

University of Groningen

## An HI perspective on galaxies 2.5 billion years ago

Gogate, Avanti

DOI:  
[10.33612/diss.206445119](https://doi.org/10.33612/diss.206445119)

**IMPORTANT NOTE: You are advised to consult the publisher's version (publisher's PDF) if you wish to cite from it. Please check the document version below.**

*Document Version*  
Publisher's PDF, also known as Version of record

*Publication date:*  
2022

[Link to publication in University of Groningen/UMCG research database](#)

*Citation for published version (APA):*  
Gogate, A. (2022). *An HI perspective on galaxies 2.5 billion years ago*. University of Groningen.  
<https://doi.org/10.33612/diss.206445119>

### Copyright

Other than for strictly personal use, it is not permitted to download or to forward/distribute the text or part of it without the consent of the author(s) and/or copyright holder(s), unless the work is under an open content license (like Creative Commons).

The publication may also be distributed here under the terms of Article 25fa of the Dutch Copyright Act, indicated by the "Taverne" license. More information can be found on the University of Groningen website: <https://www.rug.nl/library/open-access/self-archiving-pure/taverne-amendment>.

### Take-down policy

If you believe that this document breaches copyright please contact us providing details, and we will remove access to the work immediately and investigate your claim.

Downloaded from the University of Groningen/UMCG research database (Pure): <http://www.rug.nl/research/portal>. For technical reasons the number of authors shown on this cover page is limited to 10 maximum.



rijksuniversiteit  
 groningen

# **An HI perspective on galaxies 2.5 billion years ago**

**Proefschrift**

ter verkrijging van de graad van doctor aan de  
 Rijksuniversiteit Groningen  
 op gezag van de  
 rector magnificus prof. dr. C. Wijmenga  
 en volgens besluit van het College voor Promoties.

De openbare verdediging zal plaatsvinden op  
 maandag 21 maart 2022 om 12.45 uur

door

**Avanti Rajendra Gogate**

geboren op 19 juni 1992  
 te Mumbai, India

**Promotores**

Prof. dr. M.A.W. Verheijen  
Prof. dr. J.M. van der Hulst

**Beoordelingscommissie**

Prof. dr. T. A. Oosterloo  
Prof. dr. A. J. Baker  
Prof. dr. D. J. Pisano



The research leading to this thesis has received funding from the Netherlands Organisation for Scientific Research (NWO) via VICI grant number 190-236000.

**Front cover:** A representation of the Westerbork Synthesis Radio Telescope observing the field containing the cluster Abell 963. The composite colour image taken with the Isaac Newton Telescope (INT) overlaid with HI contours of some of the observed galaxies forms the backdrop of the cover.

**Back cover:** Similar to the front cover, the INT image containing the cluster Abell 2192.

Printed on FSC-certified paper by Ipskamp printing, Enschede

# Contents

<b>1 Thesis Introduction</b>	<b>1</b>
1.1 Background	1
1.2 The cosmic evolution of galaxy properties	2
1.2.1 The cosmic star formation rate and gas content of galaxies	2
1.2.2 Scaling relations	3
1.3 Environmental impact on galaxy evolution	4
1.4 The HI Universe	6
1.4.1 BUDHiES	9
1.5 This thesis	11
1.5.1 Goals of this work	11
1.5.2 Thesis outline	14
<b>2 BUDHiES IV: Deep 21-cm neutral Hydrogen, optical and UV imaging data of Abell 963 and Abell 2192 at <math>z \simeq 0.2</math></b>	<b>17</b>
2.1 Introduction	19
2.2 Targets	22
2.3 Westerbork observations and data processing	24
2.3.1 Data flagging and calibration	25
2.3.2 Imaging data cubes	27
2.3.3 Residual Continuum subtraction	28
2.3.4 Quality of the data	29
2.3.5 HI source finding and galaxy identification	31
2.3.6 Completeness	32
2.3.7 HI properties of detected galaxies	33
2.3.8 The HI catalogue	37
2.4 INT Wide field optical imaging	38
2.4.1 Data processing	39
2.4.2 Optical source finding	42
2.4.3 The optical catalogue	43
2.5 GALEX - UV imaging	45
2.6 Results	46
2.6.1 Distribution of HI properties	46
2.6.2 Optical properties	51
2.6.3 The atlas	52
2.7 Summary and Conclusions	54

---

2.8	Catalogues and atlas . . . . .	55
<b>3</b>	<b>BUDHiES V: The Baryonic Tully-Fisher relation at <math>z \sim 0.2</math> based on direct HI detections</b>	<b>121</b>
3.1	Introduction . . . . .	123
3.2	The Data . . . . .	126
3.2.1	The BUDHiES data . . . . .	126
3.2.2	Reference studies from the literature . . . . .	126
3.3	Sample selection . . . . .	127
3.3.1	The Tully-Fisher Sample ( <i>TFS</i> ) . . . . .	128
3.3.2	The High-Quality Sample ( <i>HQS</i> ) . . . . .	129
3.3.3	Literature samples . . . . .	130
3.4	Corrections to the data . . . . .	130
3.4.1	Correction to the observed HI linewidths . . . . .	130
3.4.2	Photometric corrections . . . . .	133
3.4.3	Comparison of sample properties . . . . .	135
3.5	The BUDHiES TF catalogue and atlas . . . . .	142
3.5.1	The catalogues . . . . .	143
3.5.2	The atlas . . . . .	144
3.6	The Tully-Fisher Relations . . . . .	145
3.6.1	Fitting method . . . . .	145
3.6.2	The Luminosity-based TFr . . . . .	146
3.6.3	The Baryonic TFr . . . . .	148
3.6.4	The TFr from an environmental perspective . . . . .	150
3.6.5	Parameter table layout . . . . .	153
3.7	Discussion . . . . .	153
3.7.1	Impact of sample properties, observables and corrections on TFr scatter and zero points . . . . .	154
3.7.2	Evolution in the TFr with redshift . . . . .	162
3.7.3	Effect of cosmic environment on the TFr and BTFr . . . . .	163
3.7.4	Comparison with HIGHz . . . . .	165
3.8	Summary and Conclusions . . . . .	165
3.9	Catalogues and atlas . . . . .	167
<b>4</b>	<b>BUDHiES VI: The HI Mass function and <math>\Omega_{\text{HI}}</math> at <math>z = 0.2</math> using direct HI detections</b>	<b>195</b>
4.1	Introduction . . . . .	197
4.2	Survey details and Data . . . . .	199
4.3	Completeness corrections . . . . .	200
4.3.1	Creating a library of synthetic galaxies . . . . .	200
4.3.2	Inserting synthetic sources . . . . .	201
4.3.3	Source Detection and identification . . . . .	202
4.4	The BUDHiES HiMF and $\Omega_{\text{HI}}$ . . . . .	206
4.4.1	The BUDHiES HiMF fitting results . . . . .	207
4.4.2	Estimation of $\Omega_{\text{HI}}$ for BUDHiES . . . . .	208
4.5	Discussion . . . . .	211

4.5.1	Evolution in the HiMF . . . . .	212
4.5.2	Evolution in $\Omega_{\text{HI}}$ over cosmic time . . . . .	213
4.5.3	The effect of cosmic variance and environment . . . . .	215
4.6	Summary and Conclusions . . . . .	217
4.7	Acknowledgements . . . . .	218
Appendix 4.A Motivation . . . . .		219
4.A.1	HI masses . . . . .	220
4.A.2	The HI and optical radii . . . . .	221
4.A.3	Luminosities . . . . .	222
4.A.4	Rotational velocities . . . . .	224
4.A.5	Radial HI density distributions . . . . .	224
4.A.6	Other parameters . . . . .	225
4.A.7	The models . . . . .	226
<b>5</b>	<b>Conclusions and future prospects</b>	<b>233</b>
5.1	Results of this thesis . . . . .	233
5.1.1	The BUDHiES data . . . . .	233
5.1.2	The HI-based Tully-Fisher relation at $z \simeq 0.2$ . . . . .	235
5.1.3	Completeness corrections for the BUDHiES data . . . . .	237
5.1.4	The HiMF at $z \sim 0.2$ . . . . .	237
5.1.5	$\Omega_{\text{HI}}$ at $z \sim 0.2$ from direct HI detections . . . . .	238
5.2	Future work . . . . .	238
5.2.1	Giving a gas perspective to the Butcher-Oemler effect . . . . .	238
5.2.2	Ongoing and future HI surveys . . . . .	239
<b>Nederlandse Samenvatting</b>		<b>241</b>
<b>Bibliography</b>		<b>247</b>
<b>Acknowledgments</b>		<b>257</b>



# Thesis Introduction

## 1.1 Background

In the past three decades, studying the formation and evolution of galaxies has been one of the most active fields of research in astrophysics. Our view on how galaxies formed and evolved has been revolutionised thanks to the multitude of data from multi-wavelength surveys, and several tools have been developed that have allowed astronomers to map the properties of galaxies over cosmic time. Today, cosmologists have determined that the current Universe is 13.6 billion years old and has originated from an extremely energetic event known as the ‘Big Bang’. Subsequently, cosmological models such as  $\Lambda$ CDM presented further improvements in the understanding of the origin of our Universe, by introducing dark matter, which is believed to make up most of the physical matter present in the Universe. Within the  $\Lambda$ CDM paradigm, it was found that the Universe, just after it began, was essentially homogeneous. However, as it cooled, small density fluctuations began to appear and grow, which led to the concentration of dark matter. These pockets or clumps of dark matter are seen today as resultant gravitational potential wells, known as dark matter halos. Galaxies are found to have formed (and evolved) within these dark matter halos (e.g., Riess et al. 1998; Perlmutter, Turner & White 1999; Percival et al. 2001; Spergel et al. 2003), and their properties are a direct consequence of their formation and evolutionary histories. The massive galaxies that are observed today were formed by the merging of smaller, less complex systems, as explained by the hierarchical structure formation scenario within  $\Lambda$ CDM. Thus, the properties of galaxies, such as their morphology, kinematics, star formation histories, etc. are shaped by their formation history (nature) and the influence of the environment in which these galaxies are embedded (nurture). Using tools developed over several years combined with the availability of exceptional multi-wavelength data, some of the most fundamental questions that we want to answer are what drove the morphological mix of galaxies in the distant past to evolve into today’s Hubble sequence, and how accurate are our current theoretical models in reproducing the properties of

infant galaxies. This thesis attempts to contribute to these insights by investigating some major aspects of galaxy evolution, with the help of unique deep 21 cm spectral line observations of galaxies 2.5 billion years in the past.

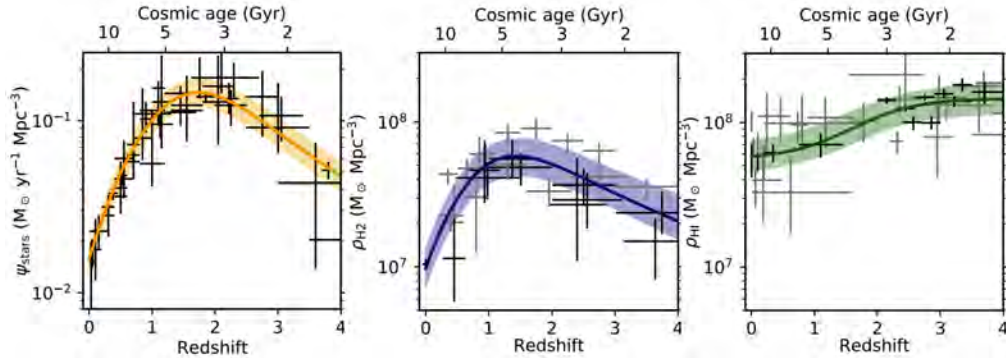


**Figure 1.1** – The evolution of various galaxy properties, taken from Walter et al. (2020). Left: The evolution of the cosmic star formation rate, compiled from Madau & Dickinson (2014). Centre: Constraints on the evolution of molecular Hydrogen with data from Decarli et al. (2019, 2020, grey) and other literature samples (black; see Appendix B of Walter et al. 2020). Right: Evolution of atomic Hydrogen, based on Neeleman et al. (2016) and other low redshift HI surveys (see Sect. 3.2.2 of Walter et al. 2020). In all sub-figures, the solid line indicates the best-fit functional form to the data, while the shaded region denotes the  $1\sigma$  interval following a Markov Chain Monte Carlo analysis.

## 1.2 The cosmic evolution of galaxy properties

### 1.2.1 The cosmic star formation rate and gas content of galaxies

Through several observational and theoretical efforts, a consistent picture on the evolution of galaxy properties has now emerged. One such significant discovery was the evolution of the cosmic star formation rate (SFR) density. Known as the ‘Madau’ plot (or the ‘Lilly-Madau’ plot; Lilly et al. 1996; Madau et al. 1996), it shows that the cosmic SFR declined exponentially with time (by a factor  $\sim 10$ ) since its peak at  $z \sim 1.9$ . Several subsequent optical, ultraviolet and far-infrared studies have been able to further quantify this with great precision (e.g., Hopkins 2004; Lapi et al. 2011; Madau & Dickinson 2014; Finkelstein et al. 2015; Gruppioni et al. 2013, 2015; Bouwens et al. 2015). The epoch between  $1 < z < 3$ , often referred to as the ‘cosmic noon’, exhibits an integrated evolution in global galaxy properties such as SFR, stellar mass and supermassive black hole growth (see review by Förster Schreiber & Wuyts 2020) and is pivotal to our understanding of how galaxies evolve.

However, this picture is incomplete without information on the cold gas content of galaxies, since it is a vital ingredient for star formation. This cold gas typically exists in both molecular and atomic form. Through measurements of carbon monoxide (CO) transitions and far-infrared dust continuum, it is found that the evolution of the molec-

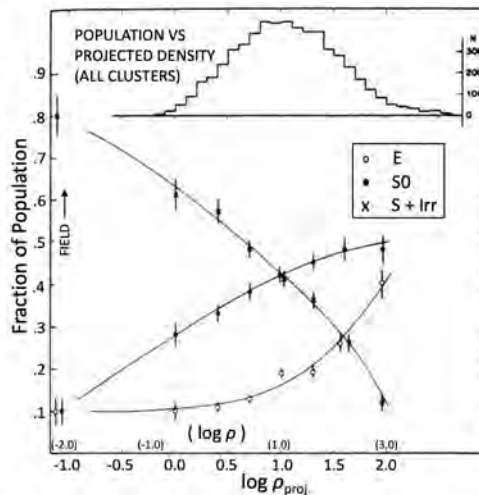
ular gas content also closely follows the trend in cosmic SFR as a function of redshift (e.g., Carilli & Walter 2013; Decarli et al. 2019, 2020; Walter et al. 2020). This is nicely illustrated in Fig. 2 of Walter et al. (2020), reproduced here as Fig. 1.1. The first two panels illustrate the cosmic SFR (panel 1) and molecular gas densities (panel 2) as a function of both redshift and cosmic age (time since the Big Bang).

The evolution of the neutral atomic hydrogen (HI) content, however, is still not well constrained, particularly at higher redshifts. In the Local Universe, large blind HI emission surveys have provided accurate measurements of the cosmic HI density (e.g., Zwaan et al. 2005; Jones et al. 2018). Beyond  $z \sim 0.1$ , other indirect methods are used, such as spectral stacking (e.g., Rhee et al. 2016; Chowdhury et al. 2020) and at  $z > 1$ , constraints are provided through quasar absorption spectroscopy (e.g., Prochaska, Herbert-Fort & Wolfe 2005; Rao et al. 2017). In addition, numerical simulations (e.g., Davé et al. 2017; Neeleman et al. 2016) have made it possible to predict the trend in the cosmic density of HI over time. Through these efforts, it has been found that the cosmic density of cold gas evolves differently than the cosmic SFR densities and molecular gas, through a much more gradual decline. This can be seen in the last panel of Fig. 1.1. However, tighter constraints on the evolution of HI beyond the Local Universe are required to effectively link SFR and the buildup of stellar population to the cold atomic gas content of galaxies. The HI emission in galaxies is further discussed in Sect.1.4.

### 1.2.2 Scaling relations

Early efforts in empirically understanding galaxies were made by studying their morphology (e.g., Hubble's tuning fork, de Vaucouleurs classification). Subsequently, with the advent of larger data sets, astronomers sought to deduce the origin and evolution of galaxies by classifying them based on patterns or trends through the correlation of their properties, thus reflecting their physics. Several fundamental scaling relations have been found to exist, such as the Faber-Jackson relation (e.g., Faber & Jackson 1976), the Kennicutt-Schmidt relation (e.g., Schmidt 1959; Kennicutt 1998), the mass-size relation (Kauffmann et al. 2003), mass-metallicity relation (e.g., Lequeux et al. 1979), the Tully-Fisher relation (Tully & Fisher 1977) and the Fundamental Plane (e.g., Djorgovski & Davis 1987; Dressler et al. 1987), among others. Particularly at higher redshifts, establishing the existence of scaling relations between global galaxy properties has been one of the main aims of large look-back surveys. It is now known that several of these relations hold at least out to  $z \sim 2$ , implying that there were already regulatory mechanisms that controlled the growth and life-cycles of galaxies. However, whether these relations evolve over cosmic time is still a matter of debate. Reducing the scatter around these scaling relations is vital for distance measurements and understanding the intrinsic scatter is important for constraining theoretical models of galaxy formation and evolution.

**Figure 1.2** – The morphology-density relation, showing the fractions of elliptical (open circles), S0 (solid circles), and a combination of spiral and irregular galaxies (crosses) as a function of the projected local density. The sample consisted of  $\sim 6000$  galaxies belonging to 55 galaxy clusters. The histogram at the top shows the number of galaxies found in these environments. Image taken from Dressler (1980).

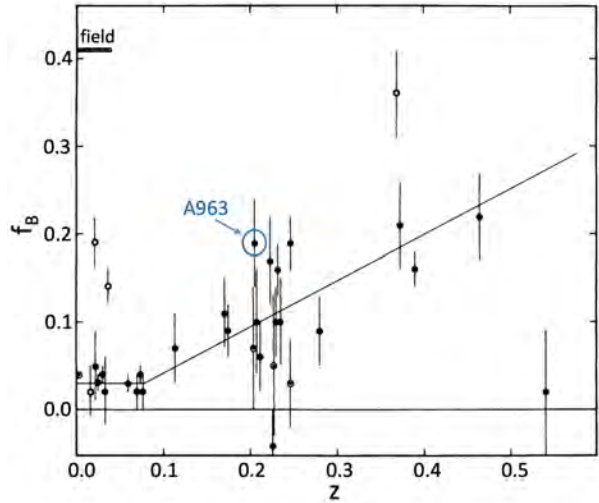


### 1.3 Environmental impact on galaxy evolution

Numerical simulations such as the Millennium (Springel, Frenk & White 2006), Illustris (Vogelsberger et al. 2014), and EAGLE, (Schaye et al. 2015; Crain et al. 2015) simulations and subsequent spectroscopic observations of galaxies (e.g., SDSS, York et al. 2000; 2dFGRS, Colless et al. 2001; GAMA, Driver et al. 2011; 2MASS, Huchra et al. 2012) have revealed a cosmic web with massive clusters and superclusters interconnected with thread-like filaments. The vast and nearly empty regions between these filaments are known as voids (e.g., Bond, Kofman & Pogosyan 1996; Cautun et al. 2014). Within the cosmic web, galaxies reside in a range of cosmic environments, conventionally characterised by the local density of galaxies. These environments are broadly classifiable into three categories: Extremely dense environments such as galaxy clusters, intermediate environments such as galaxy groups, cluster outskirts and filaments, and low density environments such as voids. These broad categories have no clear boundaries, and the definition of environment is somewhat subjective. However, galaxy properties in the most extreme overdense environments (clusters) are found to be very distinct from those in low-density environments (voids). The most massive, red and passive galaxies are formed through interactions and mergers with other galaxies in overdense environments, while void galaxies are less massive and actively star-forming (e.g., Grogin & Geller 2000, 1999; Rojas et al. 2004, 2005; Kreckel et al. 2011, 2012).

High-density regions such as clusters and groups of galaxies offer an excellent environment to study galaxy evolution. One of the earliest and most significant manifestations of environment-driven galaxy evolution is the morphology-density relation (Dressler 1980), shown in Fig. 1.2. This relation suggests that the fraction of early-type and S0 galaxies seems to increase towards denser environments at the expense of the spiral population, implying that galaxies undergo radical changes in their morphologies and kinematics with increasing galaxy density. Similarly, a significant decrease in the SFR

**Figure 1.3** – The fraction of blue galaxies as a function of redshift for a sample of 33 galaxy clusters up to  $z \sim 0.5$  from Butcher & Oemler (1984). The markers are defined by the concentration index of the clusters: solid circles are compact clusters, open circles are irregular clusters and dotted circles are intermediate clusters. Abell 963, which is a part of this thesis, is located at  $z \simeq 0.206$ , and has the largest blue fraction ( $f_b=0.19$ ) at that redshift (encircled in blue).



of galaxies is found towards the interiors compared to the outskirts of clusters (Peng et al. 2010b). This is because galaxies undergo mechanisms such as tidal interactions, mergers, harassment and starvation (e.g., Holmberg 1941; Toomre & Toomre 1972; White 1978; Smith, Davies & Nelson 2010; Bekki, Couch & Shioya 2002; Maier et al. 2016) as they fall into high density regions due to an increase in local galaxy density. In addition, the invisible, hot X-ray gas making up the Intra-Cluster Medium (ICM) also significantly contributes to the removal of gas in galaxies through ram-pressure stripping (e.g., Gunn & Gott 1972; Oosterloo & van Gorkom 2005; Jaffé et al. 2018). These processes ultimately deplete the gas reservoirs of these infalling galaxies and thus quench their SFRs. A mechanism known as ‘preprocessing’ is also an important facet of the  $\Lambda$ CDM structure formation scenario (Tonnesen, Bryan & van Gorkom 2007). Several studies have analysed the time-scales of SF quenching processes in infalling galaxies, and have concluded that in many cases, the clusters themselves were not able to account for the deficit of gas and star-formation observed in these galaxies. Thus, the notion of preprocessing came into existence, wherein these galaxies began to transform prior to their infall into the cluster potential (Zabludoff et al. 1996; Solanes et al. 2001; Fujita 2004; Bahé et al. 2013; Wetzel et al. 2013; Haines et al. 2015; Yoon et al. 2015). Much of this preprocessing is found to have occurred in infalling galaxy groups (e.g., Yoon et al. 2017; Bianconi et al. 2018).

Even at higher redshifts, several environment-based evolutionary trends have been observed. One such indicator was presented as part of a series of publications, starting with Butcher & Oemler (1984), known as the ‘Butcher-Oemler (BO) effect’, subsequently confirmed with photometric and spectroscopic studies (e.g., Couch et al. 1994; Lavery & Henry 1986; Ellingson et al. 2001; Tran et al. 2005; Lerchster et al. 2011). Butcher & Oemler (1984) found that at  $z > 0.1$  the fraction of blue, star-forming galaxies was unusually high in the cluster cores and this effect increased with redshift. The key figure from the seminal paper is presented in Fig. 1.3. Their study also suggested

1 that environmental processes were possibly playing a role in this observed increase in blue fraction. In addition, other similar studies have found an overall increase in the fraction of luminous infrared galaxies (e.g., Coia et al. 2005; Haines et al. 2009) as well as an increase in the number of spiral galaxies in high redshift clusters (e.g., Fasano et al. 2000; van Dokkum et al. 2000). These observed effects give rise to several fundamental questions regarding the physical processes governing galaxy evolution at higher redshifts. Are all these observed effects a consequence of different cluster accretion rates compared to the present epoch (e.g., Berrier et al. 2009; Poggianti et al. 2006), or the result of a higher gas content at higher redshifts coupled with a lower effectiveness of ram pressure stripping in clusters? Or are these blue galaxies post-starburst or back-splash galaxies with very little/no gas and no new star formation? Insights into the evolution of the gas content of galaxies as they migrate into denser environments are central to answering these questions.

## 1.4 The HI Universe

Owing to the synergy between theoretical and observational efforts, much progress has been made in boosting our understanding of the physical processes that govern galaxy formation and evolution. Large-scale structure and the cosmic web are now easily traced with the help of large scale optical surveys, identifying and characterising the different cosmic environments in which galaxies reside. Furthermore, with the discovery of galactic and extragalactic atomic Hydrogen several decades ago, HI synthesis imaging has now added a dramatic view of galaxies in the Universe. Detected at 1420.405752 MHz, the HI emission line is the result of the hyperfine structure of atomic Hydrogen. Despite it being a forbidden transition (Einstein  $A$  coefficient with a value of  $2.9 \times 10^{-15} \text{ s}^{-1}$ ), the abundance of neutral Hydrogen in the Interstellar Medium (ISM) of galaxies not only excites the HI through collisions, but also allows us to detect extragalactic HI. On the other hand, HI can also be detected through absorption against bright background radio sources. The HI signal has the advantage of not being affected by extinction due to dust, and it penetrates the Earth's atmosphere where it can be detected with the help of ground-based radio telescopes.

HI represents an intermediary phase of Hydrogen between the ionised gas making up the intergalactic medium of galaxies and the molecular gas that is present in the stellar disc of galaxies, from which stars form. Studying the distribution and kinematics of this cold atomic hydrogen in galaxies has revolutionised our understanding of how galaxies form and evolve. In most cases, the rotational velocities of the outer HI discs make the most robust tracers of the mass of the dark matter halos of galaxies.

Traditionally, single-dish telescopes were used for targeted HI emission studies of optically selected galaxies (e.g., Richter & Huchtmeier 1989, Fisher & Tully 1981). Subsequently, large area, blind HI emission surveys such as the Arecibo HI Strip Survey (AHISS; Zwaan et al. 1997), the HI Parkes All Sky Survey (HIPASS; Zwaan et al. 2005), and the Arecibo Legacy Fast ALFA survey (ALFALFA; Jones et al. 2018) were conducted. Despite their poor angular resolution, these surveys were crucial in gaining an unbiased insight into the HI content of galaxies. With the advent of synthesis imaging,

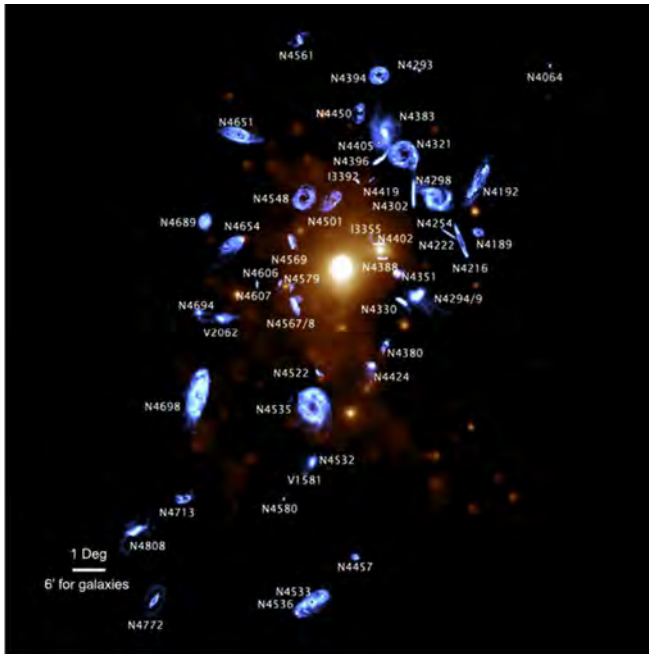


**Figure 1.4** – A composite image of the Virgo cluster, taken from Chung et al. (2009). The X-ray image in the background (orange) is taken from ROSAT (Böhringer et al. 1994) on top of which magnified ( $\times 10$ ) HI maps of the individual galaxies are overlaid in blue.

HI science became a game-changer in our quest for understanding physical mechanisms driving galaxy evolution (e.g., Verheijen 2001; Chung et al. 2009; van Eymeren et al. 2011; Ramatsoku et al. 2016).

HI discs of galaxies often extend out much further beyond the observable stellar discs of galaxies and into the dark matter halo, making HI discs very sensitive to external perturbations. Thus, from a morphological point of view, resolved HI imaging studies of extended discs may reveal any distortions in their structure due to environmental effects, such as tidal interactions and ram-pressure stripping. One such example is illustrated in Fig. 1.4, taken from the Very Large Array Imaging of Virgo galaxies in Atomic gas survey (VIVA; Chung et al. 2009). This study found that the truncation of HI discs became more pronounced and galaxies became HI deficient towards the cluster core. The figure, showing how HI in galaxies is affected as a function of local galaxy density, clearly demonstrates the potential of HI science. This trend in HI deficiency in clusters was initially studied by Solanes et al. (2001) using single dish observations and later confirmed by Dénes, Kilborn & Koribalski (2014).

One of the drawbacks of the HI signal is its intrinsic weakness, limiting HI imaging surveys mostly to the Local Universe, corresponding to  $z < 0.1$ . Beyond this redshift, HI emission observations become increasingly challenging, firstly due to excessively long integration times and secondly due to severe Radio Frequency Interference (RFI), caused by the Global Navigation Satellite System (GLONASS), Galileo satellites and the Global System for Mobile Communications (GSM) emitting in frequency ranges corresponding to  $z > 0.1$ . Typically, more than 1000 hours of telescope time are required to achieve the

Survey	Sky area (deg <sup>2</sup> )	Bandwidth (MHz)	Freq. Range (MHz)	$\Delta f$ (kHz)	Beam Size (arcsec <sup>2</sup> )	$T_{\text{int}}$ (hrs)	$\log(M_{\text{HI}}/M_{\odot})$
(1)	(2)	(3)	(4)	(5)	(6)	(7)	(8)
LADUMA	1 × (1 × 1)	850	580-1750	26.1	15 × 15	3424	8.25
CHILES	1 × (0.25 × 0.25)	15 × 32	950-1430	15.6	6 × 6	1001	8.27
DINGO	5 × (30 × 30)	288	1130-1430	18.5	30 × 30	500	9.18
MIGHTEE-HI	32 × 32	520	900-1420	26.1	12 × 12	23.4	9.06
BUDHiES	2 × (1 × 1)	60	1160-1220	39	23 × 38	~2200	7.97
AUDS100	1 × (0.68 × 0.68)	300	1225-1525	21.4	210 × 210	~700	-

**Table 1.1** – Survey details of some major completed, ongoing or upcoming blind HI surveys. Column description from left to right: (1) refers to the survey; (2) is the sky coverage in square degrees (the number outside the parentheses indicates the number of pointings); (3) and (4) refers to the total bandwidth and the frequency range respectively of the survey; (5) refers to the spectral resolution of the survey (at  $z=0$ ) in kHz; (6) gives the typical angular resolution in arcseconds; (7) provides the total telescope integration time per pointing; (8) refer to the mass limit of the survey, assuming a  $5\sigma$  detection at  $z=0.1$  for an HI emission line width of  $150 \text{ km s}^{-1}$ . Note that for BUDHiES, the mass limit provided is below the frequency range covered by the survey. In the case of LADUMA, the bandwidth includes Phase 2.

sensitivity needed to comfortably detect  $M_{\text{HI}}^*$  galaxies in HI emission, which is not easily achieved with current radio facilities. Consequently, very few HI imaging (emission) surveys have been carried out beyond the Local Universe. The only blind surveys aimed at direct HI detections are the Blind Ultra-Deep HI Environmental Survey (BUDHiES Gogate et al. 2020) covering  $0.164 < z < 0.224$ , the Arecibo Ultra-Deep Survey (AUDS, Hoppmann et al. 2015; Xi et al. 2021 between  $0 < z < 0.16$  and the COSMOS HI Large Extragalactic Survey (CHILES, Fernández et al. 2013; Hess et al. 2019) between  $0 < z < 0.45$ . On the other hand, the presence of HI in galaxies at higher redshifts can be probed with HI absorption (intervening or associated absorbing systems) detected along sightlines towards strong continuum sources (e.g., Sadler et al. 2020; Allison et al. 2020; Gupta et al. 2021). To detect HI absorption against a background radio source requires considerably less integration time compared to HI emission studies. However, in most cases HI absorption allows us to only trace a single sightline through galaxies and therefore do not always robustly measure their HI content.

Several efforts are being made in upgrading existing or building new radio facilities to push the frontiers of HI observations to higher lookback times and explore the evolution of galaxy properties, both globally for a given epoch and in different cosmic environments. Next-generation HI surveys, such as those envisaged with the upcoming Square Kilometre Array (SKA) will have a profound impact on our understanding of galaxy formation and evolution. The SKA is a global project, and several countries are participating with their own radio interferometers, also known as SKA pathfinders. With these pathfinders alone, we will enable the direct detection of HI out to  $z \sim 1$  through upcoming surveys such as the Looking At the Distant Universe with the MeerKAT Array (LADUMA; Holwerda, Blyth & Baker 2012; Blyth et al. 2016; Baker, Blyth & Holwerda 2019) survey and the Deep Investigation of Neutral Gas Origins (DINGO;

Meyer 2009; Chen et al. 2021) survey. Provided in Table 1.1 are the details of some of these major blind HI surveys which are of relevance to this thesis. Finally, SKA-mid (phase 1) is deemed to be the most powerful radio interferometer in the world. Comprising  $\sim 197$  dishes in the Karoo desert in South Africa, it aims to map the radio skies with unprecedented detail and transform our view of both the near and distant radio Universe.

### 1.4.1 BUDHiES

Until the advent of next-generation surveys, one of the only studies that provides an HI perspective on galaxy evolution at higher redshifts is the Blind Ultra-Deep HI Environmental Survey (BUDHiES). It was carried out between 2005 and 2008 with the Westerbork Synthesis Radio Telescope (WSRT) and consists of two single-pointing fields, each centred on an Abell cluster along with their surrounding large-scale structure. The redshift range of BUDHiES is  $0.164 < z < 0.224$ , corresponding to a range in look-back time  $2.05 < T < 2.69$  Gyr. The two galaxy clusters, Abell 963 and Abell 2192 are very different in their properties. Abell 963, also part of the seminal BO study (Butcher & Oemler 1984), is a massive, virialised lensing cluster at  $z \simeq 0.206$  with a 19 percent blue galaxy fraction associated with its core. It emits strong X-ray emission from its ICM. Contrastingly, Abell 2192 is a small cluster, still in the process of forming and is almost invisible in X-rays. While the detected HI sources are spatially unresolved/partially resolved (angular resolution is  $23 \times 38$  arcsec<sup>2</sup>), the spectral resolution is  $19 \text{ km s}^{-1}$ . With a depth of 328 Mpc corresponding to a total volume of  $73,400 \text{ Mpc}^3$  within the FWQM (Full Width at Quarter Maximum) of the primary beam, the data consists of a range of cosmic environments in the foreground and background of the two clusters (Verheijen et al. 2007; Jaff  et al. 2013).

Apart from the HI data, there also exists deep B- and R-band photometry of the two BUDHiES fields, centred on the two Abell clusters, obtained with the Isaac Newton (INT) telescope in La Palma. These images are significantly deeper than those available from the Sloan Digital Sky Survey (SDSS, York et al. 2000). Additionally, deep near-UV and far-UV images were obtained using the Galaxy Evolution Explorer (GALEX) for the two BUDHiES fields. These optical and UV images assisted us in the counterpart identification during the HI source finding process. Apart from two HI sources in the field containing Abell 963, all HI sources have optical and UV counterparts, and several with confirmed spectroscopic optical redshifts.

Some other available ancillary data include Hubble Space Telescope (HST) imaging of the centre of Abell 963, optical spectroscopy from the William Herschel Telescope (WHT, Jaff  et al. 2013) as well as additional redshifts from Hwang et al. (2014) and Lavery & Henry (private communication). Moreover, new spectroscopic observations of Abell 2192 were carried out in 2019 with the WIYN telescope, but are not taken advantage of in this thesis. A series of studies were already carried out using the BUDHiES HI data. The BUDHiES pilot survey presented by Verheijen et al. (2007) provided the first answers to whether or not the blue galaxies in the centre of Abell 963 were gas rich. Their stacking exercises revealed no evidence of HI within the central 1

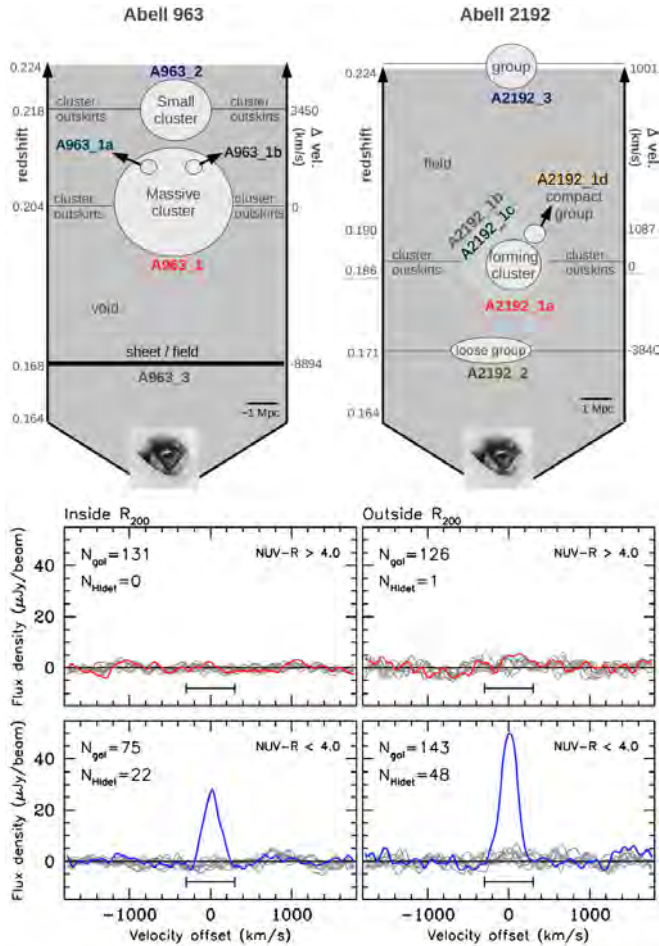


**Figure 1.5** – Top: Schematic overview of the two main Abell clusters, Abell 963 and Abell 2192 based on the environment characterisation presented in Jaffé et al. (2013). The cluster sizes are roughly scaled for the purpose of this illustration. Bottom: Stacked HI spectra of galaxies from Abell 963, taken from (Jaffé et al. 2016). Stacks from actively star forming cluster members are shown in blue (bottom panel) while passive cluster members are shown in red (top panel) inside  $R_{200}$  (left) and outside  $R_{200}$  (right) of the cluster.

Mpc of the cluster core. Using their new WHT spectroscopy data, Jaffé et al. (2013) presented an environmental analysis of the two BUDHiES volumes. They identified a range of cosmic environments (Fig. 1.5, top), including the two main Abell clusters which showed well-defined substructures. A detailed substructure analysis of Abell 963 in projected phase-space (Jaffé et al. 2015, 2016) showed that the cluster galaxies were likely stripped of their HI during their first pericentric passage, at least down to the BUDHiES detection limit of  $2 \times 10^9 M_{\odot}$ . Moreover, they revisited the stacking exercises

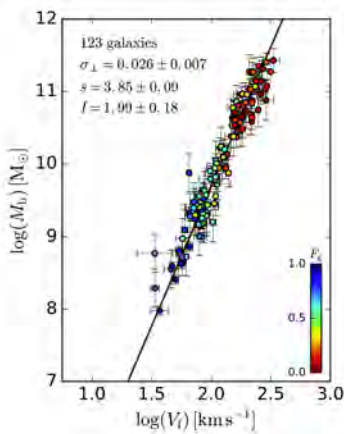


**Figure 1.6** – The Local baryonic TFR taken from Lelli et al. (2019), showing the baryonic masses of 153 galaxies belonging to the SPARC sample, as a function of their rotational velocities. These rotational velocities are derived from the flat part of the rotation curves from resolved HI observations. The line fit to the data is shown in black and the scatter points are coloured by their gas fraction, as indicated in the colour bar at the bottom-right.

carried out by Verheijen et al. (2007) and found that the blue galaxies in the cluster core are much more HI deficient than in the outskirts. These stacks from Jaffé et al. (2016) are shown in Fig. 1.5 (bottom). These results imply that the blue galaxies observed in the cluster core of Abell 963 have already lost most of their gas via ram-pressure stripping, and will eventually transition to the red sequence. Lastly, there also exist targeted CO observations for 23 galaxies belonging to the two Abell clusters (Cybulski et al. 2016). This study found an overall abundance of molecular gas compared to the HI and stellar components, higher than those proposed by previous studies (e.g., Saintonge et al. 2011). Finally, the full survey is presented in Gogate et al. (2020), which is also a part of this thesis.

## 1.5 This thesis

This thesis is based on the HI and optical and data from BUDHiES. Until data from surveys such as CHILES and subsequently DINGO and LADUMA become available, this survey still remains exquisite and unique in its ability to provide key insights into some significant aspects of galaxy evolution. The survey volume and depth samples large-scale structure and different cosmic environments, allowing us to perform statistical tests and investigate HI-based scaling relations beyond the Local Universe. Three such science goals are a part of this thesis and are briefly described below.

### 1.5.1 Goals of this work

#### The HI-based luminosity and baryonic Tully-Fisher relations at $z \sim 0.2$

In Sect. 1.2.2, we mentioned the fundamental scaling relations between global galaxy properties. One particular scaling relation is the Tully-Fisher relation (TFR, Tully & Fisher 1977), which is a fundamental manifestation of the connection between the visible and dark matter in galaxies. It tightly correlates the intrinsic luminosity with the rotational velocities of the dark matter halos of galaxies. In its baryonic form, it is

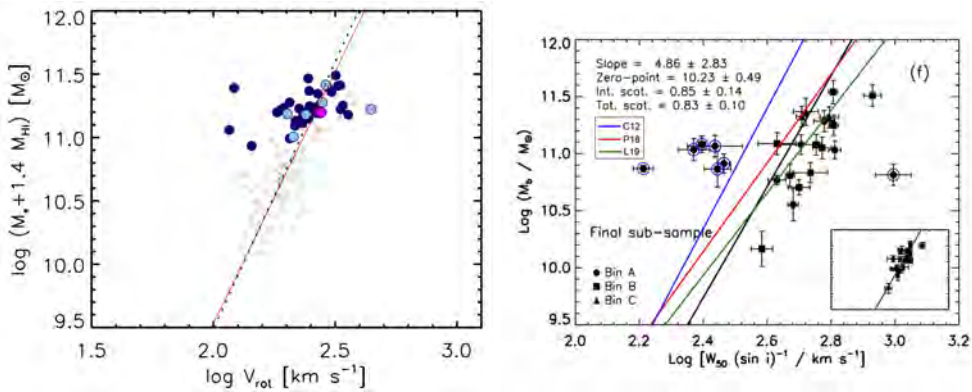


**Figure 1.7** – Left: The optically selected HI sample at  $z \sim 0.34$  (Catinella & Cortese 2015) shown in blue overlaid on the local BTFR (grey open circles and dashed line) from GASS (Catinella et al. 2012). The red solid line shows the TFr from McGaugh et al. (2000). Right: The CO-based BTFR from Topal et al. (2018) at  $z \leq 0.3$ . The blue points indicate outliers (included in the fit). The three different symbols (circles, squares and diamonds) correspond to three redshift bins. The inset shows the BTFR when outliers are excluded. The blue, red and green coloured lines correspond to BTFRs from Catinella et al. (2012), Ponomareva et al. (2018) and Lelli et al. (2019) respectively. These are not a part of the original work but are overlaid for illustrative purposes.

known as the Baryonic TFr (BTFR; e.g., McGaugh et al. 2000). Not only is this relation used extensively for distance measurements to other galaxies, but also for determining the Hubble constant, mapping cosmic flows and providing constraints to numerical simulations (e.g., Kashibadze 2008; Tully et al. 2013; Vogelsberger et al. 2014; Schaye et al. 2015; Boruah, Hudson & Lavaux 2020; Kourkchi et al. 2020). Finally, studying the evolution of the TFr at different redshifts allows us key insights into the evolution of galaxy properties.

The TFr and BTFR are extremely well constrained in the Local Universe, with accurate photometry, rotational velocities and inclinations from resolved HI kinematics and the availability of statistically significant samples (e.g., Verheijen 2001; Ponomareva et al. 2017; de Blok et al. 2016; Lelli et al. 2019; Ponomareva et al. 2021). One such example is shown in Fig. 1.6, taken from Lelli et al. (2019). Rotational velocities inferred from spatially resolved HI kinematics prove to be the most accurate representations of the circular velocities of the dark matter halos of galaxies, and thus are desirable even at higher redshifts. As already discussed in Sect. 1.4, HI observations are mostly limited to  $z < 0.1$  due to the limitations in HI detectability at higher redshifts. Thus, no HI-based TFr and BTFR studies exist at such redshifts, with the exception of the HIGHz survey presented by Catinella & Cortese (2015), who cursorily showed that their sample of optically selected, massive, gas-rich systems at  $z \sim 0.25$  lie on the local BTFR derived by Catinella et al. (2012) and McGaugh et al. (2000). However, this is not a dedicated TFr study, leaving no room for quantification of the TFr parameters due to limited ranges in luminosities and HI line widths. Their BTFR is provided in Fig. 1.7 (left).

Beyond the Local Universe, other emission line tracers are used instead to derive rotational velocities (e.g., optical and CO tracers; Conselice et al. 2005; Flores et al. 2006; Kassin et al. 2007; Ho 2007; Puech et al. 2008; Topal et al. 2018). Shown in Fig. 1.7 (right) is the BTFR from Topal et al. (2018), the first and only direct CO-based BTFR out to  $z \sim 0.3$ . These optical and CO tracers, however, are in several cases limited to the star-forming disc of galaxies, and often tend to over or underestimate the rotational velocity of the dark matter halo. So far, research on the redshift evolution of the TFR parameters (the slope and zero point of the linear regression line) has not yet converged due to inconsistencies in the choice of tracer, sample selection and methodology.

With the availability of high-resolution global HI profiles from BUDHIES, our aim is to make more robust measurements of the rotational velocities of galaxies and carry out a first consistent and thorough analysis of the HI-based TFR and BTFR at  $z \sim 0.2$ .

### The HI Mass Function at $z \sim 0.2$

Despite advancements in HI-based science in the past few decades, little is known about how the HI mass of galaxies has evolved over cosmic time through direct observations. Numerical and hydrodynamical simulations instead have allowed us to take stock of theoretical galaxy formation models by informing us how the distribution function of the HI masses of galaxies evolved with time. This distribution function, known as the HI Mass Function (HiMF), is characterised by a Schechter function (Schechter 1976), and is described by a power law at the low-mass end followed by an exponential drop-off towards the high-mass end. With the help of the HiMF parameters, namely the low-mass slope ( $\alpha$ ), the ‘knee’ or turnover mass ( $M_{\text{HI}}^*$ ) and the normalisation ( $\Phi_{\text{HI}}^*$ ), investigating the galaxy distribution function of HI at a given epoch becomes possible. With current single-dish radio telescopes, the HiMF has been well constrained in the Local Universe over the past two decades by means of large, blind HI studies (e.g., Zwaan et al. 2005; Martin et al. 2010; Jones et al. 2018). The HiMF is also shown to be affected by the local environment and cosmic variance as can be seen from Fig. 1.8 (left), which shows a dichotomous HiMF when splitting the ALFALFA sample into the ‘Spring’ and ‘Fall’ skies (see Jones et al. 2018).

At higher redshifts, the only other HiMF study has been carried out with the AUDES survey (Hoppmann et al. 2015; Xi et al. 2021) out to  $z \sim 0.16$ . Their HiMF (from Xi et al. 2021) for the full AUDES sample as well as the low- $z$  and high- $z$  sub-samples are illustrated in Fig. 1.8 (right). Their HiMF parameters are consistent with Local measurements from HIPASS and ALFALFA within the errors. In this thesis, our aim is to construct, for the first time, an HiMF at  $z \sim 0.2$  by taking advantage of the large survey volume, a statistically significant sample, and the wide range of cosmic environments encompassed by BUDHIES.

### The cosmic HI density at $z \sim 0.2$

The need for accurate measurements of the cosmic HI density beyond the Local Universe has already been motivated in Sect. 1.2. The cosmic HI density  $\Omega_{\text{HI}}$  is measured in the Local Universe by integrating the HiMF. However, at higher redshifts, limitations in the

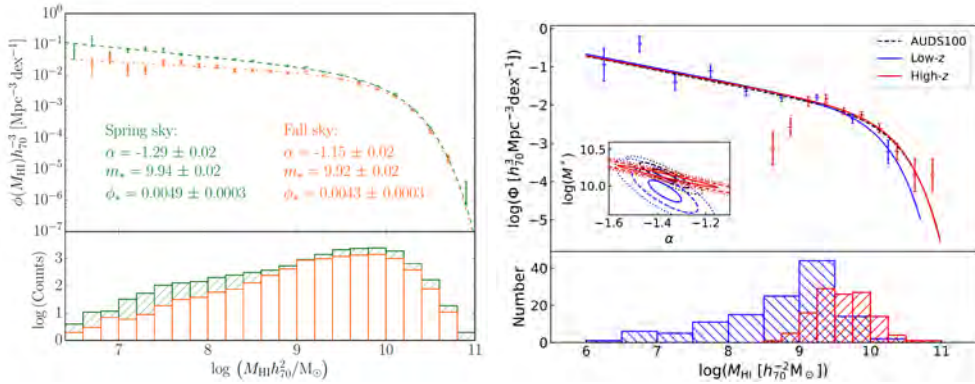


**Figure 1.8** – Left: The local HiMF from ALFA100 (Jones et al. 2018), showing the dichotomy in the HiMF parameters due to the cosmic variance present in the Spring (green) and Fall (red) skies. The best fit parameters for the respective fits are printed in the plot. The green and red HI mass histograms in the lower panel indicate the ALFA100 galaxies in the Spring and Fall regions respectively. Right: The AUFS100 HiMF (Xi et al. 2021) out to  $z \sim 0.16$  using the full sample shown as the black dashed line. Also shown are the low- $z$  (blue) and high- $z$  (red) sub-samples, split at  $z = 0.09$ . The lower panel shows the mass histograms of the low- $z$  and high- $z$  sub-samples separately.

detectability of HI have restricted the number of blind HI surveys and  $\Omega_{\text{HI}}$  is estimated instead by more indirect means, such as spectral stacking (e.g., Rhee et al. 2016; Bera et al. 2018; Chowdhury et al. 2020) and from Damped Lyman- $\alpha$  (DLA) absorbers (Prochaska, Herbert-Fort & Wolfe 2005; Rao et al. 2017; Noterdaeme et al. 2012). Such indirect methods however, do not shed light on the exact nature of these galaxies, and interpreting these observations becomes somewhat complicated. While that is so, these studies have been crucial in mapping the evolution of  $\Omega_{\text{HI}}$  with redshift, as shown in Fig. 1.9, which shows a compilation of all major  $\Omega_{\text{HI}}$  studies in the past two decades, presented by Xi et al. (2021). Our aim is to use our constructed BUDHIES HiMF to provide the first  $\Omega_{\text{HI}}$  estimate at  $z \sim 0.2$  with direct HI detections.

### 1.5.2 Thesis outline

Chapter 2, based on Gogate et al. (2020), describes the data processing and source finding of the HI, optical and UV imaging data. Counterpart identification was carried out with the help of all three data sets. Additionally, a preliminary analysis of the 166 confirmed HI sources is presented, along with an atlas and catalogues containing the HI and optical properties of the galaxies.

In chapter 3, we present, for the first time, a dedicated study of the HI-based Tully-Fisher relation and Baryonic TFR beyond the Local Universe ( $z \lesssim 0.2$ ). The motivation behind studying the TFR in the context of galaxy evolution has been discussed in Sect. 1.5.1. Our aim is to make precise and consistent comparisons with the local HI-based TFR and BTFR (Verheijen 2001), and investigate a possible evolution in the relation.

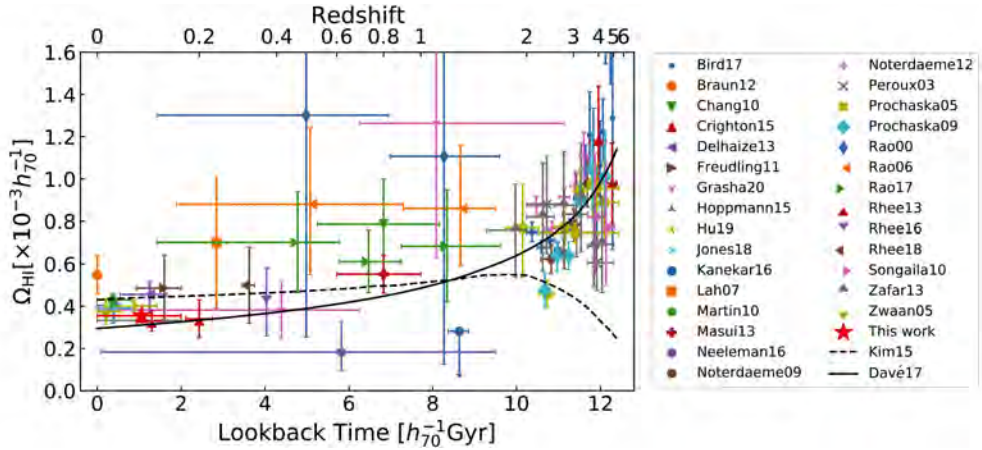


**Figure 1.9** –  $\Omega_{\text{HI}}$  as a function of redshift and lookback time taken from (Xi et al. 2021). The plot includes  $\Omega_{\text{HI}}$  estimates from direct HI detections ( $z < 0.16$ ), spectral stacking and DLAs and additionally, predictions from simulations (Davé et al. 2017) and semi-analytic modelling (Kim et al. 2015) shown by the solid and dashed black lines respectively.

Since the range in rotational velocities of the BUDHIES galaxies is limited, this comparison is restricted to the study of the offsets in the zero points of the TFrs.

Chapter 4 concerns the measurement of the HI mass function (HiMF) and  $\Omega_{\text{HI}}$  at  $z \simeq 0.2$ . For an overview of the HiMF and  $\Omega_{\text{HI}}$ , see Sect. 1.5.1. For a flux-limited blind HI survey such as BUDHIES, it is essential to first correct for survey incompleteness. The most reliable empirical method for completeness corrections is the injection of artificial galaxies in the noise cubes and testing their recovery rate by applying the same source finding scheme as used for the real data. For this purpose, a library of realistic synthetic galaxies was created, which has been described in detail in the appendix of chapter 4. These galaxies follow standard scaling relations and cover the full range of inclinations and position angles. This chapter also describes the completeness procedure used to correct the data. An HiMF is then fit to the completeness corrected mass histogram of the BUDHIES galaxies, and compared with the Local HiMF (Jones et al. 2018).  $\Omega_{\text{HI}}$  is derived by integrating the HiMF and is compared with other studies at similar redshifts. The work in this thesis is the first attempt at constructing the HiMF and measuring  $\Omega_{\text{HI}}$  through direct HI detections at  $z \sim 0.2$ .

Finally, chapter 5 summarises the results obtained in this thesis in the context of the role of HI in galaxies, and the usefulness of HI observations for tracing galaxy evolution. The final aim of this thesis is to provide a benchmark for future HI surveys with science goals similar to those presented here.

This thesis follows standard  $\Lambda$ CDM cosmology with  $\Omega_{\text{M}} = 0.3$ ,  $\Omega_{\Lambda} = 0.7$  and a Hubble constant  $H_0 = 70 \text{ km s}^{-1} \text{ Mpc}^{-1}$ .



## BUDHIES IV: Deep 21-cm neutral Hydrogen, optical and UV imaging data of Abell 963 and Abell 2192 at $z \simeq 0.2$

Avanti Gogate<sup>a</sup>, Marc Verheijen<sup>a</sup>, Boris Deshev<sup>b</sup>, Jacqueline van Gorkom<sup>c</sup>, Maria Montero-Castaño<sup>d</sup>, Thijs van der Hulst<sup>a</sup>, Yara Jaffé<sup>e</sup>, Bianca Poggianti<sup>f</sup>

<sup>a</sup> Kapteyn Astronomical Institute, University of Groningen, PO box 800, 9700AV, Groningen

<sup>b</sup> Astronomical Institute, Czech Academy of Sciences, Boční II 1401, CZ-14131 Prague, Czech Republic

<sup>c</sup> Columbia University, 550 W 120th St, New York NY 10027, United States

<sup>d</sup> Dunlap Institute for Astronomy and Astrophysics, 50 St George St, Toronto, ON M5S 3H4, Canada

<sup>e</sup> Instituto de Física y Astronomía, Universidad de Valparaíso, Avda. Gran Bretaña 1111, Casilla 5030, Valparaíso, Chile

<sup>f</sup> INAF, Osservatorio Astronomico di Padova, Vicolo dell'Osservatorio 5, 35122, Padova, Italy

*Published in Monthly Notices of the Royal Astronomical Society, Volume 496, Issue 3, pages 3531–3552, August 2020.*

## Abstract

In this chapter we present data from the Blind Ultra-Deep HI Environmental Survey (BUDHiES), which is a blind 21-cm HI spectral line imaging survey undertaken with the Westerbork Synthesis Radio Telescope (WSRT). Two volumes were surveyed, each with a single pointing and covering a redshift range of  $0.164 < z < 0.224$ . Within these two volumes, this survey targeted the clusters Abell 963 and Abell 2192, which are dynamically different and offer unique environments to study the process of galaxy evolution within clusters. With an integration time of  $117 \times 12\text{h}$  on Abell 963 and  $72 \times 12\text{h}$  on Abell 2192, a total of 166 galaxies were detected and imaged in HI. While the clusters themselves occupy only 4 per cent of the  $73,400 \text{ Mpc}^3$  surveyed by BUDHiES, most of the volume consists of large scale structures in which the clusters are embedded, including foreground and background overdensities and voids. We present the data processing and source detection techniques and counterpart identification based on a wide-field optical imaging survey using the Isaac Newton Telescope (INT) and deep ultra-violet GALEX imaging. Finally, we present HI and optical catalogues of the detected sources as well as atlases of their global HI properties, which include integrated column density maps, position-velocity diagrams, global HI profiles, and optical and UV images of the HI sources.

## 2.1 Introduction

Fundamental properties of galaxies are shaped by internal processes during and after their formation (nature) but are also found to be strongly influenced by their environment (nurture). The  $\Lambda$ CDM cosmological framework suggests that galaxies form in dark matter structures and do not evolve in isolation (Efstathiou, Sutherland & Maddox 1990; Sugimotohara & Suto 1991; Gnedin 1996). Within the  $\Lambda$ CDM model, many galaxies are predicted to transition from low to high-density environments at some point in their evolution. Galaxy properties such as star formation activity (Balogh et al. 1999; Poggianti et al. 2006; De Lucia et al. 2012), morphology (Dressler 1980) and gas content (Dénes, Kilborn & Koribalski 2014) have been found to have a strong dependence on the environment in which these galaxies reside. Dressler (1980) found high-density regions like clusters to be dominated by early type and lenticular galaxies, unlike the general field, which is mostly dominated by gas-rich spirals and dwarfs. Similarly, the Star Formation Rates (SFR) of galaxies are greatly reduced in the interiors of clusters as compared to their outskirts (Peng et al. 2010b, and references therein).

One of the main physical processes that cause environmentally driven evolution in and near galaxy clusters is ram pressure stripping (Gunn & Gott 1972; Farouki & Shapiro 1980; Chung et al. 2009; Oosterloo & van Gorkom 2005; Poggianti et al. 2017; Jaffé et al. 2018), a notion also supported by simulations (Vollmer 2003; Tonnesen & Bryan 2009; Kapferer et al. 2009). Other mechanisms, like tidal interactions and mergers (Holmberg 1941; Toomre & Toomre 1972; White 1978), harassment (Moore et al. 1996; Smith, Davies & Nelson 2010) and strangulation (Larson, Tinsley & Caldwell 1980; Balogh, Navarro & Morris 2000; Bekki, Couch & Shioya 2002; Kawata & Mulchaey 2008; Maier et al. 2016) also play a significant role in the depletion of gas and the quenching of the SFR. These processes are also more dominant in high-density environments like groups and clusters and observational evidence is provided by studies such as those by Poggianti & van Gorkom (2001) and Owers et al. (2019), pointing towards the truncation and eventual exhaustion of the atomic hydrogen (HI) in galaxies as they approach the core of clusters. These accreted cluster galaxies may also have been members of smaller groups, making preprocessing an important factor in the  $\Lambda$ CDM structure formation scenario, as indicated in simulations (Berrier et al. 2009; McGee et al. 2009; Han et al. 2018), as well as large optical surveys, such as the SDSS and 2dF surveys (Lewis et al. 2002; Gómez et al. 2003).

Due to their sensitivity to external perturbations and being the reservoir that fuels star formation, HI discs of galaxies prove to be ideal tracers for evolutionary processes. Blind HI imaging surveys have been crucial in the unbiased quantification of the environmental dependence of galaxy evolution (Williams 1981; Chung et al. 2009; Ramatsoku et al. 2016). While this is the case, HI imaging requires long integration times which proves to be challenging at redshifts beyond 0.08. Consequently, very few blind HI surveys at higher redshifts, such as the Arecibo Ultra-Deep Survey (AUDS, Hoppmann et al. 2015) and the COSMOS HI Large Extragalactic Survey (CHILES, Fernández et al. 2013; Hess et al. 2019), have been carried out so far.

The cosmological evolution of the above mentioned astrophysical processes becomes

2

evident at higher redshifts. For instance, Butcher & Oemler (1984) (BO84 hereafter) found an unusually high fraction of blue, star-forming galaxies in cluster cores at higher redshifts compared to the present epoch. This trend, known as the ‘Butcher-Oemler Effect’ (BO effect), was later confirmed by photometric as well as spectroscopic studies (e.g., Couch et al. 1994, 1998; Lubin 1996; Margoniner & de Carvalho 2000; Lavery & Henry 1986; Couch & Sharples 1987; Ellingson et al. 2001; Tran et al. 2003). Numerous other studies have addressed the cause and nature of the BO effect (Tran et al. 2005; De Propriis et al. 2004; Urquhart et al. 2010; Lerchster et al. 2011). Trends that are likely related to the BO effect were also found, for example, by Poggianti et al. (1999), Fasano et al. (2000) and van Dokkum et al. (2000) who found an increase in the spiral fraction in clusters at higher redshifts at the expense of the lenticular (S0) fraction (Dressler et al. 1997), while studies by Duc et al. (2002); Saintonge, Tran & Holden (2008) and Haines et al. (2009) found an increase in the fraction of dusty blue galaxies in clusters with increasing redshift. The fraction of early-type galaxies in the field was also found to be reduced at higher redshifts (e.g., Bell et al. 2007). Based on these findings, some fundamental questions arise regarding the physical processes that govern galaxy evolution at higher redshifts, such as the effectiveness of ram-pressure stripping, the possibility of a higher gas content of infalling galaxies (Catinella et al. 2008), different cluster accretion rates (Berrier et al. 2009), or the possibility of blue cluster galaxies simply being post-starburst or backsplash systems that are no longer actively star forming (Haines et al. 2009; Oman, Hudson & Behroozi 2013; Bahé et al. 2013). It is also argued that the BO effect is the result of an optical selection bias by preferential inclusion of clusters with bluer populations (e.g., Andreon, Lobo & Iovino 2004; Andreon et al. 2006).

While the BO effect has been extensively studied in the optical and infrared, there has been no study to date concerning the gas content of these blue galaxies in clusters at higher redshifts. With the idea of obtaining an HI perspective on the nature of the blue galaxies responsible for the BO effect, we have conducted a deep, blind HI imaging survey known as the Blind Ultra-Deep HI Environmental Survey (BUDHIES) carried out with the Westerbork Synthesis Radio Telescope (WSRT). The main aim of this survey is to study two galaxy clusters, Abell 963 and Abell 2192 at  $z \simeq 0.2$  corresponding to a look-back time of  $\sim 2.5$  Gyr, since signatures of cosmic galaxy evolution start becoming evident at such redshifts. Abell 963 is a BO cluster with a large fraction of blue galaxies in its core, while Abell 2192 has no identified population of blue galaxies associated with it but seems to host star forming galaxies in its outskirts based on the detection of OII emission lines by Jaffé et al. (2012). The properties of the two clusters are described in detail in Sect. 2.2.

Apart from the HI data presented in this chapter, ancillary optical imaging data is available in  $B$ - and  $R$ - bands obtained with the Isaac Newton Telescope (INT) and presented in this chapter. In addition, deep imaging data is available at ultraviolet wavelengths (NUV and FUV) obtained with *GALEX*, as well as optical photometry and spectroscopy provided by the SDSS and supplemented with optical spectroscopy obtained with the William Herschel Telescope (WHT, Jaffé et al. 2013). Targeted CO observations of 23 galaxies within the two surveyed volumes have also been obtained

with the Large Millimeter Telescope (LMT) (Cybulski et al. 2016). Additionally, 89 and 111 redshifts were also available in Abell 963 from Lavery & Henry (Lavery & Henry 1986) and Czoske (private communication) respectively. Furthermore, optical redshifts are available for Abell 963 from Hwang et al. (2014) and from the Local Cluster Substructure Survey (see Jaffé et al. 2016).

A BUDHiES pilot study of these two clusters with integration times of  $20 \times 12^{hr}$  for Abell 963 and  $15 \times 12^{hr}$  for Abell 2192 was presented by Verheijen et al. (2007). Upon stacking of the HI spectra, they found no evidence of HI in the cluster core of Abell 963. These observations, however, were of limited sensitivity and revealed only a fraction of HI detections obtained from the full survey. A total of 42 galaxies were detected in HI that had optical counterparts in SDSS, and the lowest detected HI mass was  $5 \times 10^9 M_{\odot}$ . The full survey, details of which are provided in Sect. 2.3, is much more sensitive and provides a better picture on the gas content in the cores of the two clusters and other overdensities in the surveyed volume. A detailed environment characterisation by Jaffé et al. (2013), based on optical redshifts, showed significant substructure associated with both clusters. For Abell 963, Jaffé et al. (2015, 2016) constructed a phase-space diagram of the cluster galaxies and carried out some preliminary HI stacking. They deduced that the large fraction of blue galaxies observed in the core of Abell 963 may be the result of preprocessing, having caused a temporary enhancement of star formation, while the galaxies lost their gas down to the BUDHiES detection limit during their first infall due to ram-pressure stripping.

In this chapter, along with the Westerbork, INT and GALEX data, including source catalogues and an atlas, we present a preliminary analysis of the HI, optical and UV data of the galaxies within the surveyed volume in preparation of a more detailed comparative study of the two clusters with a focus on the BO effect. Additionally, the BUDHiES data will be used in a forthcoming paper to measure the HI Mass Function (HiMF) and the cosmic HI density ( $\Omega_{\text{HI}}$ ), from direct HI detections at  $z \simeq 0.2$  by virtue of its total survey volume of  $73,400 \text{ Mpc}^3$ , encompassing a wide range of cosmic environments. The HI and  $\Omega_{\text{HI}}$  have been well constrained in the Local Universe (Rosenberg & Schneider 2002; Zwaan et al. 2005; Springob, Haynes & Giovanelli 2005; Martin et al. 2010; Jones et al. 2018) but only one study exists based on direct HI detections at a higher redshift (Hoppmann et al. 2015) out to  $z \approx 0.16$ . Another application of the data will be the study of the HI-based Tully-Fisher relation (TFr, Tully & Fisher 1977) at  $z \simeq 0.2$ . The HI-based TFr, though extensively used in the Local Universe, cannot be easily studied at higher redshifts (Catinella & Cortese 2015) by cause of the intrinsic weakness of the HI signal. Other gas tracers like CO are therefore used beyond the Local Universe (e.g., Topal et al. 2018), though the CO emission does not usually extend beyond the peak of the rotation curve and into the Dark Matter halo. Bright emission lines from the ionized ISM, such as  $\text{H}\alpha$ ,  $\text{H}\beta$ ,  $\text{OII}$  and  $\text{OIII}$  are also often used (e.g., Flores et al. 2006; Kassin et al. 2007; Puech et al. 2008; Di Teodoro, Fraternali & Miller 2016). Like CO, however, their presence is confined to the inner part of the rotation curve since they emit within the stellar disc. The choice of tracer, therefore, may lead to systematic differences in the kinematic measures and hence in the statistical properties of the TFr (de Blok & Walter 2014; de Blok et al. 2016, and references therein). With our HI

data, we have identified several TFR candidate galaxies for a forthcoming study of the HI-based TFR at  $z \approx 0.2$ . This will allow us to directly and consistently compare the HI-based TFR obtained from Local Universe observations with our work at a higher redshift.

This chapter is organised as follows: In Sect. 2.2 we provide a detailed description of the two target volumes. Sect. 2.3 summarises the WSRT observing strategy and includes technical details of the observations, data processing, source finding, completeness tests as well as an introduction to the HI catalogues, the samples of which are given in tables 2.5 and 2.6 for A963 and A2192 respectively. Details on the INT wide field optical imaging are provided in Sect. 2.4, as well as information on the optical source catalogues, is given in tables 2.7 and 2.8. Sect. 2.5 presents the UV imaging data and the procedures undertaken for the data reduction and source finding. In Sect. 2.6 we discuss the observed and derived HI properties of the galaxies, show the colour-magnitude diagram and present the HI atlas for all HI detected galaxies. A brief analysis of the data sets is summarised in Sect. 2.7. Throughout this chapter, we assume a  $\Lambda$ CDM cosmology, with  $\Omega_M = 0.3$ ,  $\Omega_\Lambda = 0.7$  and a Hubble constant  $H_0 = 70 \text{ km s}^{-1} \text{ Mpc}^{-1}$ .

## 2.2 Targets

BUDHiES is a blind 21 cm survey comprising two single-pointing fields, each containing an Abell cluster along with the large scale structure surrounding them. The two volumes encompass a wide range of environments, which includes the two clusters along with smaller groups, sheets and large voids. The two volumes are indicated by the two red boxes in the pie diagram from the SDSS footprint in Fig. 2.1. These two clusters, Abell 2192 at  $z \simeq 0.188$  and Abell 963  $z \simeq 0.206$ , occupy only  $\sim 4\%$  of the total surveyed volume. They were chosen to represent a well studied BO cluster (Abell 963) and a control cluster (Abell 2192), both very distinct in their dynamical properties. The clusters and the volumes containing them will henceforth be referred to as A963 and A2192 respectively. The properties of both clusters are summarised in Table 2.1. A963, which is also in the seminal BO84 sample, is a massive, virialised lensing BO cluster, bright in X-rays (Allen et al. 2003; Smith et al. 2005). It was chosen as one of the two BUDHiES targets because of its unusually large fraction of blue galaxies (19%); the largest blue fraction at  $z \sim 0.2$  in the BO84 sample. It contains a cD galaxy with a stellar mass of  $10^{12} M_\odot$ , surrounded by multiple blue arcs of lensed star-forming background galaxies at  $0.731 < z < 3.269$  (Henry & Lavery 1984). The estimated total mass of the cluster is  $1.4 \times 10^{15} M_\odot$  (Jaffé et al. 2016). Haines et al. (2018, see Fig. 6) found three X-ray groups falling into the main cluster. While the core of A963 is relaxed, the outskirts show a large degree of substructure, according to the environmental analysis undertaken by Jaffé et al. (2013), who found two groups within the cluster and two structures outside the cluster (see Fig. 10 in their paper). In the foreground, they found an overdensity in the same field-of-view which is group/sheet-like and separated from A963 by a large void. Another overdensity is located in the background of A963, well outside its turnaround radius, and does not show much evidence for substructure. In A963, a total of 134 galaxies with optical redshifts were identified in the magnitude

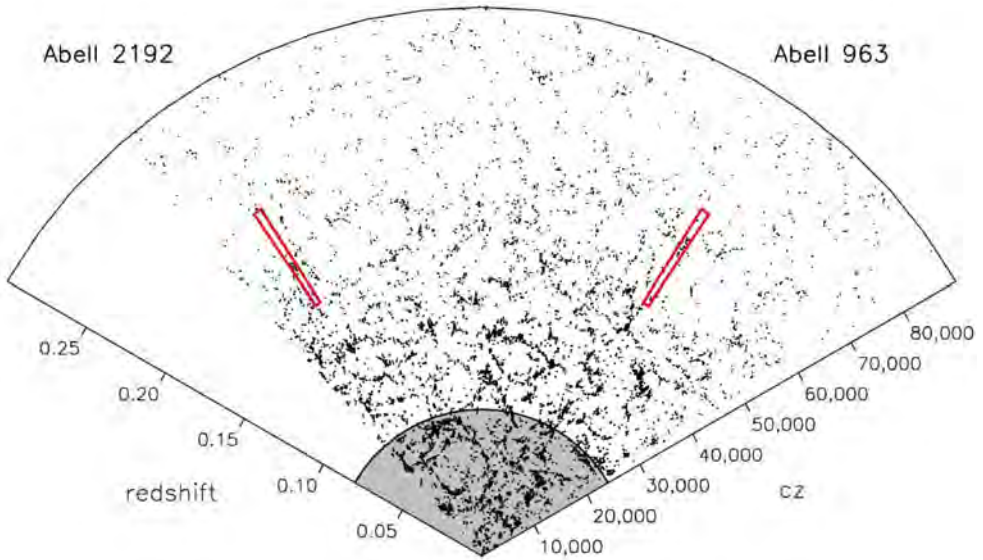


**Figure 2.1** – An SDSS pie diagram including both clusters taken from Verheijen et al. (2007), showing the distribution of SDSS galaxies out to  $z \approx 0.3$ . The grey shaded area indicates the extent of the ALFALFA and HIPASS surveys. The two red boxes show the two volumes surveyed by BUDHiES, demonstrating that not only the clusters but also large volumes in front and behind the clusters are included, encompassing all cosmic environments.

range  $m_3$  and  $m_3 + 2$ , where  $m_3$  is the magnitude of the third brightest cluster member, corresponding to a cluster richness class 3 (Abell 1958).

	A963	A2192
RA	10h17m14.22s	16h26m36.99 s
Dec	+39d01m22.1s	+42d40m10.1 s
$z$	0.206 <sup>(1)</sup>	0.188 <sup>(1)</sup>
Richness class	3 <sup>(2)</sup>	1 <sup>(2)</sup>
$L_x$	$3.4 \times 10^{44}$ <sup>(3)</sup>	$7 \times 10^{43}$ <sup>(4)</sup>
$\sigma$	993 <sup>(5)</sup>	653 <sup>(6)</sup>
$n_{det}$	127	39
$f_B$	19 <sup>(7)</sup>	–

**Table 2.1** – General properties of the two clusters. Top to bottom: Pointing centre coordinates [J2000], Redshift of the cluster, richness class, X-ray luminosity [ $\text{ergs s}^{-1}$ ], velocity dispersion [ $\text{km s}^{-1}$ ], number of HI detections and the fraction of blue galaxies [%].

[1] Jaffé et al. (2013), [2] Abell (1958), [3] Haines et al. (2018), [4] Voges et al. (1999), [5] Jaffé et al. (2016), [6] Jaffé et al. (2012), [7] Butcher & Oemler (1984)

Similar to A963, the volume containing A2192 also consists of a range of environments,

which includes three distinct overdensities and two voids. Jaffé et al. (2013) found that the central overdensity comprises the cluster A2192, which is dynamically younger and less massive than A963. With a total mass estimated at  $2.3 \times 10^{14} h^{-1} M_{\odot}$ , A2192 has a large degree of substructure and is in the process of accreting a nearby compact group and a population of gas-rich, field-like galaxies (Jaffé et al. 2012). It is very weak in X-rays (Voges et al. 1999), and the blue fraction for this cluster is still unknown. In the foreground and background of A2192, there exist group-like overdensities separated from the cluster by large voids. A2192 is of richness class 1 and 62 cluster galaxies were identified in the magnitude range  $m_3$  and  $m_3 + 2$  (Abell 1958).

## 2.3 Westerbork observations and data processing

The HI imaging survey was carried out with the Westerbork Synthesis Radio Telescope (WSRT) during eight semesters between 2005 and 2008, using the cooled Multi-Frequency Front Ends and the digital DZB backend. The 14 dishes of the WSRT provided baselines ranging from 36 to 2700m. To reach a minimum detectable HI mass of  $2 \times 10^9 M_{\odot}$  at the field centres at their respective cluster redshifts over an emission line width of  $\sim 150 \text{ km s}^{-1}$  and a signal-to-noise of 4 in each of three adjacent spectral resolution elements, A963 was observed for a total of  $118 \times 12^{\text{hr}}$  and A2192 for a total of  $72 \times 12^{\text{hr}}$  (see Table 2.2). The integration time was 60 seconds as a compromise between tangential smearing near the edges of the field and a manageable data volume. The primary beam Full Width at Quarter Maximum (FWQM) is 61 arcminutes at 1190 MHz or corresponding to  $z=0.194$  for HI emission. The observations of A963 were centred on 4C +39.29 ( $\alpha=10:17:14.20$ ,  $\delta=+39:01:21.6$ , J2000), a 1.13 Jy bright radio continuum source at 2.4 arcminutes to the south-east of the cluster core. The observations of A2192 were centred on the cluster proper at ( $\alpha=16:26:37.00$ ,  $\delta=+42:40:10.8$ , J2000). To obtain complex gain and bandpass calibrations, each 12-hour measurement was preceded and followed by a 30 minute observation of a flux calibrator: 3C147 and CTD93 for A963, and 3C286 and 3C48 for A2192.

Volume	Year	Number of $12^{\text{hr}}$ observations
A963	2005	23
	2006	34
	2007	31
	2008	30
A2192	2005	15
	2006	20
	2007	14
	2008	23

**Table 2.2** – The number of  $12^{\text{hr}}$  measurements obtained for both the BUDHiES volumes between 2005 - 2008.

The backend and correlator were configured to cover 1160–1220 MHz in dual-polarisation mode with eight partially overlapping IF bands each 10 MHz wide and divided into 256 channels, providing a channel width of 39.0625 kHz corresponding to a rest-frame velocity width of 9.84 km/s at 1190 MHz. The spectra were Hanning smoothed to suppress the Gibbs phenomenon near the bandpass edges, resulting in a velocity resolution of 19.7 km/s. This setup remained unchanged throughout all observations. For the HI emission line, it covers a redshift range of  $0.16427 < z < 0.22449$ , corresponding to a recession velocity range of  $49,246 < cz < 67,300 \text{ km s}^{-1}$ . Given the adopted cosmology, this redshift range corresponds to a luminosity distance of  $789 < D_{\text{lum}} < 1117 \text{ Mpc}$ , a range in look-back time of  $2.05 < T_{\text{lookback}} < 2.69 \text{ Gyr}$ , and a range in primary beam diameter of  $7.09 < \text{FWQM} < 9.55 \text{ Mpc}$ . The spatial scales at the distances of the two clusters are  $3.4 \text{ kpc arcsec}^{-1}$  for A963 and  $3.1 \text{ kpc arcsec}^{-1}$  for A2192. The total surveyed comoving volume within the FWQM of the primary beam is  $73,400 \text{ Mpc}^3$ , equivalent to a spherical volume of the Local Universe within 26 Mpc.

### 2.3.1 Data flagging and calibration

The visibility data obtained for BUDHiES were processed and Fourier transformed with the help of the NRAO Astronomical Image Processing System (AIPS; Greisen 1990). The datacubes were further processed and analysed with the Groningen Image Processing System (GIPSY; van der Hulst et al. 1992).

#### Cross-calibration and data flagging

The visibility data of each 12-hour measurement and the bracketed two calibrators were imported and combined into a single AIPS data set. The temporal behaviour of the system temperatures was inspected to assess the overall health of each antenna throughout the observation, and an initial flagging of disfunctional antennae was carried out manually. Visibilities of the calibrators that were affected by strong Radio Frequency Interference (RFI) were flagged by clipping visibilities with excessive amplitudes. Subsequently, a preliminary, normalised bandpass was determined for each of the two calibrators. After applying this antenna-based bandpass, a linear fit was made to the amplitudes of each baseline-based spectrum and visibilities with an amplitude in excess of  $8\sigma$  above this fit were flagged. After this flagging, a new, normalised bandpass was determined for each calibrator, each polarisation and each of the eight IF bands separately.

After applying the new bandpass to the calibrator data, the central 75 percent of each 10 MHz IF band was averaged to form continuum data sets for the calibrators. The observed, complex continuum visibilities were then calibrated to match the expected, known flux density of the calibrators. These complex gain and bandpass solutions were applied to the spectral line visibilities of the science fields by interpolating the solutions for the two calibrators in time across the 12-hour measurement. This was done for each of the eight IF bands independently.

After this cross-calibration, RFI was removed from the science data in an iterative manner. A linear fit was made to the visibility amplitudes of the central channels

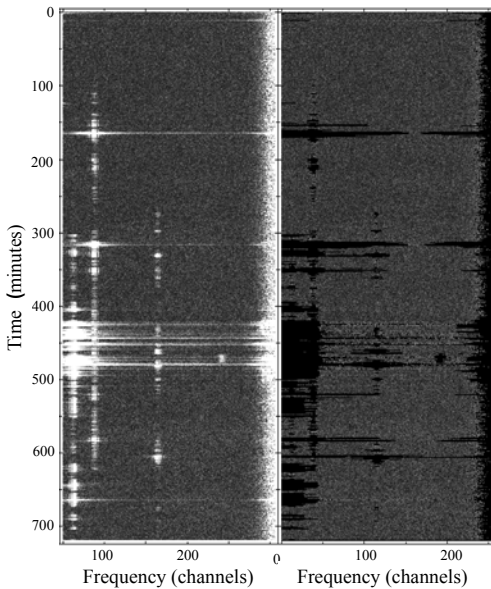


**Figure 2.2** – An example illustrating the RFI removal algorithm adopted in the data processing for one polarisation of one IF of a random 12-hour measurement consisting of all 256 channels. The left and right panels show the data before and after RFI flagging.

(26 to 217) and subtracted. Each visibility spectrum was then boxcar smoothed with different kernel widths to reduce the noise. After each smoothing operation, visibilities with an amplitude in excess of  $4.5\sigma$  were flagged, followed by a new linear, censored fit. After several iterations, the accumulated flags were applied to the original, cross-calibrated visibility data of the science targets. Figure 2.2 shows the results of this RFI removal algorithm.

### Self-calibration and Continuum subtraction

After cross-calibration and flagging, the visibilities of each measurement of the target fields were self-calibrated for each IF separately by iteratively building a sky model of the continuum sources in each field, consisting of clean components. For each IF, the central channels were averaged to produce a continuum data set, which was Fourier transformed to the image domain and cleaned with the standard Högbom algorithm, using manually controlled search areas centred on visually identified continuum sources out to a distance of several degrees from the phase centre. The clean components were subsequently used to derive and apply corrected gain solutions over increasingly shorter time intervals, followed by a new Fourier transform to produce an improved image. For the field containing A963, four phase-only self-calibrations were carried out with solution intervals of 10, 5, 2 and 1 minute, followed by three phase-and-amplitude calibrations with solution intervals of 15, 10 and 5 minutes, for each IF separately. For the field with A2192, the four phase-only self-calibrations were sufficient. The self-calibration results were inspected visually at every step. This resulted in sixteen sky models, one for each of the eight IFs for each of the two fields. The accumulated gain corrections

were applied to the corresponding spectral line data and the clean components that produced the final self-calibration solutions were subtracted from the visibilities using *uvsb* followed by *wlin* in order to remove the continuum flux from the spectral line data.

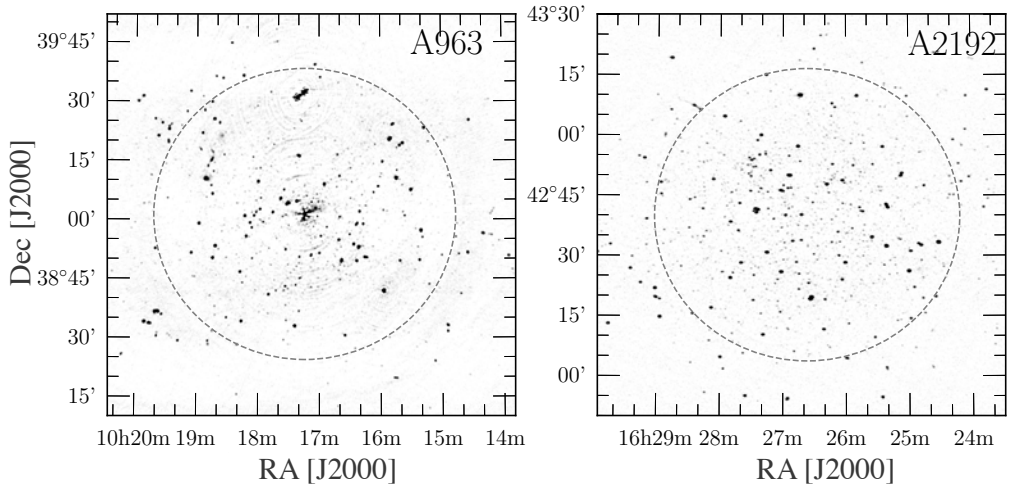


**Figure 2.3** – Radio continuum maps of the two BUDHiES fields with self-calibration applied. The dashed grey circles indicate the FWQM of the primary beam at the redshift of the respective clusters. The arcs observed in A963 are instrumental artefacts caused by the strongest continuum sources in the field, locally limiting the dynamic range of the image, and are completely unrelated to the physical lensing properties of A963.

Figure 2.3 shows the continuum maps for both fields. These maps were made separately at a higher resolution than the line data, using most of the available 60 MHz band. Use of a *Robust* weighting of -5 (uniform weighting) resulted in Gaussian beams with Full Width Half Maxima (FWHM) equivalent to  $15.7'' \times 23.2''$  for A963 and  $20'' \times 20''$  for A2192. The noise is not uniform over the entire image because source confusion and dynamic range artefacts locally enhance the noise in the field centres above the thermal level, making the estimation of the rms noise in the maps problematic. In the corners of the fields we measure average thermal noise values of  $8 \mu\text{Jy}/\text{beam}$  for A963 and  $6.5 \mu\text{Jy}/\text{beam}$  for A2192. Figure 3 of Zwart et al. (2015) provides a theoretical confusion noise limit at 1.4 GHz as a function of angular resolution. For our synthesised beam sizes, our measured thermal noise values are below the expected confusion noise of  $\sim 13$  and  $\sim 14 \mu\text{Jy}/\text{beam}$  for A963 and A2192 respectively, at 1.19 GHz.

### 2.3.2 Imaging data cubes

The self-calibrated and continuum subtracted visibility data of each IF of each measurement were Fourier transformed with *imagr* with a *Robust* weighting parameter of +1 and no further baseline tapering. This produced ‘dirty’ image cubes of  $512 \times 512$  pix-

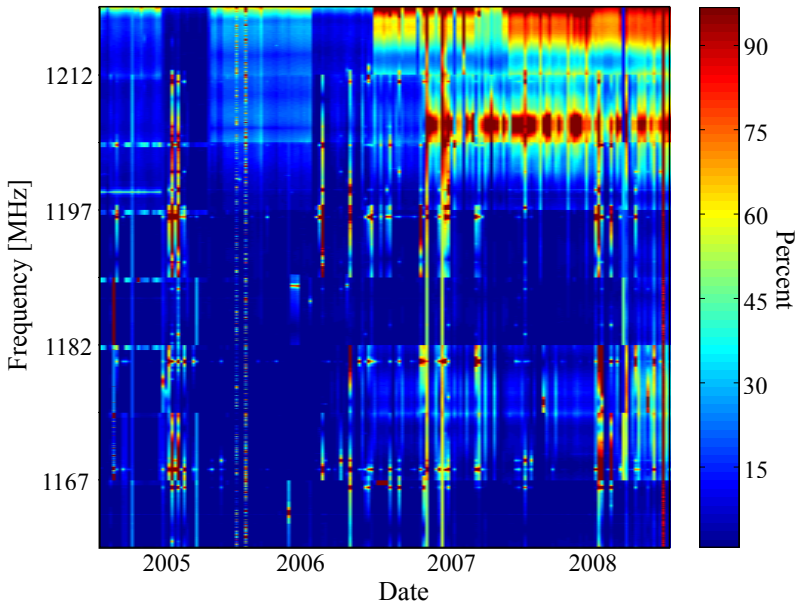


**Figure 2.4** – RFI at different frequencies plotted as a function of time for all measurements combined. The colour range indicates the percentage of RFI-induced data loss.

els and 256 channels, as well as cubes with the frequency-dependent synthesised beam pattern to be used for cleaning the HI line emission. With  $8''$  pixels the channel maps covered  $68 \times 68$  arcmin<sup>2</sup> on the sky. The FWHM of the Gaussian beams with which clean components were restored are  $23'' \times 37''$  for A963 and  $23'' \times 39''$  for A2192 independent of frequency. Data cubes from all epochs were averaged channel-by-channel with weights based on the measured rms noise in a channel. The same weights were used to average the cubes with the synthesised beams.

### 2.3.3 Residual Continuum subtraction

The combined image cubes, by virtue of their significantly lower noise, again revealed residuals from the brightest continuum sources, mainly due to temporal bandpass variations. The grating rings of the residuals were cleaned and the continuum sources themselves were masked out. The area removed from the survey due to these masks was  $< 2\%$  for the field of A963 and  $0.5\%$  for A2192.

Fitting and subtraction of the continuum with *uvlin* also removed some of the underlying HI signal, resulting in negative baselines in spectra containing HI emission. This bias was corrected in two steps. The first involved an iterative procedure in which the spectrum containing the HI signal was clipped, fitted and subtracted with the help of the GIPSY task *conrem*. This step was repeated until all of the negative baselines were corrected for to the best possible extent. This step, however, may have clipped some of

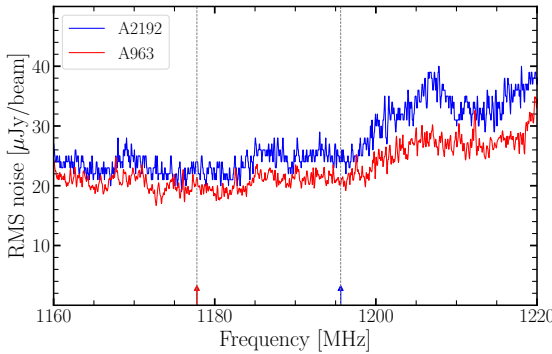


**Figure 2.5** – The rms noise variation as a function of frequency in the continuum subtracted cubes for A963 (red) and A2192 (blue) when smoothed to a velocity resolution of  $38 \text{ km s}^{-1}$ . The trend with frequency is similar for the two cubes, and the peak in the rms noise is likely caused by low-level RFI at those frequencies, which could not be entirely removed from individual measurements. The vertical dashed lines with the colour-coded arrows correspond to the redshifts of the two clusters.

the low column density HI signal as well, which had to be restored. For this purpose, a source detection algorithm (see Sect. 2.3.5 for details on the algorithm) was run on the cubes which masked the HI signal recovered in the previous step. These masks were then applied to the cubes that still contained the imperfections due to *wvlin*. A direct, censored *conrem* was then used again, and the baselines were then fit linearly and subtracted, thus bringing all negative baselines as close to zero as possible, without losing any HI signal due to clipping. The final cubes were free of offending imperfections, only containing HI signals.

### 2.3.4 Quality of the data

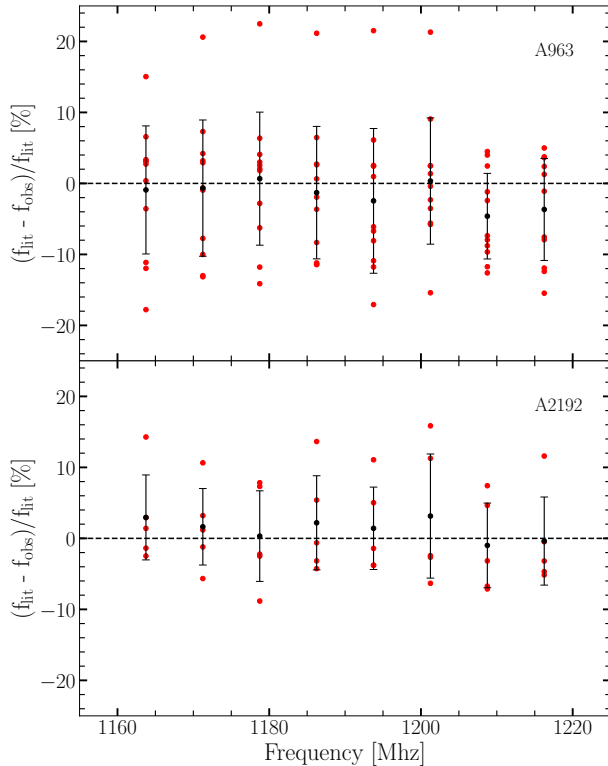
#### RFI

Figure 2.4 shows the trend in RFI at all frequencies as a function of time. The colours indicate the percentage of data lost due to RFI within the duration of the survey, and do not include data from antennae that did not work. From the figure, it is evident that the data are relatively RFI-free in the initial measurements between 2005 and 2006, with a drastic increase in RFI at higher frequencies in the more recent measurements post 2006. This increasing RFI is mostly caused by the buildup of navigation satellite constellations, particularly Galileo and GLONASS, transmitting in this frequency range.

#### Noise variation

Figure 2.5 shows the rms noise variation as a function of frequency in the two cubes after continuum subtraction and at a velocity resolution of  $38 \text{ km s}^{-1}$  (R4, see Sect. 2.3.5). The variations in both the volumes show very similar trends even though the data processing was carried out independently. The increase in noise, particularly towards higher frequencies above 1200 MHz, can be attributed to the increase in RFI and frequency dependent flagging, with about 5 - 8 % of the visibilities below 1200 MHz needed to be flagged, while more than 15 % were flagged above 1200 MHz. This increase in RFI is also seen in Fig. 2.4, as explained in Sect. 2.3.4. With achieved noise levels comparable to the expected thermal noise of the system, imperfections in

the bandpass calibration become more apparent in the combined measurements, particularly the frequency-dependent residuals from those continuum sources which could not be properly subtracted. However, while one can avoid confusion with real sources due to the coherent spatial and frequency information that these residuals possess, they still add to the overall noise in channel maps. The errors in the cubes are based on the rms noise only, and do not include uncertainties due to the masks or continuum subtraction imperfections.



**Figure 2.6** – Comparison of continuum flux densities measured with BUDHiES with those from FIRST and WENSS, shown as the mean flux difference between literature flux densities and those measured by us as a function of frequency (MHz). Top: A963, Bottom: A2192. Eleven continuum sources were chosen in the field of A963 and five in A2192. These sources are given by the red points. The expected fluxes for the eight IF bands of our measurements were calculated assuming a single spectral index between the known FIRST and WENSS fluxes. The black points and the error bars indicate the mean and standard deviation of the flux differences respectively at each IF frequency.

### Comparison of continuum flux densities

Since none of the HI sources were previously detected, we compared instead the flux densities of the detected continuum sources with those published in the literature, namely, the FIRST (Becker, White & Helfand 1995) and WENSS (Rengelink et al. 1997) surveys, which were used for their continuum flux measurements at 1400 and 325 MHz respectively. Eleven continuum sources in the field of A963 and five in that of A2192 were found to have reliable measurements in all the 8 IF bands of our survey, and also had both, FIRST and WENSS flux densities. Upon calculating the spectral index  $\alpha$ , from the two literature surveys, the expected flux density for a continuum source at each IF frequency from our survey was calculated. The differences between the expected and measured flux densities are shown in Fig. 2.6, illustrating the mean flux difference of

these continuum sources as a function of frequency. These differences in all bands were found to be consistently less than 10%, within the errors. Outlying sources could be variable over time. We concluded that the continuum flux density measurements in all bands were consistent with those obtained by FIRST and WENSS. By inference, the HI fluxes we measure also have estimated calibration errors of  $< 10\%$ .

### 2.3.5 HI source finding and galaxy identification

Source finding was carried out using GIPSY. The two processed cubes were first smoothed in velocity to four velocity resolutions consisting of an initial Hanning smoothing followed by further smoothing with a Gaussian kernel to a nearly Gaussian frequency response with a FWHM of 4, 6 and 8 channels. These four cubes, referred to as R2, R4, R6, and R8 hereafter, were made for each field. R2 corresponds to a Hanning smoothed cube ( $19 \text{ km s}^{-1}$ ), whereas the other resolutions correspond to Gaussian response functions corresponding to four ( $38 \text{ km s}^{-1}$ ), six ( $57 \text{ km s}^{-1}$ ) and eight ( $76 \text{ km s}^{-1}$ ) channels respectively at 1190 MHz. Locations in the cubes that contained residuals from strong radio continuum sources, as well as a perimeter of 5 pixels along the edges where aliasing effects occur, were masked out. The pixels between  $\pm 3$ , 4, 5 and 8 times the rms noise in each channel were then clipped, and the remaining positive and negative pixels connected to multiple adjacent velocity channels were searched for. Negative pixels were included to estimate false detections. The detection criteria were selected to combat imaging artefacts and noise in the cubes. They are as follows: A single spectral resolution element with an  $8\sigma$  peak, two adjacent elements at  $5\sigma$ , three adjacent elements at  $4\sigma$  and four adjacent elements at  $3\sigma$  were considered as solid detections, while the rest of the data was discarded. The algorithm returned three-dimensional masks of the detected sources. The source finding algorithm revealed 153 positive detections in the field of A963 and 41 in A2192. To confirm the reliability of our HI detections, these positive detections returned by the source finding process were corroborated by the existence of optical and UV counterparts, located within the FWHM of the synthesised beam centred on the HI detection. We cross-matched our HI data with the SDSS and our own wide-field optical images from the INT (see Sect. 2.4) and ultra-violet images from GALEX (see Sect. 2.5). In most cases, there is an obvious stellar counterpart within the HI contours. In many cases, this galaxy also had a corresponding optical redshift, which unambiguously settled the identification. From those unambiguous cases, we learned that the corresponding galaxies were also bright in UV. Therefore, if multiple possible stellar counterparts existed within the HI contours and no optical redshifts were available to confirm or reject a counterpart, then we used the GALEX images and assigned the brightest UV source with an optical counterpart to be the plausible stellar counterpart of the HI detection. A total of 28 spurious HI detections without an optical or UV counterpart were rejected. The HI centres of all confirmed HI detections were determined by fitting 2D Gaussians to the total HI maps. The final sample comprises 127 galaxies in A963 and 39 galaxies in A2192. These numbers are an update from those mentioned in previous BUDHiES publications, and are the result of a re-analysis of the line cubes which included the deblending of confused sources. Images of these optical and UV counterparts with overlaid HI contours are

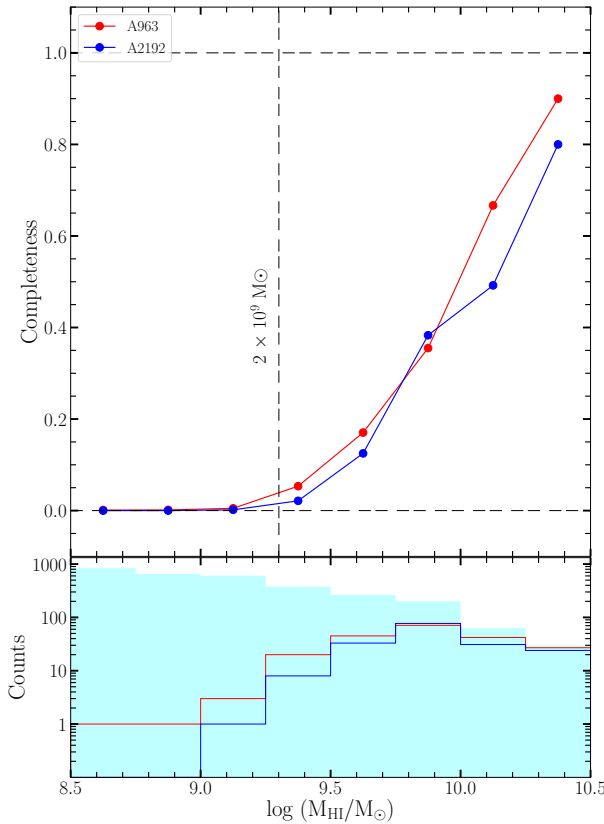


**Figure 2.7** – Top panel: Completeness of the two surveyed volumes per HI mass bin. Red: A963; Blue: A2192. Horizontal black dashed lines at the bottom and the top indicate 0 and 100 % completeness respectively, while the vertical dashed line indicates the intended detection limit of  $2 \times 10^9 M_{\odot}$  at the redshifts of the two clusters. Bottom panel: injection and recovery rates of artificial galaxies in the two volumes. The inserted artificial galaxies are given by the cyan filled histogram, while the line histograms show the recovered galaxies in the two volumes, colour-coded as in the top panel.

provided in the HI atlas (Sect. 2.6.3).

### 2.3.6 Completeness

We studied the completeness of the two detected galaxy samples based on an empirical approach by inserting artificial galaxies throughout the entire survey volume and subsequently determining the rate of recovery of these sources using the same source finding scheme as described in Sect. 2.3.5. For the purpose of the completeness tests, a library of artificial galaxies in the mass range  $10^{8.5}$  to  $10^{10.5} M_{\odot}$  was created following standard scaling relations (e.g., the HiMF, the HI mass-diameter and the Tully-Fisher relation) and covered all inclinations. These galaxies were created using the GIPSY task *galmod*.

A total of 3000 galaxies were inserted into two synthetic cubes corresponding to the two volumes such that they followed the observed cosmic large scale distribution of galaxies in these volumes. 700 of these galaxies were above the nominal survey detection limit of  $2 \times 10^9 M_{\odot}$ . These noise-free synthetic cubes were then multiplied by the primary beam and added to the observed data cubes. The new data sets containing real and artificial sources were searched again for HI detections using the same source detec-

tion method. To reduce confusion, the real sources recovered in the new data cubes were first subtracted before identifying the artificial galaxies. Source identification was carried out by cross-matching the positions of the recovered artificial sources with the input catalogue. Some sources needed to be manually identified due to the effects of blending. The search recovered a total of 210 artificial sources for the volume of A963 and 169 sources for A2192. The completeness of the survey was estimated as the ratio of input to recovered artificial sources per mass bin. This is illustrated in Fig. 2.7, from which it is evident that the survey is not fully complete in any of the mass bins, with a rapid decrease in the recovery of galaxies towards lower masses. The detectability of galaxies depends on three main parameters: firstly, their position in the cube, and their distance and thereby the extent of the attenuation by the primary beam; secondly, their inclinations, and thirdly, the nonuniform noise distribution. Consequently, we found that at higher redshifts and galaxies near the edges of the field of view, as well as those that are highly inclined have a lower detection probability. The process of source insertion, detection, and identification carried out for the completeness tests will be described in more detail in an upcoming publication focusing, for the first time, on the HiMF and  $\Omega_{\text{HI}}$  based on direct HI detections at  $z \sim 0.2$ .

### 2.3.7 HI properties of detected galaxies

This section describes the methods involved in measuring the HI properties of the individual galaxies detected in both volumes. Some of these properties are included in the HI source catalogues and atlas, described separately in Sect. 2.3.8 and Sect. 2.6.3 respectively.

#### Global HI profiles

The primary beam corrected fluxes required for the global HI profiles were determined using the GIPSY task *flux* within the frequency-dependent HI emission masks made during source finding and applied to the R2 cubes. The uncertainty in the flux calculation was determined by first applying the HI mask to 8 line-free areas in the cube over the same channels as the actual line, offset by one synthesised beam from the source and then subsequently measuring the signal in these offset regions. The rms scatter in these 8 measurements provides an empirical uncertainty in the flux values obtained for each galaxy. Peak flux densities were then measured for three equal velocity sections of the profiles, corresponding to the approaching ( $F_{\text{app}}^{\text{max}}$ ), middle ( $F_{\text{mid}}^{\text{max}}$ ) and receding ( $F_{\text{rec}}^{\text{max}}$ ) bins, and were used in quantifying the shape of the global profile: double-horned (type 1), single Gaussian-like (type 2) or asymmetric (type 3) respectively. These three types of profiles are illustrated in Fig. 2.8.

The observed frequency widths [MHz] at 20 % and 50 % ( $\Delta\nu_{\text{obs},\%}$ ) of the overall peak flux densities were determined at each resolution (R) based on the widths obtained from a linear interpolation between the data points moving outwards from the profile centre on both the approaching and receding sides ( $\nu_{r,\%}$  and  $\nu_{a,\%}$  respectively). These observed line widths were converted to velocity widths [ $\text{km s}^{-1}$ ] as per Eq. 2.1.

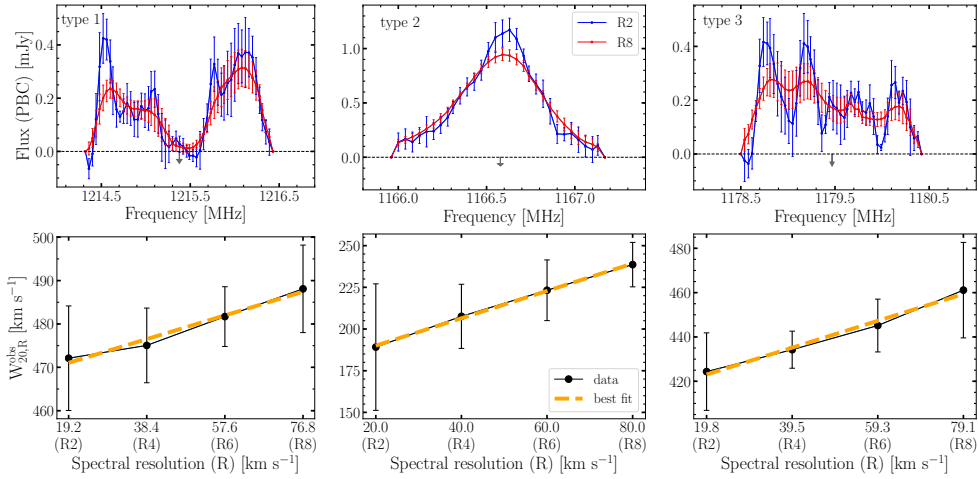


**Figure 2.8** – Three galaxies chosen to represent the entire BUDHiES sample, showing the effect of instrumental broadening as a function of spectral resolution. The top panels show the global HI profiles at the R2 and R8 resolutions (red and blue lines respectively) along with errors. The grey arrows indicate their central frequency corresponding to their systemic velocities. For the entire sample, these profiles are broadly categorised as double-horned (type 1), single gaussian (type 2) and asymmetric (type 3). In the bottom panels we show in black the measured line widths against their respective resolutions: R2, R4, R6 and R8 (See sect. 2.3.5), measured in the galaxy rest frame, along with errors. The dashed orange lines indicate the best linear fits.

$$W_{\%R}^{\text{obs}} = \frac{\Delta\nu_{\text{obs},\%}}{\nu_{\text{rest}}}(1+z)c \quad (2.1)$$

where  $\nu_{\text{rest}}$  is the rest frequency of the Hydrogen emission line. The errors on the line widths were calculated from the errors on the global profiles, also based on Eq. 2.1.

The rest-frame channel widths in  $\text{km s}^{-1}$  were calculated as

$$\Delta V_{\text{rest}}^{\text{chan}} = c \frac{\Delta f}{\nu_{\text{obs}}} \quad (2.2)$$

where  $\Delta f$  is the width of the spectral channel in MHz and  $\nu_{\text{obs}}$  is the observed frequency of the HI line. The total primary beam corrected HI flux (S) for each galaxy was calculated by integrating their global profiles, given by

$$S^{\text{V}_{\text{rest}}} = \sum S_{\nu} \Delta V_{\text{rest}}^{\text{chan}} \quad (2.3)$$

where  $S^{\text{V}_{\text{rest}}}$  is in  $\text{Jy km s}^{-1}$  and  $S_{\nu}$  is the primary beam corrected flux density within the mask in each channel, given in Jy.

The observed line widths (Eqs. 2.1) of galaxies increase with decreasing spectral resolution, and hence need to be corrected for instrumental broadening. Ideally, the corrected widths at all velocity resolutions should be the same, or, in other words, a line fit to the corrected widths plotted as a function of velocity resolution, should have a zero slope. For each source, a first-order polynomial was fit to the observed rest frame line widths in  $\text{km s}^{-1}$  at each of their respective four resolutions R2, R4, R6 and R8 (see Sect. 2.3.5). An average correction factor C was then derived from all slopes of the individual fits. Under the assumption that the required correction factor (C) is linear with resolution (R), the universal correction ( $\delta W_{\%,R}$ ) to be applied to the measured line widths of galaxies at different resolutions was calculated as:

$$\delta W_{\%,R} = C \times R \quad (2.4)$$

The observed line widths were then corrected following:

$$W_{\%}^{\text{corr}} = W_{\%,R}^{\text{obs}} - \delta W_{\%,R} \quad (2.5)$$

where  $W_{\%}^{\text{corr}}$  is the corrected line width after applying the correction factor to the observed line width  $W_{\%,R}^{\text{obs}}$ . Figure 2.8 illustrates three galaxies chosen to represent the entire sample. The global HI profiles in the top panels are shown for two resolutions, R2 (black) and R8 (blue). One can notice that the line width increases at lower spectral resolutions. In the bottom panels we plot the observed line widths as a function of rest frame velocity resolution, with the dashed line indicating the line that best fits the data. The corrections in the line widths were calculated based on Eq. 2.4. The final corrected line widths in  $\text{km s}^{-1}$  are calculated according to:

$$W_{20}^{\text{corr}} = W_{20,R}^{\text{obs}} - 0.36R \quad (2.6)$$

$$W_{50}^{\text{corr}} = W_{50,R}^{\text{obs}} - 0.29R \quad (2.7)$$

To confirm that these corrected line widths were not systematically over/under-corrected, we first calculated the expected linewidth per galaxy based on the individual correction factor ( $c^{\text{ind}}$ ) obtained from the slopes of the respective polynomial fits, such that Eq. 2.4 becomes

$$\delta W_{\%,R}^{\text{ind}} = c^{\text{ind}} \times R \quad (2.8)$$

and Eq. 2.5 becomes

$$W_{\%}^{\text{corr,ind}} = W_{\%,R}^{\text{obs}} - \delta W_{\%,R}^{\text{ind}} \quad (2.9)$$

where  $\delta W_{\%,R}^{\text{ind}}$  is unique for each galaxy and would be the ideal correction required to have equal line widths at all resolutions. For each galaxy, the corrected line widths from

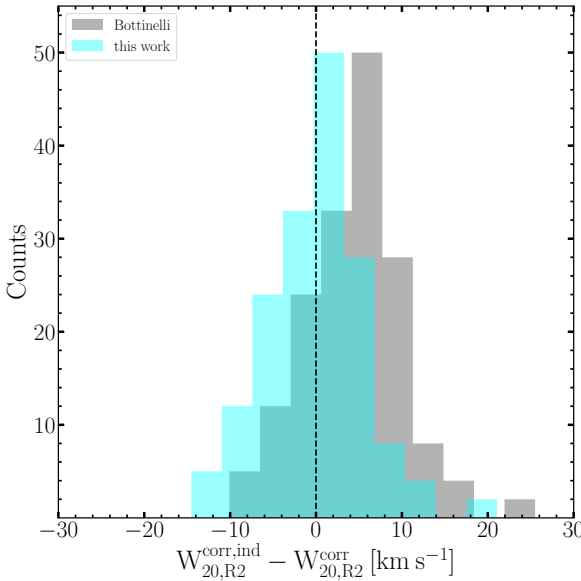


**Figure 2.9** – Histograms of the difference between the expected and corrected  $W_{20}$  line widths at the velocity resolution R2. The cyan histogram represents corrected  $W_{20}$  widths based on the difference between Eq. 2.6 and Eq. 2.9. Given as reference is a grey histogram that follows a similar procedure but is based on the correction factor taken from Bottinelli et al. (1990). The overlap between the two histograms is shown in dark cyan, and the dashed line implies zero difference between the expected and corrected  $W_{20}$  widths at R2.

Eq. 2.5 were subsequently subtracted from these expected line widths (Eq. 2.9). Ideally, this difference should amount to zero for all galaxies. We compared these values with corrected  $W_{\%,R}^{\text{corr}}$  line widths based on Bottinelli et al. (1990), who claim a correction factor of  $0.55R$  and  $0.19R$  for  $W_{20,R}^{\text{obs}}$  and  $W_{50,R}^{\text{obs}}$  respectively. The histograms in Fig. 2.9 illustrate this comparison of corrected  $W_{20,R}^{\text{corr}}$  line widths at the R2 resolution. From the figure, it is clear that our corrections have a closer convergence around zero compared to those from Bottinelli et al. (1990), which are slightly offset. We find similar results for the  $W_{50,R}^{\text{corr}}$  line widths.

### HI masses and column density maps

The total HI mass  $M_{\text{HI}}$  ( $M_{\odot}$ ) of each galaxy was calculated as:

$$M_{\text{HI}} = \frac{2.36 \times 10^5}{(1+z)} \times D_{\text{lum}}^2 S^{\text{V}_{\text{rest}}} \quad (2.10)$$

where  $D_{\text{lum}}$  (Mpc) is the luminosity distance to the galaxy, based on its redshift and the adopted cosmology.

Total HI maps were constructed from the emission within masks that outlined the HI emission from the cleaned data cubes. All the channels were then co-added to make the maps, which were subsequently corrected for primary beam attenuation. Though most galaxies in our volumes were barely resolved, we computed column densities from the HI maps by converting pixel values from  $\text{Jy beam}^{-1}$  to  $\text{cm}^{-2}$  by using Equations 2.11

and 2.12. These column densities were used for choosing appropriate HI contour levels (see Sect. 2.6.3).

$$N_{\text{HI}} = 1.82 \times 10^{18} \int T_{\text{b}} dV_{\text{rest}}^{\text{chan}} \quad (2.11)$$

where  $T_{\text{b}}$  is the brightness temperature, given by

$$T_{\text{b}} [\text{K}] = \frac{6.05 \times 10^5}{\Theta_x \Theta_y} (1+z)^3 S_{\nu} [\text{Jy beam}^{-1}] \quad (2.12)$$

Here,  $\Theta_x$  and  $\Theta_y$  correspond to the major and minor axes of the clean beam in arcseconds, and  $z$  is the redshift of the HI emission line. It is to be noted, that total HI column density maps are meaningful only for spatially resolved sources. The equations 2.1, 2.2, 2.3, 2.10, 2.11 and 2.12 have been adopted from Meyer et al. (2017) and take cosmological effects into account.

For extended sources larger than the synthesised beam, the column density sensitivity at 5 times the rms noise ( $N_{\text{HI}}^{5\sigma}$ ) at the redshift of the clusters is  $0.91 \times 10^{19} \text{ cm}^{-2}$  for A963 and  $1.1 \times 10^{19} \text{ cm}^{-2}$  for A2192. The rms values are based on Fig. 2.5. These column density limits are remarkably low and can be attributed to the exceptionally long integration times.

### Position-Velocity diagrams

Position-velocity diagrams (PVD) along the kinematic major axis give an impression of the projected rotation curve of the HI disc of a galaxy. For our sample, PVDs were extracted from the cubes with velocity resolutions of  $19 \text{ km s}^{-1}$  (R2) and  $76 \text{ km s}^{-1}$  (R8) respectively. The centres of the PVDs are based on the HI centres, while the position angles were obtained from SExtractor fits made to the R-band INT data as described in Sect. 2.4.

#### 2.3.8 The HI catalogue

Tables 2.5 and 2.6 list the derived HI parameters for all confirmed HI detected galaxies in the two volumes. The contents of the tables are given below, from columns (1) to (10):

**Column (1):** Serial number assigned to each HI detection, based on which optical properties can be correlated with Tables 2.7 and 2.8 for the two volumes respectively.

**Column (2):** Galaxy ID based on the Right Ascension (J2000) and Declination (J2000) of the HI centres derived from our observations.

**Columns (3) & (4):** Right Ascension and Declination of the HI centres (J2000).

**Column (5):** HI redshift  $z_{\text{HI}}$ .

**Column (6)** : Luminosity distance  $D_{\text{lum}}$  in Mpc to the galaxy derived from co-moving distances based on the HI redshifts and the adopted cosmology.

**Column (7) & (8)**: HI linewidths  $W_{20,R4}^{\text{obs}}$  and  $W_{50,R4}^{\text{obs}}$  measured in  $\text{km s}^{-1}$  at 20% and 50% of the peak HI flux, respectively, derived from the R4 cubes. These line widths have not been corrected for instrumental broadening.

**Column (9)**: Primary beam corrected integrated HI flux density  $S_{\text{int}}$  in  $\text{mJy km s}^{-1}$  obtained from the R4 cubes.

**Column (10)**: The total HI mass in  $M_{\odot}$ .

**Column (11)**: Type of profile. As mentioned in Sect. 2.3.7, all HI sources have been classified into three categories based on their global HI profiles: Double horned (Type 1), single Gaussian-like (Type 2) and asymmetric (Type 3).

## 2.4 INT Wide field optical imaging

Both fields have been imaged by the Sloan Digital Sky Survey (SDSS DR7, Abazajian et al. 2009). However, as the SDSS has limited surface brightness sensitivity and probes mostly the brightest galaxies on the red sequence at these redshifts, optical counterparts for some of the fainter HI detections were not available. Identification of these missing optical counterparts is important, however, for obtaining rough optical morphologies of the HI detected galaxies to probe the nature of the galaxies in our sample in relation to the BO effect. For this purpose, wide-field optical Harris images of the two BUDHiES fields were obtained with the Wide Field Camera (WFC) on the 2.54m Isaac Newton Telescope (INT) at the ‘Observatorio de la Roque Muchachos’, La Palma. As a motivation for carrying out this study, Fig. 2.10 shows the central region of A963 in both, the SDSS and the final INT composite images. From the figure, it is evident that the INT image is significantly deeper than SDSS, which is essential for subsequent studies.

The WFC consists of four CCDs with  $2148 \times 4128$  pixels of 13.5 microns, corresponding to 0.33 arcseconds. The largest gap between the chips is 1098 microns, corresponding to  $\sim 27$  arcseconds on the sky. For both fields, the entire FWQM of the WSRT primary beam was imaged in the Harris B- and R- filters by mosaicing 30 individual exposures, distributed over 6 partially overlapping pointings. At each pointing position, 5 individual exposures were collected, slightly dithered with 35 arcsecond offsets around the centre of the pointing, in order to fill the gaps between the chips. The integration time for every individual exposure was 480s for the B-band and 360s for the R-band. The total integration time per field amounted to 14400 seconds or 4 hours for the B-band and 10800 seconds or 3 hours for the R-band imaging.

In total, 9 observing nights were allocated in April 2007, 2008, and 2009, of which 6 yielded usable scientific data. A summary of the number of exposures used in the making of the mosaic images and the atmospheric conditions during the observations is presented in Table 2.3. Bias frames and at least three sky flatfields in both filters were taken at the beginning and the end of each night. The dark current (considerably less than  $1 \text{ e}^-/\text{hour}$ ) was neglected during the data processing. The nights were non-



**Figure 2.10** – A comparison of the area within the central  $2 \times 2$  arcmin<sup>2</sup> region of A963, showing our composite optical INT image (left) and SDSS (right). The contrasts in both images have been increased to demonstrate the depth. The INT images were created using Harris B- and R- bands, while the SDSS image is a composite of g, r and i bands. Multiple arcs and low surface brightness sources can be observed around the central cD galaxy in our image. Note the number of blue galaxies in the centre of A963.

Date	Used exposures	Seeing	Weather conditions
17 April 2007	20	1.0 - 1.2	cirrus
18 April 2007	12	>1.1	clouds
19 April 2007	25	1.2 - 1.4	good
04 April 2008	3	1.2 - 1.4	clouds
05 April 2008	0	-	high humidity
06 April 2008	0	-	storm
26 April 2009	0	-	high humidity
27 April 2009	29	>1.4	cirrus
28 April 2009	31	<1.1	good

**Table 2.3** – Exposures used in the final mosaic images along with their seeing conditions.

photometric and no standard star fields were observed.

### 2.4.1 Data processing

The imaging data from the INT WFC were processed with the *ccdred* and *mscred* packages of IRAF (Tody 1986).

## Bias removal, flat fielding, and sky subtraction

Each exposure yielded four ‘science frames’ from the four CCD chips. The following procedure was carried out individually for every science frame from every exposure. The value of the overscan region was first subtracted, the frames were trimmed, and a bad pixel mask was created. A median bias frame was then made per observing run and subtracted from all science frames and flatfields. A median of the normalised flats was made and used as a master flat field for each filter for each night. Every master flat image was then normalised to the highest median from all four chips. All science frames were then divided by the corresponding flat field image.

For the sky subtraction, masks were made and grown to various sizes to censor the faintest galaxies and scattered light from bright stars. A single first-order plane was then fit to the masked images and subtracted. The images were inspected interactively and any residual sky imperfection was then manually estimated and subtracted. A fringe correction was then made by subtracting the median of all available R-band images from each individual R-band image. A preliminary coordinate system was attached to the images by aligning the catalogue stars taken from the NOAO USNO - A2.0 to the corresponding stars in the science frames. The astrometric solutions derived from this step were applied to all the individual science frames.

All four science frames from a single exposure were combined into a single 4-CCD mosaic image, once the detector and filter-induced artefacts were removed. An additional refinement of the coordinate system was carried out for each 4-CCD mosaic image to reduce any additional astrometric residuals, by re-aligning the NOAO USNO-A2.0 stars with those in the 4-CCD mosaic images.

Since the observations were carried out in non-photometric conditions and over a range of airmasses, the 30 4-CCD mosaics obtained through a particular filter for a particular field, 5 at each of the 6 pointing locations, had to be scaled to match the brightness of selected stars in the various overlap regions between the 30 4-CCD mosaics. First, the 5 dithered 4-CCD mosaics around a particular pointing location were scaled and combined into a single pointing mosaic to fill the gaps within each of the five individual 4-CCD images. Subsequently, the 6 pointing mosaics were scaled with respect to each other, again by using selected stars in their overlap regions. After this scaling the 6 pointing mosaics were combined into a single  $1 \times 1 \text{ deg}^2$  mosaic that covers the FWQM of the WSRT primary beam. This procedure resulted in four mosaiced images in total, one for each filter and each field. The photometric calibration and consistency across the mosaics will be discussed in Sect. 2.4.1.

## Astrometric calibration

The produced images were then further processed for an additional refinement of the astrometric calibration solutions. The images were first reprojected to match the projection centres of the HI maps produced by the WSRT for the two fields. About 150 stars taken from the USNO-A2.0 catalogue were identified in the INT images. The GIPSY task *astrom* was used to measure any deviations and the corrections were subsequently applied using *reproj*. Figure 2.11 shows the amplitude and direction of the

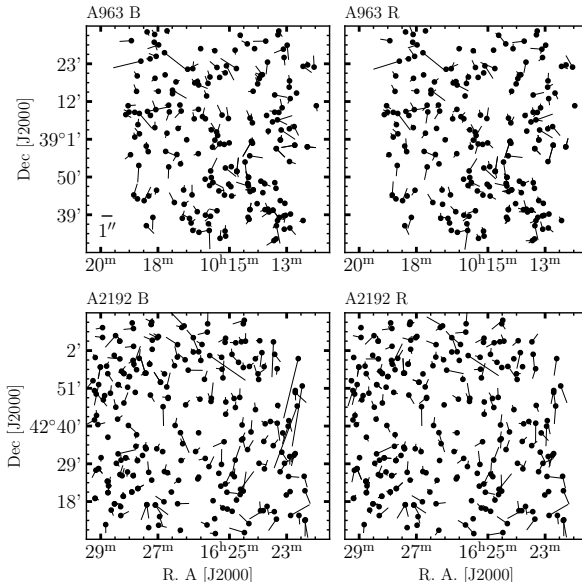


**Figure 2.11** – For the 150 stars used for astrometric calibration, vectors showing the residual differences in the positions of the stars derived from our INT images and those from the USNO-A2.0 catalogue. These vectors have been enlarged by a factor of 250 for clarity. Top two panels: A963; bottom two panels: A2192. A size bar showing 1 arcsecond, also enlarged 250 times, is given in the bottom left corner of A963 B.

residuals in the astrometry for all the images at the positions of the 150 reference stars. These offsets are enlarged by a factor of 250 for clarity. Note that we ignored the effect of proper motion of the stars in the astrometric solutions. We do not find systematic residuals in the plate scale, rotation angle or projection system.

### Photometric calibration

For photometric calibration, a catalogue of roughly 900 stars per field with  $17.66 < r < 19.66$  was extracted from the SDSS database. The lower magnitude limit was set to ensure that the stars are within the linear regime of the WFC CCD chips, while the upper limit ensured a sufficiently high SNR. Their SDSS  $u$ ,  $g$ ,  $r$  and  $i$  magnitudes were then converted to the Johnson B- and Kron-Cousin R-band magnitude filters based on the transformation equations (2.13, 2.14, see Lupton (2005)). These filters match closely with the Harris B- and R- filters used for this study, and hence an additional conversion factor was not necessary.

$$B = u - 0.8116 (u - g) + 0.1313; \quad \sigma = 0.0095 \quad (2.13)$$

$$R = r - 0.2936 (r - i) - 0.1439; \quad \sigma = 0.0072 \quad (2.14)$$

Out of the 900 stars in the catalogue, stars which were in relative isolation and with a uniform background in our INT images were identified and used for aperture photometry. The remainder of the stars were masked out. Apertures were made around the stars out to a radius of 15 arcseconds. The outermost annuli were used for the

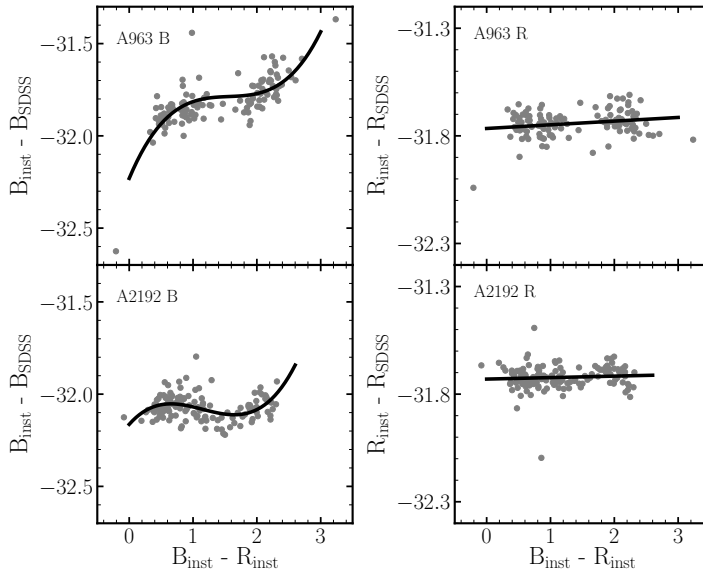


**Figure 2.12** – Zero points derived from our photometric calibration for A963 (Top) and A2192 (Bottom). The grey points denote the zero points for both, the B - (left panel) and the R-bands (right panel). Horizontal axes show the instrumental colour derived from our images, whereas vertical axes indicate the photometric zero points, calculated as the difference between INT and SDSS magnitudes. Lines indicate polynomial fits made to the scatter points.

estimation of the local sky background, which was subtracted from each of the other annuli. The annulus corresponding to the first dip in flux below the sky level was used as the outermost radius of the aperture. The measured fluxes were converted to instrumental INT B- and R- magnitudes derived from our images. Photometric zero points, calculated as the difference between the instrumental magnitudes and the converted SDSS magnitudes, were calculated for the two bands. Illustrated in Fig. 2.12, these zero points are plotted as a function of the instrumental colour of the INT data. For both fields and filters, a polynomial fit to the data showed a strong colour dependence in the B-band. The instrumental INT magnitudes of the galaxies were corrected following this calibration.

#### 2.4.2 Optical source finding

We used SExtractor to identify and catalogue all the extended sources within the two fields. The program was run in dual mode, with the R-band image used as a detection image. The images were filtered with a Gaussian with a FWHM of 2.5 pixels. Sources were selected to have at least five contiguous pixels with values larger than  $2\sigma$  above the local background. The deblending parameter was set to zero since this provided the best results for cluster galaxies at  $z \simeq 0.2$ . Those galaxies rarely showed any structures

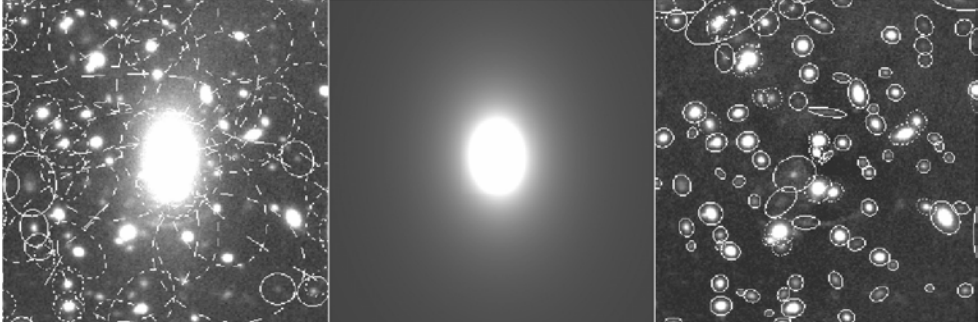


**Figure 2.13** – Automatic apertures made with SExtractor before (left) subtraction of the model cD galaxy in A963 (middle), and after (right) the subtraction of the model.

that would cause SExtractor to fragment them. No other deblending setup was able to separate all galaxies in the crowded central region of A963. The local background was estimated and subtracted using a mesh size of 128 pixels and a mean filtering box of 9 pixels. This adequately removed the extended halos around bright stars, which otherwise would have caused an erroneous estimation of the Kron radius and hence unreasonably big apertures for the photometry. Apertures close to the brightest stars affect sources out to a few arcminutes away and tended to be larger, thereby causing a systematic offset in the measured magnitudes. After subtracting the local background, these apertures became much smaller than before, but were nevertheless flagged in the final catalogue. In addition, the extended light from the cD galaxy in the centre of A963 was causing a similar problem for the aperture photometry of galaxies in the centre of the cluster. The cD galaxy was modelled with *galfit* (Peng et al. 2002) and subtracted to allow for a better estimation of the Kron radii of the surrounding galaxies. Figure 2.13 shows the automatic apertures in the centre of A963, before and after subtracting the cD galaxy. Not only were the automatic apertures more appropriate, but nearby sources were also better deblended. For all the objects in the catalogue, magnitudes were estimated in automatic apertures based on the default scaling parameters given by the SExtractor task *mag\_auto*.

The final B- and R- band magnitudes are provided in the optical source catalogues (Tables 2.7 and 2.8). Many low surface brightness sources, as well as arcs around the central cD galaxy can be seen in the INT image, which are absent in the SDSS image of the same field. Figure 2.14 shows the central  $7 \times 7$  arcmin<sup>2</sup> of the final images of the two clusters as constructed from our INT data.

### 2.4.3 The optical catalogue

Tables 2.7 and 2.8 list the derived optical properties for all confirmed HI detections in the two volumes with available INT or SDSS photometry. These optical counterparts are identified in either SDSS or our INT observations, or both. The contents of the

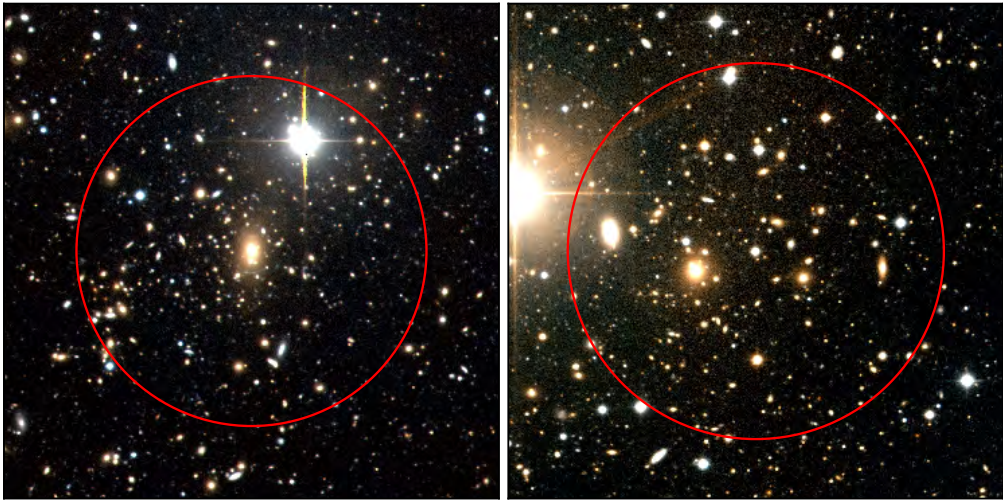


**Figure 2.14** – Optical images constructed from the B- and R-band images of the two clusters A963 (left) and A2192 (right) at  $z \simeq 0.206$  and  $z \simeq 0.188$  respectively, taken with the WFC of the INT. The two images show the central  $7 \times 7$  arcmin<sup>2</sup> of the entire 1 degree<sup>2</sup> field surveyed by the INT. The red circles indicate the central 1 Mpc region in diameter centred on the two clusters at their respective redshifts.

tables are summarised as follows:

**Column (1):** Serial number corresponding to Tables 2.5 and 2.6.

**Column (2):** SDSS Galaxy ID based on the Right Ascension (J2000) and Declination (J2000) of the optical centre. For those sources which did not have an SDSS counterpart, INT IDs have been provided.

**Column (3) & (4):** Right Ascension and Declination (J2000) of the optical centres derived from our INT observations.

**Column (5):** Position angle of the detected galaxies.

**Column (6):** Optical redshift  $z$  from the literature for those objects which have optical spectroscopy.

**Column (7):** B-magnitudes for all sources calculated after INT data reduction and source extraction. These values have not been extinction or k-corrected.

**Column (8):** R-magnitudes for all sources calculated after INT data reduction and source extraction. These values have not been extinction or k-corrected.

**Column (9) & (10):** Observed FUV and NUV magnitudes extracted from GALEX (see Sect. 2.5).

## 2.5 GALEX - UV imaging

While information on the HI content of blue galaxies is useful in the context of the BO effect, it is necessary to link the gas content with the recent SF History (SFH) of the galaxies that are responsible for the BO effect. To properly assess the impact of environmental effects on the SFH and the evolution of galaxies it would be very helpful to resolve the recent SFH on time scales that are relevant to the environment dependent astrophysical processes that act upon the galaxies, where some of these processes such as ram pressure stripping can act on rather short time scales. While the average SF activity over the past few 100 Myrs can be estimated in the HI detected blue galaxies using our optical photometry and radio continuum fluxes, the currently ongoing SF activity can only be accurately measured with the help of UV photometry as the UV luminosity of a galaxy is dominated by the short-lived but bright O- and B-type stars. Therefore, we obtained deep UV imaging photometry of the two BUDHIES fields in order to help us disentangle the currently ongoing SF activity from the average SFR over the past few 100 Myrs in the HI detected blue galaxies.

	A963	A2192
RA (J2000)	10h 17m 09.6s	16h 26m 37s
Dec (J2000)	39d 01m 00s	42d 40m 20s
Date	15 Feb 2008	26 May 2008
$n_{orb}$	24	29
$T_{exp}$ (s)	29040	25815 (NUV) 25796 (FUV)

**Table 2.4** – Table with details on the pointing centres, dates of observations, number of orbits per field and the exposure times for the GALEX UV observations of the two fields.

The Galaxy Evolution Explorer (GALEX) satellite, launched on 28 April 2003 and decommissioned on 28 June 2013, was used to simultaneously obtain deep near-UV (NUV, 1771-2831 Å) and far-UV (FUV, 1344-1786 Å) images for both fields separately. GALEX provides a circular field-of-view with 1.24 and 1.28 degree diameters for the NUV and FUV respectively, which is a good match to the FWQM of the WSRT primary beam. The angular resolution of the GALEX images is 5.3 arcsec in the NUV and 4.3 arcsec in the FUV. The pointing centres, observation dates, number of orbits, and exposure times for the two fields are given in Table 2.4. The achieved limiting magnitude for point sources in both the NUV and FUV was  $m_{AB} \sim 25.5$  mag. The UV images and photometry reported in this chapter are produced with the GALEX Pipeline, which uses SExtractor to measure magnitudes by applying a variable extraction area (aperture) depending on the object size. A detailed explanation of the data products from the GALEX Data Analysis Pipeline can be found in Morrissey et al. (2007).

Around 400 UV sources in A963 and 300 UV sources in A2192 were detected. This is strikingly more than the number of HI detections in the two fields, but obviously, the HI detections are restricted to the redshift range surveyed by the WSRT while GALEX also detected foreground and background galaxies. The correspondence between the GALEX

and radio continuum sources will be investigated in a forthcoming paper. Interestingly, we noted that many of our HI detections are also clearly detected in the GALEX images. This allowed us to take advantage of the UV images for counterpart identification as discussed in Sect. 2.3.5. The measured FUV and NUV magnitudes for most of our HI detections are presented in Tables 2.7 and 2.8. The NUV images corresponding to the HI detections are included in the atlas (see Sect. 2.6.3). Apart from two HI sources in A963 which lie just outside the GALEX field-of-view, all HI sources have optical and UV counterparts, most of them with confirmed optical redshifts. Nearly all HI detections have an NUV counterpart and only a few are missing a FUV detection. Occasionally, only an FUV counterpart for an HI detection could be identified.

## 2.6 Results

In this section, we bring forth a discussion on some galaxy properties derived from a preliminary analysis of the various data sets.

### 2.6.1 Distribution of HI properties

To study the distribution of the global HI properties of the detected HI sources, we present plots of the various observed and derived HI parameters in this section.

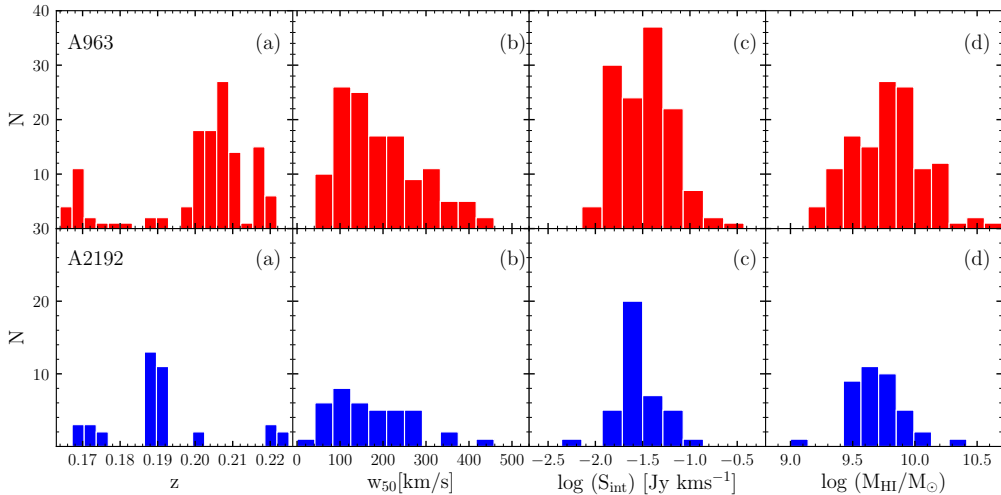


**Figure 2.15** – Histograms illustrating various global HI properties of the detected galaxies derived from the R4 cubes shown as the red and blue histograms for A963 (top panel) and A2192 (bottom panel) respectively. From left to right: Redshift (a), HI line width ( $w_{50}$ ) (b), integrated flux (c), HI mass (d).

Figure 2.15 shows the distribution of HI redshifts, intrinsic line widths, integrated HI fluxes and derived HI masses of the galaxies. The large scale structure along the line-of-

sight is clearly evident in both volumes in Fig. 2.15 (a) and has been described briefly in Sect. 2.2. For further details, we refer to Jaffé et al. (2013).

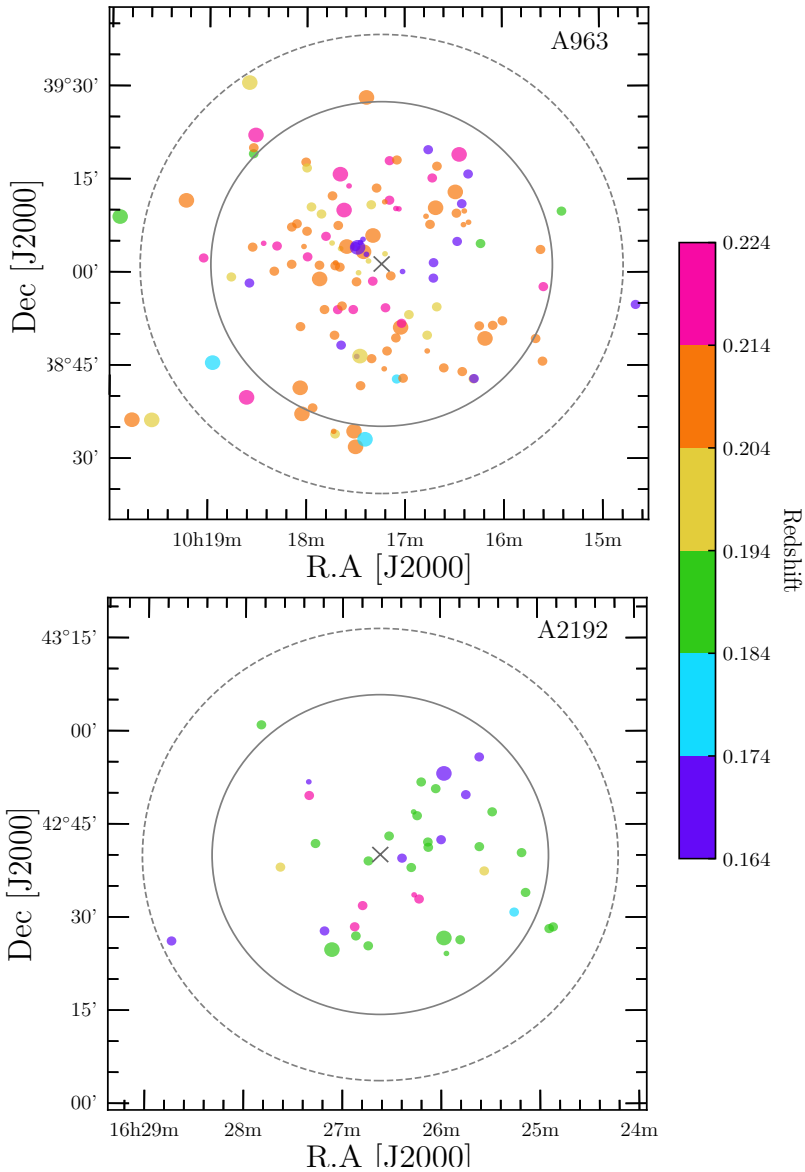
Figure 2.15 (b) shows histograms of the intrinsic  $W_{50}$  line widths of galaxies which range from 61 to 451  $\text{km s}^{-1}$  for A963 and 26 to 453  $\text{km s}^{-1}$  for A2192. The average line widths for galaxies in A963 and A2192 are  $193 \pm 91$  and  $172 \pm 92$   $\text{km s}^{-1}$  respectively. The different distributions of the line widths for the two volumes could be due to differences in sensitivity, large scale structure, galaxy populations and sample sizes, A963 being statistically more significant than A2192.

Figures 2.15 (c) and (d) show the histograms of the integrated HI fluxes ( $\text{Jy km s}^{-1}$ ) and the derived HI masses ( $M_{\odot}$ ) for the galaxies in the two volumes. The integrated HI fluxes span a range between 7.5 to 229  $\text{mJy km s}^{-1}$  for A963 and 5 to 124  $\text{mJy km s}^{-1}$  for A2192. The average integrated flux values are  $42 \pm 32$  and  $34 \pm 22$   $\text{mJy km s}^{-1}$  for A963 and A2192 respectively.

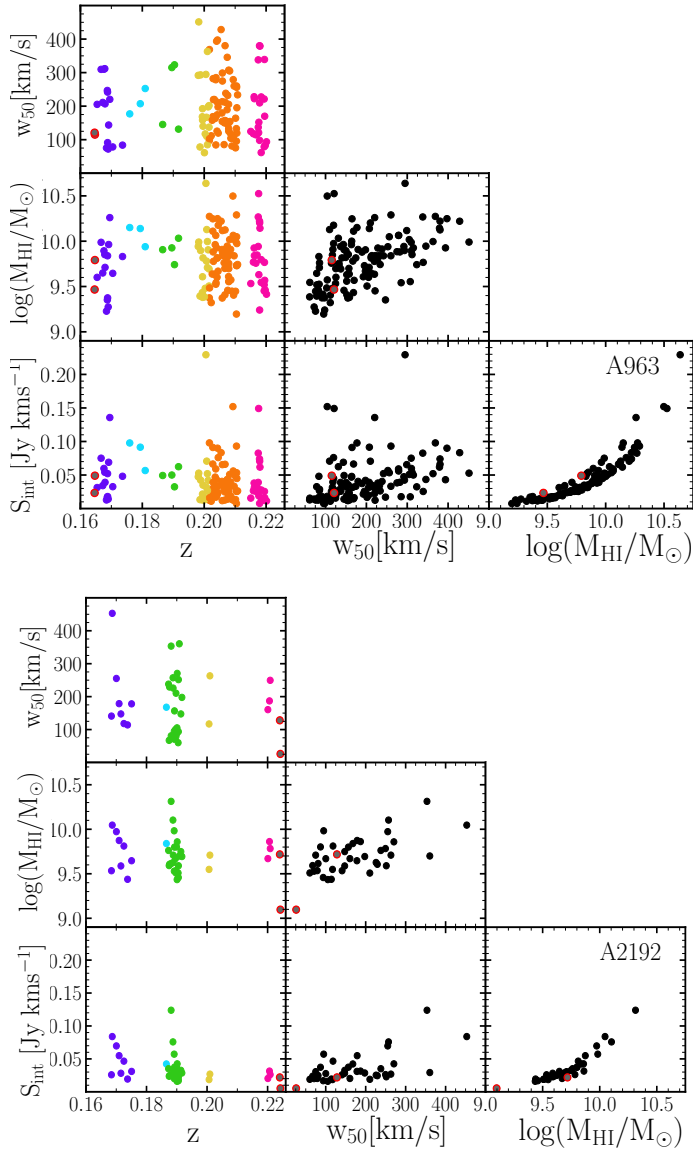
The HI masses of the galaxies in the survey lie within a mass range  $\log(M_{\text{HI}}/M_{\odot}) = 9.2$  to 10.64. The average  $\log(M_{\text{HI}}/M_{\odot})$  values are  $9.8 \pm 0.3$  and  $9.7 \pm 0.2$  for A963 and A2192 respectively. The distribution appears to peak around the local  $M_{\text{HI}}^*$  (Jones et al. 2018) for A963 but is slightly shifted towards lower masses for A2192. The significance and reason for this shift will be investigated with the help of HI mass-to-light ratios of the galaxies in an upcoming paper since it is beyond the scope of this study. There also seems to exist a tail towards higher HI masses, which could be associated with galaxy mergers or interactions, or compact galaxy groups. Due to the large synthesised beam of the WSRT at these redshifts, such systems may not be resolved and hence a more detailed inspection of their optical counterparts and global profiles needs to be carried out.

Figure 2.16 illustrates the distribution on the sky of all the HI sources in the two fields. They are colour coded based on their redshift and sized based on their HI mass. Note that most of the lowest HI masses are detected only near the centre of the two volumes within the FWHM of the primary beam at the redshifts of the clusters, while a few gas-rich systems are detected beyond the FWQM of the primary beam. This is due to the primary beam attenuation of the telescope, causing sensitivity to drop as a function of distance from the centre. The spatial distribution of A963 is relatively symmetric, whereas A2192 shows clear asymmetry, with a majority of the HI detections to the west of the pointing centre. From their colour-coding and Fig. 2.15 (a), it is evident that most of the detected galaxies have redshifts similar to the clusters within the redshift range  $0.204 < z < 0.211$  for A963 and  $0.188 < z < 0.192$  for A2192.

Figure 2.17 shows multivariate distributions of the derived HI parameters for the two volumes. The left column with three panels shows the distribution of the intrinsic HI line widths, inferred HI masses, and integrated HI fluxes as a function of redshift. The colours follow the same colour bar as Fig. 2.16. There exists a large void in the foreground of A963 and a smaller void in the background. In the case of A2192, there appear to be smaller overdensities separated by voids from the main cluster at  $z \simeq 0.188$ . The large-scale structure in the two volumes has been studied in detail by Jaffé et al. (2013). The middle column with two panels shows the distribution of integrated



**Figure 2.16** – Distributions on the sky of the detected HI sources in the two volumes; Top: A963, Bottom: A2192. The distribution is colour coded based on redshift, as indicated by the colour bar, whereas the three marker sizes indicate three mass ranges of the galaxies: massive ( $\log(M_{\text{HI}}/M_{\odot}) > 10$ ), intermediate ( $9.5 < \log(M_{\text{HI}}/M_{\odot}) < 10$ ) and low ( $9 < \log(M_{\text{HI}}/M_{\odot}) < 9.5$ ). The pointing centres for the two fields are indicated by the grey crosses. The FWQM and FWHM of the primary beam at cluster redshifts are indicated by the outer (dashed) and inner circles respectively.



**Figure 2.17** – Multivariate distribution of the observed and derived HI properties, namely redshift ( $z$ ), line width ( $W_{50}$ ), HI mass ( $\log(M_{\text{HI}}/M_{\odot})$ ) and integrated flux HI ( $S_{\text{int}}$ ) for the two volumes. Top: A963; Bottom: A2192. The colours in the first (vertical) panel in both figures are based on the same colour distribution as in Fig. 2.16. The grey sources encircled in red are to be treated as lower limits, since they are very close to the band edges or bright continuum sources.

HI fluxes and HI masses as a function of their line widths ( $W_{50}$ ), while the last column shows the integrated fluxes as a function of HI mass. Despite the modest HI mass and redshift ranges, trends in the various distributions are clearly visible. From Fig. 2.17, a clear trend is observed in  $W_{50}$  as a function of mass. It is observed that only the lower-mass galaxies with narrower line widths were detected, while galaxies with higher masses were found over a larger range of line widths. Since the HI line widths of galaxies depend on factors such as their inclinations and rotational velocities, the undetected low-mass galaxies with higher line widths in the bottom-right of this panel could be fast-rotating early-type gas-poor galaxies. As mentioned in the previous section, the detection limit of the survey was  $2 \times 10^9 M_{\odot}$  at the distances of the two clusters over a line width of  $150 \text{ km s}^{-1}$ . However, we still notice galaxies below the mass limit being detected at those redshifts and beyond. This is caused by line widths narrower than  $150 \text{ km s}^{-1}$ , which brings the detection limit down to lower masses. In the case of A2192, the galaxy with the lowest HI mass lies at the edge of the bandpass, and has a corresponding line width of about  $15 \text{ km s}^{-1}$ . Such galaxies were cut at the edge of the bandpass and only show a small section of their line profiles and hence low HI masses, and are to be treated as lower limits. These could also be some of the possible causes for the difference observed in the peaks of the histograms seen in Fig. 2.15 (d).

No HI was detected in galaxies within a projected distance of 1 Mpc of the cluster A963, whereas for A2192 we found one HI source. As mentioned in Sect. 2.1, A963 being a BO cluster, it is essential to know the nature of the blue galaxies using information on the gas content from this survey. Using the pilot sample, Verheijen et al. (2007) stacked the HI spectra of the blue galaxies in the core of both clusters and compared them with the stacked spectra of the blue galaxies within and outside the central 1 Mpc region. They concluded that the central blue galaxies are significantly more HI deficient than those outside this region. A further analysis of the stacked spectra of galaxies with available optical redshifts inside and outside  $R_{200}$  of A963 was carried out by Jaffé et al. (2016) using the entire data set. They found that the HI content of galaxies in the cluster core, inside  $R_{200}$ , was reduced by half compared to those in the outskirts. They also concluded from stacking exercises in phase-space that the blue galaxies in the centre of A963, which are possibly infalling from the field, have been stripped of a large fraction of their HI during their transition into the stripping zone, i.e. their first passage through the ICM. Most of these blue galaxies were not detected in HI individually as any remaining HI in these galaxies is below our detection threshold. In an upcoming paper, we will revisit the results for the HI stacking and relative gas content in terms of a comparative analysis of A963 and A2192, thereby building on the works of Verheijen et al. (2007) and Jaffé et al. (2016) on an HI perspective of the BO effect, using the full data set.

Figure 2.18 illustrates the B - R versus R colour-magnitude diagram (CMD) of all galaxies in the two volumes that have optical or HI redshifts. These colours and magnitudes have not been corrected for galactic extinction or reddening. A similar CMD was presented by Jaffé et al. (2013) for the two clusters separately, while Jaffé et al. (2016) presented the NUV - R versus R CMD of the cluster A963. From Fig. 2.18, it is evident that most of the galaxies with SDSS redshifts lie at the bright tip of the

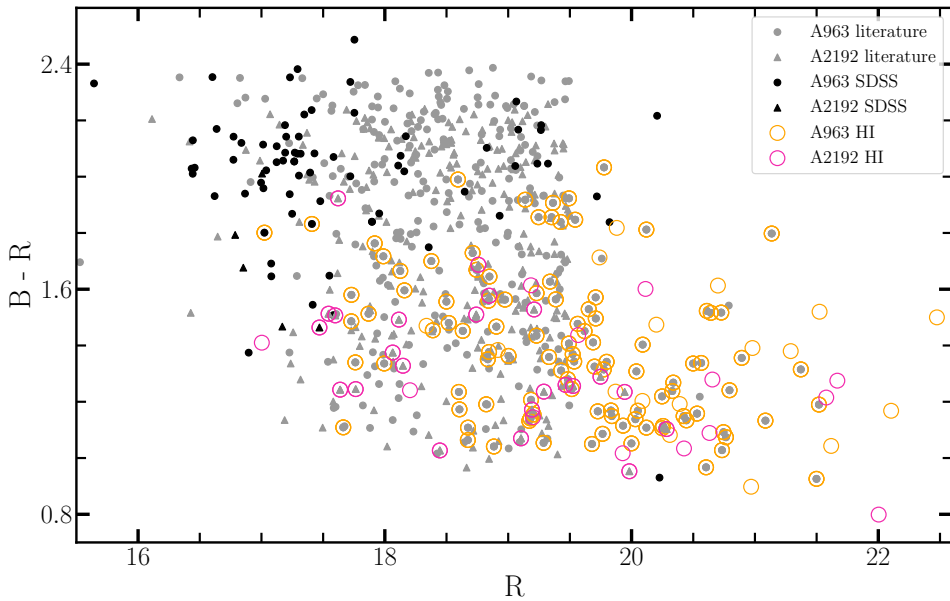


**Figure 2.18** – The combined colour-magnitude diagram of all galaxies lying in the redshift range  $0.164 < z < 0.224$ . Galaxies with optical redshifts are indicated in grey, while those from SDSS are marked in black. These galaxies are mostly located within the ‘red sequence’. HI detections are indicated as open circles. Most of the HI detections are located within the ‘blue cloud’.

red sequence, while most of the HI detected galaxies are located in the ‘blue cloud’. However, we find that some HI detected galaxies lie close to the red sequence, in the so-called ‘green valley’. The brightest HI detected galaxies are found to be as bright as the most luminous red galaxies, and could possibly be merging or post-starburst systems. A further study of the optical morphologies of all these galaxies is required in order to study these bright blue gas rich galaxies in greater detail.

## 2.6.2 Optical properties

Figure 2.19 compares the HI redshifts with optical spectroscopic redshifts available in the literature (SDSS, Henry & Lavery 1984; Jaffé et al. 2013). The plot shows a tight correlation between the two redshifts with a small scatter of  $70 \text{ km s}^{-1}$  and  $168 \text{ km s}^{-1}$  for A963 and A2192 respectively. The scatter for both volumes combined is  $94 \text{ km s}^{-1}$ . This scatter becomes particularly significant for stacking exercises as well as for TFR studies, as it indicates the extent of broadening that can be expected in the width of the stacked profiles due to errors in the optical redshifts.

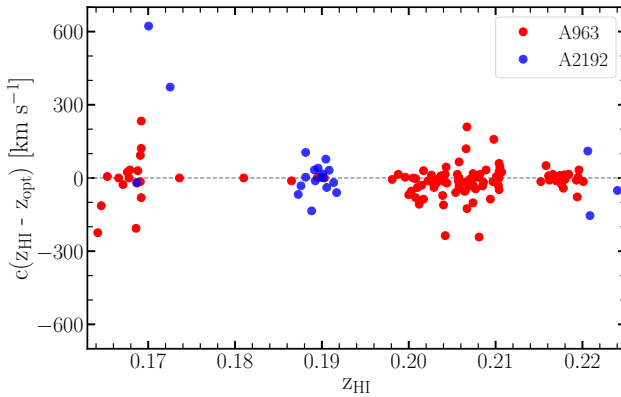


**Figure 2.19** – For those sources with literature spectroscopic redshifts (SDSS, Henry & Lavery 1984; Jaffé et al. 2013), a plot showing a comparison between literature redshifts as a function of HI redshifts obtained from this survey.

### 2.6.3 The atlas

The HI atlas illustrates the most important HI properties described in Sect. 2.3.7 for each individual detected galaxy along with its INT R-band image (see Sect. 2.4), and ultra-violet GALEX image (see Sect. 2.5 for details). Figure 2.20 illustrates the layout of the panels presented in the atlas pages. A sample atlas page is provided in Fig. 2.21. The panels in the respective atlas pages are briefly described below.

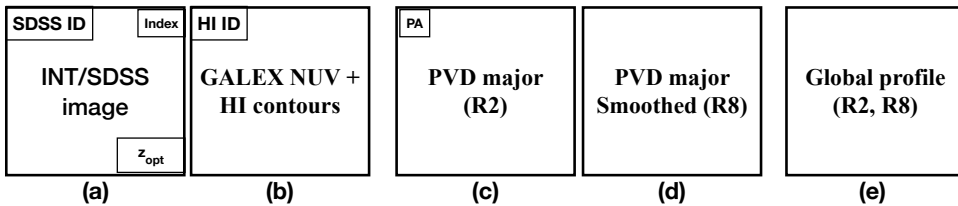


**Figure 2.20** – Schematics of the arrangement of the derived HI parameters given in the atlas.

(a) *INT R-band image*: Identified optical counterparts obtained with the INT are encircled in orange. The SDSS ID is indicated in the top-left corner for those galaxies that have SDSS counterparts, while some with missing SDSS data have their corresponding INT ID. The optical redshift is given in the bottom-right of the image for those sources with optical spectroscopy. The atlas entries are numbered (top-right) according to their respective index numbers in column 1 of the catalogues.

(b) *GALEX NUV image with HI contours*: GALEX NUV image of the HI source with overlaid HI contours. The contours are set at column density levels of 1, 2, 4, 8, 16 and  $32 \times 10^{19} \text{ cm}^{-2}$ . A red cross indicates the location of the HI centre, while the orange circle indicates the same galaxy as in panel (a). The HI ID is provided in the top-left corner.

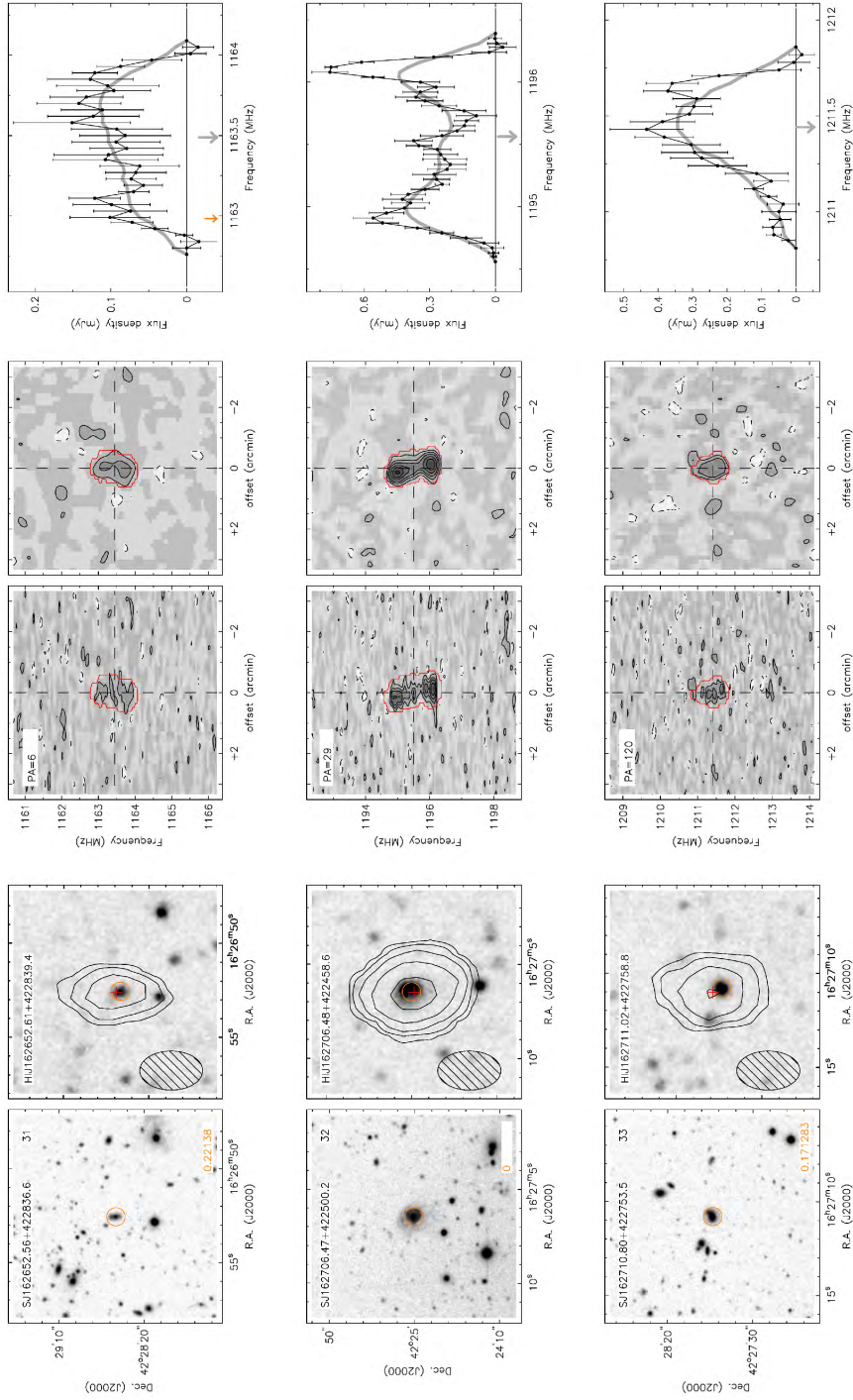


**Figure 2.21** – A sample atlas page showing the data products for three of the HI detections in A963. The full atlas is available online.

(c) & (d) *Position-Velocity diagrams*: The position-velocity slices along the optical major axis were extracted from the R2 ( $19 \text{ km s}^{-1}$ ) and R8 ( $76 \text{ km s}^{-1}$ ) cubes given in the two panels respectively. The red outline indicates the HI mask within which the HI flux was determined. The position angle is given in the top left corner of the diagram.

Vertical and horizontal lines correspond to the systemic velocity and the HI centre respectively. Contours are drawn at -2 (dashed), 2, 4, 6, 9, 12, 15, 20 and 25 times the local rms noise level.

(e) *Global HI profiles*: Global HI profiles for each galaxy correspond to the flux density derived from the R2 cubes ( $19 \text{ km s}^{-1}$ ), shown in black. The smooth grey line illustrates the HI profiles extracted from cubes smoothed to the R8 resolution. The vertical grey arrow indicates the frequency corresponding to the HI redshift of the galaxy, while the orange arrows indicate the frequency corresponding to the optical redshift of the galaxy, if available. Error bars are based on the methodology described in Sect. 2.3.7.

## 2.7 Summary and Conclusions

In this chapter, we have presented the results of a blind, 21-cm HI imaging survey with the WSRT, covering a redshift range of  $0.164 < z < 0.224$  in each of two pointings, thereby surveying a total volume of  $73,400 \text{ Mpc}^3$  within the FWQM of the primary beam with a velocity resolution of  $19 \text{ km s}^{-1}$  and an average angular resolution of  $23 \times 38 \text{ arcsec}^2$ . We have described in detail the radio data processing procedure, the HI source detection methodology and an initial assessment of the completeness of our HI detected sample. The two surveyed volumes each contain an Abell cluster, as well as foreground and background over-densities. The HI detection limit in the field centres and at the distances of the clusters is  $2 \times 10^9 \text{ M}_\odot$  over an emission line width of  $150 \text{ km s}^{-1}$  with a significance of  $4\sigma$  in each of 3 adjacent, independent spectral resolution elements. A total of 166 galaxies are detected within the total survey volume, none of which have been previously detected in HI. We have also presented ancillary optical imaging data of the two fields in the Harris B- and R-bands, obtained with the Wide-Field Camera on the Isaac Newton Telescope on La Palma. We have described the mosaicing data processing in detail, including the astrometric and photometric calibration. In addition, we have obtained deep, near- and far-ultraviolet ancillary imaging data of the two fields with the GALEX satellite. These optical and ultraviolet images have assisted us in identifying the stellar counterparts of the HI detected galaxies in case optical redshifts for them were unavailable. We have catalogued the observed and derived HI properties of the detected galaxies, such as their HI coordinates and redshifts, HI line widths, integrated fluxes and HI masses. We have also tabulated the optical and ultraviolet properties of the HI detected galaxies such as their SDSS identifiers, available optical spectroscopic redshifts, and their derived absolute R, B, NUV and FUV magnitudes. The HI, optical and ultraviolet data are compiled in an atlas showing the R-band image from the INT, a contoured HI map overlaid on the NUV image from GALEX, position-velocity diagrams at two velocity resolutions, as well as the global HI profiles with empirically estimated errors. The HI redshift distributions in the two fields outline a well-defined large scale structure along the 328 Mpc deep line-of-sight, with a dominant

overdensity at the redshifts of the Abell clusters, near-empty voids in front and behind the clusters and smaller over-densities with HI detected galaxies in the near-foreground and far-background of those voids. The volumes surveyed with the WSRT, hence, encompass the widest range of cosmic environments from a deep void to the most dense core of a lensing galaxy cluster. Abell 963 is a relatively nearby, massive Butcher-Oemler cluster with a large fraction of blue galaxies, while Abell 2192 is much less massive and dynamically less evolved. The blue galaxies in the core of A963 were not individually detected in HI above the survey HI mass limit. Nearly all HI detected galaxies associated with Abell 2192 are located to the South-West of the cluster, indicating an anisotropic accretion of field galaxies.

In a series of forthcoming papers, we will exploit the data provided in this chapter to derive the HI Mass Function and  $\Omega_{\text{HI}}$  from direct HI detections at  $z=0.2$ , study the H<sub>I</sub>-based Tully-Fisher relation at this redshift, and provide an HI perspective on the Butcher-Oemler effect. These studies and the HI data presented here will also have implications for future HI surveys at intermediate redshifts with APERTIF, MeerKAT, ASKAP, and the Square Kilometre Array.

## Acknowledgements

AG and MV acknowledge the Netherlands Foundation for Scientific Research support through VICI grant 016.130.338. We acknowledge the Leids Kerkhoven-Bosscha Fonds (LKBF) for travel support. BD acknowledges the support of the Czech Science Foundation grant 19-18647S and the institutional project RVO 67985815. This research was supported in part by a grant from the US National Science Foundation to Columbia University. JMvdH acknowledges support from the European Research Council under the European Union's Seventh Framework Programme (FP/2007-2013)/ERC Grant Agreement nr. 291531. Y.J. acknowledges financial support from CONICYT PAI (Concurso Nacional de Inserción en la Academia 2017) No. 79170132 and FONDECYT Iniciación 2018 No. 11180558. AG thanks Kyle A. Oman and Pooja V. Bilimogga for useful comments on the contents of the chapter. This work is partly based on observations made with the NASA Galaxy Evolution Explorer (GALEX). The WSRT is operated by the Netherlands Foundation for Research in Astronomy, supported by the Netherlands Foundation for Scientific Research. The full acknowledgement of the Sloan Digital Sky Survey Archive used in this chapter can be found at <http://www.sdss.org>. IRAF is distributed by the National Optical Astronomy Observatory, which is operated by the Association of Universities for Research in Astronomy (AURA) under cooperative agreement with the National Science Foundation.

## 2.8 Catalogues and atlas

The following pages contain the HI and optical catalogues of the whole BUDHIES survey (Tables 2.5, 2.6, 2.7 and 2.8 respectively). Following the two tables is an atlas of the optical and HI properties of all the BUDHIES galaxies.

**Table 2.5** – Catalogue containing the HI properties of the detected galaxies in A963. The description of each column is provided in Sect. 2.3.8 of this chapter.

Index	HI ID	R.A. (J2000) hh:mm:ss.ss	Dec (J2000) dd:mm:ss.ss	z	$D_{\text{lum}}$ Mpc	$w_{20}$ km s $^{-1}$	$w_{50}$ mJy km s $^{-1}$	$S_{\text{int}}$ mJy km s $^{-1}$	$M_{\text{HI}}$ ( $\times 10^9$ ) $M_{\odot}$	Type
(1)	(2)	(3)	(4)	(5)	(6)	(7)	(8)	(9)	(10)	(11)
1	H1J101439.00+385444.8	10:14:39.00	38:54:44.8	0.17361	836.7	110.2 $\pm$ 9.4	83.7 $\pm$ 11.4	48.1 $\pm$ 4.2	6.77 $\pm$ 0.59	2
2	H1J101523.89+390949.7	10:15:23.89	39:09:49.7	0.1904	926.7	349.1 $\pm$ 9.8	323.3 $\pm$ 9.5	32.4 $\pm$ 1.7	5.51 $\pm$ 0.3	1
3	H1J101535.30+385740.8	10:15:35.30	38:57:40.8	0.21954	1086.8	222.6 $\pm$ 10.3	170.0 $\pm$ 20.8	16.2 $\pm$ 1.4	3.7 $\pm$ 0.33	3
4	H1J101536.08+384540.9	10:15:36.08	38:45:40.9	0.20575	1010.5	222.6 $\pm$ 20.1	179.7 $\pm$ 17.0	40.5 $\pm$ 2.9	8.1 $\pm$ 0.58	2
5	H1J101536.90+390339.7	10:15:36.90	39:03:39.7	0.2104	1036.3	206.6 $\pm$ 32.6	133.0 $\pm$ 20.4	25.8 $\pm$ 1.7	5.39 $\pm$ 0.37	2
6	H1J101540.21+384919.4	10:15:40.21	38:49:19.4	0.20356	998.5	257.4 $\pm$ 28.6	163.4 $\pm$ 44.1	46.9 $\pm$ 2.3	9.16 $\pm$ 0.46	3
7	H1J101600.44+385211.7	10:16:00.44	38:52:11.7	0.20861	1026.3	126.2 $\pm$ 10.4	104.3 $\pm$ 12.0	18.2 $\pm$ 1.7	3.74 $\pm$ 0.36	2
8	H1J101606.37+385128.0	10:16:06.37	38:51:28.0	0.20739	1019.7	257.0 $\pm$ 23.1	189.3 $\pm$ 29.7	37.3 $\pm$ 2.1	7.58 $\pm$ 0.43	3
9	H1J101611.10+384921.7	10:16:11.10	38:49:21.7	0.20674	1016.0	407.5 $\pm$ 8.1	380.3 $\pm$ 10.4	66.0 $\pm$ 2.9	13.32 $\pm$ 0.59	2
10	H1J101613.62+390438.4	10:16:13.62	39:04:38.4	0.18954	922.2	372.1 $\pm$ 15.3	315.0 $\pm$ 17.8	50.0 $\pm$ 2.0	8.44 $\pm$ 0.34	3
11	H1J101614.58+385123.2	10:16:14.58	38:51:23.2	0.20679	1016.6	255.8 $\pm$ 21.3	211.6 $\pm$ 20.8	33.4 $\pm$ 1.8	6.46 $\pm$ 0.37	3
12	H1J101617.91+384254.2	10:16:17.91	38:42:54.2	0.17046	819.9	109.1 $\pm$ 8.1	78.4 $\pm$ 12.6	32.6 $\pm$ 2.9	4.42 $\pm$ 0.39	2
13	H1J101618.31+384251.6	10:16:18.31	38:42:51.6	0.20105	984.9	124.9 $\pm$ 17.2	84.9 $\pm$ 15.9	26.8 $\pm$ 2.4	5.11 $\pm$ 0.45	2
14	H1J101620.93+390804.8	10:16:20.93	39:08:04.8	0.2067	1015.8	222.5 $\pm$ 10.4	152.2 $\pm$ 40.4	12.7 $\pm$ 1.2	2.56 $\pm$ 0.24	2
15	H1J101621.10+391550.8	10:16:21.10	39:15:50.8	0.16722	802.7	260.7 $\pm$ 15.0	211.1 $\pm$ 33.4	34.2 $\pm$ 1.9	4.46 $\pm$ 0.25	2
16	H1J101623.51+390953.7	10:16:23.51	39:09:53.7	0.21013	1034.7	120.5 $\pm$ 13.0	75.7 $\pm$ 14.5	13.4 $\pm$ 0.9	2.8 $\pm$ 0.19	2
17	H1J101624.03+390741.4	10:16:24.03	39:07:41.4	0.20173	988.6	171.0 $\pm$ 10.9	103.0 $\pm$ 18.0	15.9 $\pm$ 1.2	3.05 $\pm$ 0.22	2
18	H1J101625.05+384401.9	10:16:25.05	38:44:01.9	0.2076	1020.4	291.3 $\pm$ 20.1	232.1 $\pm$ 53.1	34.2 $\pm$ 2.3	6.97 $\pm$ 0.46	2
19	H1J101625.06+391104.0	10:16:25.06	39:11:04.0	0.1676	804.8	359.1 $\pm$ 16.0	310.2 $\pm$ 17.7	59.8 $\pm$ 3.4	7.83 $\pm$ 0.45	3
20	H1J101626.57+391900.1	10:16:26.57	39:19:00.1	0.21746	1075.2	375.2 $\pm$ 13.6	338.0 $\pm$ 15.1	82.6 $\pm$ 3.8	18.51 $\pm$ 0.84	2
21	H1J101627.94+390459.4	10:16:27.94	39:04:59.4	0.16541	793.5	297.3 $\pm$ 10.8	205.3 $\pm$ 15.2	31.3 $\pm$ 1.8	3.99 $\pm$ 0.23	3
22	H1J101628.33+390932.3	10:16:28.33	39:09:32.3	0.21055	1037.1	173.3 $\pm$ 10.2	119.8 $\pm$ 11.2	44.9 $\pm$ 2.0	9.42 $\pm$ 0.43	2
23	H1J101629.00+391257.8	10:16:29.00	39:12:57.8	0.21043	1036.1	396.2 $\pm$ 16.1	260.2 $\pm$ 12.7	93.1 $\pm$ 2.9	19.49 $\pm$ 0.61	3
24	H1J101636.32+384437.8	10:16:36.32	38:44:37.8	0.20746	1020.3	276.0 $\pm$ 18.0	149.2 $\pm$ 31.3	32.5 $\pm$ 2.1	6.62 $\pm$ 0.42	2
25	H1J101640.22+391706.5	10:16:40.22	39:17:06.5	0.20299	995.5	321.9 $\pm$ 20.3	219.6 $\pm$ 23.6	30.8 $\pm$ 1.8	5.99 $\pm$ 0.35	2
26	H1J101640.53+385427.6	10:16:40.53	38:54:27.6	0.20157	987.6	230.4 $\pm$ 7.3	201.6 $\pm$ 14.2	16.7 $\pm$ 1.0	3.2 $\pm$ 0.19	2
27	H1J101641.11+391025.1	10:16:41.11	39:10:25.1	0.21047	1036.3	334.6 $\pm$ 22.2	256.1 $\pm$ 10.4	53.4 $\pm$ 2.0	11.19 $\pm$ 0.41	3
28	H1J101642.43+390134.5	10:16:42.43	39:01:34.5	0.16469	789.7	182.7 $\pm$ 4.7	115.2 $\pm$ 15.2	49.0 $\pm$ 2.3	6.19 $\pm$ 0.3	2
29	H1J101642.56+385905.1	10:16:42.56	38:59:05.1	0.16877	809.9	379.4 $\pm$ 42.8	241.9 $\pm$ 10.6	52.1 $\pm$ 2.3	6.9 $\pm$ 0.3	3
30	H1J101643.13+391512.8	10:16:43.13	39:15:12.8	0.21841	1080.6	97.2 $\pm$ 15.9	61.6 $\pm$ 16.4	15.5 $\pm$ 1.8	3.51 $\pm$ 0.4	2
31	H1J101644.55+390744.6	10:16:44.55	39:07:44.6	0.20788	1022.4	257.1 $\pm$ 21.4	205.4 $\pm$ 22.9	19.9 $\pm$ 1.3	4.07 $\pm$ 0.27	3
32	H1J101645.59+391946.1	10:16:45.59	39:19:46.1	0.16913	812.5	313.5 $\pm$ 14.3	143.7 $\pm$ 32.5	69.0 $\pm$ 3.3	9.19 $\pm$ 0.44	2
33	H1J101646.39+384721.5	10:16:46.39	38:47:21.5	0.20896	1028.2	116.8 $\pm$ 12.0	81.2 $\pm$ 8.9	13.6 $\pm$ 1.1	2.81 $\pm$ 0.22	2
34	H1J101646.41+384953.8	10:16:46.41	38:49:53.8	0.20074	982.8	223.7 $\pm$ 6.1	166.8 $\pm$ 21.0	31.7 $\pm$ 2.0	6.03 $\pm$ 0.38	2
35	H1J101646.99+390903.0	10:16:46.99	39:09:03.0	0.2095	1031.3	151.2 $\pm$ 27.0	111.8 $\pm$ 14.8	12.3 $\pm$ 0.9	2.54 $\pm$ 0.18	2
36	H1J101657.55+385312.9	10:16:57.55	38:53:12.9	0.19824	969.7	545.8 $\pm$ 22.2	451.2 $\pm$ 21.7	52.8 $\pm$ 4.2	9.78 $\pm$ 0.77	3
37	H1J101701.14+384258.2	10:17:01.14	38:42:58.2	0.20328	996.9	266.7 $\pm$ 21.5	219.9 $\pm$ 23.0	22.2 $\pm$ 1.7	4.32 $\pm$ 0.33	2

Table 2.5 – continued

Index	Hi ID	R.A. (J2000) hh:mm:ss.ss	Dec (J2000) dd:mm:ss.ss	z	D <sub>HI</sub> Mpc	w <sub>20</sub> km s <sup>-1</sup>	w <sub>50</sub> km s <sup>-1</sup>	S <sub>HI</sub> mJy km s <sup>-1</sup>	M <sub>HI</sub> (×10 <sup>9</sup> ) M <sub>⊙</sub>	Type
(1)	(2)	(3)	(4)	(5)	(6)	(7)	(8)	(9)	(10)	(11)
38	H1J101701.41+390009.2	10:17:01.41	39:00:09.2	0.16459	789.0	137.5 ± 4.4	120.9 ± 7.8	23.3 ± 1.7	2.93 ± 0.21	3
39	H1J101702.04+385149.1	10:17:02.04	38:51:49.1	0.21622	1067.3	270.9 ± 13.8	222.2 ± 12.0	31.4 ± 1.5	6.93 ± 0.34	3
40	H1J101702.64+385109.6	10:17:02.64	38:51:09.6	0.20587	1011.2	341.4 ± 6.9	298.8 ± 5.6	65.5 ± 2.4	13.1 ± 0.48	3
41	H1J101703.64+391014.5	10:17:03.64	39:10:14.5	0.21937	1085.9	258.2 ± 23.6	221.3 ± 13.1	12.4 ± 0.7	2.83 ± 0.17	3
42	H1J101704.83+391806.8	10:17:04.83	39:18:06.8	0.20794	1022.5	188.2 ± 16.0	125.1 ± 19.1	24.4 ± 1.9	4.98 ± 0.38	2
43	H1J101705.07+384250.6	10:17:05.07	38:42:50.6	0.18094	875.8	354.5 ± 26.4	252.6 ± 14.7	56.7 ± 3.0	8.69 ± 0.45	2
44	H1J101705.47+391018.1	10:17:05.47	39:10:18.1	0.2197	1087.6	178.7 ± 9.2	82.4 ± 12.6	12.6 ± 1.1	2.89 ± 0.24	2
45	H1J101705.51+384927.4	10:17:05.51	38:49:27.4	0.20401	1000.8	445.6 ± 18.5	393.6 ± 13.4	43.0 ± 2.3	8.44 ± 0.45	1
46	H1J101708.63+385927.0	10:17:08.63	38:59:27.0	0.20792	1022.6	174.2 ± 9.9	133.0 ± 29.0	27.8 ± 2.1	5.68 ± 0.42	1
47	H1J101709.38+391800.2	10:17:09.38	39:18:00.2	0.21938	1085.9	112.4 ± 8.0	78.8 ± 9.5	14.4 ± 0.9	3.3 ± 0.21	2
48	H1J101709.40+391138.3	10:17:09.40	39:11:38.3	0.21842	1080.6	259.8 ± 11.0	227.5 ± 14.4	27.7 ± 1.3	6.26 ± 0.29	1
49	H1J101710.92+384721.4	10:17:10.92	38:47:21.4	0.20699	1017.2	333.9 ± 36.1	155.7 ± 30.7	35.3 ± 2.1	7.14 ± 0.42	2
50	H1J101711.87+385419.0	10:17:11.87	38:54:19.0	0.21613	1067.8	308.0 ± 15.6	228.1 ± 40.7	38.0 ± 2.6	8.41 ± 0.58	2
51	H1J101712.15+390300.7	10:17:12.15	39:03:00.7	0.1994	975.8	216.4 ± 8.8	168.4 ± 10.9	14.5 ± 1.0	2.71 ± 0.19	2
52	H1J101712.30+391122.4	10:17:12.30	39:11:22.4	0.21041	1036.3	125.1 ± 11.0	95.5 ± 14.0	7.5 ± 0.8	1.57 ± 0.16	2
53	H1J101712.64+384429.1	10:17:12.64	38:44:29.1	0.20582	1011.0	186.3 ± 10.4	154.6 ± 21.1	11.8 ± 1.1	2.36 ± 0.23	2
54	H1J101717.31+391335.5	10:17:17.31	39:13:35.5	0.21079	1038.1	300.2 ± 8.7	233.7 ± 58.4	26.3 ± 1.4	5.53 ± 0.3	2
55	H1J101719.53+390557.3	10:17:19.53	39:05:57.3	0.21015	1034.7	230.8 ± 12.2	164.1 ± 38.0	47.9 ± 2.3	10.01 ± 0.48	2
56	H1J101719.65+385835.8	10:17:19.65	38:58:35.8	0.21746	1075.3	239.1 ± 13.8	136.9 ± 20.5	39.0 ± 1.5	8.75 ± 0.35	2
57	H1J101720.34+384607.3	10:17:20.34	38:46:07.3	0.20667	1015.6	264.2 ± 5.1	157.2 ± 33.5	24.8 ± 1.8	5.01 ± 0.37	2
58	H1J101720.60+391054.4	10:17:20.60	39:10:54.4	0.19808	968.2	432.5 ± 28.2	291.8 ± 23.7	47.4 ± 2.6	8.75 ± 0.48	3
59	H1J101722.26+390151.1	10:17:22.26	39:01:51.1	0.19864	972.0	119.6 ± 27.3	78.2 ± 16.7	13.3 ± 1.2	2.48 ± 0.22	2
60	H1J101723.55+392811.2	10:17:23.55	39:28:11.2	0.20279	994.4	206.1 ± 9.4	168.6 ± 10.4	66.4 ± 3.7	12.89 ± 0.72	3
61	H1J101723.56+390255.5	10:17:23.56	39:02:55.5	0.16871	810.5	267.4 ± 12.3	246.8 ± 6.6	17.0 ± 1.3	2.25 ± 0.18	1
62	H1J101724.32+383308.2	10:17:24.32	38:33:08.2	0.17985	867.9	284.0 ± 11.4	207.3 ± 10.9	91.5 ± 5.0	13.79 ± 0.75	3
63	H1J101725.27+390320.1	10:17:25.27	39:03:20.1	0.20822	1024.0	338.3 ± 8.1	305.0 ± 17.5	50.8 ± 2.0	10.41 ± 0.41	1
64	H1J101725.64+390520.3	10:17:25.64	39:05:20.3	0.16898	812.0	105.1 ± 15.7	72.1 ± 13.0	14.1 ± 1.0	1.88 ± 0.13	2
65	H1J101727.06+384146.0	10:17:27.06	38:41:46.0	0.20643	1014.4	130.3 ± 13.2	85.3 ± 12.4	28.7 ± 2.0	5.77 ± 0.4	2
66	H1J101727.24+390450.0	10:17:27.24	39:04:50.0	0.16843	809.0	113.6 ± 21.9	75.5 ± 13.8	12.8 ± 1.0	1.69 ± 0.13	2
67	H1J101727.44+384632.2	10:17:27.44	38:46:32.2	0.20104	984.8	449.0 ± 21.5	363.1 ± 14.4	52.0 ± 2.7	9.91 ± 0.51	3
68	H1J101728.35+385957.3	10:17:28.35	38:59:57.3	0.19947	976.1	209.1 ± 6.1	158.6 ± 18.4	12.8 ± 1.0	2.4 ± 0.18	2
69	H1J101728.95+390403.0	10:17:28.95	39:04:03.0	0.1695	815.2	311.7 ± 6.9	220.3 ± 14.8	135.7 ± 2.2	18.2 ± 0.3	3
70	H1J101729.42+384628.8	10:17:29.42	38:46:28.8	0.16879	811.0	119.1 ± 8.9	91.3 ± 16.5	17.9 ± 1.5	2.37 ± 0.21	3
71	H1J101729.58+385829.8	10:17:29.58	38:58:29.8	0.20381	999.8	318.5 ± 10.6	285.1 ± 23.1	17.7 ± 1.0	3.48 ± 0.19	2
72	H1J101730.09+383155.4	10:17:30.09	38:31:55.4	0.20453	1003.8	269.0 ± 29.9	119.7 ± 29.4	76.0 ± 4.5	15.0 ± 0.89	2
73	H1J101730.18+390409.9	10:17:30.18	39:04:09.9	0.16796	806.3	290.1 ± 28.5	206.8 ± 29.7	39.1 ± 1.8	5.14 ± 0.23	2
74	H1J101731.03+383425.9	10:17:31.03	38:34:25.9	0.20374	999.3	336.3 ± 33.7	278.7 ± 23.1	59.1 ± 3.4	11.58 ± 0.67	3
75	H1J101731.57+385401.7	10:17:31.57	38:54:01.7	0.2159	1066.8	259.0 ± 19.5	117.7 ± 38.1	26.6 ± 1.9	5.88 ± 0.42	2
76	H1J101734.23+391356.2	10:17:34.23	39:13:56.2	0.21791	1077.8	141.0 ± 27.2	97.9 ± 16.2	7.7 ± 0.7	1.74 ± 0.15	2

Table 2.5 – continued

Index	Hi ID	R.A. (J2000) hh:mm:ss.ss	Dec (J2000) dd:mm:ss.ss	z	D <sub>lum</sub> Mpc	w <sub>20</sub> km s <sup>-1</sup>	w <sub>50</sub> km s <sup>-1</sup>	S <sub>int</sub> mJy km s <sup>-1</sup>	M <sub>HI</sub> (×10 <sup>9</sup> ) M <sub>⊙</sub>	Type
(1)	(2)	(3)	(4)	(5)	(6)	(7)	(8)	(9)	(10)	(11)
77	HJ101735.53+390410.4	10:17:35.53	39:04:10.4	0.20938	1030.5	372.7 ± 9.2	279.0 ± 339.9	56.0 ± 3.0	11.59 ± 0.61	3
78	HJ101737.25+391003.1	10:17:37.25	39:10:03.1	0.21788	1077.5	457.1 ± 49.5	380.2 ± 17.2	74.0 ± 2.5	16.64 ± 0.56	1
79	HJ101738.43+385436.1	10:17:38.43	38:54:36.1	0.20588	1011.4	363.8 ± 13.7	274.9 ± 17.5	38.3 ± 1.9	7.66 ± 0.38	3
80	HJ101738.96+384817.8	10:17:38.96	38:48:17.8	0.16788	806.3	414.5 ± 8.6	311.7 ± 24.1	54.1 ± 2.8	7.11 ± 0.36	2
81	HJ101739.35+390350.1	10:17:39.35	39:03:50.1	0.20007	979.2	92.0 ± 11.6	61.1 ± 7.1	12.9 ± 0.8	2.43 ± 0.15	2
82	HJ101739.56+391549.4	10:17:39.56	39:15:49.4	0.21802	1078.2	410.2 ± 13.6	379.0 ± 8.7	61.8 ± 2.4	13.91 ± 0.55	1
83	HJ101739.79+390051.4	10:17:39.79	39:00:51.4	0.20832	1024.7	190.3 ± 13.0	154.1 ± 7.9	34.8 ± 1.2	7.13 ± 0.25	2
84	HJ101740.82+390734.0	10:17:40.82	39:07:34.0	0.20853	1025.5	167.7 ± 9.4	118.0 ± 13.5	39.5 ± 1.6	8.11 ± 0.34	2
85	HJ101741.04+385400.4	10:17:41.04	38:54:00.4	0.21506	1061.9	176.7 ± 28.6	124.6 ± 12.8	15.6 ± 1.1	3.41 ± 0.23	2
86	HJ101742.36+390133.5	10:17:42.36	39:01:33.5	0.20761	1020.8	167.5 ± 7.9	145.2 ± 9.2	14.1 ± 0.8	2.87 ± 0.17	2
87	HJ101742.53+388335.1	10:17:42.53	38:33:59.1	0.20157	987.5	203.6 ± 4.0	137.3 ± 29.8	25.8 ± 2.3	4.94 ± 0.44	3
88	HJ101742.65+390104.7	10:17:42.65	39:01:04.7	0.20793	1022.5	335.1 ± 12.0	307.4 ± 12.5	17.5 ± 1.0	3.58 ± 0.21	1
89	HJ101742.99+384953.3	10:17:42.99	38:49:53.3	0.20655	1014.8	232.6 ± 21.8	150.1 ± 18.5	38.9 ± 2.4	7.83 ± 0.49	2
90	HJ101743.40+388342.0	10:17:43.40	38:34:25.0	0.20166	988.1	119.6 ± 3.8	97.4 ± 12.6	12.4 ± 1.1	2.37 ± 0.21	2
91	HJ101744.37+391220.1	10:17:44.37	39:12:20.1	0.21056	1037.1	252.5 ± 7.6	195.2 ± 56.3	25.6 ± 1.6	5.37 ± 0.34	3
92	HJ101744.58+390444.3	10:17:44.58	39:04:44.3	0.20033	981.0	162.7 ± 12.4	117.2 ± 10.9	16.0 ± 0.9	3.02 ± 0.16	2
93	HJ101748.32+390548.9	10:17:48.32	39:05:48.9	0.21947	1086.6	404.6 ± 19.3	339.1 ± 14.4	25.5 ± 1.3	5.84 ± 0.31	1
94	HJ101749.14+385401.5	10:17:49.14	38:54:01.5	0.20697	1017.5	328.5 ± 10.7	238.3 ± 39.4	40.4 ± 2.1	8.19 ± 0.43	2
95	HJ101751.11+390924.4	10:17:51.11	39:09:24.4	0.19962	976.6	243.9 ± 24.0	140.2 ± 42.9	34.9 ± 2.1	6.54 ± 0.4	2
96	HJ101752.16+388585.7	10:17:52.16	38:58:57.1	0.20169	988.2	468.7 ± 15.2	368.8 ± 56.7	97.9 ± 2.8	18.77 ± 0.54	3
97	HJ101752.28+390109.5	10:17:52.28	39:01:09.5	0.20259	993.3	276.9 ± 13.7	158.0 ± 89.4	22.4 ± 2.4	4.34 ± 0.47	2
98	HJ101756.24+388811.3	10:17:56.24	38:38:11.3	0.20424	1002.2	243.9 ± 14.4	211.7 ± 19.0	33.1 ± 2.1	6.52 ± 0.42	2
99	HJ101757.27+391032.7	10:17:57.27	39:10:32.7	0.19946	976.1	252.5 ± 45.2	192.4 ± 38.6	21.6 ± 1.4	4.05 ± 0.27	2
100	HJ101759.55+390230.4	10:17:59.55	39:02:30.4	0.21766	1076.1	209.7 ± 20.5	152.0 ± 16.4	19.0 ± 1.1	4.27 ± 0.25	3
101	HJ101759.95+390637.9	10:17:59.95	39:06:37.9	0.20966	1032.0	345.0 ± 11.2	260.0 ± 10.9	33.2 ± 1.5	6.9 ± 0.31	1
102	HJ101800.61+391649.2	10:18:00.61	39:16:49.2	0.19884	972.6	339.9 ± 21.5	293.2 ± 62.1	42.4 ± 3.0	7.89 ± 0.57	2
103	HJ101800.62+391745.8	10:18:00.62	39:17:45.8	0.20377	999.8	217.9 ± 17.5	84.4 ± 27.4	17.1 ± 1.7	3.35 ± 0.32	3
104	HJ101801.79+390410.3	10:18:01.79	39:04:10.3	0.20227	991.5	144.0 ± 8.6	111.6 ± 10.4	10.9 ± 0.9	2.1 ± 0.18	2
105	HJ101802.74+388713.4	10:18:02.74	38:37:13.4	0.20278	994.0	204.8 ± 10.6	164.8 ± 6.8	91.1 ± 3.3	17.65 ± 0.64	2
106	HJ101803.78+388511.6	10:18:03.78	38:51:16.2	0.20448	1003.5	250.8 ± 28.4	197.5 ± 23.1	23.7 ± 1.8	4.67 ± 0.36	3
107	HJ101803.86+384125.1	10:18:03.86	38:41:25.1	0.20546	1009.1	507.2 ± 18.0	428.3 ± 45.2	83.3 ± 4.0	16.61 ± 0.79	3
108	HJ101806.12+390750.0	10:18:06.12	39:07:50.0	0.20802	1023.0	194.5 ± 27.0	151.8 ± 13.7	17.7 ± 1.0	3.62 ± 0.2	2
109	HJ101809.30+390718.2	10:18:09.30	39:07:18.2	0.20745	1019.9	391.7 ± 9.1	345.7 ± 28.7	43.4 ± 1.8	8.82 ± 0.36	2
110	HJ101809.30+390118.4	10:18:09.30	39:01:18.4	0.20419	1002.2	226.9 ± 10.6	174.1 ± 18.8	33.2 ± 1.9	6.54 ± 0.38	3
111	HJ101818.30+390414.7	10:18:18.30	39:04:14.7	0.2167	1070.9	198.2 ± 7.4	114.5 ± 33.3	25.7 ± 1.7	5.72 ± 0.37	2
112	HJ101819.92+390011.2	10:18:19.92	39:00:11.2	0.20586	1011.1	303.1 ± 13.7	213.5 ± 18.3	34.7 ± 1.4	6.93 ± 0.29	2
113	HJ101826.50+390440.4	10:18:26.50	39:04:40.4	0.22013	1090.1	130.5 ± 12.3	93.7 ± 27.5	11.3 ± 1.1	2.6 ± 0.25	2
114	HJ101831.52+392206.9	10:18:31.52	39:22:06.9	0.21759	1076.0	207.6 ± 19.2	121.0 ± 10.5	149.2 ± 3.7	33.48 ± 0.83	2
115	HJ101832.84+392003.8	10:18:32.84	39:20:03.8	0.20415	1001.8	181.5 ± 6.3	125.5 ± 37.5	20.3 ± 1.9	4.0 ± 0.38	2

Table 2.5 – continued

Index	HI ID (2)	R.A. (J2000) hh:mm:ss.ss (3)	Dec (J2000) dd:mm:ss.ss (4)	z (5)	D <sub>lum</sub> Mpc (6)	w <sub>20</sub> km s <sup>-1</sup> (7)	w <sub>50</sub> mJy km s <sup>-1</sup> (8)	S <sub>int</sub> mJy km s <sup>-1</sup> (9)	M <sub>HI</sub> (×10 <sup>9</sup> ) M <sub>⊙</sub> (10)	Type (11)
116	HLJ101832.89+391905.5	10:18:32.89	39:19:05.5	0.18658	906.3	211.3 ± 25.7	145.4 ± 27.0	49.3 ± 2.8	8.06 ± 0.46	2
117	HLJ101833.23+390403.3	10:18:33.23	39:04:03.3	0.20288	994.8	343.1 ± 22.5	282.1 ± 9.6	39.2 ± 2.4	7.61 ± 0.47	1
118	HLJ101835.11+385816.3	10:18:35.11	38:58:16.3	0.16669	800.1	380.7 ± 18.2	309.7 ± 38.6	75.1 ± 3.5	9.72 ± 0.46	1
119	HLJ101835.52+393033.1	10:18:35.52	39:30:33.1	0.20082	983.4	151.2 ± 16.2	110.0 ± 17.2	70.7 ± 6.8	13.44 ± 1.3	2
120	HLJ101836.50+383951.5	10:18:36.50	38:39:51.5	0.21792	1078.1	370.7 ± 23.8	209.7 ± 19.7	70.6 ± 3.9	15.91 ± 0.88	2
121	HLJ101846.20+385914.4	10:18:46.20	38:59:14.4	0.20128	985.9	254.4 ± 24.0	197.7 ± 35.4	42.0 ± 3.0	8.03 ± 0.58	3
122	HLJ101857.33+384526.0	10:18:57.33	38:45:26.0	0.17594	848.8	232.9 ± 13.1	177.0 ± 14.1	97.8 ± 4.0	14.14 ± 0.57	2
123	HLJ101903.22+390217.0	10:19:03.22	39:02:17.0	0.21708	1073.4	164.2 ± 9.5	116.8 ± 16.9	31.5 ± 1.9	7.03 ± 0.43	2
124	HLJ101914.04+391132.9	10:19:14.04	39:11:32.9	0.2043	1002.5	434.3 ± 8.4	397.2 ± 11.4	90.0 ± 4.2	17.72 ± 0.82	3
125	HLJ101934.16+383610.4	10:19:34.16	38:36:10.4	0.20055	981.9	330.3 ± 12.6	294.7 ± 13.1	229.3 ± 8.1	43.46 ± 1.54	3
126	HLJ101946.23+383611.4	10:19:46.23	38:36:11.4	0.20928	1030.2	150.7 ± 11.2	104.1 ± 18.8	152.0 ± 14.4	31.48 ± 2.99	2
127	HLJ101954.60+390853.7	10:19:54.60	39:08:53.7	0.1917	933.8	171.8 ± 9.3	131.4 ± 10.5	62.4 ± 3.4	10.78 ± 0.59	2

**Table 2.6** – Catalogue containing the HI properties of the detected galaxies in A2192. The description of each column is provided in Sect. 2.3.8 of this chapter.

Index	HI ID	R.A. (J2000) hh:mm:ss.ss	Dec (J2000) dd:mm:ss.ss	z	D <sub>lum</sub> Mpc	w <sub>20</sub> km s <sup>-1</sup>	w <sub>50</sub> mJy km s <sup>-1</sup>	S <sub>int</sub> mJy km s <sup>-1</sup>	M <sub>HI</sub> (×10 <sup>9</sup> ) M <sub>⊙</sub>	Type
(1)	(2)	(3)	(4)	(5)	(6)	(7)	(8)	(9)	(10)	(11)
1	H1J162451.47+422835.4	16:24:51.47	42:28:35.4	0.18956	922.2	128.5 ± 6.5	100.2 ± 11.3	27.7 ± 2.3	4.67 ± 0.38	3
2	H1J162453.90+422819.1	16:24:53.90	42:28:19.1	0.18915	920.2	93.6 ± 5.5	70.8 ± 6.0	20.1 ± 1.6	3.38 ± 0.27	2
3	H1J162508.17+423409.0	16:25:08.17	42:34:09.0	0.18746	910.8	154.2 ± 10.5	67.2 ± 8.5	23.7 ± 1.3	3.91 ± 0.22	2
4	H1J162510.48+424033.8	16:25:10.48	42:40:33.8	0.18727	909.9	262.7 ± 8.5	237.9 ± 12.5	35.1 ± 1.8	5.78 ± 0.3	3
5	H1J162515.22+423059.6	16:25:15.22	42:30:59.6	0.18656	906.1	201.8 ± 9.0	167.8 ± 14.5	42.3 ± 2.0	6.91 ± 0.33	2
6	H1J162528.35+424708.7	16:25:28.35	42:47:08.7	0.18914	919.9	140.2 ± 5.5	94.9 ± 11.0	57.2 ± 2.0	9.61 ± 0.34	2
7	H1J162533.39+423737.8	16:25:33.39	42:37:37.8	0.20094	984.0	293.0 ± 12.6	263.2 ± 17.7	26.9 ± 2.0	5.12 ± 0.38	1
8	H1J162536.15+425559.3	16:25:36.15	42:55:59.3	0.16842	809.0	169.7 ± 19.4	140.9 ± 16.7	25.9 ± 2.4	3.42 ± 0.32	2
9	H1J162536.33+424132.7	16:25:36.33	42:41:32.7	0.19046	927.1	84.5 ± 9.3	60.1 ± 10.5	19.0 ± 1.8	3.23 ± 0.3	2
10	H1J162544.48+424955.2	16:25:44.48	42:49:55.2	0.17005	817.6	301.2 ± 13.3	255.2 ± 20.4	69.7 ± 3.7	9.4 ± 0.5	3
11	H1J162548.25+422633.2	16:25:48.25	42:26:33.2	0.18993	924.4	120.7 ± 8.8	86.9 ± 6.8	37.3 ± 1.8	6.33 ± 0.3	2
12	H1J162556.66+422421.2	16:25:56.66	42:24:21.2	0.19008	925.2	149.8 ± 17.5	105.2 ± 17.0	16.0 ± 1.4	2.72 ± 0.24	2
13	H1J162557.88+425320.7	16:25:57.88	42:53:20.7	0.16869	810.5	475.1 ± 8.6	452.9 ± 6.6	83.9 ± 4.1	11.13 ± 0.55	1
14	H1J162558.15+422650.8	16:25:58.15	42:26:50.8	0.18874	917.6	288.8 ± 7.3	257.2 ± 6.8	75.8 ± 2.7	12.68 ± 0.45	1
15	H1J162559.73+424240.3	16:25:59.73	42:42:40.3	0.17507	844.4	225.1 ± 12.9	178.1 ± 34.1	31.0 ± 2.3	4.43 ± 0.33	2
16	H1J162602.94+425053.5	16:26:02.94	42:50:53.5	0.1888	918.1	328.1 ± 16.5	226.0 ± 21.5	25.3 ± 1.9	4.23 ± 0.32	2
17	H1J162607.60+424126.7	16:26:07.60	42:41:26.7	0.19014	925.4	375.6 ± 11.5	270.6 ± 20.0	42.5 ± 2.0	7.22 ± 0.33	3
18	H1J162607.84+424218.2	16:26:07.84	42:42:18.2	0.18975	923.3	235.4 ± 8.3	210.4 ± 13.8	19.0 ± 1.3	3.22 ± 0.23	2
19	H1J162611.86+425158.2	16:26:11.86	42:51:58.2	0.18813	914.6	133.1 ± 13.3	81.0 ± 19.8	24.8 ± 1.7	4.12 ± 0.28	2
20	H1J162613.28+423307.4	16:26:13.28	42:33:07.4	0.22403	1111.4	147.6 ± 6.7	128.1 ± 8.2	21.9 ± 1.4	5.22 ± 0.33	3
21	H1J162614.39+424632.3	16:26:14.39	42:46:32.3	0.1917	933.7	237.3 ± 9.0	197.7 ± 38.4	28.6 ± 1.7	4.94 ± 0.29	3
22	H1J162616.29+423347.7	16:26:16.29	42:33:47.7	0.22421	1112.5	62.4 ± 7.7	26.0 ± 10.1	5.2 ± 0.5	1.25 ± 0.13	3
23	H1J162616.50+424709.4	16:26:16.50	42:47:09.4	0.19054	927.6	149.6 ± 21.3	93.7 ± 24.1	16.9 ± 1.7	2.87 ± 0.29	2
24	H1J162618.03+423811.8	16:26:18.03	42:38:11.8	0.19084	929.2	381.3 ± 8.8	360.5 ± 9.3	29.3 ± 1.7	5.01 ± 0.3	1
25	H1J162623.68+423942.3	16:26:23.68	42:39:42.3	0.17154	825.6	170.4 ± 5.9	147.5 ± 8.9	28.2 ± 2.0	3.87 ± 0.28	2
26	H1J162631.59+424316.2	16:26:31.59	42:43:16.2	0.19136	932.0	188.1 ± 6.0	147.5 ± 18.8	32.6 ± 1.3	5.61 ± 0.23	2
27	H1J162644.27+423915.5	16:26:44.27	42:39:15.5	0.19056	927.7	278.4 ± 7.5	251.6 ± 16.0	22.8 ± 1.7	3.89 ± 0.29	1
28	H1J162644.34+422535.4	16:26:44.34	42:25:35.4	0.18924	920.5	200.0 ± 13.5	156.7 ± 14.0	37.4 ± 2.3	6.3 ± 0.38	3
29	H1J162647.77+423204.0	16:26:47.77	42:32:04.0	0.22062	1092.9	211.5 ± 7.5	187.1 ± 7.5	34.5 ± 1.9	7.27 ± 0.43	1
30	H1J162651.87+422710.8	16:26:51.87	42:27:10.8	0.18759	911.6	278.7 ± 6.5	229.2 ± 17.0	21.5 ± 1.5	4.04 ± 0.25	1
31	H1J162652.61+422839.4	16:26:52.61	42:28:39.4	0.22086	1094.3	279.9 ± 9.8	249.5 ± 12.6	26.2 ± 1.9	6.07 ± 0.45	3
32	H1J162706.48+422458.6	16:27:06.48	42:24:58.6	0.18813	914.6	379.4 ± 8.3	353.4 ± 5.3	123.9 ± 3.7	20.58 ± 0.62	1
33	H1J162711.02+422758.8	16:27:11.02	42:27:58.8	0.17253	831.2	167.6 ± 17.8	118.2 ± 12.1	46.6 ± 2.3	6.48 ± 0.31	2
34	H1J162716.67+424203.3	16:27:16.67	42:42:03.3	0.18974	923.3	138.2 ± 9.5	78.9 ± 14.8	20.3 ± 1.3	3.43 ± 0.22	2
35	H1J162720.61+424947.4	16:27:20.61	42:49:47.4	0.22009	1089.9	204.2 ± 22.3	160.5 ± 19.5	20.3 ± 1.5	4.68 ± 0.35	2
36	H1J162720.90+425159.4	16:27:20.90	42:51:59.4	0.17374	837.4	190.5 ± 21.7	114.1 ± 25.7	19.4 ± 1.6	2.74 ± 0.23	2
37	H1J162738.09+423814.7	16:27:38.09	42:38:14.7	0.20066	982.8	140.0 ± 7.8	117.0 ± 10.6	18.6 ± 2.1	3.54 ± 0.4	2
38	H1J162750.18+430109.2	16:27:50.18	43:01:09.2	0.18882	918.3	117.6 ± 9.5	74.8 ± 17.3	30.6 ± 2.2	5.12 ± 0.37	2
39	H1J162844.33+422617.8	16:28:44.33	42:26:17.8	0.17095	822.5	212.2 ± 25.1	178.7 ± 17.7	54.9 ± 3.7	7.48 ± 0.51	2

**Table 2.7** – The optical properties of the HI detected galaxies in A963. The description of each column is provided in Sect. 2.4.3 of this chapter.

Index	SDSS ID	R.A (J2000) hh:mm:ss.ss	Dec (J2000) dd:mm:ss.s	P.A °	$z_{\text{opt}}$	$M_B$	$M_R$	$M_{\text{NUV}}$	$M_{\text{FUV}}$
(1)	(2)	(3)	(4)	(5)	(6)	(7)	(8)	(9)	(10)
1	SJ101438.70+385445.0	10:14:38.70	38:54:45.0	2	0.17360	21.8	19.8	23.3	24.4
2	SJ101523.65+390941.2	10:15:23.65	39:09:41.2	64	0.19030	20.0	18.5	21.5	22.2
3	SJ101534.80+385746.4	10:15:34.80	38:57:46.4	39	0.0	22.4	21.0	22.9	23.7
4	SJ101536.22+384532.7	10:15:36.22	38:45:32.7	168	0.20555	19.8	18.6	20.6	21.2
5	SJ101537.01+390334.6	10:15:37.01	39:03:34.6	84	0.21040	21.2	19.7	22.1	22.6
6	SJ101540.19+384913.7	10:15:40.19	38:49:13.7	89	0.20351	19.8	18.1	21.0	21.5
7	SJ101600.10+385205.5	10:16:00.10	38:52:05.5	64	0.20866	21.2	20.1	21.5	22.0
8	SJ101605.77+385121.6	10:16:05.77	38:51:21.6	23	0.0	21.4	20.3	22.6	23.1
9	SJ101611.13+384924.3	10:16:11.13	38:49:24.3	89	0.20600	19.2	17.4	21.0	21.6
10	SJ101613.68+390437.8	10:16:13.68	39:04:37.8	79	0.18949	20.5	18.8	22.2	22.8
11	SJ101613.95+385122.4	10:16:13.95	38:51:22.4	60	0.20712	21.1	19.7	22.1	22.8
12	iJ101617.72+384255.5	10:16:17.72	38:42:55.5	44	0.0	19.8 <sup>†</sup>	18.9 <sup>†</sup>	20.1	21.5
13	SJ101618.23+384254.4	10:16:18.23	38:42:54.4	86	0.20107	19.8	18.4	20.9	21.5
14	SJ101621.18+390757.7	10:16:21.18	39:07:57.7	176	0.20666	21.2	20.0	21.7	22.4
15	SJ101620.90+391552.7	10:16:20.90	39:15:52.7	166	0.16719	21.6	20.3	22.4	23.1
16	iJ101623.56+390954.5	10:16:23.56	39:09:54.5	0	0.0	16.2 <sup>†</sup>	14.6 <sup>†</sup>	21.2	21.9
17	SJ101624.25+390742.4	10:16:24.25	39:07:42.4	62	0.20199	21.4	20.3	21.7	22.2
18	SJ101625.10+384405.2	10:16:25.10	38:44:05.2	138	0.20750	22.2	20.9	23.3	23.5
19	SJ101625.03+391101.0	10:16:25.03	39:11:01.0	53	0.16752	20.3	19.2	21.0	21.7
20	SJ101626.35+391900.8	10:16:26.35	39:19:00.8	23	0.21737	21.1	19.1	22.0	22.8
21	SJ101627.91+390457.6	10:16:27.91	39:04:57.6	154	0.16528	20.4	19.2	21.1	21.5
22	SJ101628.18+390931.9	10:16:28.18	39:09:31.9	58	0.21035	19.1	17.8	20.3	21.3
23	SJ101629.17+391256.0	10:16:29.17	39:12:56.0	21	0.21020	19.3	18.0	20.5	21.2
24	SJ101636.11+384434.4	10:16:36.11	38:44:34.4	25	0.20774	20.9	19.5	20.8	21.5
25	SJ101640.03+391706.1	10:16:40.03	39:17:06.1	153	0.0	22.7	21.6	22.5	22.9
26	SJ101640.94+385449.5	10:16:40.94	38:54:49.5	18	0.0	20.5	18.0	23.1	23.5
27	SJ101641.08+391025.7	10:16:41.08	39:10:25.7	83	0.21031	20.0	18.8	20.6	21.2
28	SJ101642.81+390135.4	10:16:42.81	39:01:35.4	95	0.16498	19.7	18.7	20.5	21.2
29	SJ101642.34+385900.5	10:16:42.34	38:59:00.5	133	0.16877	20.4	19.2	21.2	21.9
30	SJ101643.17+391510.3	10:16:43.17	39:15:10.3	73	0.21835	20.9	19.5	21.5	22.1
31	SJ101644.46+390744.6	10:16:44.46	39:07:44.6	128	0.20785	21.0	19.6	22.3	22.7
32	SJ101645.41+391940.7	10:16:45.41	39:19:40.7	84	0.16879	20.8	19.2	20.6	21.1
33	SJ101646.51+384720.3	10:16:46.51	38:47:20.3	71	0.20879	20.8	19.5	21.9	22.3
34	SJ101645.33+384953.0	10:16:45.33	38:49:53.0	161	0.0	23.3	22.1	24.1	24.1
35	SJ101646.94+390901.6	10:16:46.94	39:09:01.6	61	0.20969	21.1	20.0	21.4	21.9
36	SJ101658.04+385323.9	10:16:58.04	38:53:23.9	96	0.0	22.3	20.7	22.5	23.3
37	SJ101701.11+384258.9	10:17:01.11	38:42:58.9	87	0.20327	20.7	19.3	21.5	22.1
38	SJ101701.54+390008.6	10:17:01.54	39:00:08.6	26	0.16495	20.9	19.8	21.4	21.7
39	SJ101702.66+385143.1	10:17:02.66	38:51:43.1	80	0.21623	22.9	21.1	24.7	0.0
40	SJ101702.77+385115.5	10:17:02.77	38:51:15.5	145	0.20558	21.3	19.7	22.9	23.4
41	SJ101703.62+391018.0	10:17:03.62	39:10:18.0	88	0.21949	21.2	19.7	21.8	22.6
42	SJ101705.11+391755.4	10:17:05.11	39:17:55.4	155	0.0	21.7	20.2	22.7	23.4
43	SJ101704.47+384251.0	10:17:04.47	38:42:51.0	97	0.18100	21.4	19.5	22.4	23.0
44	SJ101705.62+391016.1	10:17:05.62	39:10:16.1	58	0.0	21.6	20.4	22.0	22.3
45	SJ101705.49+384924.8	10:17:05.49	38:49:24.8	92	0.20437	20.1	18.4	21.5	22.2
46	SJ101708.63+385924.4	10:17:08.63	38:59:24.4	54	0.21000	21.6	20.4	21.8	22.3
47	SJ101709.20+391800.5	10:17:09.20	39:18:00.5	15	0.21933	21.7	20.5	22.0	22.5
48	SJ101709.09+391136.2	10:17:09.09	39:11:36.2	15	0.21835	21.1	19.8	21.8	22.3
49	SJ101710.61+384714.8	10:17:10.61	38:47:14.8	155	0.20702	22.2	21.1	22.6	22.3
50	SJ101711.90+385421.6	10:17:11.90	38:54:21.6	61	0.21607	21.9	20.1	24.3	24.5
51	SJ101712.50+390254.7	10:17:12.50	39:02:54.7	131	0.0	21.5	19.7	23.2	23.4
52	SJ101712.50+391124.3	10:17:12.50	39:11:24.3	70	0.21040	22.0	20.8	22.3	22.7
53	SJ101712.30+384426.5	10:17:12.30	38:44:26.5	46	0.20574	21.1	19.6	22.1	22.7
54	SJ101717.55+391334.5	10:17:17.55	39:13:34.5	136	0.21062	20.3	19.3	20.7	21.3
55	SJ101719.62+390556.5	10:17:19.62	39:05:56.5	99	0.21008	21.0	19.8	21.6	22.0
56	SJ101719.41+385833.7	10:17:19.41	38:58:33.7	129	0.21737	21.2	20.1	21.7	21.9
57	SJ101719.92+384608.0	10:17:19.92	38:46:08.0	78	0.20620	20.9	19.5	21.7	22.0
58	SJ101721.45+391052.0	10:17:21.45	39:10:52.0	105	0.19812	20.6	18.6	22.7	23.4
59	SJ101722.03+390153.8	10:17:22.03	39:01:53.8	132	0.19892	20.4	19.0	21.4	21.9
60	SJ101723.76+392801.3	10:17:23.76	39:28:01.3	1	0.20271	21.8	20.8	21.7	22.0

<sup>†</sup> Galaxies close to bright stars or at the edge of the field (A963 only) with incorrect/unavailable INT magnitudes. The values given are converted from SDSS u, g, r, and i magnitudes.

Table 2.7 – continued

Index	SDSS ID	R.A (J2000) hh:mm:ss.ss	Dec (J2000) dd:mm:ss.s	P.A. °	$z_{\text{opt}}$	$M_B$	$M_R$	$M_{\text{NUV}}$	$M_{\text{FUV}}$
(1)	(2)	(3)	(4)	(5)	(6)	(7)	(8)	(9)	(10)
61	SJ101723.76+390253.9	10:17:23.76	39:02:53.9	114	0.0	20.3	18.9	21.6	22.1
62	SJ101724.17+383309.4	10:17:24.17	38:33:09.4	123	0.0	22.7	19.8	24.2	-
63	SJ101725.11+390316.5	10:17:25.11	39:03:16.5	73	0.20815	20.4	18.8	21.7	22.2
64	SJ101725.91+390522.2	10:17:25.91	39:05:22.2	89	0.16929	20.7	19.7	21.3	21.5
65	SJ101727.08+384143.6	10:17:27.08	38:41:43.6	20	0.20658	19.7	18.0	20.9	21.3
66	SJ101727.05+390453.2	10:17:27.05	39:04:53.2	86	0.0	21.9	21.0	21.8	22.4
67	SJ101727.72+384627.8	10:17:27.72	38:46:27.8	69	0.20113	20.1	18.5	21.3	22.0
68	SJ101728.04+385952.1	10:17:28.04	38:59:52.1	72	0.12000	20.9	19.7	21.4	22.0
69	SJ101729.04+390402.8	10:17:29.04	39:04:02.8	67	0.16947	18.8	17.7	19.5	20.1
70	SJ101729.66+384631.0	10:17:29.66	38:46:31.0	79	0.16870	21.6	20.3	22.3	22.6
71	SJ101730.00+390830.6	10:17:30.00	38:58:30.6	68	0.20414	21.0	19.4	21.8	22.6
72	SJ101730.24+383154.6	10:17:30.24	38:31:54.6	155	0.0	21.7	19.9	21.3	22.0
73	SJ101730.01+390407.7	10:17:30.01	39:04:07.7	84	0.16780	19.8	18.7	20.6	21.3
74	SJ101731.48+383418.3	10:17:31.48	38:34:18.3	106	0.20367	19.4	17.9	20.6	21.3
75	SJ101731.91+385401.2	10:17:31.91	38:54:01.2	15	0.21563	20.7	19.4	21.6	22.1
76	SJ101734.62+391353.5	10:17:34.62	39:13:53.5	79	0.21794	21.0	19.7	21.8	22.3
77	SJ101735.30+390413.5	10:17:35.30	39:04:13.5	79	0.20927	20.5	19.0	21.5	22.2
78	SJ101737.03+391005.8	10:17:37.03	39:10:05.8	86	0.21786	20.4	18.7	21.7	22.5
79	SJ101738.53+385431.9	10:17:38.53	38:54:31.9	104	0.205906	20.7	19.2	21.4	22.0
80	SJ101738.32+384806.7	10:17:38.32	38:48:06.7	84	0.16779	21.1	19.8	21.7	22.0
81	SJ101739.14+390345.9	10:17:39.14	39:03:45.9	104	0.20023	21.0	19.8	21.2	21.9
82	SJ101739.82+391547.9	10:17:39.82	39:15:47.9	94	0.21802	21.3	19.4	22.6	23.2
83	IJ101739.86+390055.6	10:17:39.86	39:00:55.6	109	0.0	21.1	19.9	21.1	22.0
84	SJ101740.72+390733.9	10:17:40.72	39:07:33.9	47	0.20861	20.3	19.2	20.9	21.3
85	SJ101741.33+385358.5	10:17:41.33	38:53:58.5	23	0.21525	21.5	20.2	22.2	22.5
86	SJ101742.42+390135.8	10:17:42.42	39:01:35.8	80	0.0	21.3	20.1	21.8	22.2
87	SJ101742.86+383358.8	10:17:42.86	38:33:58.8	117	0.20160	22.2	20.7	23.0	25.1
88	SJ101742.99+390105.4	10:17:42.99	39:01:05.4	98	0.20891	21.3	19.4	23.1	23.7
89	SJ101742.98+384949.4	10:17:42.98	38:49:49.4	87	0.20668	21.8	20.7	22.3	22.4
90	SJ101742.88+383414.4	10:17:42.88	38:34:14.4	159	0.0	23.0	21.5	23.7	24.6
91	SJ101744.26+391217.7	10:17:44.26	39:12:17.7	167	0.21056	21.0	19.3	21.8	22.5
92	SJ101744.57+390446.4	10:17:44.57	39:04:46.4	91	0.20048	20.8	19.5	21.6	22.2
93	SJ101748.10+390544.4	10:17:48.10	39:05:44.4	122	0.21949	21.4	19.5	22.4	23.0
94	SJ101748.72+385356.5	10:17:48.72	38:53:56.5	109	0.0	24.0	22.5	22.6	23.0
95	SJ101751.16+390922.8	10:17:51.16	39:09:22.8	142	0.19959	21.0	19.9	21.6	22.1
96	SJ101752.21+385857.3	10:17:52.21	38:58:57.3	30	0.20160	21.1	19.2	22.7	23.2
97	SJ101752.29+390111.2	10:17:52.29	39:01:11.2	36	0.20256	21.6	20.4	21.9	22.2
98	SJ101756.25+383807.3	10:17:56.25	38:38:07.3	54	0.20499	19.9	18.9	20.5	21.0
99	SJ101757.22+391039.6	10:17:57.22	39:10:39.6	106	0.0	22.7	21.3	22.5	23.1
100	SJ101759.77+390238.7	10:17:59.77	39:02:38.7	35	0.21769	21.9	20.6	0.0	22.9
101	SJ101759.72+390636.5	10:17:59.72	39:06:36.5	22	0.20975	20.2	18.8	21.2	21.8
102	SJ101759.13+391658.1	10:17:59.13	39:16:58.1	55	0.19875	22.1	20.6	23.4	24.0
103	SJ101800.16+391743.6	10:18:00.16	39:17:43.6	175	0.20580	21.8	20.7	22.4	22.9
104	SJ101801.71+390407.2	10:18:01.71	39:04:07.2	179	0.20224	22.7	21.4	23.0	23.4
105	SJ101802.66+383703.9	10:18:02.66	38:37:03.9	166	0.20271	19.8	18.6	20.6	21.0
106	SJ101803.84+385107.1	10:18:03.84	38:51:07.1	26	0.20447	22.4	21.5	21.8	22.9
107	SJ101803.65+384119.7	10:18:03.65	38:41:19.7	111	0.20560	19.3	17.7	20.3	20.8
108	SJ101806.11+390753.2	10:18:06.11	39:07:53.2	115	0.20799	20.4	18.7	21.8	22.4
109	SJ101809.25+390716.6	10:18:09.25	39:07:16.6	107	0.20750	20.4	18.9	21.5	22.1
110	SJ101809.12+390118.5	10:18:09.12	39:01:18.5	137	0.20415	22.7	21.5	23.3	23.4
111	SJ101818.32+390418.1	10:18:18.32	39:04:18.1	99	0.21655	21.2	19.4	22.5	22.8
112	SJ101819.97+390009.6	10:18:19.97	39:00:09.6	175	0.20593	20.2	18.8	20.8	21.0
113	SJ101826.87+390434.9	10:18:26.87	39:04:34.9	155	0.22015	21.4	20.2	22.0	22.4
114	SJ101831.47+392158.2	10:18:31.47	39:21:58.2	147	0.21753	18.8	17.0	20.2	20.7
115	SJ101833.02+391954.8	10:18:33.02	39:19:54.8	89	0.20415	21.3	20.0	22.3	22.6
116	SJ101832.47+391912.3	10:18:32.47	39:19:12.3	69	0.18654	21.6	20.6	21.9	21.8
117	SJ101833.28+390356.5	10:18:33.28	39:03:56.5	83	0.20287	19.2	17.7	20.5	21.4
118	SJ101835.20+385816.9	10:18:35.20	38:58:16.9	133	0.16660	19.7	17.9	21.1	21.7
119	SJ101835.83+393032.8	10:18:35.83	39:30:32.8	96	0.20081	22.2	20.6	22.1	23.6
120	SJ101836.67+383949.7	10:18:36.67	38:39:49.7	103	0.21786	21.8	20.5	19.9	20.5
121	SJ101846.27+385915.1	10:18:46.27	38:59:15.1	69	0.20156	20.1	18.6	21.2	22.0
122	SJ101857.32+384517.6	10:18:57.32	38:45:17.6	5	0.0	19.8	18.3	21.1	21.7
123	SJ101903.39+390207.6	10:19:03.39	39:02:07.6	140	0.21704	21.5	20.1	22.2	22.8
124	SJ101913.95+391122.2	10:19:13.95	39:11:22.2	90	0.20415	19.8	18.2	21.0	21.8
125	SJ101933.54+383626.6	10:19:33.54	38:36:26.6	0	0.20050	18.9 <sup>†</sup>	16.9 <sup>†</sup>	0.0	0.0

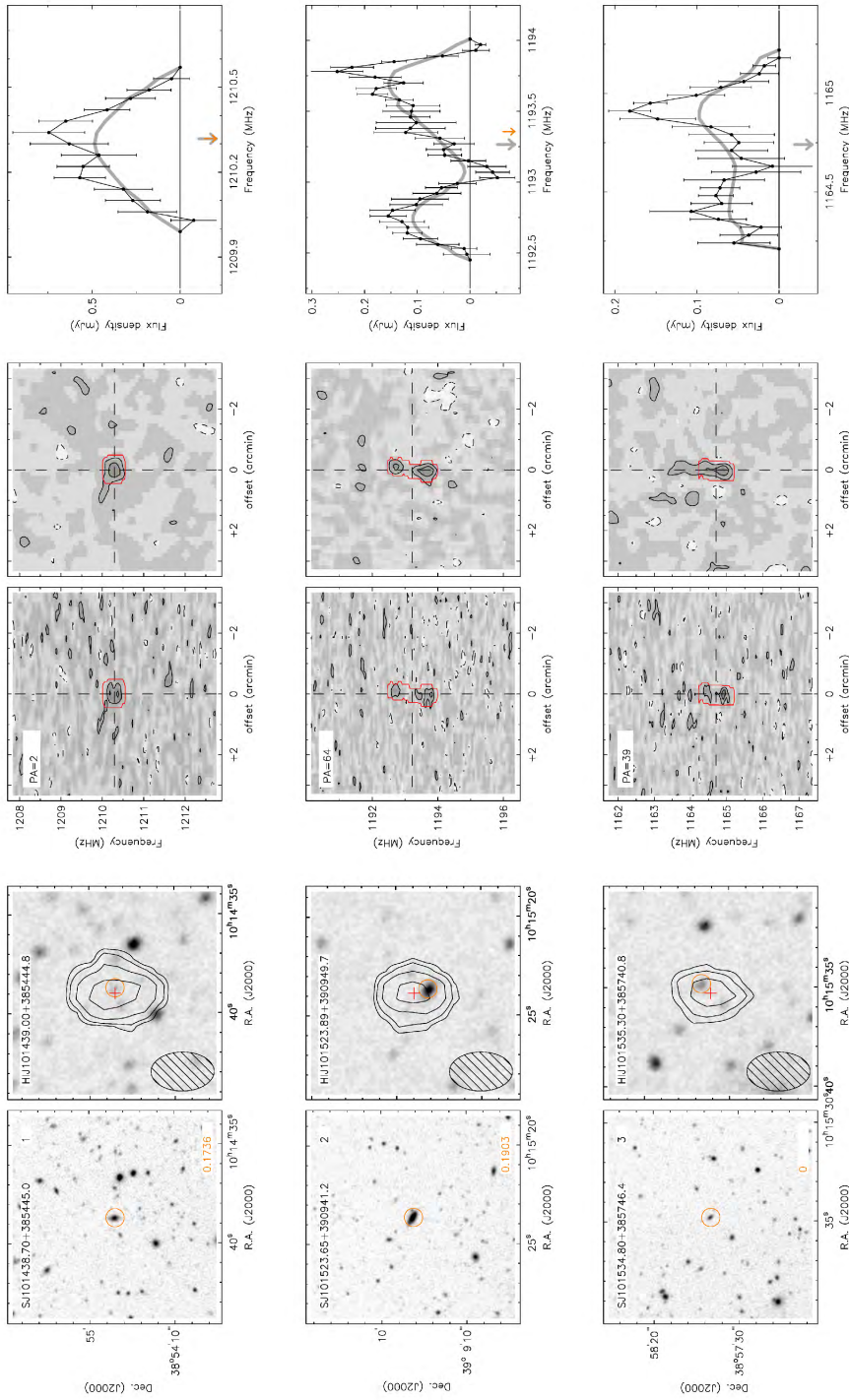
Table 2.7 – continued

Index	SDSS ID	R.A (J2000) hh:mm:ss.ss	Dec (J2000) dd:mm:ss.s	P.A. °	$z_{\text{opt}}$	$M_{\text{B}}$	$M_{\text{R}}$	$M_{\text{NUV}}$	$M_{\text{FUV}}$
(1)	(2)	(3)	(4)	(5)	(6)	(7)	(8)	(9)	(10)
126	SJ101944.68+383614.0	10:19:44.68	38:36:14.0	0	0.0	22.1 <sup>†</sup>	19.6 <sup>†</sup>	0.0	0.0
127	SJ101954.68+390844.26	10:19:54.68	39:08:44.26	0	0.0	22.4 <sup>†</sup>	22.0 <sup>†</sup>	20.4	21.2

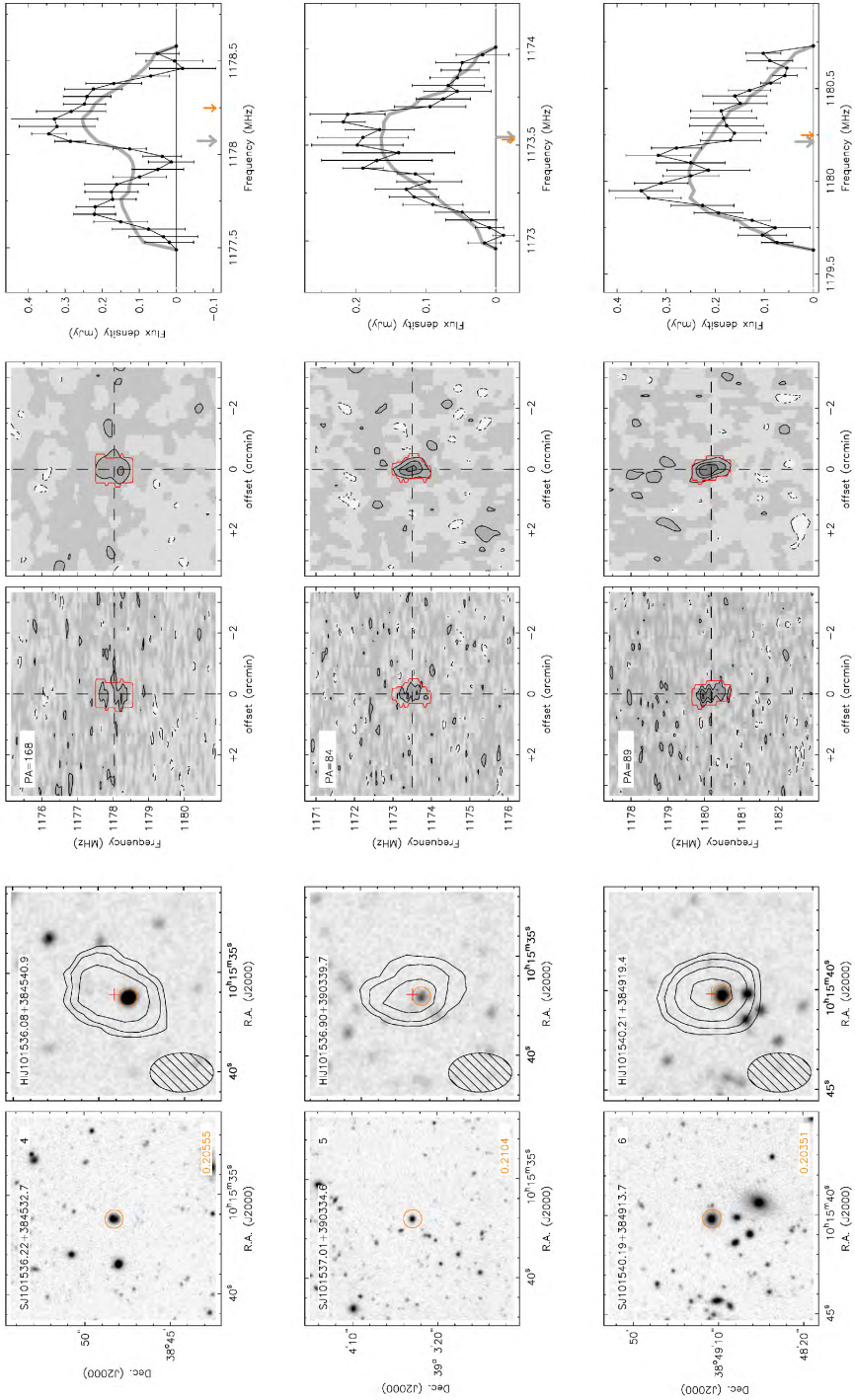
Table 2.8 – The optical properties of the HI detected galaxies in A2192. The description of each column is provided in Sect. 2.4.3 of this chapter.

Index	SDSS ID	R.A (J2000) hh:mm:ss.ss	Dec (J2000) dd:mm:ss.s	P.A. °	$z_{\text{opt}}$	$M_{\text{B}}$	$M_{\text{R}}$	$M_{\text{NUV}}$	$M_{\text{FUV}}$
(1)	(2)	(3)	(4)	(5)	(6)	(7)	(8)	(9)	(10)
1	SJ162451.64+422828.0	16:24:51.64	42:28:28.0	37	0.18943	20.9	20.0	21.3	21.7
2	SJ162454.44+422823.9	16:24:54.44	42:28:23.9	158	0.0	21.7	20.1	22.5	24.6
3	SJ162507.59+423408.6	16:25:07.59	42:34:08.6	20	0.0	19.4	18.2	20.3	21.0
4	SJ162510.56+424028.8	16:25:10.56	42:40:28.8	111	0.18750	20.4	19.2	21.3	21.8
5	SJ162515.35+423057.0	16:25:15.35	42:30:57.0	99	0.0	20.0 <sup>†</sup>	18.8 <sup>†</sup>	19.3	19.7
6	SJ162528.34+424708.8	16:25:28.34	42:47:08.8	4	0.18903	19.0	17.8	19.9	20.6
7	SJ162533.32+423742.8	16:25:33.32	42:37:42.8	41	0.0	22.4 <sup>†</sup>	20.8 <sup>†</sup>	21.8	23.1
8	SJ162536.21+425558.8	16:25:36.21	42:55:58.8	167	0.0	20.3	19.2	21.2	21.6
9	SJ162536.16+424131.8	16:25:36.16	42:41:31.8	31	0.19020	20.7	19.5	21.6	22.1
10	SJ162544.36+424953.1	16:25:44.36	42:49:53.1	156	0.16797	19.5	17.6	21.4	22.0
11	SJ162548.41+422632.3	16:25:48.41	42:26:32.3	73	0.18993	19.5	18.4	20.1	20.8
12	SJ162556.96+422416.0	16:25:56.96	42:24:16.0	103	0.19003	21.0	19.7	21.5	22.0
13	SJ162558.03+425319.4	16:25:58.03	42:53:19.4	171	0.16875	19.1	17.5	20.5	21.2
14	SJ162558.29+422651.3	16:25:58.29	42:26:51.3	54	0.0	19.1	17.6	20.3	20.8
15	SJ162600.24+424235.8	16:26:00.24	42:42:35.8	108	0.0	20.4	18.8	20.5	22.2
16	SJ162602.68+425054.8	16:26:02.68	42:50:54.8	61	0.0	20.8	19.2	22.4	23.0
17	SJ162607.85+424128.4	16:26:07.85	42:41:28.4	119	0.19014	19.4	18.1	20.6	21.3
18	SJ162607.94+424215.9	16:26:07.94	42:42:15.9	93	0.0	21.7	20.6	22.5	22.8
19	SJ162612.06+425147.8	16:26:12.06	42:51:47.8	172	0.18778	20.5	19.3	21.2	21.8
20	SJ162613.37+423303.7	16:26:13.37	42:33:03.7	33	0.22420	19.5	18.1	20.4	21.0
21	SJ162614.11+424631.5	16:26:14.11	42:46:31.5	151	0.19190	21.0	19.6	22.5	23.2
22	SJ162616.39+423348.0	16:26:16.39	42:33:48.0	62	0.0	21.9	20.7	22.6	22.7
23	SJ162616.42+424703.6	16:26:16.42	42:47:03.6	107	0.0	22.9	21.7	23.4	23.9
24	SJ162618.09+423808.9	16:26:18.09	42:38:08.9	100	0.19073	20.7	19.2	22.0	22.6
25	SJ162623.81+423938.8	16:26:23.81	42:39:38.8	162	0.0	21.5	20.4	22.3	22.4
26	SJ162631.71+424315.3	16:26:31.71	42:43:15.3	148	0.19142	18.9	17.6	19.9	20.5
27	SJ162644.36+423918.2	16:26:44.36	42:39:18.2	86	0.19107	21.2	19.9	21.9	22.3
28	SJ162644.64+422529.7	16:26:44.64	42:25:29.7	130	0.18960	18.4	17.0	19.6	20.3
29	SJ162647.80+423205.7	16:26:47.80	42:32:05.7	123	0.22025	20.3	18.7	21.2	21.8
30	SJ162651.30+422709.9	16:26:51.30	42:27:09.9	19	0.18770	21.4	20.3	22.2	22.7
31	SJ162652.56+422836.6	16:26:52.56	42:28:36.6	6	0.22138	20.8	19.5	21.3	22.0
32	SJ162706.47+422500.2	16:27:06.47	42:25:00.2	29	0.18812	18.9	17.5	20.0	20.3
33	SJ162710.80+422753.5	16:27:10.80	42:27:53.5	120	0.17128	19.6	18.1	20.8	21.5
34	SJ162716.61+424205.6	16:27:16.61	42:42:05.6	167	0.0	22.8	22.0	22.0	22.4
35	SJ162720.95+424951.1	16:27:20.95	42:49:51.1	134	0.0	20.4	18.8	21.1	22.5
36	SJ162721.54+425148.4	16:27:21.54	42:51:48.4	105	0.0	22.8	21.6	22.5	23.8
37	SJ162737.70+423817.6	16:27:37.70	42:38:17.6	105	0.0	15.4 <sup>†</sup>	13.9 <sup>†</sup>	19.6	21.5
38	SJ162750.22+430105.7	16:27:50.22	43:01:05.7	55	0.18927	20.2	19.1	20.6	20.9
39	SJ162843.80+422618.2	16:28:43.80	42:26:18.2	43	0.0	20.9	19.9	21.6	22.0

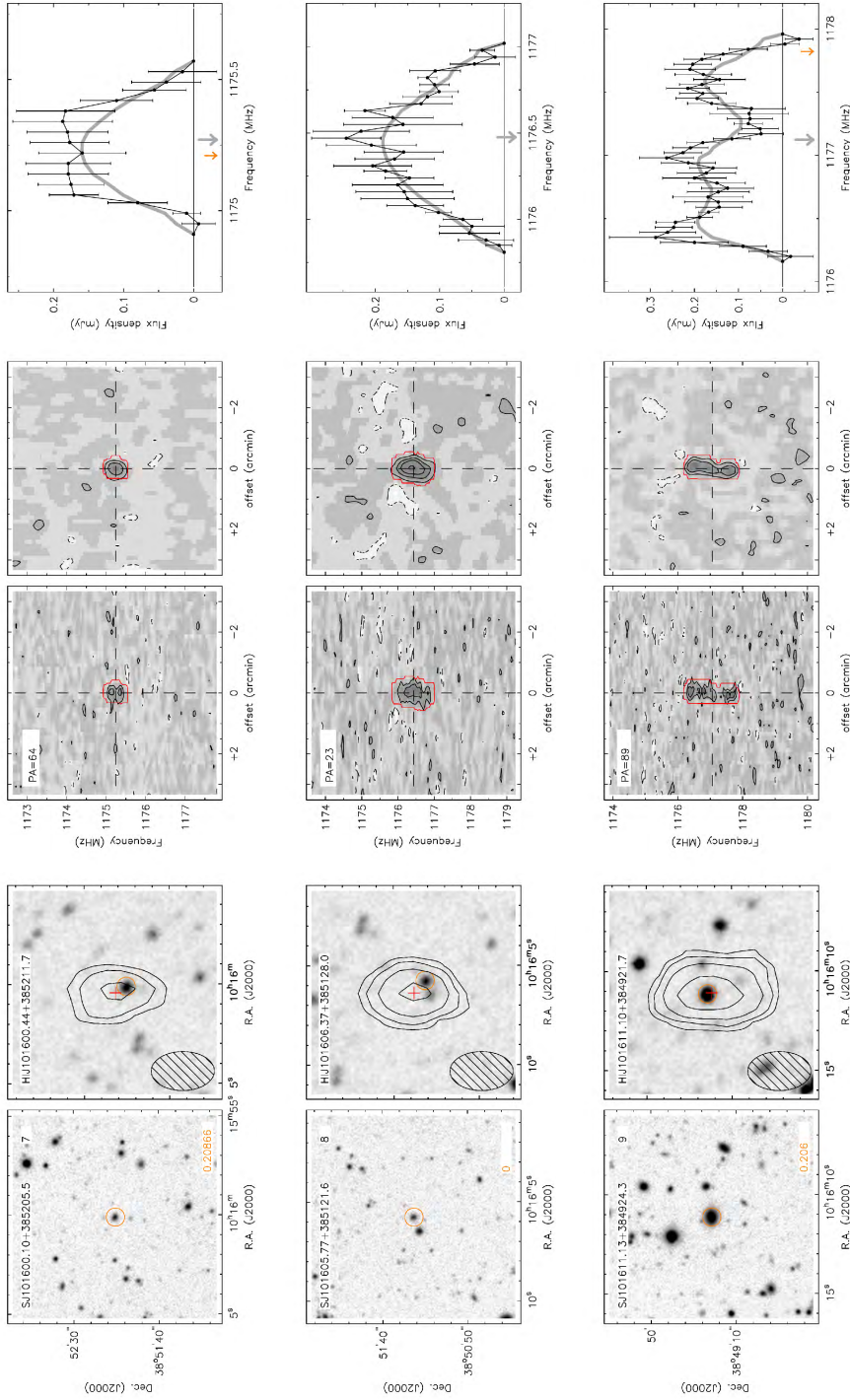
<sup>†</sup> Galaxies close to bright stars or at the edge of the field (A963 only) with incorrect/unavailable INT magnitudes. The values given are converted from SDSS u, g, r, and i magnitudes.



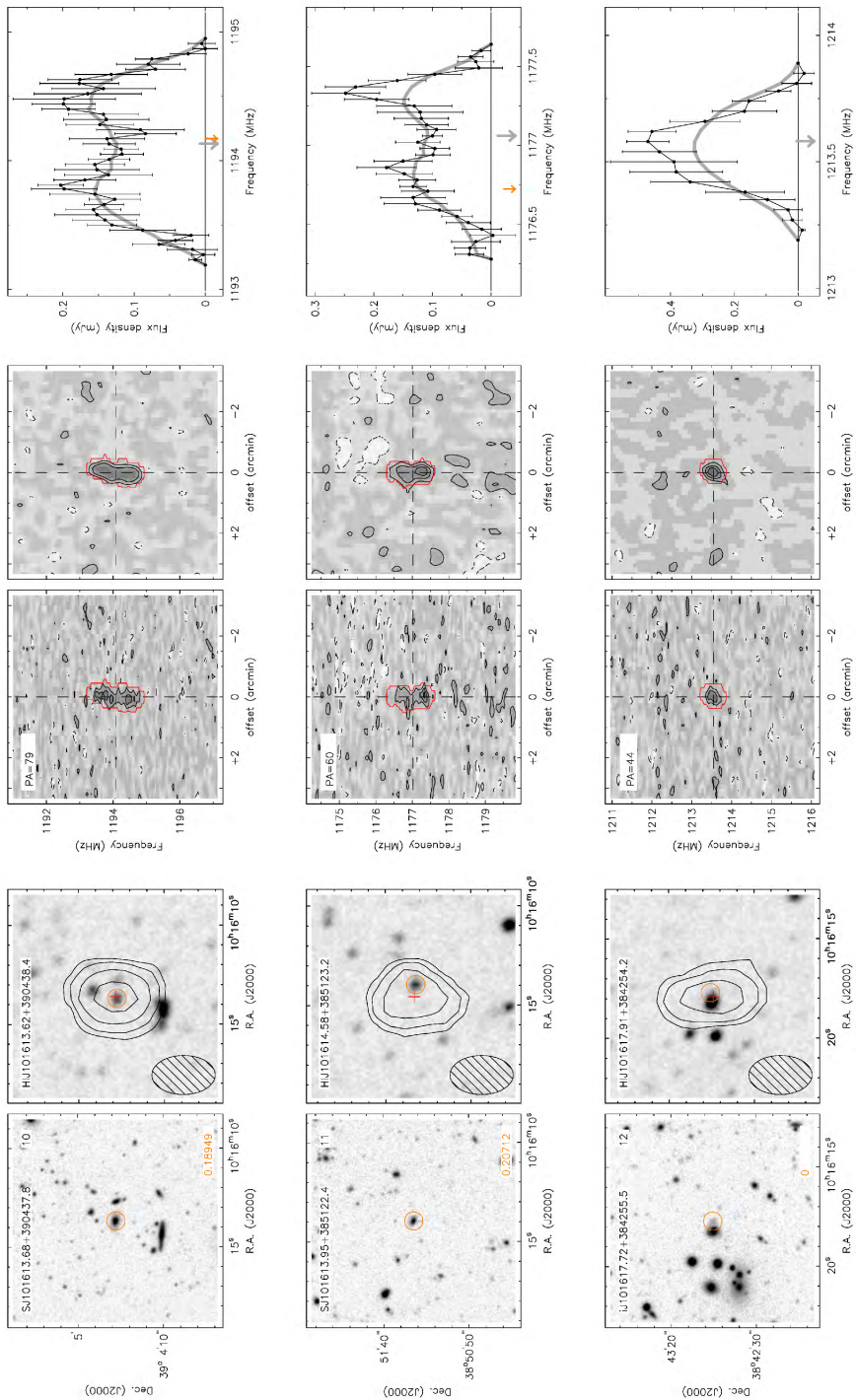
Atlas of HI detections in A963.



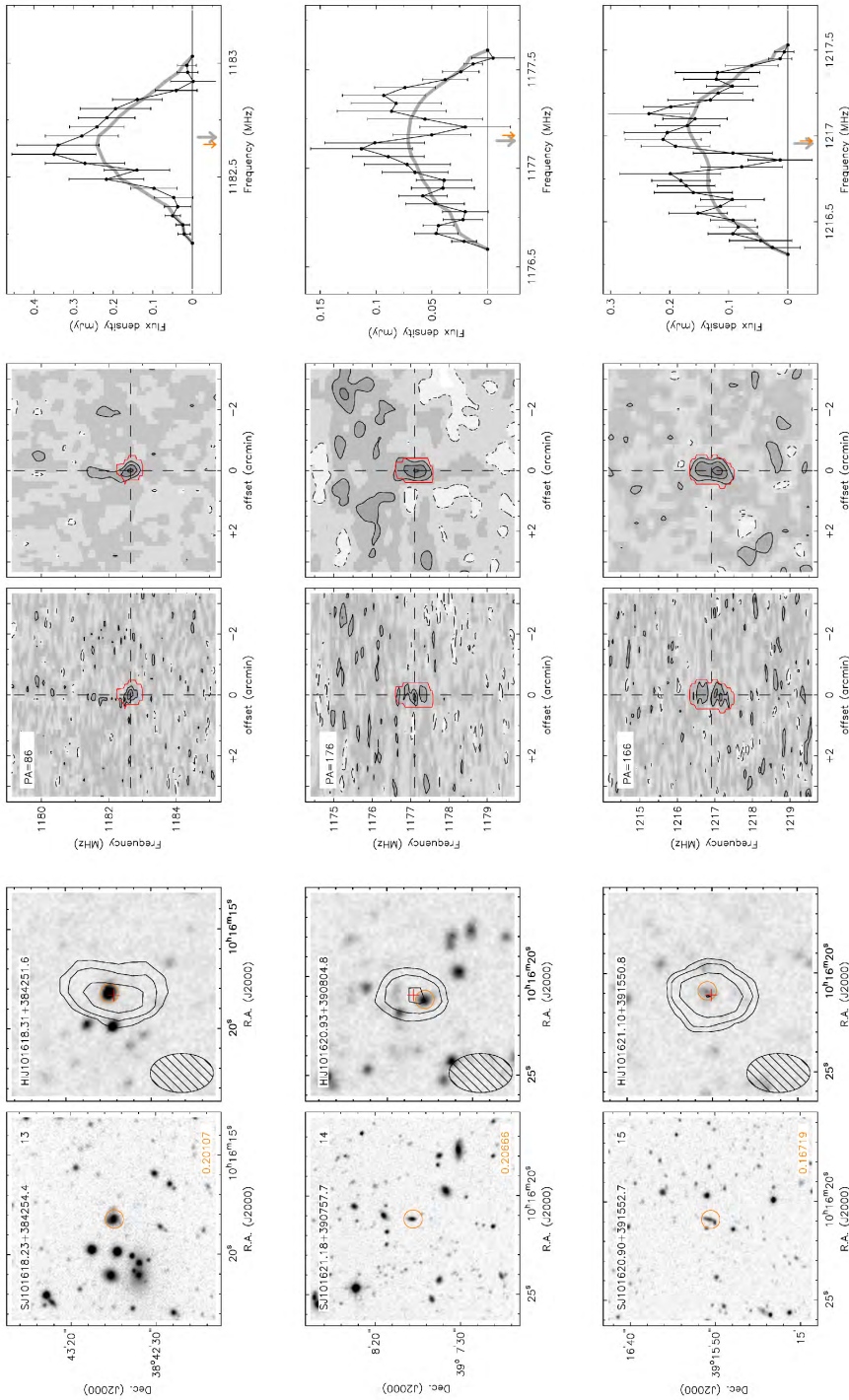
Atlas of HI detections in A963.



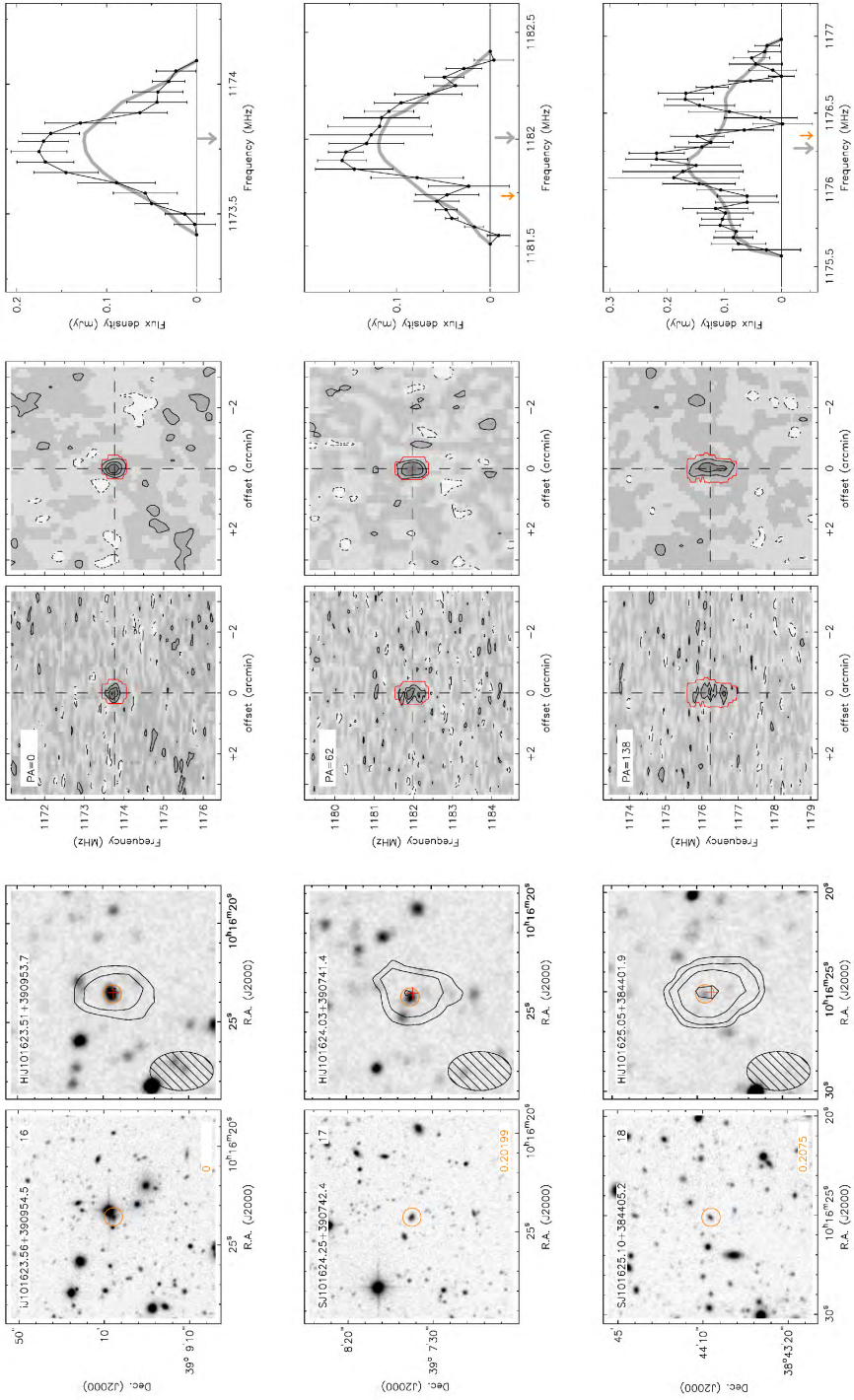
Atlas of HI detections in A963.



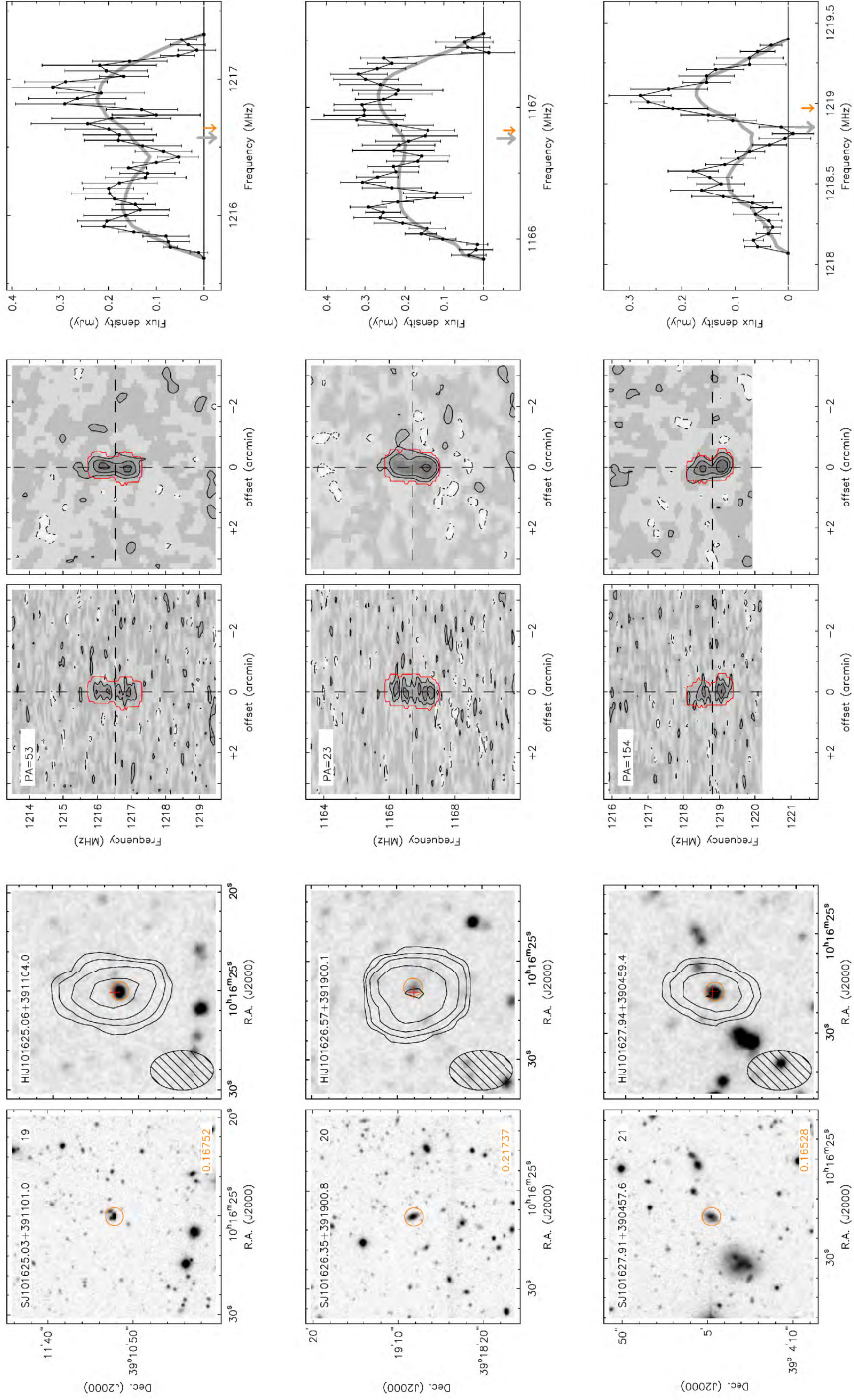
Atlas of HI detections in A963.



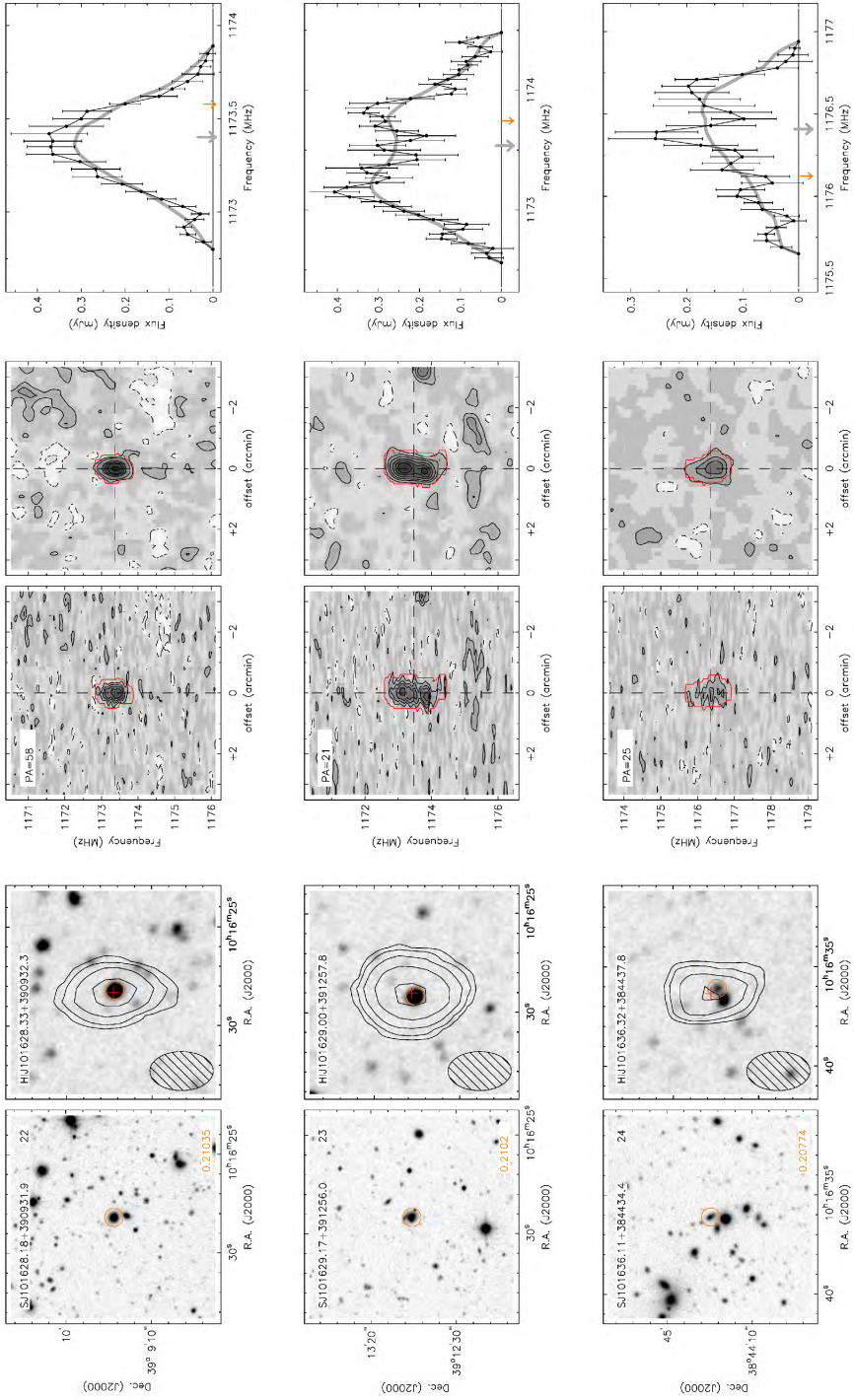
Atlas of HI detections in A963.



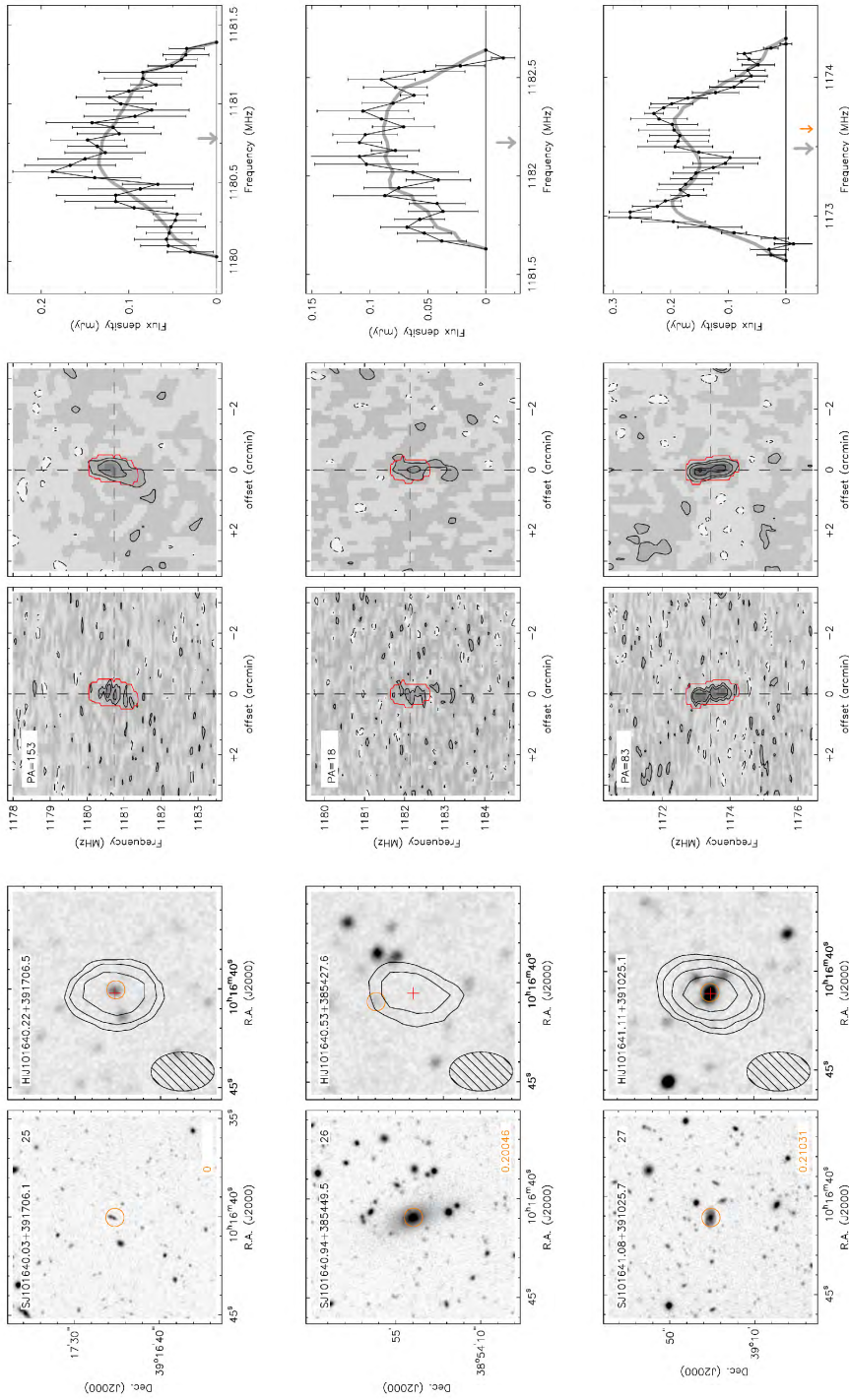
Atlas of HI detections in A963.



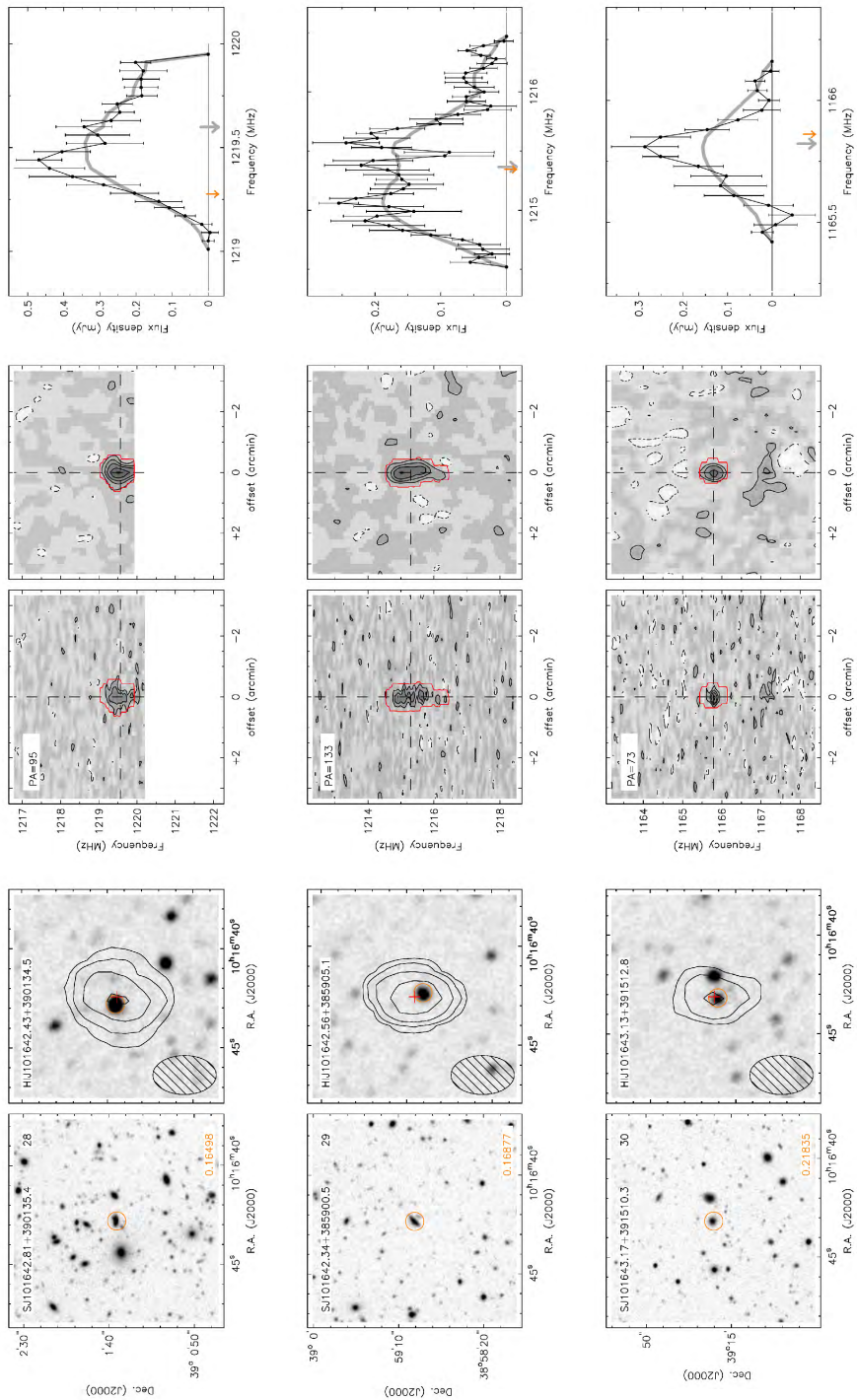
Atlas of HI detections in A963.



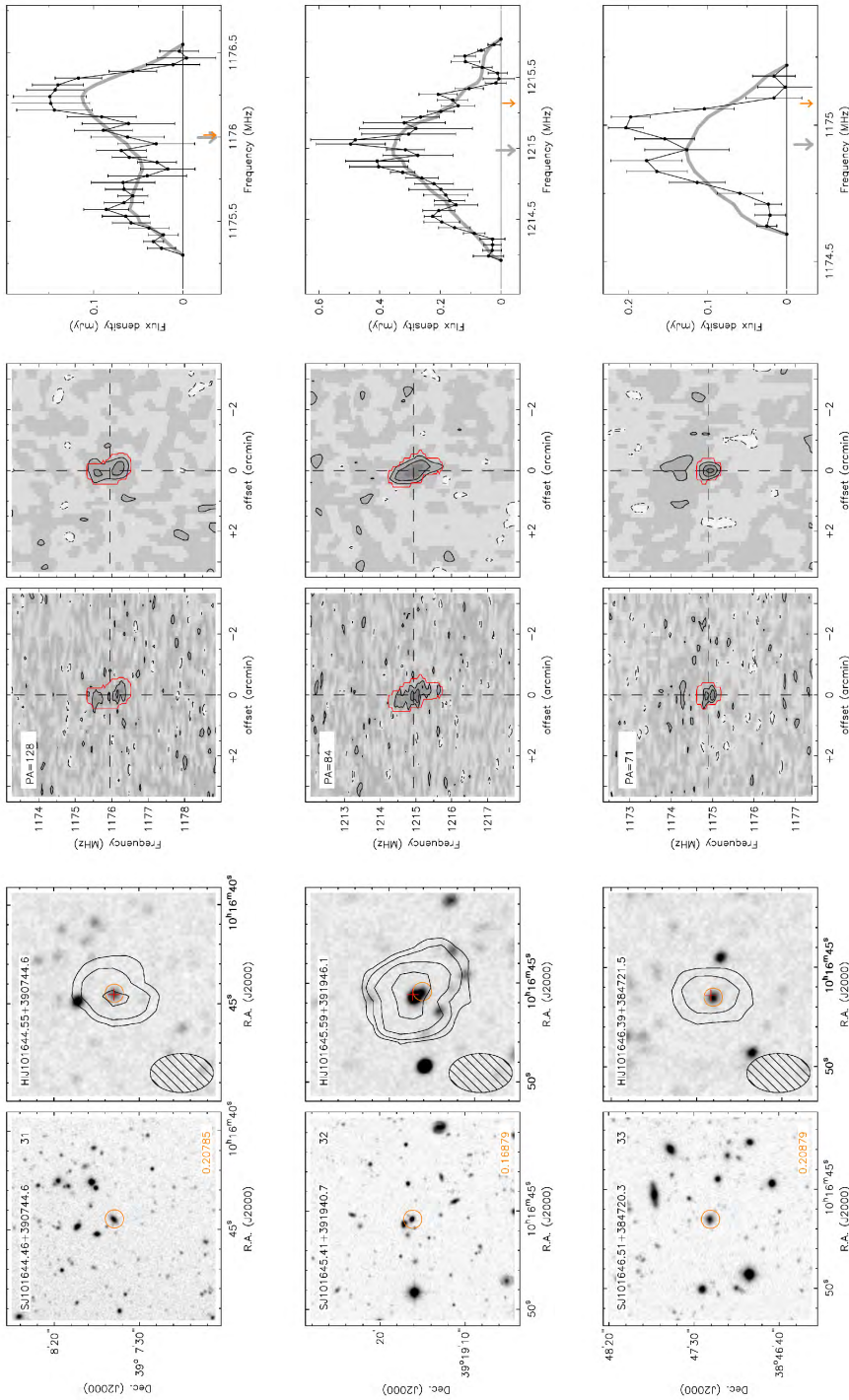
Atlas of HI detections in A963.



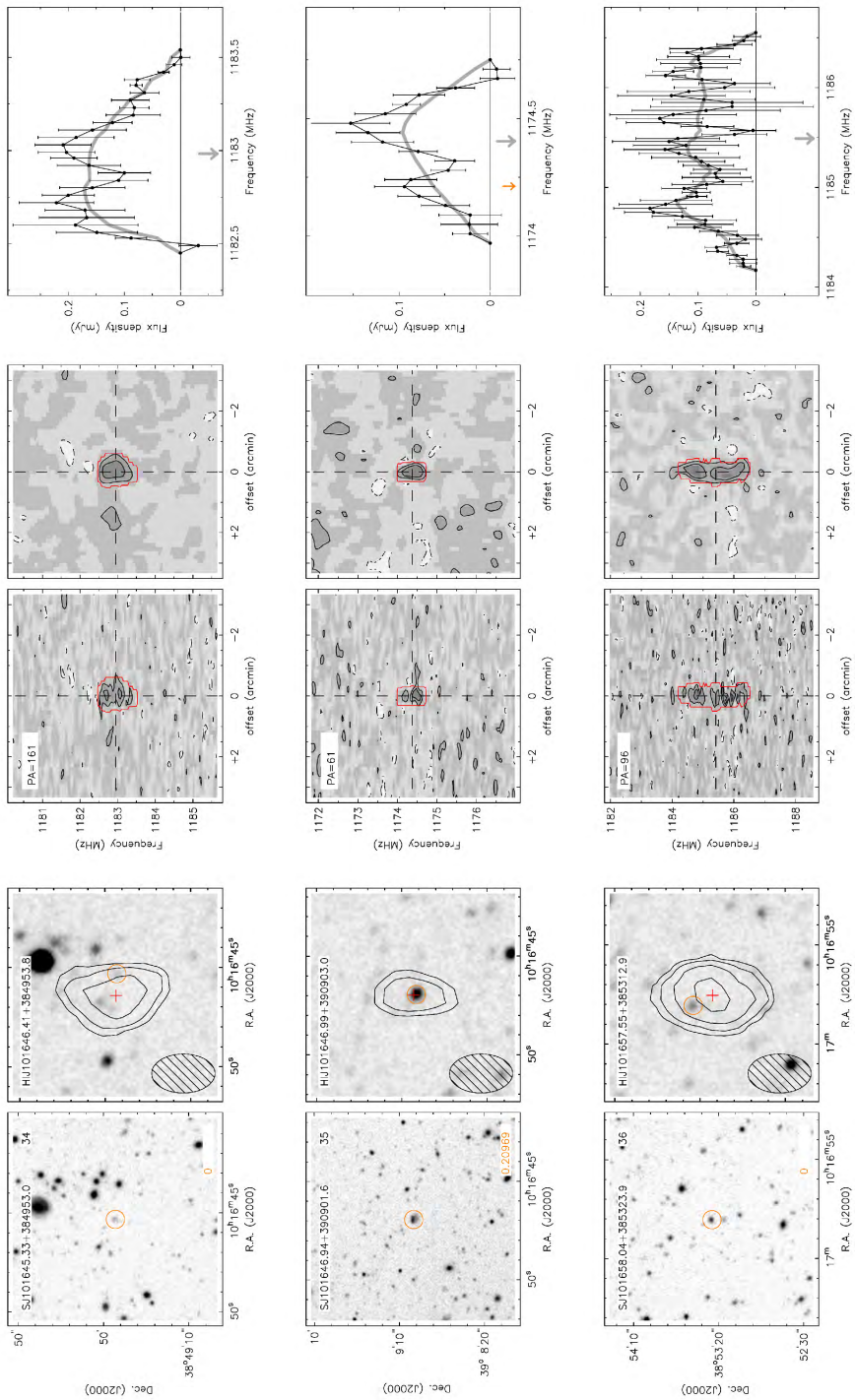
Atlas of HI detections in A963.



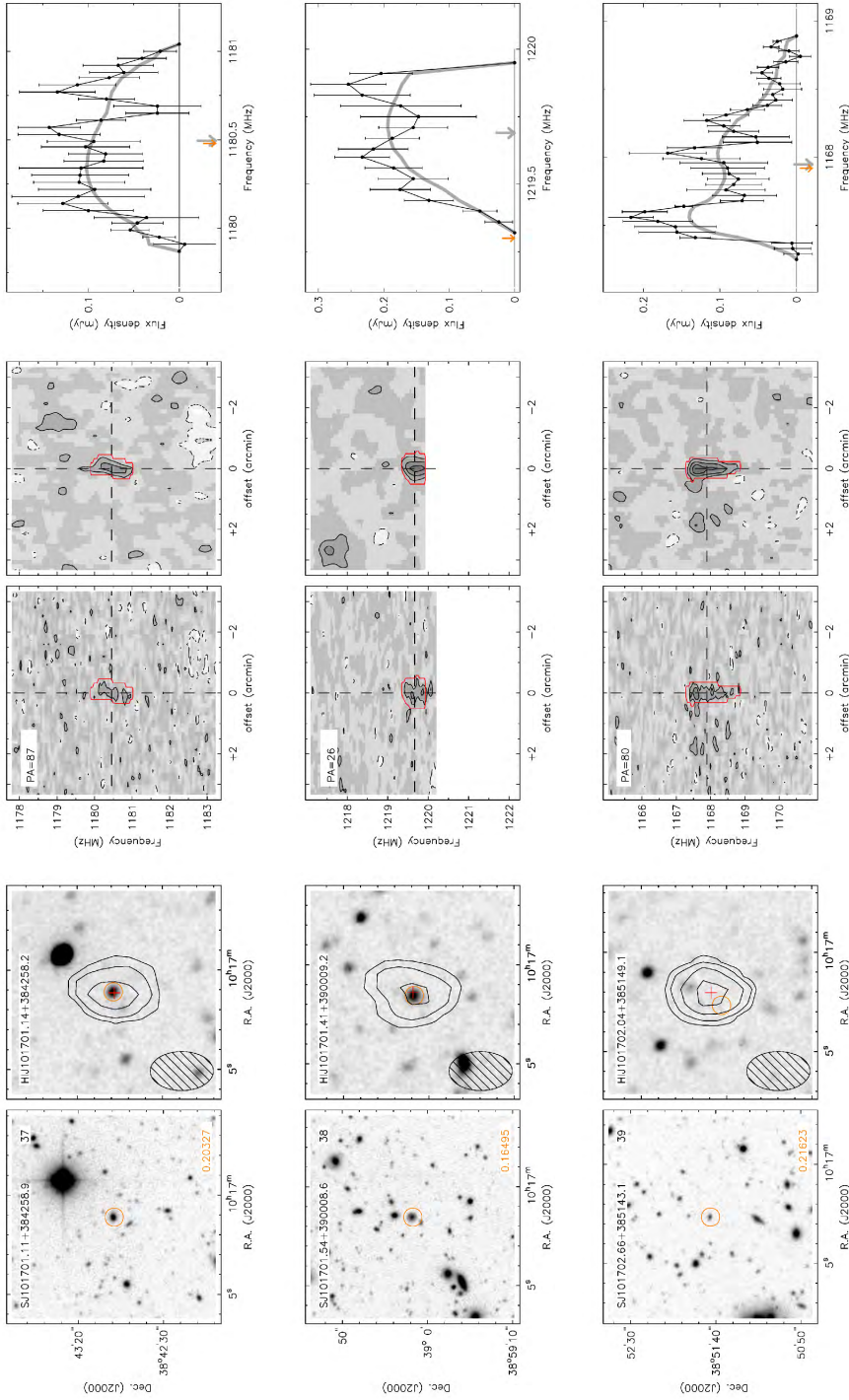
Atlas of HI detections in A963.



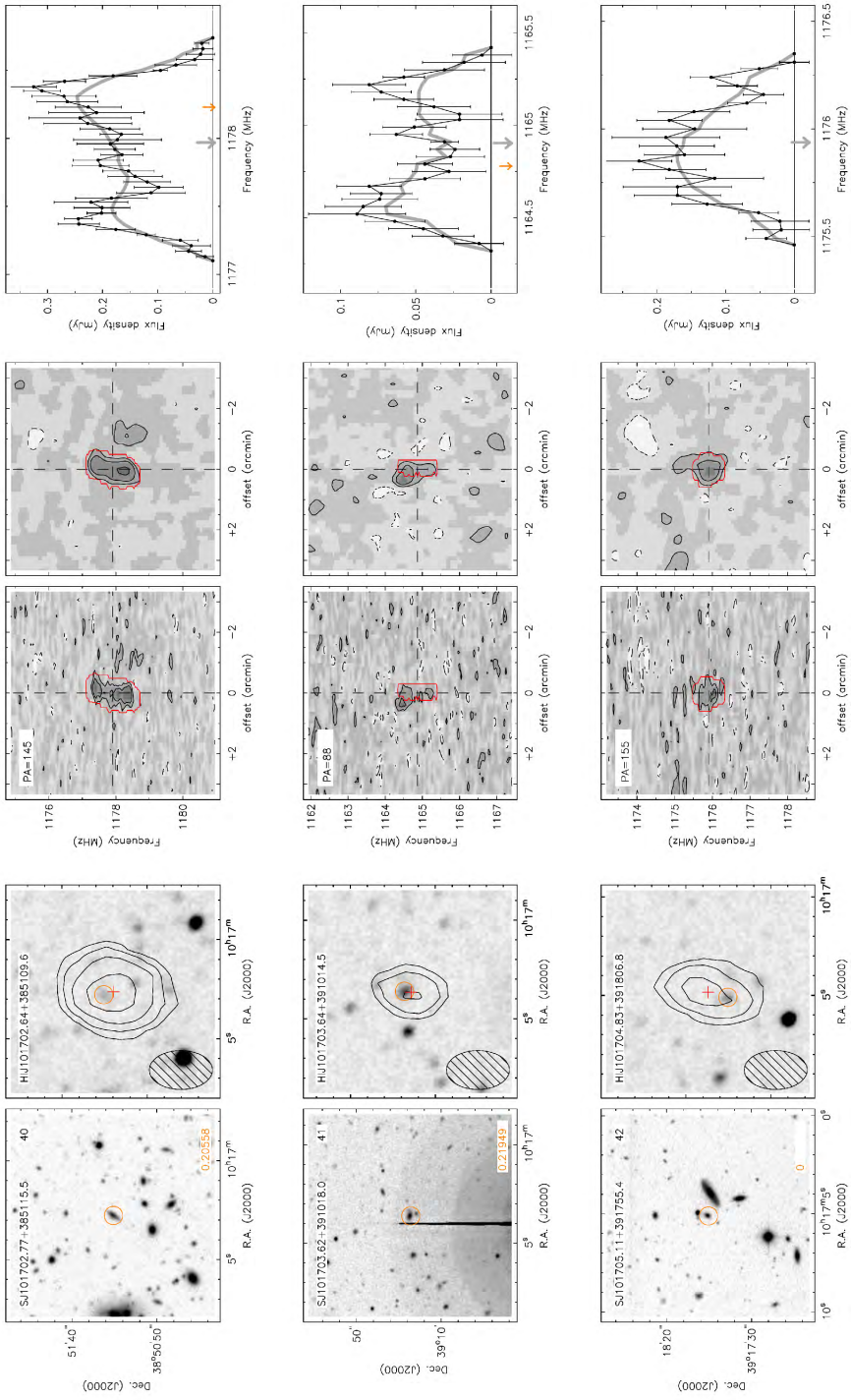
Atlas of HI detections in A963.



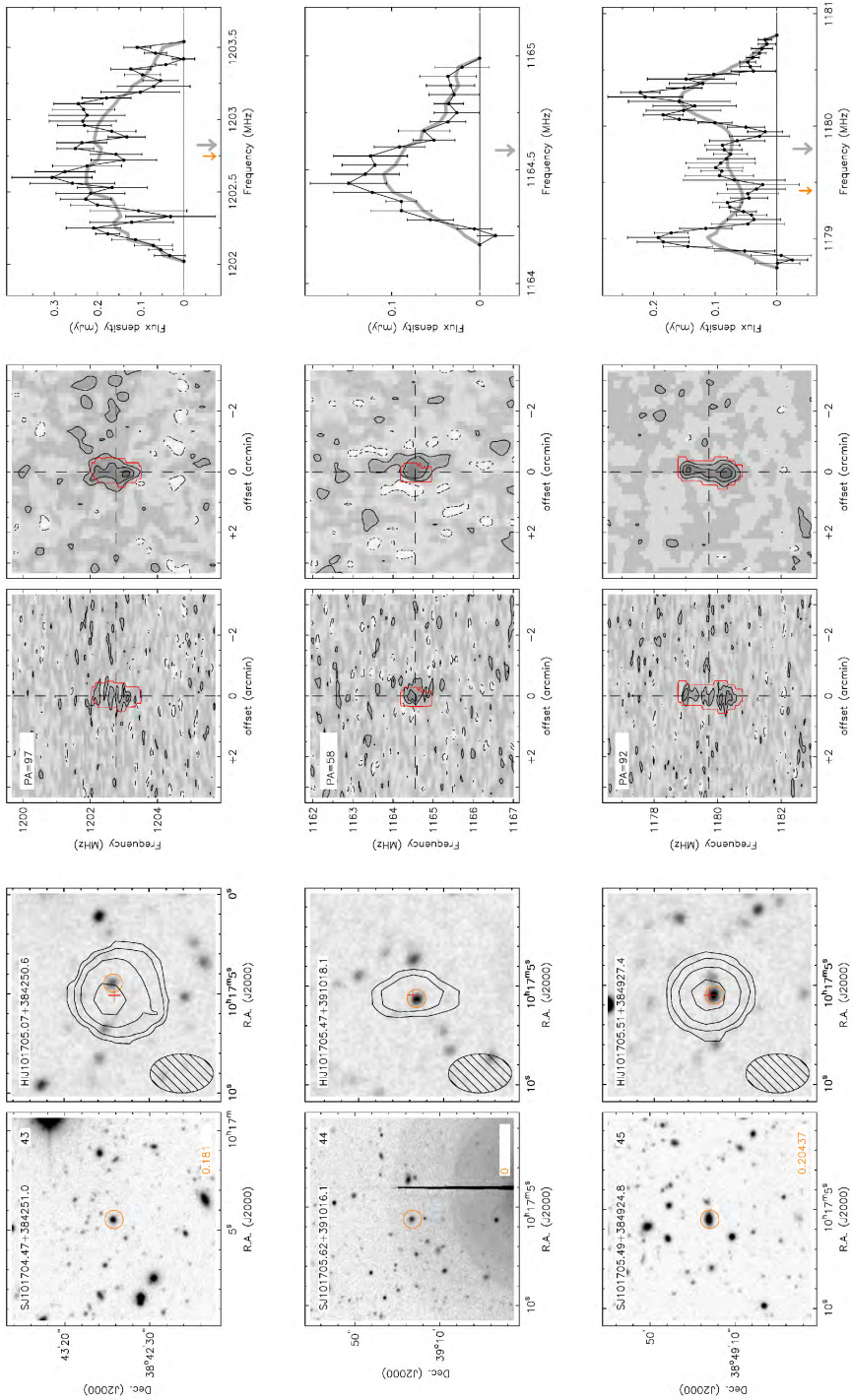
Atlas of HI detections in A963.



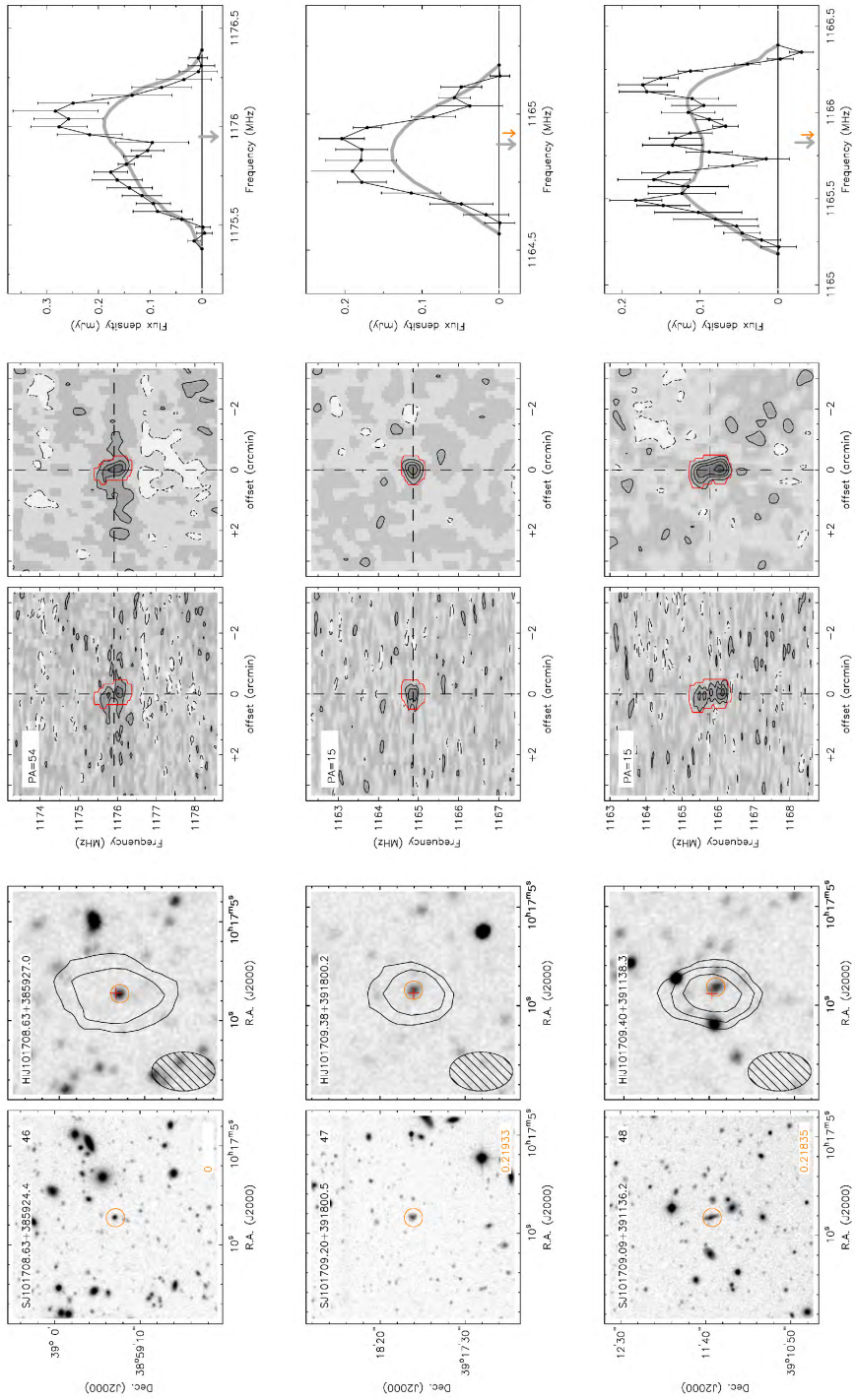
Atlas of HI detections in A963.



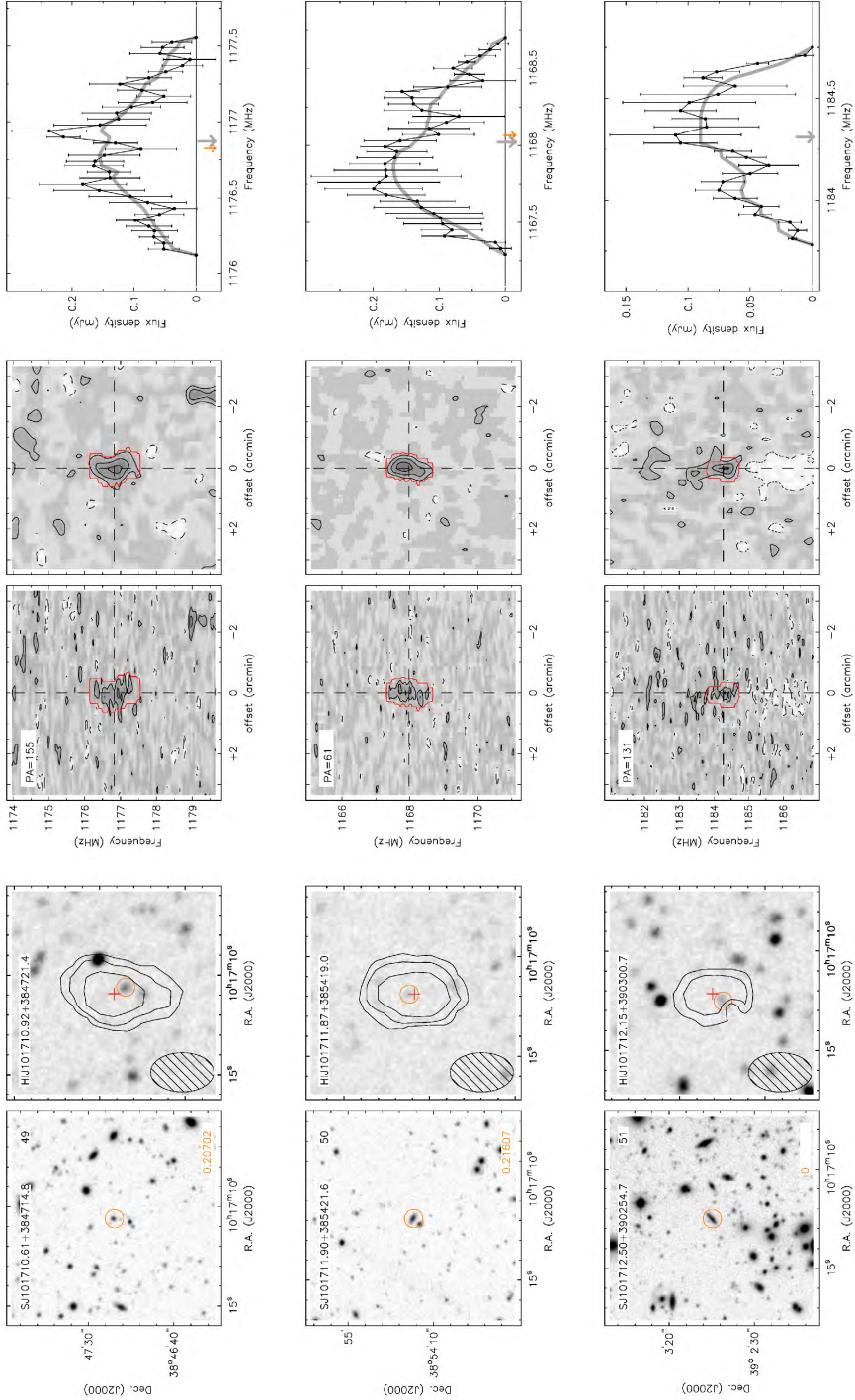
Atlas of HI detections in A963.



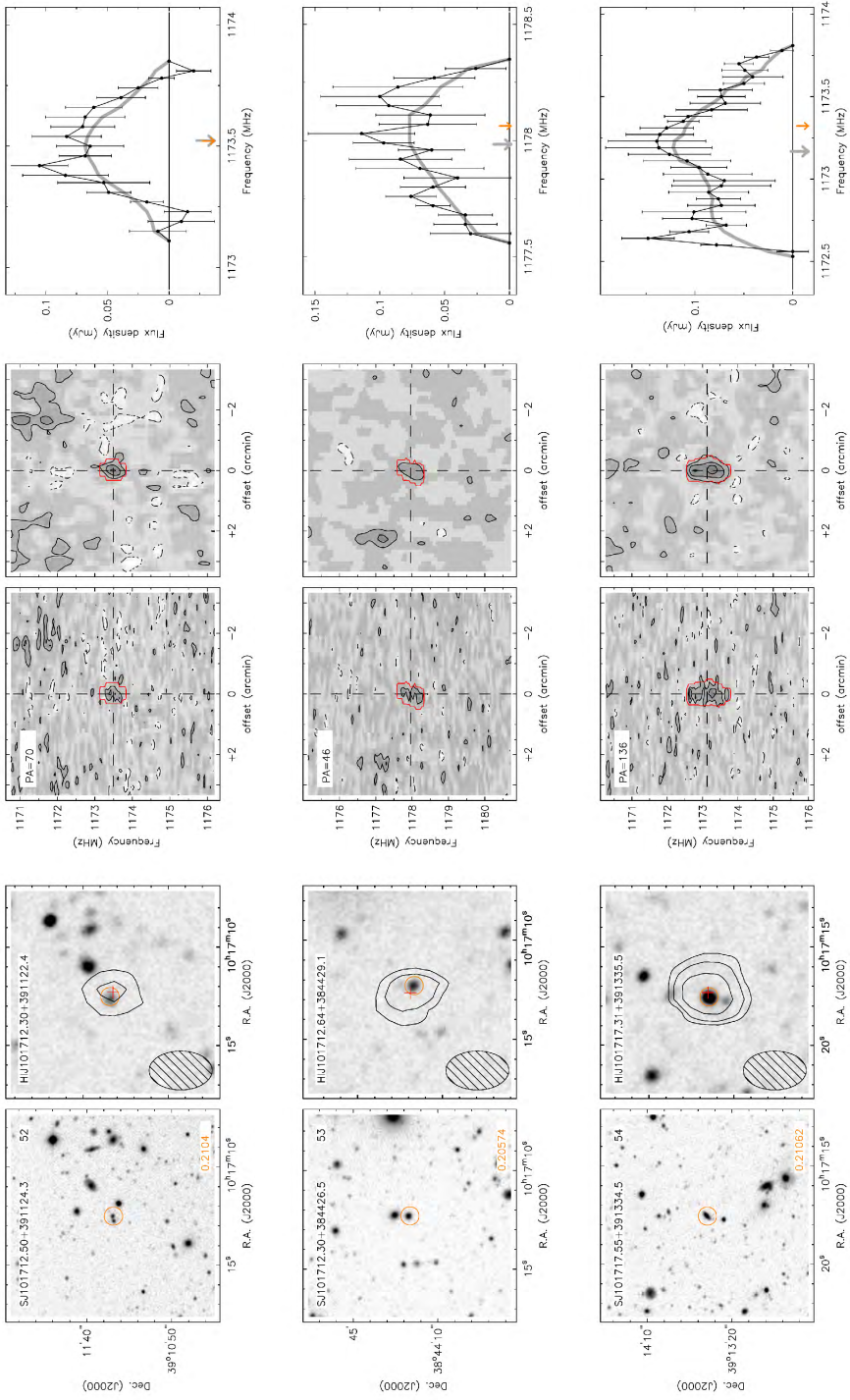
Atlas of HI detections in A963.



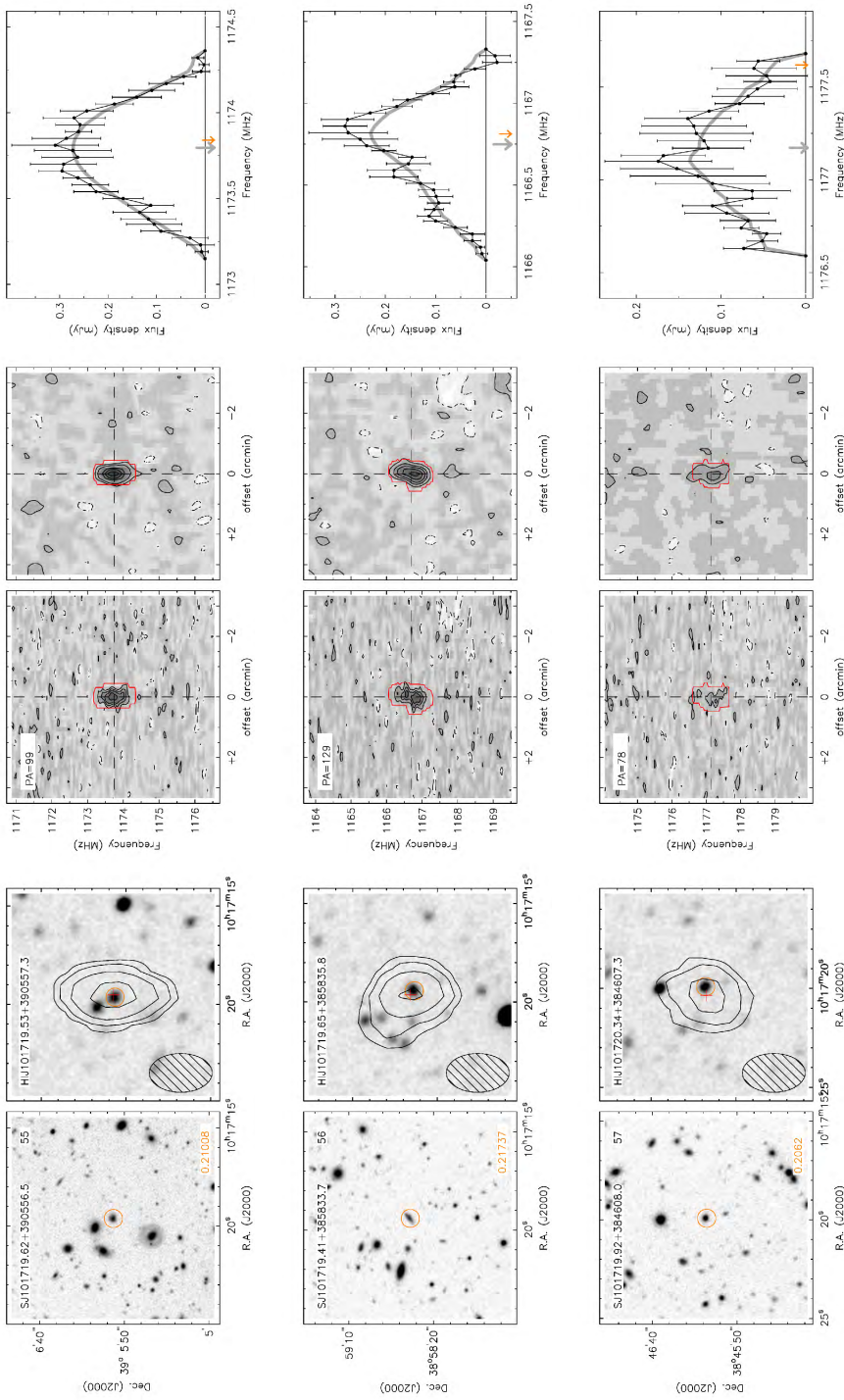
Atlas of HI detections in A963.



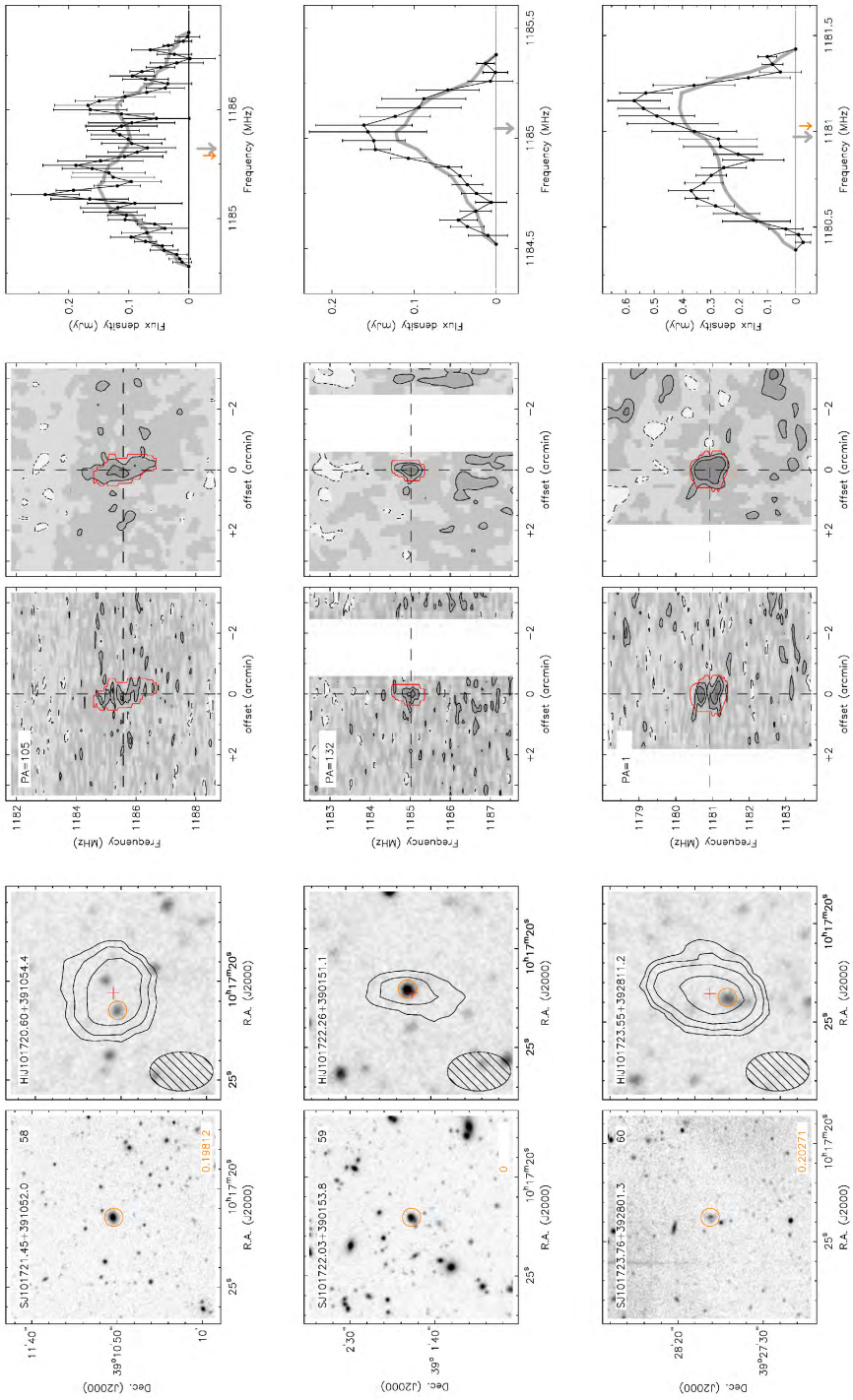
Atlas of HI detections in A963.



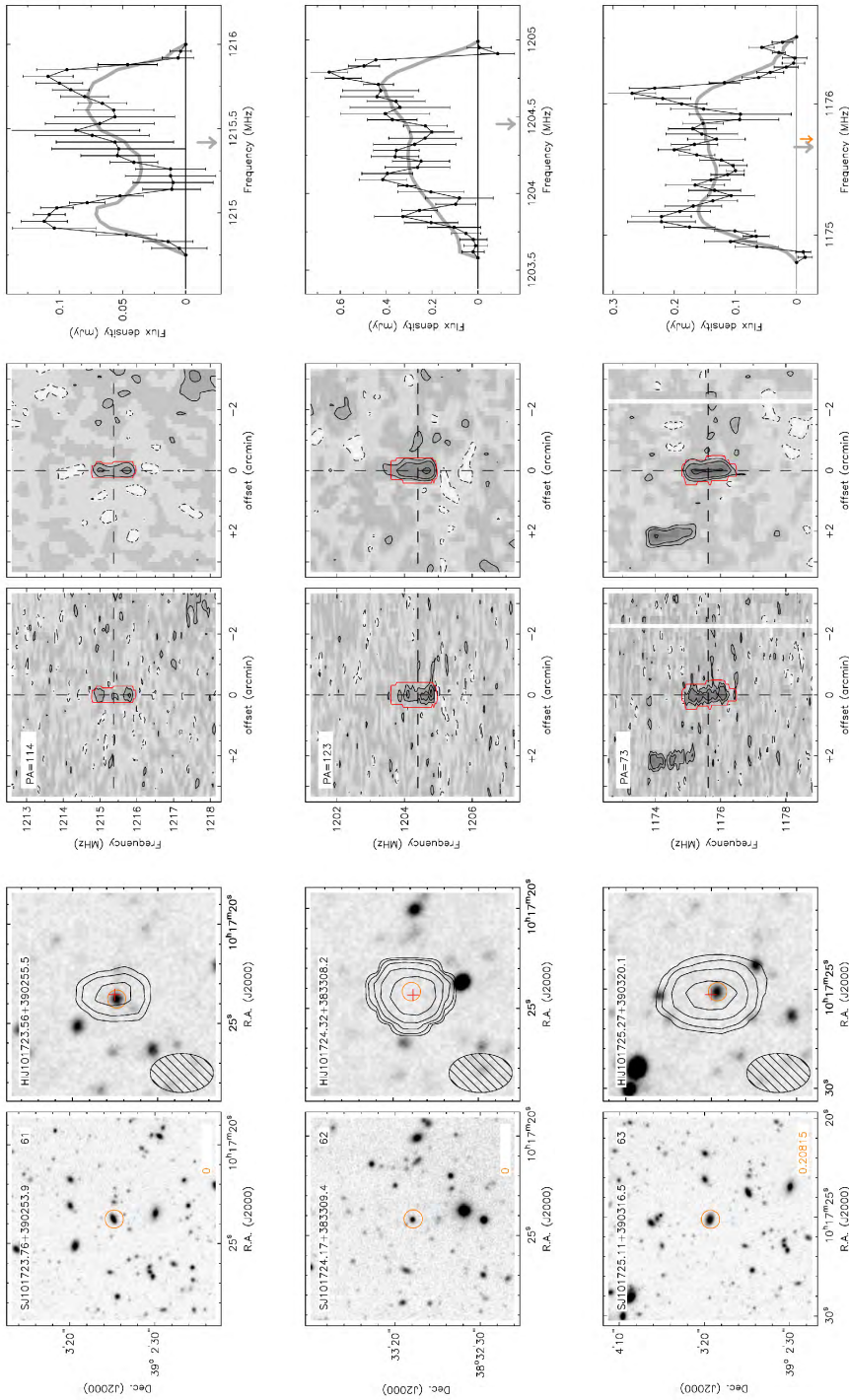
Atlas of HI detections in A963.



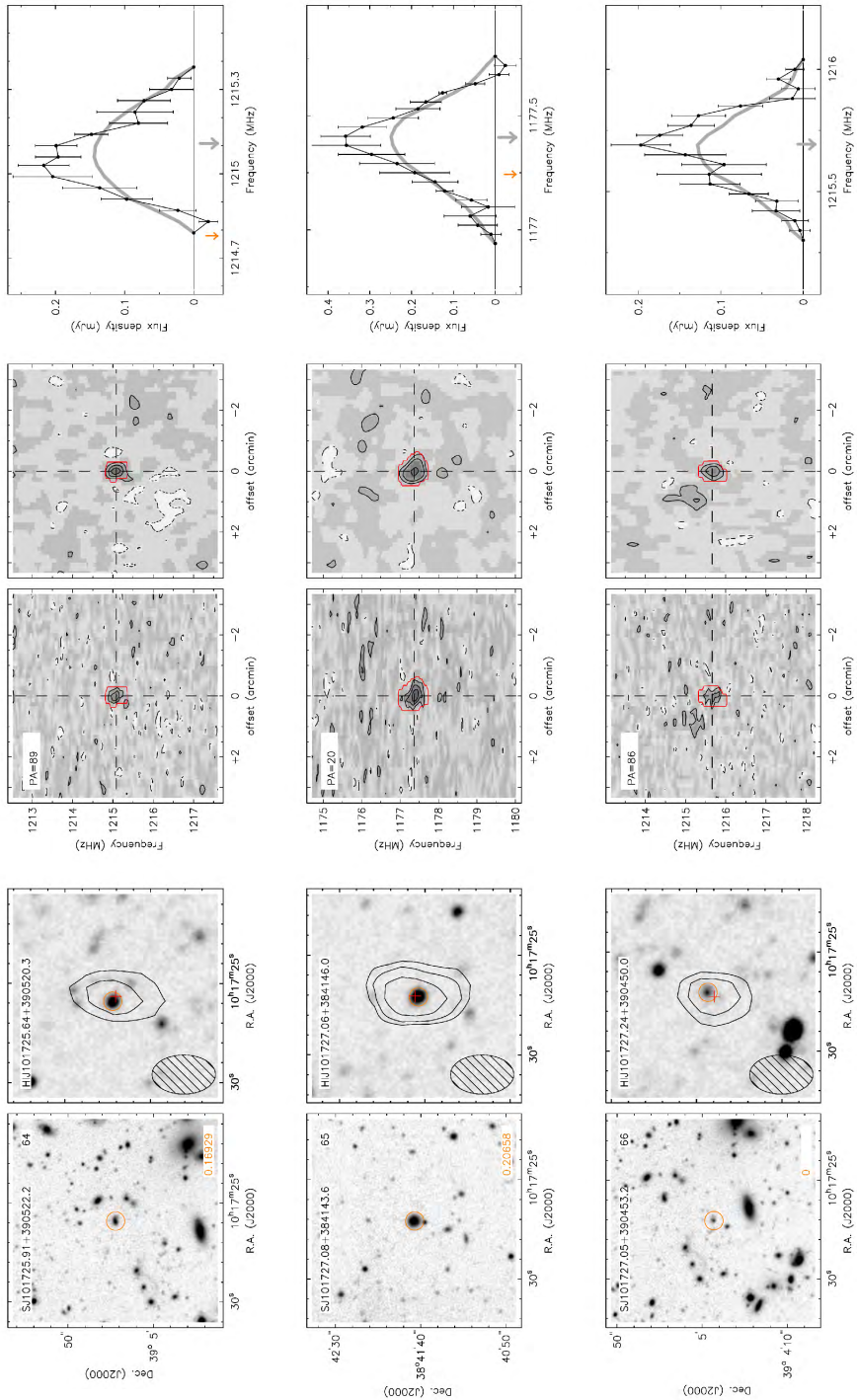
Atlas of HI detections in A963.



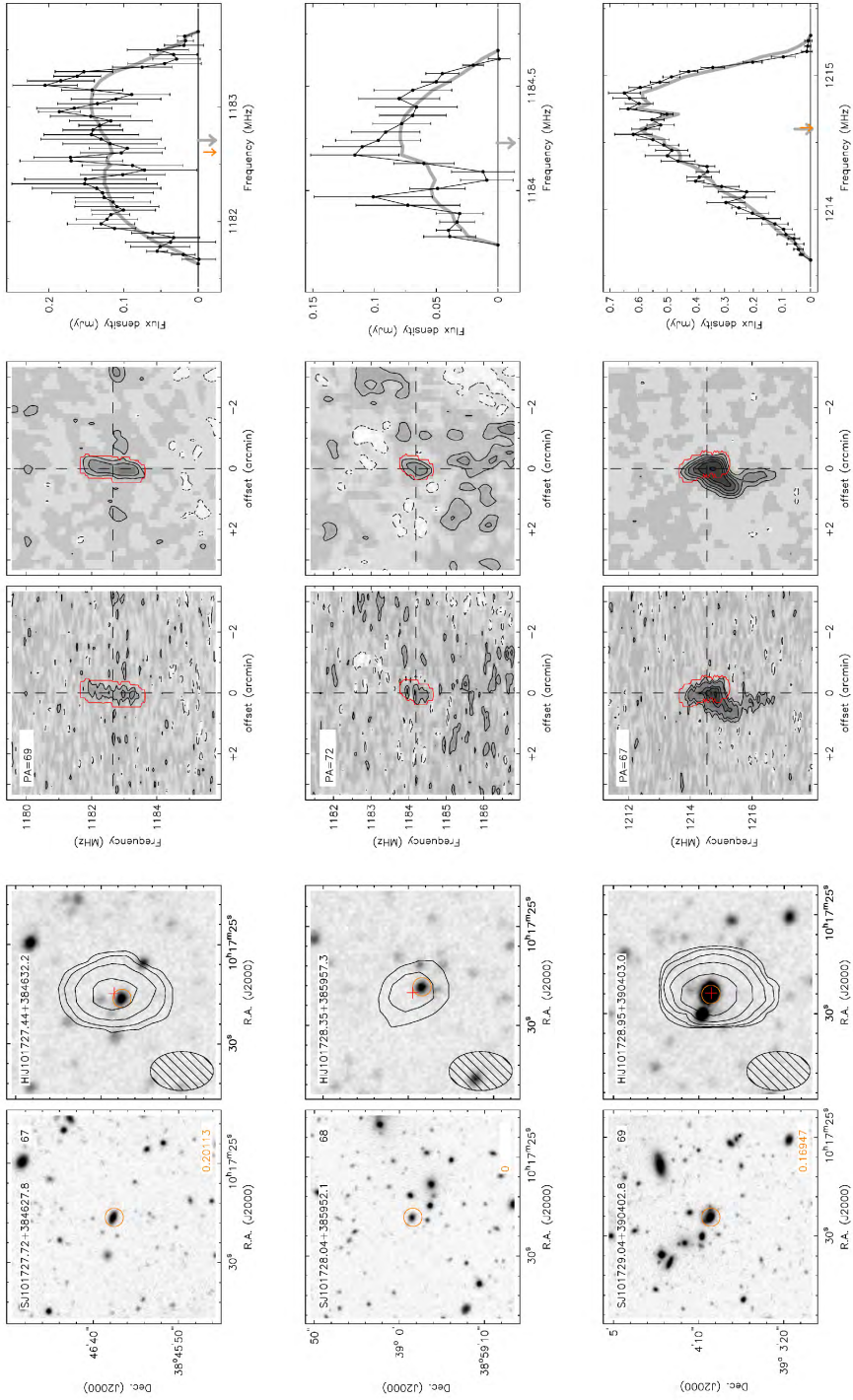
Atlas of HI detections in A963.



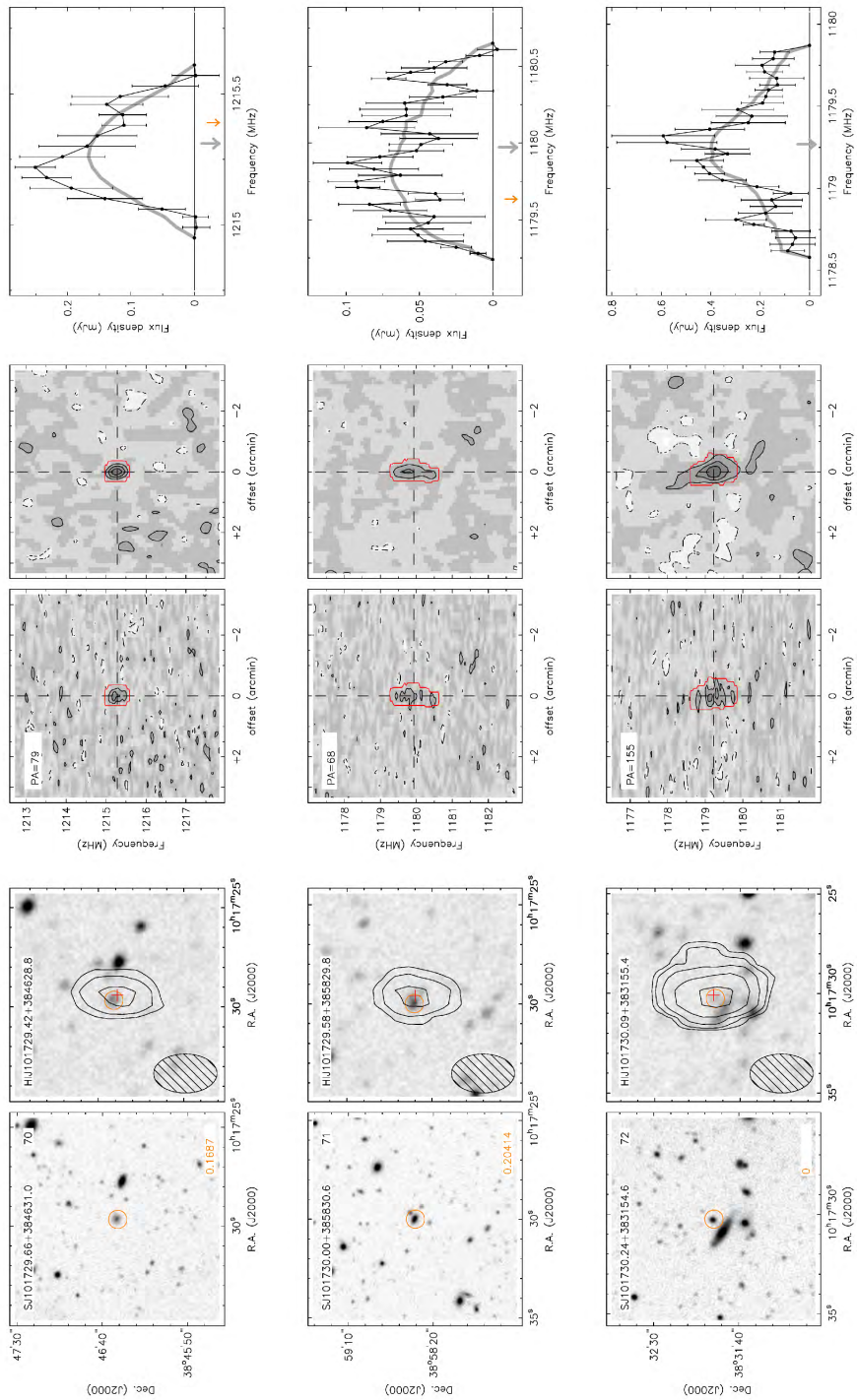
Atlas of HI detections in A963



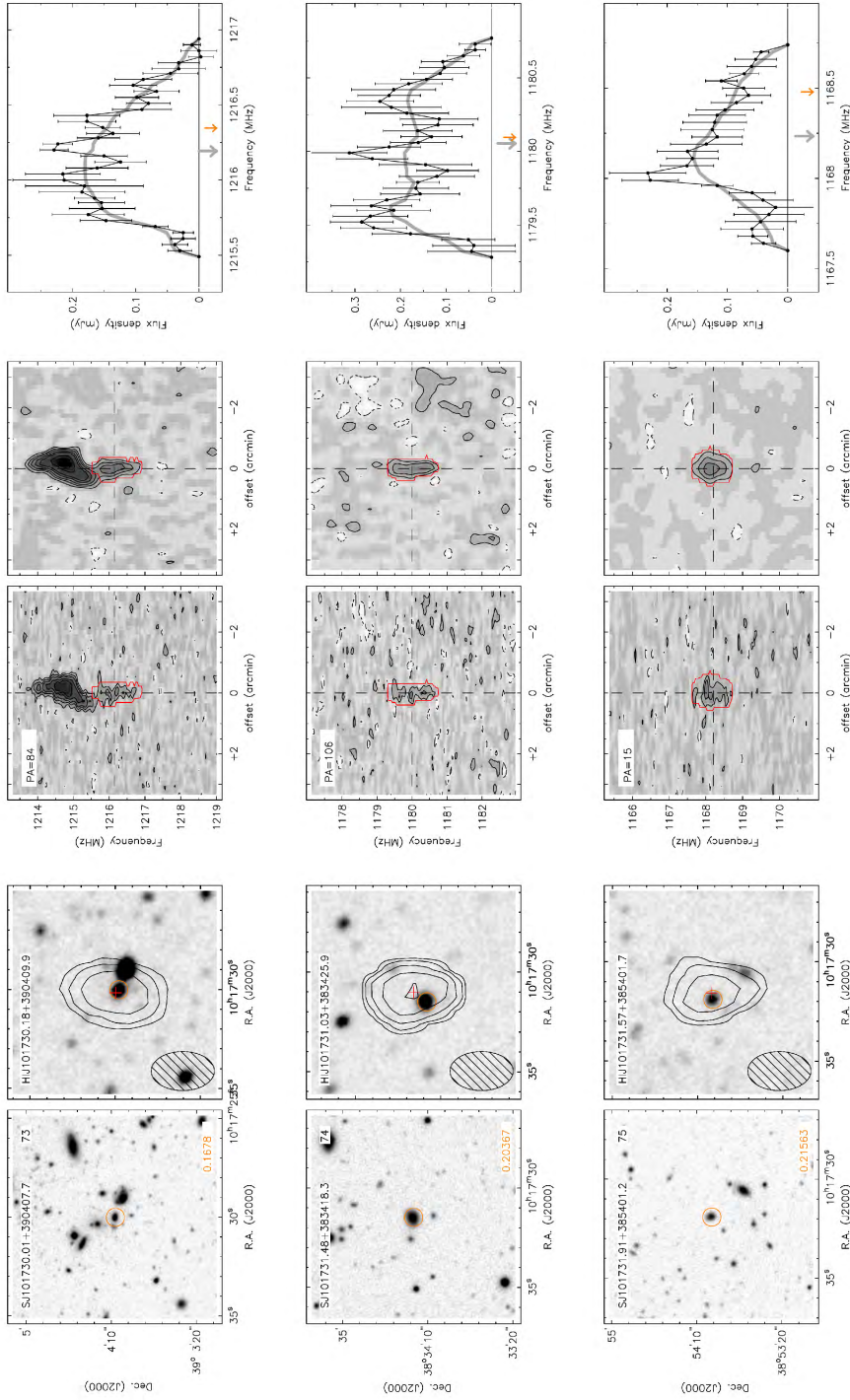
Atlas of HI detections in A963



Atlas of HI detections in A963

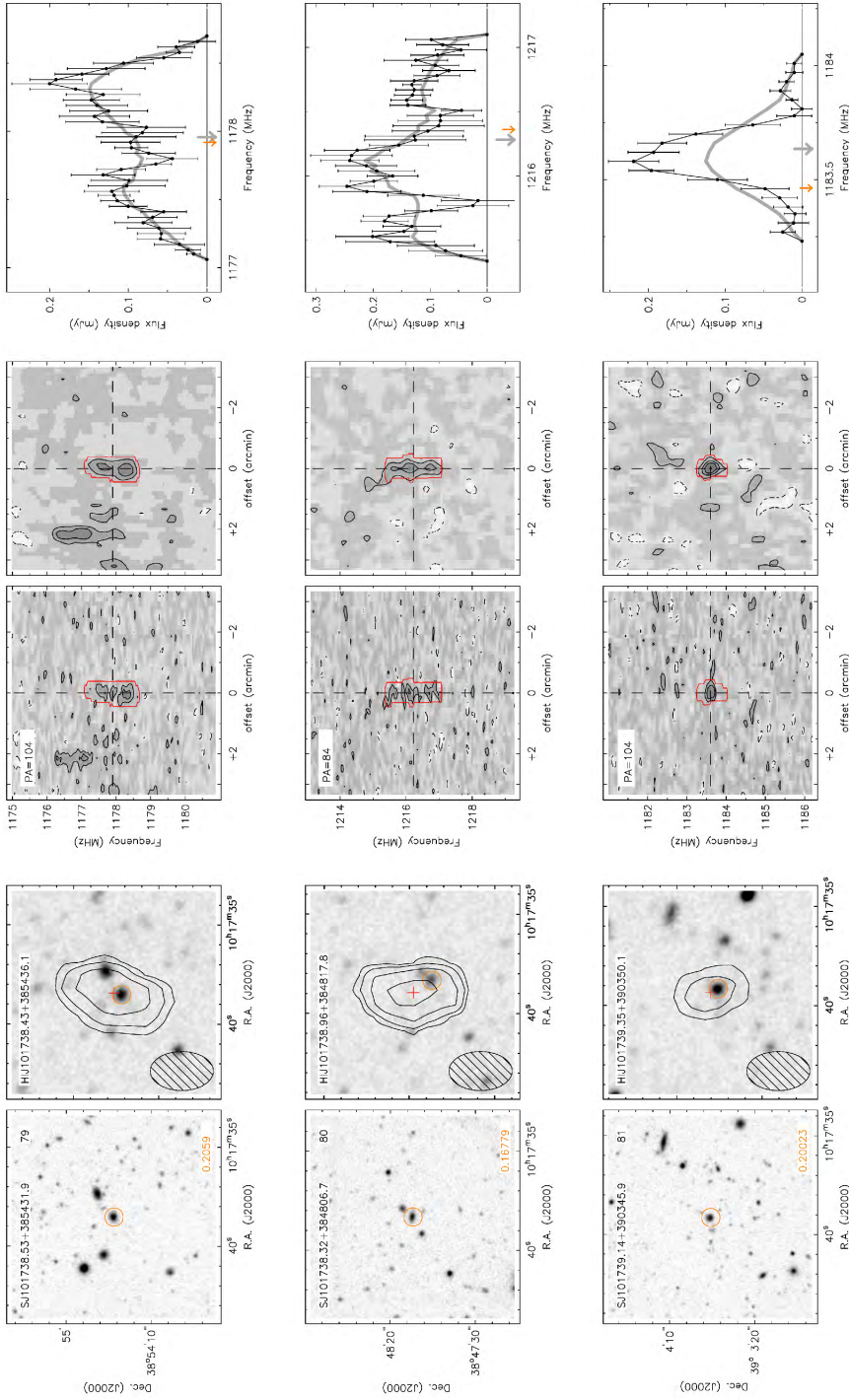


Atlas of HI detections in A963

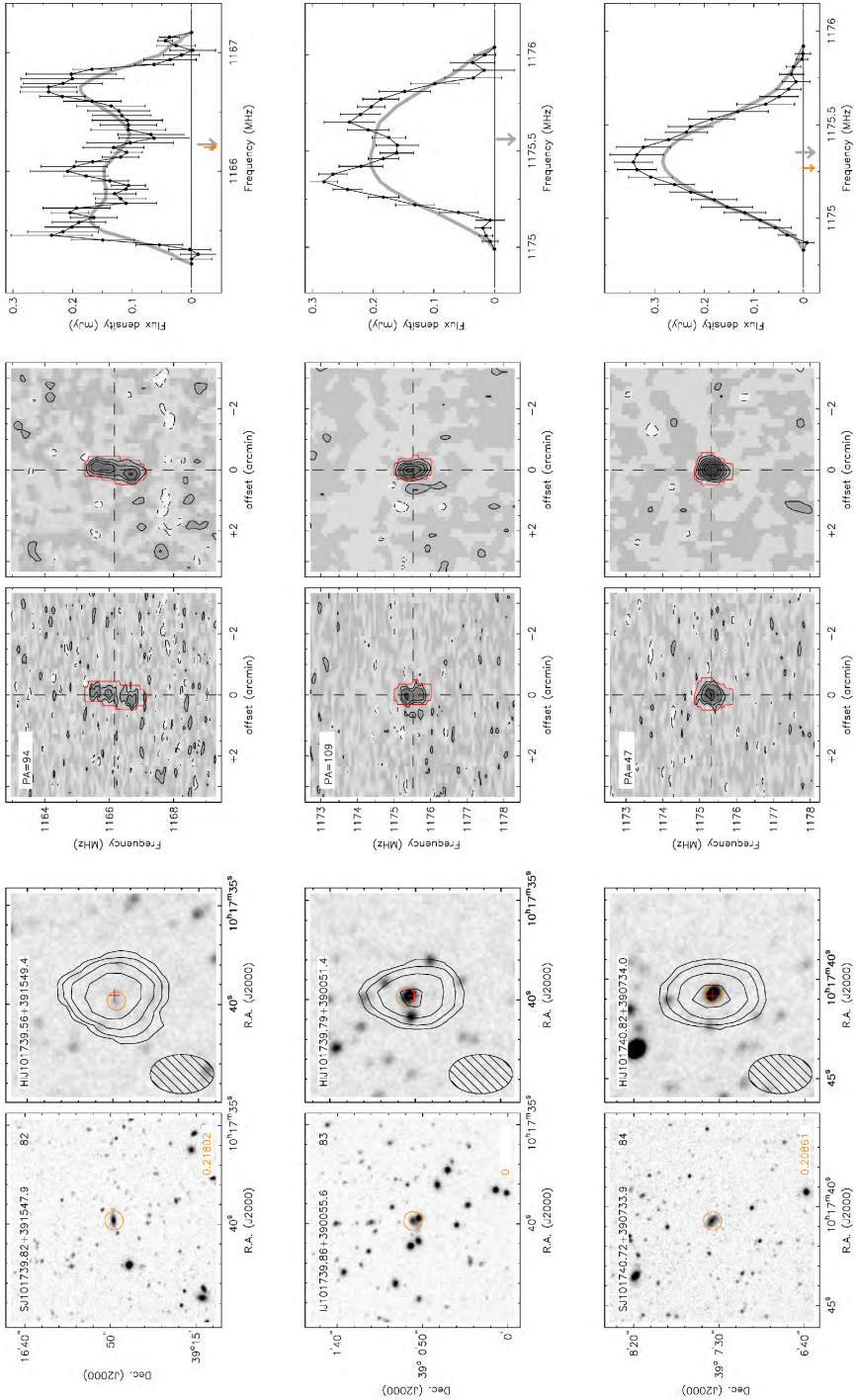


Atlas of HI detections in A963

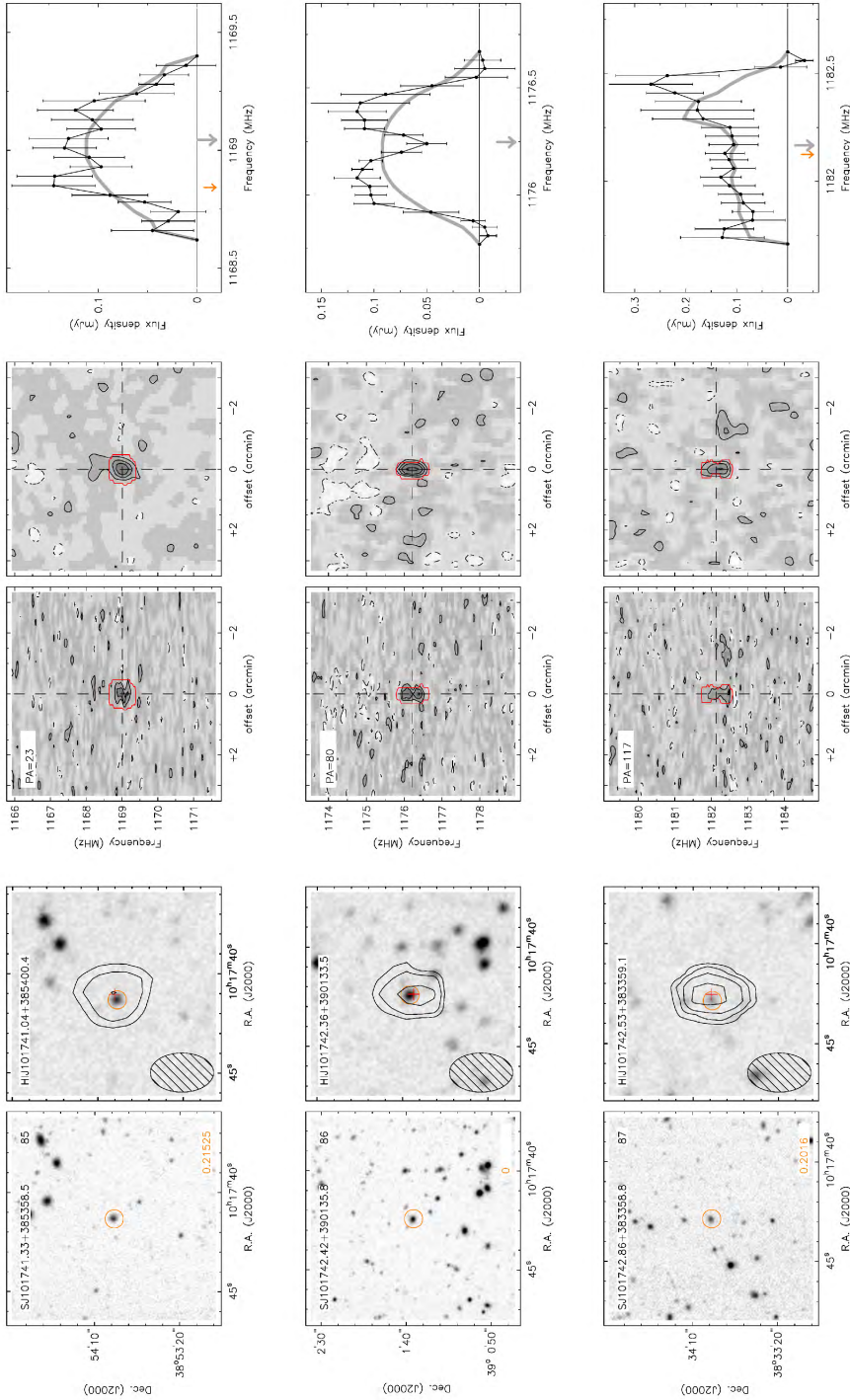




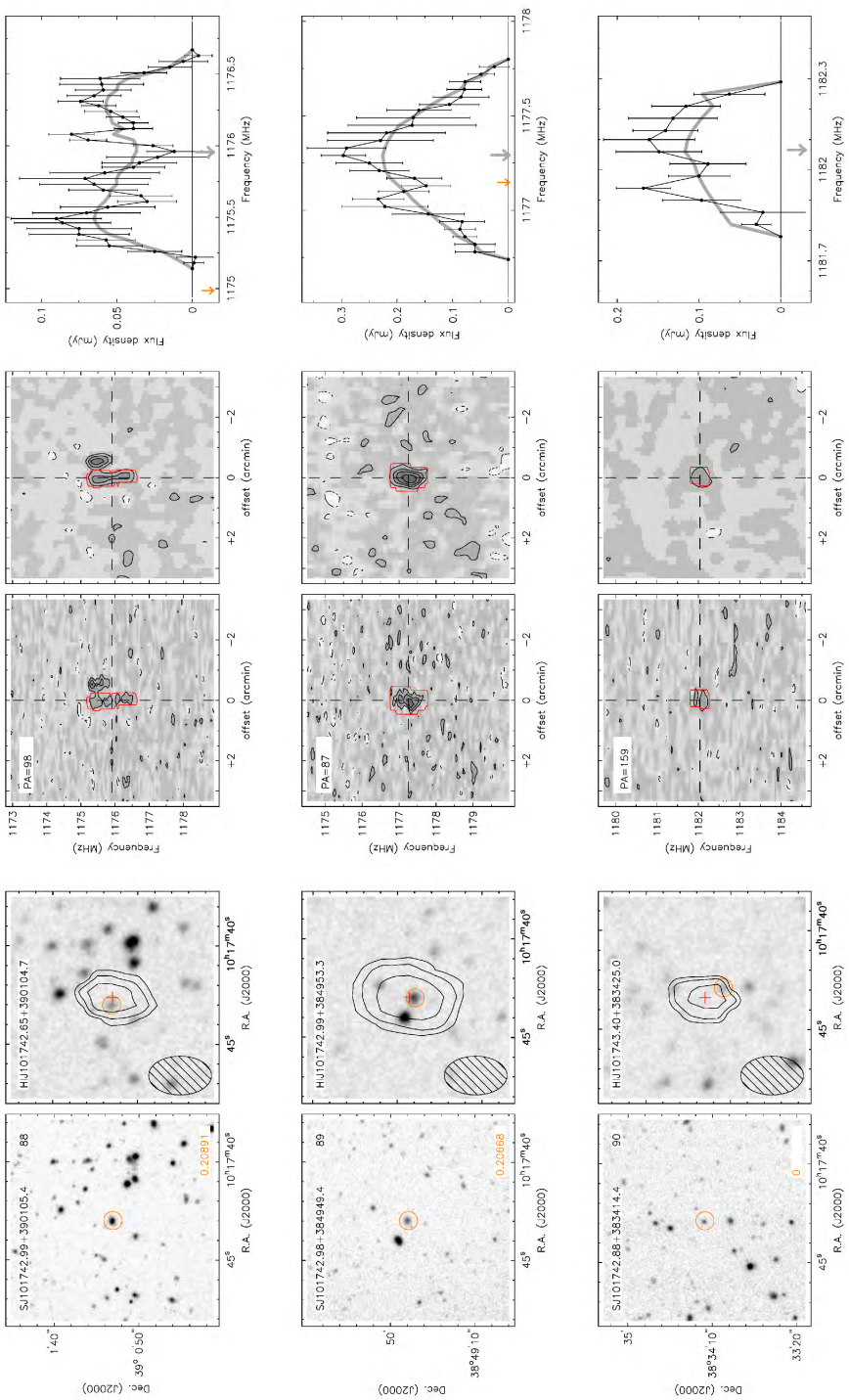
Atlas of HI detections in A963



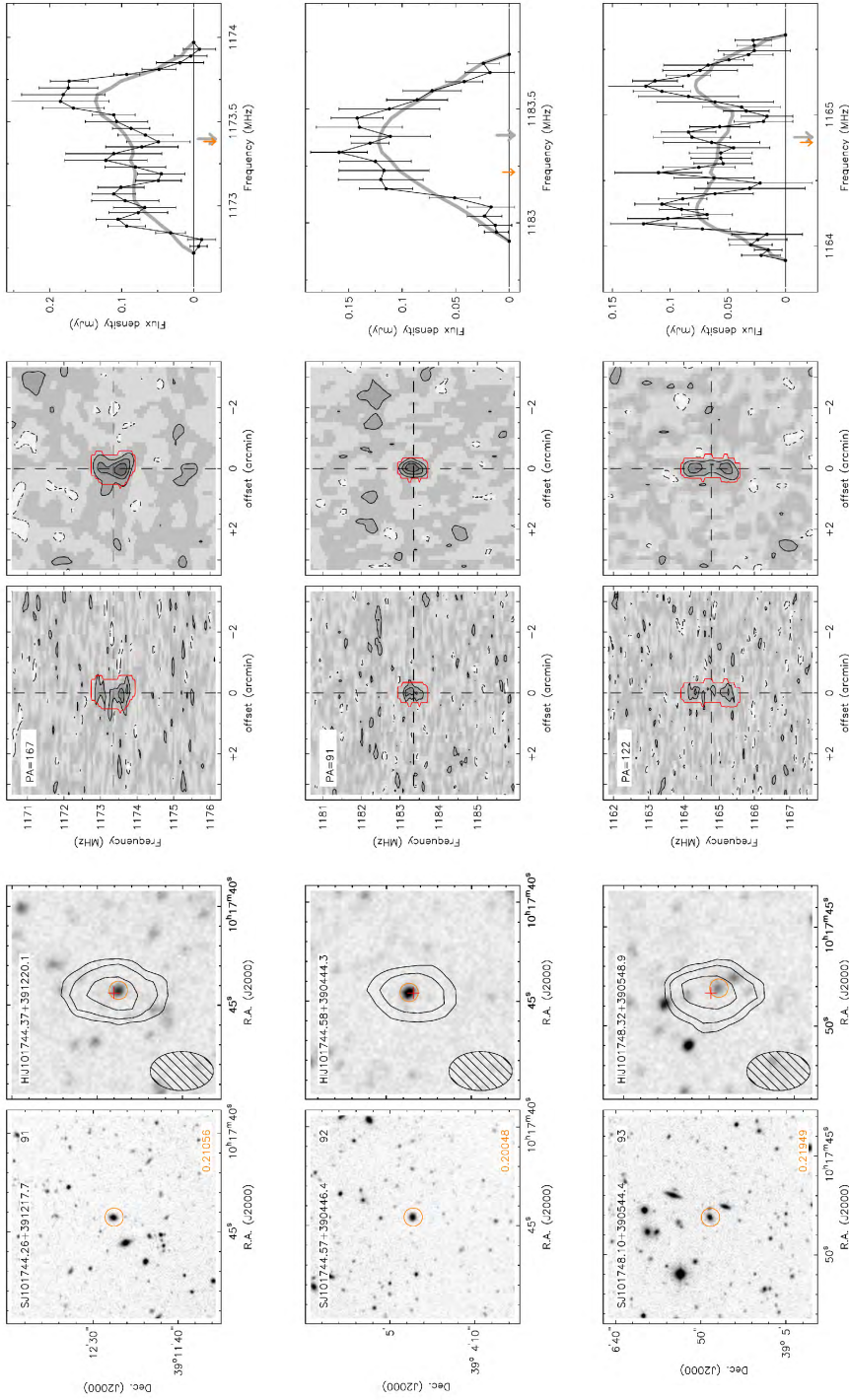
Atlas of HI detections in A963



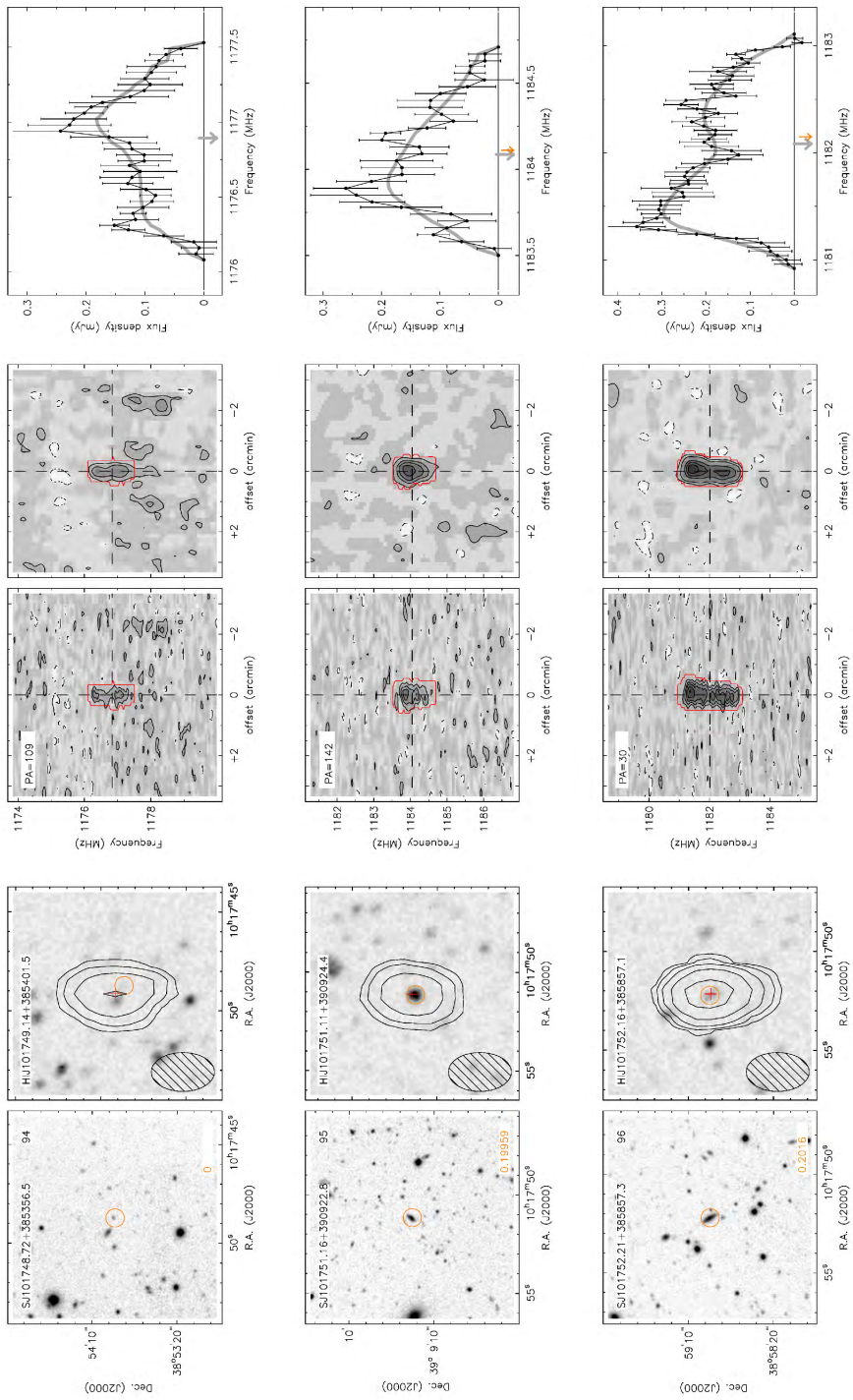
Atlas of HI detections in A963



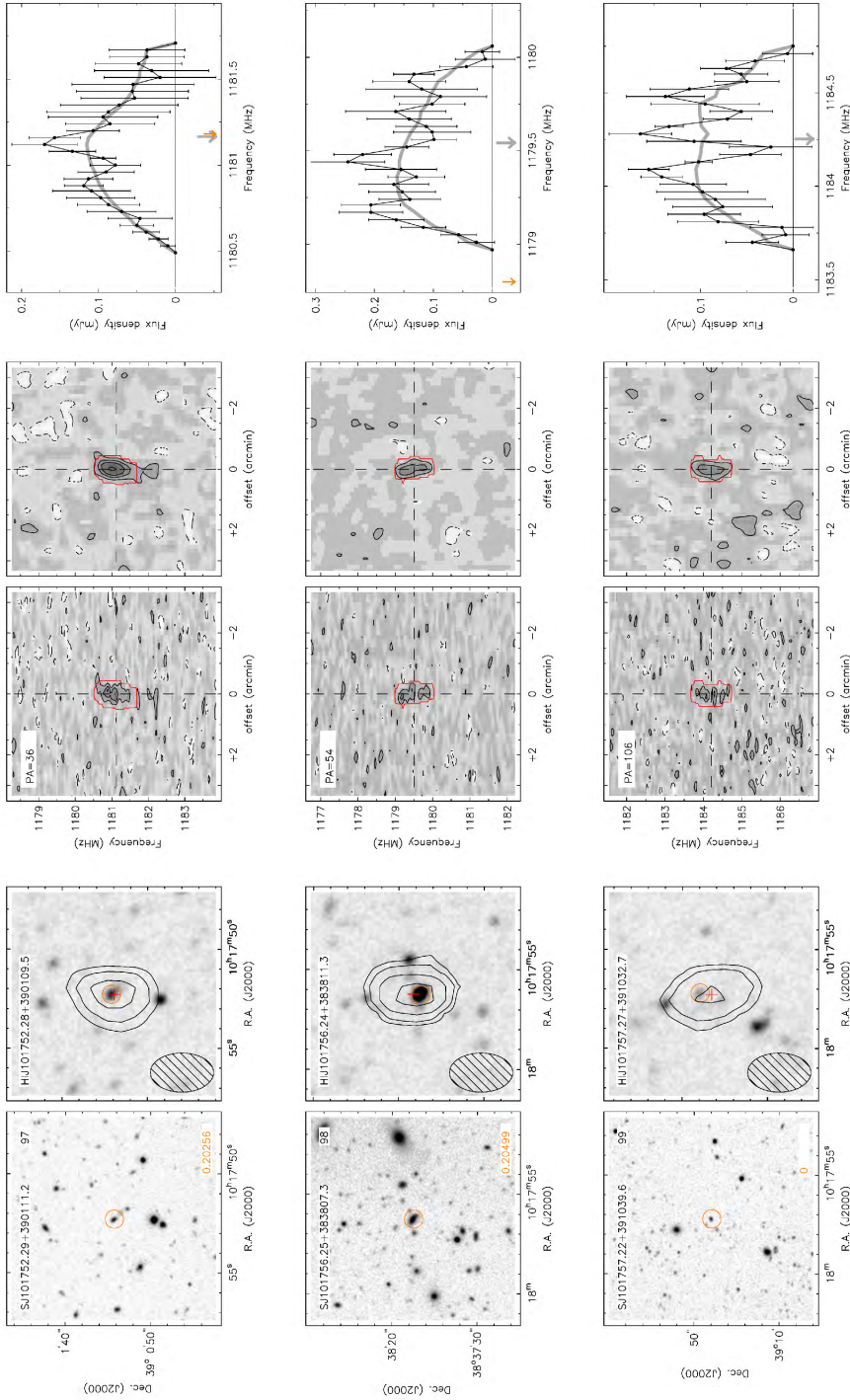
Atlas of HI detections in A963



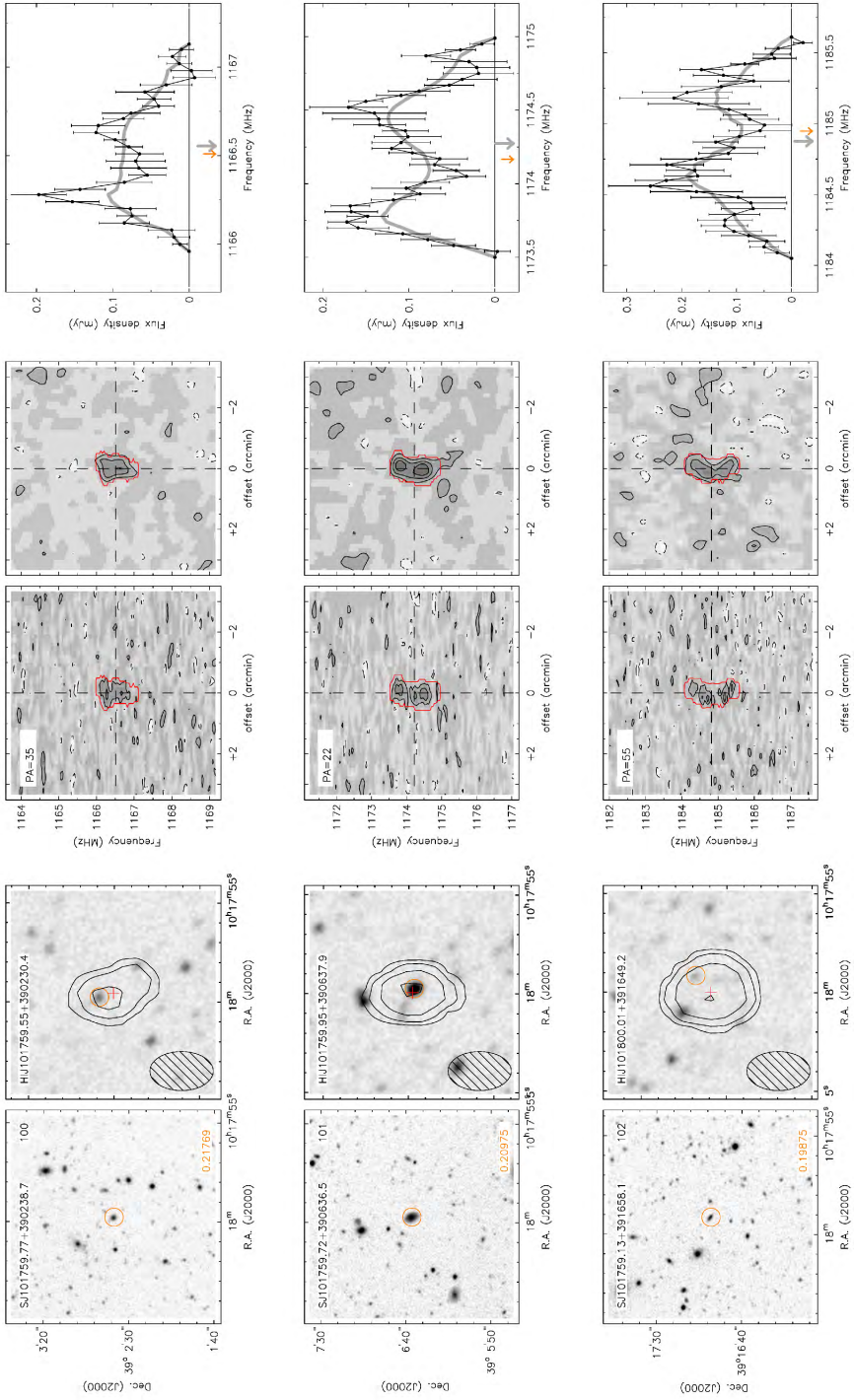
Atlas of HI detections in A963



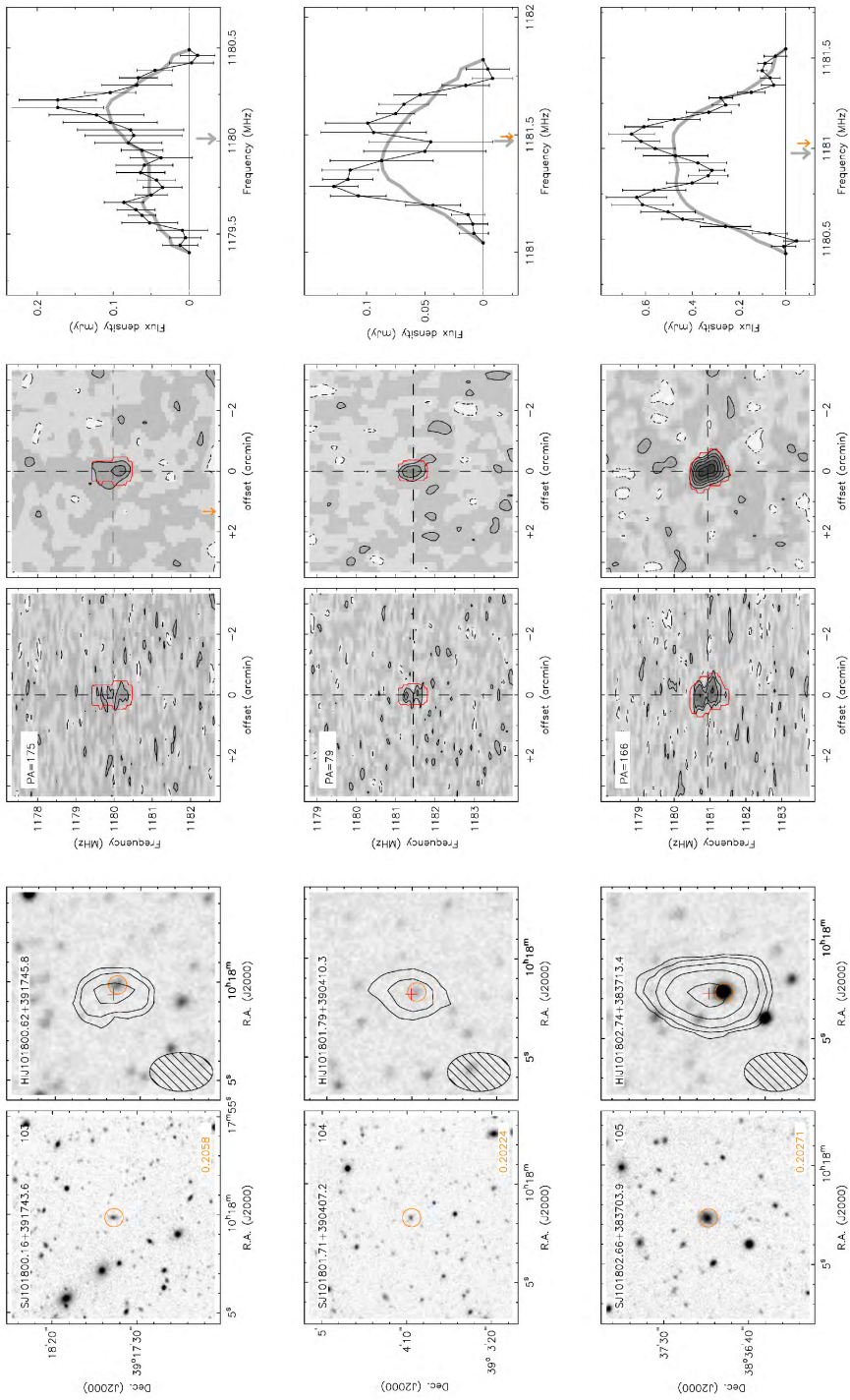
Atlas of HI detections in A963



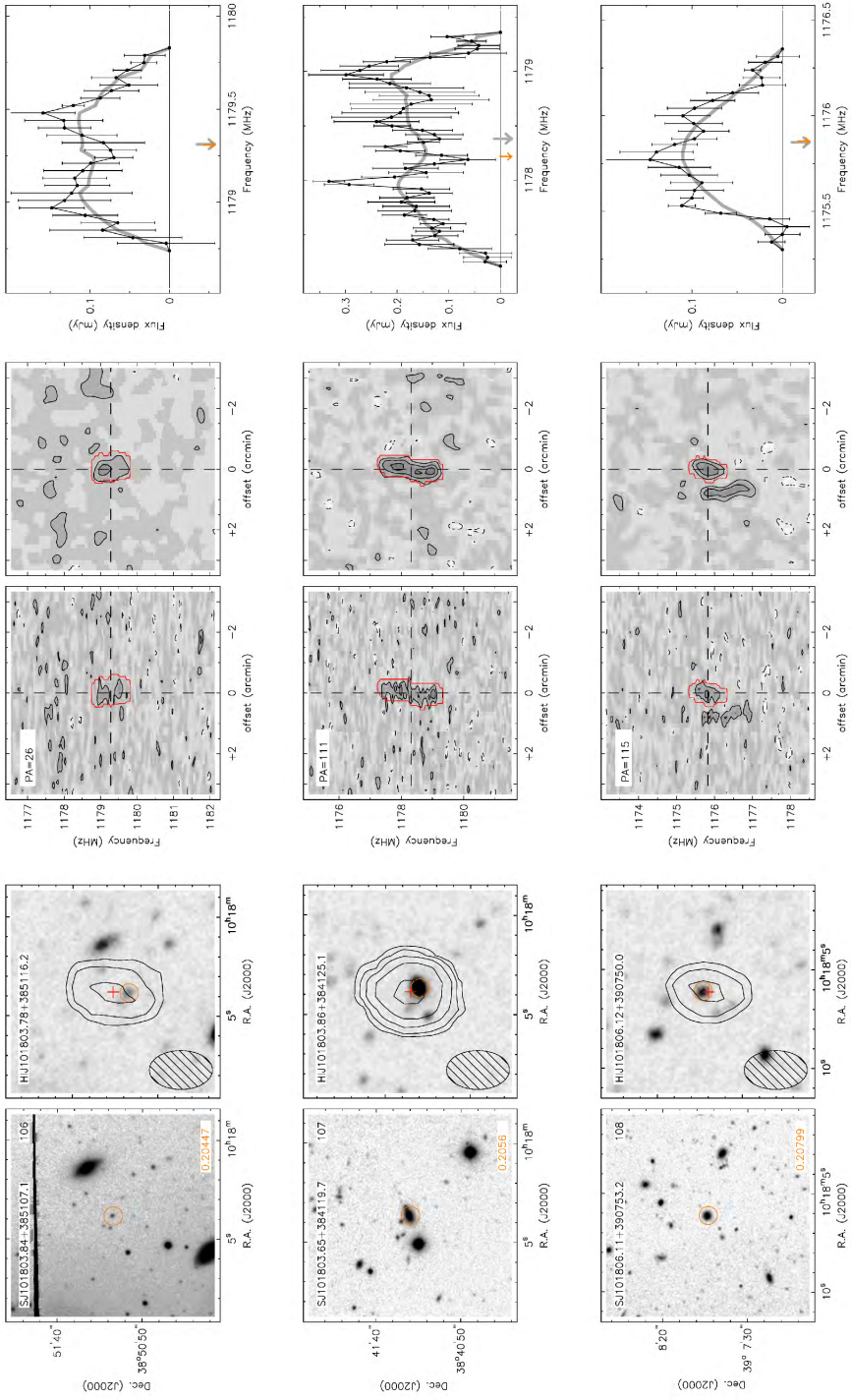
Atlas of HI detections in A963



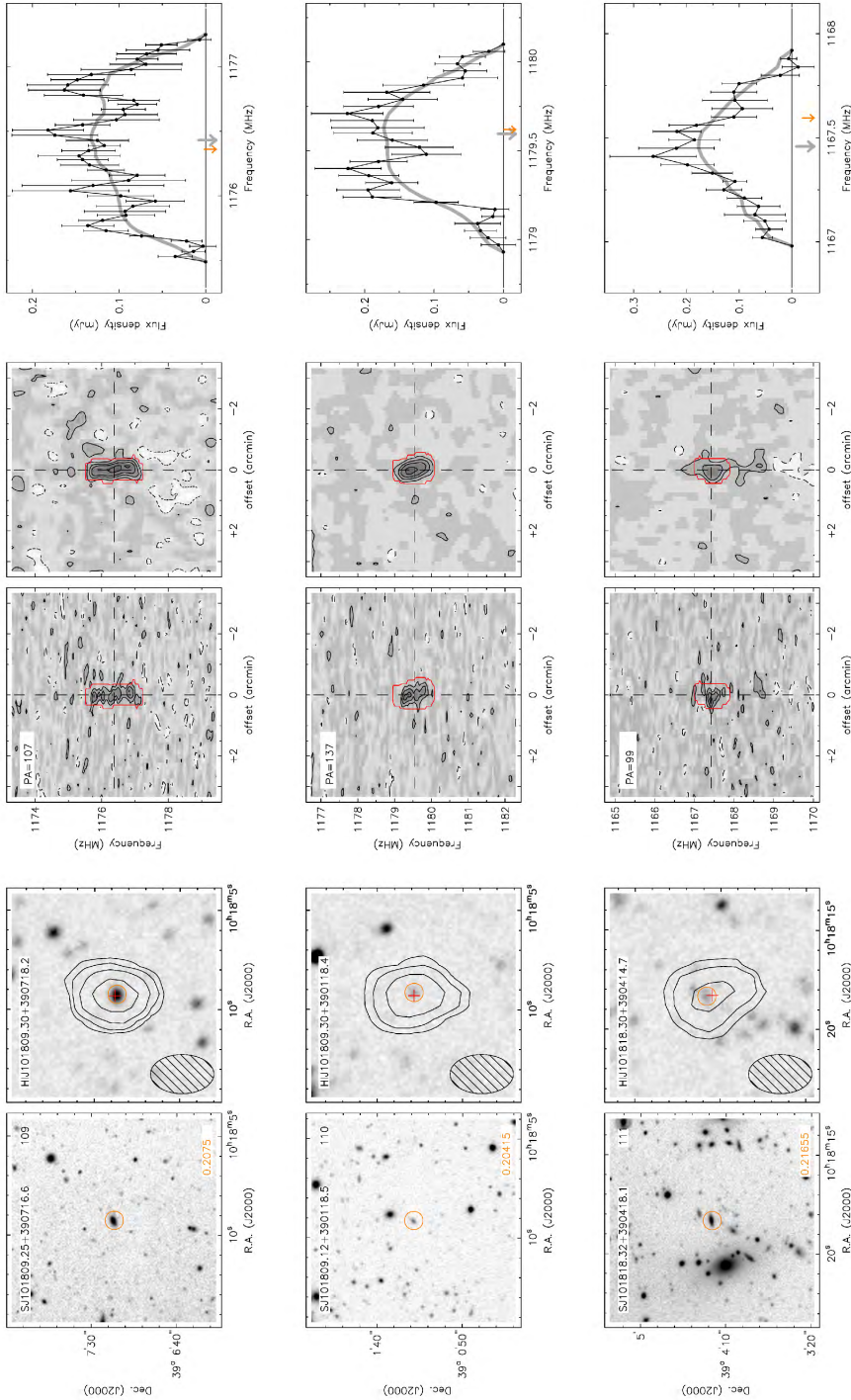
Atlas of HI detections in A963



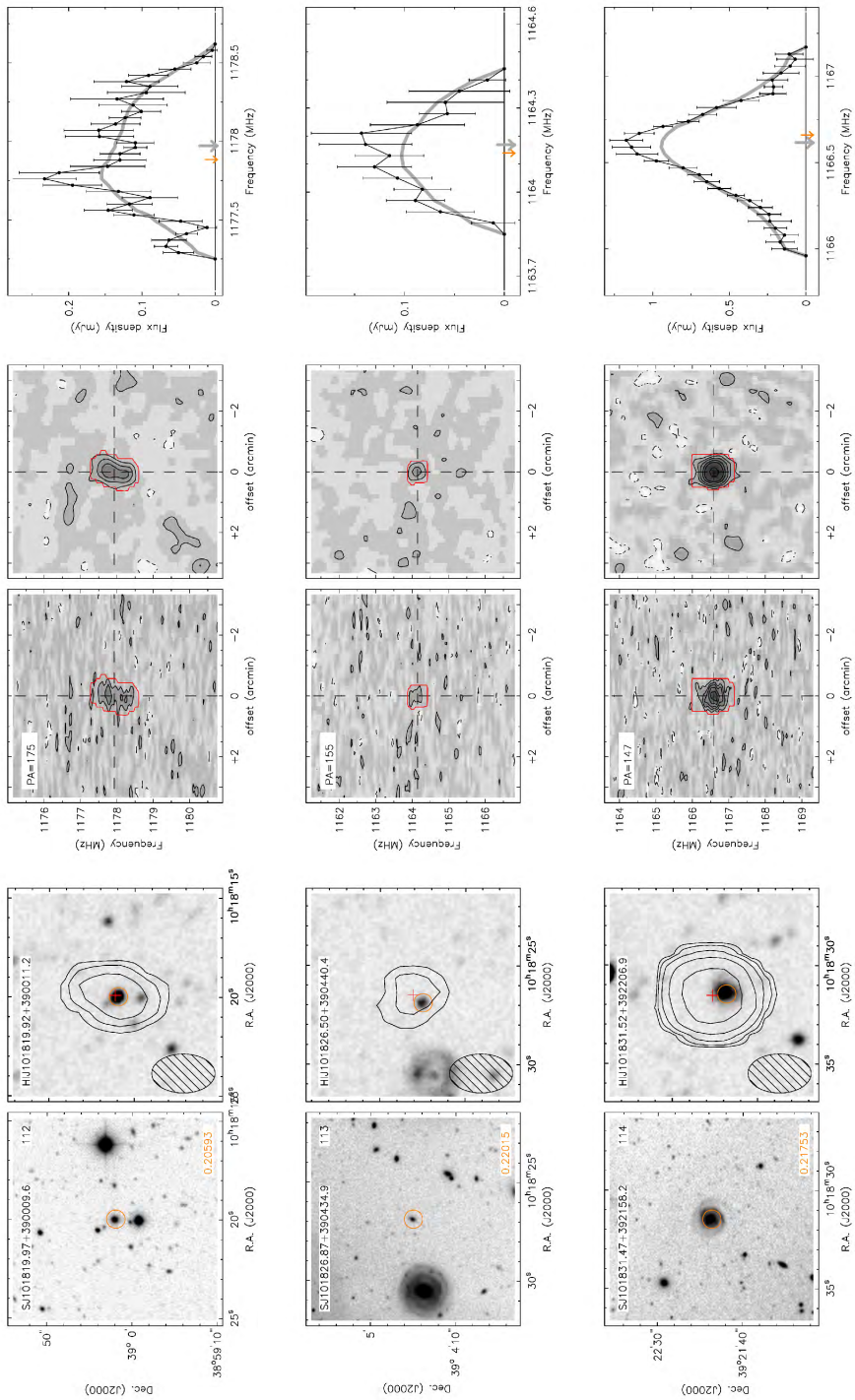
Atlas of HI detections in A963



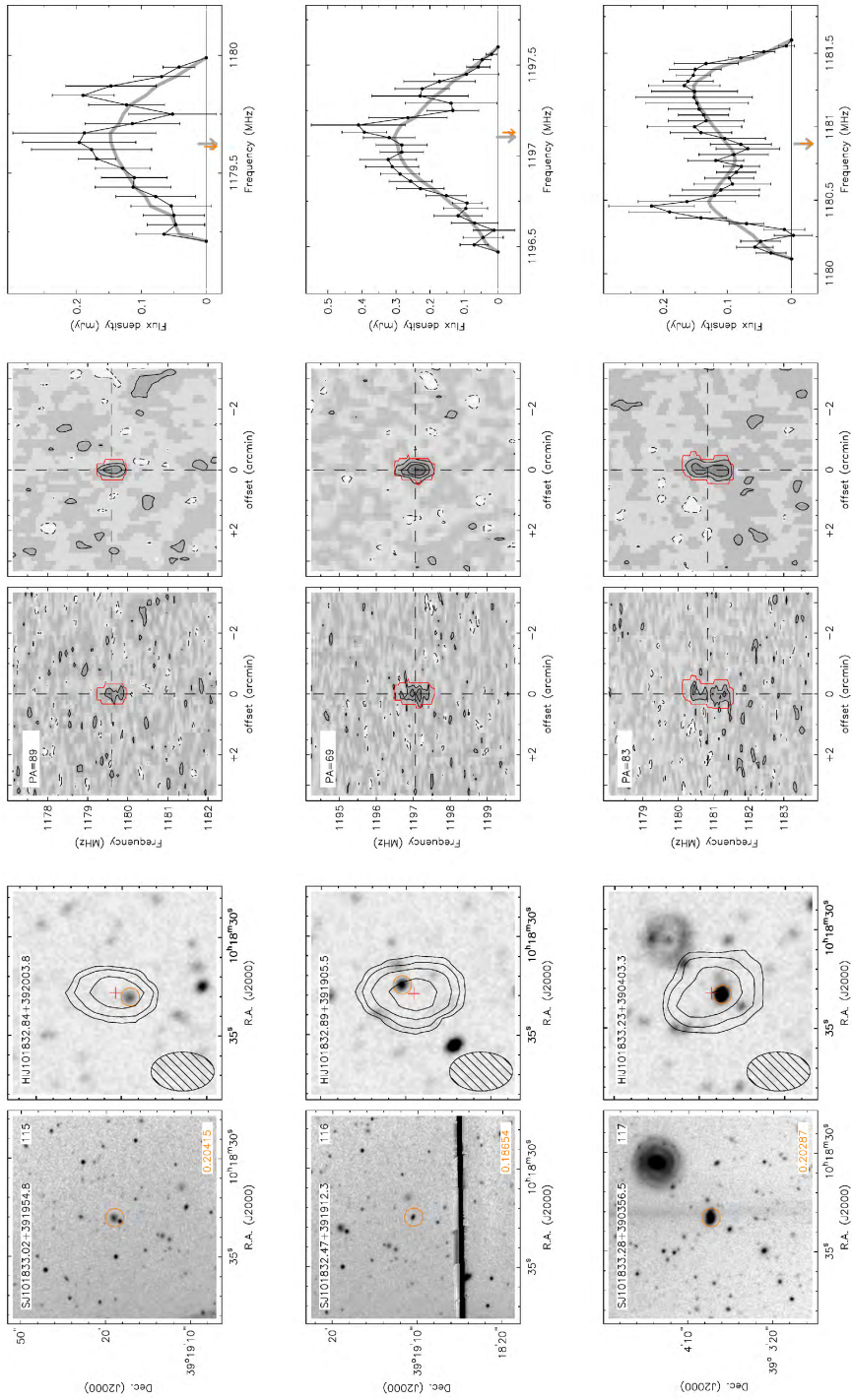
Atlas of HI detections in A963



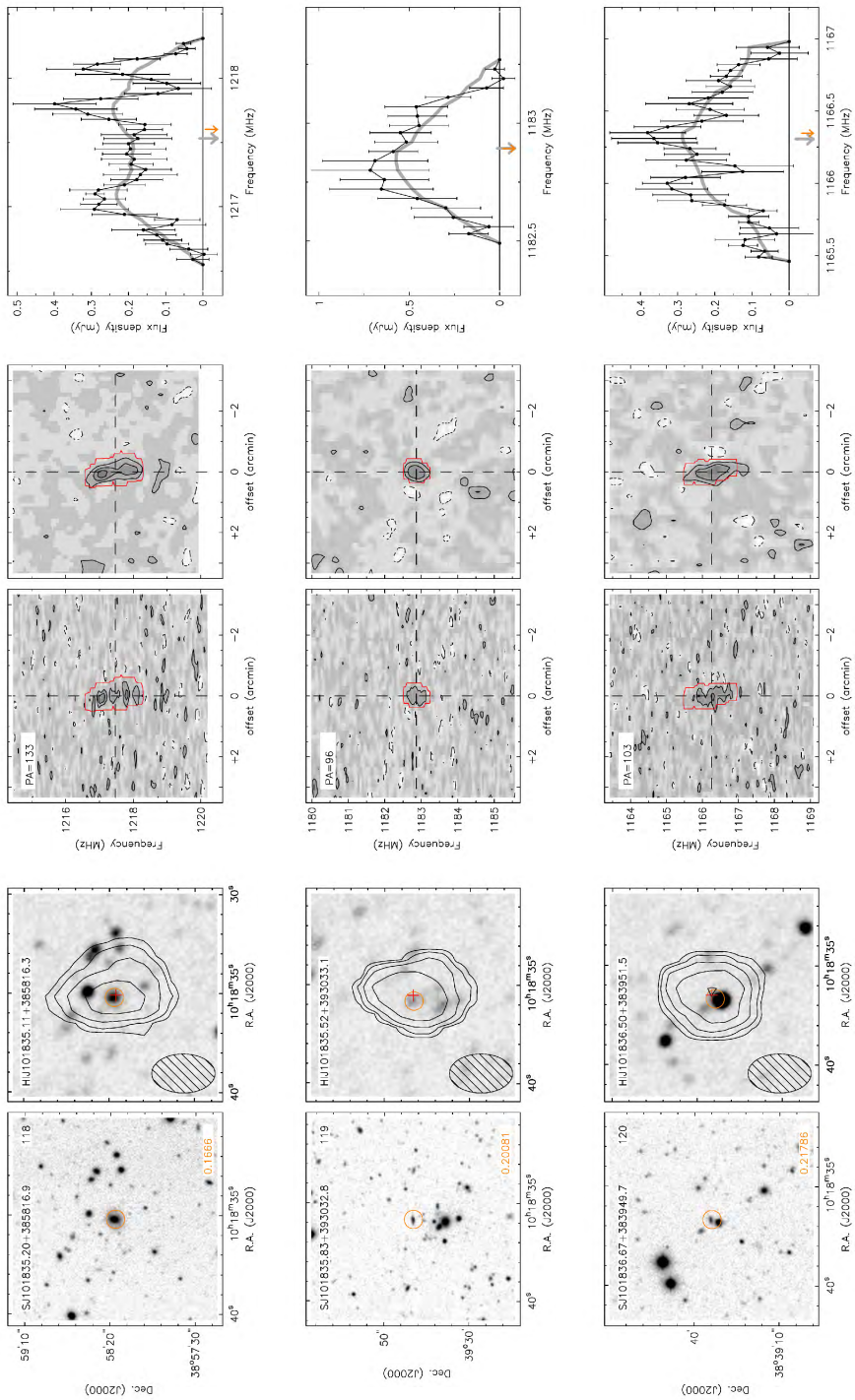
Atlas of HI detections in A963



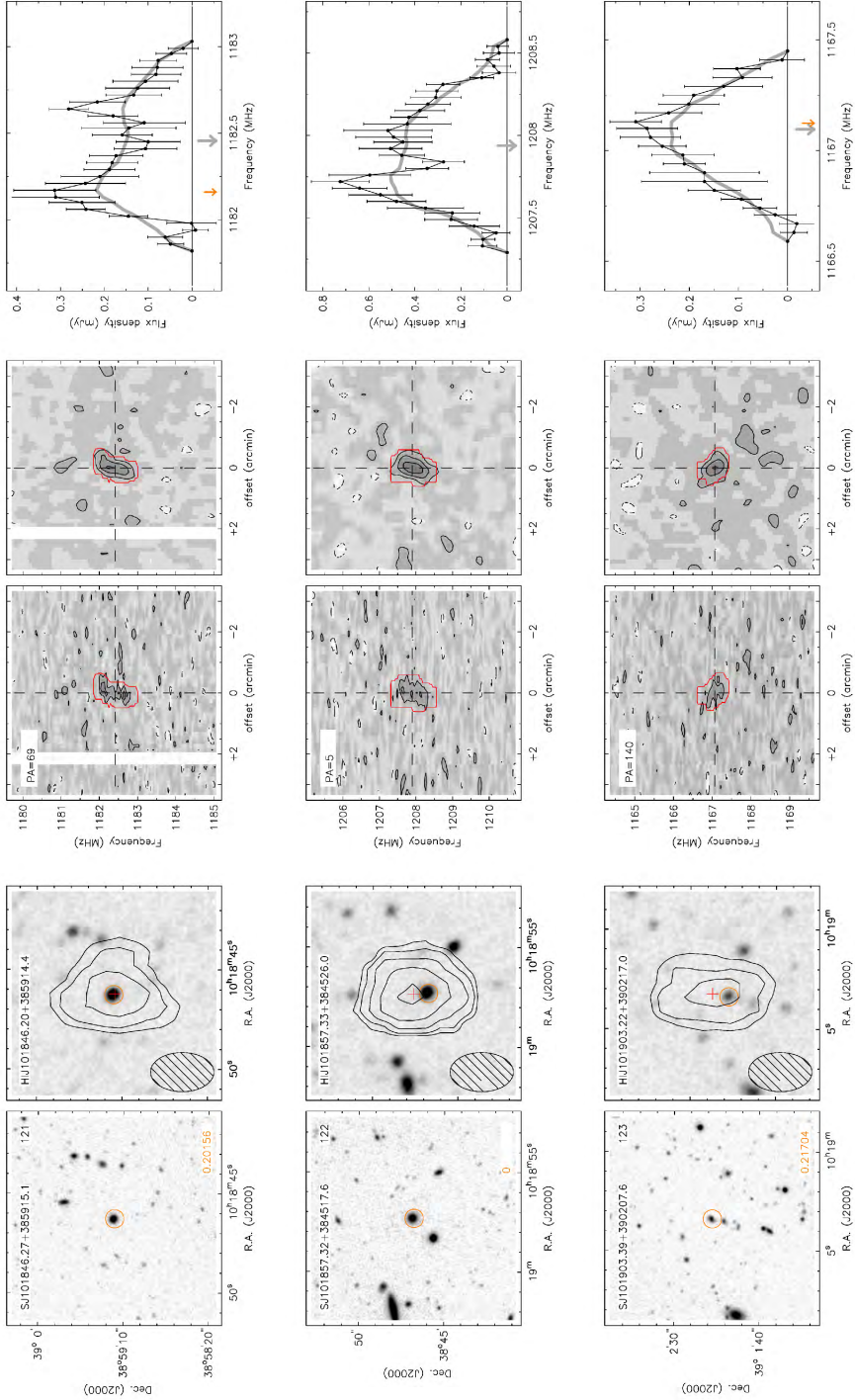
Atlas of HI detections in A963



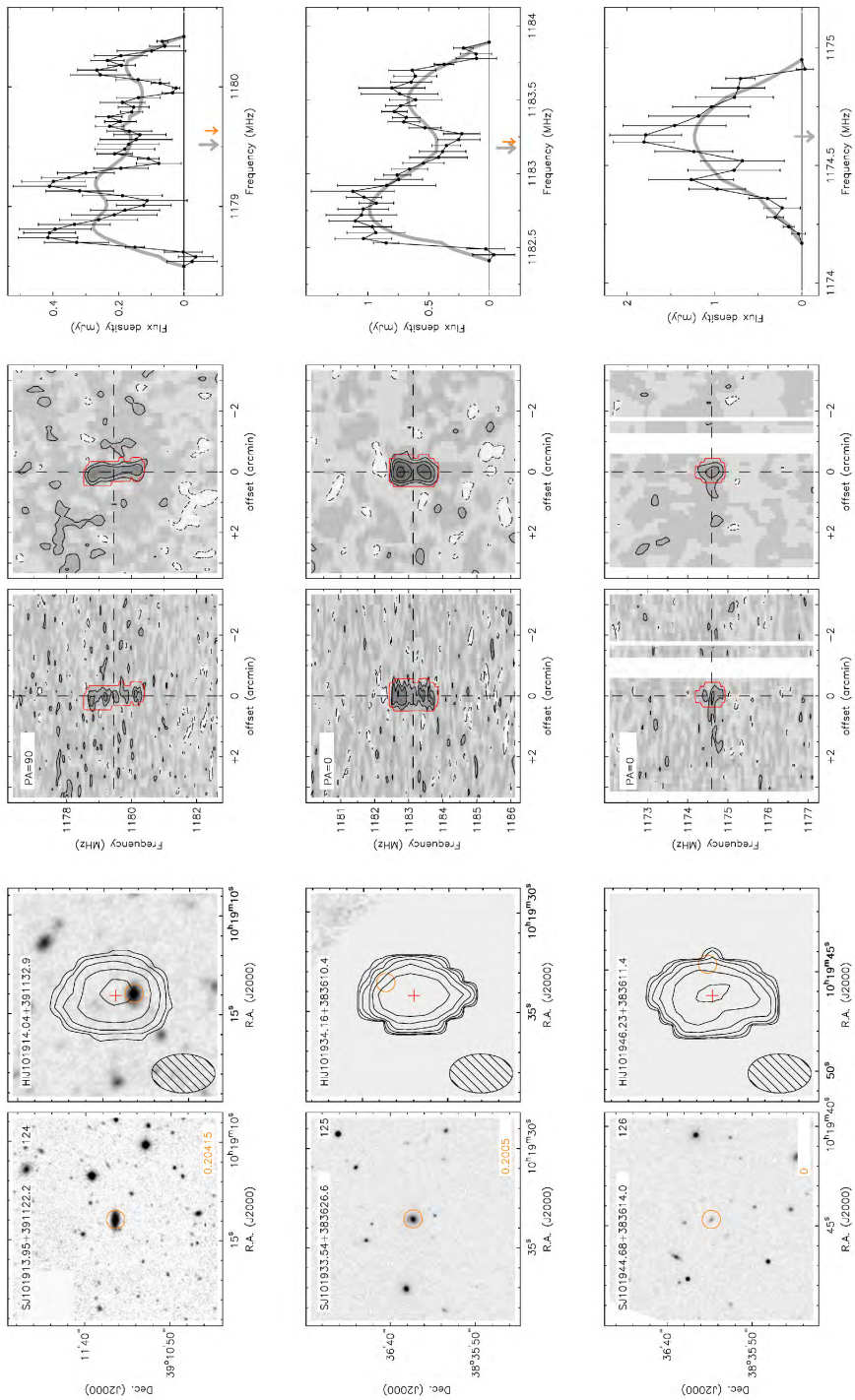
Atlas of HI detections in A963



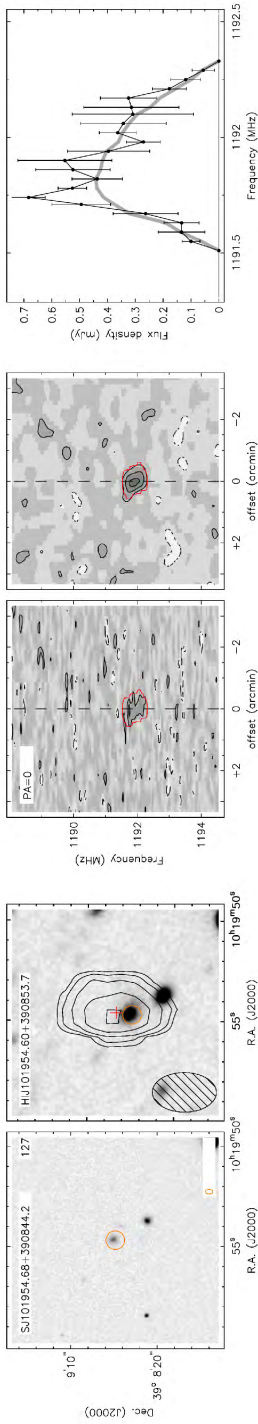
Atlas of HI detections in A963



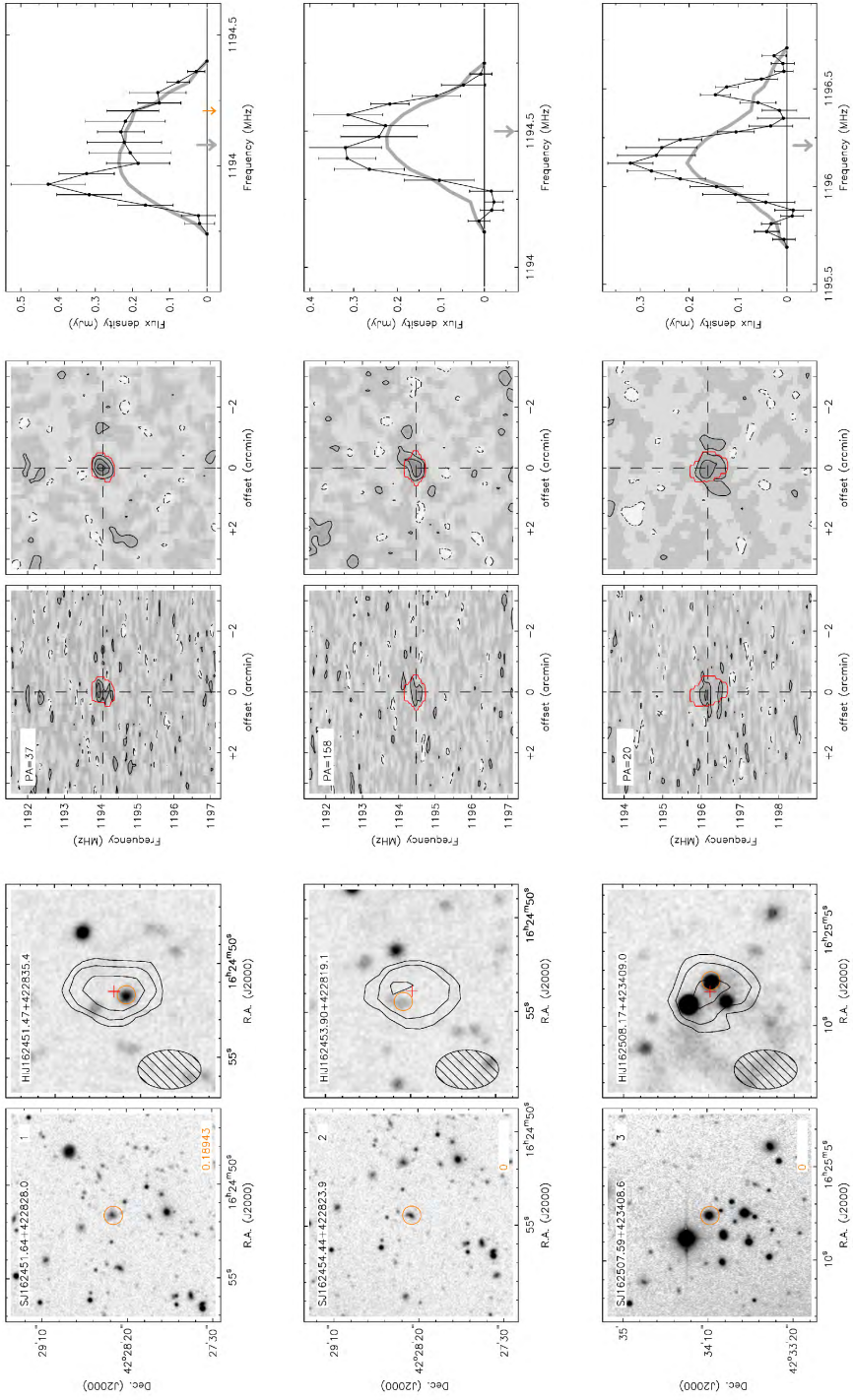
Atlas of HI detections in A963



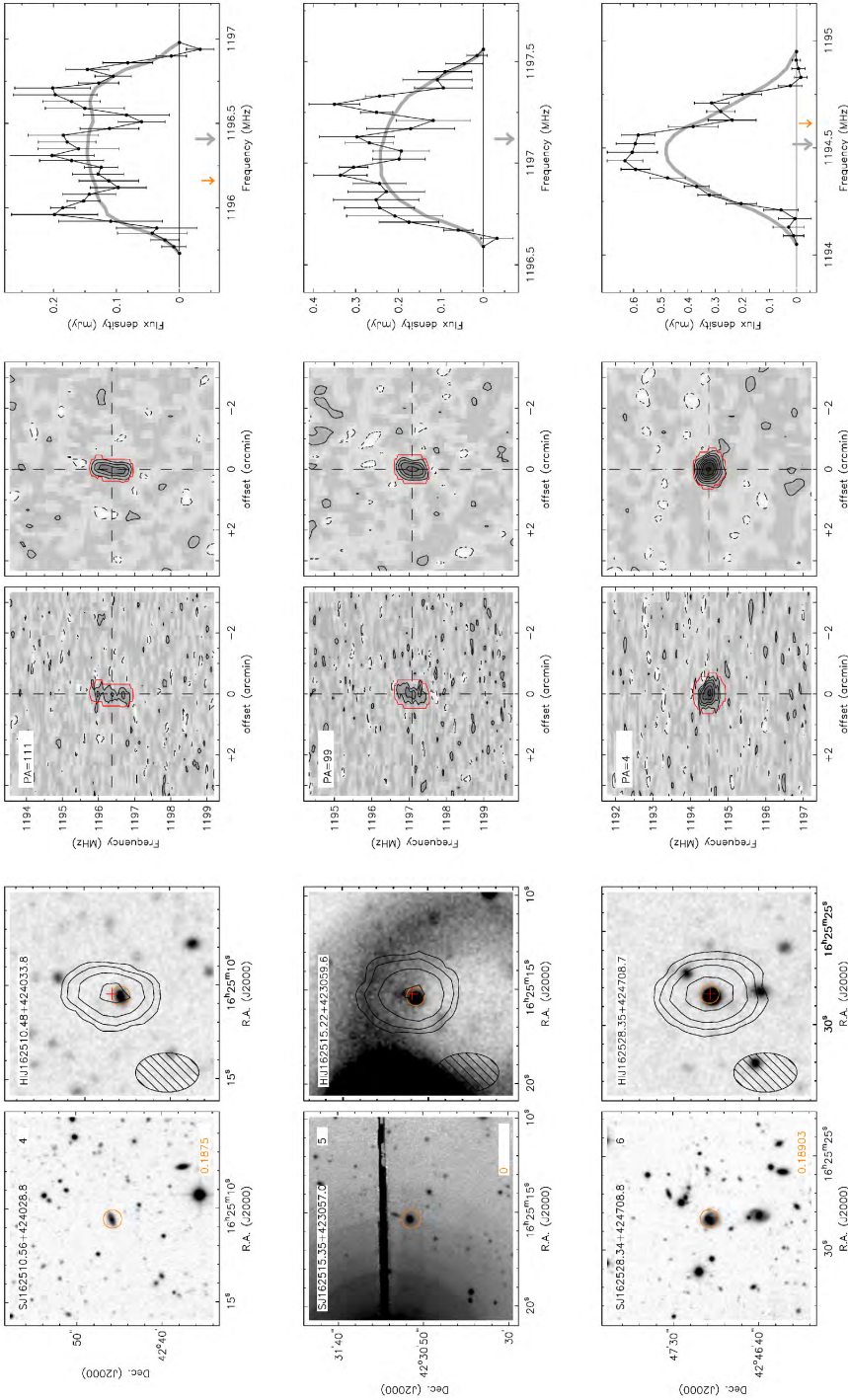
Atlas of HI detections in A963



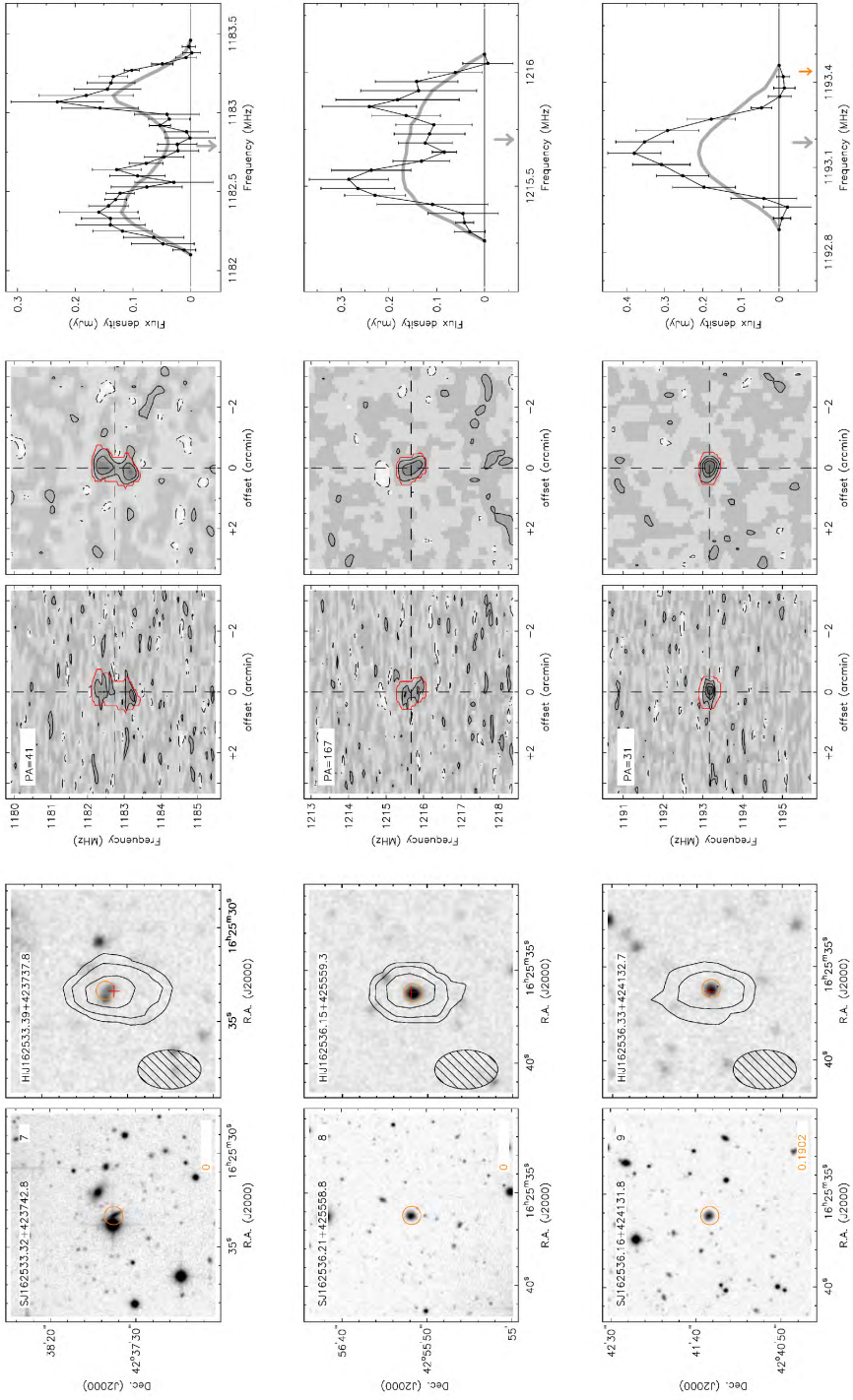
Atlas of HI detections in A963



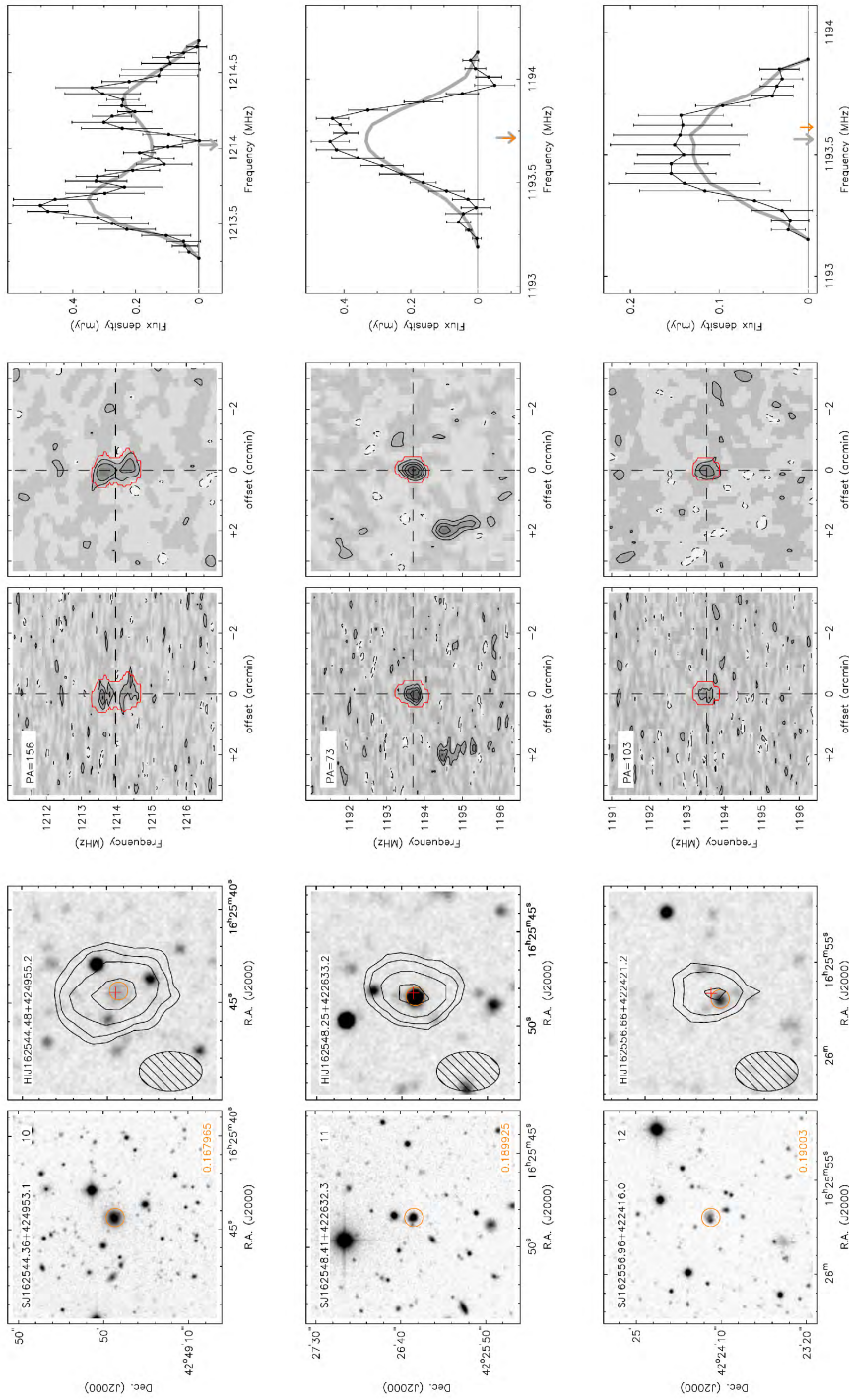
Atlas of HI detections in A2192



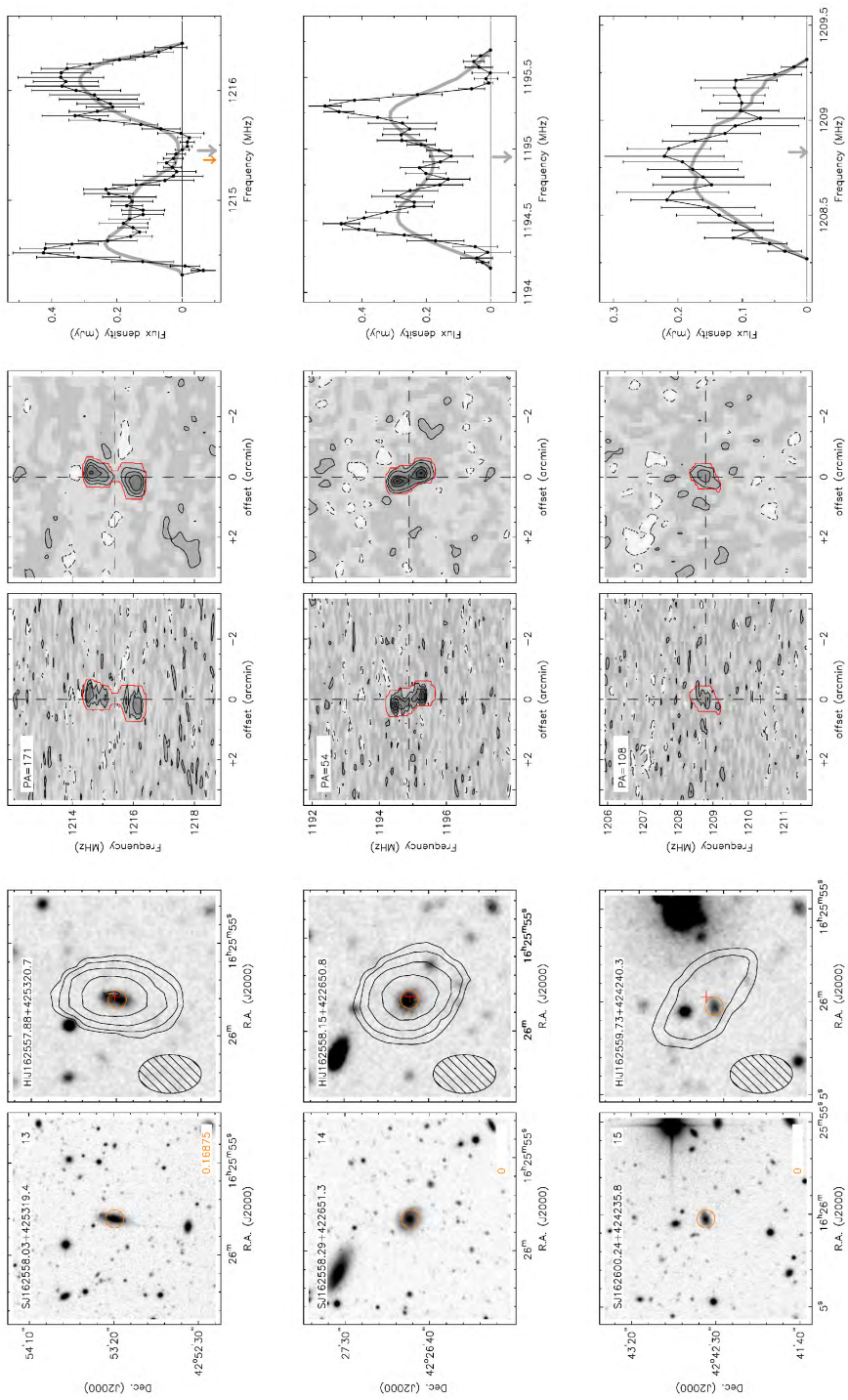
Atlas of HI detections in A2192



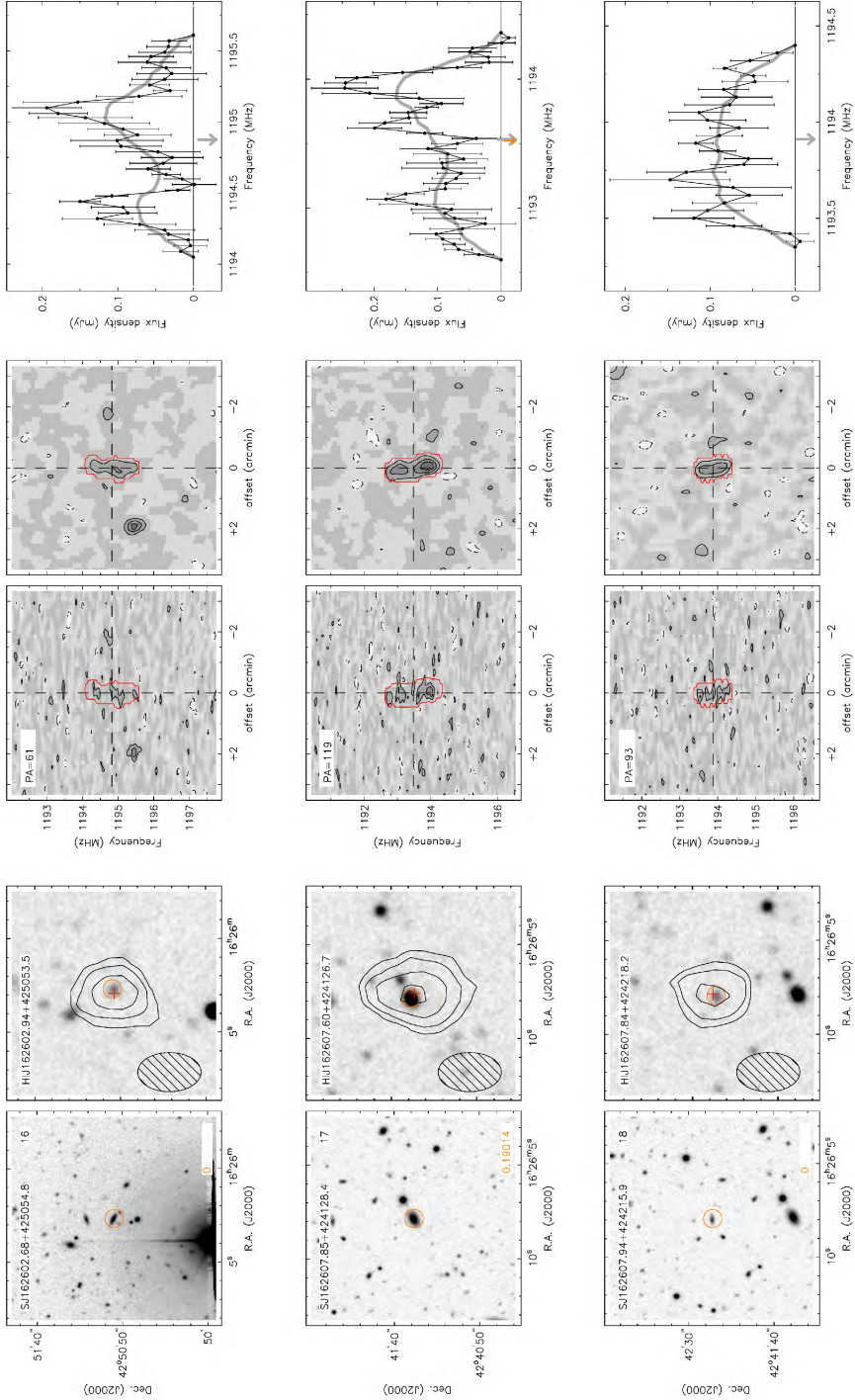
Atlas of HI detections in A2192



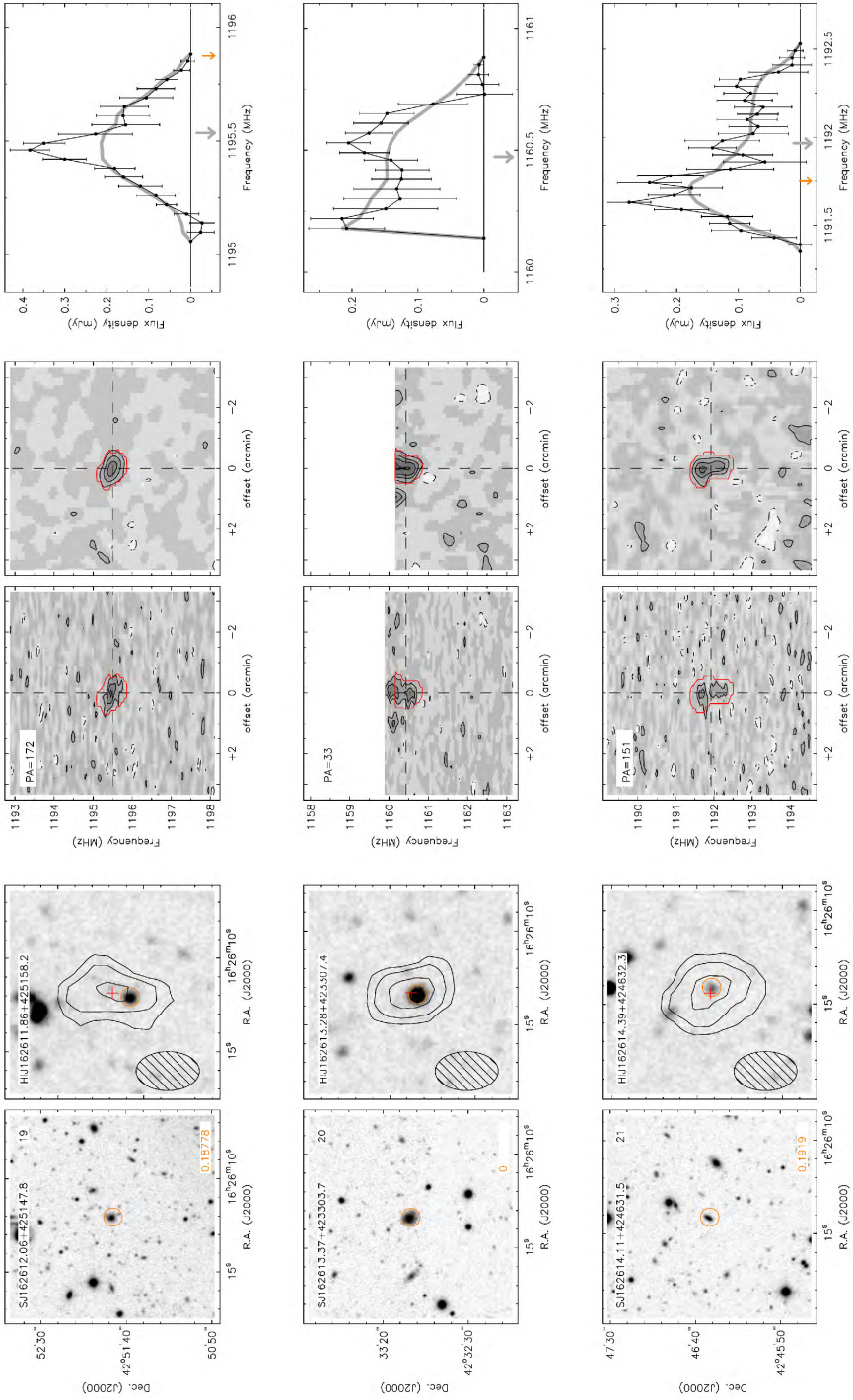
Atlas of HI detections in A2192



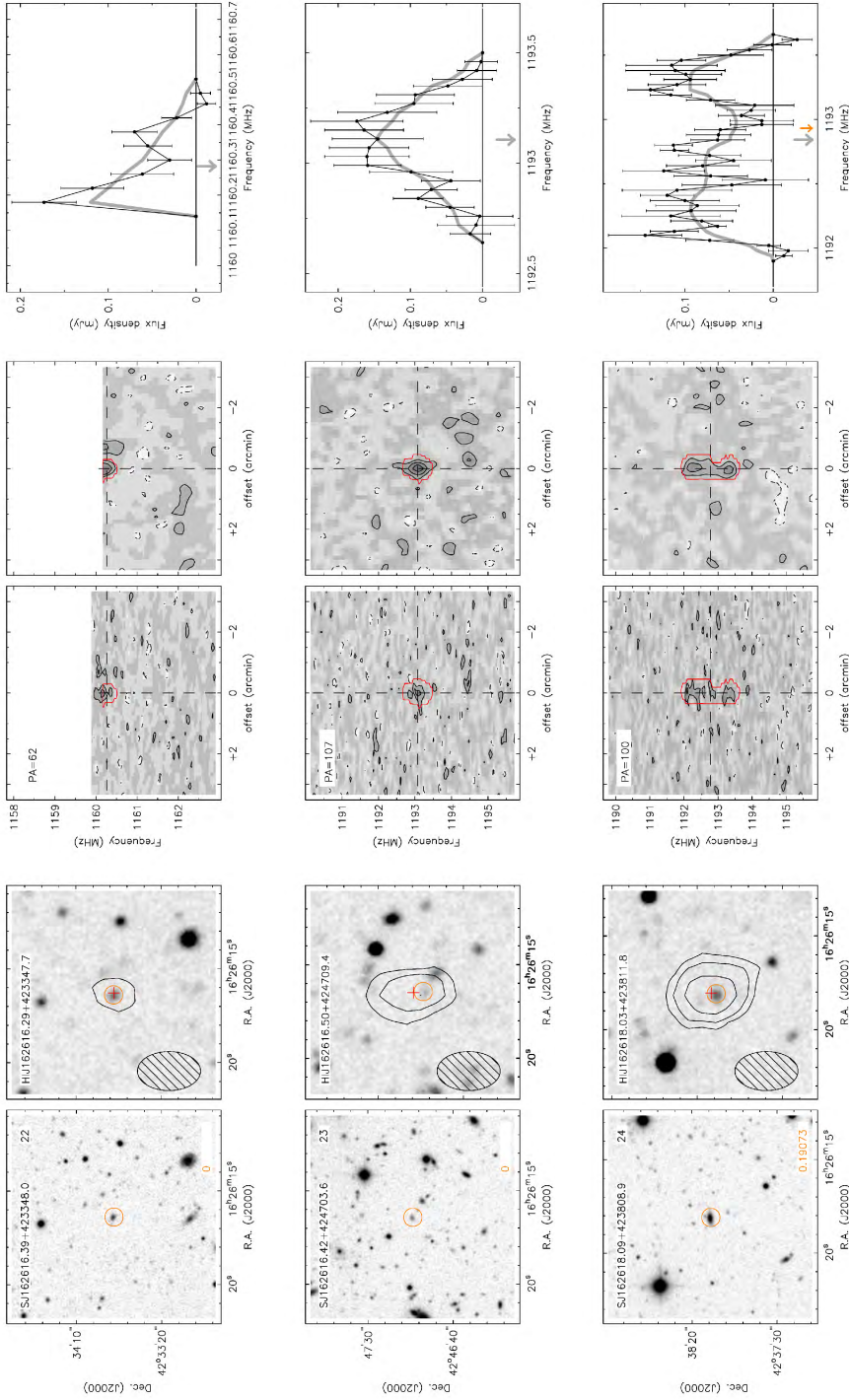
Atlas of HI detections in A2192



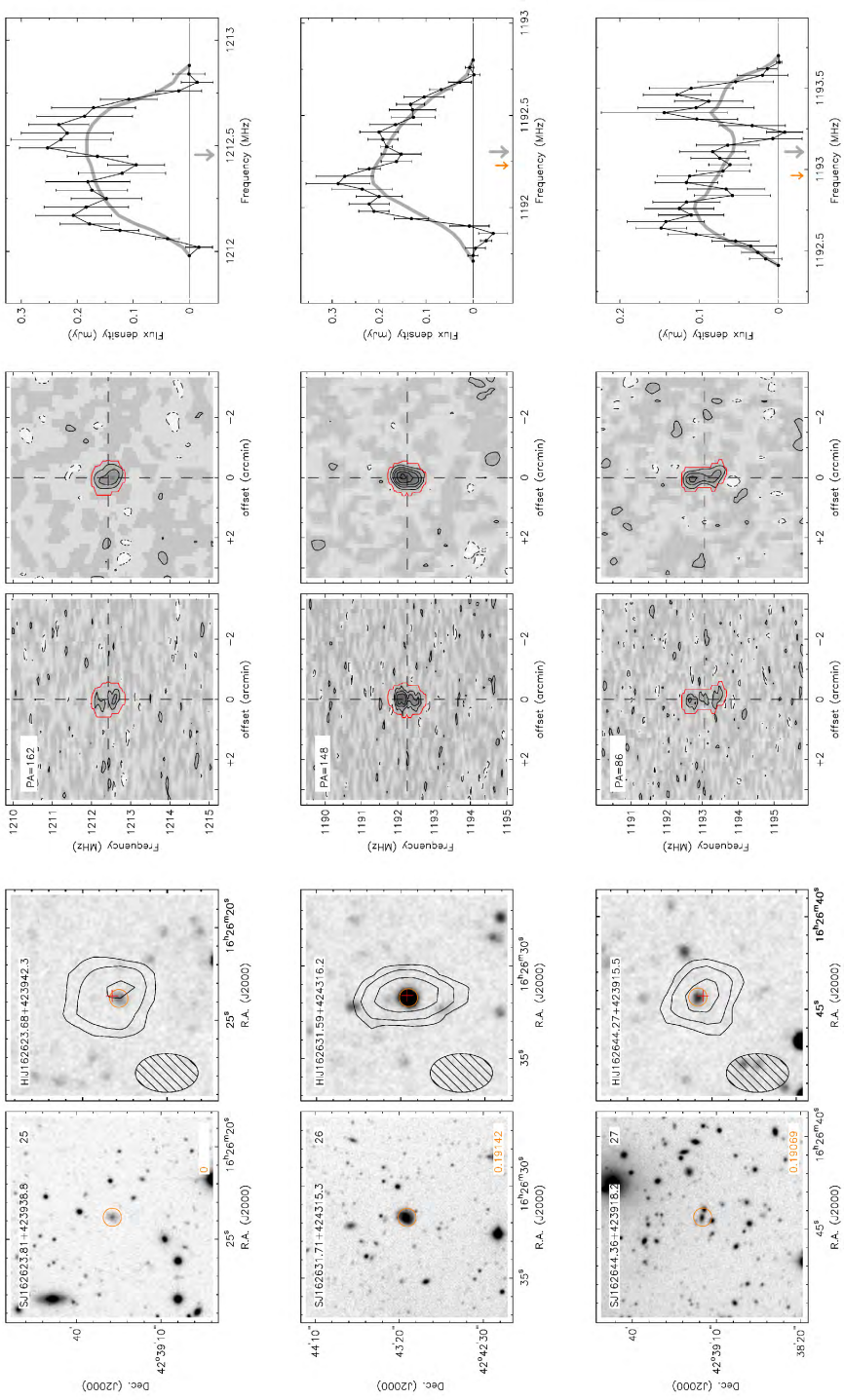
Atlas of HI detections in A2192



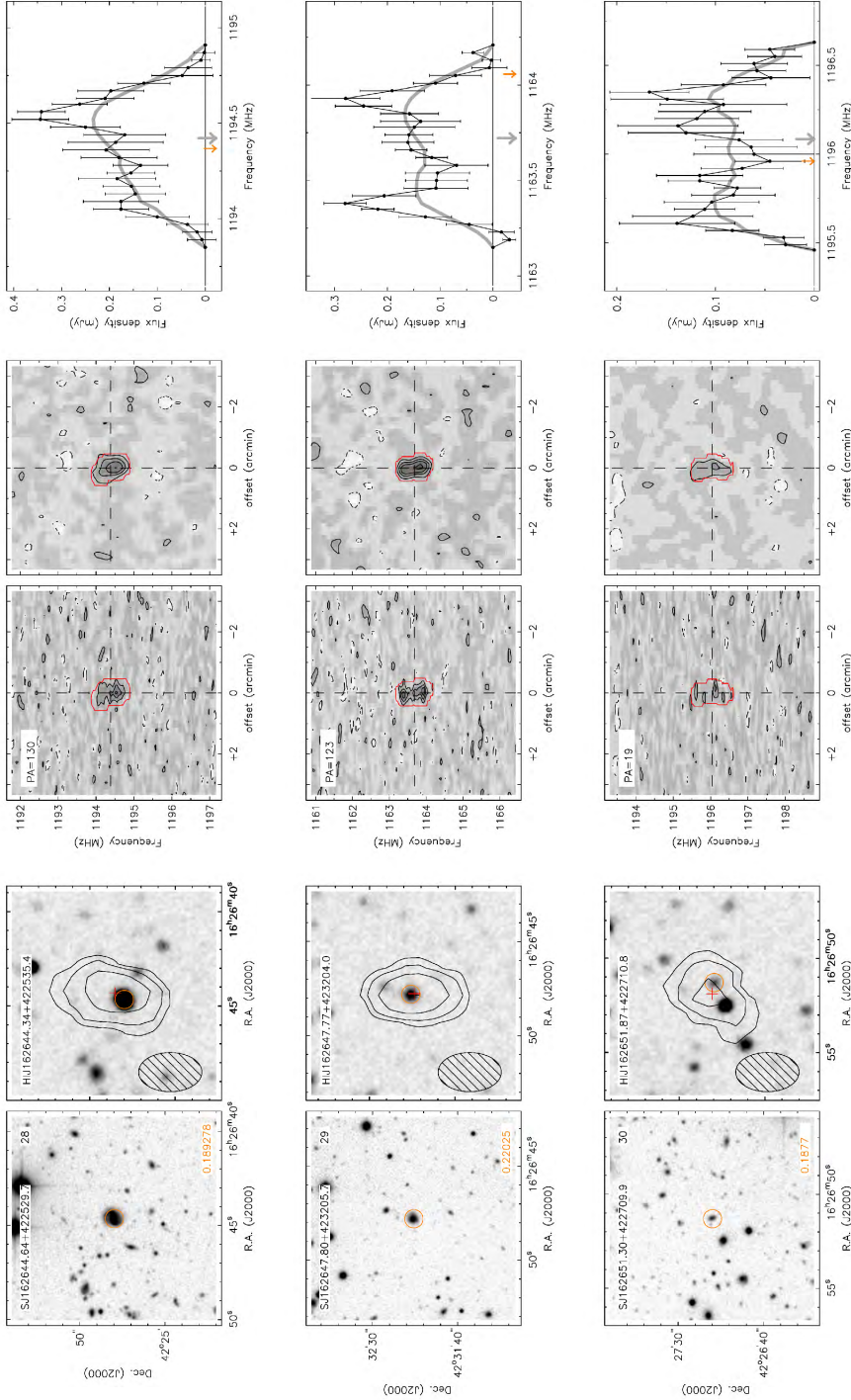
Atlas of HI detections in A2192



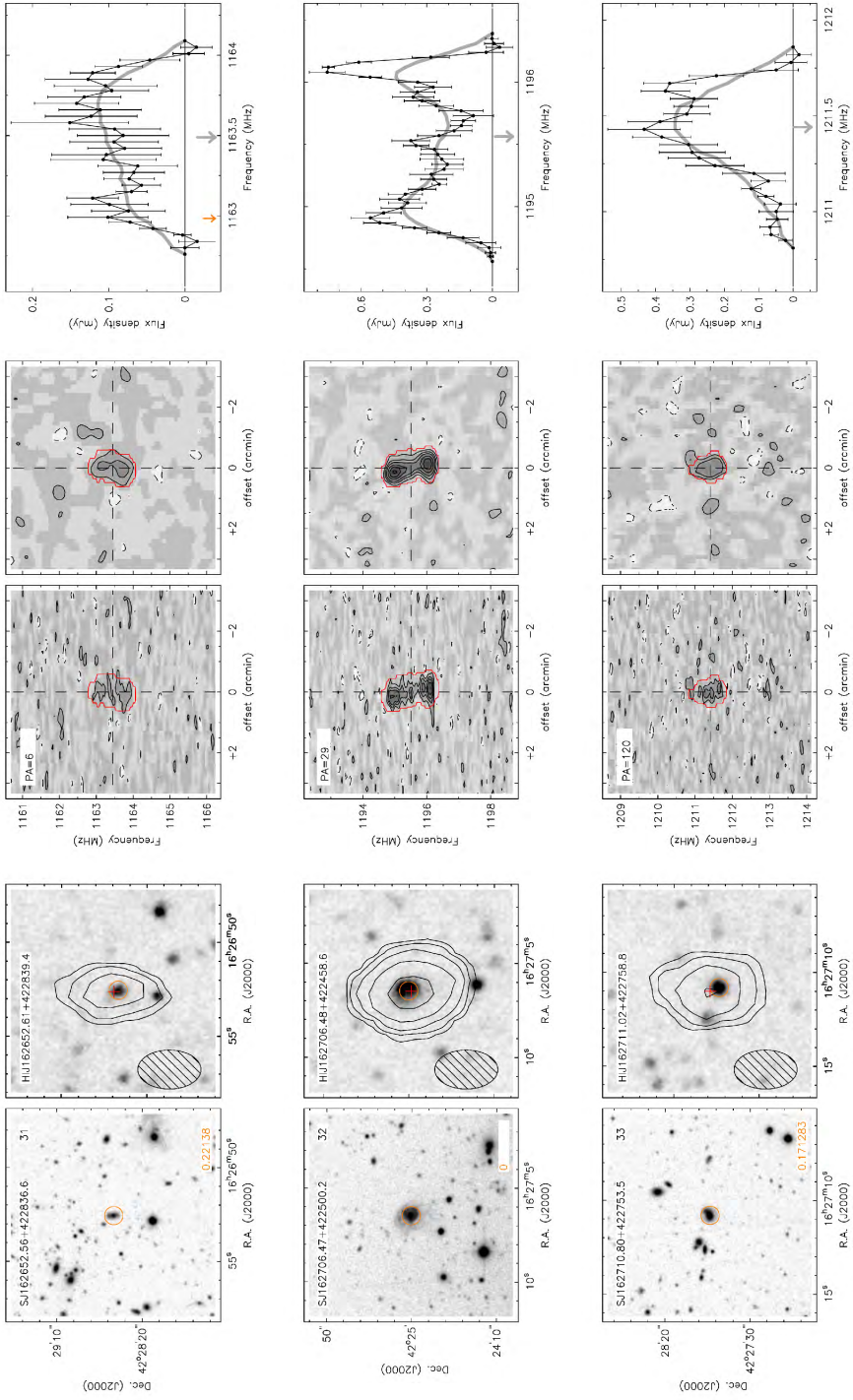
Atlas of HI detections in A2192



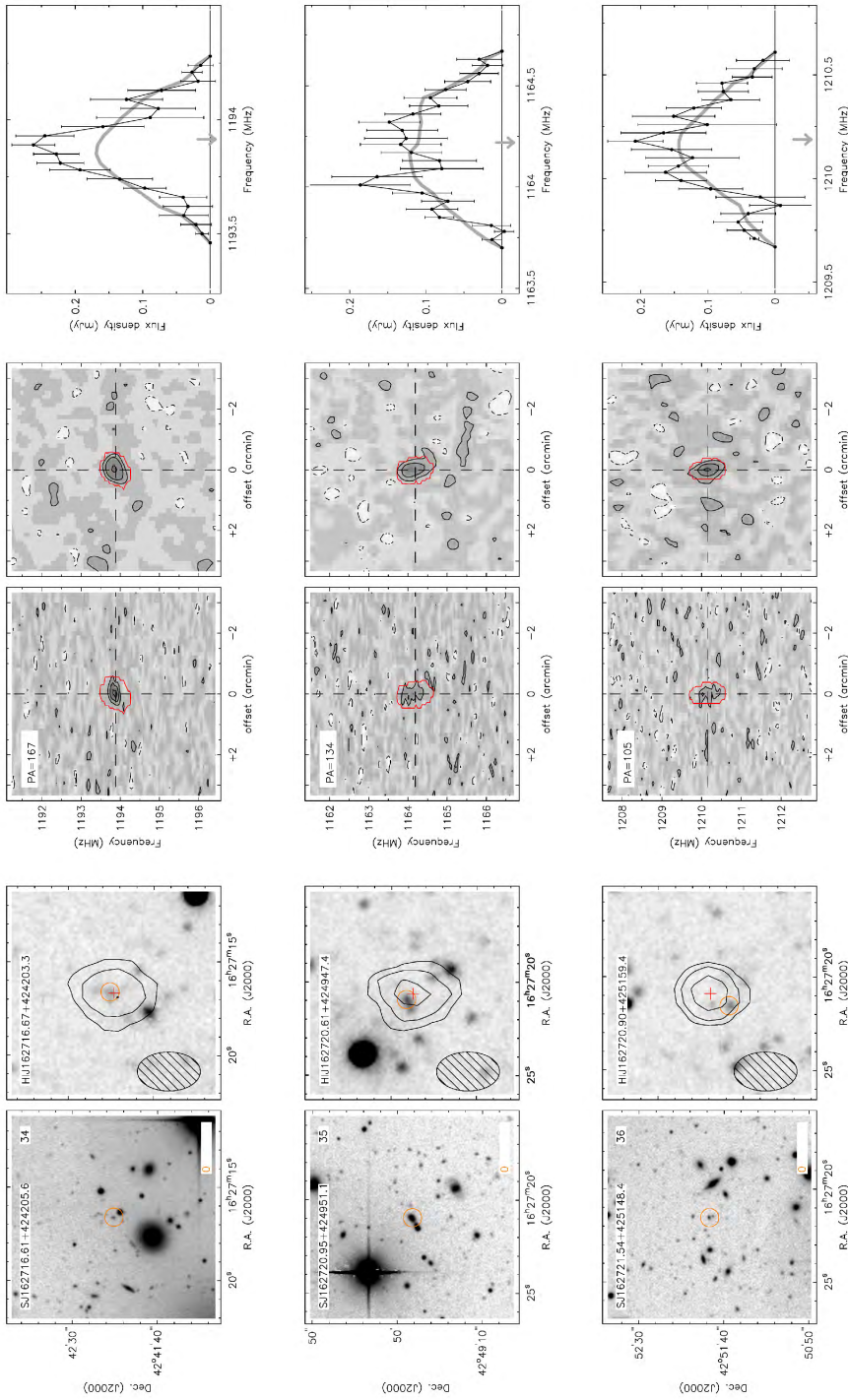
Atlas of HI detections in A2192



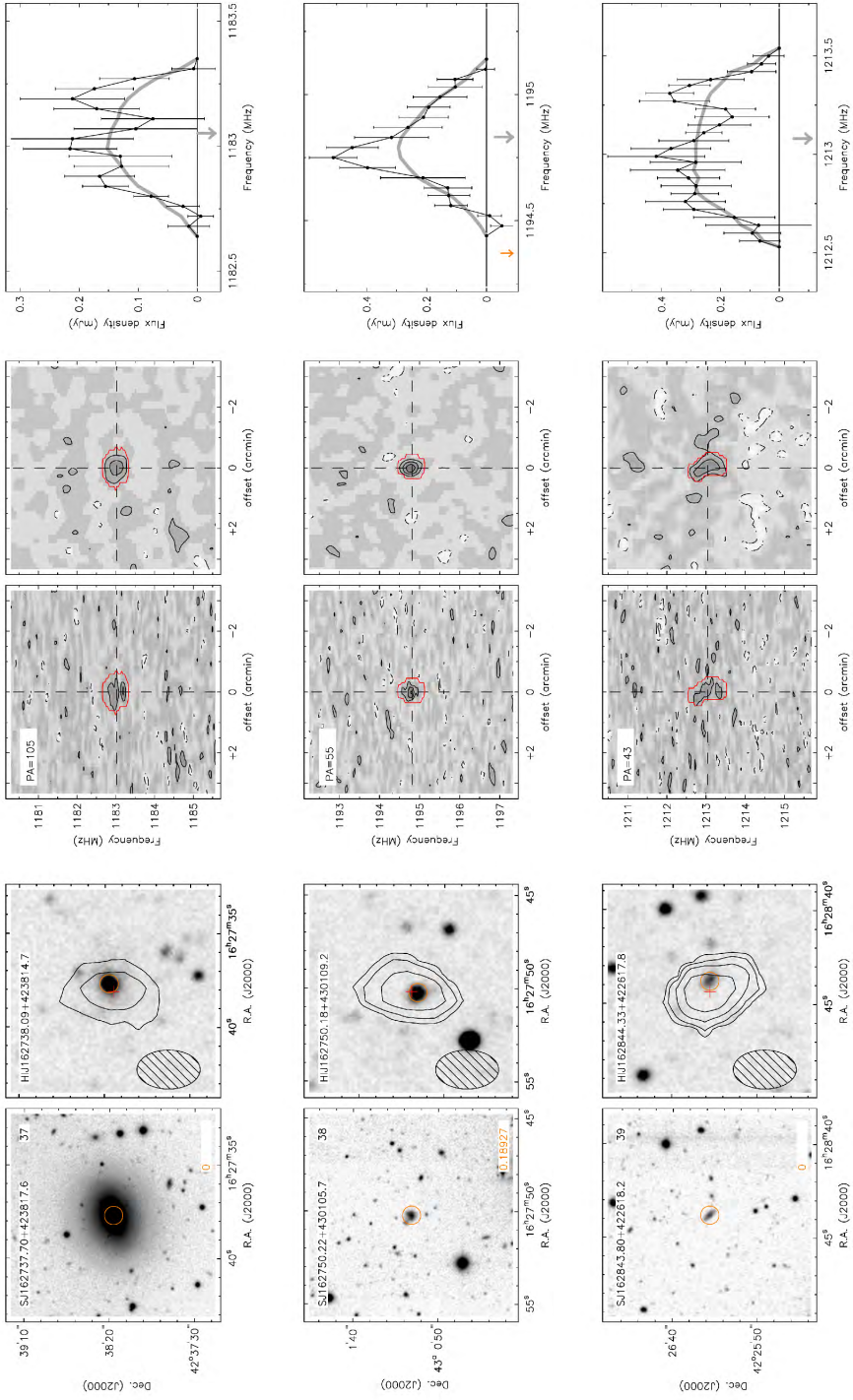
Atlas of HI detections in A2192



Atlas of HI detections in A2192



Atlas of HI detections in A2192



Atlas of HI detections in A2192



# BUDHIES V: The Baryonic Tully-Fisher relation at $z \sim 0.2$ based on direct HI detections

Avanti Gogate<sup>a</sup>, Marc Verheijen<sup>a</sup>, Thijs van der Hulst<sup>a</sup> Yara Jaffé<sup>b</sup>

<sup>a</sup> Kapteyn Astronomical Institute, University of Groningen, PO box 800, 9700AV, Groningen

<sup>b</sup> Instituto de Física y Astronomía, Universidad de Valparaíso, Avda. Gran Bretaña 1111, Casilla 5030, Valparaíso, Chile

*Resubmitted to MNRAS after first review.*

## Abstract

We present HI-based B- and R-band Tully-Fisher relations (TFrs) and the Baryonic TFr (BTFR) at  $z \sim 0.2$  using direct HI detections from the Blind Ultra-Deep HI Environmental Survey (BUDHiES). Deep photometry from the Isaac Newton Telescope was used for 36 out of 166 HI sources, matching the quality criteria required for a robust TFr analysis. Two velocity definitions at 20% and 50% of the peak flux were measured from the global HI profiles and adopted as proxies for the rotational velocities. We compare our results with an identically constructed  $z=0$  TFr from the Ursa Major association of galaxies. All the samples were treated identically regarding sample selection and corrections applied to ensure an unbiased comparison of the TFr. We provide an atlas and catalogues showcasing the properties of the galaxies. Our analysis is focused on the zero points of the TFr and BTFR with their slopes fixed to the  $z=0$  relation. Our main results are: (1) The BUDHiES sample consists of shallower and more asymmetric HI profiles than UMa, which is likely due to the environment in which the galaxies reside, (2) The luminosity-based  $z \sim 0.2$  TFrs are brighter and bluer than the  $z=0$  TFrs, even when cluster galaxies are excluded from the BUDHiES sample, (3) The BTFR shows no evolution in its zero point over the past 2.5 billion years and does not significantly change on inclusion of cluster galaxies, and (4) Proper sample selection and consistent corrections are crucial for an unbiased analysis of the evolution of the TFr.

## 3.1 Introduction

In the past few decades, several efforts have been made to improve our understanding of fundamental scaling relations between various properties of galaxies. For rotationally supported systems, i.e. for regular, late-type disc galaxies, the Tully-Fisher relation (TFr, Tully & Fisher 1977) is one such scaling relation, correlating two observed quantities of galaxies: the intrinsic luminosity, which is a proxy for the stellar mass of the galaxy, and the width of an emission line from the interstellar medium (ISM), which is directly linked to the galaxy's rotational velocity. It is now also general practice to study other manifestations of the TFr, such as the Stellar-mass TFr (STFr) and the Baryonic TFr (BTFr), by converting the luminosity and gas content of a galaxy into derived quantities such as stellar and baryonic masses. Rotational velocities can be inferred from various distance independent, kinematic measures such as the width of a global profile and the amplitude of a rotation curve (see Verheijen 2001; Ponomareva et al. 2017; Lelli et al. 2019). While the TFr is standardly studied using galaxies with regular, disc-like morphologies, it is found that early-type and S0 galaxies in the Local Universe also follow a similar relation (see Trujillo-Gomez et al. 2011; Cortese et al. 2014). In theory, however, an offset in the zero-point of the TFr for early-types can be expected due to the higher stellar Mass-to-Light ratios (M/L) of their older stellar populations. This has also been confirmed by a number of studies (Bedregal, Aragón-Salamanca & Merrifield 2006; Aragón-Salamanca, Bedregal & Merrifield 2006; Williams, Bureau & Cappellari 2010; Davis et al. 2011; den Heijer et al. 2015). Furthermore, massive, compact galaxies tend to have declining rotation curves, resulting in the measured global profile width to over-estimate the circular velocity of the dark matter halo (Casertano & van Gorkom 1991; Noordermeer & Verheijen 2007), which also results in an offset of the zero point when using the width of the global profile.

The TFr has been used extensively for distance measurements, wherein the distance modulus to disc galaxies can be recovered from the TFr if their distance independent rotational velocities are measured properly. The observed and intrinsic scatter in the TFr, however, leads to uncertainties in the inferred distances and several studies have tried to quantify and reduce this scatter to thereby attain the tightest TFr. Using distances derived from the TFr, the Hubble constant (see Schombert, McGaugh & Lelli 2020) as well as local cosmic flows have been studied (Kashibadze 2008; Tully et al. 2013; Boruah, Hudson & Lavaux 2020; Kourkchi et al. 2020). Additionally, the TFr is a useful tool to provide constraints for numerical simulations of galaxy formation (Navarro & Steinmetz 2000; Dutton et al. 2007; Vogelsberger et al. 2014; Schaye et al. 2015; Macciò et al. 2016), wherein the slope, scatter and zero point of the TFr need to be accurately reproduced at various cosmic epochs in order to verify the plausibility of galaxy formation scenarios. The TFr may also provide insights into internal galaxy structure and kinematics, such as the prevalence of warps and non-circular motions (Franx & de Zeeuw 1992).

In the Local Universe, it is general practice to use the 21-cm atomic hydrogen (HI) emission line for TFr studies. HI proves to be an excellent tracer of galaxy dynamics due to several factors; firstly, HI discs generally extend much farther out than stellar discs

and in most cases, probe the outer, flat part of the rotation curve, which provides the ideal velocity measurement for a TFr study. Secondly, atomic gas has a lower velocity dispersion compared to ionised gas and hence is more directly associated with circular velocities. Thirdly, it also has a relatively constant surface density and a high area-covering factor. Notably, several HI-based TFr studies using spatially resolved rotation curves have been carried out in the recent past (e.g., Verheijen 2001; Ponomareva, Verheijen & Bosma 2016; Noordermeer & Verheijen 2007; de Blok & Walter 2014), providing more accurate measures of the circular velocity compared to the corrected width of the global profile.

One drawback of using HI measurements, however, is that HI emission is intrinsically weak and, therefore, its detectability is restricted to the Local Universe. At higher redshifts, HI becomes increasingly difficult to detect with the current generation of radio telescopes, thus requiring extremely long integration times. Consequently, HI surveys carried out beyond the Local Universe are limited in number (Fernández et al. 2013; Hoppmann et al. 2015; Gogate et al. 2020; Catinella & Cortese 2015). A recent study by Ponomareva et al. (2021) provides the deepest HI-based TFr study out to  $z \sim 0.08$  using resolved HI kinematics. Beyond this redshift, only one study (Catinella & Cortese 2015) has presented the BTFR at an intermediate redshift ( $z \sim 0.2$ ) using targeted HI observations. Their sample of extremely massive and luminous galaxies, optically selected from the Sloan Digital Sky Survey (SDSS, York et al. 2000) seems to follow the  $z=0$  BTFR from Catinella et al. (2012) and McGaugh et al. (2000). However, no corrections or fits were made to this sample or offsets quantified, and this study is hence considered inconclusive.

With an increase in the amount of observational data sets over the past decade, several TFr studies of galaxy samples have been carried out using other emission line tracers of a galaxy's kinematics, such as  $H\alpha$ ,  $H\beta$ , OII and OIII and CO (Dickey & Kazes 1992; Schoniger & Sofue 1994; Tutui & Sofue 1997; Lavezzi & Dickey 1998; Tutui et al. 2001; Ho 2007; Davis et al. 2011; Tiley et al. 2016). All these tracers are usually confined to the inner, star forming regions of galaxies and typically do not accurately probe the circular velocity of the Dark Matter halo. While several TFr studies have been carried out beyond the Local Universe using optical emission lines (Conselice et al. 2005; Flores et al. 2006; Kassin et al. 2007; Puech et al. 2008; Jaffé et al. 2011b), only one TFr study based on CO observations (Topal et al. 2018) exists to date. At intermediate redshifts, CO is a preferred kinematic tracer as compared to ionised gas due to its lower intrinsic velocity dispersion, while its emission line is relatively brighter compared to HI.

Despite the plethora of information on the TFr at intermediate and high redshifts, there is no convergence yet on the results for the redshift evolution of the TFr (see discussion in Sect. 3.7.2). Inconsistencies in the TFr parameters are often encountered in the literature, due to factors such as the choice of tracer and differences in photometric bands, sample selection and size, methodology adopted for the measurement of galaxy properties, corrections applied to the data etc., making it particularly difficult to consistently compare and study the evolution of the TFr slope, scatter and zero point over cosmic time. Consequently, these observational and selection biases often tend to introduce systematic offsets, which could be mistaken for an intrinsic evolution in the parameters

of the TFr. For instance, Verheijen & Sancisi (2001) found that a galaxy with an uncertainty of just 1 degree on the measured inclination alone could lead to a scatter of 0.04 magnitudes (assuming a slope of -10). Another study by Bedregal, Aragón-Salamanca & Merrifield (2006) indicates a downward shift of the Local TFr (adopted in their case, from Tully & Pierce 2000) by about 1.2 mags for a sample of lenticular galaxies, emphasising the importance of selecting proper comparison samples. For an unbiased TFr comparison, one has to ensure that the methodology adopted for measuring and correcting the observed galaxy properties used in the TFr is consistent, since it is the relative offsets between these properties that are of significance (Ponomareva et al. 2017). While the observed scatter in the TFr can be minimised when using a carefully selected sample of regular, disc-like systems with extended, flat rotation curves or clear double-horned global profiles, the same cannot be expected for studies of galaxy samples at higher redshifts due to, for example, the use of a kinematically hot tracer with limited radial extent, survey limitations such as poor spatial and velocity resolution or smaller sample sizes and uncertainties in the measurement of inclinations.

In this chapter, we aim to provide, for the first time, a meaningful and detailed comparison of the HI-based TFr and BTFR at  $z=0$  and  $z=0.2$  in a careful and consistent manner using a blind HI sample, namely the Blind Ultra-Deep HI Environmental Survey (BUDHIES, Gogate et al. 2020, referred to as Paper 1 hereafter). BUDHIES was undertaken using the Westerbork Synthesis Radio Telescope (WSRT) and is one of the first blind HI imaging surveys at  $z > 0.1$ . The surveyed volume includes a range of cosmic environments, effectively encompassing a total volume of  $73,400 \text{ Mpc}^3$  with a depth of 328 Mpc and covering a redshift range of  $0.164 < z < 0.224$ . From the 166 direct HI detections, a subset of suitable galaxies was chosen to represent the BUDHIES TF sample. With this study, we present the first thorough analysis of an HI-based TFr by comparing our results to the  $z=0$  HI-based TFr from a previous study of the Ursa Major association of galaxies (Verheijen 2001). The data reduction procedures and extraction of galaxy properties were carried out in an identical manner for both samples, which is crucial for a proper analysis. Our goal is to also present the effect on the observed statistical properties of the TFr due to the choice of corrections and prescriptions applied to the observables. It is our objective to provide this study as a reference for the next-generation HI surveys that will be able to study the HI-based TFr out to higher redshifts.

Sect. 3.2 describes the BUDHIES sample and the TFr sample down-selection process. The rigorous sample selection process is given in Sect. 3.3. In Sect. 3.4, we describe the corrections applied to the data. The HI and optical catalogues as well as an atlas containing the various observed properties of the BUDHIES TF galaxies, are presented in Sect. 3.5. Sect. 3.6 provides the main results from this study. Finally, we discuss our findings in Sect. 3.7 and summarise our work in Sect. 3.8. Throughout this chapter, we assume a  $\Lambda$ CDM cosmology, with  $\Omega_M = 0.3$ ,  $\Omega_\Lambda = 0.7$  and a Hubble constant  $H_0 = 70 \text{ km s}^{-1} \text{ Mpc}^{-1}$ . All magnitudes used in this chapter are Vega magnitudes.

## 3.2 The Data

### 3.2.1 The BUDHiES data

BUDHiES is a blind HI imaging survey undertaken with the primary aim of providing an HI perspective on the so-called Butcher-Oemler (BO) effect (Butcher & Oemler 1984) at an intermediate redshift of  $z \simeq 0.2$ , corresponding to a look-back time of  $\sim 2.5$  Gyr. To this effect, the survey was centred on two galaxy clusters: Abell 963 at  $z = 0.206$ , which is a massive, virialised, lensing BO cluster with a large fraction (19%) of blue galaxies in its core and strong in X-ray emission from the Intra-Cluster Medium (ICM), and Abell 2192 at  $z = 0.188$ , which is a much smaller, non-BO cluster still in the process of forming and weak in X-rays. The two surveyed volumes also include the large-scale structure in which the clusters are embedded. The volumes within the Abell radii of these clusters occupy as little as 4 percent of the total surveyed volume, which is  $73,400 \text{ Mpc}^3$  within the Full Width at Quarter Maximum (FWQM) of the primary beam. The average angular resolution of BUDHiES is  $23 \times 38 \text{ arcsec}^2$  (corresponding to  $65 \times 107 \text{ kpc}^2$  at  $z \sim 0.164$ ) while the rest-frame velocity resolution is  $19 \text{ km s}^{-1}$ . The achieved HI mass limits at the redshifts of the clusters and in the field centres is  $2 \times 10^9 \text{ M}_\odot$  at the redshift of the two clusters, for an emission line width of  $150 \text{ km s}^{-1}$ . A total of 127 galaxies with confirmed optical counterparts were detected in HI in the cube containing Abell 963 (A963 hereafter), while 39 HI-detected galaxies were identified in the cube containing Abell 2192 (A2192 hereafter).

Apart from the HI data, a deep B- and R-band imaging survey of the two fields was carried out with the Isaac Newton Telescope (INT), which was utilised for counterpart identification, photometry, assessing optical morphologies as well as estimating inclinations. Additionally, u, g, r, i, z photometry as well as optical spectroscopy from the SDSS is available for the two fields. Other supporting data include deep NUV and FUV imaging with the GALaxy Evolution eXplorer (GALEX; Martin et al. 2005), spectroscopic redshifts from the William Herschel Telescope (WHT, Jaffé et al. 2013) and CO observations using the Large Millimeter Telescope (LMT, Cybulski et al. 2016). These data, however, have not been used in this chapter. Details on the BUDHiES data processing, source finding and stellar counterpart identification can be found in Paper 1.

### 3.2.2 Reference studies from the literature

For comparison with the Local Universe TFr, we adopt Verheijen (2001)'s study of the Ursa Major association of galaxies (UMa, hereafter). In particular, we adopt the global HI profiles of the 22 UMa galaxies for which the amplitude of the outer flat part of the HI rotation curve could be measured from spatially resolved HI synthesis imaging data obtained with the WSRT (Verheijen & Sancisi 2001), and for which photometric imaging data is available in the B, R, I and  $K'$ -band (Tully et al. 1996). These UMa galaxies are nearly equidistant at 18.6 Mpc (Tully & Pierce 2000), consistent with the average of the Cosmicflows-3 distances (Tully, Courtois & Sorce 2016) to the 22 individual galaxies

as provided by the Extragalactic Distance Database\* (Tully et al. 2009). The radio and photometric data reduction and analysis procedures used for the BUDHiES sample and those employed by Verheijen (2001) are essentially identical. Note that the UMa BRIK' and the INT B- and R-band images for the two BUDHiES fields are significantly deeper than the SDSS images. From his analysis, Verheijen (2001) found that the K'-band TFr using rotational velocities derived from the outer flat part of the rotation curves has the tightest correlation; however, for an unresolved HI study, the R-band TFr using corrected global HI line widths as proxies for rotational velocities is the preferred choice. While other, more recent HI-based  $z=0$  TFr studies exist (e.g., Ponomareva, Verheijen & Bosma 2016; Lelli et al. 2019), we chose the UMa sample because of its many observational similarities with BUDHiES such as similar HI data sets, both obtained with the WSRT, and the availability of B- and R-band photometric images. Moreover, the UMa sample is volume-limited and complete to a limiting magnitude of  $m_{z_w}=15.2$  for late-type galaxies, while the data reduction procedures are identical to ours.

For a cursory high-redshift comparison we use the HIGHz sample by Catinella & Cortese (2015), which is a targeted HI survey with Arecibo and consists of 39 isolated galaxies optically selected from the SDSS, covering a redshift range of  $0.17 < z < 0.25$ . These galaxies were selected to represent a sample of extremely massive, luminous, and star-forming galaxies at  $z \sim 0.2$ . From a preliminary analysis they found that these rare galaxies lie on the local BTFR adopted from Catinella et al. (2012), suggesting that they are scaled-up versions of local disc galaxies. To make this sample available for our comparative study, the SDSS photometry of these 39 galaxies was re-extracted from the DR7 database and transformed to Johnson-B and Cousins-R bands using the transformation equations by Cook et al. (2014). While the HI and photometric data acquisitions by Catinella & Cortese (2015) differ from those for the BUDHiES and UMa samples, we consistently applied identical corrections (including K-corrections) to the line widths and photometry (see Sect. 3.4) for all three samples. It is to be noted, however, that the comparison with the HIGHz sample is limited in scope, firstly due to the absence of direct B- and R- band photometry, which is required for a consistent analysis, secondly, since a reliable quantification of the offset from the  $z=0$  TFr for the HIGHz sample is impossible due to the limited ranges in the luminosities and  $W_{50}$  line widths. In addition, the HIGHz sample also does not overlap in parameter space (see Sect. 3.4.3), making it unrepresentative for this analysis. Thus, it is included for illustrative purposes only in the various figures that follow.

### 3.3 Sample selection

For a robust TFr study, one of the fundamental requirements is to be able to accurately measure the rotational velocities of the Dark Matter halos of galaxies. In the Local Universe, this is best achieved with resolved HI studies, which can provide rotational velocities from the HI rotation curves of galaxies. However, for blind HI imaging at intermediate redshifts, such as BUDHiES, galaxies are only marginally resolved at best, making rotation curve measurements unattainable. For this study, therefore, rotational

\* available at <https://edd.ifa.hawaii.edu>

velocities were inferred from HI global profile measurements. The corrected HI profile line widths at 20% and 50% of the peak flux are often used as proxies for the rotational velocities at the flat part of the rotation curve (see Sect. 3.7.1 for a further discussion). This makes it necessary to carefully select galaxies with larger inclinations and suitable HI profiles. We constructed two sub-samples from the parent sample of 166 galaxies, as described below. A full break-down of the galaxies rejected at every stage of the sample selection is provided in Table 3.5.

### 3.3.1 The Tully-Fisher Sample (*TFS*)

This BUDHiES sub-sample was constructed based on a qualitative inspection of the optical images and an objective assessment of the HI profile shapes. Galaxies were rejected up-front due to the following observational and qualitative constraints:

#### A. Qualitative observational rejection criteria:

- A1. Galaxies with global HI profiles that are cut-off at the edges of the observed WSRT bandpass;
- A2. Galaxies lying outside the field-of-view of the INT mosaic;
- A3. Galaxies with corrupted or uncertain INT photometry due to imaging artefacts from nearby bright stars, with stars superimposed on the optical image of the galaxy, or with nearby, overlapping companion(s).

#### B. Rejection criteria based on optical morphologies or potential confusion of the stellar counterpart:

- B1. HI detections with multiple nearby, UV-bright companions within the WSRT synthesised beam that lack an optical redshift. Such cases do not allow for an unambiguous identification of the stellar counterpart of an HI detection.
- B2. Galaxies with obvious disturbed optical morphologies such as tidal features or strong asymmetries. The HI gas in these galaxies is likely not on circular orbits while the optical morphologies preclude an accurate measurement of the inclination.

#### C. HI profile shapes:

Galaxies with Gaussian or strongly asymmetric HI profiles were rejected. An automated profile classifier was constructed which compared the maximum fluxes in three equally-spaced velocity bins of the HI profiles and classified them into five categories: Double-Horned (type 1), Single-Gaussian (type 2), Boxy (type 3), Skewed Boxy (type 4) and Asymmetric (type 5). We retained types 1, 3 and 4, in an effort to ensure the inclusion of only galaxies with steep HI profile edges. Resolved HI synthesis imaging studies and simulations (e.g., Verheijen 2001; Lelli, McGaugh & Schombert 2016; El-Badry et al. 2018) have shown that Gaussian profiles (type 2) are generally associated

with rising rotation curves, and are thus unsuitable for a TFR analysis. In addition, they also often correspond to face-on systems with low inclinations. Asymmetric (type 5) profiles could be the result of blending of nearby, possibly interacting galaxies, given the relative large size of the synthesised beam in kpc. Since the primary aim of the HI data is to procure reliable measurements of the rotational velocities of the Dark Matter halo, such galaxies have therefore been excluded from this analysis.

#### D. Inclinations:

Finally, the inclinations of the galaxies that were not rejected by the criteria mentioned above were computed using the available INT R-band images. Since inclinations based on our SExtractor photometry were not very robust, the galaxies were modelled with *galfit* (Peng et al. 2010a). Parameters computed by SExtractor were used as the initial estimates required by *galfit*. We fit Sérsic models to all our galaxies. From the axis ratios ( $b/a$ ) returned by *galfit*, inclinations were calculated following:

$$\cos i = \sqrt{\frac{(b/a)^2 - q_0^2}{1 - q_0^2}} \quad (3.1)$$

where  $a$  and  $b$  are the semi-major and semi-minor axes of the model ellipse and the disc thickness ( $q_0$ ) was chosen to be 0.2. For consistency with other comparison samples, galaxies with an inclination more face-on than  $45^\circ$  were rejected. Note the two galaxies (no. 14 and 26 in Column (1) of Table 3.1) which were both assigned an inclination of  $90^\circ$  since the axis ratios returned by *galfit* were less than the assumed disk thickness.

These rejection criteria resulted in a sample of 36 galaxies, of which 29 belong to A963 and 7 belong to A2192 (note that A963 and A2192 refer to the entire survey volume, not just the Abell clusters themselves).

#### 3.3.2 The High-Quality Sample (HQS)

From the 36 galaxies in the *TFS*, we constructed a high-quality sub-sample by applying three additional quantitative criteria to the global HI profile shapes. This was done to ensure the best possible comparison with the high-quality data of the UMa sample. These criteria concern the signal-to-noise, symmetry and shape of the HI profiles and are described below.

#### E. Quantitative rejection criteria:

Galaxies were rejected based on their HI properties subject to pre-defined quantitative thresholds:

- E1. *Signal-to-noise of the HI profiles:* To ensure an accurate measurement of the widths of the global HI profiles, we imposed a threshold on the HI profile line width uncertainties and rejected galaxies with uncertainties in excess of 10% of

the respective line widths.

- E2. *Symmetry of the HI profiles*: Galaxies with asymmetric HI profiles do not provide robust circular velocity measurements. One method of assessing an asymmetric profile is to assess the systemic velocities ( $V_{\text{sys}}$ ) derived from the  $W_{20}^{\text{obs}}$  and  $W_{50}^{\text{obs}}$  line widths. If this difference  $\delta V_{\text{sys}}$  is large, then the profile is most likely asymmetric. Based on our assessment, galaxies with absolute fractional differences in  $V_{\text{sys}}$  following  $|\delta V_{\text{sys}}/W_{20}^{\text{obs}}| > 0.05$  were rejected.
- E3. *Steepness of the HI profile edges*: To assess the steepness of the HI profile edges, the differences in  $W_{20}^{\text{obs}}$  and  $W_{50}^{\text{obs}}$  were considered. Based on our assessment, galaxies with  $|W_{20}^{\text{obs}} - W_{50}^{\text{obs}}| > 50 \text{ km s}^{-1}$  were rejected.

These stricter, objective criteria on the quality of the global profiles resulted in the rejection of 17 more galaxies and yielded a sample of 19 galaxies, of which 12 galaxies are in the A963 volume and 7 galaxies are in the A2192 volume.

### 3.3.3 Literature samples

For the Uma sample we used the ‘RC/FD’ sample of 22 galaxies from Verheijen (2001) for which spatially resolved HI rotation curves confirm that the corrected widths of the corresponding global HI profiles properly represent their rotational velocities. These Uma galaxies abide by the same qualitative selection criteria as the BUDHIES *HQS* galaxies. Due to some limitations of the HIGHz sample (see Sect. 3.2.2), it was not used for a quantitative assessment of the TFr. All the galaxies in the HIGHz sample with inclinations above  $45^\circ$ , however, are included in the illustrations of the  $W_{50}$  TFrs in this chapter.

## 3.4 Corrections to the data

Before Tully-Fisher relations can be constructed, the observed HI line widths  $W_{\%}^{\text{obs}}$  and total apparent magnitudes  $m_{\text{B,R}}^{\text{obs}}$  need to be corrected for various instrumental, astrophysical and geometric effects such as finite spectral resolution, turbulent motions of the gas, Galactic and internal extinction, K-corrections and inclination. We ensure that these corrections are applied consistently to all galaxies in the BUDHIES, Uma and HIGHz samples. In this section we describe these corrections in some detail.

### 3.4.1 Correction to the observed HI linewidths

#### Conversion to rest-frame line widths

For the BUDHIES galaxies, the observed widths of the redshifted global HI profiles were measured in MHz at 20% and 50% of the peak flux ( $\Delta\nu_{\%}^{\text{obs}}$ ) and converted to observed, uncorrected rest-frame line widths ( $W_{\%}^{\text{obs}}$ ) in  $\text{km s}^{-1}$  using the following equation.

$$W_{\%}^{\text{obs}} = \frac{\Delta\nu_{\%}^{\text{obs}}}{\nu_{\text{rest}}}(1+z)c \quad (3.2)$$

where  $\nu_{\text{rest}}$  is the rest frequency of the Hydrogen emission line (1420.4057517667 MHz).

For the HIGHz galaxies, Catinella & Cortese (2015) provide observed line widths at 50% of the peak flux, expressed as  $W_{50} = \Delta cz$  in  $\text{km s}^{-1}$  (column 6 in their Table 2), which we divide by  $(1+z)$  to obtain the observed rest-frame line widths in  $\text{km s}^{-1}$  such that we can consistently apply our correction for instrumental broadening as explained in the next subsection. For the galaxies in the UMa sample, we do not apply any correction for this relativistic effect and adopt the measured line widths as the rest-frame values.

### Correction for instrumental broadening

The effect of instrumental broadening on the observed line widths, caused by a finite spectral resolution  $R$  of the radio spectrometers, was corrected using the following equations, adopted from Paper 1, in which the authors studied this effect at different velocity resolutions:

$$W_{20}^{\text{R}} = W_{20}^{\text{obs}} - 0.36R \quad (3.3)$$

$$W_{50}^{\text{R}} = W_{50}^{\text{obs}} - 0.29R \quad (3.4)$$

For the BUDHiES galaxies, we measured the line widths after the data were spectrally smoothed to a Gaussian line spread function with a FWHM of four channels or 0.15625 MHz (R4, hereafter), corresponding to a rest-frame velocity resolution of  $R=33.0 \times (1+z)$   $\text{km s}^{-1}$ . For the UMa galaxies, the spectral resolution varied in the range  $R=5.0 - 33.2$   $\text{km s}^{-1}$  (Verheijen & Sancisi 2001) while we adopted the rest-frame velocity resolutions for the HIGHz galaxies presented in Table 2 in Catinella & Cortese (2015).

### Correction for turbulent motion

After correcting for instrumental velocity resolution effects, corrections for broadening due to turbulent motions of the HI gas were then made to the data. Following Verheijen & Sancisi (2001) we adopt the prescription by Tully & Fouque (1985), which corresponds to a linear subtraction by  $w_{t,\%}$  for HI profiles with  $W_{\%}^{\text{R}} > w_{c,\%}$  and a quadratic subtraction if  $W_{\%}^{\text{R}} < w_{c,\%}$  where  $w_{c,20}=120$   $\text{km s}^{-1}$  and  $w_{c,50}=100$   $\text{km s}^{-1}$ . Since all the BUDHiES and HIGHz galaxies in our samples have  $W_{\%}^{\text{R}} > w_{c,\%}$ , and assuming that they have monotonically rising rotation curves that properly sample the outer flat parts of the rotation curve, we adopt the values for  $w_{t,\%}$  from Verheijen & Sancisi (2001) as

$$w_{t,20}^{\text{flat}} = 32 \text{ km s}^{-1} \quad \text{and} \quad w_{t,50}^{\text{flat}} = 15 \text{ km s}^{-1},$$

and thus our corrected line widths become:

$$W_{\%}^{R,t} = W_{\%}^R - w_{t,\%}^{\text{flat}} \quad (3.5)$$

Although Verheijen & Sancisi (2001) did not provide uncertainties related to the turbulent motion corrections, it can be noted that the values of  $w_{t,\%}^{\text{flat}}$  in comparable studies (Broeils 1992; Rhee 1996) are quite similar and hence we adopt the corresponding errors of 5 and 4 km s<sup>-1</sup> for  $w_{t,20}^{\text{flat}}$  and  $w_{t,50}^{\text{flat}}$  by Broeils (1992) respectively. It is important to note that these corrections are based on a sample average. A few resultant non-physical corrected line widths ( $W_{50}^{\text{corr}} > W_{20}^{\text{corr}}$ ) are caused by the scatter around the sample, which may affect individual systems. Other statistical corrections in the literature would show similar results.

### Correction for inclination

Uncertainties in corrections involving the inclination contribute significantly to the scatter in the TFR. Hence, it is crucial, to calculate the inclinations as accurately as possible, and to propagate the corresponding uncertainties through the relevant correction formulas. Sect. 3.3.1 describes our method for inferring inclinations based on the observed ellipticity  $\epsilon = 1 - (b/a)$  of the optical images. For completeness, we note here that *galfit* takes the smoothing of the BUDHIES INT images due to the seeing into account while the value of  $(b/a)$  as returned by *galfit* pertains to the effective radius instead of a specified isophotal contour of the outer stellar disc. In case a significant spherical bulge is present in a galaxy, this approach may result in a slight overestimate of  $(b/a)$  and, consequently, an underestimate of the inclination of the disc component and thereby an overestimate of the circular velocity. Table 2 lists the  $(b/a)$  values for the BUDHIES galaxies as returned by *galfit*, along with the formal errors.

For the UMa galaxies, Tully et al. (1996) measured the  $(b/a)$  ratio as a function of radius and selected the value that is representative of the outer disc, taking the optical morphology of the galaxy into account, including the presence of a bar, bulge and spiral arms. They converted this representative  $(b/a)$  into an inclination using the same equation (1) and  $q_0=0.2$ . They assigned an uncertainty of 3 degrees to the inferred inclinations.

For the HIGHz galaxies, Catinella & Cortese (2015) adopted the  $(b/a)$  values from an exponential fit to the r-band SDSS images (*expAB<sub>r</sub>* in the SDSS database) and  $q_0=0.2$  while employing the same equation (1) to infer an inclination. This axis ratio is representative at the effective radius of a galaxy. They do not provide an error estimate for either the  $(b/a)$  values or the inferred inclinations.

Although the measurements of the optical minor-to-major axis ratio  $(b/a)$  may have been slightly different for the galaxies in the three samples, the same formula and value of the intrinsic thickness  $q_0$  was used in all studies. With the inferred inclinations, we corrected the already partially corrected line width according to:

$$W_{\%}^{\text{R},\text{t},\text{i}} = \frac{W_{\%}^{\text{R},\text{t}}}{\sin i} \quad (3.6)$$

where  $W_{\%}^{\text{R},\text{t}}$  is the HI line width corrected for instrumental broadening and turbulent motion and  $i$  is the inclination of the galaxy. Hereafter, we refer to  $W_{\%}^{\text{R},\text{t},\text{i}}$  as  $W_{\%}^{\text{corr}}$  in the text for the sake of simplicity.

### 3.4.2 Photometric corrections

For the BUDHIES sample, deep Harris B- and R-band imaging was carried out with the INT on La Palma. Photometric calibration of these images was carried out using the photometry of selected stars from the SDSS DR7 catalogue, transformed to Johnson B and Cousins R bands using the transformation equations provided by Lupton 2005\* (see Paper 1). Subsequently, instrumental aperture B- and R-band magnitudes were derived with SExtractor by summing all the background subtracted pixels within adaptive Kron elliptical apertures defined by the R-band images and also applied to the B-band images. For our analysis, the resulting AUTO magnitudes from SExtractor needed to be converted to the equivalent of total model magnitudes for a consistent comparison with the other literature data sets, which consist of total extrapolated magnitudes for the UMa galaxies (Tully et al. 1996) or SDSS model magnitudes for the HIGHz galaxies. For this purpose, we extracted and analysed the luminosity profiles of several galaxies in the *HQS*, measured the sky levels, identified the radial range where the exponential disc dominates the light, fitted an exponential profile to this radial range and calculated the total extrapolated magnitudes following Tully et al. (1996). From this exercise, we found that the differences between the SExtractor aperture (AUTO) magnitudes and our extrapolated total magnitudes were quite small: 0.038 for A963 and -0.014 for A2192. The INT aperture magnitudes were corrected accordingly to make up for these differences. Note that this statistical correction does not alter the results of our study.

To obtain intrinsic absolute magnitudes in the B- and R-bands, the total, extrapolated model magnitudes of the galaxies require further corrections for Galactic extinction, cosmological reddening and internal extinction as described below. These corrections were applied consistently to all galaxies in the three samples under consideration.

### Galactic extinction

The total apparent magnitudes were corrected for Galactic extinction ( $A_{\text{B,R}}^{\text{g}}$ ) following Schlegel, Finkbeiner & Davis (1998). The BUDHIES galaxies within a WSRT pointing are all close together on the sky and received the same correction according to

$$\text{A963} \quad : \quad A_{\text{B}}^{\text{g}} = 0.052 \quad ; \quad A_{\text{R}}^{\text{g}} = 0.031$$

$$\text{A2192} \quad : \quad A_{\text{B}}^{\text{g}} = 0.039 \quad ; \quad A_{\text{R}}^{\text{g}} = 0.023$$

\* <http://classic.sdss.org/dr4/algorithms/sdssUBVRITransform.html>

Galactic extinction corrections for UMa galaxies were also adopted from Schlegel, Finkbeiner & Davis (1998) and are provided in Table 1 of Verheijen & Sancisi (2001). In the case of the HIGHz sample, de-reddened SDSS magnitudes (dered\_u, dered\_g, dered\_r, dered\_i, dered\_z) were used, since they also follow Schlegel, Finkbeiner & Davis (1998).

### K-corrections

Corrections for cosmological reddening, known as K-corrections ( $\kappa_{B,R}$ ), were carried out with the help of the K-correction calculator by Chilingarian, Melchior & Zolotukhin (2010)\*. This was done for both the high redshift samples. As expected, we find that the K-corrections are larger in the B-band (average  $\kappa_B = 0.65$  mags) than the R-band (average  $\kappa_R = 0.12$  mags).

### Internal extinction

Finally, the apparent magnitudes were corrected for internal extinction following Tully et al. (1998). Based on their prescription, the internal extinction correction is dependent on both the inclination and the corrected HI line widths of the galaxies, and is given by

$$A_{B,R}^i = \gamma_{B,R} \log(a/b) \quad (3.7)$$

where  $a/b$  is the major-to-minor axis ratio. The  $\gamma_{B,R}$  coefficient is line width dependent and calculated as

$$\gamma_B = 1.57 + 2.75 (\log(W_{\%}^{\text{corr}}) - 2.5) \quad (3.8)$$

$$\gamma_R = 1.15 + 1.88 (\log(W_{\%}^{\text{corr}}) - 2.5) \quad (3.9)$$

where  $W_{\%}^{\text{corr}}$  is the corrected HI line width as derived in Eq. 3.6. The final corrected magnitudes were calculated as

$$m_{B,R}^{g,\kappa,i} = m_{B,R}^{\text{obs}} - A_{B,R}^g - \kappa_{B,R} - A_{B,R}^i \quad (3.10)$$

where  $m_{B,R}^{\text{obs}}$  is the uncorrected, total apparent magnitude. The subscripts signify the choice of filter, namely B or R. Note that this internal extinction correction method depends on both the inclination and the HI line width, recognising that galaxies of lower mass are usually less dusty.

\* the online K-corrections calculator can be found at <http://kcor.sai.msu.ru/>

### Absolute magnitudes and luminosities

Absolute B- and R-magnitudes, corrected for Galactic extinction, cosmological reddening and internal extinction, were calculated from the distance modulus equation, which takes into account the luminosity distance to each galaxy based on the adopted cosmology.

$$M_{B,R} = m_{B,R}^{g,\kappa,i} - 5 \log(D_{\text{lum}}/10) \quad (3.11)$$

where  $m_{B,R}^{g,\kappa,i}$  is the corrected apparent magnitude, and the luminosity distance,  $D_{\text{lum}}$ , is in parsecs. As mentioned before, a common distance of 18.6 Mpc was assumed for all galaxies in the UMa sample. Luminosities were computed from the corrected absolute magnitudes following the standard prescription, with adopted solar absolute magnitudes of  $M_{\odot,B} = 5.31$  and  $M_{\odot,R} = 4.60$ .

#### 3.4.3 Comparison of sample properties

As mentioned previously, all galaxies in the BUDHiES sample are selected to be isolated, HI rich, rotationally supported and geometrically inclined systems. In this section, some properties of the galaxy populations in the three comparison samples will be discussed.

#### Distribution of observables

Figure 3.1 presents the distributions of the various parameters for the BUDHiES galaxies on the left, distinguishing the *HQS* galaxies in the A963 and A2192 volumes, and the reference samples of UMa and HIGHz on the right. The full BUDHiES *TFS* (29+7 galaxies) is shown by the light-grey histogram while the *HQS* galaxies are indicated by the hatched histograms for A963 (12 galaxies: teal) and A2192 (7 galaxies: magenta) separately. Note that all 7 galaxies in the *TFS* of A2192 are in the *HQS* as well.

The top panels (a) and (b) of Fig. 3.1 show the redshift distributions of the BUDHiES and HIGHz galaxies. Compared to the BUDHiES sample, the HIGHz sample reaches slightly further in redshift, out to  $z=0.245$ , but only 2 of the 28 galaxies are beyond the maximum redshift of the BUDHiES sample ( $z=0.224$ ). The majority of the *TFS* galaxies in the BUDHiES sample (29 out of 36) are located in the volume containing A963, with a significant fraction of galaxies (11 out of 29) in the redshift bin that contains the large-scale structure in which A963 is embedded. The UMa sample is not shown in panel (b) as it is located at  $z=0$ , with an assumption that all galaxies in this sample are at a common distance of 18.6 Mpc. The HIGHz sample contains galaxies selected over a large area on the sky and, therefore, does not target a specific cosmic over-density.

Panels (c) and (d) of Fig. 3.1 show the distribution of HI gas masses of the sample galaxies, and there are some striking differences between the samples. The BUDHiES galaxies have HI masses in the range  $9.3 < \log(M_{\text{HI}}) < 10.2$  while the UMa galaxies have notably smaller HI masses, covering the range  $8.7 < \log(M_{\text{HI}}) < 9.9$ . The HIGHz galaxies, however, have significantly higher HI masses, covering the range  $10.4 < \log(M_{\text{HI}}) < 10.9$ .

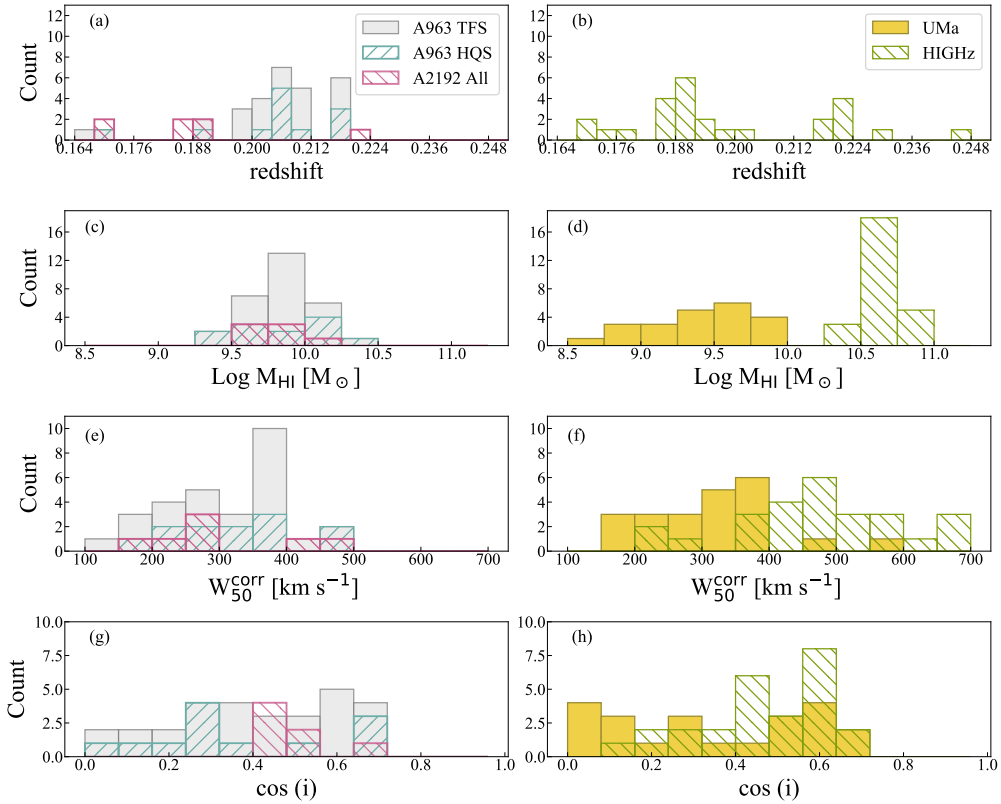


**Figure 3.1** – Histograms showing the various properties of the samples used for the TFr analysis. The BUDHiES samples are shown on the left. For A963, the grey histograms show the *TFS*, and the hatched cyan histograms show the *HQS*. Note that the *HQS* is a subset of the *TFS*. For A2192, the *TFS* and *HQS* are identical, hence shown by the hatched magenta histograms. On the right, the histograms show the UMa and HIGHz samples, in orange and green (hatched) respectively. (a) and (b) illustrate the redshift distribution of the samples. The UMa sample is not a part of these histograms, since we assume an average distance of 18.6 Mpc, corresponding to  $z \simeq 0$ . The HI mass distributions are shown in panels (c) and (d), while (e) and (f) illustrate the distribution of the HI line widths measured at 50% of the peak flux. Lastly, panels (g) and (h) show the distribution of the cosine of the inclinations of galaxies in the various samples.

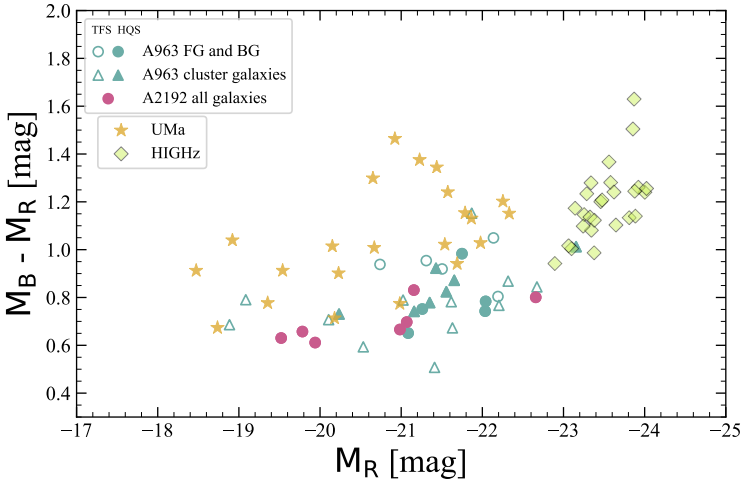
None of the BUDHiES or UMa galaxies have an HI mass as high as the lowest HI mass of any HIGHz galaxy. This is not surprising as the HIGHz galaxies were selected as the most extreme, massive HI-rich galaxies at  $z > 0.16$  while the global HI profiles of the 'code 1' galaxies from Catinella & Cortese (2015), that constitute the HIGHz subsample considered here, have the highest signal-to-noise and thereby a relatively high HI content.

Figure 3.1 (e) and (f) show histograms of the HI line widths measured at 50% of the peak flux. The fastest rotators belong to the HIGHz sample ( $\langle W_{50}^{\text{corr}} \rangle = 477 \text{ km s}^{-1}$ ), which is expected since this sample is selected to contain massive and luminous galaxies. On the other hand, the distributions of the BUDHiES (*TFS*) and UMa samples are quite similar ( $\langle W_{50}^{\text{corr}} \rangle = 313.5$  and  $313.8 \text{ km s}^{-1}$  respectively). The two UMa galaxies with larger line widths are NGC 3953 and NGC 3992.

Lastly, panels (g) and (h) in Fig. 3.1 illustrate the distribution of the inclinations of all our sample galaxies. Based on our sample selection criteria (see Sect. 3.3), only galaxies with inclinations  $> 45^\circ$  were retained for this analysis. From the histograms, it is evident that the BUDHiES and UMa samples have flat distributions as expected for randomly oriented discs in a volume limited sample, whereas the HIGHz sample is biased towards more face-on systems with lower inclinations. This is an expected observational bias as galaxies with lower inclinations tend to have narrower HI emission lines that are easier to detect and measure.

### The colour–magnitude diagram

The rest-frame  $M_B - M_R$  versus  $M_R$  colour-magnitude diagram (CMD) of the three samples is shown in Fig. 3.2. The magnitudes were corrected for galactic extinction, cosmological reddening and internal extinction as described in Sect. 3.4.2. The three samples occupy different areas in the CMD. The BUDHiES and UMa samples cover a similar range in absolute magnitude ( $-23 < M_R < -19$ ) but the BUDHiES galaxies ( $\langle M_B - M_R \rangle = 0.79$ ) are on average 0.26 magnitudes bluer than the UMa galaxies ( $\langle M_B - M_R \rangle = 1.05$ ) although there is some overlap in colour. The HIGHz galaxies ( $\langle M_B - M_R \rangle = 1.20$ ) have similar colours as the UMa galaxies but are significantly brighter ( $-24 < M_R < -23$ ) than the galaxies in both the BUDHiES and UMa samples. Only one BUDHiES galaxy falls in the magnitude range of the HIGHz sample. It should be recalled here that the applied correction for internal extinction not only depends on inclination but also on the corrected line width, which correlates with absolute luminosity through the TFr. This is discussed in more detail in Sect. 3.7.1 as this correction for internal extinction will eventually have some impact on the slope and zero point of the TFr. The fact that the HIGHz sample is so 'disjoint' from the BUDHiES and UMa samples in the CMD is another motivation to consider the HIGHz sample for illustrative purposes only and exclude it from a quantitative assessment of the cosmic evolution of the TFr zero point.



**Figure 3.2** – The R-band colour-magnitude diagram of the various samples after photometric corrections have been applied. Cyan triangles represent galaxies belonging to the cluster Abell 963. Circles indicate galaxies from the foreground (FG) and background (BG) of the volume A963 (cyan) and all of the volume A2192 (magenta) which together make up the BUDHiES *TFS* (open symbols), of which the *HQS* is shown by the solid symbols. The UMa sample is indicated by the orange stars. The HIGHz *u*, *g*, *r*, *i* magnitudes were transformed to Cousins R magnitudes using Cook et al. (2014) and are shown by the green diamonds. Magnitudes were corrected using the inclination and line width dependent corrections by Tully et al. (1998).

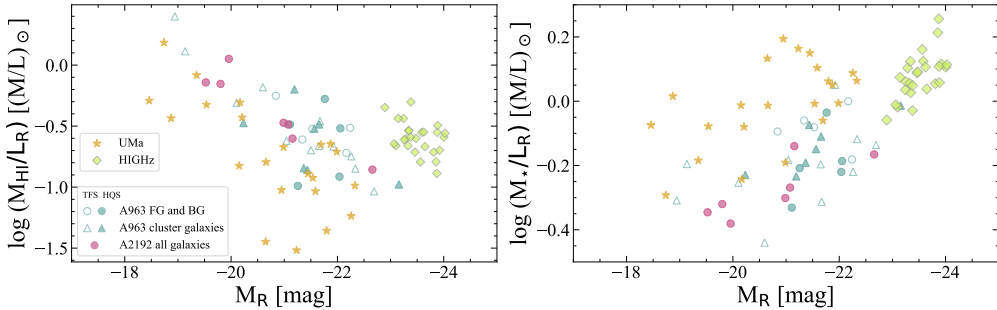


**Figure 3.3** – Comparison of R-band mass-to-light ratios for the various samples; left:  $M_{\text{HI}}/L$  ratios, right:  $M_{\star}/L$  ratios. The colours and markers used to represent the samples are identical to Figure 3.2 and are also provided in the legend. Stellar masses shown here are based on Eq. 3.16.

### HI and stellar mass-to-light ratios

The left panel of Fig. 3.3 shows the HI mass-to-light ( $M_{\text{HI}}/L_{\text{R}}$ ) ratios of the galaxies in the various samples. As expected, the BUDHiES and UMa galaxies show a general increasing trend in the HI mass-to-light ratio with decreasing luminosity. For a given

magnitude, however, the BUDHiES galaxies tend to have a slightly higher  $M_{\text{HI}}/L_{\text{R}}$  ratio. The sample averages are  $\langle \log(M_{\text{HI}}/L_{\text{R}}) \rangle = -0.52$  for the BUDHiES galaxies and  $\langle \log(M_{\text{HI}}/L_{\text{R}}) \rangle = -0.75$  for the UMa galaxies. The HIGHz galaxies do not follow the extrapolated trend to brighter magnitudes as they are overly gas rich with a sample average of  $\langle \log(M_{\text{HI}}/L_{\text{R}}) \rangle = -0.65$ .

The right panel of Fig. 3.3 shows the maximum-disc inferred stellar mass-to-light ratio in the R-band ( $M_{\star}^{\text{mxd}}/L_{\text{R}}$ ) according to Eq. 3.16 as motivated in Sect. 3.6.3. Since there is a rather strong dependence on the  $M_{\text{B}}-M_{\text{R}}$  colour, the distribution of points is similar to that in the CMD, with  $0.4 < (M_{\star}/L_{\text{R}}) < 1.6$ . The HIGHz galaxies have similar stellar mass-to-light ratios compared to most of the UMa galaxies. The BUDHiES galaxies have a notably lower stellar mass-to-light ratio with a clear trend of lower  $M_{\star}/L_{\text{R}}$  values toward fainter galaxies. The sample average values  $\langle M_{\star}/L_{\text{R}} \rangle$  are 0.63 for the BUDHiES galaxies, 0.98 for the UMa galaxies and 1.2 for the HIGHz galaxies.

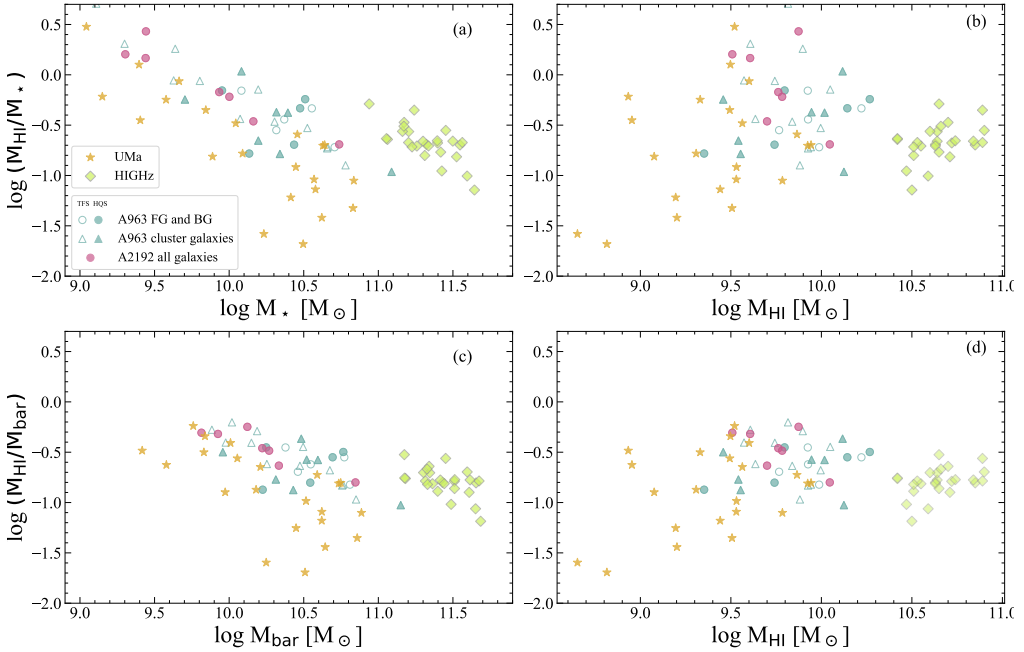


**Figure 3.4** – Gas fractions of the galaxies in the various samples. Panels (a) and (b) show the  $M_{\text{HI}}/M_{\star}$  ratios as a function of  $M_{\star}$  and  $M_{\text{HI}}$  respectively, while panels (c) and (d) show the  $M_{\text{HI}}/M_{\text{bar}}$  ratios as a function of  $M_{\text{bar}}$  and  $M_{\text{HI}}$  respectively. The colours and markers are identical to Fig. 3.2. Stellar and baryonic masses shown here are based on Eq. 3.16.

### HI mass fractions

The HI mass to stellar mass ratios ( $M_{\text{HI}}/M_{\star}$ ) as a function of stellar mass are shown in panel (a) of Fig. 3.4. Not surprisingly, we see the same trend as in the left panel of

Fig. 3.3 where we used the R-band luminosity instead of stellar mass. We confirm the well-known trend that lower mass galaxies tend to have a larger ratio of HI-to-stellar mass while the HIGHz galaxies seem to lie above the trend defined by the BUDHiES and UMa galaxies, as expected given the selection criteria for the HIGH z sample. In panel (b) of Fig. 3.4 we plot  $M_{\text{HI}}/M_{\star}$  as a function of  $M_{\text{HI}}$  and note that the correlation seen in panel (a) has disappeared. The  $M_{\text{HI}}/M_{\star}$  ratios for the BUDHiES galaxies tend to be higher than for the UMa and HIGHz galaxies with sample averages of  $\langle \log(M_{\text{HI}}/M_{\star}) \rangle = -0.74$  and  $-0.73$  for the UMa and HIGHz samples respectively, while  $\langle \log(M_{\text{HI}}/M_{\star}) \rangle = -0.31$  for the BUDHiES sample.

In panels (c) and (d) of Fig. 3.4 we plot the  $M_{\text{HI}}/M_{\text{bar}}$  fractions as a function of  $M_{\text{bar}}$  and  $M_{\text{HI}}$  respectively. We observe in panel (c) that, compared to panel (a), the trend of  $M_{\text{HI}}/M_{\text{bar}}$  versus  $M_{\text{bar}}$  has become shallower as the HI mass is a larger fraction of  $M_{\text{bar}}$  for galaxies with a lower  $M_{\text{bar}}$ . Interestingly, in panel (d), plotting  $M_{\text{HI}}/M_{\text{bar}}$  versus  $M_{\text{HI}}$  instead of plotting  $M_{\text{HI}}/M_{\star}$  versus  $M_{\text{HI}}$  shows a significantly smaller scatter, while the HIGHz galaxies do not stand out significantly.

It is evident that the sample of BUDHiES galaxies tends to have a higher  $M_{\text{HI}}/M_{\star}$  ratio than the UMa and HIGHz galaxies. The sample averages for the UMa and HIGHz galaxies are  $\langle \log(M_{\text{HI}}/M_{\text{bar}}) \rangle = -0.89$  and  $-0.83$  respectively, while  $\langle \log(M_{\text{HI}}/M_{\text{bar}}) \rangle = -0.58$  for the BUDHiES samples. From Fig. 3.4 we conclude that the BUDHiES galaxies at  $z=0.2$  are relatively more HI-rich than the UMa galaxies at  $z=0$ , even though they have similar baryonic masses.

Finally, we remark that the larger vertical spread of the UMa sample in Figs. 3.3 and 3.4 is due to the fact that the UMa sample has a better HI mass sensitivity than both BUDHiES and HIGHz, and hence includes galaxies with lower HI masses.

### HI profile shapes

Ideally, the HI profiles of isolated spiral galaxies with suitable inclinations should have steep edges, allowing the two line width measures  $W_{20}$  and  $W_{50}$ , once properly corrected for instrumental spectral resolution, turbulent motion and inclination, to yield the same circular velocity. To inspect this notion in some detail, we compared the  $W_{20}$  and  $W_{50}$  width of the galaxies in the various TFR samples, as illustrated in Fig 3.5. The figure shows the fractional differences between the observed  $W_{20}$  and  $W_{50}$  line widths (a), and the same after accumulative corrections for instrumental resolution (b), turbulent motion (c) and inclination (d). For details on the applied corrections, see Sect. 3.4.1. Along with the BUDHiES *TFS* and *HQS* samples, we also included the UMa sample, as well as an HI sample from a blind VLA HI imaging survey of part of the Perseus-Pisces (PP) filament at a distance of 66 Mpc (Bilimogga et al., in prep). In panel (a), all samples deviate from the zero line, which is expected since the HI profile edges are not infinitely steep ( $W_{20}^{\text{obs}} > W_{50}^{\text{obs}}$  always).

In the case of the UMa and PP samples, this offset is corrected as we move downwards to panel (c), in which the line widths are corrected for both, instrumental spectral resolution and turbulent motion. It is also immediately evident that in panel (c) there still exists an offset and a larger scatter in the BUDHiES samples that could not be

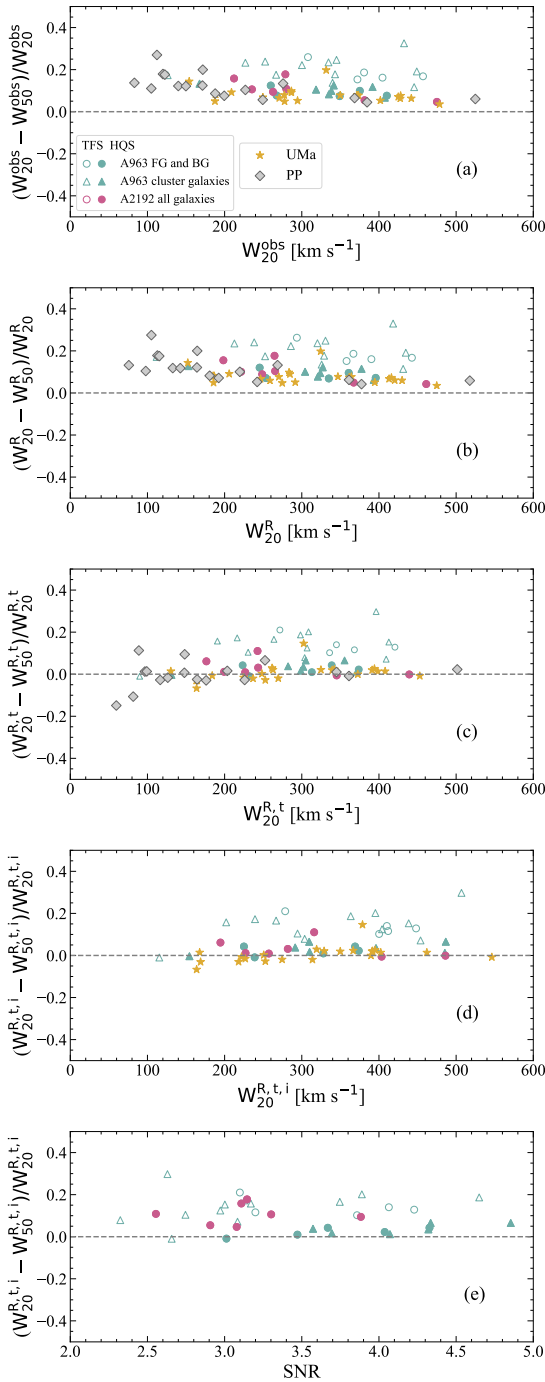


**Figure 3.5** – Fractional differences in the HI line widths, defined as  $(W_{20}-W_{50})/W_{20}$  for the various comparison samples. The colours and markers used to represent the samples are identical to Figure 3.2 and are also provided in the legend. Additionally, an HI sample from VLA observations of the Perseus-Pisces filament (grey diamonds) is also included in the figure (Bilimogga et al., in prep). From top to bottom: (a) fractional differences in the observed line widths, (b) after correcting for instrumental broadening, (c) after turbulent motion corrections, (d) after inclination corrections. Panel (e) illustrates the fractional differences in the corrected line widths as a function of the average SNR derived from the HI profiles for the BUDHiES volumes.

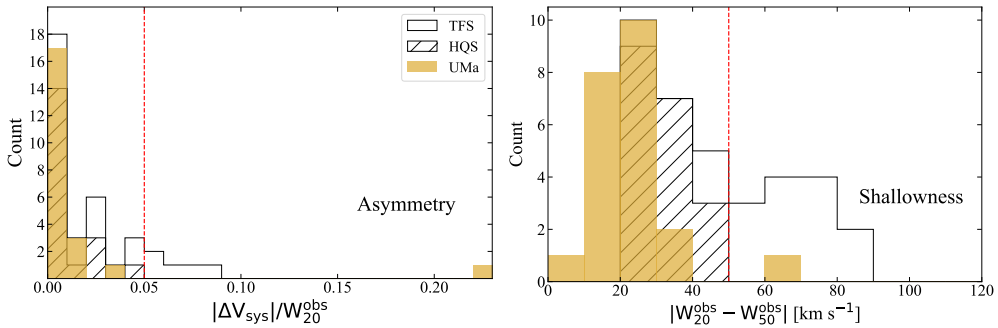


**Figure 3.6** – Histograms comparing the HI properties of the comparison samples; the open histogram shows the *TFS* while the hatched histogram shows the *HQS* (which is a subset of the *TFS*). The UMa sample is shown in orange. The red dashed lines indicate the thresholds applied during the sample selection process for creating the *HQS*. Right: Histograms showing the difference in the observed line widths which is a quantification of the shallowness of the HI profiles; Left: histograms showing asymmetries in the form of the absolute fractional differences in the systemic velocities derived from  $W_{20}^{\text{obs}}$  and  $W_{50}^{\text{obs}}$  respectively.

eliminated by applying the same corrections. The offset, however, is smaller for the *HQS* (solid symbols) than for the *TFS* (open symbols) by merit of the more stringent, quantitative criteria applied to the profiles of the *HQS* galaxies. The average fractional difference between the  $W_{20}^{\text{R,t}}$  and  $W_{50}^{\text{R,t}}$  line widths is 0.16 for the BUDHiES *TFS* galaxies, compared to 0.08 for the UMa galaxies. Naturally, correcting for inclination, as shown in panel (d), does not further reduce the fractional difference for any of the samples. It is important to point out in panel (e) that no trend is observed in the fractional differences as a function of the average Signal-to-Noise Ratio (SNR) of the HI profiles. In Sect. 3.7 we address the possible reasons for this offset of the BUDHiES galaxies.

Figure 3.6 shows the histograms of the asymmetries and the shallowness of the HI profile edges of the BUDHiES and UMa galaxies. The red dashed lines indicate the applied cuts in the asymmetry and shallowness of the profiles given in Sect. 3.3 (E2 and E3) respectively. It can be noted that while these thresholds do exclude BUDHiES galaxies with the most asymmetric profiles or shallow profile edges from the *TFS*, the profiles of the *HQS* galaxies are still more asymmetric and with shallower edges than the profiles of the UMa galaxies. The origin of such profiles is discussed in Sect. 3.7.1. From the UMa sample, we note that the profile of NGC 3729 is more asymmetric than the imposed threshold while NGC 4138 has a profile with shallower edges compared to the threshold applied for the selection of the BUDHiES *HQS* galaxies.

### 3.5 The BUDHiES TF catalogue and atlas

We present here the tables as well as an atlas containing the HI and optical properties of the galaxies chosen to represent the TF sample from BUDHiES. The tables include observed, corrected and inferred properties following the methodology as described in

Sect. 3.4.

### 3.5.1 The catalogues

The HI and optical catalogues for the BUDHiES TF sample are provided in Tables 3.1 and 3.2 respectively. The contents of the HI catalogue as presented in Table 3.1 are as follows:

*Column* (1): The running identification number of the galaxies for easy cross-reference with entries in Table 3.2.

*Column* (2): The catalogue number assigned to these galaxies in Paper 1, for easy cross-reference to the atlas pages.

*Column* (3): The HI ID which contains the Right Ascension and Declination of the HI source [J2000].

*Column* (4): The rest-frame velocity resolution  $R$  at which the HI profile, total HI map and Position-Velocity diagrams were extracted from the data cubes. The velocity resolution is set at  $4 \times \Delta v$  ( $R4$ ), where  $\Delta v$  is the redshift-dependent rest-frame width of the channel in  $\text{km s}^{-1}$ .

*Column* (5): The channel-average SNR of the extracted HI profiles of each galaxy.

*Column* (6): The galaxy redshift based on the HI profile.

*Column* (7): The luminosity distance to the galaxy, calculated using its HI redshift and the adopted cosmology.

*Columns* (8) & (9): The observed (rest frame)  $W_{20}$  and  $W_{50}$  line widths, including their errors.

*Column* (10) & (11): The  $W_{20}^{\text{corr}}$  and  $W_{50}^{\text{corr}}$  line widths corrected for instrumental resolution, turbulent motions and inclination, following the methodology described in Sect. 3.4.

*Column* (12): HI masses ( $\times 10^9 M_{\odot}$ ) calculated from the integrated flux densities of the extracted HI profiles, including their uncertainties. For further details, see Paper 1.

*Column* (13): The volume (A963 or A2192) and sample (*TFS* or *HQS*) that a galaxy belongs to.

The contents of the optical catalogue as presented in Table 3.2 are as follows:

*Column* (1): The running identification number of the galaxies for easy cross-reference with entries in Table 3.1.

*Column* (2): The SDSS ID of the adopted optical counterpart of the HI detection, indicating the optical coordinates of the galaxy.

*Column* (3): The minor-to-major axis ratios ( $b/a$ ) obtained from *galfit*.

*Column* (4): The inclination as inferred from the optical axis ratio ( $b/a$ ), following Eq. (1) and assuming an intrinsic disc thickness  $q_0$  of 0.2.

*Columns* (5) & (6): Total apparent INT B- and R- band magnitudes, respectively, including a small aperture correction as described in Sect. 4.2.

*Columns* (7) & (8): The k-corrections applied to the Galactic extinction corrected, apparent B- and R- band magnitudes, as described in Sect. 3.

*Columns* (9) & (10): The internal extinction corrections applied to the Galactic extinction and k-corrected B- and R- band magnitudes, as described in Sect. 3.

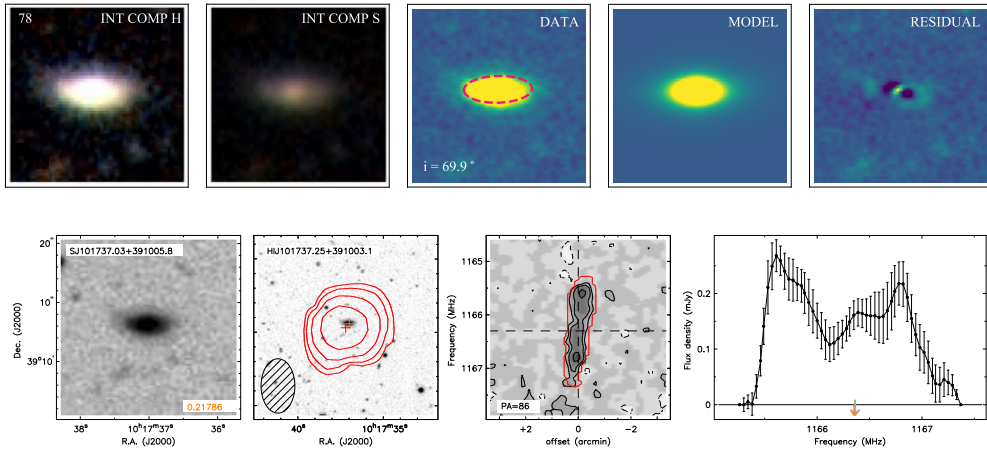


**Figure 3.7** – An example of the layout of the atlas, showing a galaxy from the *TFS*. The top row shows the optical properties and *galfit* outputs, whereas the bottom panel mostly shows the HI properties. The atlas layout has been described in detail in Sect. 3.5.

*Columns* (11) & (12): The corrected, absolute B- and R- band magnitudes, respectively.

*Column* (13): Log stellar mass ( $M_{\odot}$ ) calculated using Eq. 3.16.

*Column* (14): Log baryonic mass ( $M_{\odot}$ ) calculated from the HI masses in Col. (12) of Table 3.1, and the stellar masses in Col. (13) respectively.

### 3.5.2 The atlas

The catalogue presented in Tables 3.1 and 3.2 is accompanied by an atlas page for each galaxy. Figure 3.7 illustrates an example of the atlas layout, consisting of two rows. The top row consists of 5 panels highlighting the optical morphology and the results from the *galfit* modelling. The bottom row consists of 4 panels highlighting the HI data, similar to the atlas pages in Paper 1. Each panel is briefly described below.

From left to right, the top row displays the following:

*Panels* (1) and (2): INT colour composite images ( $20 \times 20$  arcsec<sup>2</sup>) with a hard and soft contrast, respectively. The top-left corner of panel (1) shows the catalogue number as listed in Col. (2) of Table 3.1.

*Panel* (3): The optical R-band image of the galaxy. The red dashed ellipse depicts the fitting result returned by *galfit* as derived at the effective radius and deconvolved from the seeing. For clarity, it is enlarged by an arbitrary factor and therefore not representative for the radius at which it is drawn.

*Panel* (4): The resulting model as returned by *galfit*.

*Panel* (5): The residual image as returned by *galfit*.

From left to right, the bottom row of each atlas page displays the following:

*Panel (1):* INT R-band image ( $30 \times 30$  arcsec<sup>2</sup>) of the optical counterpart. The SDSS ID is given in the top-left corner. The optical redshift is printed in the bottom-right corner of the image for those sources with optical spectroscopy.

*Panel (2):* A zoomed-out INT R-band image ( $2 \times 2$  arcmin<sup>2</sup>) with HI contours from the total HI map overlaid in red. The HI ID is provided in the top-left corner. The optical centre is indicated by the orange cross while the HI centre is given by the red cross. The contours are set at HI column density levels of 1, 2, 4, 8, 16, and  $32 \times 10^{19}$  cm<sup>-2</sup>.

*Panel (3):* The Position–velocity diagram along the optical major axis, extracted from the R4 ( $\sim 38$  km s<sup>-1</sup>) cube. The contour levels correspond to  $-2$  (dashed), 2, 4, 6, 9, 12, 15, 20, and 25 times the local rms noise level. The mask within which the HI flux was determined is outlined in red. The position angle is given in the bottom-left corner of the diagram. The central frequency and the HI centre are given by the vertical and horizontal dashed lines, respectively.

*Panel (4):* The global HI profile as extracted from the R4 cube within the mask indicated in panel (3). The frequencies corresponding to the HI and optical redshifts are indicated by the grey and orange arrows respectively. Further details about the data processing can be found in Paper 1.

## 3.6 The Tully-Fisher Relations

Presented in this section are the TFrs obtained using the corrected HI line widths as tracers of the rotational velocities, and different photometric bands as well as derived quantities such as baryonic masses. We begin with explaining the fitting methods applied to the various samples, followed by a presentation of the luminosity-based TFrs and the baryonic TFrs relations using rotational velocities derived from the corrected  $W_{20}$  and  $W_{50}$  HI line widths.

### 3.6.1 Fitting method

The fitting method adopted in this chapter closely resembles that of Verheijen (2001) and for this study, our choice of the fiducial TFr in the Local Universe is from that study as well.

In order to minimise the Malmquist bias, inverse, weighted-least-square fits were made to the data, identical to the procedure followed by Verheijen (2001). A custom-made fitting algorithm using the python package *scipy.optimize.curve\_fit* was implemented for the fitting. Uncertainties in the corrected line widths were estimated using standard error propagation of the errors on the observed line widths. Uncertainties in the model parameters featuring in the various correction formulas were not considered. Only errors in the corrected line widths were taken into account during the fitting, and the small inclination related co-variance between the errors in the corrected luminosities and in the line widths were ignored. The parameters of the inverse TFr and BTFr fits are

provided in Tables 3.3 and 3.4 (see Sect. 3.6.5 for more details).

### 3.6.2 The Luminosity-based TFr

The best-fit TFrs for the full *TFS* with both the slope and the zero point left free and using both velocity measures  $W_{20}^{\text{corr}}$  and  $W_{50}^{\text{corr}}$ , combined with the two photometric bands B and R are given by Eqs. 3.12, 3.13, 3.14 and 3.15.

$$M_B = (-10.6 \pm 0.73)\log(W_{20}^{\text{corr}}) + (6.35 \pm 1.49) \quad (3.12)$$

$$M_B = (-8.2 \pm 0.54)\log(W_{50}^{\text{corr}}) + (0.14 \pm 1.39) \quad (3.13)$$

$$M_R = (-10.9 \pm 0.71)\log(W_{20}^{\text{corr}}) + (6.27 \pm 1.47) \quad (3.14)$$

$$M_R = (-8.4 \pm 0.54)\log(W_{50}^{\text{corr}}) + (-0.33 \pm 1.41) \quad (3.15)$$

We note that the TFrs based on the smaller *HQS* are very similar to the TFrs to the larger *TFS* (see Sect. 3.7.1) and hence are not considered here.

Due to the rather limited range ( $2.25 < \log W_{\%}^{\text{corr}} < 2.75$ ) and relatively larger errors on the HI line widths for the BUDHiES galaxies, however, we limit our analysis to fitting and comparing the TFr zero points only. For this purpose, fits to the *TFS* and *HQS* were made with the slopes fixed to the corresponding TFr of the UMa sample, which displays a significantly smaller scatter. The figures corresponding to Eqs. 3.12, 3.13, 3.14 and 3.15 are not provided in this chapter, since our main focus is on the evolution in the TFr zero points. Note that we did not make fits to the HIGHz sample because of the very limited range in luminosity of its constituent galaxies. They are instead plotted for illustrative purposes only, by including them in the various  $W_{50}^{\text{corr}}$  TFr plots. In all the figures displaying the TFrs (except Fig. 3.11), the TFrs for the *TFS* and *HQS* are shown by the *grey* and *red* lines respectively. All symbols and colours are kept consistent throughout the chapter except, again, for Fig. 3.11.

Fig. 3.8 presents the luminosity-based TFr fits based on the two velocity measures  $W_{20}^{\text{corr}}$  (left) and  $W_{50}^{\text{corr}}$  (right), and the absolute B-band (top) and R-band (bottom) magnitudes. The slope was fit to the UMa sample and then kept fixed for the fits to the BUDHiES samples. In all cases we find an offset of the BUDHiES TFr zero point towards brighter luminosities. These offsets are smallest when using the  $W_{20}^{\text{corr}}$  line widths (left panels) with  $0.47 \pm 0.06$  in the B-band and  $0.19 \pm 0.06$  in the R-band. The offsets in the zero point are significantly larger when using  $W_{50}^{\text{corr}}$  (right panels) with  $0.72 \pm 0.06$  and  $0.44 \pm 0.06$  in the B and R bands respectively. In all four cases, the vertical scatters are comparable, between 0.56 and 0.69 magnitudes (see Table 3.3). The numbers quoted are for the *TFS*, but there are no significant differences in the zero point offsets when fitting to the *TFS* or the more restrictive *HQS* (again, see Table 3.3).

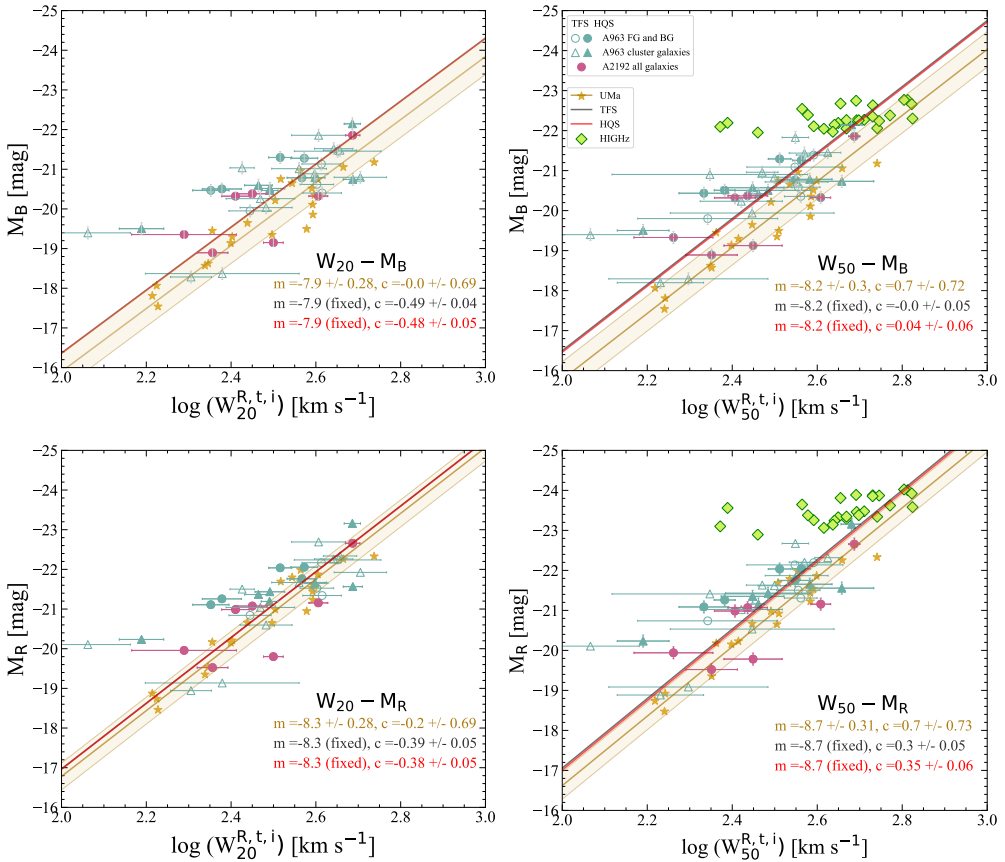


**Figure 3.8** – Top panel: The Hi-TFRs using  $W_{20}^{\text{CORR}}$  (left) and  $W_{50}^{\text{CORR}}$  (right) line widths as velocity tracers in the B-band. Bottom panel: Similar to the top panel but in the R-band. In comparison, the Local TFR (Verheijen 2001) is shown by the orange markers and a corresponding orange best-fit line, while the orange band framing the UMA TFR represents the total observed rms scatter in the UMA data points. Overlays of the HIGHz galaxies are shown in the  $W_{50}^{\text{CORR}}$  TFRs for illustrative purposes. The colours and symbols used are identical to Fig. 3.2. Open (pink and cyan) symbols indicate the *TFS*, while the coloured symbols represent the *HQS* (which is a subset of the *TFS*). The respective best fit TFRs with slopes fixed to UMA are shown by the grey and red lines. The best-fit parameters of the UMA and *TFS* TFRs are printed to the bottom-right of the sub-figures.

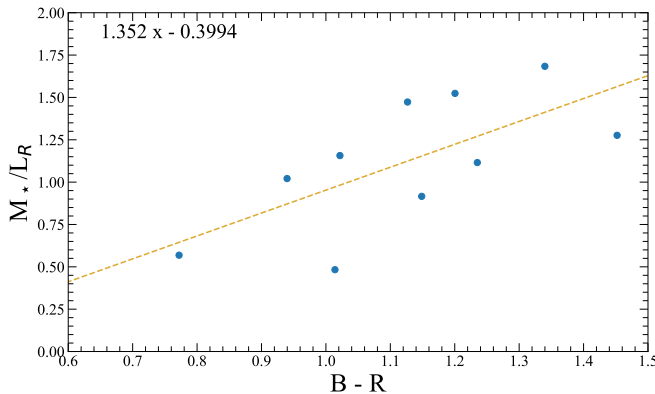


**Figure 3.9** –  $M_*/L_R$  vs  $B-R$  for the UMA HSB galaxies using maximum-disc fits, assuming an isothermal halo. The line of best fit given to the top-left is the same as Eq. 3.16.

### 3.6.3 The Baryonic TFR

For the purpose of constructing baryonic TFRs, stellar masses were calculated by converting the corrected, absolute B– and R–band magnitudes using two different prescriptions that both involve a  $(B-R)$  colour term but with a different degree of dependency. With the first prescription, stellar masses ( $M_*$ ) were determined empirically from maximum-disc rotation curve mass decompositions (Verheijen 1997, Chapter 6) of the UMA galaxies, using K–band luminosity profiles and assuming a maximum-disc fit with an isothermal dark matter halo model. The stellar masses following from these rotation curve decompositions are tabulated in Verheijen (1997, Chapter 6) and were used to calculate R–band stellar mass-to-light ratios  $M_*/L_R$ , which are plotted versus the  $(B-R)$  colour of the galaxies in Fig. 3.9. A linear correlation is observed and represented by the following expression:

$$M_*^{\text{mxd}} [M_\odot] = L_R \times (1.35(B-R) - 0.399) \quad (3.16)$$

Maximum-disc-based stellar masses computed in this way for all the BUDHiES galaxies are provided in Col. (13) of Table 3.2.

For comparison, we also adopted an alternative stellar mass estimator, following Zibetti, Charlot & Rix (2009). This prescription was also adopted by Cybulski et al. (2016) who calculated stellar masses for 23 BUDHiES galaxies using the INT B– and R–band photometry following:

$$M_*^{\text{zib}} [M_\odot] = L_R \times 10^{-1.2+1.066(B-R)} + 10^{0.04} \quad (3.17)$$

where the term  $10^{0.04}$  accommodates a conversion to the Kroupa initial mass function (Kroupa 2001). Stellar masses computed using this prescription are not tabulated.

From the estimated stellar and HI masses, the baryonic masses were calculated for all galaxies following:

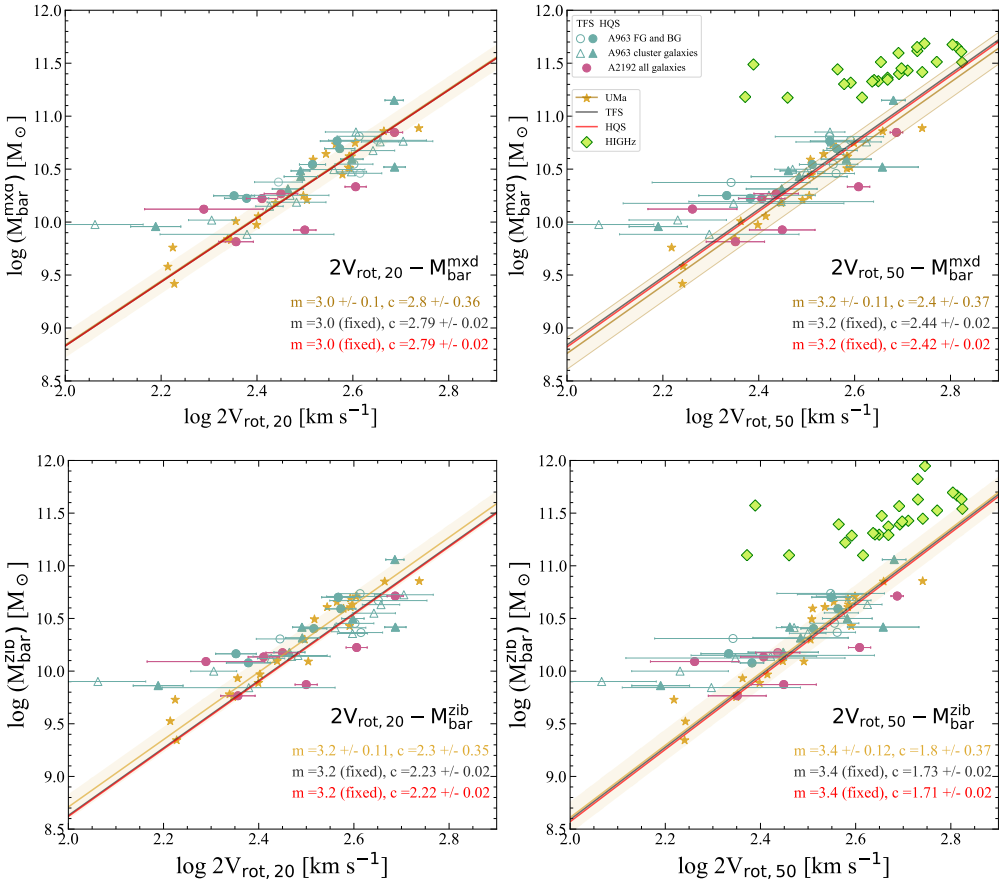


**Figure 3.10** – BTFrs based on the two velocity measures,  $\log(2V_{\text{rot},20} = W_{20}^{\text{corr}})$  (left) and  $\log(2V_{\text{rot},50} = W_{50}^{\text{corr}})$  (right). Baryonic masses ( $1.4M_{\text{HI}} + M_{\star}$ ) were computed from two different stellar mass prescriptions, Eq. 3.16 (top) and Eq. 3.17 (bottom). The layout, colours and symbols are identical to Fig. 3.8.

$$M_{\text{bar}} = M_{\star} + 1.4M_{\text{HI}} \quad (3.18)$$

where the factor 1.4 accounts for the contribution by Helium and metals. Molecular gas is not accounted for since its contribution to the statistical properties of the BTFR is found to be negligible (e.g., Ponomareva et al. 2018). The velocity measures for the BTFRs are given in the form of  $\log(2V_{\text{rot},\%})$  for which  $\log(W_{\%}^{\text{corr}})$  is an approximation.

The best fit inverse BTFRs with both the slope and the zero point left free are described by:

$$\log(M_{\text{bar}}/M_{\odot}) = (3.7 \pm 0.23)\log(2V_{\text{rot},20}) + (1.1 \pm 0.65) \quad (3.19)$$

$$\log(M_{\text{bar}}/M_{\odot}) = (3.4 \pm 0.20)\log(2V_{\text{rot},50}) + (1.89 \pm 0.61) \quad (3.20)$$

These are based on the stellar masses computed using Eq. 3.16. Again, the corresponding figures for these BTFRs are not shown, since our focus is on the zero point of the BTFRs with their slopes fixed to the BTFR of UMa. Instead, we show in Fig. 3.10 the BTFRs based on the two stellar mass prescriptions given by Eqs. 3.16 and 3.17. The zero points of the BTFRs based on the maximum disc approach (top panels) are indistinguishable from the zero points of the UMa BTFRs, with a maximum zero point offset of 0.08 dex when using  $W_{50}^{\text{corr}}$ . Similar statistically insignificant differential offsets in the zero point are observed for the BTFRs using Eq. 3.17 (bottom panels). These results will be discussed in detail in Sect. 3.7.

### 3.6.4 The TFR from an environmental perspective

The final versions of the TFR presented in this paper investigate the effect of the environment on the TFR, taking advantage of the fact that the BUDHiES samples also include galaxies in a cluster environment. In particular, we are interested in studying these environmental effects from a ‘Butcher-Oemler’ (BO) perspective. The BO effect (Butcher & Oemler 1984) manifests itself as a higher fraction of blue galaxies in the cores of clusters at higher redshifts. The cluster A963, part of the seminal BO paper, is a massive, lensing cluster hosting an unusual large fraction of blue galaxies in its core ( $f_b = 0.19$ ), and is one of the nearest BO clusters. In contrast, A2192, at a similar redshift as A963, is a non-BO cluster with no blue galaxies associated with its core, weak in X-rays and still in the process of forming (for more information on the two clusters, see Jaffé et al. 2012, 2013, 2015, 2016). Several studies of the BO effect using optical and other bands have been carried out, with varying results (e.g., Couch et al. 1994; Lavery & Henry 1986; Tran et al. 2003; De Propris et al. 2004; Andreon, Lobo & Iovino 2004; Andreon et al. 2006; Urquhart et al. 2010; Lerchster et al. 2011). While some confirmed the presence of this BO effect, others claimed it was a selection bias by preferential inclusion of brighter, bluer galaxies at higher redshifts.

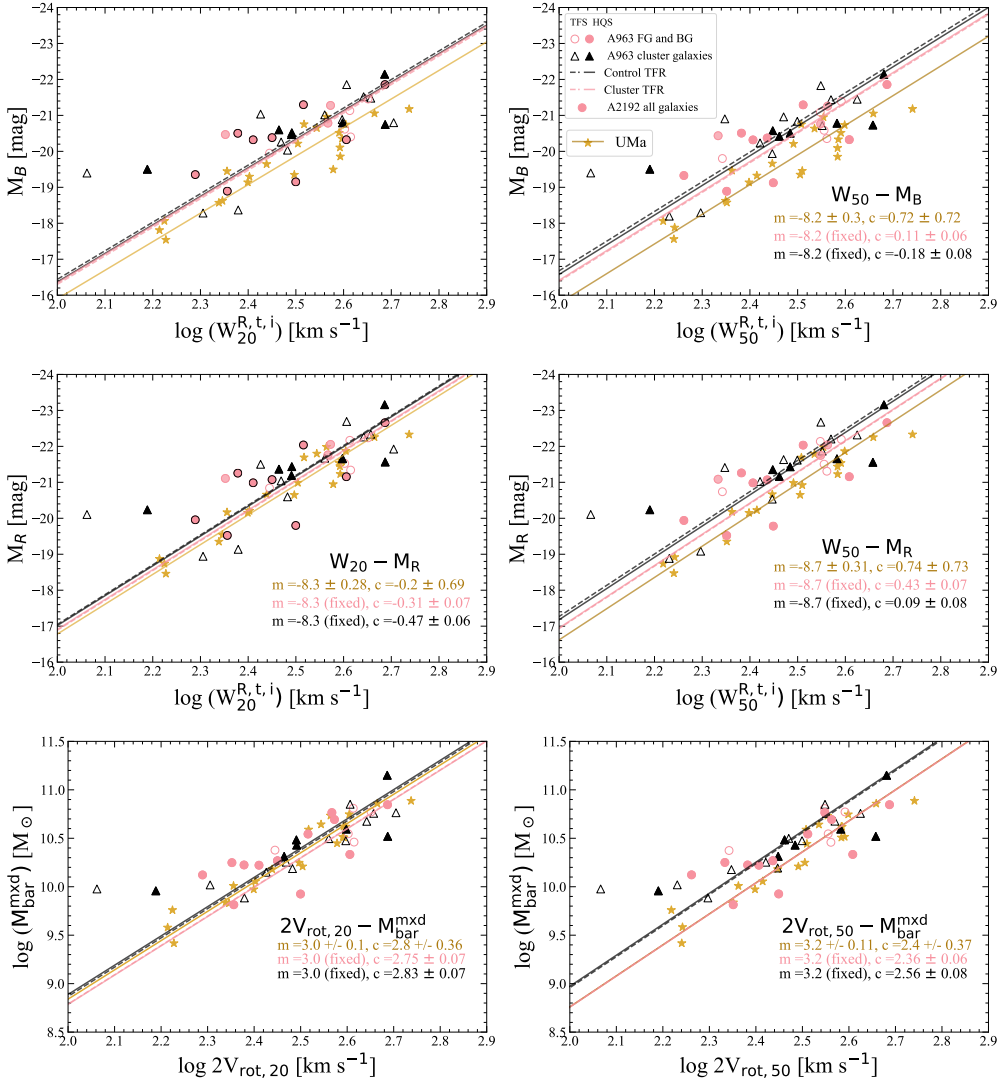


**Figure 3.11** – Top and middle: The luminosity-based TFRs for the *Cluster* and *Control* samples in B-band and R-bands respectively, using  $W_{20}^{\text{corr}}$  (left) and  $W_{50}^{\text{corr}}$  (right). Bottom: BTFRs using the same velocity measures as the luminosity based TFRs but expressed as  $2V_{\text{rot},20}$  (left) and  $2V_{\text{rot},50}$  (right). The *Control* sample and its corresponding TFR is shown by the pink circles and lines, while the *Cluster* sample and TFR is shown by the black triangles and lines. The open and solid symbols as well as the dashed and solid lines represent the *TFS* and *HQS* respectively. The UMa galaxies and TFR are given in orange. The fit parameters for UMa and the *TFS* samples are printed in the bottom-right of each panel.

However, the BO effect in relation to the cold atomic gas content of galaxies has never been investigated, and this was the primary driver for the BUDHIES survey. Previous studies of the BUDHIES data have shown that none of the blue galaxies within the central 1 Mpc region of A963 were detected in HI (see Verheijen et al. 2007; Jaffé et al. 2016). This implies that these blue galaxies may not be gas-rich and actively star-forming systems but still have their light dominated by a young, post-starburst stellar population. In a series of papers, the cluster substructure and the nature of the blue galaxies were studied based on HI stacking in phase space (Verheijen et al. 2007; Jaffé et al. 2013, 2015, 2016). These studies concluded that the blue galaxies were stripped of their HI during their first passage through the Intra-Cluster Medium (ICM) which resulted in temporarily enhanced star formation. These blue galaxies could possibly have remaining HI with masses below our detection threshold. Other blue galaxies in the vicinity of the cluster could still be gas bearing and experiencing enhanced star formation activity.

Our topic of interest is to investigate whether the galaxies outside the cluster core of A963 are responsible for the blueing and brightening of the TFR observed in Fig. 3.8. The advantage of having HI data from galaxies associated with a BO cluster and field galaxies at the same redshift therefore allows us to study its effect on the TFR and BTFR.

For both the *TFS* and *HQS*, we constructed two sub-samples, distinguished by their environment. Galaxies belonging to the cluster A963 alone, defined as the velocity range within  $2.5\sigma_{\text{cl}}$  from the cluster recession velocity, with  $\sigma_{\text{cl}} = 933 \text{ km s}^{-1}$  being the velocity dispersion of A963, made up the *Cluster* sub-sample. The remainder of the galaxies in both survey volumes, consisting of those in the foreground and background of A963 as well as those in the entire A2192 survey volume, made up the *Control* sub-sample. While A2192 is also classified as a ‘cluster’, we include it in the *Control* sample since A2192 has a much smaller velocity dispersion ( $\sigma_{\text{cl}} = 645 \text{ km s}^{-1}$ ) and a negligible ICM compared to A963. Note that, only one direct HI detection exists within a projected distance of 1 Mpc from the cluster centre and this galaxy is not a member of the *TFS*. A total of 19 galaxies from the *TFS* belong to the *Cluster* sub-sample, while 17 belong to the *Control* sub-sample. From the *HQS*, 7 and 12 galaxies belong to the *Cluster* and *Control* sub-samples respectively. The various environment-based TFRs and BTFRs are illustrated in Fig. 3.11. The fit results for all these TFRs are provided in Table 3.4.

Compared to the *TFS*, which consists of galaxies from all environments, the TFRs derived using the *Control* sample show smaller offsets from the UMa sample in all cases. The *Cluster* TFR is significantly brighter and bluer ( $\Delta M_B = 0.90 \pm 0.09 \text{ mags}$  and  $\Delta M_R = 0.65 \pm 0.09 \text{ mags}$ ) than UMa, using  $W_{50}^{\text{corr}}$ . The same trend, though milder, is also observed in the *Control* sample, with galaxies being both brighter and bluer ( $\Delta M_B = 0.61 \pm 0.07 \text{ mags}$  and  $\Delta M_R = 0.31 \pm 0.08 \text{ mags}$ ) than UMa. The BTFRs, however, are still comparable to UMa even with the exclusion of cluster galaxies. This is discussed further in Sect. 3.7.3.

### 3.6.5 Parameter table layout

The fit results for the various TFrs in this chapter are given in Tables 3.3 and 3.4. Table 3.3 provides the fit parameters for the luminosity-based TFrs and BTFRs for the three samples in consideration: UMa, *TFS* and *HQS*. Table 3.4 is similar, but provides the fit parameters for the *Cluster* and *Control* samples (see Sect. 3.6.4). In addition, the tables also provide the offset differences with respect to each other as well as with UMa. Offsets greater than  $5\sigma$  are highlighted. Given below is a description of the columns.

*Column (1)*: Describes which TFr has been fit. Given in bold are the headers, consisting of the TF categories, for instance, the  $W_{20}$ -R band,  $W_{20}$ -B band etc. The numbers given next to the headers for the BTFRs indicate the stellar mass prescription used. *1* represents Eq. 3.16 while *2* represents Eq. 3.17.

*Column (2)*: The number of galaxies belonging to the specified sample.

*Column (3)*: The slopes with errors obtained at the time of fitting. This is true for the UMa sample. For the others, the slope is fixed to the UMa value.

*Column (4)*: The zero points with errors obtained at the time of fitting.

*Column (5)*: The reduced  $\chi_{\text{red}}^2$  signifying whether the observed scatter can be explained given the errors.

*Column (6)*: The total vertical rms scatter taking into account all the data points.

*Columns (7)*: Offsets in zero points with UMa. Offsets in the zero points calculated from the re-fitted UMa line with the slope fixed to the UMa sample with all parameters left free.

*Columns (8)*: Offset in zero point of the *HQS* with the larger *TFS*.

## 3.7 Discussion

Several high redshift studies of the TFr exist (see Sect. 3.7.2), though there are none that make use of HI as the choice of kinematic tracer. The only known HI study beyond the Local Universe ( $z \sim 0.2$ ) by Catinella & Cortese (2015) shows that an optically selected sample of extremely massive, gas rich and luminous galaxies also seems to follow the local BTFR from GASS (Catinella et al. 2012); however, their work is not a dedicated TFr study and the limited range in their magnitudes and line widths does not allow further analysis. TFr studies based on cosmological numerical simulations provide some insights into the *expected* redshift evolution of the TFr, with a possibility to carefully construct a sample of suitable galaxies with accurate inclination measurements. Regardless, the number of such studies using the extended HI discs of galaxies to trace the evolution in the TFr is limited. Using semi-analytical models, Obreschkow et al. (2009) concluded that their simulated TFrs in the Local Universe are in good agreement with the fiducial, observed TFr based on the HIPASS survey, but at higher redshifts, found an increase in the scatter and a shift in the zero points towards higher velocities for a given baryonic mass (their Fig. 14). On the other hand, Glowacki, Elson & Davé (2020, 2021) studied the evolution of the BTFR using the SIMBA simulation, and found that the zero point of the BTFR at higher redshifts is shifted towards lower velocities (their Fig. 3) and

only detectable for disc-like galaxies with  $V_{\text{flat}}$  as the kinematic measure. Thus, a proper morphological classification is abundantly important for an apt evaluation of the redshift evolution of the TFr.

This section provides a discussion of our observational findings and presents caveats that the reader needs to keep in mind, to ensure that possible systematic differences in the comparison samples are not mistaken for an evolution in the TFr parameters.

### 3.7.1 Impact of sample properties, observables and corrections on TFr scatter and zero points

The differences in the scatter and zero points of the luminosity-based TFrs as presented in Fig. 3.8 may be the result of a number of factors, such as the choice of photometric band (B versus R), the velocity measure ( $W_{20}^{\text{corr}}$  versus  $W_{50}^{\text{corr}}$ ), the inclusion of different galaxy populations in the sample, inaccuracies in the measurement of inclinations, intrinsic differences in the kinematics and morphologies of galaxies at higher redshifts and the effect of environment on these galaxies. Interestingly, the BTFRs as presented in Fig. 3.10 show a notably smaller scatter and offsets than the TFrs, as also reported in the literature (e.g., Lelli, McGaugh & Schombert 2016). In all cases, however, the  $z=0.2$  TFrs show a larger vertical scatter and zero point compared to the  $z=0$  TFr. Below, we explore some of the factors mentioned above in more detail.

### Sample selection

Galaxies at higher redshifts are more often found to have kinematical and morphological anomalies than local galaxies (Kannappan, Fabricant & Franx 2002; Flores et al. 2006; Kassin et al. 2007). In all these studies, inclusion of these galaxies with disturbed and complex optical morphologies introduced a large scatter in the TFr. Weiner et al. (2006) and Kassin et al. (2007) showed in their studies that the scatter in the stellar mass TFr was greatly reduced by adopting a kinematic estimator  $S_{0.5}$ , which adds a measure of disordered, non-circular motions to the rotational velocity, effectively accounting for pressure support. This empirical approach to reduce the scatter was also confirmed by simulations (see, for instance, Covington et al. 2010). Furthermore, including different galaxy types in the sample may also result in different slopes and systematic offsets in the TFr zero points. For instance, galaxies with rising or declining rotation curves are systematically offset from the TFr defined by regular spirals with flat rotation curves (e.g., Verheijen 2001; Bedregal, Aragón-Salamanca & Merrifield 2006; den Heijer et al. 2015).

In the extensive sample selection procedure adopted for this chapter (see Sect. 3.3), we filtered out optically disturbed and interacting galaxies since our goal is to construct a robust TFr using galaxies with reliable photometry and HI line widths that reflect the rotational velocities as a tracer of the total dynamical mass. Due to the limitations in the resolution and quality of both the HI and the optical data, however, it is likely that some kinematically disturbed systems may still have been included in our sample selection process, despite our best efforts.

It is noteworthy that there is almost no difference in the TFRs of the two BUDHIES subsamples (*HQS* and *TFS*), implying that an even stricter control over the HI properties of galaxies, in particular the symmetry of the HI global profile, does not significantly alter the TFR zero points or reduce the scatter. The offsets in the zero points of the *HQS* and the *TFS* are given in Col. (9) of Table 3.3, and in all cases, the differences are less than 0.1 magnitude. For simplicity, we will limit the rest of the discussion based on the results of the larger *TFS*.

### Inclinations

Improper inclination measurements are a dominant source of scatter in the TFR, since inclination corrections are applied not just to the kinematic measures but also to the magnitudes, and thus deserve special attention. Inclinations and their uncertainties can be estimated in a number of ways, such as making tilted-ring fits to the HI velocity fields, measuring HI disc ellipticities or optical axis ratios. With spatially unresolved HI data, inclinations are based on the ellipticity of the optical images. For the BUDHIES data, the optical axis ratios were computed from Sérsic models fit to our deep INT R-band images (Gogate et al. 2020) of the galaxies using *galfit*, which also corrects for the seeing. These axis ratios were determined at the effective radius and converted to inclinations adopting a disc thickness ( $q_0$ ) of 0.2. We found that adopting a different value of  $q_0$  would not significantly impact the zero point offsets. For instance, a  $q_0$  of 0.1 would result in a difference of  $\sim 1$  per cent in the corrected line widths for an observed axis ratio ( $b/a$ ) of 0.7 ( $i=46.5^\circ$ ), and  $\sim 1.6$  per cent for an observed  $b/a$  of 0.3 ( $i=76.8^\circ$ ). Several other studies with spatially unresolved HI data also commonly use a similar approach (e.g., Tully & Fisher 1977; Topal et al. 2018).

For the UMA and HIGHz samples, we adopted the inclinations from the respective papers (Verheijen 2001; Catinella & Cortese 2015). For the UMA sample, inclination measurements are based on both, optical axis ratios and HI kinematics. These inclinations are robust because the UMA galaxies are nearby and also have spatially resolved HI kinematics. For the HIGHz sample, these inclinations are based on the  $(b/a)_r$  axis ratios provided in the SDSS database.

### Choice of velocity measures

Conventional HI based TFR studies make use of several velocity definitions, depending on the type of data available. The choice of velocity measure can have significant effects on the statistical properties of the TFR. Spatially resolved studies provide rotation curves, which allow measurements of the outer flat part, the inner peak velocity or the velocity at a radius of 2.2 scale lengths of the stellar disc. Flat, extended rotation curves are generally exhibited by late-type, rotationally supported disc galaxies, whereas smaller, irregular systems usually exhibit rising rotation curves up to the outermost measured radius, and are unsuitable for a TFR analysis. Very massive and compact galaxies often show declining rotation curves for which a corrected global HI profile width usually overestimates the amplitude of the outer flat part. A galaxy with a flat or declining rotation curve is typified by a classic ‘double-horned’ HI profile, with steep profile edges.

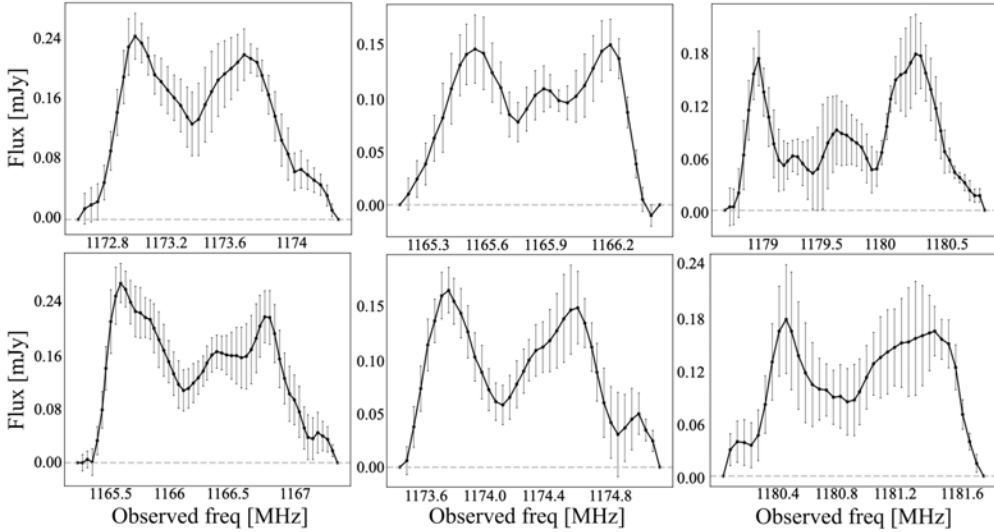


**Figure 3.12** – Some examples of asymmetric HI profiles that show the presence low-level HI which is responsible for broadening the observed  $W_{20}$  line widths. The velocity resolution of these profiles is  $38 \text{ km s}^{-1}$ .

For single dish and spatially unresolved HI studies, the classic approach for estimating the rotational velocities of galaxies is based on the corrected widths of the global HI profiles (Tully & Fisher 1977). These are measured at the 20% and 50% of the peak flux density ( $W_{20}^{\text{corr}}$  and  $W_{50}^{\text{corr}}$  respectively), where inferred rotational velocities are roughly half of the corrected HI profile line widths. Lelli et al. (2019) found significantly tighter TFrs using HI line-widths as proxies for rotational velocities, as compared to other velocity tracers such as the  $H\alpha$  and CO emission lines, which probe velocities in the inner parts of galaxies. This implies that HI line widths, while indirect velocity measures, are better kinematic tracers of the dark matter potential than other tracers originating from the inner star-forming discs of galaxies. Rotational velocities measured along the flat part of HI rotation curves are found to provide the tightest TFrs (Verheijen 2001; Ponomareva et al. 2017; Lelli et al. 2019). However, such measurements require spatially resolved HI kinematics from interferometric observations, which are often not available. Additionally, Glowacki, Elson & Davé (2020) found, for their sample of galaxies from the SIMBA simulation, that  $W_{20}$  line widths were the best proxies for  $V_{\text{flat}}$ , whereas  $W_{50}$  suggested smaller rotational velocities by definition. However, when considering only disc galaxies, both velocity measures traced  $V_{\text{flat}}$  quite well, except for dispersion-dominated low mass galaxies, which lie off the 1:1 relation between  $2V_{\text{flat}}$  and  $W_{50}$ . This also highlights the importance of proper sample selection.

Since the BUDHiES sample consists mostly of spatially unresolved HI sources, the corrected HI profile line widths  $W_{20}^{\text{corr}}$  and  $W_{50}^{\text{corr}}$  were used as proxies for the rotational velocities. Interestingly, we found a striking difference in  $W_{20}^{\text{corr}}$  and  $W_{50}^{\text{corr}}$  without any

correlation with the average SNR of the HI profiles (see Fig. 3.5). We concluded that galaxies in our sample have intrinsically shallower HI profile wings compared to the Local Universe counterparts. Furthermore, the HI profiles of the BUDHiES galaxies also tend to be more asymmetric than the UMa galaxies.

Our sample selection procedure resulting in the *HQS* (described in detail in Sect. 3.3) involved further stringent quantitative constraints on the HI profile to ensure a more reliable estimate of the rotational velocity. The first criterion ensured a higher SNR in the HI profiles. The second imposed constraints on the symmetry in the profiles, while the third criterion assessed the steepness of the profile edges. Figure 3.6 shows histograms of the steepness and symmetry of these profiles. From these histograms, it is clear that the galaxies in the *HQS* still have more asymmetric profiles with shallow edges compared to the UMa galaxies. However, we find that these more stringent quantitative criteria do not significantly reduce the TFR scatter or zero point offset of the *HQS* compared to the *TFS*.

The differences observed in the  $W_{20}^{\text{corr}}$  and  $W_{50}^{\text{corr}}$  line widths pose the question about the correct choice of velocity measure, since they both result in two different TFRs (illustrated in Fig. 3.8). Further analysis of galaxies with asymmetric HI profile shapes in the two BUDHiES samples suggests the presence of low-level unresolved HI which is likely not participating in the rotation of these galaxies but appears to broaden the HI profiles at low flux levels, thus affecting the  $W_{20}^{\text{corr}}$  line widths. The  $W_{50}^{\text{corr}}$  line widths on the other hand, seem less affected by this broadening. Some of these asymmetric profiles are shown in Fig. 3.12. Thus, smaller offsets with UMa seen in the  $W_{20}^{\text{corr}}$  luminosity-based TFRs (Fig. 3.8, left) are likely due to an overestimation of the rotational velocities derived from the  $W_{20}^{\text{corr}}$  line widths, causing the BUDHiES galaxies to shift towards larger rotational velocities and negating the vertical offset of the BUDHiES sample. Notably, plotting the vertical offsets of all individual galaxies from the UMa TFRs as a function of increasing asymmetry ( $|\Delta V_{\text{sys}}|/W_{20}^{\text{obs}}$ ) and increasing shallowness ( $\Delta W = |W_{20}^{\text{corr}} - W_{50}^{\text{corr}}|$ ) in Fig. 3.13, we do not see any particular trend.

To explore a possible correlation between the environment and the occurrence of asymmetric and shallow HI profiles, the BUDHiES samples were categorised further into two sub-samples, the *Cluster* and *Control* samples (see Sect. 3.6.4). Histograms similar to Fig. 3.6 are shown for these sub-samples in Fig. 3.14. Most of these asymmetric and shallow HI profiles originate from the *Cluster* sample, though the *Control* sample also exhibits some asymmetric and shallow profiles. Jaffé et al. (2011a) also found similar disturbances in their optical emission-line profiles of cluster galaxies. Probing the nature of these differences in the context of evolutionary signatures as seen by studies such as Kannappan, Fabricant & Franx (2002); Kassin et al. (2007) amongst others, would require further analysis of the HI profiles and a larger sample, which is beyond the scope of this thesis. See sect. 3.7.3 for a further discussion on the environmental effects on the TFR and BTFR.

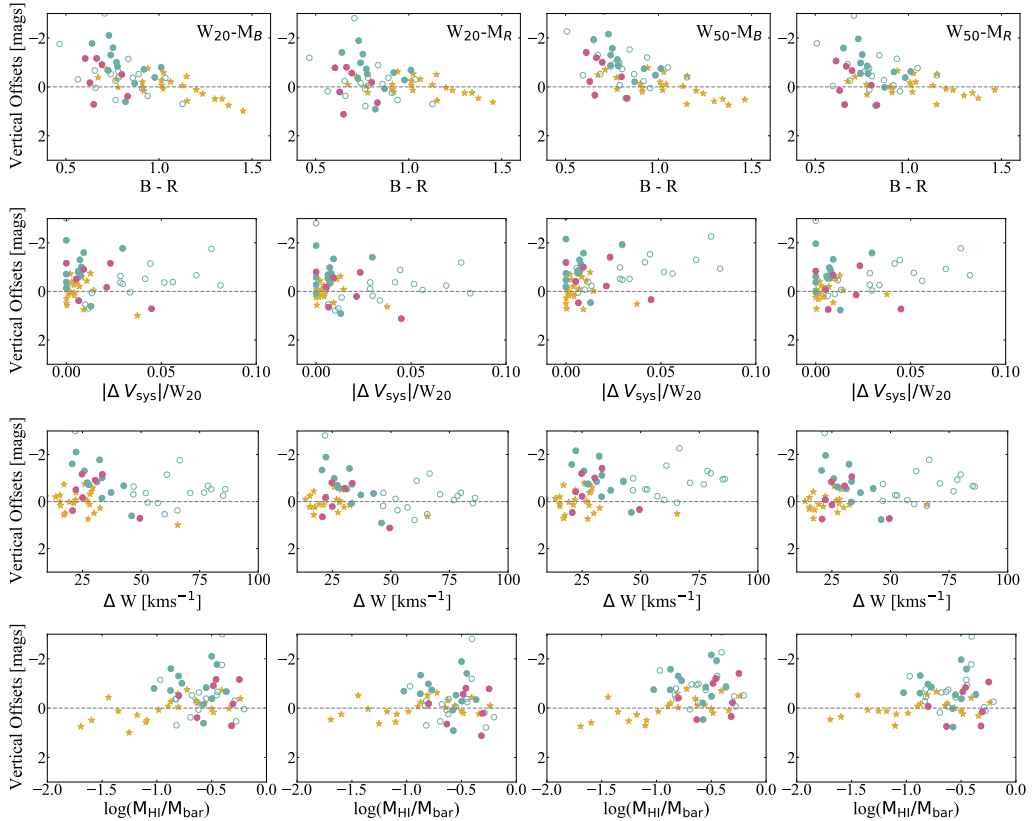


**Figure 3.13** – Scatter plot of the vertical offsets (difference in magnitudes) of the individual galaxies points from the luminosity-based TFR from UMa, as a function of (a) B-R colour, (b) quantified asymmetry, (c) quantified shallowness and (d) ratio of the HI to baryonic mass. Points lying above the dashed ‘zero’ line are brighter than the UMa TFR while those below are fainter. From first to the last columns are the TFRs from the two photometric bands and velocity measures:  $W_{20}-M_B$ ,  $W_{20}-M_R$ ,  $W_{50}-M_B$ ,  $W_{50}-M_R$ . All colours and symbols are identical to Fig. 3.2.

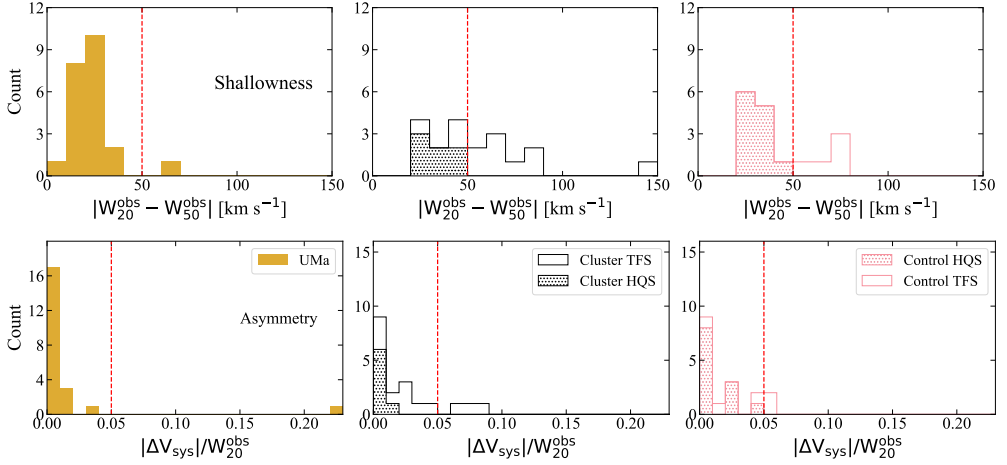


**Figure 3.14** – Similar to Fig. 3.6 but for the control (pink) and cluster (black) samples, respectively: Top: histograms showcasing the difference in the observed line widths (shallowness); Bottom: histograms showing the absolute fractional differences in the systemic velocities derived from the two line width measures (asymmetry). The orange histograms show the UMA sample. Open histograms correspond to the *TFS*, while the hatched histograms show the *HQS*.

### Choice of corrections for turbulent motion and internal extinction

In the previous sections, we have already stressed the importance of having homogeneous samples with consistently applied corrections to properly compare the parameters of different TFr. Moreover, the corrections themselves may affect the samples differently, depending on their underlying properties, and could play a significant role in altering the parameters of the TFr. For instance, an inconsistent choice of corrections applied to the line widths would impact the inferred evolution in the TFr. The turbulent motion corrections used in this chapter are adopted from Verheijen & Sancisi (2001), which were optimised for the UMA galaxies based on rotation curve measurements. For an unresolved sample like BUDHiES, however, there is no way of knowing if these corrections are adequate.

Furthermore, we consider two different internal extinction correction methods. The first is from Tully et al. (1998, referred to as T98), which is the standard correction adopted for this chapter and described by Eq. 3.7 in Sect. 3.4.2. The second is from Tully & Fouque (1985, referred to as TFq) which is dependent on inclination only, and is given as follows:

$$A_{\lambda}^{i, \text{TFq}} = -2.5 \log \left[ f(1 + e^{-\tau_{\lambda} \sec i}) + (1 - 2f) \left( \frac{1 - e^{-\tau_{\lambda} \sec i}}{\tau_{\lambda} \sec i} \right) \right] \quad (3.21)$$

where, for a slab of dust containing a homogeneous mixture of stars of fraction  $(1-2f)$ ,  $f$  signifies the fraction of stars above and below this slab, while  $\tau_{\lambda}$  gives the optical

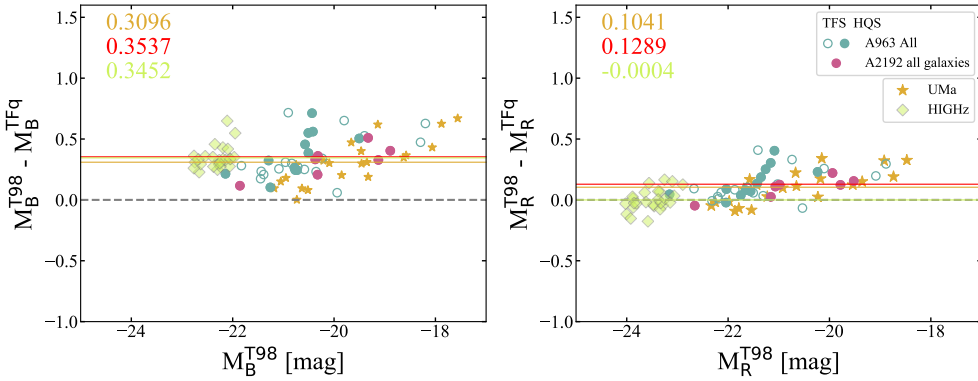


**Figure 3.15** – Difference in the absolute magnitudes based on two different internal extinction corrections for the two available photometric bands, B (left) and R (right). The magnitudes were corrected for Galactic extinction, K-corrections and the internal extinction corrections were adopted from Tully et al. (1998) and Tully & Fouque (1985) respectively. The differences are plotted against the absolute magnitudes based on Tully et al. (1998), which is the standard correction used in this chapter. The colours and symbols are identical to Fig. 3.2. The horizontal lines indicate the average differences for each sample, denoted by their respective colours, with their corresponding values printed at the top-left. The dashed black line indicates no differences between the T98 and TFq corrections.

depth of the dust layer as a function of wavelength. We used  $f = 0.1$ ,  $\tau_B = 0.81$  and  $\tau_R = 0.40$  (Verheijen 1997). This extinction prescription is applicable for galaxies with  $45^\circ < i < 80^\circ$ . For more edge-on galaxies, the TFq prescription assigns reddening corrections corresponding to  $i=80^\circ$ , assuming the extinction to plateau for extremely inclined systems, as the ‘back’ of the disk and bulge becomes visible below the dustlane.

Fig. 3.15 shows the differences in the absolute magnitudes of the various samples, based on the two internal extinction corrections (T98 and TFq), for both photometric bands. Four, two and two galaxies in the UMa, BUDHiES and HIGHz samples respectively had  $i > 80^\circ$ , and thus were assigned TFq corrections  $A_\lambda^{i,TFq} = A_\lambda^{80,TFq}$ . The average difference between the two prescriptions is larger for the B-band (up to  $\sim 0.35$  mags) than the R-band (up to  $\sim 0.13$  mags), suggesting large systematic offsets in the TFR zero points if the samples were to be treated with different internal extinction prescriptions. However, the sample averages in the figure seem to be consistent with each other, with a maximum difference  $\sim 0.04$  in the B-band and an even smaller difference  $\sim 0.025$  in the R-band. This suggests that the choice of prescription would have an insignificant impact on our results, given that they are consistently applied to all the samples. The spread in the UMa and BUDHiES samples is similar due to similar distributions of their inclinations and linewidths, and smaller for the more face-on HIGHz galaxies. Finally, the figure suggests an increasing difference in corrections with decreasing magnitude. This is probably due to the fact that lower mass galaxies tend to be less dusty, an effect accommodated by the T98 prescription but not TFq. This would also introduce a change in the slope of the TFR if different prescriptions are used for different samples.

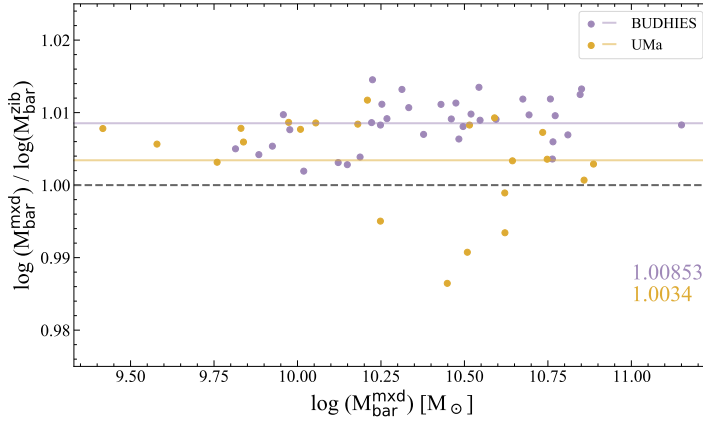


**Figure 3.16** – Ratio of the baryonic masses derived from the two stellar mass prescriptions, Eq. 3.16 (referred to as  $M_{\text{bar}}^{\text{mxd}}$ ) and Eq. 3.17 (referred to as  $M_{\text{bar}}^{\text{zib}}$ ) as a function of  $M_{\text{bar}}^{\text{mxd}}$ . The purple circles are the BUDHiES TFS galaxies while the orange circles indicate the UMA galaxies. The solid purple and orange lines and the corresponding coloured numbers printed to the bottom-right indicate the mean ratios of the baryonic masses for the TFS and UMA samples, respectively. The dashed grey line indicates the line of equality.

### Choice of photometric band

Some studies such as Flores et al. (2006,  $z \sim 0.6$ ) claim to find a larger scatter in the B-band TFR compared to other bands. We find that both the K-corrections and internal extinction corrections are larger in the B-band than the R-band, and after applying these corrections the vertical scatters in the BUDHiES TFRs are similar in the B and R bands (see Fig. 3.8 and Table 3.3). This implies that the choice of photometric band does not seem to affect the observed scatter in the BUDHiES TFRs. The applied corrections, however, do result in differences in the zero-points between the BUDHiES TFRs and the  $z=0$  TFR from UMA, with the offsets being larger (brighter) in the B-band than in the R-band in all cases. Furthermore, Fig. 3.13 illustrates the vertical offsets (offset in magnitude) of each individual BUDHiES galaxy from the  $z=0$  UMA TFR as a function of B-R colour using both,  $W_{20}^{\text{corr}}$  and  $W_{50}^{\text{corr}}$ . We find a mild colour dependence for the UMA galaxies, particularly in the B-band, in the sense that bluer UMA galaxies have a positive offset. This mild trend is continued towards bluer colours by the BUDHiES galaxies, albeit with a larger scatter. The TFRs in the respective photometric bands are discussed in more detail in Sect. 3.7.2.

### Choice of stellar mass estimator

Similar to Sect. 3.7.1, here we discuss the systematics involved in the choice of stellar mass prescription used to estimate baryonic masses. Studies such as Ponomareva et al. (2018, 2021), whose stellar masses are based on Spectral Energy Distribution (SED) fitting, have shown that the choice of stellar mass estimator can impact the statistical properties of the BTFR and are dependent on the quality of the photometry. To verify

this notion, two different stellar mass prescriptions, Eqs. 3.16 and 3.17, were used to derive stellar and baryonic masses. Figure 3.16 shows the ratios of these two baryonic masses derived for both, BUDHiES and UMa. Contrary to the results of Ponomareva et al. (2018), we find that the baryonic masses derived from our chosen stellar mass prescriptions are consistent. The fit parameters of the resulting BTFRs from the two stellar mass estimators are given in Table 3.3. For instance, if stellar masses were derived using Eq. 3.16 for the UMa galaxies and Eq. 3.17 for BUDHiES we find the difference in the zero points of the BTFRs to be  $\sim 0.01$  dex.

In conclusion of this subsection 3.7.1, we find that some choices such as the chosen velocity measure, the photometric band and the choice of corrections applied to the data may affect the TFR and BTFR offsets and thus need to be suitably chosen. More importantly, it is essential that these choices are consistent throughout all comparison samples to avoid the influence of any systemic biases on the measured TFR offsets.

3

### 3.7.2 Evolution in the TFR with redshift

There are no HI studies of similarly constructed TFRs at higher redshifts in the literature to compare our results to. Other works at higher redshifts make use of other kinematic tracers and are based on optical or CO measurements, which originate from the inner regions of galaxies. There are currently many conflicting results and ongoing debates regarding the evolution of the TFR parameters with redshift (e.g., Vogt et al. 1997; Rix et al. 1997; Simard & Pritchett 1998; Ferreras & Silk 2001; Ziegler et al. 2002; Böhm et al. 2004; Ferreras et al. 2004; Conselice et al. 2005; Flores et al. 2006; Bamford, Aragón-Salamanca & Milvang-Jensen 2006; Weiner et al. 2006; Kassin et al. 2007; Puech et al. 2008). More recent studies such as Di Teodoro, Fraternali & Miller (2016) analysed  $H\alpha$  velocity fields from integral field unit (IFU) spectroscopy to derive the stellar mass TFR and reported no significant evolution out to  $z \sim 1$ . Topal et al. (2018) presented the first CO-based TFR, stellar mass TFR and BTFR beyond the Local Universe ( $0.05 < z < 0.3$ ) and also found no significant redshift evolution of the zero-point for any of their TFRs.

Conflicting results in the literature are likely caused by differences in the construction of the comparison samples and inconsistencies in the applied corrections, which, as discussed previously, could introduce systematic offsets that may be mistaken for evolutionary signatures. In our analysis, we have chosen to compare our BUDHiES TFRs with the local UMa TFR from Verheijen (2001) because of the similarities in the available data and the fact that the UMa galaxies are nearly equidistant.

### Evolution in the luminosity-based TFR

In Sect. 3.7.1 we discussed in detail the differences observed in the  $W_{20}^{\text{corr}}$  and  $W_{50}^{\text{corr}}$  line widths, and the possible reasons for the asymmetries and the shallow edges seen in the HI profiles of the BUDHiES galaxies. We limit this discussion to the offsets in the zero points from the  $W_{50}^{\text{corr}}$  TFRs, which imply that galaxies in the past were both brighter and bluer ( $\Delta ZP_B = 0.72 \pm 0.06$  mags and  $\Delta ZP_R = 0.44 \pm 0.06$  mags) than galaxies in the present epoch. This is most likely due to the rest frame B-band

luminosity being significantly more sensitive to star formation activity compared to the R-band luminosity. Qualitatively, this is expected, since galaxies at higher redshifts are predicted to have younger stellar populations, and it is known that the cosmic star formation rate density increases towards higher redshifts (e.g., Dutton et al. 2011; Madau & Dickinson 2014). Such offsets are also reported in the literature. For example, Böhm & Ziegler (2016) found that their sample of higher redshift field galaxies ( $0.05 < z < 1$ ) were either brighter in the B-band for their dynamical masses or had lower dynamical masses for their B-band luminosities. The underlying difference in colour seen in the CMD presented in Fig. 3.2 and discussed in Sect. 3.4.3 could be the reason behind the brightening of the BUDHiES TFr with respect to UMa. However, the fact that our BUDHiES galaxies are not only brighter in the B-band but also bluer suggests that, indeed, galaxies were brighter for their dynamical mass.

### Evolution in the Baryonic TFr

Turning our attention to the BUDHiES BTFRs, we find that their zero points are comparable to the  $z=0$  BTFRs, using either stellar mass estimator (Eqs. 3.16 and 3.17). For the  $2V_{50}$  BTFRs constructed with the *TFS*, the offsets in the zero points are as small as  $+0.08 \pm 0.02$  dex and  $-0.02 \pm 0.03$  dex, based on Eqs. 3.16 and 3.17 respectively. We therefore conclude that there is no evolution in the zero point of the BTFR with redshift up to  $z \sim 0.2$ . This supports the finding by Dutton et al. (2011), who concluded that the scaling relations using baryonic masses show a weak evolution.

Interestingly, as shown in Fig. 3.4, the higher  $M_{\text{HI}}/M_{\text{bar}}$  ratios of the BUDHiES galaxies compared to UMa (see Sect. 3.4.3) imply that a larger fraction of the baryonic content in the BUDHiES galaxies is in the form of HI. Figure 3.4 also shows a larger intrinsic spread in  $M_{\text{HI}}/M_{\text{bar}}$  for the UMa sample, which is not reflected in a larger scatter in the TFr or BTFR. In particular, the two UMa galaxies (NGC 3729 and NGC 4102) with the lowest  $M_{\text{HI}}/M_{\star}$  and  $M_{\text{HI}}/M_{\text{bar}}$  ratios in Fig. 3.4 (b) and (d) have the lowest HI masses and small HI discs, yet they follow the TFr and BTFR. This implies that the BTFR is insensitive to the gas fraction of the galaxies at least out to  $z \sim 0.2$ . Shown in the last panel of Fig. 3.13 are the vertical offsets of the UMa and BUDHiES galaxies from the luminosity-based UMa TFrs as a function of  $M_{\text{HI}}/M_{\text{bar}}$ . From the figure it is evident that the higher gas fraction in the BUDHiES galaxies does result in a higher star formation activity, which makes the BUDHiES galaxies brighter and bluer.

In conclusion to this section 3.7.2, we find that while the baryonic content of galaxies in the past has remained largely unchanged, the components making up the baryonic content (HI and stellar masses) have changed in the past 2.5 Gyrs. At the same time, the higher gas fraction of the BUDHiES galaxies seems to be linked to a higher star formation rate, which makes the BUDHiES galaxies brighter and bluer.

### 3.7.3 Effect of cosmic environment on the TFr and BTFR

There are several literature studies linking scaling relations such as the TFr to the evolution of galaxies in different environments. In dense cluster environments, for instance, kinematically anomalous galaxies are expected to be more common than in the field due

to mechanisms such as ram-pressure stripping, tidal interactions, mergers, harassment and strangulation (e.g., Oosterloo & van Gorkom 2005; Poggianti et al. 2017; Jaffé et al. 2018; Toomre & Toomre 1972; White 1978; Smith, Davies & Nelson 2010; Kawata & Mulchaey 2008; Maier et al. 2016). Inclusion of such galaxies in a TFR analysis are expected to lead to a larger scatter and systematic offsets in the TFR parameters, as discussed in Sect. 3.7.1 on sample selection.

There are some environment- and morphology-specific studies of the TFR, both at low (e.g., Vogt et al. 2004; Mocz et al. 2012) and high redshifts. At higher redshifts, several environment-specific TFR studies reported no significant differences in the TFRs in cluster and field populations (Ziegler et al. 2003; Nakamura et al. 2006; Jaffé et al. 2011a; Pérez-Martínez et al. 2021), while other authors such as Bamford et al. (2005), Milvang-Jensen et al. (2003) and Pérez-Martínez et al. (2021, for  $z \sim 1.5$ ) found an overall brightening of cluster galaxies at a fixed rotational velocity. Other morphology-specific studies such as Bedregal, Aragón-Salamanca & Merrifield (2006); Jaffé et al. (2014) reported fainter magnitudes at a given rotational velocity for lenticular and early-type galaxies compared to spiral galaxies.

Our thorough selection criteria were aimed at ensuring the selection of isolated, inclined systems with symmetric HI profiles with steep edges. However, it is still possible that the local environment around these galaxies may contribute to the scatter or offsets observed in Figs. 3.8 and 3.10, since a significant fraction of the BUDHiES galaxies lie in the vicinity of the massive, Butcher-Oemler cluster A963. It is of particular interest to investigate the offset and scatter in the TFR in the context of the BO effect (Butcher & Oemler 1984), motivated in Sect. 3.6.4.

To probe the effect of the environment on the TFR and BTFR parameters, the BUDHiES galaxies in the *TFS* and *HQS* were further classified into two categories: the ‘*Cluster*’ and the ‘*Control*’ sub-samples (see Sect. 3.6.4 for the sample construction). We have discussed the correlation between asymmetric and shallow HI profiles, and the environment in Sect. 3.7.1. Here, we discuss the environment-specific TFRs and BTFRs shown in Fig. 3.11. The fit results to the various subsamples are tabulated in Table 3.4. Note that we provide the results for both,  $W_{20}^{\text{corr}}$  and  $W_{50}^{\text{corr}}$ , but we only discuss the  $W_{50}^{\text{corr}}$  TFRs (motivated in Sect. 3.7.1). In the figure, the top two panels show the luminosity-based TFRs for the *Cluster* and *Control* samples. We note that the brightening and blueing of the *Control* galaxies is still significant compared to the UMa sample, with  $\Delta M_B = 0.61 \pm 0.07$  mags and  $\Delta M_R = 0.31 \pm 0.08$  mags. The sub-sample of *Cluster* galaxies, however, shows a much more extreme brightening with  $\Delta M_B = 0.90 \pm 0.09$  mags and  $\Delta M_R = 0.65 \pm 0.09$  mags, but a similar blueing to the *Control* sample. The extreme brightening of the *Cluster* galaxies could be the result of enhanced star formation induced by the cluster environment, while they still contain a detectable amount of HI gas (e.g., Mahajan, Raychaudhury & Pimblet 2012; Jaffé et al. 2016; Vulcani et al. 2018). This finding indicates that though the cluster environment increases the zero point offset, field galaxies in the past were still intrinsically bluer and brighter than local galaxies for a given rotational velocity.

Focusing instead on the environment-specific BTFRs (Fig. 3.11, bottom panel), we find

that the  $V_{50}$ -BTFR of the *Control* sample is identical to the UMa BTFR within the uncertainties, with  $\Delta\log(M_{\text{bar}}) = 0.00 \pm 0.06$  dex. The *Cluster* BTFR, while marginally offset from both, the *Control* and the UMa BTFR, is still consistent within the errors at the  $2.5\sigma$  level, with  $\Delta\log(M_{\text{bar}}) = 0.20 \pm 0.08$  dex. Thus, we conclude that the cluster environment does not seem to remove the baryonic mass from the dark matter halos of galaxies, contrary to one's expectations that the cluster environment might remove gas from infalling galaxies (e.g. due to ram-pressure stripping and starvation). We do not find hints of these gas removal processes in our *Cluster* sample galaxies since they have similar  $M_{\text{HI}}/M_{\text{bar}}$  ratios as our *Control* sample galaxies (see Fig. 3.4). This is not surprising, as our *Cluster* sample galaxies are all outside the estimated stripping cone of A963 (see Fig. 7 in Jaffé et al. 2015). Nevertheless, since the *Cluster* galaxies are brighter than the *Control* galaxies, the outer cluster environment may already be enhancing the star formation activity compared to field galaxies.

Thus, reiterating our conclusion from Sect. 3.7.2, while the baryonic content of these galaxies do not show an evolution with redshift for a given rotational velocity, the  $M_{\text{HI}}/M_{\text{bar}}$  ratio seems to have evolved. At the same time, our results also show that the star-formation activity was higher in the past and further enhanced by the cluster environment.

### 3.7.4 Comparison with HIGHz

Lastly, for a cursory comparison, we also indicated the HIGHz sample in various the  $W_{50}^{\text{corr}}$  TFR and BTFR figures. The HIGHz sample consists of optically selected massive, luminous galaxies at redshifts similar to BUDHIES (see Sect. 3.4.3 for more details). Catinella & Cortese (2015) found that they lie on the local BTFR defined by Catinella et al. (2012) and McGaugh et al. (2000), though the galaxies had not been corrected for turbulent motion or internal extinction. In our work, however, corrections applied to the BUDHIES galaxies were identically applied to the HIGHz galaxies, including the correction for internal extinction. We do find that applying the extinction corrections to the HIGHz galaxies results in offsets from the local BTFR (see Fig. 3.10), underlining the importance of applying consistent corrections to all samples.

We find that the HIGHz galaxies are more consistent with our luminosity-based TFRs (Fig. 3.8) compared to the local TFR. However, a correlation between luminosity and line width is nearly absent for the HIGHz sample. In the case of the BTFR (Fig. 3.10), we find that the HIGHz galaxies seem to have significantly larger baryonic masses for their rotational velocities compared to both the Local BTFR and BUDHIES.

## 3.8 Summary and Conclusions

With this work, we present the first dedicated study of an HI-based TFR beyond the Local Universe using direct HI detections. We have studied the luminosity-based B- and R-band TFRs as well as the BTFR at  $z \sim 0.2$  from a meticulously selected sample of HI detected galaxies from the Blind Ultra-Deep HI Environmental Survey (BUDHIES, Gogate et al. 2020). In addition, we used deep B- and R-band images, obtained with

the IN. The BUDHiES TF sample (*TFS*) comprises 36 galaxies, of which 29 are in the survey volume containing A963 and 7 in the volume containing A2192. Of these, 11 and 7 galaxies together make up the *High Quality* sub-sample (*HQS*) based on stringent quantitative thresholds imposed on the shape of the HI global profile. Our results were compared with an identically constructed TFr from the Ursa Major association of galaxies in the Local Universe at a distance of 18.6 Mpc (UMa, Verheijen 2001). Our main results are as follows:

(1) The best fit inverse R-band and baryonic TFrs for the BUDHiES TF sample with all parameters left free are:

$$M_R = (-8.4 \pm 0.54) \log(W_{50}^{\text{corr}}) + (-0.33 \pm 1.41);$$

$$\log(M_{\text{bar}}/M_{\odot}) = (3.4 \pm 0.20) \log(2V_{50}^{\text{corr}}) + (1.98 \pm 0.61);$$

These are based on the  $W_{50}^{\text{corr}}$  velocity measures and stellar masses computed according to Eq. 3.16. Fits using other velocity measures and stellar mass estimators are given in Sects. 3.6.2 and 3.6.3. Due to the relatively large scatter of the BUDHiES sample compared to UMa, further analysis was restricted to the TFr zero points only, by fixing the slope to the UMa TFr.

(2) The scatter in the *TFS* and *HQS* TFrs are very similar, suggesting that stricter quantitative selection criteria on the shapes of the HI profiles do not reduce the scatter.

(3) Similarly, differences in the zero points of the *TFS* and *HQS* TFrs are always less than 0.05 magnitudes, implying that stricter selection criteria also do not affect the TFr zero points. These thresholds were chosen to improve the quality of the sample without compromising too much on the sample size. However, the BUDHiES galaxies in the *HQS* still seem to have more asymmetric HI profiles with shallower wings than the UMa galaxies. Further inspection of these asymmetric profiles suggests the presence of low-level unresolved HI gas that likely does not participate in the rotation of the galaxies, possibly from optically unidentified nearby companions, but broadens the  $W_{20}^{\text{corr}}$  in some cases. This leads to the intrinsic differences in the two corrected line width measures. The majority of these disturbed HI profiles are from galaxies belonging to the cluster A963.

(4) The zero point offsets depend on the choice of photometric band and velocity measure. Offsets in the B-band are always larger than in the R-band. An overestimation of rotational velocities using  $W_{20}^{\text{corr}}$  causes the BUDHiES galaxies to shift towards larger rotational velocities and thus negate the above mentioned vertical offset of the BUDHiES sample.

(5) Adopting  $W_{50}^{\text{corr}}$  as the velocity measure, the BUDHiES TFr is both bluer and brighter than the  $z=0$  TFr. We further divided the *TFS* into a *Cluster* and a *Control* sub-sample. While the *Control* sample is brighter and bluer than the UMa sample ( $\Delta M_B = 0.61 \pm 0.07$  mags and  $\Delta M_R = 0.31 \pm 0.08$  mags), the *Cluster* sample is even brighter but not bluer ( $\Delta M_B = 0.90 \pm 0.09$  mags and  $\Delta M_R = 0.65 \pm 0.09$  mags).

(6) The Baryonic TFr at  $z \sim 0.2$  is consistent with the local BTfr despite the fact that

the  $M_{\text{HI}}/M_{\text{bar}}$  ratio of the BUDHiES galaxies is somewhat higher than that of the UMa galaxies. Although the  $M_{\text{HI}}/M_{\text{bar}}$  ratios are similar for the *Cluster* and *Control* galaxies, the cluster environment seems to enhance the luminosities of the *Cluster* sample galaxies.

(7) Lastly, it is very important to ensure that the comparison samples trace similar galaxy populations for a proper and unbiased comparison, since the various corrections, even if consistently applied, may affect different galaxy populations differently.

Finally, we reinforce the fact that HI as a kinematical tracer of the rotational velocities of galaxies is an important tool to further our knowledge of the evolution of such scaling relations. With this study, we have provided an important reference for future HI-based surveys at higher redshifts such as the Deep Investigation of Neutral Gas Origins (DINGO; Meyer 2009) with the Australian Square Kilometre Array Pathfinder (ASKAP) and the Looking At the Distant Universe with the MeerKAT Array (LAD-UMA; Holwerda, Blyth & Baker 2012; Blyth et al. 2016), and ultimately, the Square Kilometre Array (SKA-1)\*, which may have similar HI selection effects as BUDHiES and limitations in spatial resolution.

## Acknowledgements

AG and MV would like to acknowledge the Netherlands Foundation for Scientific Research support through VICI grant 016.130.338 and the Leids Kerkhoven-Bosscha Fonds (LKBF) for travel support. AG thanks P. Bilimogga for useful discussions, for providing the HI profile widths for the Perseus-Pisces data and the systemic velocities for the Ursa Major sample. AG also thanks N. Choque. and J. Healy for useful discussions on galaxy modelling with *galfit*. JMvdH acknowledges support from the European Research Council under the European Union’s Seventh Framework Programme (FP/2007-2013)/ERC Grant Agreement nr. 291531. Y.J. acknowledges financial support from CONICYT PAI (Concurso Nacional de Insercion en la Academia 2017) No. 79170132 and FONDECYT Iniciacion 2018 No. 11180558. The WSRT is operated by the Netherlands Foundation for Research in Astronomy, supported by the Netherlands Foundation for Scientific Research. The full acknowledgement of the Sloan Digital Sky Survey Archive used in this chapter can be found at <http://www.sdss.org>.

## 3.9 Catalogues and atlas

The following pages contain the HI and optical catalogues of the BUDHiES TF sample (Tables 3.1 and 3.2 respectively). Following the two tables is an atlas of the optical and HI properties of all the BUDHiES TF galaxies.

---

\* <https://www.skatelescope.org>

**Table 3.1** – HI properties of the BUDHIES TF galaxies. The columns are described in detail in Sect. 3.5.1

Sr. no.	Cat. no.	HI ID	R	SNR	$z_{\text{HI}}$	$D_{\text{lum}}$	$w_{20}^{\text{obs}}$	$w_{50}^{\text{obs}}$	$w_{20}^{\text{R,t,1}}$	$w_{50}^{\text{R,t,1}}$	$\log M_{\text{HI}}$	Volume
(1)	(2)	(3)	(4)	(5)	(6)	(7)	(8)	(9)	(10)	(11)	(12)	(13)
			$\text{km s}^{-1}$			Mpc	$\text{km s}^{-1}$	$\text{km s}^{-1}$	$\text{km s}^{-1}$	$\text{km s}^{-1}$	$M_{\odot}$	
1	2	HLJ101523.89+390949.7	39.09	3.47	0.1904	926.7	349.1 ± 9.8	323.3 ± 9.5	328.0 ± 20.5	324.7 ± 19.9	5.5 ± 0.3	A963
2	7	HLJ101600.44+385211.7	39.69	2.66	0.20861	1026.3	126.2 ± 10.4	104.3 ± 12.0	115.4 ± 26.7	116.5 ± 30.8	3.7 ± 0.4	A963
3	9	HLJ101611.10+384921.7	39.63	4.07	0.20674	1016	407.5 ± 8.1	380.3 ± 10.4	485.4 ± 21.4	479.6 ± 27.4	13.3 ± 0.6	A963
4	10	HLJ101613.62+390438.4	39.06	3.86	0.18954	922.2	372.1 ± 15.3	315.0 ± 17.8	400.2 ± 36.5	359.3 ± 42.4	8.4 ± 0.3	A963
5	20	HLJ101626.57+391900.1	39.98	3.67	0.21746	1075.2	375.2 ± 13.6	338.0 ± 15.1	369.1 ± 29.7	353.4 ± 32.9	18.5 ± 0.8	A963
6	27	HLJ101641.11+391025.1	39.75	4.65	0.21047	1036.3	334.6 ± 22.2	256.1 ± 10.4	363.4 ± 54.1	295.5 ± 25.4	11.2 ± 0.4	A963
7	37	HLJ101701.14+384258.2	39.51	2.75	0.20328	996.9	266.7 ± 21.5	219.9 ± 23.0	294.5 ± 55.0	263.8 ± 58.8	4.3 ± 0.3	A963
8	40	HLJ101702.64+385109.6	39.6	4.85	0.20587	1011.2	341.4 ± 6.9	298.8 ± 5.6	309.6 ± 14.0	289.5 ± 11.4	13.1 ± 0.5	A963
9	45	HLJ101705.51+384927.4	39.54	3.08	0.20401	1000.8	445.6 ± 18.5	393.6 ± 13.4	453.9 ± 41.1	421.5 ± 29.8	8.4 ± 0.4	A963
10	48	HLJ101709.40+391138.3	40.01	4.33	0.21842	1080.6	259.8 ± 11.0	227.5 ± 14.4	225.0 ± 22.2	215.4 ± 29.0	6.3 ± 0.3	A963
11	50	HLJ101711.87+385419.0	39.94	3.1	0.21613	1067.8	308.0 ± 15.6	228.1 ± 40.7	278.5 ± 32.0	219.9 ± 83.5	8.4 ± 0.6	A963
12	54	HLJ101717.31+391335.5	39.76	3.75	0.21079	1038.1	300.2 ± 8.7	233.7 ± 58.4	266.7 ± 17.6	222.5 ± 118.1	5.5 ± 0.3	A963
13	58	HLJ101720.60+391054.4	39.34	2.63	0.19808	968.2	432.5 ± 28.2	291.8 ± 23.7	506.9 ± 72.2	356.1 ± 60.7	8.8 ± 0.5	A963
14	61	HLJ101723.56+390255.5	38.38	3.01	0.16871	810.5	267.4 ± 12.3	246.8 ± 6.6	239.0 ± 25.4	241.1 ± 13.6	2.2 ± 0.2	A963
15	63	HLJ101725.27+390320.1	39.68	4.32	0.20822	1024	338.3 ± 8.1	305.0 ± 17.5	396.2 ± 21.4	382.4 ± 46.0	10.4 ± 0.4	A963
16	67	HLJ101727.44+384632.2	39.44	3	0.20104	984.8	449.0 ± 21.5	363.1 ± 14.4	438.5 ± 45.7	371.5 ± 30.6	9.9 ± 0.5	A963
17	71	HLJ101729.58+385829.8	39.53	3.57	0.20381	999.8	318.5 ± 10.6	285.1 ± 23.1	291.4 ± 21.9	280.5 ± 47.7	3.5 ± 0.2	A963
18	78	HLJ101737.25+391003.1	40	4.23	0.21788	1077.5	457.1 ± 49.5	380.2 ± 17.2	448.1 ± 105.5	390.5 ± 36.7	16.6 ± 0.6	A963
19	82	HLJ101739.56+391549.4	40	4.04	0.21802	1078.2	410.2 ± 13.6	379.0 ± 8.7	373.8 ± 27.2	365.4 ± 17.4	13.9 ± 0.6	A963
20	86	HLJ101742.36+390133.5	39.66	5.52	0.20761	1020.8	167.5 ± 7.9	145.2 ± 9.2	154.4 ± 18.6	155.0 ± 21.7	2.9 ± 0.2	A963
21	88	HLJ101742.65+390104.7	39.67	3.69	0.20793	1022.5	335.1 ± 12.0	307.4 ± 33.9	310.1 ± 24.9	305.0 ± 70.4	3.6 ± 0.2	A963
22	93	HLJ101748.32+390548.9	40.05	3.2	0.21947	1086.6	404.6 ± 19.3	339.1 ± 14.4	411.9 ± 43.2	364.1 ± 32.2	5.8 ± 0.3	A963
23	99	HLJ101757.27+391032.7	39.39	3.13	0.19946	976.1	252.5 ± 45.2	192.4 ± 38.6	239.4 ± 100.0	198.1 ± 85.4	4.0 ± 0.3	A963
24	101	HLJ101759.95+390637.9	39.72	3.89	0.20966	1032	345.0 ± 11.2	260.0 ± 10.9	395.4 ± 28.8	315.7 ± 28.0	6.9 ± 0.3	A963
25	102	HLJ101800.01+391649.2	39.37	2.32	0.19884	972.6	339.9 ± 21.5	293.2 ± 62.1	303.7 ± 43.0	279.8 ± 124.2	7.9 ± 0.6	A963
26	109	HLJ101809.30+390718.2	39.65	4.33	0.20745	1019.9	391.7 ± 9.1	345.7 ± 28.7	486.6 ± 25.2	454.8 ± 78.6	8.8 ± 0.4	A963
27	110	HLJ101809.30+390118.4	39.54	3.17	0.20419	1002.2	226.9 ± 10.6	174.1 ± 18.8	202.0 ± 22.5	170.2 ± 39.8	6.5 ± 0.4	A963

Table 3.1 – continued

Sr. no.	Cat. no.	H $\alpha$ ID	R km s $^{-1}$	SNR	$z_{\text{HI}}$	$D_{\text{lum}}$ Mpc	$w_{20}^{\text{obs}}$ km s $^{-1}$	$w_{50}^{\text{obs}}$ km s $^{-1}$	$w_{20}^{\text{R,t,l}}$ km s $^{-1}$	$w_{50}^{\text{R,t,l}}$ km s $^{-1}$	log M $_{\text{HI}}$ $M_{\odot}$	Volume
(1)	(2)	(3)	(4)	(5)	(6)	(7)	(8)	(9)	(10)	(11)	(12)	(13)
28	117	HLJ101833.23+390403.3	39.5	2.97	0.20288	994.8	343.1 $\pm$ 22.5	282.1 $\pm$ 9.6	404.0 $\pm$ 59.3	353.7 $\pm$ 25.4	7.6 $\pm$ 0.5	A963
29	118	HLJ101835.11+385816.3	38.31	4.06	0.16669	800.1	380.7 $\pm$ 18.2	309.7 $\pm$ 38.6	410.3 $\pm$ 43.3	352.8 $\pm$ 91.8	9.7 $\pm$ 0.5	A963
30	4	HLJ162510.48+424033.8	38.99	3.88	0.18727	909.9	262.7 $\pm$ 8.5	237.9 $\pm$ 12.5	257.3 $\pm$ 19.3	254.9 $\pm$ 28.4	5.8 $\pm$ 0.3	A2192
31	13	HLJ162557.88+425320.7	38.38	3.08	0.16869	810.5	475.1 $\pm$ 8.6	452.9 $\pm$ 6.6	486.2 $\pm$ 19.0	486.7 $\pm$ 14.6	11.1 $\pm$ 0.6	A2192
32	18	HLJ162607.84+424218.2	39.07	3.3	0.18975	923.3	235.4 $\pm$ 8.3	210.4 $\pm$ 13.8	227.1 $\pm$ 18.9	224.5 $\pm$ 31.4	3.2 $\pm$ 0.2	A2192
33	24	HLJ162618.03+423811.8	39.11	2.91	0.19084	929.2	381.3 $\pm$ 8.8	360.5 $\pm$ 9.3	403.5 $\pm$ 20.6	405.7 $\pm$ 21.8	5.0 $\pm$ 0.3	A2192
34	30	HLJ162651.87+422710.8	39	3.15	0.18759	911.6	278.7 $\pm$ 6.5	229.2 $\pm$ 17.0	316.0 $\pm$ 17.0	281.2 $\pm$ 44.3	4.0 $\pm$ 0.2	A2192
35	31	HLJ162652.61+422839.4	40.09	2.55	0.22086	1094.3	279.9 $\pm$ 9.8	249.5 $\pm$ 12.6	281.9 $\pm$ 22.7	273.1 $\pm$ 29.2	6.1 $\pm$ 0.4	A2192
36	39	HLJ162844.33+422617.8	38.45	3.11	0.17095	822.5	212.2 $\pm$ 25.1	178.7 $\pm$ 17.7	194.6 $\pm$ 55.4	182.7 $\pm$ 39.1	7.5 $\pm$ 0.5	A2192

**Table 3.2** – Optical properties of the BUDHIES TF galaxies. The columns are described in detail in Sect. 3.5.1

Sr. no.	SDSS ID	b/a	incl deg	M <sub>B</sub>	M <sub>R</sub>	M <sub>B</sub> <sup>corr</sup>	M <sub>R</sub> <sup>corr</sup>	M <sub>B</sub> <sup>tfq</sup>	M <sub>R</sub> <sup>tfq</sup>	log L <sub>R</sub> L <sub>⊙</sub>	log M <sub>*</sub> M <sub>⊙</sub>	log M <sub>bar</sub> M <sub>⊙</sub>
(1)	(2)	(3)	(4)	(5)	(6)	(7)	(8)	(9)	(10)	(11)	(12)	(13)
1	SJ101523.65+390941.2	0.354 ± 0.002	72.65	-21.3	-22.04	-21.62	-22.12	10.66	10.42	10.25	10.53	10.4
2	SJ101600.10+385205.5	0.646 ± 0.011	51.2	-19.4	-20.1	-19.93	-20.36	9.88	9.62	9.44	9.97	9.9
3	SJ101611.13+384924.3	0.662 ± 0.002	49.89	-22.14	-23.16	-22.36	-23.2	11.1	11.09	10.98	11.15	11.06
4	SJ101613.68+390437.8	0.568 ± 0.003	57.1	-20.62	-21.53	-20.84	-21.56	10.45	10.36	10.22	10.54	10.45
5	SJ101626.35+391900.8	0.437 ± 0.004	66.64	-20.78	-21.76	-21.01	-21.79	10.54	10.51	10.39	10.76	10.7
6	SJ101641.08+391025.7	0.594 ± 0.007	55.16	-21.01	-21.67	-21.27	-21.73	10.51	10.18	10.01	10.49	10.41
7	SJ101701.11+384258.9	0.642 ± 0.006	51.5	-20.26	-21.04	-20.57	-21.15	10.26	10.06	9.89	10.25	10.14
8	SJ101702.77+385115.5	0.26 ± 0.004	80.27	-20.46	-21.19	-21	-21.48	10.32	10.07	9.89	10.48	10.42
9	SJ101705.49+384924.8	0.468 ± 0.002	64.41	-21.48	-22.34	-21.62	-22.31	10.78	10.65	10.49	10.75	10.63
10	SJ101709.09+391136.2	0.232 ± 0.003	83.13	-20.47	-21.11	-21.38	-21.74	10.28	9.94	9.77	10.24	10.16
11	SJ101711.90+385421.6	0.294 ± 0.022	77.26	-19.95	-20.84	-20.45	-21.07	10.18	10.08	9.93	10.37	10.31
12	SJ101717.55+391334.5	0.245 ± 0.006	81.65	-21.04	-21.5	-21.74	-21.94	10.44	9.76	9.74	10.13	10.12
13	SJ101721.45+391052.0	0.643 ± 0.01	51.43	-20.8	-21.92	-20.99	-21.95	10.61	10.66	10.61	10.76	10.72
14	SJ101723.76+390253.9	0.314 ± 0.004	75.74	-20.5	-21.26	-21.06	-21.51	10.34	10.12	9.95	10.22	10.08
15	SJ101725.11+390316.5	0.665 ± 0.002	49.67	-20.79	-21.66	-21.05	-21.73	10.5	10.39	10.23	10.59	10.5
16	SJ101727.72+384627.8	0.386 ± 0.002	70.27	-21.52	-22.26	-21.67	-22.23	10.74	10.51	10.33	10.67	10.55
17	SJ101730.00+385830.6	0.315 ± 0.01	75.59	-20.6	-21.37	-21.03	-21.54	10.39	10.19	10.01	10.31	10.18
18	SJ101737.03+391005.8	0.392 ± 0.004	69.86	-21.46	-22.24	-21.6	-22.2	10.74	10.54	10.37	10.77	10.67
19	SJ101739.82+391547.9	0.176 ± 0.005	90	-21.28	-22.05	-22.44	-23.58	10.66	10.47	10.29	10.69	10.59
20	SJ101742.42+390135.8	0.554 ± 0.011	58.19	-19.5	-20.23	-20.01	-20.46	9.93	9.69	9.51	9.95	9.86
21	SJ101742.99+390105.4	0.33 ± 0.009	74.5	-20.52	-21.44	-20.89	-21.56	10.41	10.33	10.19	10.43	10.31
22	SJ101748.10+390544.4	0.483 ± 0.015	63.37	-20.4	-21.34	-20.59	-21.34	10.38	10.31	10.18	10.46	10.37
23	SJ101757.22+391039.6	0.465 ± 0.031	64.64	-18.37	-19.14	-18.77	-19.28	9.49	9.29	9.11	9.88	9.84
24	SJ101759.72+390636.5	0.644 ± 0.003	51.33	-20.89	-21.65	-21.13	-21.72	10.5	10.29	10.12	10.47	10.36
25	SJ101759.13+391658.1	0.111 ± 0.032	90	-20.03	-20.6	-21.08	-22.03	10.08	9.61	9.48	10.18	10.15
26	SJ101809.25+390716.6	0.698 ± 0.011	46.93	-20.74	-21.56	-20.98	-21.63	10.47	10.31	10.14	10.51	10.42

Table 3.2 – continued

Sr. no.	SDSS ID	b/a	incl deg	M <sub>B</sub>	M <sub>R</sub>	M <sub>B<sup>corr</sup></sub>	M <sub>R<sup>corr</sup></sub>	M <sub>B<sup>ftq</sup></sub>	M <sub>R<sup>ftq</sup></sub>	log L <sub>R</sub> L <sub>⊙</sub>	log M <sub>*</sub> M <sub>⊙</sub>	log M <sub>bar</sub> M <sub>⊙</sub>
(1)	(2)	(3)	(4)	(5)	(6)	(7)	(8)	(9)	(10)	(11)	(12)	(13)
27	SJ101809.12+390118.5	0.381 ± 0.022	70.69	-18.28	-18.94	-18.83	-19.18	9.42	9.09	8.92	10.02	10
28	SJ101833.28+390356.5	0.668 ± 0.004	49.43	-21.86	-22.69	-22.11	-22.77	10.92	10.77	10.61	10.84	10.71
29	SJ101835.20+385816.9	0.567 ± 0.006	57.21	-21.13	-22.17	-21.34	-22.2	10.71	10.7	10.61	10.81	10.74
30	SJ162510.56+424028.8	0.505 ± 0.001	61.76	-20.32	-20.99	-20.68	-21.11	10.23	9.92	9.74	10.21	10.13
31	SJ162558.03+425319.4	0.465 ± 0.002	64.63	-21.86	-22.66	-21.97	-22.61	10.9	10.73	10.56	10.84	10.71
32	SJ162607.94+424215.9	0.51 ± 0.004	61.36	-18.89	-19.52	-19.29	-19.68	9.65	9.29	9.12	9.81	9.77
33	SJ162618.09+423808.9	0.545 ± 0.001	58.83	-20.32	-21.15	-20.53	-21.18	10.3	10.15	9.99	10.33	10.22
34	SJ162651.30+422709.9	0.659 ± 0.003	50.16	-19.15	-19.8	-19.45	-19.91	9.76	9.42	9.25	9.92	9.87
35	SJ162652.56+422836.6	0.533 ± 0.004	59.73	-20.38	-21.08	-20.7	-21.18	10.27	9.99	9.81	10.26	10.17
36	SJ162843.80+422618.2	0.46 ± 0.002	65	-19.35	-19.96	-19.84	-20.16	9.82	9.42	9.27	10.12	10.09

**Table 3.3** – Parameters and offsets of the various TFRs.

TFR (1)	<i>Parameters</i>					<i>ZP Offsets</i>	
	Count (2)	a (3)	b (4)	$\chi^2_{\text{red}}$ (5)	$\sigma$ (6)	Offset UMa (7)	Offset TFS (8)
<b>W<sub>20</sub>-R</b>							
UMa (free)	22	-8.29 ± 0.28	-0.2 ± 0.69	3.88	0.34	-	-
UMa	22	-8.29 (fixed)	-0.20 ± 0.04	3.69	0.34	-	-
TFS	36	-8.29 (fixed)	-0.39 ± 0.05	6.35	0.68	0.19 ± 0.06	-
HQS	19	-8.29 (fixed)	-0.38 ± 0.05	10.0	0.70	0.18 ± 0.06	0.01 ± 0.07
<b>W<sub>50</sub>-R</b>							
UMa (free)	22	-8.68 ± 0.31	0.74 ± 0.73	3.50	0.34	-	-
UMa	22	-8.68 (fixed)	0.74 ± 0.04	3.33	0.34	-	-
TFS	36	-8.68 (fixed)	0.30 ± 0.05	3.40	0.56	<b>0.44 ± 0.06</b>	-
HQS	19	-8.68 (fixed)	0.35 ± 0.06	5.20	0.57	<b>0.39 ± 0.07</b>	0.05 ± 0.08
<b>W<sub>20</sub>-B</b>							
UMa (free)	22	-7.94 ± 0.28	-0.02 ± 0.69	7.62	0.45	-	-
UMa	22	-7.94 (fixed)	-0.02 ± 0.04	7.26	0.45	-	-
TFS	36	-7.94 (fixed)	-0.49 ± 0.04	7.02	0.69	<b>0.47 ± 0.06</b>	-
HQS	19	-7.94 (fixed)	-0.48 ± 0.05	10.23	0.68	<b>0.46 ± 0.06</b>	0.01 ± 0.06
<b>W<sub>50</sub>-B</b>							
UMa (free)	22	-8.25 ± 0.3	0.72 ± 0.72	6.56	0.44	-	-
UMa	22	-8.25 (fixed)	0.72 ± 0.04	6.25	0.44	-	-
TFS	36	-8.25 (fixed)	-0.0 ± 0.05	3.73	0.56	<b>0.72 ± 0.06</b>	-
HQS	19	-8.25 (fixed)	0.04 ± 0.06	5.55	0.56	<b>0.68 ± 0.07</b>	0.04 ± 0.08
<b>BTFr V<sub>20</sub>: 1</b>							
UMa (free)	22	3.02 ± 0.1	2.8 ± 0.36	3.64	0.12	-	-
UMa	22	3.02 (fixed)	2.80 ± 0.01	3.46	0.12	-	-
TFS	36	3.02 (fixed)	2.79 ± 0.02	5.28	0.23	0.01 ± 0.02	-
HQS	19	3.02 (fixed)	2.79 ± 0.02	8.85	0.24	0.01 ± 0.02	0.0 ± 0.03
<b>BTFr V<sub>50</sub>: 1</b>							
UMa (free)	22	3.2 ± 0.11	2.36 ± 0.37	3.79	0.13	-	-
UMa	22	3.20 (fixed)	2.36 ± 0.01	3.61	0.13	-	-
TFS	36	3.20 (fixed)	2.44 ± 0.02	3.38	0.21	0.08 ± 0.02	-
HQS	19	3.20 (fixed)	2.42 ± 0.02	5.35	0.21	0.06 ± 0.02	0.02 ± 0.03
<b>BTFr V<sub>20</sub>: 2</b>							
UMa (free)	22	3.2 ± 0.11	2.31 ± 0.35	3.52	0.12	-	-
UMa	22	3.20 (fixed)	2.31 ± 0.01	3.36	0.12	-	-
TFS	36	3.20 (fixed)	2.23 ± 0.02	5.27	0.24	0.08 ± 0.02	-
HQS	19	3.20 (fixed)	2.22 ± 0.02	8.46	0.25	0.09 ± 0.02	0.01 ± 0.03
<b>BTFr V<sub>50</sub>: 2</b>							
UMa (free)	22	3.43 ± 0.12	1.75 ± 0.37	4.35	0.15	-	-
UMa	22	3.43 (fixed)	1.75 ± 0.02	4.14	0.15	-	-
TFS	36	3.43 (fixed)	1.73 ± 0.02	3.83	0.24	0.02 ± 0.03	-
HQS	19	3.43 (fixed)	1.71 ± 0.02	6.15	0.25	0.04 ± 0.03	0.02 ± 0.03

**Table 3.4** – Fit parameters of the environment-based TFRs

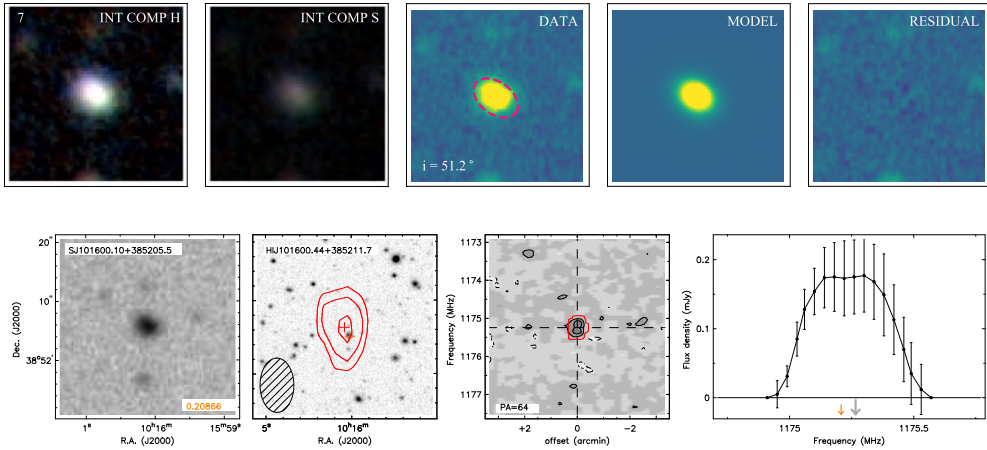
TFR (1)	<i>Parameters</i>					<i>ZP Offsets</i>	
	Count (2)	a (3)	b (4)	Chisq (5)	Scatter (6)	UMa (7)	Cluster sample (8)
<i>W<sub>20</sub> R</i>							
UMa	22	-8.29 (fixed)	-0.2 ± 0.04	3.69	0.34	-	-
TFS Cluster	19	-8.29 (fixed)	-0.47 ± 0.06	5.78	0.68	0.27 ± 0.08	-
TFS Control	17	-8.29 (fixed)	-0.31 ± 0.07	7.20	0.70	0.11 ± 0.08	0.16 ± 0.09
HQS Cluster	7	-8.29 (fixed)	-0.44 ± 0.08	11.43	0.61	0.24 ± 0.09	-
HQS Control	12	-8.29 (fixed)	-0.33 ± 0.07	10.03	0.72	0.13 ± 0.08	0.11 ± 0.1
<i>W<sub>20</sub> B</i>							
UMa	22	-7.94 (fixed)	-0.02 ± 0.04	7.26	0.45	-	-
TFS Cluster	19	-7.94 (fixed)	-0.56 ± 0.06	6.58	0.68	<b>0.54 ± 0.07</b>	-
TFS Control	17	-7.94 (fixed)	-0.42 ± 0.06	7.80	0.70	<b>0.40 ± 0.07</b>	0.14 ± 0.09
HQS Cluster	7	-7.94 (fixed)	-0.49 ± 0.07	11.28	0.61	<b>0.47 ± 0.08</b>	-
HQS Control	12	-7.94 (fixed)	-0.47 ± 0.07	10.72	0.72	<b>0.45 ± 0.08</b>	0.02 ± 0.1
<i>W<sub>50</sub> R</i>							
UMa	22	-8.68 (fixed)	0.74 ± 0.04	3.33	0.34	-	-
TFS Cluster	19	-8.68 (fixed)	0.09 ± 0.08	1.58	0.44	<b>0.65 ± 0.09</b>	-
TFS Control	17	-8.68 (fixed)	0.43 ± 0.07	5.03	0.60	0.31 ± 0.08	0.34 ± 0.11
HQS Cluster	7	-8.68 (fixed)	0.18 ± 0.11	2.21	0.39	0.56 ± 0.12	-
HQS Control	12	-8.68 (fixed)	0.41 ± 0.07	7.02	0.61	0.33 ± 0.08	0.23 ± 0.13
<i>W<sub>50</sub> B</i>							
UMa	22	-8.25 (fixed)	0.72 ± 0.04	6.25	0.44	-	-
TFS Cluster	19	-8.25 (fixed)	-0.18 ± 0.08	2.14	0.44	<b>0.90 ± 0.09</b>	-
TFS Control	17	-8.25 (fixed)	0.11 ± 0.06	6.29	0.60	<b>0.61 ± 0.07</b>	0.29 ± 0.10
HQS Cluster	7	-8.25 (fixed)	-0.08 ± 0.10	3.73	0.39	<b>0.80 ± 0.11</b>	-
HQS Control	12	-8.25 (fixed)	0.08 ± 0.07	8.30	0.61	<b>0.64 ± 0.08</b>	0.16 ± 0.12
<i>2V<sub>20</sub> BTFr</i>							
UMa	22	3.02 (fixed)	2.8 ± 0.01	3.46	0.12	-	-
TFS Cluster	19	3.02 (fixed)	2.83 ± 0.07	5.03	0.22	0.03 ± 0.07	-
TFS Control	17	3.02 (fixed)	2.75 ± 0.07	5.55	0.22	0.05 ± 0.07	0.08 ± 0.09
HQS Cluster	7	3.02 (fixed)	2.85 ± 0.08	11.60	0.22	0.05 ± 0.08	-
HQS Control	12	3.02 (fixed)	2.75 ± 0.07	7.51	0.23	0.05 ± 0.07	0.10 ± 0.11
<i>2V<sub>50</sub> BTFr</i>							
UMa	22	3.20 (fixed)	2.36 ± 0.01	3.61	0.13	-	-
TFS Cluster	19	3.20 (fixed)	2.56 ± 0.08	1.41	0.15	0.20 ± 0.08	-
TFS Control	17	3.20 (fixed)	2.36 ± 0.06	4.20	0.20	0.00 ± 0.06	0.2 ± 0.10
HQS Cluster	7	3.20 (fixed)	2.57 ± 0.10	1.98	0.15	0.21 ± 0.11	-
HQS Control	12	3.20 (fixed)	2.36 ± 0.06	5.83	0.21	0.00 ± 0.06	0.22 ± 0.12

**Table 3.5** – Detailed break-down of the galaxies rejected at each step of the sample selection process

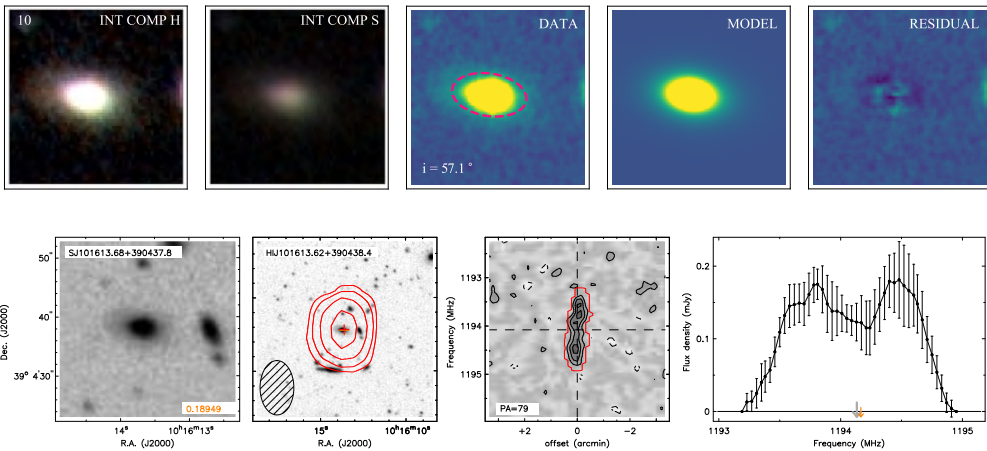
Criteria (1)	A963		A2192		Final sample size (6)
	Rejected cat no. (2)	Final sample size (3)	Rejected cat no. (4)	Final sample size (5)	
<b>Parent Sample</b>	<b>127</b>	-	<b>39</b>	-	
<b>Observational criteria</b>					
Galaxies cut off at band edges	28, 38	125	20, 22	37	162
Galaxies without INT photometry	12, 16, 125, 126, 127	120	7, 37	35	155
Galaxies with unreliable INT photometry due to nearby stars or other galaxies	41, 44, 83	117	5, 16, 34	32	149
<b>Qualitative criteria</b>					
Nearby optical companions (UV bright) might lead to H $\alpha$ profile disturbances, kinematical disturbances in main galaxy	4, 8, 15, 19, 23, 24, 25, 26, 29, 32, 35, 52, 64, 73, 80, 97, 107, 120	99	2, 27, 33, 35	28	127
Obvious disturbance in optical image	34, 47, 59, 60, 66, 69, 77, 84, 98, 123	89	6, 11, 12, 28, 32, 38	22	111
H $\alpha$ profile shape (reject type 2,5)	1, 3, 5, 6, 11, 13, 14, 17, 18, 21, 22, 30, 31, 33, 39, 42, 46, 49, 51, 55, 56, 57, 62, 65, 68, 70, 72, 75, 76, 79, 81, 87, 90, 91, 92, 94, 95, 96, 100, 103, 105, 111, 112, 114, 115, 116, 119, 122, 124	40	1, 3, 9, 10, 15, 17, 19, 21, 23, 26, 36	11	51
Inclinations < 45 degrees	4, 36, 43, 53, 85, 89, 104, 106, 108, 113, 121	29	8, 14, 25, 29	7	36

Table 3.5 – continued

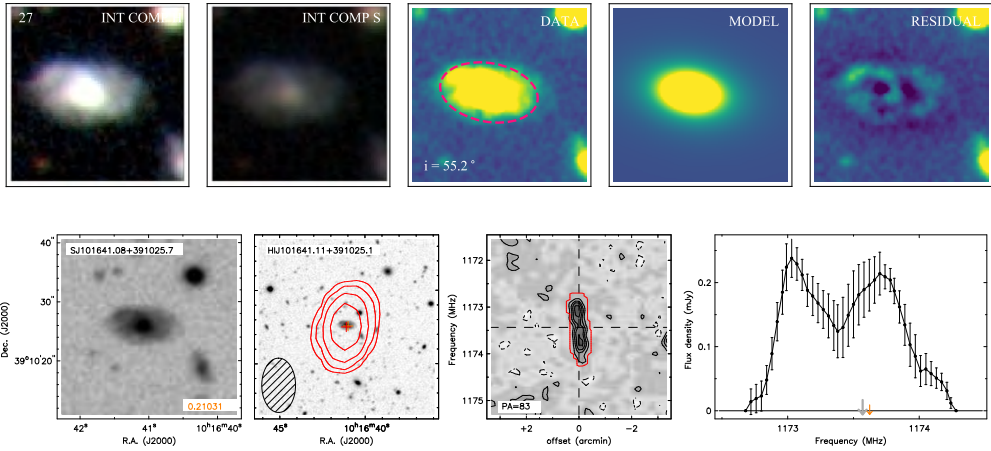
Criteria (1)	A963		A2192	
	Rejected cat no. (2)	Final sample size (3)	Rejected cat no. (4)	Final sample size (5)
<b>Quantitative criteria</b>				
Error on $W_{20}^{\text{obs}}$ and $W_{50}^{\text{obs}} < 10\%$	7, 37, 50, 54, 99, 102, 110, 118	21	-	7
$0.05 <  \Delta V_{\text{sys}}/W_{20}^{\text{obs}}  < 0.05$	27, 78, 101	18	-	7
$W_{20}^{\text{obs}} - W_{50}^{\text{obs}} < 50 \text{ km s}^{-1}$	10, 45, 58, 67, 93, 117	12	-	7
				Final sample size (6)



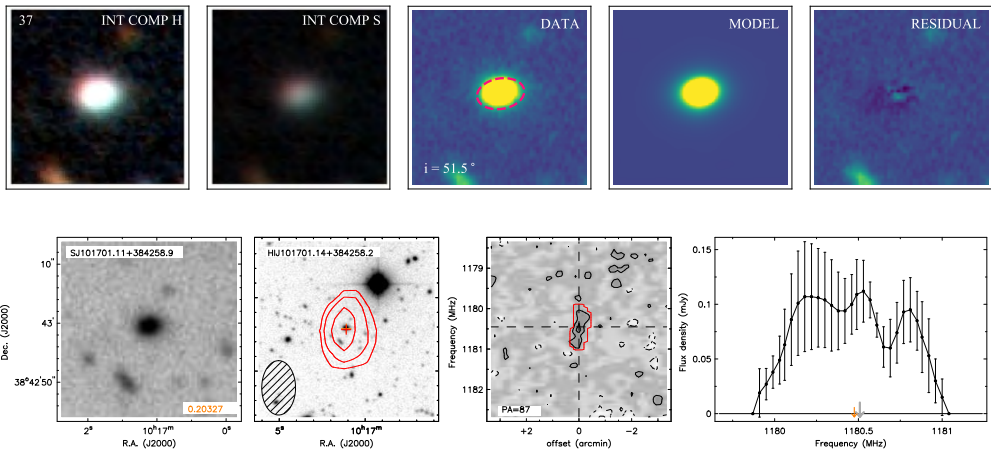
A963 TFS cat no. 7



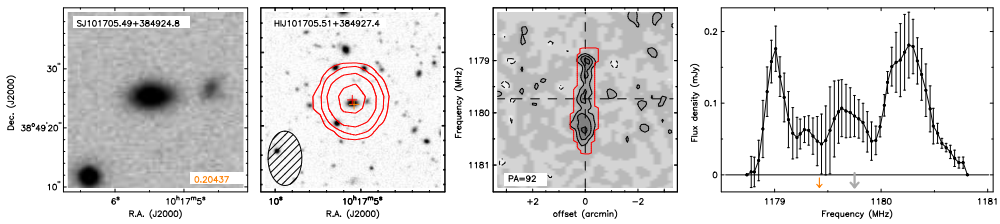
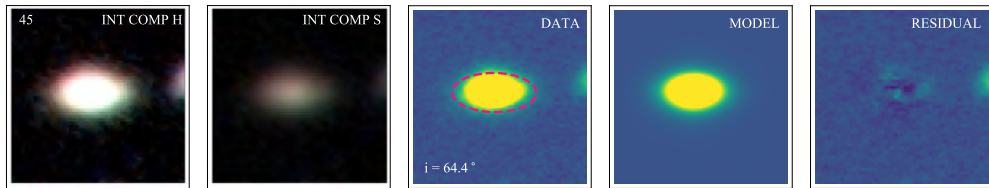
A963 TFS cat no. 10



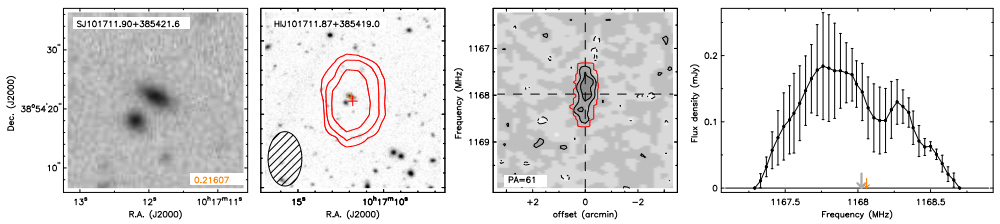
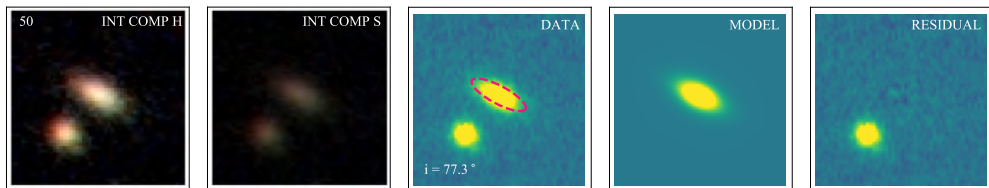
A963 TFS cat no. 27



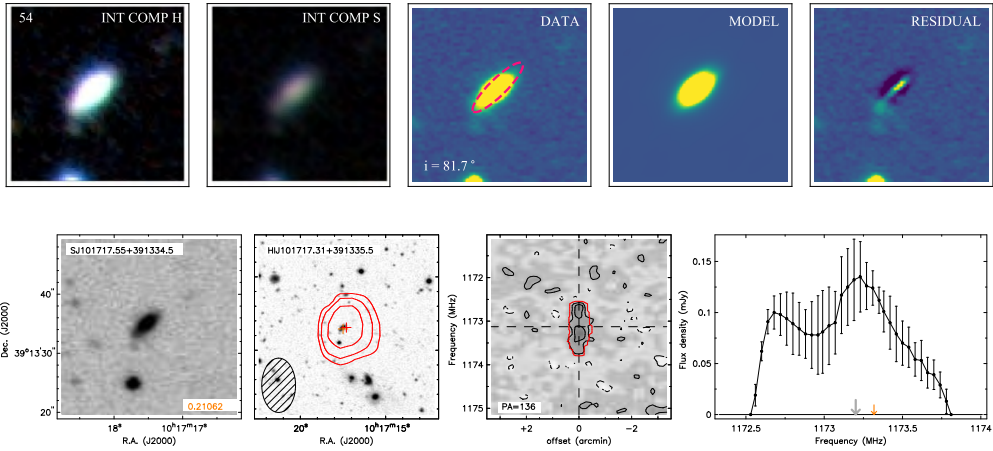
A963 TFS cat no. 37



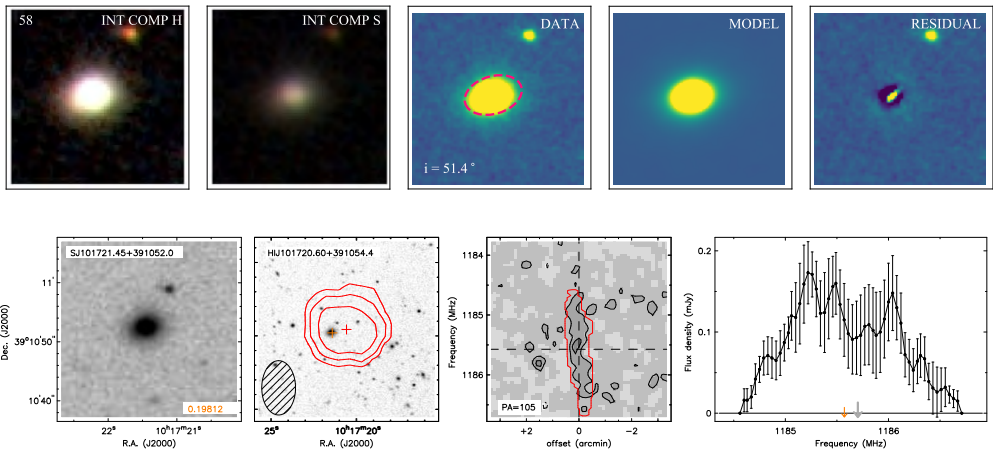
A963 TFS cat no. 45



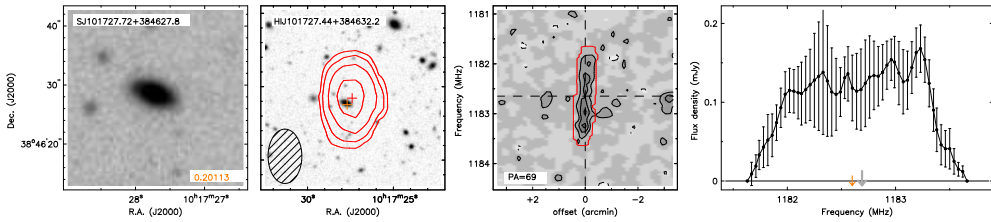
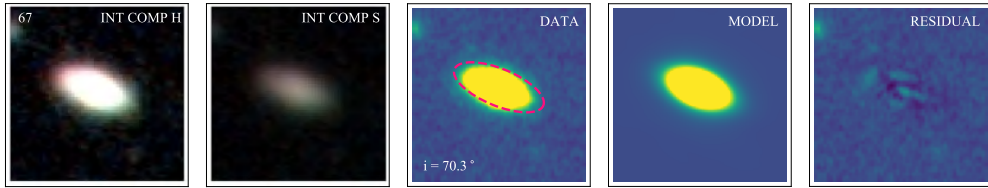
A963 TFS cat no. 50



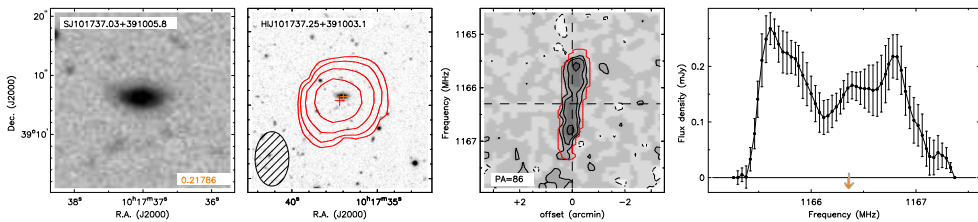
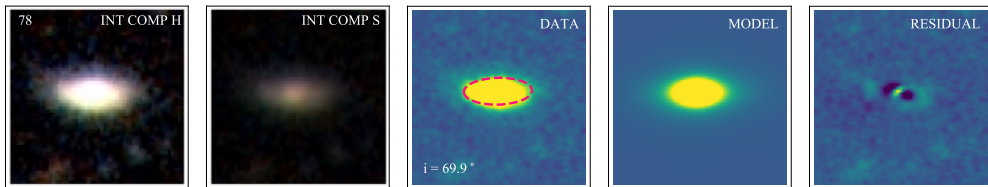
A963 TFS cat no. 54



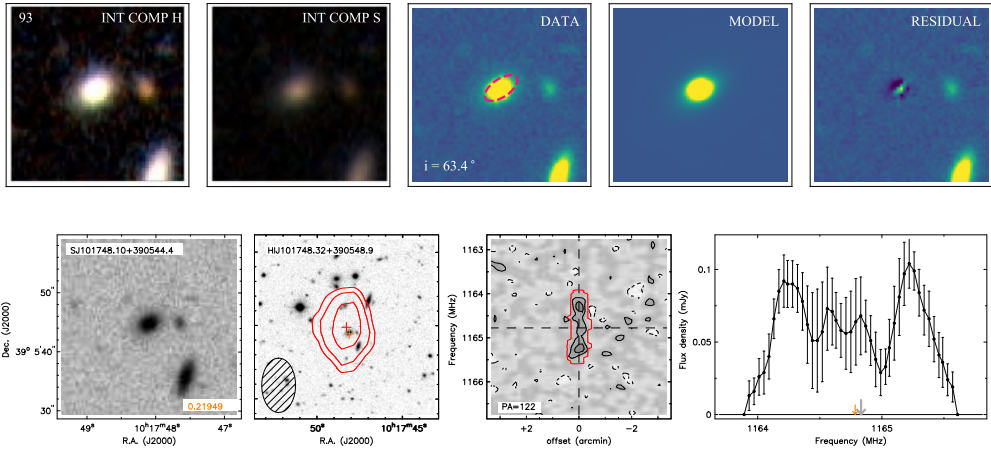
A963 TFS cat no. 58



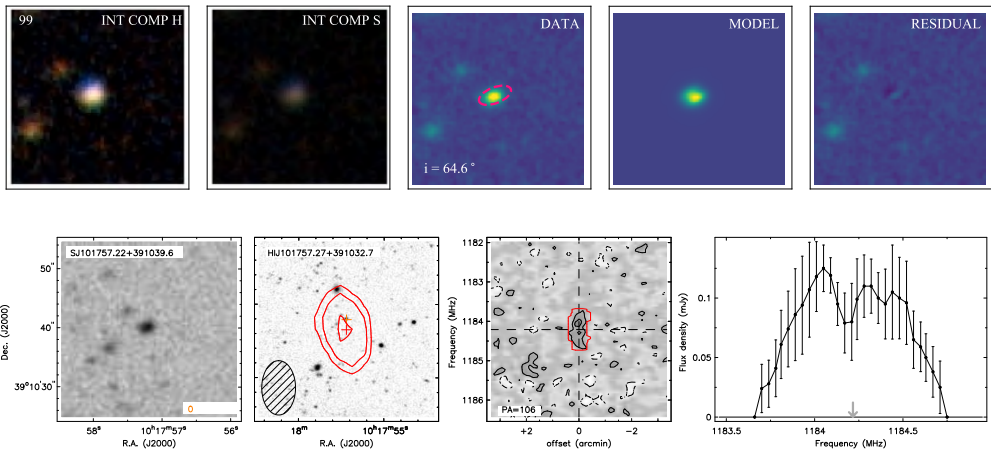
A963 TFS cat no. 67



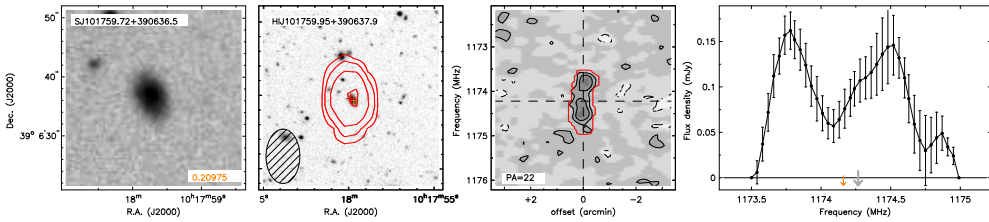
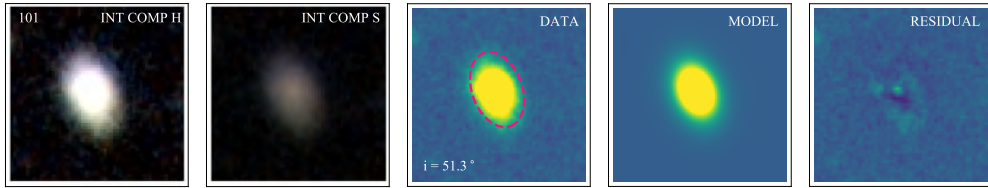
A963 TFS cat no. 78



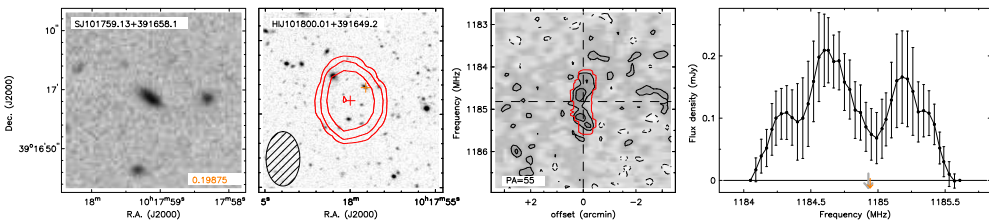
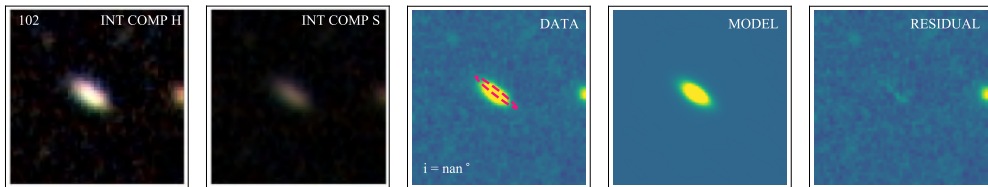
A963 TFS cat no. 93



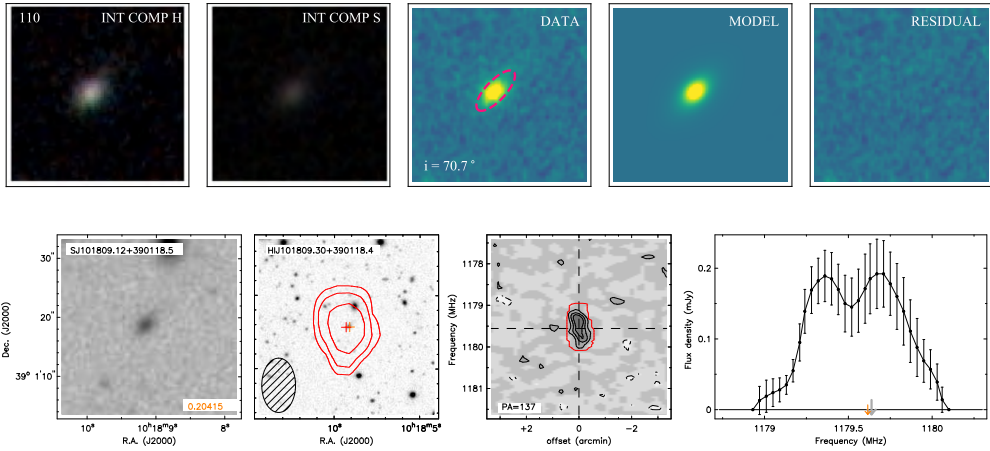
A963 TFS cat no. 99



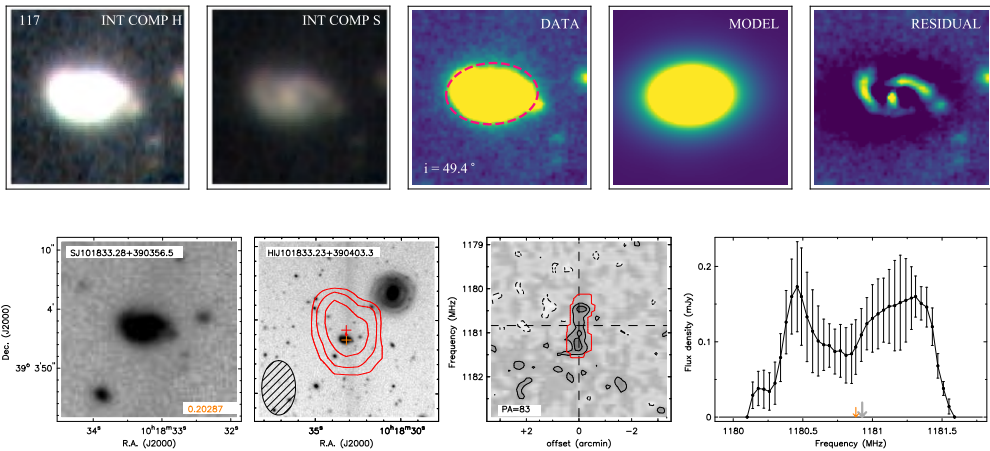
A963 TFS cat no. 101



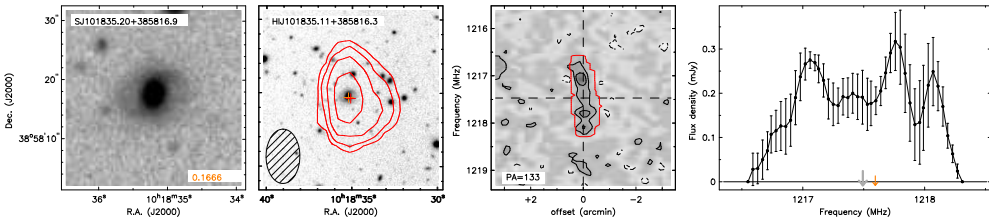
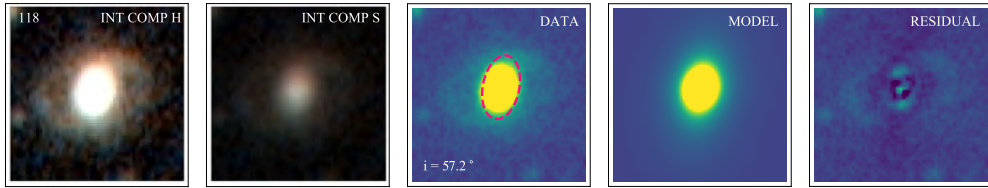
A963 TFS cat no. 102



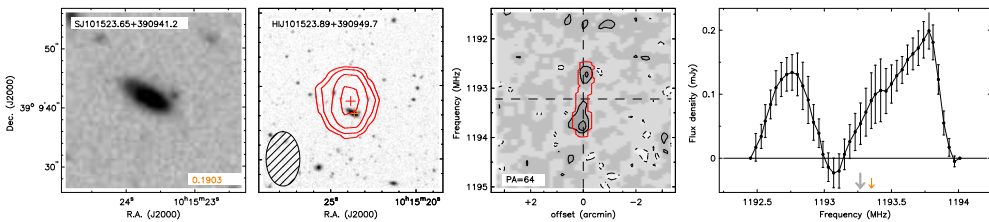
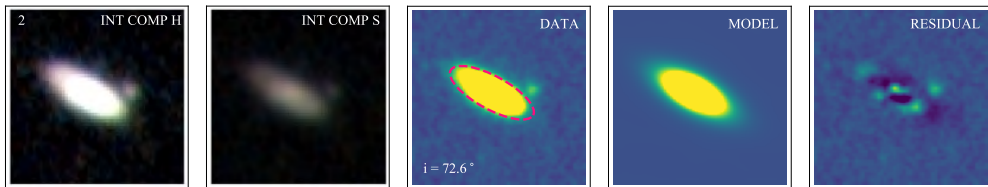
A963 TFS cat no. 110



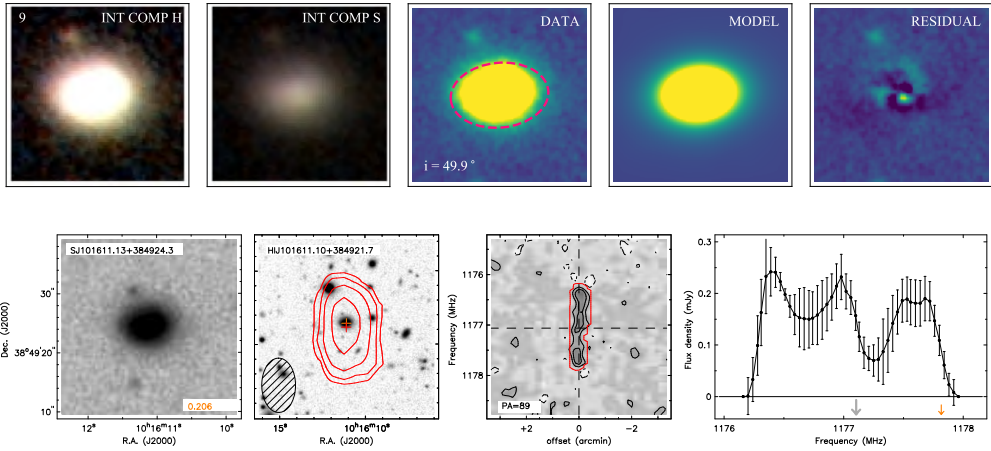
A963 TFS cat no. 117



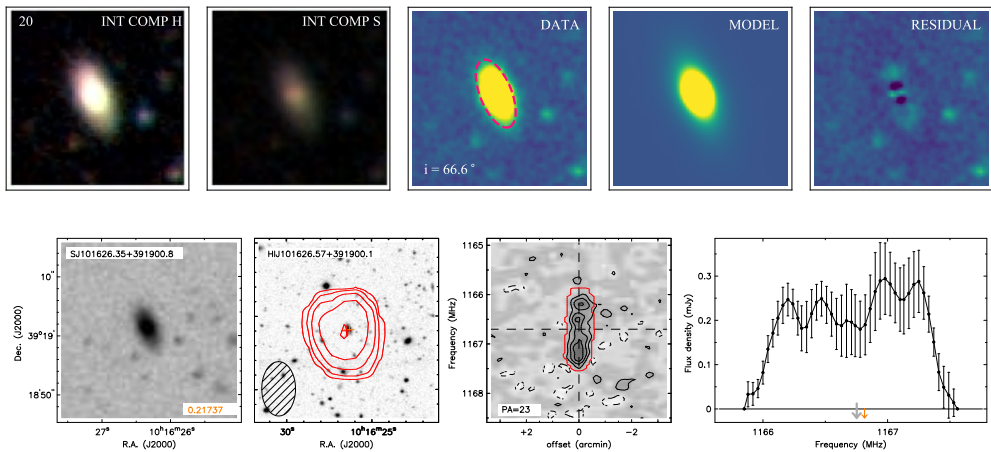
A963 TFS cat no. 118



A963 TFS/HQS cat no. 2

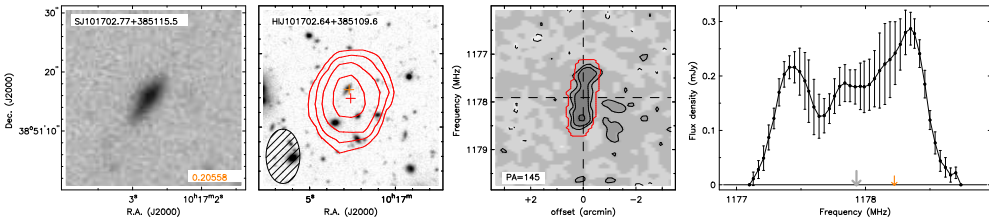
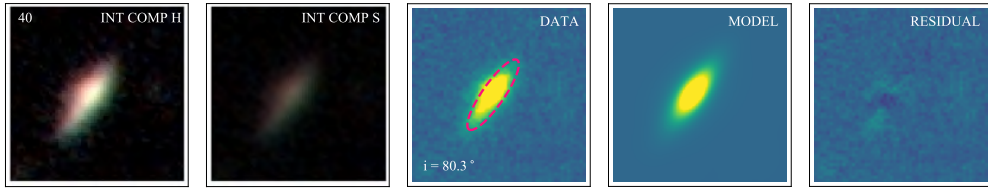


A963 TFS/HQS cat no. 9

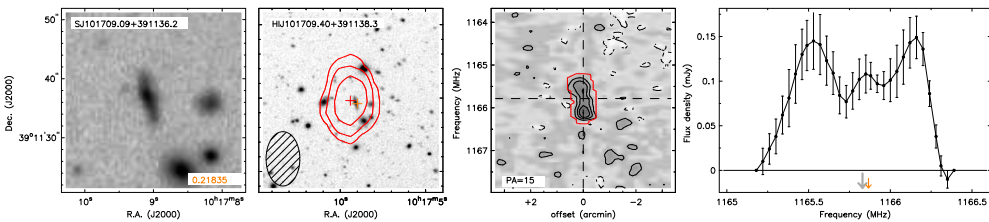
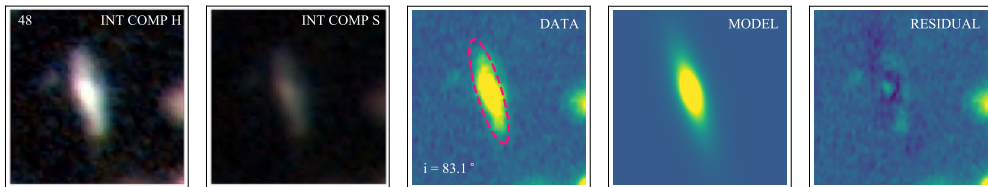


A963 TFS/HQS cat no. 20

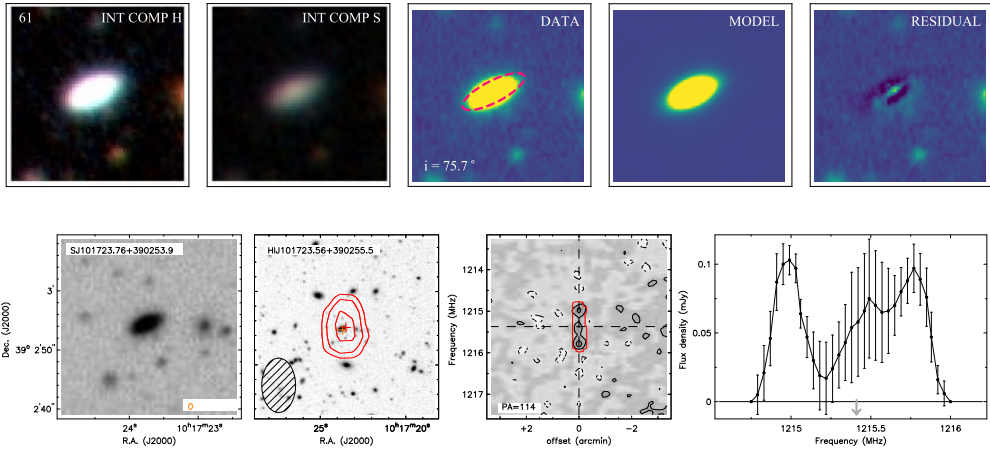
3



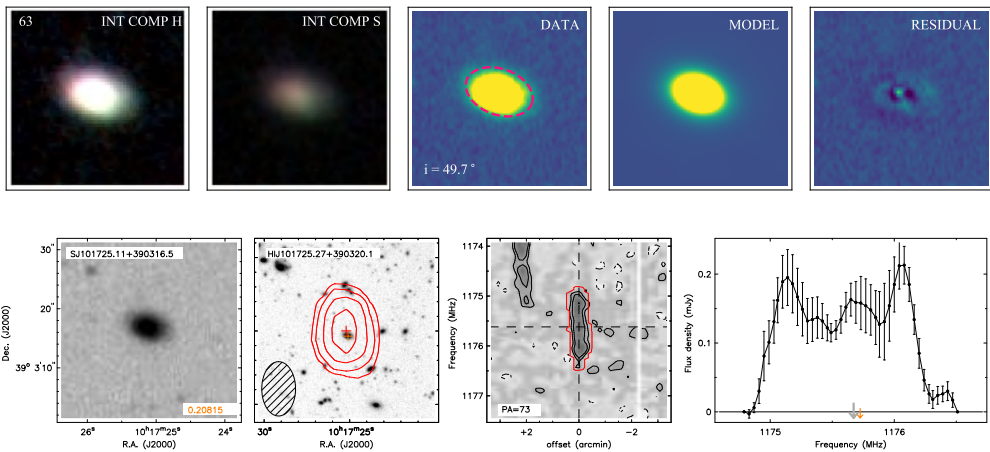
A963 TFS/HQS cat no. 40



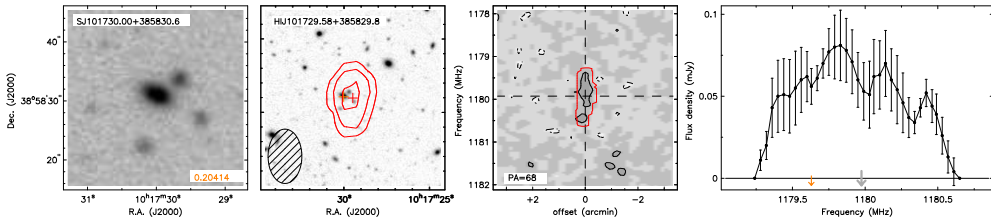
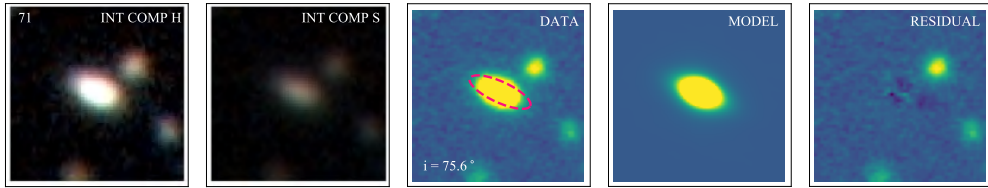
A963 TFS/HQS cat no. 48



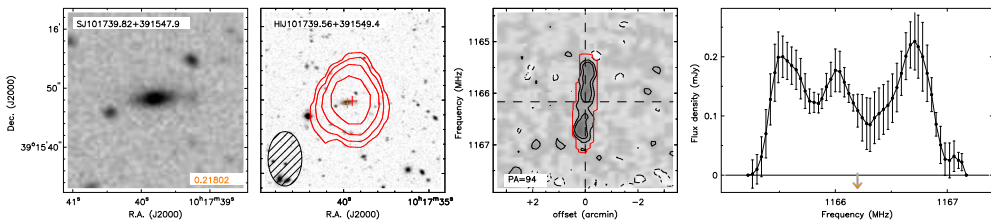
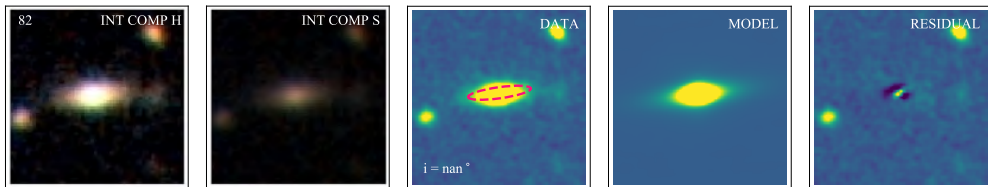
A963 TFS/HQS cat no. 61



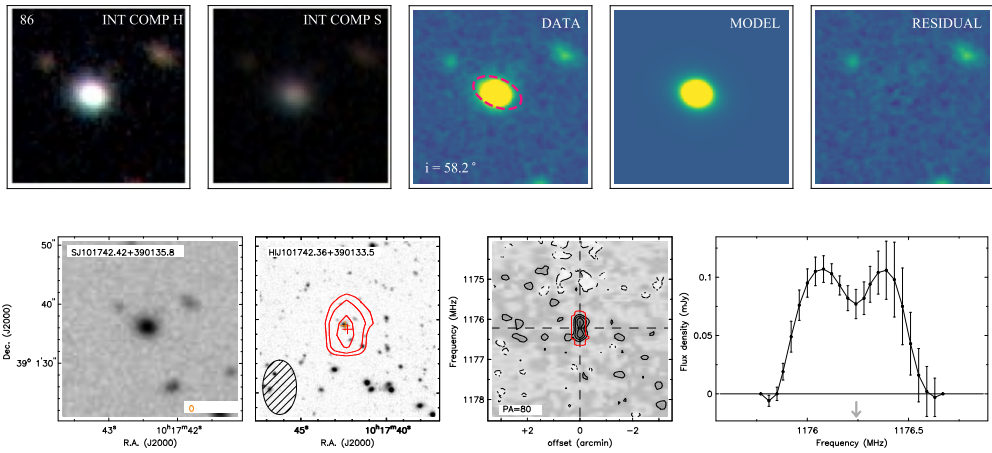
A963 TFS/HQS cat no. 63



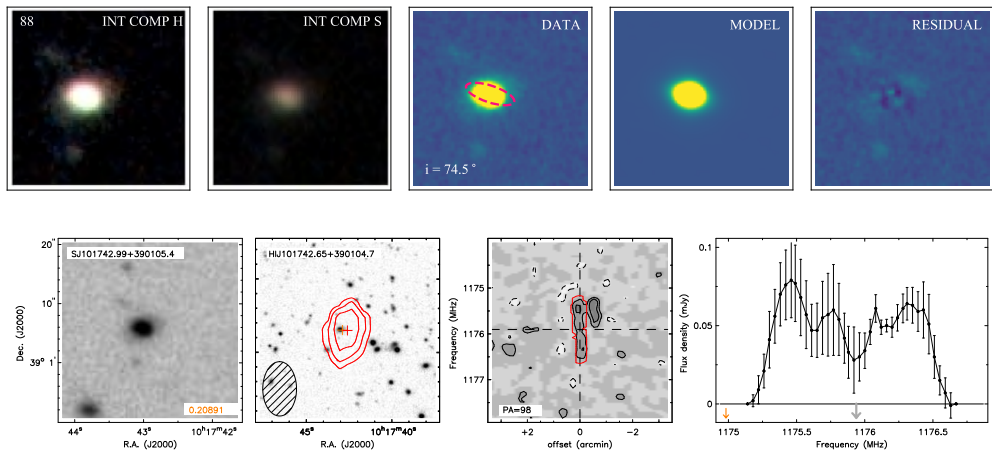
A963 TFS/HQS cat no. 71



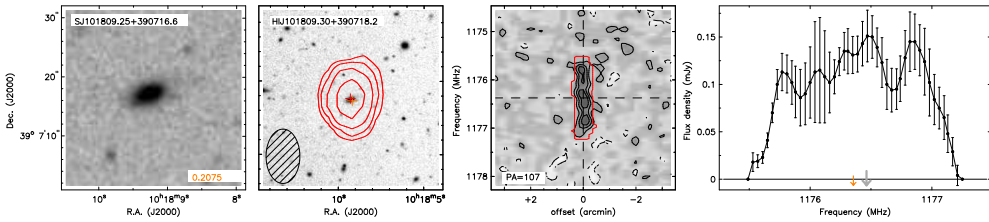
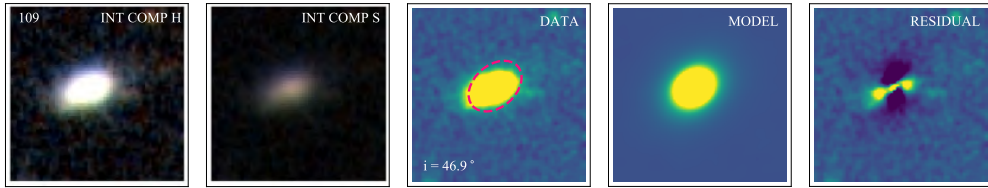
A963 TFS/HQS cat no. 82



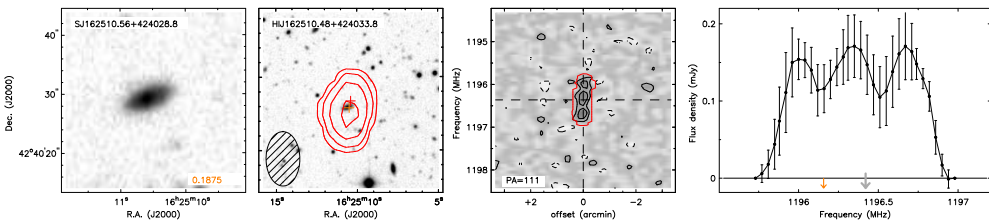
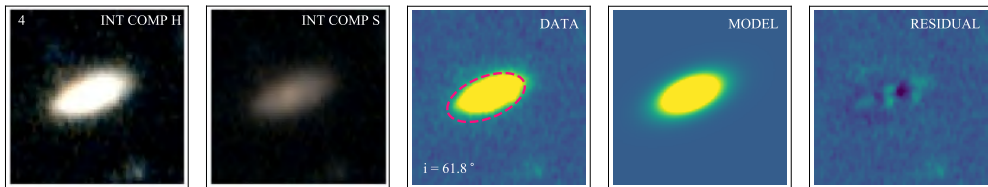
A963 TFS/HQS cat no. 86



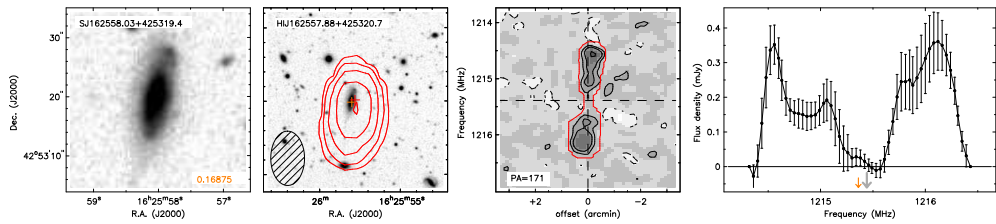
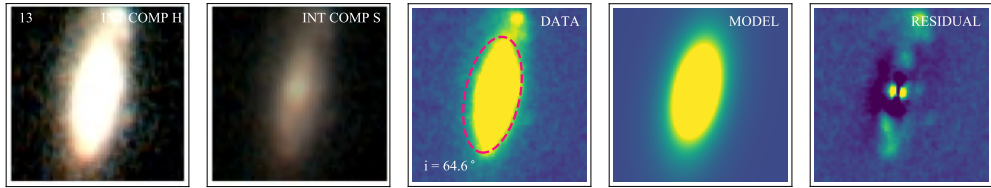
A963 TFS/HQS cat no. 88



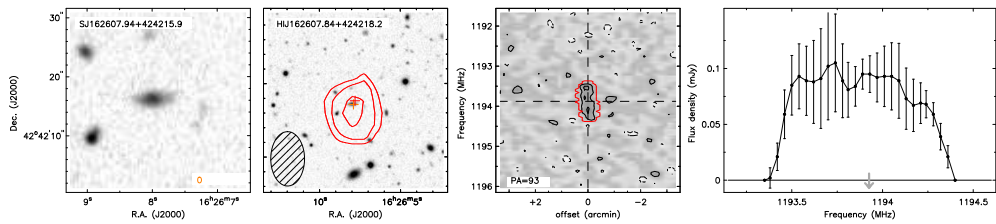
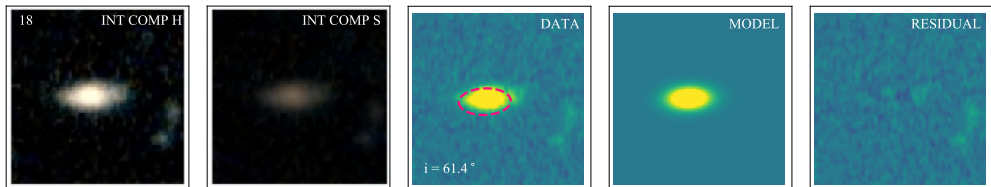
A963 TFS/HQS cat no. 109



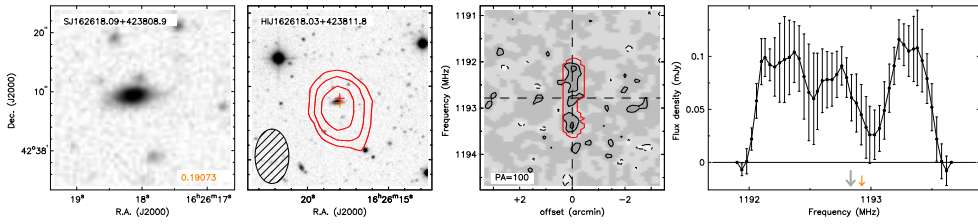
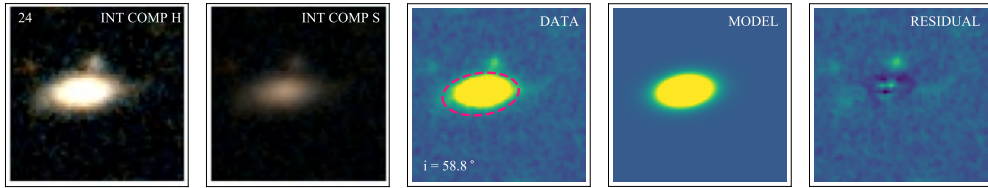
A2192 TFS/HQS cat no. 4



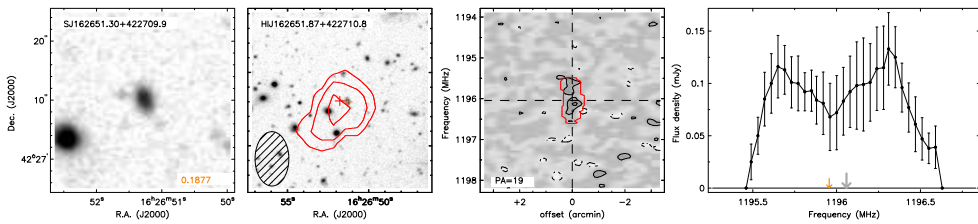
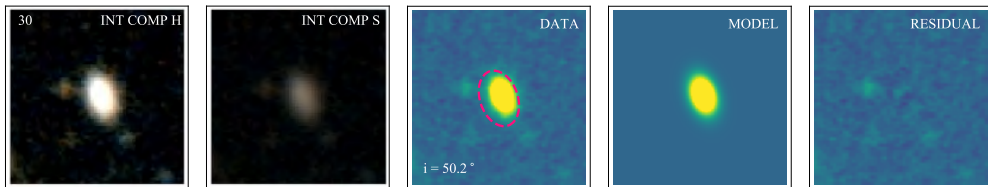
A2192 TFS/HQS cat no. 13



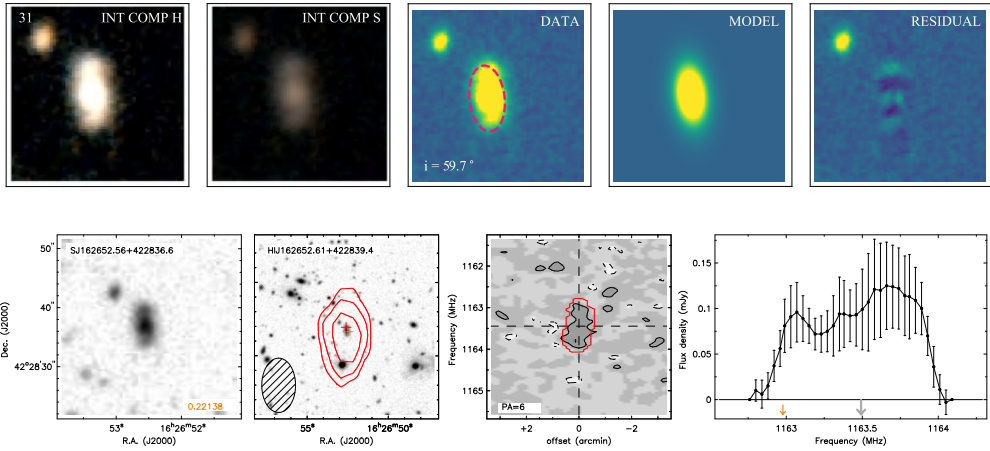
A2192 TFS/HQS cat no. 18



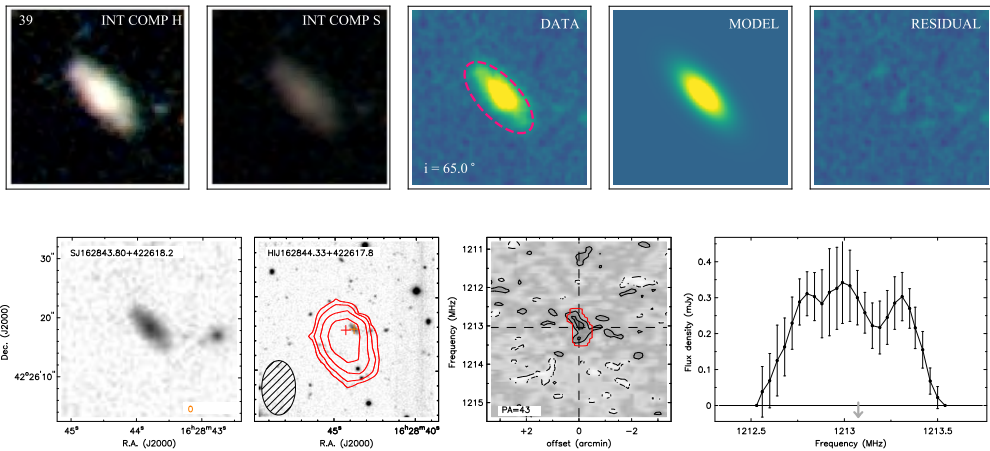
A2192 TFS/HQS cat no. 24



A2192 TFS/HQS cat no. 30



A2192 TFS/HQS cat no. 31



A2192 TFS/HQS cat no. 39



## BUDHIES VI: The HI Mass function and $\Omega_{\text{HI}}$ at $z = 0.2$ using direct HI detections

Avanti Gogate<sup>a</sup>, Marc Verheijen<sup>a</sup>, Kyle Oman<sup>b</sup> Thijs van der Hulst<sup>a</sup>

---

<sup>a</sup> Kapteyn Astronomical Institute, University of Groningen, Landleven 12, 9747AD Groningen

<sup>b</sup> Department of Physics, Durham University, Stockton Road, DH1 3LE Durham

In prep, to be submitted to MNRAS.

## Abstract

While the global HI mass function is well constrained in the Local Universe, little is known about its evolution with redshift. Several predictions exist for its evolution from hydrodynamical and semi-analytical simulations, however, the weakness of the HI signal beyond  $z \sim 0.1$  does not allow for similar observational studies. In this work, we construct, for the first time, an HiMF at  $z \sim 0.2$ , using direct HI detections from the Blind Ultra-Deep HI Environmental Survey (BUDHiES), which consists of a wide range of environments spanning clusters, voids and other over-densities. With a volume of  $73,400 \text{ Mpc}^3$  within the Full-Width-at-Quarter-Maximum (FWQM) of the primary beam, the flux-limited BUDHiES sample has an HI-mass limit of  $2 \times 10^9 M_\odot$  at the redshifts of the two Abell clusters that were the central targets for BUDHiES. We present completeness techniques and results of the first measurement of the global HiMF and  $\Omega_{\text{HI}}$  at  $z \sim 0.2$ . Completeness tests were carried out by injecting artificial sources into the BUDHiES volumes and testing their recovery rate. Real data were corrected for incompleteness and a Schechter function fit to the corrected data provided the following three parameters of the HiMF: the knee mass  $\log(M_{\text{HI}}^* h_{70}^2 / M_\odot) = 9.78 \pm 0.16$ , the low mass slope  $\alpha = -1.49 \pm 0.48$  and the normalisation parameter  $\Phi_{\text{HI}}^* = (4.9 \pm 3.2) \times 10^{-3}$ . The large uncertainty on  $\alpha$  is due to the relatively higher mass limit of BUDHiES and incompleteness in the lower-mass regime. For constraining the cosmic HI density ( $\Omega_{\text{HI}}$ ) at  $z \sim 0.2$ , we assumed non-evolution of the slope  $\alpha$  as a function of  $z$ , and estimated  $\Omega_{\text{HI}} = (3.2 \pm 0.7) \times 10^{-4}$ , corrected for self-absorption. We explore possible interpretations of these results and discuss the possible effects of environment and cosmic variance on our sample. Finally, we discuss the implications of these results with respect to future HI and  $\Omega_{\text{HI}}$  studies.

## 4.1 Introduction

Within the  $\Lambda$ CDM paradigm, several attempts have been made to understand the process of galaxy formation and the crucial role physical mechanisms such as galaxy mergers, interactions, gas accretion, etc. play in the evolution of galaxies up to the present epoch (e.g., Holmberg 1941; Toomre & Toomre 1972; De Propriis et al. 2014; Somerville & Davé 2015; Pearson et al. 2019). One of the best ways to obtain a complete understanding of this process would be to combine studies on the evolution of stellar populations with those on the evolution of the gas content at different epochs. This is because, in the present epoch, most of the baryonic matter is contained within stars, while a large part was in the form of gas at some point in the past. Optical studies such as those by Hopkins & Beacom (2006); Madau & Dickinson (2014); Bouwens et al. (2014) showed that the star formation rate (SFR) increased by almost an order of magnitude around  $z \sim 2$ . Thus, while the evolution of stellar populations and SFR has been well constrained by optical and radio observations (Condon 1992; Kennicutt & Evans 2012; Magnelli et al. 2015; Bera et al. 2018), a clear picture has not yet emerged on the evolution of cold gas in galaxies. In particular, the evolution of the neutral atomic hydrogen (HI) content in galaxies is still not well understood, since it is a challenge for present day radio telescopes to achieve the sensitivities required to detect HI at cosmologically significant redshifts. This is because the HI emission line becomes increasingly difficult to detect at larger distances due to radio frequency interference (RFI) and the requirement of longer telescope integration times. As a consequence, very few blind HI surveys have been carried out so far beyond the Local Universe (Fernández et al. 2013; Gogate et al. 2020; Xi et al. 2021).

One method to study the evolution of the neutral gas content in galaxies is the HI mass function (HiMF) and the variations seen in its parameters as a function of redshift and environment. The HiMF, for a given sample of galaxies is simply the number density of galaxies in a range of HI mass bins. It is characterised by a Schechter function (Schechter 1976), expressed by a power law with slope  $\alpha$  at the low mass end and an exponential decline at a turnover, or ‘knee’ HI mass ( $M_{\text{HI}}^*$ ) at the high mass end. It was first measured by Briggs (1990) and has been improved upon ever since, thanks to large blind HI surveys such as the HI Parkes All Sky Survey (HIPASS, Zwaan et al. 2005), and more recently, the Arecibo Legacy Fast ALFA survey (ALFALFA, Giovanelli et al. 2005; Martin et al. 2010; Jones et al. 2016; Jones et al. 2018). Covering much larger volumes in the Local Universe, these surveys enabled their HI measurements to be relatively free of selection effects and other biases. With a relatively flat low-mass slope  $\alpha = -1.25$  and a knee mass  $\log_{10}(M_{\text{HI}}^*/M_{\odot}) = 9.94$ , the HiMF from the ALFALFA 100 percent survey (ALFA100 hereafter; Jones et al. 2018) implies that most of the gas seems to be present in the high mass galaxies close to  $M_{\text{HI}}^*$ . Additionally, this study also illustrates the effect of the cosmic variance and environment on the HiMF: the dichotomy observed in  $\alpha$  when the sample is divided into the Spring and Fall skies, due to the presence of the centre of the Local Supercluster in the Spring sample and void in the Fall sample. They also report a change in  $M_{\text{HI}}^*$  when only part of the sample is used, indicating an environmental dependence on where these  $M_{\text{HI}}^*$  galaxies are located in the sample. This environmental influence on the HiMF has also been confirmed by studies such as

Pisano et al. (2011); Moorman et al. (2014); Westmeier et al. (2017) and Busekool et al. (2021), which show a flattening of the low-mass slope in high-density environments such as groups and clusters. Thus, the parameters of the HiMF are influenced by the local and global environment in which the galaxies are embedded, making an environment-specific HiMF largely different from a global HiMF, which measures the global HI mass distribution in galaxies at a given epoch.

Accurate measurements of the HiMF have so far only been achieved in the Local Universe, out to a redshift of 0.06 (Jones et al. 2018). However, at redshifts beyond the Local Universe, statistical measurements become increasingly challenging, ultimately providing very little information on the HiMF at higher look-back times. So far, the Arecibo Ultra-Deep Survey (AUDS, Hoppmann et al. 2015; Xi et al. 2021), spanning a redshift range  $0 < z < 0.16$ , is the only other available study of the HiMF beyond the Local Universe. The results from this survey are in good agreement with those from HIPASS and ALFALFA, particularly with respect to the low-mass slope,  $\alpha$ .

4

With the help of an accurate HiMF, the cosmic HI density ( $\Omega_{\text{HI}}$ ) can be measured for a given epoch and is an important tool in assessing the evolution of HI in galaxies.  $\Omega_{\text{HI}}$  is well constrained in the Local Universe with the help of direct 21-cm emission line observations, especially with the aid of blind HI surveys (e.g., Zwaan et al. 2005; Giovanelli et al. 2005; Martin et al. 2010; Haynes et al. 2011; Jones et al. 2018). However, the limitations of blind HI imaging at higher redshifts make  $\Omega_{\text{HI}}$  estimates based on direct HI detections more challenging beyond the Local Universe. The AUDS survey (Hoppmann et al. 2015; Xi et al. 2021) provides the only available  $\Omega_{\text{HI}}$  estimate out to  $z \sim 0.16$  based on direct detections. At such redshifts and beyond, an indirect estimation method known as spectral stacking is used instead to estimate  $\Omega_{\text{HI}}$  (e.g., Lah et al. 2007; Delhaize et al. 2013; Rhee et al. 2016; Kanekar, Sethi & Dwarakanath 2016; Rhee et al. 2018; Bera et al. 2019; Chowdhury et al. 2020). Spectral stacking exercises extract HI information of galaxies based on coordinates from optical catalogues, and subsequently co-add the HI spectra to achieve a higher signal-to-noise ratio, thereby determining  $\Omega_{\text{HI}}$  from the co-added HI flux. While spectral stacking studies have provided crucial insights into the trend of  $\Omega_{\text{HI}}$  with redshift, measurements often suffer from selection biases and cosmic variance. Thus, a more detailed understanding of  $\Omega_{\text{HI}}$  at intermediate redshifts requires accurate measurements from direct HI detections. At very high redshifts ( $z \approx 0.8$  and above)  $\Omega_{\text{HI}}$  has been well constrained with the help of Damped Lyman- $\alpha$  (DLA) systems which exhibit wide absorption lines due to high HI column densities (e.g., Prochaska, Herbert-Fort & Wolfe 2005; Noterdaeme et al. 2009, 2012; Crighton et al. 2015; Bird, Garnett & Ho 2017). These absorption features can be seen against bright Quasi-Stellar Objects (Péroux et al. 2003). All these direct and indirect  $\Omega_{\text{HI}}$  estimation methods as well as predictions from simulations indicate that the evolution of  $\Omega_{\text{HI}}$  is gradual out to  $z \sim 1$ , after which it rapidly increases. There seems to be no significant change in  $\Omega_{\text{HI}}$  at least out to  $z \sim 0.4$ . A compilation of the various  $\Omega_{\text{HI}}$  studies showing  $\Omega_{\text{HI}}$  as a function of cosmic time is illustrated in Fig. 19 of Xi et al. (2021), also shown in Chapter 1.

In this work, we aim to construct, for the first time, the global HiMF at  $z \sim 0.2$  using direct HI detections from the Blind Ultra-Deep HI Environmental Survey (BUDHiES,

Gogate et al. 2020). In addition, we provide the first direct measurement of  $\Omega_{\text{HI}}$  derived from the integrated BUDHiES HiMF. With a total surveyed volume of 73,400 Mpc<sup>3</sup> within the Full-Width at Quarter Maximum (FWQM) of the primary beam, BUDHiES consists of two pointings covering a depth of 328 Mpc, both hosting a range of cosmic environments, from clusters to voids and other overdensities. A brief description of the survey and data is provided in Sect. 4.2, while an extensive overview can be found in Gogate et al. (2020). This work is aimed to be a reference study for future HI surveys with similar science goals such as the Deep Investigation of Neutral Gas Origins (DINGO; Meyer 2009) with the Australian Square Kilometre Array Pathfinder (ASKAP) and the Looking At the Distant Universe with the MeerKAT Array (LADUMA; Holwerda, Blyth & Baker 2012; Blyth et al. 2016), which will overcome sensitivity and resolution limitations that currently plague HI emission studies beyond the Local Universe.

This chapter is organised as follows. In Sect. 4.2, we summarise the survey details and the data used for this analysis. Sect. 4.3 provides the methodology used for completeness corrections carried out by inserting artificial galaxies. The making of these galaxies is described in detail in Appendix A. In Sect. 4.4 we present our results on the measurement of the HiMF and  $\Omega_{\text{HI}}$  estimation. Sect. 4.5 provides an extensive discussion which includes the evolution of the HiMF and  $\Omega_{\text{HI}}$ , and addresses the issue of cosmic variance. Finally, we summarise and conclude our results in Sect. 4.6. Throughout this work, we assume a  $\Lambda$ CDM cosmology, with  $\Omega_{\text{M}} = 0.3$ ,  $\Omega_{\Lambda} = 0.7$  and a Hubble constant  $H_0 = 70 \text{ km s}^{-1} \text{ Mpc}^{-1}$ .

## 4.2 Survey details and Data

BUDHiES (Gogate et al. 2020) is a blind 21-cm pencil-beam imaging survey covering  $0.164 < z < 0.224$ , undertaken with the Westerbork Synthesis Radio Telescope (WSRT). It is one of the first blind HI surveys that combines gas content (HI) and optical properties of galaxies at such redshifts. It comprises a wide range of environments, from clusters and cluster outskirts to other overdensities, sheets, and low density voids (the environment characterisation of the two volumes has been carried out in Jaffé et al. 2013). The two pointings were each centred on an Abell cluster, namely Abell 963 ( $z=0.206$ ) and Abell 2192 ( $z=0.187$ ). Within their Abell radii, these two clusters occupy only  $\sim 4$  per cent of the total surveyed volume of 73,400 Mpc<sup>3</sup>, within the FWQM of the primary beam. Both clusters are very different in their properties. Abell 963 is a massive lensing cluster, strong in X-rays, while Abell 2192 is a less massive, diffuse cluster in the process of forming and almost invisible in X-rays.

For three adjacent spectral resolution elements of  $4\sigma$  each, the theoretical mass limit of the survey is  $\sim 2 \times 10^9 M_{\odot}$  at the redshifts of the respective Abell clusters, for an HI emission line width of  $150 \text{ km s}^{-1}$  at the field centres. The data processing was carried out with the help of AIPS (Greisen 1990) and GIPSY (van der Hulst et al. 1992). The final image cubes generated after the data processing have spatial resolutions of  $65 \times 104 \text{ kpc}^2$  and  $65 \times 110 \text{ kpc}^2$  at  $z \sim 0.164$  for the cube containing Abell 963 (referred to as B1) and Abell 2192 (referred to as B2) respectively. Note that most galaxies in the two

cubes are spatially unresolved. For the purpose of source finding, the cubes were first smoothed in velocity to four different velocity resolutions: an initial Hanning smoothing with a resolution corresponding to two channels (R2 hereafter) and further smoothing with a Gaussian kernel to a nearly Gaussian frequency response with a Full Width at Half Maximum (FWHM) of 4, 6, and 8 channels (R4, R6 and R8 hereafter). At 1190 MHz, these four resolutions correspond to 19, 38, 57 and 76 km s<sup>-1</sup> respectively. Source finding was then carried out using a smooth-and-clip algorithm, as described in Sect. 4.3.3. These HI sources were then confirmed based on counterpart identification using R-band images obtained with the Isaac Newton Telescope (INT), as well as deep UV images from GALEX. From this exercise, 127 galaxies were confirmed in B1 and 39 in B2. Further details on the data processing and analysis, as well as the HI and optical properties of the BUDHiES galaxies can be found in Gogate et al. (2020) as well as Chapter 2 of this thesis.

## 4.3 Completeness corrections

To perform any statistical analysis on a sample, it is essential to first estimate the completeness of the survey. At higher redshifts, it becomes increasingly difficult to detect low mass galaxies due to several limitations faced by current radio telescopes. These include the effects of primary beam attenuation, RFI, non-uniform noise distribution and limited spatial (and/or spectral) resolution. Furthermore, the detectability of HI in galaxies largely depends on their inclinations and dynamical mass and therefore the width of the HI line (see Sect. 4.3.3 for further discussion). These factors tend to greatly weaken and bias the detectability of the HI signal, and hence allow only the most gas rich galaxies in the survey volume to be detected. To determine the completeness of our survey, we made use of an empirical method of injecting artificial sources into our data cubes and testing their recovery rate using the same detection criteria used for the survey. This method is one of the most reliable ways to probe the completeness of a survey.

### 4.3.1 Creating a library of synthetic galaxies

We carried out our completeness corrections by inserting artificial sources into the BUDHiES volumes and recording their recovery rate. These artificial galaxies were created with the help of the GIPSY package *galmod* (van der Hulst et al. 1992), which approximated them as discs consisting of concentric circular rings with increasing radii. They were created such that the sample mimicked the ALFA40 HiMF (Martin et al. 2010), with parameters  $\alpha = -1.33$ ,  $M_{\text{HI}}^* = 10^{9.96} M_{\odot}$  and  $\Phi_{\text{HI}}^* = 4.3 \times 10^{-3}$ . These galaxies were also made to follow standard scaling relations such as the HI mass-diameter relation (Wang et al. 2016) and the Tully-Fisher relation (Tully & Fisher 1977) which we used for generating the parameters required by *galmod*. The final library consists of  $\sim 2000$  synthetic sources covering, at random, all inclinations and position angles, with HI masses between  $10^{8.5} M_{\odot} < M_{\text{HI}}^{\text{gal}} < 10^{10.5} M_{\odot}$ . An example atlas from the library is provided in Fig. 4.1, which shows the various properties of the illustrated mock galaxies. The process of creating these galaxies as well as a description of the atlas is given in

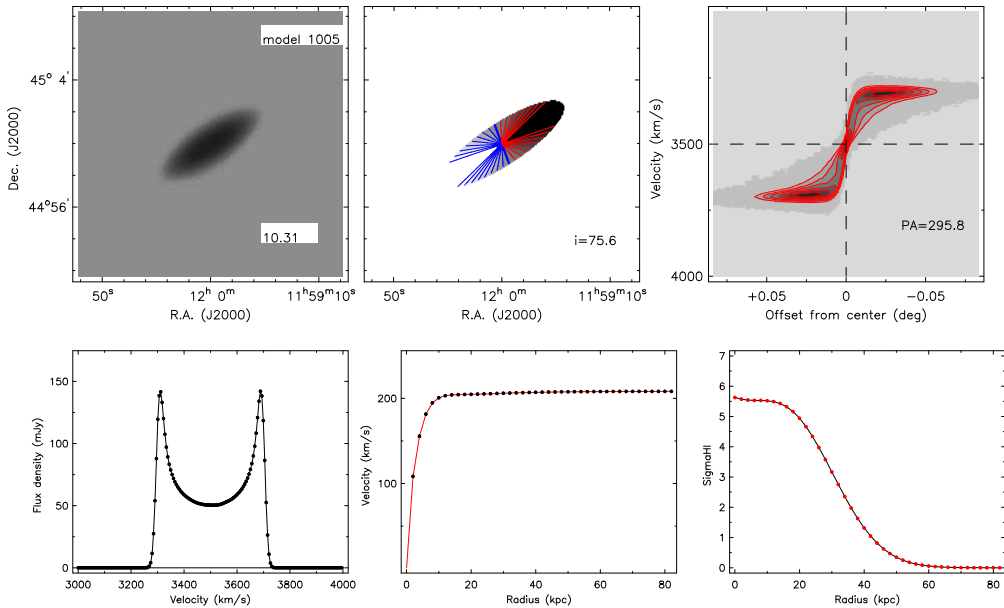


**Figure 4.1** – An atlas showing the properties of a typical artificial source from the  $\sim 2000$  mock galaxies created for completeness corrections. The full description of the layout of the atlas along with other examples is given in Appendix A.

detail in Appendix A of this chapter.

### 4.3.2 Inserting synthetic sources

The BUDHiES cubes (B1 and B2) cover a range of redshifts, probing different physical scales from the near to the far end. Therefore, our synthetic galaxies needed to be corrected and adjusted for various cosmological effects depending on where in B1 and B2 they were inserted.

We started by creating model master cubes identical to the two BUDHiES cubes (referred to as M1 and M2 corresponding to B1 and B2 respectively) with all pixel values set to zero. The much smaller individual synthetic galaxy cubes were then randomly picked out of the library, spatially smoothed, and regridded to match the resolutions and pixel sizes at the positions chosen for insertion in the master cubes. Spatial smoothing was carried out using a custom Fast Fourier Transform (FFT) algorithm. The appropriate pixel and beam sizes required for the above steps were calculated using comoving distances based on the adopted cosmology. Finally, the model galaxy cubes were regridded in velocity to match the velocity widths of the master cubes. In this way, 3030 artificial sources were projected and inserted in each master cube such that

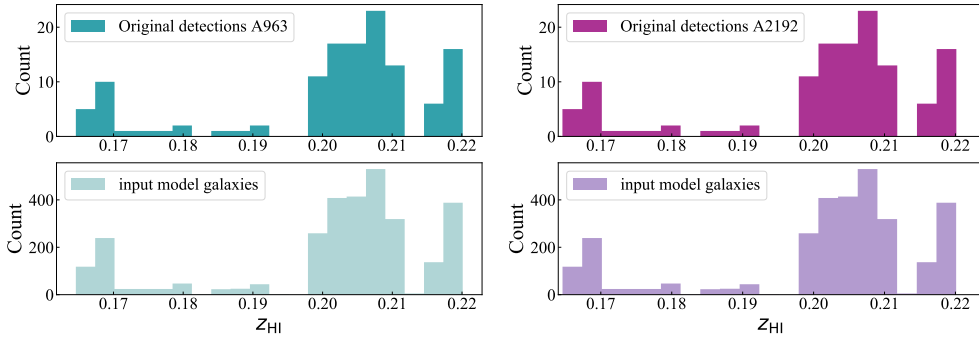


**Figure 4.2** – Redshift distribution of the model galaxies (bottom) and original HI detections (top) in A963 (left) and A2192 (right). Note that the inserted mock galaxies follow the same cosmic Large scale structure as the real galaxies.

4

they followed the observed large-scale structure in B1 and B2. This is illustrated in the histograms in Fig. 4.2. The top panel of the figure shows the redshift distribution of the 166 real sources detected in the two survey volumes, while the bottom panel shows a similar distribution of the injected mock galaxies. Spatially, they were distributed randomly in both the  $1 \times 1$  square degree fields.

Once all the galaxies were inserted into the model cubes, the cubes M1 and M2 were primary beam attenuated as observed in the original data cubes, B1 and B2. Subsequently, they were smoothed to the various velocity resolutions R2, R4, R6, and R8 (described in Sect. 4.2) and then added to B1 and B2, respectively. These new cubes (referred to as C1 and C2 hereafter) consisted of 3030 artificial sources along with the observed noise and real sources. Although limitations in the survey sensitivity do not allow for sources with  $\log(M_{\text{HI}}/M_{\odot}) < 9$  to be detected, such galaxies were still included in the completeness tests to mimic the observed data. It is safe to assume that such low mass galaxies would exist, but given the sensitivity of the survey, would lie below the detection threshold and add to the local noise in the cubes. Out of all galaxies in the library, only  $\sim 700$  galaxies lie above the theoretical detection limit, while the other undetected galaxies possibly make a significant contribution to the noise.

### 4.3.3 Source Detection and identification

Once C1 and C2 were ready, they were passed to the same custom-made smooth-and-clip algorithm, which was applied to find the real sources in the BUDHIES data (see Gogate et al. 2020). It is to be noted that current, more sophisticated source finding software such as SoFiA (Serra et al. 2015) have become available. In principle, SoFiA also works as a smooth-and-clip source finder, but we chose to work with our own algorithm for the sake of consistency with preceding source finding exercises carried out on the real BUDHIES data. Our algorithm uses clip levels of  $8\sigma$ ,  $5\sigma$ ,  $4\sigma$  and  $3\sigma$  on the channel maps, and works such that detections with only the following criteria were

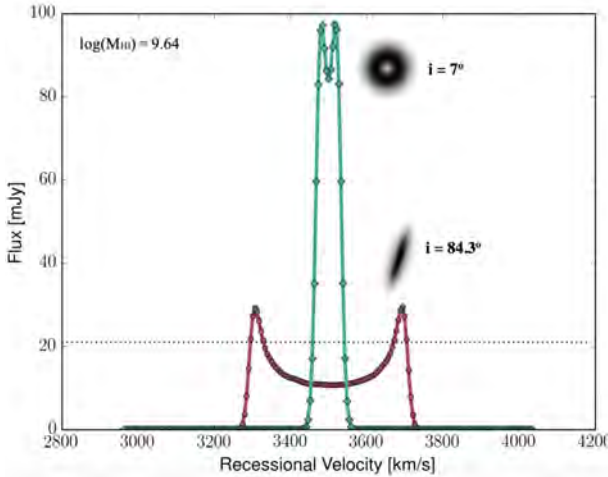


**Figure 4.3** – An example illustrating the dependence of the inclination of a galaxy in the source finding process. Face-on systems have a higher detectability than edge-on systems, which could be mistaken to be two separate sources depending on the local noise level (e.g., the horizontal dashed line).

accepted: A single velocity element with an  $8\sigma$  detection, 2 adjacent velocity resolution elements with  $5\sigma$  detections, 3 adjacent velocity resolution elements with  $4\sigma$  detections and 4 adjacent velocity resolution elements with  $3\sigma$  detections. All the pixels above the specified clip levels were combined to form masks, while the other pixels were set to zero. These masks were applied to isolate the HI emission in the real data, C1 and C2. After this source finding exercise, these new noiseless data cubes (F1 and F2) now contained only the sources extracted by the detection algorithm, which included both, the real and artificial galaxies. To avoid confusion during source identification, the real sources were first subtracted from F1 and F2.

The detectability of an HI source is heavily dependent on the inclination of the galaxy. Face-on systems are generally more easily detected out to larger distances. To illustrate this, we refer to Fig. 4.3, which shows the global HI profiles of two galaxies from our library, with the same HI mass but different inclinations. The figure shows that the HI profile of a nearly face-on galaxy (cyan line) is much narrower and therefore has a higher peak flux density than of an edge-on system (purple line) with the same HI mass. Additionally, a highly inclined system with a double-horned, broad HI line could be detected by the source finder as two separate sources, if the flux in between the peaks lies below the detection threshold. Apart from inclination, other factors that affect the detectability of a galaxy are the extent of the primary beam attenuation and thereby the position of the source in the cubes, as well as the non-uniform noise distribution across the cubes.

From our exercise, a total of 210 and 169 artificial galaxies were recovered from F1 and F2 respectively, most of which were low-inclination sources positioned close to the cube centres. All of these galaxies were cross-matched with the input catalogues of artificial galaxies and identified. The corresponding mass and positional information were extracted and tabulated. Spurious noise peaks were identified and rejected, while blended sources were visually analysed and assigned their respective counterparts from

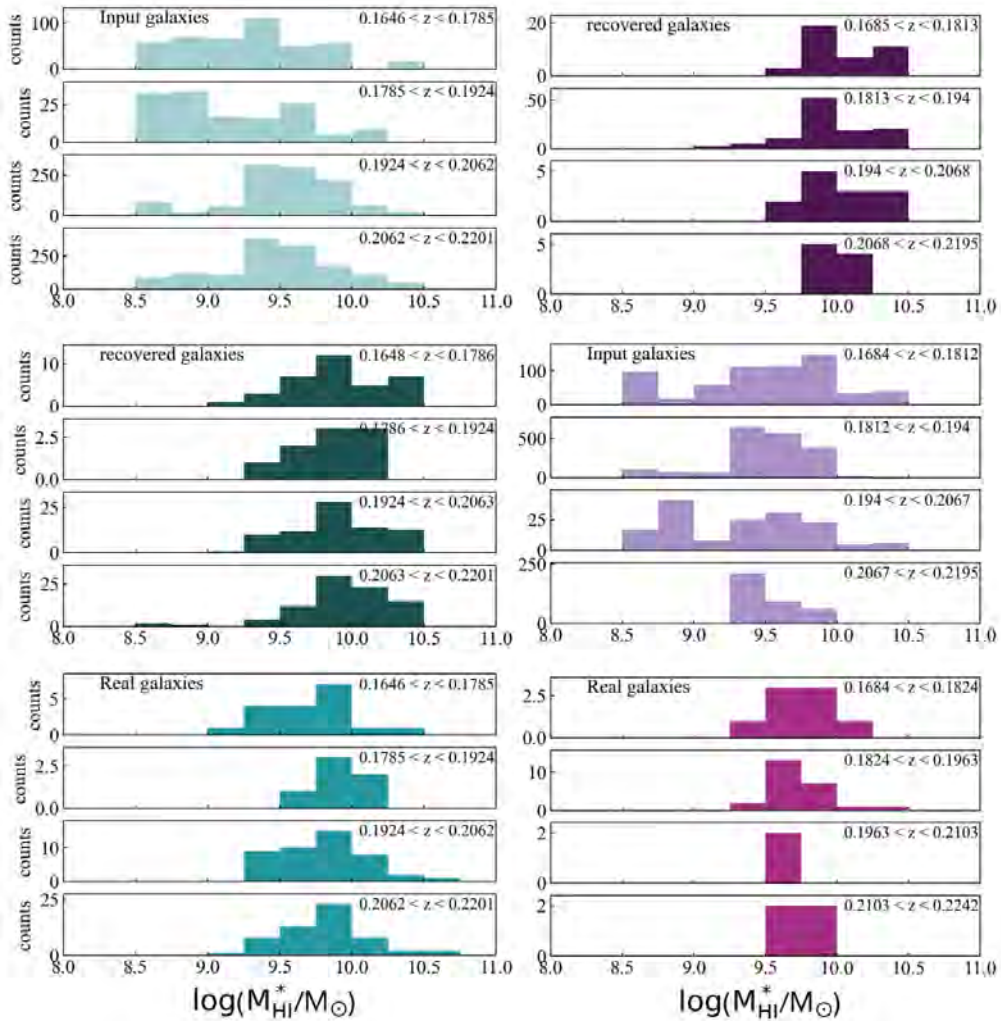


**Figure 4.4** – Mass histograms at different redshifts; Left: A963, right: A2192. The top row indicates the input artificial galaxies, the middle shows the recovered artificial galaxies, while the real galaxies are shown in the bottom row. Galaxies below the survey detection limit of  $2 \times 10^9 M_{\odot}$  are not detected, even at lower redshifts.

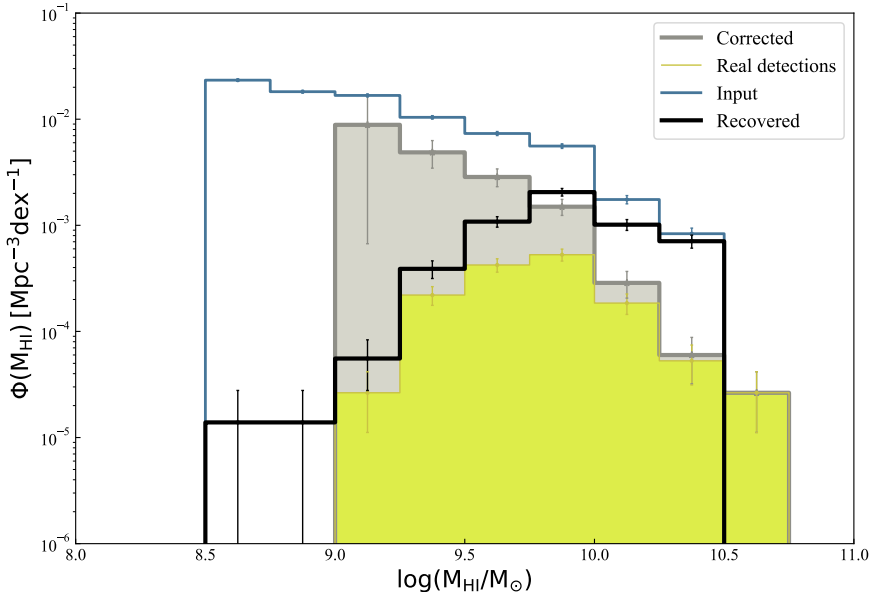


**Figure 4.5** – The open blue histogram indicates the total number of artificial galaxies that were injected in the noise cubes, per HI mass bin (set at 0.25 dex). The open black histogram shows the number of recovered galaxies based on the same source finding scheme that was used on the real data. The yellow shaded histogram shows the mass distribution of the real galaxies observed by BUDHiES, while the grey shaded histogram shows the corrected mass distribution of the BUDHiES galaxies after applying completeness corrections (ratio of the number of injected to recovered artificial sources per mass bin). Note that the artificial galaxies were created within the mass range  $10^{8.5}$  to  $10^{10.5} M_{\odot}$ . Thus, no completeness correction was applied to the mass bin beyond  $10^{10.5} M_{\odot}$ , under the assumption that the survey is complete in this mass range. The errors on the histograms are Poisson counting errors.

the input catalogues. Fig. 4.4 shows HI mass histograms at different redshift intervals. We find that none of the artificial low mass galaxies below the detection threshold are recovered by the source finder, except three sources in the highest redshift bin in A963. These unusual detections could be a result of the addition of local noise peaks included in the masks. Shown in Fig 4.5 are the various HI mass histograms at different stages of the completeness estimation, for both F1 and F2 combined. The distribution of input and recovered artificial galaxies are given by the open blue and black histograms respectively, while the real BUDHiES histogram on which the completeness corrections are to be applied is shown by the filled yellow histogram. The completeness correction factors were estimated as the ratio of the input to recovered artificial sources per mass bin, applied to the real data. The final completeness corrected BUDHiES histogram is shown in grey in the figure. It can be noticed that the highest mass bin ( $\log M_{\text{HI}} > 10.5$ ) is not a part of our completeness tests. This is due to an oversight while making the artificial sources, which were limited to  $\log M_{\text{HI}} \leq 10.5$ . However, since this bin consists of the largest HI sources to be found in the survey, it is reasonable to assume that the

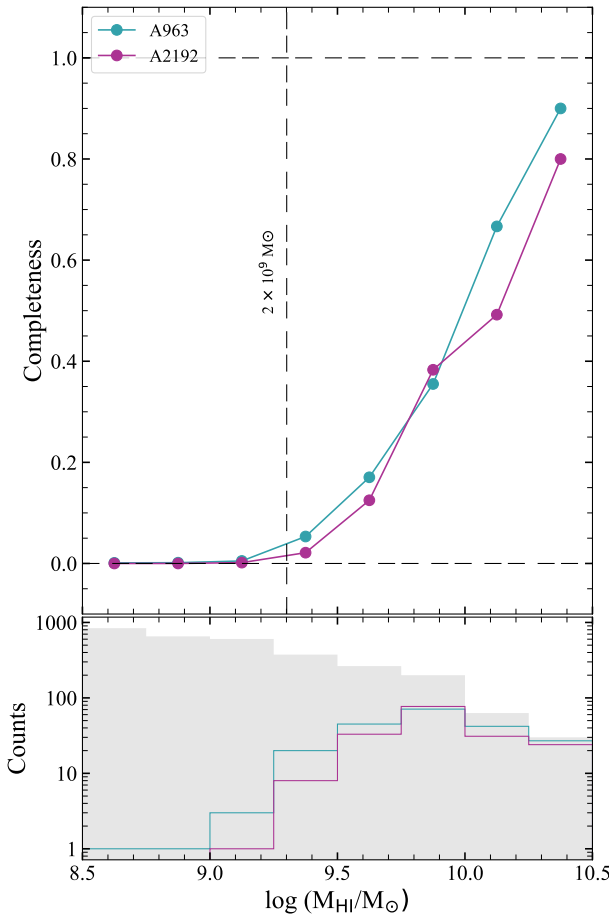


**Figure 4.6** – Top panel: Completeness of the two surveyed volumes per HI mass bin, where completeness ranges from 0 (incomplete) to 100 (fully complete), shown by the two horizontal black dashed lines. Cyan points denote the completeness level for each mass bin in the volume A963 while pink points denote the same for A2192. The vertical dashed line indicates the theoretical detection limit of  $2 \times 10^9 M_{\odot}$  at the redshifts of the two clusters. Bottom panel: Similar to Fig. 4.5 but for the two volumes separately, histograms showing the injection and recovery rates of artificial galaxies. The inserted artificial galaxies are given by the grey filled histogram, while the line histograms show the recovered galaxies in the two volumes, colour-coded as in the top panel.

completeness of this bin is 1, i.e., such galaxies would be detectable at all redshifts and at any spatial position in the cube. The completeness factor per mass bin is shown in Fig. 4.6. Based on this figure, our final completeness tests yield the following results: While the survey becomes rapidly incomplete towards lower HI masses, as one would expect, even the higher mass bins are not fully complete and some of the more massive galaxies are not detected in our tests, contrary to our expectations. Note that more low-mass galaxies are recovered in B1 because it has a lower noise compared to B2.

#### 4.4 The BUDHIES HIMF and $\Omega_{\text{HI}}$

For a given epoch, the HIMF ( $\Phi(M_{\text{HI}})$ ) is the number density of HI bearing galaxies over a range of HI mass bins. It was originally parameterised as

$$\Phi(M_{\text{HI}}) = \frac{dN_{\text{gal}}}{dV d\log_{10}(M_{\text{HI}})} \quad (4.1)$$

Here,  $dN_{\text{gal}}$  is the average galaxy number density in a cosmic box of volume  $dV$ , whose HI mass lies within a small logarithmic bin centred around  $M_{\text{HI}}$ .

Subsequently, studies such as Zwaan et al. (2003, 2005); Martin et al. (2010) and more recently Jones et al. (2018) have shown that the HiMF can be characterised by a functional form, known as the ‘Schechter function’ (Press & Schechter 1974; Schechter 1976), given by

$$\Phi(M_{\text{HI}}) = \ln(10) \Phi_{\text{HI}}^* \left( \frac{M_{\text{HI}}}{M_{\text{HI}}^*} \right)^{\alpha+1} e^{-\left( \frac{M_{\text{HI}}}{M_{\text{HI}}^*} \right)} \quad .$$

where  $\alpha$  is the power law slope at the faint end of the mass function,  $M_{\text{HI}}^*$  is the knee HI mass above which the power law changes into an exponential drop-off and  $\Phi_{\text{HI}}^*$  is the normalisation constant.

From the HiMF, one can derive the cosmic HI density  $\Omega_{\text{HI}}$ , at a given epoch. It is a useful parameter to study the evolution of the HI content of galaxies over cosmic time. The calculation of  $\Omega_{\text{HI}}$  requires knowing the comoving HI mass density  $\rho_{\text{HI}}$ , which can be derived by integrating the HiMF. Subsequently,  $\Omega_{\text{HI}}$  can be calculated by

$$\Omega_{\text{HI}}(z) = \frac{\rho_{\text{HI}}(z)}{\rho_{\text{crit}}(z=0)} = \frac{8\pi G}{3H_0^2} \rho_{\text{HI}}(z) \quad (4.2)$$

where  $\rho_{\text{HI}}(z) = \Gamma(\alpha + 2)M_{\text{HI}}^*\Phi_{\text{HI}}^*$  is the HI mass density, scaled by the critical density of the Universe ( $\rho_{\text{crit}}(z=0)$ ), assuming  $\Lambda$ CDM cosmology. Here,  $\Gamma$  is Euler’s Gamma function, while  $\alpha$ ,  $M_{\text{HI}}^*$  and  $\Phi_{\text{HI}}^*$  are the best fit parameters of the HiMF. The gravitational constant  $G$  has the value  $4.30 \times 10^{-9} \text{ Mpc } M_{\odot}^{-1}(\text{km s}^{-1})^2$  and the Hubble constant,  $H_0 = 70 \text{ km s}^{-1} \text{ Mpc}^{-1}$ .

#### 4.4.1 The BUDHiES HiMF fitting results

A Schechter function was fit to the corrected BUDHiES histogram with the help of the Kapteyn package (Terlouw & Vogelaar 2016), which makes use of the non-linear least square fitting method. Fig 4.7 indicates the HiMF obtained when all its parameters are left free and the results of this fit are provided in Table 4.1. The shaded regions in the figure indicate the error on each parameter. For comparison, the figure also shows the ALFA100 HiMF (black dashed line), whose parameters are also provided in Table 4.1. Since the BUDHiES detection limit is  $2 \times 10^9 M_{\odot}$ , the BUDHiES HiMF was extrapolated down to  $10^6 M_{\odot}$  for the purpose of calculating  $\Omega_{\text{HI}}$ . For our fitting results (FIT1), Fig. 4.8 shows the  $\alpha - M_{\text{HI}}^*$  covariance plot, comparing the BUDHiES

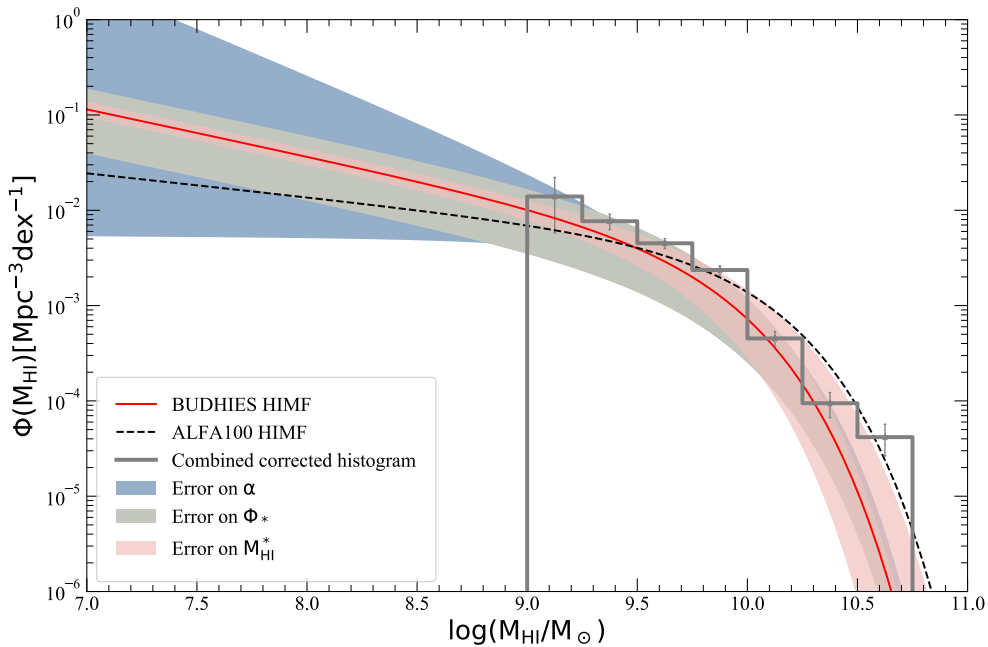


**Figure 4.7** – The BUDHiES HiMF, with all parameters left free, shown by the red line. The shaded regions indicate the errors on the HiMF parameters, with grey for  $\Phi_{\text{HI}}^*$ , blue for  $\alpha$  and pink for  $M_{\text{HI}}^*$ . The open histogram is the completeness corrected BUDHiES histogram with mass bins of 0.25 dex. The black dotted line denotes the ALFA100 HiMF (Jones et al. 2018).

(orange point) and literature HiMF, which include ALFA100, HIPASS and AUDS100 (their high redshift sample). The contours indicate  $1\sigma$ ,  $2\sigma$  and  $3\sigma$  confidence intervals around the best fit BUDHiES  $\alpha$  and  $M_{\text{HI}}^*$ . The figure shows that both the ALFA100 and AUDS100 parameters are well outside the  $3\sigma$  confidence contour of the BUDHiES HiMF parameters, though the HIPASS parameters are more comparable to our results, lying within the confidence contours. Also worth noting is that the variation is largest in  $M_{\text{HI}}^*$  while the  $\alpha$  estimates of the various samples are more or less consistent with BUDHiES within the errors.

#### 4.4.2 Estimation of $\Omega_{\text{HI}}$ for BUDHiES

In simple terms,  $\Omega_{\text{HI}}$  is derived by integrating the mass-weighted HiMF, scaled by the critical density of the Universe. In this study, different realisations of the BUDHiES HiMF were explored for constraining  $\Omega_{\text{HI}}$ . The HiMF fitting results and corresponding  $\Omega_{\text{HI}}$  values for these realisations are tabulated in Table 4.1, and described below. The  $\Omega_{\text{HI}}$  values have been corrected for self-absorption of 11 per cent based on Jones et al. (2018).

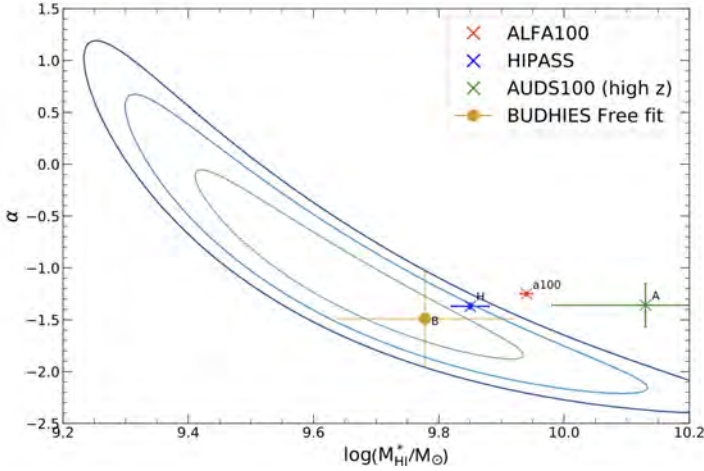


**Figure 4.8** – The covariance between the derived slope and knee mass of the BUDHiES HiMF in  $\alpha$ - $M_{\text{HI}}^*$  space. The best fit parameters returned by the fit are given by the orange point. The contours indicate the 1, 2 and 3 $\sigma$  confidence intervals around the BUDHiES best fit values. Also shown for reference are the literature HiMF parameters taken from ALFA100 (Jones et al. 2018), HIPASS (Zwaan et al. 2005) and AUDES100 (Xi et al. 2021). These are shown as red, blue and green crosses respectively. Note that the AUDES100 value is based on their high redshift sample, defined between  $0.09 < z < 0.16$ .

	$\alpha$	$\log_{10}(M_{\text{HI}}^*/M_{\odot})$	$\Phi_{\text{HI}}^*(\times 10^{-3})$	$\chi_{\nu}^2$	$\Omega_{\text{HI}}(\times 10^{-4})$
FIT 1	$-1.49 \pm 0.48$	$9.78 \pm 0.16$	$4.9 \pm 3.2$	1.13	$4.1 \pm 4.6$
FIT 2	$-1.85 \pm 0.15$	<b>9.94</b>	$2.4 \pm 0.3$	0.99	$8.5 \pm 5.6$
FIT 3	<b>-1.25</b>	$9.70 \pm 0.05$	$6.5 \pm 1.4$	0.93	$3.2 \pm 0.7$
ALFA100	$-1.25 \pm 0.02$	$9.94 \pm 0.01$	$4.5 \pm 0.2$	-	$3.9 \pm 0.1$
HIPASS	$-1.37 \pm 0.03$	$9.86 \pm 0.03$	$4.9 \pm 0.6$	-	$3.8 \pm 0.4$
AUDES100	$-1.37 \pm 0.05$	$10.15 \pm 0.09$	$2.4 \pm 0.8$	-	$3.6 \pm 0.3$
AUDES100 (high z)	$-1.36 \pm 0.21$	$10.13 \pm 0.15$	$2.8 \pm 1.4$	-	$3.9 \pm 0.4$

**Table 4.1** – The results of the various fits to the corrected BUDHiES histogram and the corresponding  $\Omega_{\text{HI}}$  estimates. These  $\Omega_{\text{HI}}$  values are corrected for self-absorption. The results of the fits include the low-mass slope  $\alpha$ , the high-mass knee  $M_{\text{HI}}^*$ , normalisation  $\Phi_{\text{HI}}^*$  and goodness of fit,  $\chi_{\nu}^2$ . FIT 1 provides fits when all parameters are left free. FIT 2 and FIT 3 indicate fits when  $M_{\text{HI}}^*$  and  $\alpha$  are fixed to the ALFA100 values respectively. Given in the last column are the corresponding  $\Omega_{\text{HI}}$  values for each fit. Also given for reference are some literature HiMF and  $\Omega_{\text{HI}}$  results: ALFA100 (Jones et al. 2018), HIPASS (Zwaan et al. 2005), AUDES full sample and AUDES high redshift sample between  $0.09 < z < 0.16$  (Xi et al. 2021).

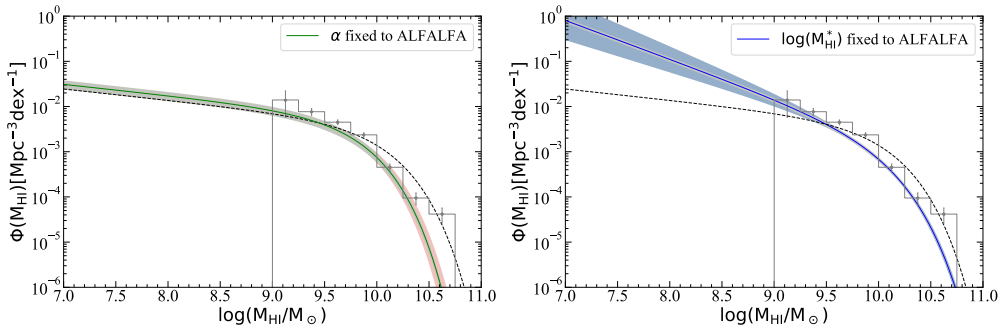


**Figure 4.9** – The two realisations of the BUDHiES HiMF, for the purpose of estimating  $\Omega_{\text{HI}}$ . Left: HiMF with the slope ( $\alpha$ ) fixed to the value of ALFA100. Right: HiMF with the knee mass ( $M_{\text{HI}}^*$ ) fixed to the value of ALFA100. The shaded regions indicate the errors on the HiMF parameters, with grey for  $\Phi_{\text{HI}}^*$ , blue for  $\alpha$  and pink for  $M_{\text{HI}}^*$ . The open histograms are the completeness corrected BUDHiES histograms with mass bins of 0.25 dex. The black dotted line denotes the ALFA100 HiMF (Jones et al. 2018).

4

Given the large uncertainties in the HiMF parameters, particularly those on the low-mass slope  $\alpha$  as a result of limited sensitivity, it is evident that  $\Omega_{\text{HI}}$  would be difficult to determine with good accuracy. As expected, we find  $\Omega_{\text{HI}} = (4.1 \pm 4.3) \times 10^{-4}$  from the HiMF (FIT1 in Table 4.1). Hence, for a more robust measurement of  $\Omega_{\text{HI}}$ , certain hypotheses were made to constrain the HiMF parameters with the largest errors, namely, the low-mass slope  $\alpha$  and the knee mass  $M_{\text{HI}}^*$ .

In the first hypothesis, it was assumed that  $M_{\text{HI}}^*$  does not change as a function of redshift. Upon fixing  $M_{\text{HI}}^*$  to the ALFA100 value, the function was fit again to the completeness corrected BUDHiES histogram, and the results of the fit are provided in Table 1 (FIT2). This version of the HiMF is illustrated in Fig 4.9 (left). By fixing  $M_{\text{HI}}^*$ , we found a  $3.9\sigma$  tension between the  $\alpha$  values obtained by BUDHiES and ALFA100. However, this value of  $\alpha = -1.85$  is extremely steep. Despite discrepant predictions in the literature (e.g., Obreschcow et al. 2009; Popping, Somerville & Trager 2014), such a steep slope has never been predicted beyond the Local Universe. This hypothesis also leads to an unrealistic value of  $\Omega_{\text{HI}}(z=0.2) = (8.5 \pm 5.6) \times 10^{-4}$  which is almost twice larger than  $\Omega_{\text{HI}}(z=0)$ . This hypothesis was hence rejected.

For our next hypothesis, we assumed that the slope  $\alpha$  does not change with redshift, and fixed our BUDHiES  $\alpha$  to the ALFA100 slope. The best fit values are provided under FIT3 in Table 4.1 and the resulting HiMF is shown in Fig. 4.9 (right). With this hypothesis, there exists a  $4.7\sigma$  tension between the BUDHiES and ALFA100 values of  $M_{\text{HI}}^*$ . There is no reason to exclude this hypothesis, since the literature also suggests that the slope  $\alpha$  of the HiMF does not evolve, at least out to  $z \sim 0.16$  (Xi et al. 2021). This is also evident from Fig. 4.8, in which the largest variations are seen in  $M_{\text{HI}}^*$ , while the slopes of all reference studies are more or less comparable. Furthermore, despite the mass limit of  $2 \times 10^9 M_{\odot}$  being close to the derived  $M_{\text{HI}}^*$  (FIT1), the fit still forces

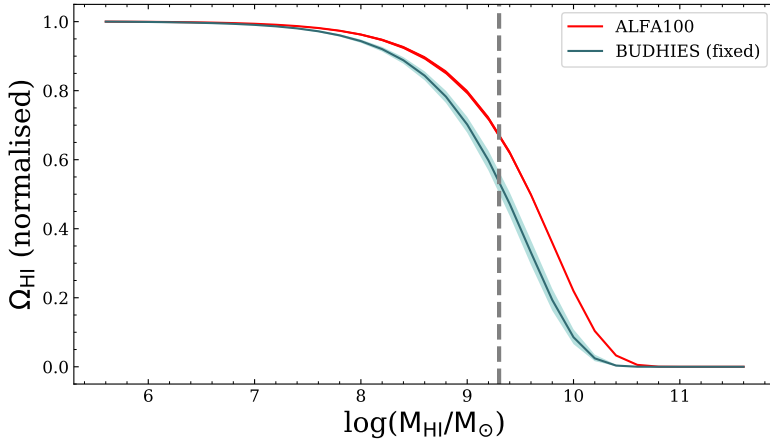


**Figure 4.10** – The cumulative distribution of  $\Omega_{\text{HI}}$  for the BUDHiES HiMF parameters with the slope fixed to ALFA100, shown as the cyan line. Also shown for comparison is the cumulative distribution of  $\Omega_{\text{HI}}$  for ALFA100 (red line). The vertical dashed line indicates the theoretical BUDHiES detection limit of  $2 \times 10^9 M_{\odot}$ . The pink and cyan shaded regions show the range of uncertainties for ALFA100 and BUDHiES respectively.

$\alpha$  to be less steep than the one derived from FIT2, thus making this hypothesis more plausible. The fit, with a  $\chi^2_{\nu} = 0.93$ , results in  $\Omega_{\text{HI}} = (3.2 \pm 0.7) \times 10^{-4}$ , corrected for self-absorption.

In Fig. 4.10, we show the cumulative distribution of the self-absorption corrected  $\Omega_{\text{HI}}$  as a function of HI mass for this chosen hypothesis of a non-evolving slope (FIT3). The ALFA100 distribution is also given for comparison. Based on the theoretical detection limit of BUDHiES, shown as the black dashed line, it is evident that the ALFA100 HiMF would recover  $\sim 70$  per cent of  $\Omega_{\text{HI}}$  down to  $2 \times 10^9 M_{\odot}$  (shown by the vertical dashed line). The small errors on the ALFA100 HiMF parameters also result in a tighter cumulative distribution, while the  $M_{\text{HI}}^*$  derived in FIT3 is smaller than ALFA100 ( $\Delta \log(M_{\text{HI}}^*/M_{\odot}) = 0.24$ ), resulting in a lower recovery of  $\Omega_{\text{HI}}$  ( $\sim 55$  per cent). Thus, our HiMF needs to be extrapolated at least down to  $3 \times 10^7 M_{\odot}$  to recover  $> 99\%$  of the  $\Omega_{\text{HI}}$ . With the BUDHiES free fit (FIT1), this would also imply a larger dependence on  $\alpha$ , thus resulting in large errors on  $\Omega_{\text{HI}}$ .

## 4.5 Discussion

In the past two decades, not only have there been several new insights into the evolution of stellar populations such as the SFR main sequence, (e.g., Baldry et al. 2002; Noeske et al. 2007; Madau & Dickinson 2014; Bera et al. 2019), but also into the evolution of molecular hydrogen ( $\text{H}_2$ ) content through blind and targeted CO observations of

galaxies (e.g., Pavese et al. 2018; Tacconi et al. 2018; Decarli et al. 2019).

Moreover, studies in the past decade suggest that SFRs of galaxies show different correlations with their gas content, depending on their gas fraction. For instance, Bigiel et al. (2008) showed a clear correlation of SFR with  $\text{H}_2$  but not with  $\text{HI}$ , while Huang et al. (2012) showed the opposite effect in high gas fraction galaxies in ALFALFA. Undeniably, galaxies also seem to contribute differently to the overall cosmic neutral gas density, as shown by semi-analytical modelling (see Lagos et al. 2014). While the SFR peaked at  $z \sim 2$ , the neutral gas density has remained fairly constant (see discussion in Sect. 4.5.2). Over similar time-scales, semi-analytical models have also suggested an evolution in the  $\text{H}_2/\text{HI}$  ratios of galaxies (Obreschkow et al. 2009). Additionally, not much is known about the evolution of the gas accretion rate onto galaxies (Sancisi et al. 2008; Dekel et al. 2009). In the study of the evolution of these baryonic components of galaxies, careful attention thus needs to be given to their neutral Hydrogen content (which is the raw fuel for star formation), to obtain a complete picture of how galaxies evolve. In contrast to the increasing number of stellar and molecular gas evolution studies, however, the study of  $\text{HI}$ , particularly direct 21-cm emission observations, is limited due to the intrinsic weakness of the  $\text{HI}$  signal. So far, conflicting results in the literature (e.g., Bigiel et al. 2008; Huang et al. 2012) demonstrate that the relation between the SFR and gas content is still not well understood. For this, it is necessary to study not only how the gas content evolves over cosmic time i.e. how much neutral atomic gas exists at a given epoch (by constraining  $\Omega_{\text{HI}}$ ), but also how it is distributed over galaxies of different masses at different epochs (by constraining the  $\text{HiMF}$ ).

$\text{HiMF}$  predictions made with the help of simulations and semi-analytic modelling (see Power, Baugh & Lacey 2010, and references therein) are conflicting and remain a topic of debate. Moreover, while techniques such as spectral stacking and observation of DLA absorbers have allowed  $\Omega_{\text{HI}}$  to be better constrained at higher redshifts (e.g., Rhee et al. 2013; Bera et al. 2019; Chowdhury et al. 2020; Noterdaeme et al. 2012; Rao et al. 2017), they still entail certain assumptions and biases (see discussion in Sect. 4.5.2). Studying the evolution of the  $\text{HiMF}$  and  $\Omega_{\text{HI}}$  with the help of direct  $\text{HI}$  detections from blind  $\text{HI}$  surveys is therefore an effective way of gaining insight into the relation between the SFR and the gas content in galaxies at intermediate redshifts.

#### 4.5.1 Evolution in the $\text{HiMF}$

The  $\text{HiMF}$  is an essential tool to understand the global role of neutral atomic gas in the context of star formation and galaxy evolution. Moreover, it helps put constraints on galaxy evolution models. Several Local  $\text{HiMF}$  studies (e.g., Jones et al. 2018; Zwaan et al. 2005; Martin et al. 2010) have made it possible to constrain the  $\text{HiMF}$  parameters, providing information on how the total  $\text{HI}$  content in galaxies is distributed among galaxies in the present epoch.

Beyond the Local Universe, the detectability of  $\text{HI}$  becomes more challenging owing to the increase in RFI and the requirement of long telescope integration time due to the intrinsic weakness of the  $\text{HI}$  signal. So far, only one survey (the Arecibo Ultra Deep Survey, AUDS), conducted with the Arecibo telescope, has been able to construct the

HiMF between  $0 < z < 0.16$ . Two studies were conducted with the AUDS data, at 60% of the final survey (AUDS60, Hoppmann et al. 2015) and the complete survey (AUDS100, Xi et al. 2021) over a 1.35 square degree area on the sky. A total of 247 HI sources were detected by AUDS100. We restrict our discussion to AUDS100, given that their results overlap with AUDS60. Overall, the AUDS100 HiMF is found to be consistent with both, the HIPASS and ALFA100 HiMF, although their  $\alpha$  is steeper than ALFA100 and their  $M_{\text{HI}}^*$  is larger, but consistent at the  $2\sigma$  level (see Fig. 4.8). However, in context with our work at a higher redshift, it is important to compare their results from their high redshift sample, covering  $0.09 < z < 0.16$ , consisting of 124 galaxies. With this sample alone, they found a larger characteristic knee mass compared to the low redshift sample ( $z < 0.09$ ). Furthermore, for the sake of consistency, they limited their comparison of the two subsamples to a  $\log(M_{\text{HI}}/M_{\odot})$  range of 8.94 to 10.4. This resulted in larger errors (similar to the BUDHiES fits) due to a reduction in sample size, but also a smaller difference in the HiMF parameters of the two AUDS100 subsamples. Other theoretical studies, while discrepant in their predictions on the evolution of the HiMF, are in broad agreement at least out to  $z \sim 0.16$ , predicting little or no evolution of the HiMF (e.g., Power, Baugh & Lacey 2010; Popping, Somerville & Trager 2014; Crain et al. 2017). The differences in these theoretical studies are reflected by their choice of gas cooling mechanisms, supernova feedback, star formation timescales, and numerical resolution, to name a few. In addition, several simulations based HiMF display an unrealistic bump at  $M_{\text{HI}}^* \simeq 10^8 - 10^{8.5} M_{\odot}$ , which is purely an artefact (e.g., Crain et al. 2017).

While it is impossible to constrain the slope of the BUDHiES HiMF due to the large errors on the fit parameters, Fig. 4.8 does show a tension in the  $\alpha$ - $M_{\text{HI}}^*$  plane between BUDHiES and ALFA100, implying that there is a difference between the  $z \sim 0.2$  HiMF and the  $z \sim 0$  HiMF. Moreover, fixing the slope to the ALFA100 value, as described and motivated in Sect. 4.4.2, results in a knee mass  $\log_{10}(M_{\text{HI}}^*/M_{\odot}) = 9.70 \pm 0.05$ , which is significantly lower than observed or predicted values in the literature. Based on the hierarchical structure formation scenario presented in the  $\Lambda$ CDM paradigm, the massive galaxies seen today are predicted to have formed from the merging of smaller halos in the past. Thus, at higher redshifts, one would expect the HiMF to have a steeper low-mass slope and a smaller knee mass. While our findings are consistent with theoretical predictions, such significant changes in the knee mass are not expected at  $z \sim 0.2$  (e.g., Popping, Somerville & Trager 2014).

#### 4.5.2 Evolution in $\Omega_{\text{HI}}$ over cosmic time

In the Local Universe,  $\Omega_{\text{HI}}$  has been well constrained with the help of direct HI detections from blind HI surveys (Zwaan et al. 2005; Martin et al. 2010; Jones et al. 2018). At higher redshifts ( $z > 0.1$ ), however, the direct detection of HI becomes significantly more difficult due to the intrinsic weakness of the HI signal. So far,  $\Omega_{\text{HI}}$  measurements based on direct HI emission studies have been limited to  $z < 0.16$  (Hoppmann et al. 2015; Xi et al. 2021). Other indirect methods are therefore utilised to measure  $\Omega_{\text{HI}}$ . One method is based on spectral stacking techniques (Bera et al. 2019; Rhee et al. 2016, 2018; Chowdhury et al. 2020). Chowdhury et al. (2020) achieved the highest

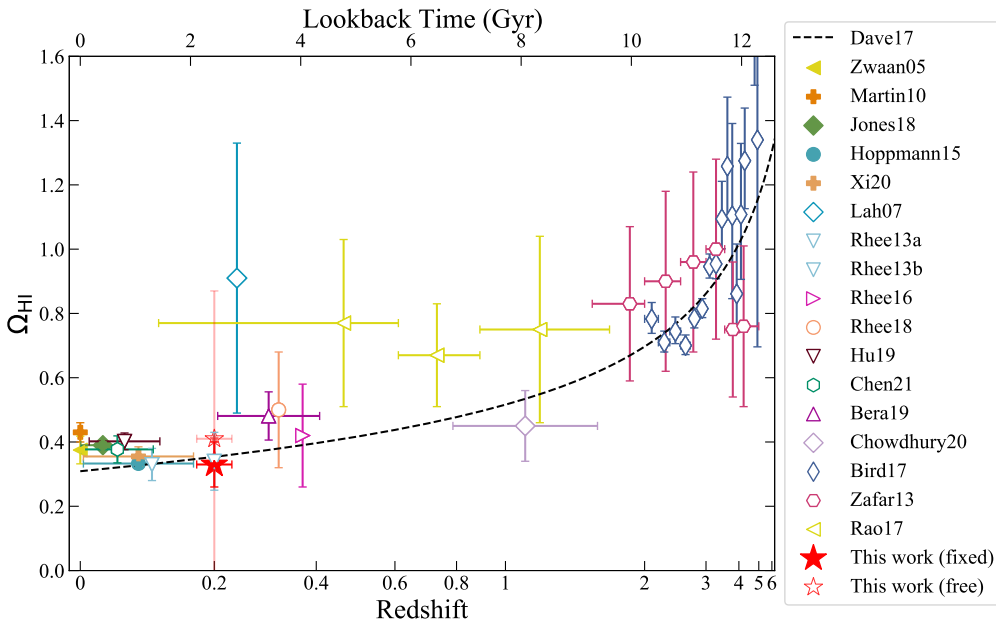


**Figure 4.11** – The cosmic HI density,  $\Omega_{\text{HI}}$ , plotted as a function of both, redshift and lookback time. Literature  $\Omega_{\text{HI}}$  estimates have been provided in the legend and are sorted by the type of study: HI emission (restricted to  $z < 0.22$ , solid symbols), stacking and Damped Lyman- $\alpha$  studies ( $0.1 < z < 6$ , open symbols). All measurements have been corrected to follow our adopted ‘737’ cosmology. Our  $\Omega_{\text{HI}}$  estimates following FIT1 (free parameters of the HiMF) and FIT3 (assuming a non-evolving HiMF slope) are shown as the light pink and red stars, respectively. The studies included are as follows:  $\Omega_{\text{HI}}$  provided by Zwaan et al. (2005); Martin et al. (2010); Jones et al. (2018); Hoppmann et al. (2015); Xi et al. (2021) are based on direct HI emission studies, out to  $z \sim 0.16$ . Spectral stacking-based studies include Lah et al. (2007); Rhee et al. (2013, 2016, 2018); Hu et al. (2019); Chowdhury et al. (2020); Bera et al. (2019); Chen et al. (2021), while DLA studies include Zafar et al. (2013), Rao et al. (2017), Bird, Garnett & Ho (2017). Finally, the evolution in  $\Omega_{\text{HI}}$  predicted by the MUFASA hydrodynamical simulation Davé et al. (2017) is provided by the dashed black line.

ever redshift measurement of  $\Omega_{\text{HI}}$  with spectral stacking, at  $z \sim 1.05$ . While stacking provides much needed insight into the evolution of  $\Omega_{\text{HI}}$  with redshift, it is important to note some assumptions and caveats that are a part of such methods. Firstly, such studies at higher redshifts are usually based on optically selected samples, leading to selection biases. Secondly, there could be a potential for confusion of sources at higher redshifts due to limited spatial resolution, particularly in denser environments. Finally, optically selected studies make the assumption that the HI and optical centres coincide, which is often not the case in disturbed or interacting systems. All these factors can possibly affect and influence the measurement of  $\Omega_{\text{HI}}$  with severity increasing with redshift.

At even higher redshifts ( $z > 0.8$  and out to  $z \sim 6$ ),  $\Omega_{\text{HI}}$  is inferred from the HI content

of galaxies based on DLA (Bird, Garnett & Ho 2017; Zafar et al. 2013; Noterdaeme et al. 2012) and MgII absorbers (Rao et al. 2017). These studies may suffer from systematic biases caused by extinction and gravitational lensing (e.g., Smette, Claeskens & Surdej 1997; Ellison et al. 2001; Jorgenson et al. 2006). Below  $z \sim 1.6$ , Lyman- $\alpha$  becomes hard to detect, and thus such studies are restricted to very high redshifts. Even next-generation HI surveys will not be able to achieve the sensitivity required to probe such redshifts through direct HI detections of individual galaxies or through stacking.

Fig. 4.11 shows the measured and inferred evolution of  $\Omega_{\text{HI}}$  as a function of redshift as well as look-back time. Several literature studies have been combined in this figure. In the context of the evolution of  $\Omega_{\text{HI}}$ , several studies have now shown, as also evident from the figure, that there has been no significant change in  $\Omega_{\text{HI}}$  over the past 4 Gyrs ( $0 < z < 0.45$ ). It is also worth noting that the measurement uncertainties are larger at intermediate redshifts. There appears to be a marginal increase in  $\Omega_{\text{HI}}$  with redshift, but this only becomes significantly stronger beyond  $z > 2$ , as suggested by DLA-based studies (e.g., Bird, Garnett & Ho 2017; Zafar et al. 2013; Noterdaeme et al. 2012). Additionally, the hydrodynamical simulation MUFASA (Davé et al. 2017) also predicts an evolution in  $\Omega_{\text{HI}}$ , given as  $\Omega_{\text{HI}} = 10^{-3.45}(1+z)^{0.74}$  (adjusted to the cosmology adopted in this chapter). This is shown by the dashed black line in Fig. 4.11 and is in excellent agreement with observational results.

Our work provides the first insight into  $\Omega_{\text{HI}}$  from direct HI detections at  $z \sim 0.2$ , as indicated in the figure. Our measurement of  $\Omega_{\text{HI}}$  from FIT1 (shown as the open red star in Fig. 4.11) is not well constrained due to large uncertainties on the HiMF parameters. However, under the assumption of an unevolving slope of the HiMF from local measurements, our completeness and self-absorption corrected  $\Omega_{\text{HI}}$  measurement of  $(3.2 \pm 0.7) \times 10^{-4}$  (shown by the red star) is almost identical to the stacking result from Rhee et al. (2013) at the same redshift. In addition, our result is also consistent, within the errors, with those measured in the Local Universe and predictions from simulations (Davé et al. 2017).

### 4.5.3 The effect of cosmic variance and environment

Cosmic variance, which describes perturbations in measurements within our Universe due to sample size and selected survey volume, is a dominant source of uncertainty in large extragalactic surveys. Due to the non-homogeneity of the Universe on the scales at which these surveys are performed, the variation observed in the sample size and galaxy density is larger than standard Poisson variation. All large-scale surveys carrying out statistical studies such as the determination of the luminosity function, the HiMF, cosmic SFR histories, etc. have to factor in the effect of cosmic variance, which becomes particularly significant for deep pencil-beam surveys, covering a smaller area on the sky. The methods for its quantification are based on underlying assumptions which may or may not be best suited for the survey in question, depending on its specifications. Cosmic variance is typically estimated empirically with Monte-Carlo or Jackknife sampling, with the help of numerical simulations, or analytically using two- or three-point correlation functions. Another approach is to empirically compare the

data set with a reference field, usually based on large optical catalogues. For instance, the only other blind HI survey that has quantified cosmic variance beyond the Local Universe is the AUDES survey (Hoppmann et al. 2015; Xi et al. 2021). Their approach for quantifying cosmic variance was to measure the relative density distribution of their two AUDES fields with a reference field from an optical catalogue (SDSS). Since blind HI surveys typically trace blue, late-type, star forming galaxies, they selected galaxies with SDSS  $u - r < 2.22$  to ensure the inclusion of representative galaxy populations. For the full ALFALFA data set, Jones et al. (2018) estimated cosmic variance as the difference between the HiMF constructed separately for the ALFALFA Spring and Fall regions. Additionally, simplified cosmic variance calculators based on optical catalogues or numerical simulations are available (e.g., Trenti & Stiavelli 2008; Driver & Robotham 2010; Moster et al. 2011).

In our case, quantifying cosmic variance proves to be non-trivial, and we have identified a few downsides of applying these cosmic variance estimates to our study, which we discuss further here. Firstly, BUDHiES, at  $z \sim 0.2$  is deeper than AUDES, and at such redshifts, large optical surveys such as SDSS ‘thin out’, meaning that they tend to trace redder, more luminous galaxy populations, which would not represent those galaxies detected by BUDHiES. Furthermore, clustering signatures of galaxy populations are different for optical and HI surveys, making the two-point correlation function different for optical and HI detected galaxies. For example, none of the galaxies in the central  $\sim 1$  Mpc region of Abell 963 were detected in HI by BUDHiES, but are obviously visible in the SDSS image. Thus far, no suitable spectroscopic data sets exist at such redshifts in this regard.

Next, we discuss the available cosmic variance calculators. Our focus is particularly on the extensively adopted Driver & Robotham (2010) calculator, in which they use  $M^* \pm 1$  mag galaxies in SDSS to empirically determine cosmic variance as a function of survey volume and survey shape. They assume fixed redshift windows, corresponding to a physical comoving distance of  $\sim 291 h_{0.7}^{-1}$  Mpc. In addition, they also point out the issue of survey volume and shape (see Sect. 3.4 in their paper), making the extrapolation of their method beyond  $z \sim 0.1$  non-trivial. As a work-around, they provide an approximation of the cosmic variance at higher redshifts (Eq. 4 of their paper), based on some underlying assumptions. Firstly, they assume that the cosmic variance in long cuboids (where one axis is much greater than the other two) scales according to Poisson statistics. Secondly, they translate the volume as the product of the median redshift transverse lengths and depth. Based on their assumptions and equations, we infer a cosmic variance of up to  $\sim 34$  per cent for the BUDHiES survey volume, based on two  $1^\circ$  fields over  $0.164 < z < 0.224$ . However, the interpretation of this number is difficult due to the underlying differences between optical and HI surveys, as discussed earlier. We thus treat it as an upper limit for our survey.

Finally, another important point to consider is that cosmic variance not only affects the normalisation parameter ( $\Phi_{\text{HI}}^*$ ) of the HiMF, but is likely to also affect the other parameters, namely,  $\alpha$  and  $M_{\text{HI}}^*$ . These are more environment-sensitive parameters and require a more detailed environmental analysis. In the Local Universe, for instance, studies have found that the HiMF of groups tends to have a flatter slope (e.g., Pisano

et al. 2011; Westmeier et al. 2017; Busekool et al. 2021), whereas the global HiMF is found to have a somewhat steeper slope (e.g., Zwaan et al. 2005; Martin et al. 2010; Jones et al. 2018; Xi et al. 2021). Furthermore, Jones et al. (2018) illustrated how treating the ALFALFA Spring and Fall skies as separate volumes resulted in a dichotomy in  $\alpha$ . They also found a suppression in  $M_{\text{HI}}^*$  by  $\sim 0.2$  dex within 60 Mpc, compared to the full depth of  $\sim 200$  Mpc. In our blind HI sample, the 166 confirmed HI sources are distributed across different cosmic environments, which include the two galaxy clusters Abell 963 and Abell 2192, foreground and background voids and overdensities unrelated to the clusters. The clusters themselves occupy as little as 4% of the total surveyed volume within their respective Abell radii. Additionally, with a survey depth of 328 Mpc and an average projected size of  $\sim 11.5 \times 11.5$  Mpc, the survey dimensions exceed the typical correlation lengths of the cosmic large-scale structure along the line-of-sight. This allows us to draw the preliminary conclusion that the cosmic variance would not significantly affect our results.

Finally, we see two other approaches that could prove to be more robust than the methods mentioned above. The first is by using numerical simulations such as the Evolution and Assembly of GaLaxies and their Environments (EAGLE, Schaye et al. 2015) simulation as a reference sample. However, it is important to note that the box size of EAGLE is much smaller (each side of 100 Mpc). In addition, the HiMF derived from EAGLE (Crain et al. 2017) is not an adequate representation of reality, as discussed in Sect. 4.5.1. The other method to derive cosmic variance is to use a large HI survey such as ALFALFA or HIPASS as a reference volume. By segmenting the reference set to match the depth and volume of BUDHiES, cosmic variance can be derived by computing the HiMF parameters in the different sections. One important caveat of this method is the assumption that the HiMF does not evolve with redshift up to  $z \sim 0.2$ . Due to the non-triviality of this estimation, it is considered beyond the scope of this thesis and hence might be addressed in future work.

## 4.6 Summary and Conclusions

In this chapter, we have attempted to construct the HiMF and measure  $\Omega_{\text{HI}}(z=0.2)$  for the first time with direct HI detections from BUDHiES, a blind, pencil-beam HI imaging survey within the redshift range  $0.164 < z < 0.224$  (Gogate et al. 2020). As part of this analysis, we have carried out completeness corrections using an empirical approach of injecting artificial sources into the observed noisy data cubes, after subtracting the real sources (see Chapter 2 for full details on the source finding and counterpart identification). The recovery of these artificial galaxies was tested by cross-matching the positions of the input and recovered sources. Based on the recovery rate of the artificial sources, the real data (binned in 0.25 dex mass bins) were corrected by our derived completeness factor. We found that no bins were complete, with incompleteness increasing at lower HI masses. The HiMF was then fit as a Schechter function to the corrected histograms using nonlinear least squares fitting. The best-fit HiMF parameters are:  $\alpha = -1.49 \pm 0.48$ ,  $\log_{10}(M_{\text{HI}}^*/M_{\odot}) = 9.78 \pm 0.16$  and  $\Phi_{\text{HI}}^* = 4.9 \pm 3.2 (\times 10^{-3})$ . The large error on the slope arises due to the high degree of incompleteness in the survey. Thus, the

HiMF parameters, in particular, the low-mass slope  $\alpha$ , cannot be constrained to make a direct comparison with the Local HiMF. However, it is evident that the slopes of the BUDHiES, ALFA100, AUDES100, and HIPASS HiMF are more comparable, while the variation is largest in  $M_{\text{HI}}^*$ . Of these, the ALFA100 and AUDES100 points lie outside the 99.9 % confidence contours of the BUDHiES HiMF in the  $\alpha$ - $M_{\text{HI}}^*$  parameter space.

With large errors on the best fit HiMF parameters, the derived cosmic HI density  $\Omega_{\text{HI}}$  also results in large errors, at  $4.1 \pm 4.6 (\times 10^{-4})$ . In order to constrain the  $\Omega_{\text{HI}}$  at  $z \sim 0.2$ , it was assumed that the slope  $\alpha$  remains unchanged with redshift (fixed to the ALFA100 value), as suggested by previous studies. This resulted in an  $\Omega_{\text{HI}}$  of  $3.2 \pm 0.7 (\times 10^{-4})$ . Based on this assumption, we find that our  $\Omega_{\text{HI}}$  measurement is consistent with other indirect  $\Omega_{\text{HI}}$  studies at similar redshifts (Rhee et al. 2013; Davé et al. 2017). This  $\Omega_{\text{HI}}(z=0.2)$  measurement has been corrected for incompleteness and self-absorption.

Our findings remain incomplete without addressing the issue of cosmic variance. With a line-of-sight depth of 328 Mpc, the BUDHiES volumes host a range of cosmic environments from clusters to voids and other unrelated overdensities. At such redshifts, however, the quantification of cosmic variance is effectively impossible due to a number of reasons, as discussed in detail in Sect. 4.5.3. With the help of the optically-based cosmic variance calculator by Driver & Robotham (2010), we estimated an upper limit of 34 per cent cosmic variance for our survey. A proper quantification of cosmic variance is desirable but beyond the scope of this thesis.

The advent of next-generation deep, blind HI surveys using SKA pathfinder telescopes such as ASKAP and MeerKAT and eventually SKA-1 will bring about a substantial improvement in our understanding of the redshift evolution of the HiMF and  $\Omega_{\text{HI}}$ . So far, such studies have been limited to  $z < 0.2$ , but these boundaries will be pushed to new horizons in the near future, with surveys such as DINGO (Meyer 2009) with the Australian SKA Pathfinder telescope (ASKAP) out to  $z \sim 0.5$ , and the LADUMA (Holwerda, Blyth & Baker 2012; Blyth et al. 2016; Baker, Blyth & Holwerda 2019) out to  $z \sim 1$  using MeerKAT. With this work, our attempt was to provide a benchmark for these future surveys, with meaningful information on the difficulties and shortcomings that can be expected when conducting such studies.

## 4.7 Acknowledgements

AG and MV acknowledge the Netherlands Foundation for Scientific Research support through VICI grant 016.130.338. We acknowledge the Leids Kerkhoven-Bosscha Fonds (LKBF) for travel support. AG thanks Martin Vogelaar for technical support in developing the python wrapper for GIPSY, Manolis Papastergis, Kelley Hess and Michael Jones for useful discussions. JMvdH acknowledges support from the European Research Council under the European Union's Seventh Framework Programme (FP/2007-2013)/ERC Grant Agreement nr. 291531. The WSRT is operated by the Netherlands Foundation for Research in Astronomy, supported by the Netherlands Foundation for Scientific Research.

## Appendix: A library of realistic mock galaxies

### 4.A Motivation

HI is a vital ingredient for star formation within galaxies, and gives great insight into the formation and evolution of the host galaxy. A drawback of using the HI signal as a tracer of galaxy evolution is its intrinsic weakness, and it thus becomes challenging to detect HI at higher redshifts ( $z > 0.1$ ). Very few blind HI surveys at higher redshifts have so far been carried out (e.g., Fernandez et al. 2015; Gogate et al. 2020; Xi et al. 2021). This thesis is focused on data from the Blind Ultra-Deep HI Environmental Survey (BUDHiES Gogate et al. 2020), which detected 166 galaxies in HI over a redshift range  $0.164 < z < 0.224$ . With a volume of  $73,400 \text{ Mpc}^3$  within the FWQM of the primary beam, the survey is sensitive to galaxies down to a mass limit of  $2 \times 10^9 M_{\odot}$ . The motivation for the work presented in this appendix was the need for realistic simulated galaxies that could quantify the number of undetected HI emitters due to the intrinsic limitations of HI surveys. This is a necessity to gain insight into the HI content of galaxies at redshifts beyond the Local Universe, where its detection becomes more challenging.

Many attempts to predict the atomic gas properties of galaxies have been made with the help of (semi)analytic and numeric modelling methods for galaxy formation (e.g., Cole et al. 2000; Obreschkow et al. 2009; De Lucia et al. 2012; Han et al. 2018; Davé et al. 2020). These models mostly follow a  $\Lambda$ CDM cosmology and reproduce large-scale structures that are observed in the universe, e.g, the Millennium simulation by Springel, Frenk & White (2006); the *SAX*<sup>3</sup> simulation by Obreschkow et al. (2009) who simulated the cosmic evolution of the H<sub>2</sub> and HI in galaxies using the virtual galaxy catalogue produced by De Lucia & Blaizot (2007); Elson, Blyth & Baker (2016) who created HI data cubes based on the catalogue presented by Obreschkow & Meyer (2014) for predicting uncertainties in HI stacking methods, among others.

Our method is based on an empirical approach, following the observed standard scaling relations. As mentioned in Sect. 4.3, the aim was to create a library consisting of model realistic galaxies with varying masses, inclinations, and other parameters with the specific aim of carrying out completeness corrections for our HI survey. This modelling does not make use of any cosmological simulations. Galaxies were created with the help of the task *galmod*, part of the software GIPSY. For each galaxy, *galmod* requires six main parameters: The radii of the galaxy disc ( $\mathcal{R}$  from 0 to  $\mathcal{R}_{max}$ ) in arcseconds, the radial HI surface density distribution ( $\Sigma_{HI}$ ) in atoms/cm<sup>2</sup>, the rotational velocities ( $V_{rot}$ ) in km s<sup>-1</sup> at each radius, the velocity dispersion ( $\sigma$ ) in km s<sup>-1</sup>, the inclination ( $i$ ) in degrees and the position angle (PA) in degrees. The models also follow  $\Lambda$ CDM cosmology with the same parameters mentioned in Sect. 1.5.1. The approximation of each of these above-mentioned parameters is described in detail in the following sections.

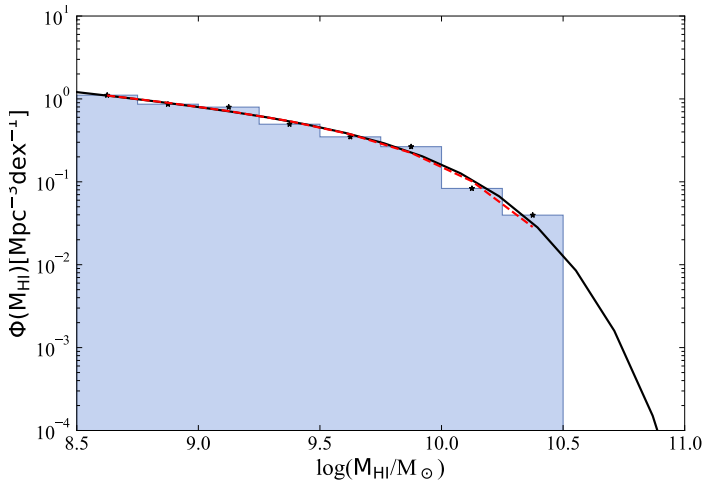


**Figure 4.12** – Randomly generated HI masses following the ALFALFA 40% HiMF with  $\alpha = -1.33$ ,  $M_{HI}^* = 10^{9.96} M_{\odot}$  and  $\Phi_{HI}^* = 4.8 \times 10^{-03}$  (solid black line). The distribution of randomly selected HI masses is shown in the form of a histogram to which a verifying HiMF is fitted (dotted red line)

#### 4.A.1 HI masses

We begin with the first and most fundamental parameter from which most of the above are calculated: the HI mass. These masses were generated with the help of a random number generator in the mass range  $10^{8.5} M_{\odot}$  to  $10^{10.5} M_{\odot}$ , following a Schechter function (Schechter 1976). The analytic form of the Schechter function has been described in Sect. 4.4. For this exercise, the parameters of the HiMF derived from the 40 % ALFALFA Survey (Martin et al. 2010) were used, with  $\alpha = -1.33$ ,  $M_{HI}^* = 10^{9.96} M_{\odot}$  and  $\Phi_{HI}^* = 4.8 \times 10^{-03}$  as shown in Fig. 4.12. We would like to point out that at the time of creating these galaxies, this mass range should have included galaxies between  $10^{10.5}$  and  $10^{11} M_{\odot}$ , since the BUDHIES sample did contain two galaxies in this range.

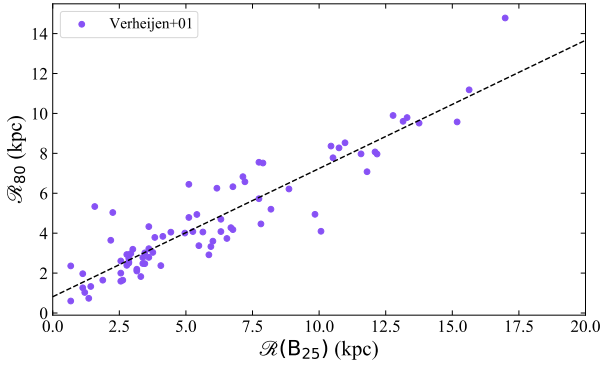


**Figure 4.13** – The  $\mathcal{R}_{80} - \mathcal{R}(B_{25})$  correlation from the Ursa Major Association of galaxies (Verheijen 2001), used for defining the optical radius ( $\mathcal{R}_{80}$ ) for the model galaxies.

However, since the process of re-simulating these galaxies was non-trivial, we decided to assume that the most massive HI galaxies were complete in the survey and would be detectable from anywhere in the cube.

#### 4.A.2 The HI and optical radii

Creating these artificial sources requires two diameter measures for each galaxy. The HI diameter from the centre out to the edge of the disc, and similarly, an approximation of the optical diameter, which encloses the majority of the light in the galaxy. The optical diameter is necessary to simulate realistic rotation curves, as described in Sect. 4.A.4.

##### HI radius

We derived the HI radius ( $\mathcal{R}_{\text{HI}}$ ) using the well constrained direct correlation between a galaxy’s HI mass and its HI disc size: the so-called  $D_{\text{HI}} - M_{\text{HI}}$  relation for determining the HI diameters of the synthetic sources. It is found, that with a slope close to 0.5, this relation indicates that the average HI surface density is constant for any given galaxy. It is given by:

$$\log(D_{\text{HI}}) = 0.54 \log(M_{\text{HI}}) - 3.646 \quad (4.3)$$

where  $D_{\text{HI}}$  is the disc size in kpc and  $M_{\text{HI}}$  is the HI mass in  $M_{\odot}$ . We adopted averaged values for the slope and zero point based on work by Broeils & Rhee (1997), Verheijen (2001), Swaters et al. (2002), Noordermeer et al. (2005) and Martinsson et al. (2016) for approximating the HI disc diameters from our preselected HI masses. This average relation corresponds well with the more recent work by Wang et al. (2016), which was published after our work was completed. Note that the HI diameter is defined by the column density level of  $1 M_{\odot}/\text{pc}^{-2}$ .

### The optical radius

The second radius measure is the radius enclosing 80 per cent of the total blue light ( $\mathcal{R}_{80}$ ). To determine this optical radius for the mock galaxy sample, we drew a correlation between the B-band radius at the isophotal level of 25 mag arcsec<sup>-2</sup> ( $\mathcal{R}(B_{25})$ ) and the  $\mathcal{R}_{80}$  for the Ursa Major sample (Verheijen & Sancisi 2001), as shown in Fig 4.13. The line of best fit for this distribution is given by:

$$\mathcal{R}_{80} = 0.642 \mathcal{R}(B_{25}) + 10.83 \quad (4.4)$$

From several studies, it is known that for a regular star forming galaxy, its optical radius can only be smaller than or equal to its HI radius. Thus, we chose, for each galaxy, a random  $\mathcal{R}(B_{25})$  such that  $0.4 \mathcal{R}_{\text{HI}} < \mathcal{R}(B_{25}) < \mathcal{R}_{\text{HI}}$  where  $\mathcal{R}_{\text{HI}}$  is the galaxy's HI radius in kpc derived from Eq. 4.3. Then, using the equation 4.4 above, we obtained the corresponding value of  $\mathcal{R}_{80}$ .

4

#### 4.A.3 Luminosities

B-band luminosities are required for each galaxy as an ingredient for the Universal Rotation Curve prescription (Sect. 4.A.4). A study of the Tully-Fisher relation (TFR) carried out by Verheijen (2001) showed that the K-band TFR was the tightest with the least scatter. Our aim was to assign each galaxy with a random but plausible luminosity, and hence we first compiled from the literature, a sample of galaxies with available K-band luminosities and HI masses: Tully et al. (1996); Swaters et al. (2002); Noordermeer et al. (2005); Spekkens & Giovanelli (2006); Cappellari et al. (2011a,b); Martinsson et al. (2016); Ponomareva, Verheijen & Bosma (2016) and Busekool et al. (in prep). From Fig. 4.14, it is evident that a galaxy with a given  $M_{\text{HI}}$  can possess a wide range of K-band luminosities. While one could define a correlation between the two parameters, the scatter is quite large. A polynomial fit to the distribution would not be an appropriate model for this distribution. For meeting our requirements, we defined a box around the scattered points to constrain the K-band magnitudes for a given HI mass. The upper limits from the Atlas 3D survey (Cappellari et al. 2011a,b) were excluded for this exercise. It is worth noting that the lower-right area of the box is devoid of galaxies, but this is likely due to survey limitations at lower HI masses and fainter magnitudes, which have not yet facilitated a study of this region. However, this region is of no concern to us, because it is well below our detection limit.

Thus, for a given HI mass, a random K-band absolute magnitude was chosen, based on the limits drawn by the box. We then converted the chosen K-band magnitudes to B-band magnitudes with the help of the B-K colour-magnitude diagram. We used B- and K-band magnitudes from Martinsson et al. (2016); Tully et al. (1996) and Noordermeer et al. (2005), as shown in Fig 4.15. Owing to the large scatter, we set boundaries to offer some constraints on the selection of B-K colour. Thus, from this diagram, we computed the values of a randomly selected B-K colour for a given absolute K-band magnitude, which provides in turn the corresponding B-band absolute magnitude. B-band luminosities were calculated with the help of the expression:

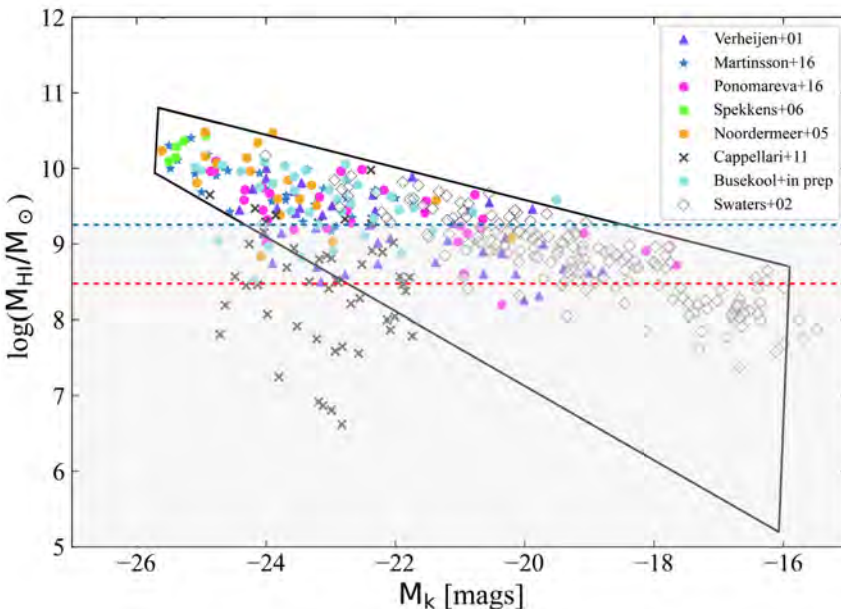


**Figure 4.14** – For those samples from the literature with available HI information along with K-band photometry, a scatter plot showing HI masses against K-band absolute magnitudes. The samples are colour-coded as given in the legend. The black bounding box enclosing most of the scatter points is our reference for choosing an appropriate K-band magnitude for a given HI mass. The blue dashed line indicates the BUDHIES detection limit of  $2 \times 10^9 M_{\odot}$ , with the shaded grey region indicating all points below this detection limit. The red dashed line indicates the mass limit of the model galaxies.

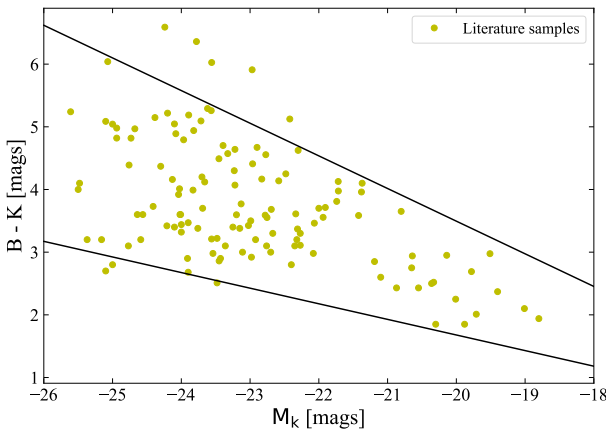


**Figure 4.15** – A Combined colour magnitude diagram for samples from the literature with available K and B-band photometry. The samples included are from Tully et al. (1996), Martinsson et al. (2016) and Noordermeer et al. (2005). The black lines are the bounds used for converting K-band magnitudes to B-band magnitudes.

$$L_B = 10^{(\text{Mag}_{\odot(B)} - M_B)/2.5} \quad (4.5)$$

where  $M_B$  is the B-band absolute magnitude derived from the B-K colour-magnitude diagram in Fig. 4.15, and  $\text{Mag}_{\odot(B)}$  is the in B-band absolute magnitude of the Sun, with  $\text{Mag}_{\odot(B)} = 5.48$ .

#### 4.A.4 Rotational velocities

Rotational velocities were derived from the empirical Universal Rotation Curve (URC) prescription by Persic, Salucci & Stel (1996). With this prescription, rotation curves can be generated for any luminosity, as well as any type of galaxy, including spirals, low-surface-brightness objects, ellipticals and dwarf irregular galaxies. The existence of a ‘universal’ rotation curve has also been claimed previously by Rubin, Burstein & Thonnard (1980). It is given by

$$V_{\text{URC}}(x) = V(\mathcal{R}_{80}) \left[ (0.72 + 0.44 \log \lambda) \frac{1.97x^{1.22}}{(x^2 + 0.78^2)^{1.43}} + 1.6e^{-0.4\lambda} \frac{x^2}{x^2 + 2.25\lambda^{0.4}} \right]^{0.5} \quad (4.6)$$

$$V(\mathcal{R}_{80}) = \frac{200\lambda^{0.41}}{\left[ 0.80 + 0.49 \log \lambda + \frac{0.75e^{-0.4\lambda}}{0.47 + 2.25\lambda^{0.4}} \right]^{0.5}} \quad (4.7)$$

Here,  $\mathcal{R}_{80}$  is the rotational velocity at the optical radius (radius enclosing 80% of the light),  $\lambda = L/L_*$  with  $\log(L_*/L_{\odot}) = 10.4$  in B-band,  $x = \mathcal{R}/\mathcal{R}_{80}$  where  $0 \leq \mathcal{R} \leq 2\mathcal{R}_{\text{HI}}$ . Note however, that a significant variety in rotation curve shapes exists for any  $L_B$  and  $\mathcal{R}_{80}$  combination, with the URC being a typical parameterisation of the average shape.

#### 4.A.5 Radial HI density distributions

The radial HI surface density profiles provide information on the distribution of neutral hydrogen in a galaxy. The radial distribution of HI often flattens or even declines near the centre of the galaxy and may extend out to large radii compared to the distribution of the stars for which the surface density peaks in the centre of the galaxy and declines exponentially with radius. The total HI mass is the value of the integral over the entire distribution. The radial HI density distribution varies significantly among galaxies. However, low mass galaxies tend to have a centrally peaked radial profile which declines exponentially with radius, while galaxies with bulges often have a HI deficient central region. In an attempt to accommodate these variations in the radial profile of the mock galaxies, we used the radial density distribution function ( $\Sigma_{\text{HI}}$ ) prescribed by Martinsson et al. (2016) as a basis and added slight modifications which would allow the inner part of the profile to change. This type of radial distribution can be described by a combination of two Gaussians:

$$\Sigma_{\text{HI},1} = e^{-(\mathcal{R} + \mathcal{R}_{\Sigma^{\text{max}}})^2 / 2\sigma_{\Sigma}^2} \quad (4.8)$$

$$\Sigma_{\text{HI},2} = e^{-(\mathcal{R} - \mathcal{R}_{\Sigma^{\text{max}}})^2 / 2\sigma_{\Sigma}^2} \quad (4.9)$$

combined as:

$$\Sigma_{\text{HI}} = \Sigma^{\text{max}} \Sigma_{\text{HI},1} + \Sigma_{\text{HI},2} \quad (4.10)$$

Where  $\Sigma_{\text{HI},1}$  and  $\Sigma_{\text{HI},2}$  are the two components of the total distribution,  $\mathcal{R}$  is the radius over which the HI is distributed,  $\mathcal{R}_{\Sigma^{\text{max}}}$  is the radius at the maximum amplitude ( $\Sigma^{\text{max}}$ ) of the first Gaussian. The amplitude of the second Gaussian is normalised to 1.  $\mathcal{R}_{\Sigma^{\text{max}}} = 0.4\mathcal{R}_{\text{HI}}$  and the radial dispersion of the profile,  $\sigma_{\Sigma} = 0.36\mathcal{R}_{\text{HI}}$ , is adopted from Martinsson et al. (2016), while  $\mathcal{R}_{\text{HI}}$  follows from the HI mass-diameter relation.

The only factor which changes the shape of the entire distribution is  $\Sigma^{\text{max}}$ , since all other parameters are common to both Gaussians. We choose  $\Sigma^{\text{max}}$  randomly from a Gaussian distribution, with centre = 0 and a dispersion  $\sigma = 1$ .

We scale the amplitude of the generalised form (4.10) of the radial HI distribution by calculating the integral:

$$I = \int_0^{\mathcal{R}} 2\pi\mathcal{R} \Sigma_{\text{HI}} d\mathcal{R}, \quad \text{with } 0 < \mathcal{R} < 2\mathcal{R}_{\text{HI}} \quad (4.11)$$

The scaled radial HI density distribution ( $\Sigma_{\text{HI}}^r$ ) is then given by:

$$\Sigma_{\text{HI}}^r = \left(\frac{M_{\text{HI}}}{I}\right) \Sigma_{\text{HI}} \quad (4.12)$$

$\Sigma_{\text{HI}}^r$  maintains the  $D_{\text{HI}} - M_{\text{HI}}$  relation where  $\mathcal{R}_{\text{HI}}(\text{pc})$  corresponds to a  $\Sigma_{\text{HI}}$  of  $1 M_{\odot} \text{pc}^{-2}$  for any given galaxy.

#### 4.A.6 Other parameters

Apart from the parameters discussed in the previous sections, *galmod* requires additional parameters such as the inclination, position angle and velocity dispersion. The inclination was chosen at random in the range  $0^\circ$  to  $90^\circ$  and the position angle of the receding side of the galaxy between  $0^\circ$  and  $360^\circ$ . These distributions of the inclinations and position angles are shown in Fig. 4.16. The velocity dispersion follows from observations, and we adopted a range between  $15\text{-}6 \text{ km s}^{-1}$ . Once these parameters were in place, *galmod* created galaxies within pre-defined data cubes, made with the GIPSY task *create*, which consist of  $400 \times 400$  pixels and 200 channels. Each pixel has a size of 5 arcseconds and a channel velocity width of  $5.2 \text{ km s}^{-1}$ . All cubes are placed at a

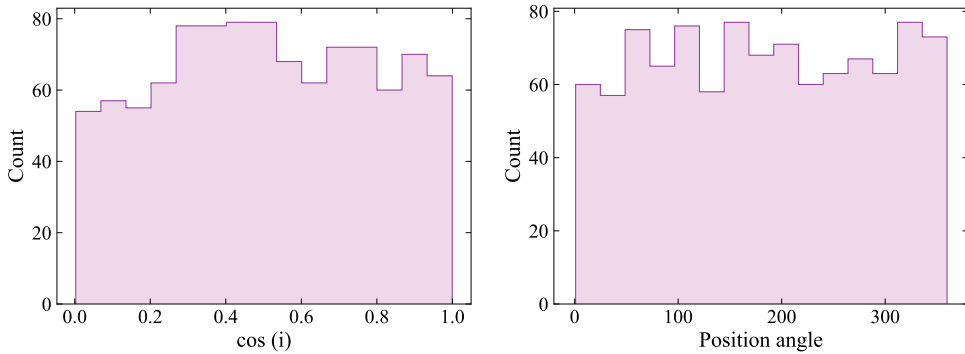


**Figure 4.16** – Histograms of the randomly assigned inclinations and position angles for all the mock galaxies.

distance of 50 Mpc and have a systemic velocity of  $3500 \text{ km s}^{-1}$ . Depending on where the cubelets with mock galaxies were inserted in the master cube, they were smoothed and regridded accordingly.

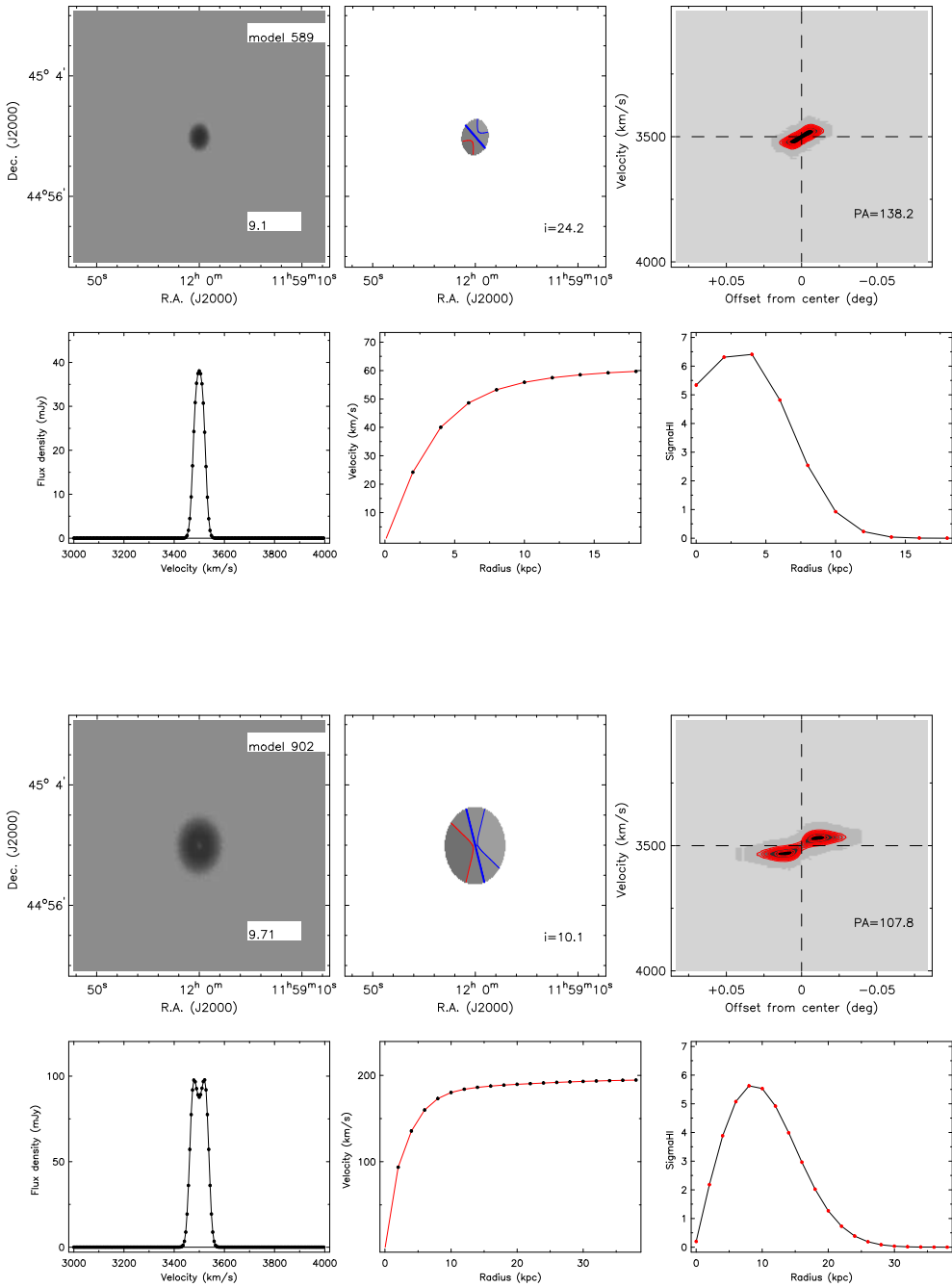
#### 4.A.7 The models

As described in the previous sections, these galaxies are realistic, created at all inclinations and position angles, and follow all standard empirical scaling relations. Some galaxies representing the mock library with varying HI masses, inclinations and position angles are illustrated below. The layout of the figures are as follows. From left to right, top panel:

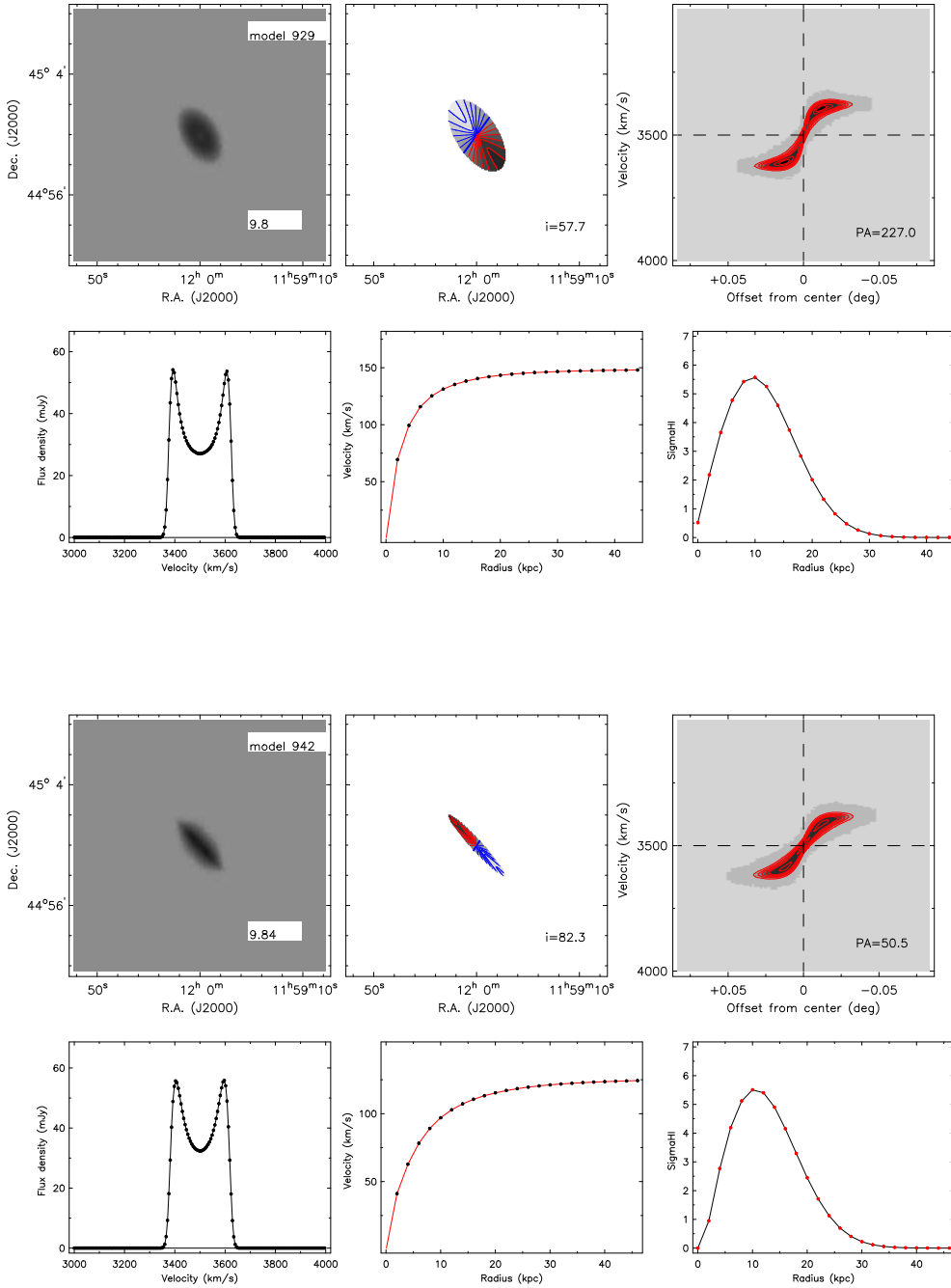
- (1) *Total HI map*: The model number is indicated at the top right while the log of the HI mass is given at the bottom-right.
- (2) *Velocity field*: Given to the bottom right is the assigned inclination of the mock galaxy. The blue line indicates the systemic velocity, while the red and blue contours show the approaching and receding sides of the galaxy respectively.
- (3) *Position-Velocity (PV) diagram*: The position angle assigned to the galaxy is printed at the bottom-right. The red contours indicate  $2, 4, 6, 9, 12, 15, 20$  and  $25 \times$  the rms in the PV diagrams.

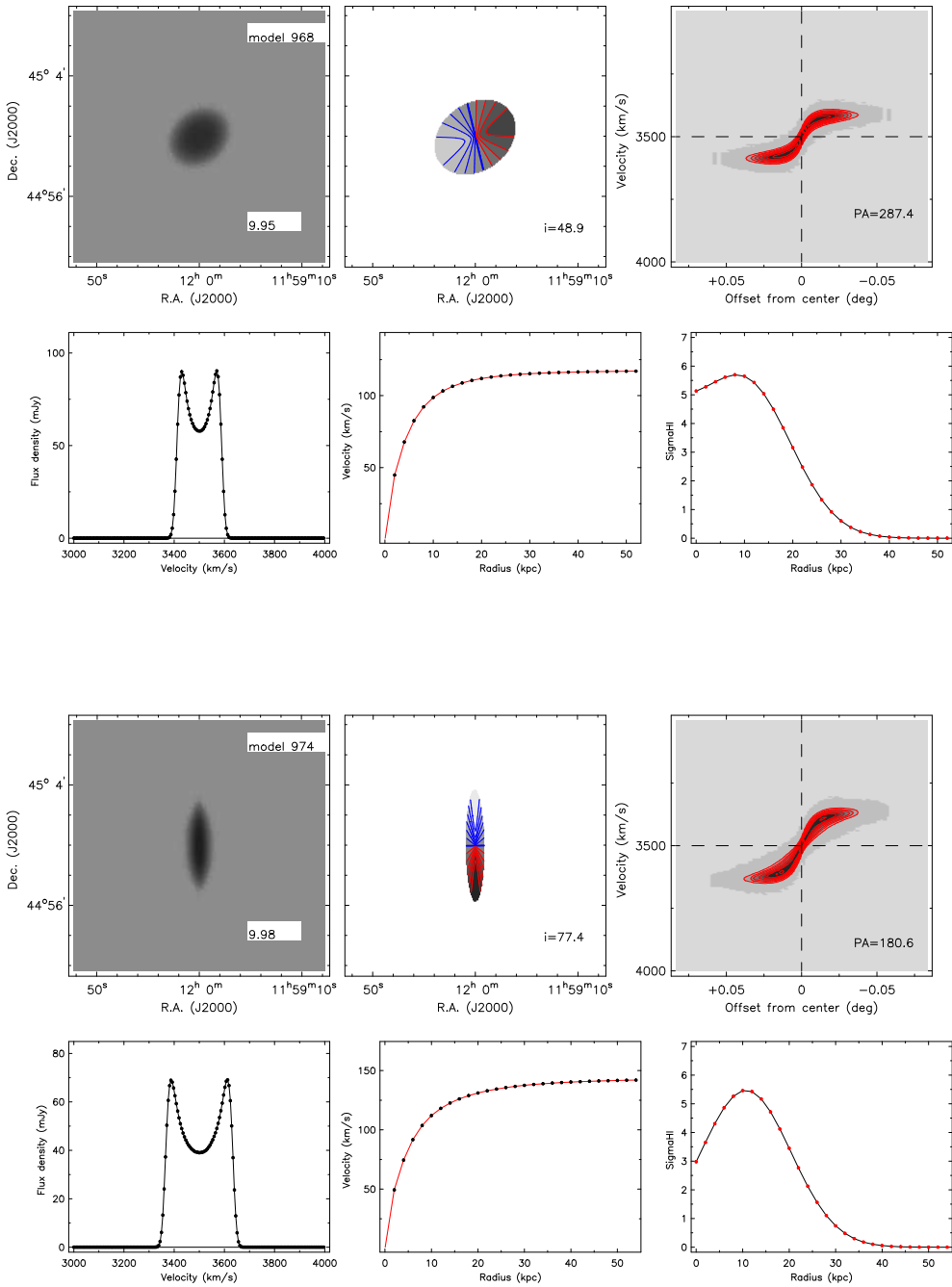
And on the bottom panel, from left to right:

- (4) *Global HI profile*: The global HI profile of the artificial galaxy.
- (5) *Rotation curve*: The assigned rotation curve of the mock galaxy based on the URC prescription (Persic, Salucci & Stel 1996).
- (6) *Radial density distribution*: The assigned radial density profile of the mock galaxy.

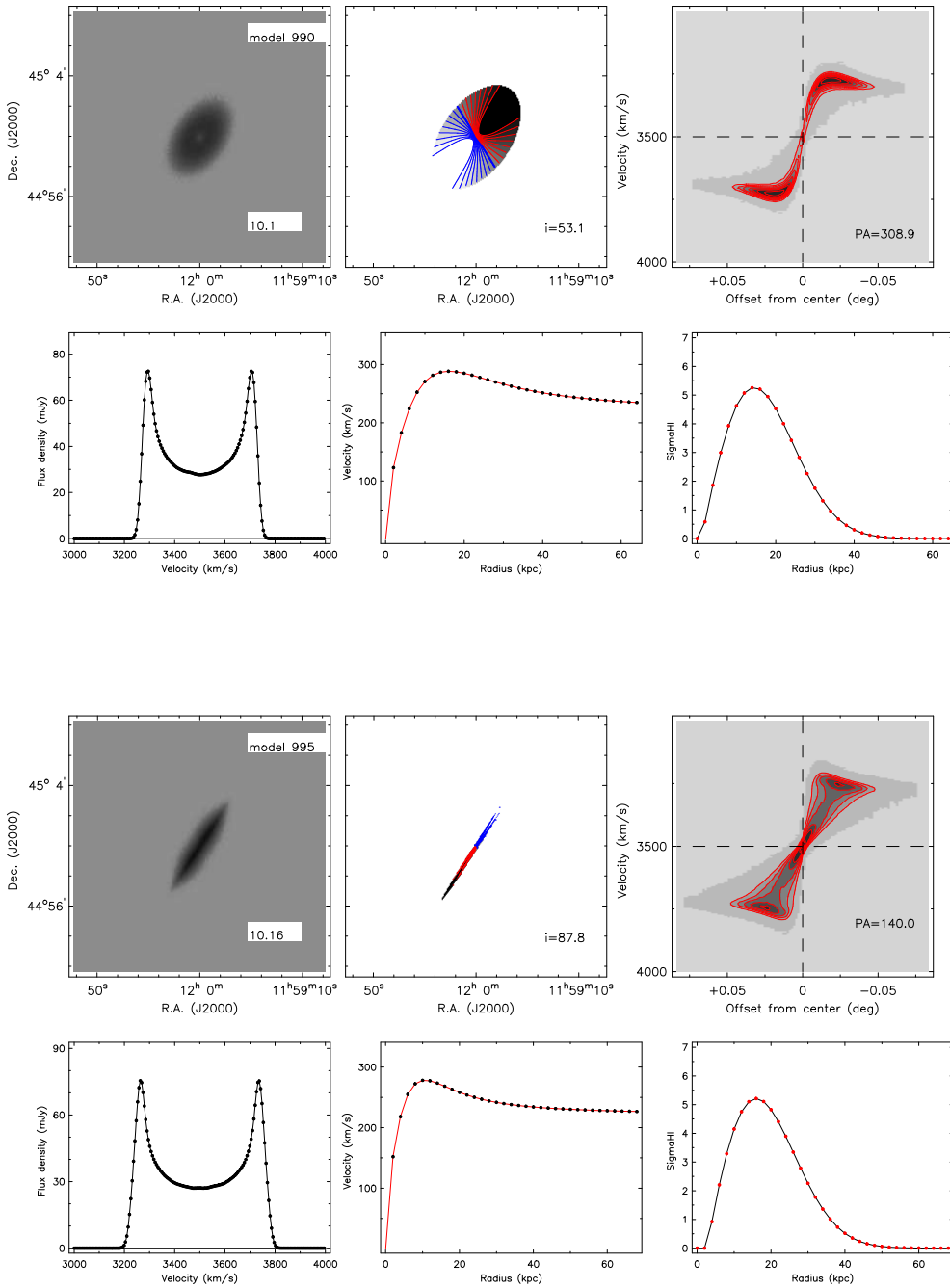


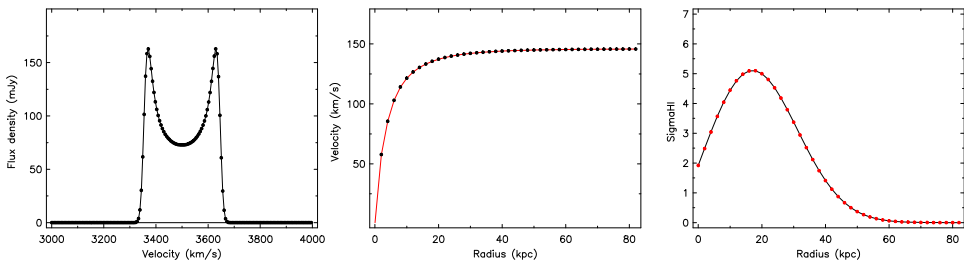
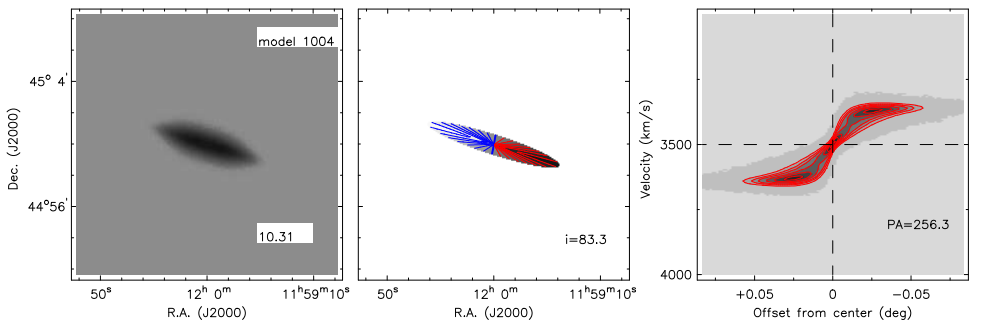
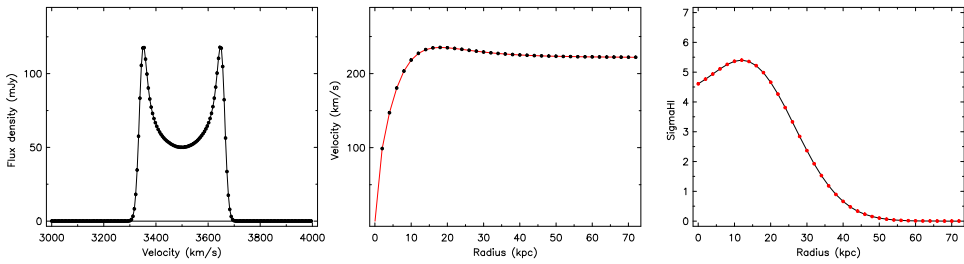
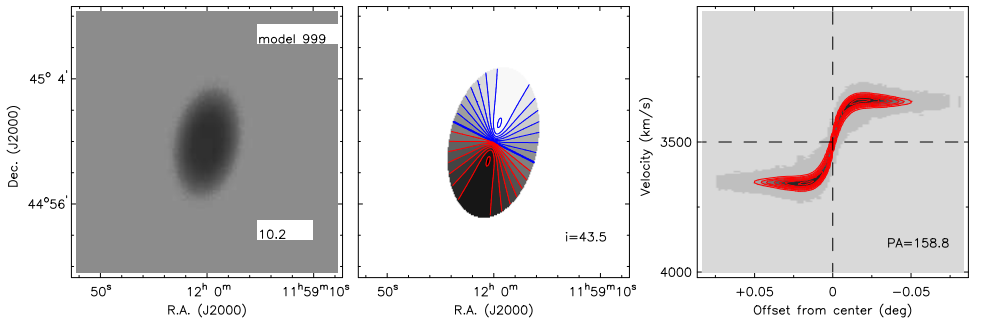
4



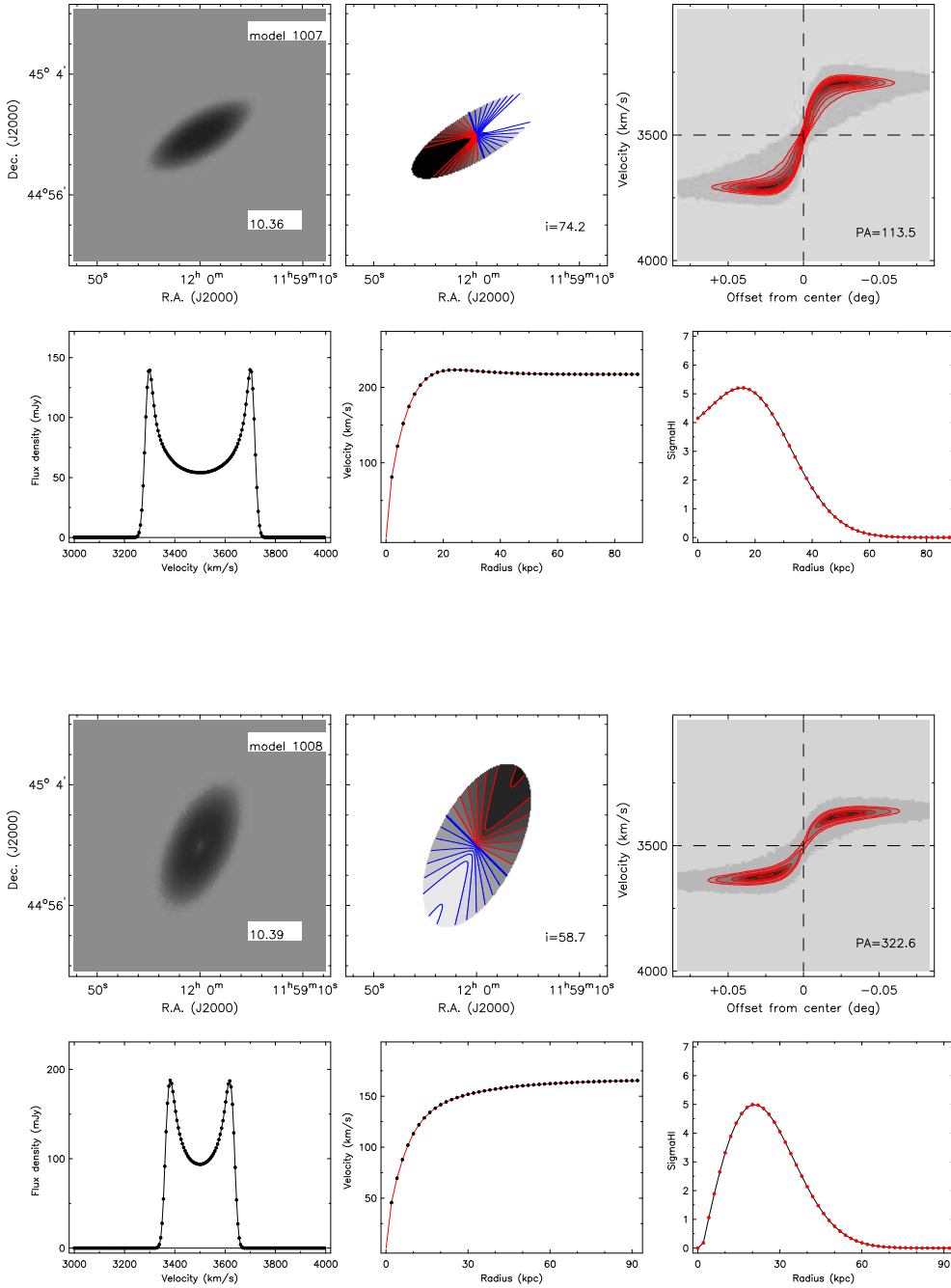


4





4



## Conclusions and future prospects

HI synthesis imaging beyond the Local Universe offers the possibility of exploring galaxy evolution through an HI perspective. It also offers important insights into the role of cosmic environments in galaxy evolution and galaxy dynamics. This was the aim of this PhD thesis, along with emphasising the importance of HI observations beyond the Local Universe. Some important HI-based measures of galaxy evolution have been explored in this thesis, all interlinked by one common data set, BUDHIES. This data set can still be considered unique, since blind HI observations beyond a redshift  $z \sim 0.1$  have so far been rare. Till date, it is still the largest and most distant blind sample of HI detected galaxies. This will soon change with the advent of next-generation HI surveys that will bring forth exceptional data and usher in the much awaited SKA era. Until then, BUDHIES offers significant insights into HI-based science beyond the Local Universe and aims to provide a benchmark for these future surveys. We cover not only the scientific results obtained through our study, but also the practical details and limitations of such observations that are relevant for future studies. The three aspects of galaxy evolution that have been explored in this thesis, namely, the redshift evolution of the Tully-Fisher relation, the HI mass function, and the cosmic HI density ( $\Omega_{\text{HI}}$ ), are the first attempts of such studies at  $z \sim 0.2$  with direct HI detections. The next section provides an overview of the main results obtained in this thesis. Finally, we discuss the prospects related to future HI-based surveys with similar science goals.

### 5.1 Results of this thesis

#### 5.1.1 The BUDHIES data

The so-called Butcher-Oemler effect (Butcher & Oemler 1984), is an observational effect indicating that the fraction of blue galaxies in cluster cores seems to increase as a function of redshift. To provide, for the first time, a gas perspective to the BO effect, a blind HI imaging survey was carried out with two pencil beam pointings each centred on an Abell cluster, along with the respective foreground and background large scale structure in which they are embedded. Known as the Blind Ultra-Deep HI Environmental Survey

(BUDHiES), this data formed the backbone of this PhD thesis. The two selected Abell clusters are strikingly different in their properties. Abell 963, at  $z \sim 0.206$  was part of the seminal BO study, and hosts 19 percent fraction of blue galaxies in its cluster core. It is a massive, virialised, lensing cluster with strong X-ray emission (Allen et al. 2003; Smith et al. 2005). In comparison, Abell 2192 at  $z \sim 0.188$  is dynamically younger, weak in X-rays (Voges et al. 1999) and not a BO cluster. The large scale structure around the two clusters within the redshift range of the survey include distinct over-densities separated by voids in the foreground and background of the two clusters. Detailed environmental analyses of the two BUDHiES volumes are provided by Jaffé et al. (2013). It is important to note that the clusters themselves, within their respective Abell radii, occupy only  $\sim 4$  per cent of the total volume surveyed by BUDHiES.

### Data processing and source finding

BUDHiES was carried out between 2005 and 2008, with a total integration time of  $\sim 183 \times 12$  hours with the Westerbork Synthesis Radio Telescope (WSRT). The survey covers a frequency range 1160 to 1220 MHz, corresponding to a redshift range  $0.164 < z < 0.224$ , effectively encompassing a volume of  $73,400 \text{ Mpc}^3$  within the FWQM of the primary beam. The resultant data cubes have an average angular resolution of  $23 \times 38 \text{ arcsec}^2$ , while the velocity resolution is  $19 \text{ km s}^{-1}$  after Hanning smoothing to suppress the Gibbs phenomenon near the bandpass edges. The survey was designed to reach a minimum detectable HI mass of  $2 \times 10^9 M_{\odot}$  at the respective cluster redshifts, at the  $4\sigma$  noise level, assuming an emission line width of  $\sim 150 \text{ km s}^{-1}$  detected over 3 adjacent spectral resolution elements. A GIPSY-based source finding algorithm was used to search for the HI emission from galaxies in the two BUDHiES volumes and yielded 194 positive detections. 166 galaxies were confirmed based on a thorough counterpart identification, and literature spectroscopic redshifts that were available for most of the galaxies. The ancillary data of the two BUDHiES fields consist of deep Harris B- and R-band imaging obtained from the INT as well as near-UV and far-UV observations with GALEX. Chapter 2 contains an extensive description of the data processing and calibration of these data sets in detail. None of the detected 166 galaxies have been previously studied in HI. At least half of the detections come from around the two clusters. However, no HI sources were detected within the projected distance of the central 1 Mpc from the cluster core of Abell 963, and one galaxy was detected in Abell 2192 (Jaffé et al. 2013).

### The HI and optical properties of BUDHiES galaxies

The average line widths at 50 per cent of the peak flux ( $W_{50}$ ) are  $193 \text{ km s}^{-1}$  for the volume containing Abell 963 (referred to as A963) and  $172 \text{ km s}^{-1}$  for the volume containing Abell 2192 (A2192). The  $\log(M_{\text{HI}})$  range of the detected galaxies is 9.0 to 10.64. Galaxies with line widths below  $150 \text{ km s}^{-1}$  were detected below the theoretical detection limit at the cluster redshifts and beyond. Some galaxies at the bandpass edges show only part of the profile and are hence treated as lower limits. Projections of the HI detected galaxies in the two fields on the sky (Fig. 2.16 in Chapter 2) show that (1) the spatial distribution in A963 appears relatively symmetric compared to A2192

which shows clear asymmetry, with most galaxies located to the west of the pointing centre; and (2) the lowest HI masses are detected closer to the field centres, an effect caused by the primary beam attenuation of the telescope.

A B-R vs R colour-magnitude diagram (Fig. 2.18 in Chapter 2) of all galaxies in the redshift range  $0.164 < z < 0.224$  with available literature spectroscopic redshifts as well as the HI detected galaxies indicates a clear distinction between the 'red sequence' and the 'blue cloud'. Most of the HI detections lie in the blue cloud, as is expected for gas-rich, star forming galaxies. Galaxies that were not detected in HI mostly lie on the red sequence, indicating that these are passive galaxies devoid of HI or at least undetectable in HI above the achieved mass limit.

### 5.1.2 The HI-based Tully-Fisher relation at $z \simeq 0.2$

The first application of the BUDHiES data in this thesis is the construction of HI-based B- and R-band TFrs as well as the baryonic TFr at  $z \sim 0.2$ . Galaxies were carefully selected based on a number of qualitative and quantitative criteria, ensuring that our final selection traced similar galaxy populations as the  $z=0$  sample. This was necessary to exclude systematic effects which often plague TFr studies. This exercise resulted in the BUDHiES TFr sample, known as the Tully-Fisher Sample (*TFS*) comprising 36 galaxies. Of these, 29 are in the survey volume containing Abell 963 and 7 are in the volume containing Abell 2192. Additionally, further rigorous quantitative thresholds were applied to the shapes of the HI profiles of the *TFS*, giving rise to the High-Quality Sample (*HQS*) consisting of 18 galaxies. Our analysis of the TFr was restricted to the analysis of the zero points, by comparing our results with an identically constructed TFr from the Ursa Major association of galaxies in the Local Universe (UMa, Verheijen 2001). We also qualitatively included an optically selected high redshift ( $z \sim 0.25$ ) sample of extremely massive and luminous galaxies from Catinella & Cortese (2015). Two important observational aspects need to be mentioned first before summarising our results:

#### 1) *Velocity measures:*

Two velocity measures i.e. the HI line widths at 20% and 50% of the peak flux were available for this analysis. These line widths were corrected for the effects of instrumental broadening, turbulent broadening and inclination, identically for all samples. It was found that at lower flux levels, several galaxies show the presence of a 'bump' in the wings of the HI profiles, which seems to broaden the HI profiles at low flux levels and cause an overestimation of the rotational velocities derived from the  $W_{20}$  line widths. This leads to a shift in the BUDHiES sample towards larger rotational velocities and reduces the vertical offset in the zero point from the UMa TFr. The  $W_{50}$  line widths are unaffected by this broadening and hence were chosen as the primary velocity measures for this analysis.

#### 2) The *TFS* and *HQS*

We assessed the difference between the *HQS* and *TFS*, and found that TFrs constructed with these two samples are very similar. This suggests that a further selection of galaxies

based on stricter quantitative measures neither affects the TFr zero points ( $\Delta ZP < 0.05$  mags), nor reduces the scatter. Thus, we only discuss the larger *TFS* further.

### The luminosity-based and baryonic TFr

The zero points of the B- and R-band TFrs constructed using the  $W_{50}^{\text{corr}}$  line widths as velocity measures were compared for the *TFS* and local UMa samples. We found that the BUDHiES TFr is both brighter and bluer ( $\Delta M_B = 0.72 \pm 0.06$  and  $\Delta M_R = 0.44 \pm 0.06$ ) than the  $z=0$  TFr when using  $W_{50}^{\text{corr}}$  line widths as measures of the rotational velocity. This blueing and brightening of the  $z \sim 0.2$  TFr suggests that galaxies were brighter for their dynamical mass, due to enhanced star formation at higher redshifts.

From our analysis, we found a striking similarity between baryonic TFrs at  $z \sim 0.2$  and  $z=0$ , within the uncertainties. For the purpose of converting luminosities to baryonic masses, two different stellar mass estimators were used, both resulting in consistent BTFRs. We conclude that galaxies in the past had similar baryonic masses as  $z=0$  galaxies for a given circular velocity. However, the  $M_{\text{HI}}/M_{\text{HI}}^*$  ratios of galaxies seems to have evolved, with HI mass making up a larger fraction of the baryonic matter in the past, unlike at  $z=0$ , where the stellar mass fraction is higher.

### Environmental assessment of the TFr

Apart from the choice of photometric band and velocity measure used for our analysis, the offsets in zero points also heavily depend on the sample selection. The above-mentioned results are based on the *TFS*, which while created using a meticulous sample selection process, also involve galaxies lying in the vicinity of the cluster Abell 963. Since the effect of the environment around the galaxies in Abell 963 may have some influence on the observed offsets, we also created further sub-samples within the *TFS* (and *HQS*). These were called the *Control* (galaxies lying outside  $2.5\sigma_{\text{cl}}$ ) and *Cluster* (galaxies within  $2.5\sigma_{\text{cl}}$ ) samples. There is still a significant difference in zero point offsets between the *Control* sample and the  $z=0$  TFr ( $\Delta M_B = 0.61 \pm 0.07$  and  $\Delta M_R = 0.31 \pm 0.08$ ). This difference becomes even more extreme in the *Cluster* sample TFr, which is significantly brighter but not bluer than the *Control* sample. The offsets in zero point with the  $z=0$  TFr are  $\Delta M_B = 0.90 \pm 0.09$  and  $\Delta M_R = 0.65 \pm 0.09$ .

In addition to the luminosity-based TFr, we also constructed the BTFRs of the various subsamples. The zero points of the *Control* sample is surprisingly similar to the  $z=0$  BTFR in contrast to the remarkable zero point difference found for the luminosity based TFr. In addition, the *Cluster* BTFR is also consistent with UMa within the errors, suggesting that the cluster environment does not seem to remove the baryonic mass from the dark matter halos of galaxies, but seem to enhance the star formation activity compared to field galaxies.

From our analysis, we conclude that the field galaxies (*Control* sample) in the past were brighter and bluer than local galaxies of the same dynamical mass, but similar in terms of baryonic content. In general, galaxies in our  $z \sim 0.2$  sample are more gas-rich than from the local sample. Galaxies lying within the  $2.5\sigma$  dispersion limit of Abell 963 seem

to be brighter but not bluer than other galaxies at similar redshifts.

It is also important to emphasise that in order to arrive at the results above, it was essential to :

- (1) carry out a proper sample selection tracing similar galaxy populations
- (2) apply consistent corrections applied to all comparative samples.

### 5.1.3 Completeness corrections for the BUDHiES data

For the purpose of constructing the HiMF and measuring  $\Omega_{\text{HI}}$  from the BUDHiES data, a completeness analysis was carried out to determine the number of undetected galaxies in the survey. This was done empirically by injecting artificial galaxies throughout the two survey volumes and subsequent testing of the recovery rate of these sources. The ratio of the number of inputs to the number of recoveries then provided us with the completeness factor per HI mass bin. For this purpose, a library of  $\sim 2000$  artificial galaxies was created to mimic the Local HiMF (Martin et al. 2010) in the mass range  $10^{8.5}-10^{10.5} M_{\odot}$ . These galaxies, created using the GIPSY task *galmod*, also follow standard scaling relations such as the HI mass-diameter relation (e.g. Wang et al. 2016) and the Tully-Fisher relation (Verheijen 2001). They cover the full range of inclinations and position angles. 3000 galaxies were inserted into the two data cubes following the observed large scale structure, of which 700 galaxies were above the survey detection limit ( $2 \times 10^9 M_{\odot}$ ). The same source finding scheme used for the real sources was run on these synthetic cubes, resulting in 210 and 169 recoveries for the volumes containing Abell 963 and Abell 2192, respectively. From our completeness analysis, we found that no mass bin is complete, with completeness rapidly decreasing as a function of decreasing HI mass. We also confirmed that the detectability of galaxies is dependent firstly on their position in the cube, with decreased sensitivity towards the edges due to primary beam attenuation. Secondly, the fraction of recovered face-on galaxies is larger than edge-on galaxies, confirming that highly inclined systems have a lower detection probability.

### 5.1.4 The HiMF at $z \sim 0.2$

We fit a Schechter function (Schechter 1976) to the completeness corrected mass histograms, set at 0.25 dex bin widths, with the help of a linear least square fitting method (Terlouw & Vogelaar 2016). The resultant HiMF parameters are as follows:  $\alpha = -1.49 \pm 0.48$ ,  $\log_{10}(M_{\text{HI}}^*) = 9.78 \pm 0.16 M_{\odot}$  and  $\Phi_{\text{HI}}^* = 4.9 \pm 3.2 (\times 10^{-3})$ . These results indicate large errors, caused by the degree of incompleteness of the survey, and thus do not allow for a meaningful direct comparison of the HiMF parameters with the Local HiMF (Jones et al. 2018). An analysis of the covariance between the low mass slope  $\alpha$  and the knee mass  $M_{\text{HI}}^*$  in the  $\alpha$ - $M_{\text{HI}}^*$  parameter space shows that literature HiMF studies (Zwaan et al. 2005; Jones et al. 2018; Xi et al. 2021) show similar slopes but a larger variation in the knee mass. The ALFA100 and AUDS100 parameters lie well outside the 99.9% confidence intervals of the BUDHiES parameters, while the HIPASS parameters lie within these contours.

### 5.1.5 $\Omega_{\text{HI}}$ at $z \sim 0.2$ from direct HI detections

By integrating the mass-weighted HiMF and scaling with the critical density of the Universe, one can derive the cosmic HI density,  $\Omega_{\text{HI}}$ . Due to the large uncertainties in the HiMF parameters caused by the considerable completeness corrections, particularly at lower HI masses, the resulting  $\Omega_{\text{HI}}$  estimate is not physical and thus we made some assumptions to obtain a better measurement. Of the various hypotheses tested, the assumption that the low-mass slope  $\alpha$  does not evolve with redshift was most reasonable (motivated by findings in the literature that indicate little to no evolution of  $\alpha$  at least out to  $z \sim 0.16$ ) and resulted in a self-absorption corrected  $\Omega_{\text{HI}}$  estimate of  $(3.2 \pm 0.7) \times 10^{-4}$ . With our best estimate of  $\Omega_{\text{HI}}$ , we confirm that it does not evolve notably as a function of increasing redshift out to  $z \sim 0.2$  and is consistent, within the errors, with other estimates of  $\Omega_{\text{HI}}$  derived from spectral stacking exercises (e.g., Lah et al. 2007; Rhee et al. 2013) and simulations (Davé et al. 2017) at similar redshifts. Our study provides the first attempt at measuring  $\Omega_{\text{HI}}$  at  $\sim 0.2$  with the help of direct HI detections.

### Cosmic variance and environment

BUDHiES hosts a variety of cosmic environments such as voids, clusters and other overdensities, and the two volumes clearly show the presence of large scale structure. The clusters themselves occupy only 4 per cent of the total volume within their respective radii. Along the line-of-sight, the dimensions of the survey exceed the typical observed correlation lengths. However, the quantification of cosmic variance for our survey is nontrivial, since conventional estimation methods are not applicable to the surveys at  $z \sim 0.2$ . This has been discussed in Chapter 5. Based on a popular cosmic variance calculator by Driver & Robotham (2010) constructed using the SDSS optical catalogue, we estimated a cosmic variance of 34 per cent or less for the two BUDHiES volumes. Due to the several differences between HI and optical surveys and the underlying assumptions associated with such calculators, we treat this estimate as an upper limit. In a future endeavour, our preferred method for quantifying cosmic variance is to use one of the Local blind HI surveys, e.g., ALFALFA, by projecting and slicing the survey data in a way as to mimic BUDHiES in terms of volume and depth. Cosmic variance would then correspond to the number of galaxies in each slice. This method, however, relies on the assumption that the HiMF does not evolve with redshift.

## 5.2 Future work

### 5.2.1 Giving a gas perspective to the Butcher-Oemler effect

The Butcher-Oemler effect (Butcher & Oemler 1984) is an observational effect showing an increase in the fraction of blue galaxies in cluster cores with increasing redshift. Abell 963, part of the seminal BO paper, has a blue galaxy fraction ( $f_b$ ) of 19 % as documented by Butcher & Oemler (1984). With available HI data for the BO cluster Abell 963 and the non-BO (control) cluster Abell 2192, it will be possible to provide a gas perspective of the BO effect with the help of the following additional steps:

- A consistent measurement of the blue fraction in both clusters.  $f_b$  must be remeasured for Abell 963 and then consistently measured for Abell 2192, with the help of our available INT imaging.
- Assessment of kinematic substructure within the two clusters. This can be done with the help of a Dressler-Schechtman (DS) test, consistently for the two clusters. While the substructure in Abell 963 has been studied in detail (Jaffé et al. 2013, 2015, 2016), such a detailed study has not been performed for Abell 2192. WIYN-HYDRA observations of Abell 2192 were carried out in 2019, providing us with additional new optical redshifts and these spectroscopic data await analysis.
- Morphological classification of galaxies based on visual identification. Visual classification of the galaxies detected in HI into their respective morphological types will be carried out using the available INT imaging.
- Inferring the evolutionary status of the blue galaxies in Abell 963 by analysing HI mass-to-light ( $M_{\text{HI}}/L$ ) ratios and phase-space diagrams of the two clusters.
- Comparison of the blue galaxies within Abell 963 with those in the field. The comparison can be based on the optical magnitude and colour, as well as the statistical significance of the flux densities of the stacked spectra in the cluster and field.

With this information, it will be possible to examine whether the blue galaxies in A963 are HI rich due to longer stripping timescales or higher galaxy accretion rates; whether they are HI deficient, post-starburst or back-splash systems that are no longer actively star forming; or whether previous BO studies suffered optical selection bias by preferential inclusion of clusters with bluer populations.

### 5.2.2 Ongoing and future HI surveys

Other surveys with science goals similar to ours are currently being conducted or planned for the near future. One such survey, known as the COSMOS HI Large Extragalactic Survey (CHILES; Fernández et al. 2013; Hess et al. 2019; Blue Bird et al. 2020) is already underway with the Very Large Array (VLA, B-configuration). Conducted with over 1000h of VLA time, this single-pointing survey is defined by a tier that is deeper and narrower than BUDHIES, out to  $0 < z < 0.45$ . Around 300 galaxies are expected to be detected across the surveyed redshift range. Similarly, HI studies with the Giant Metrewave Radio Telescope (GMRT) and the upgraded GMRT have already probed redshifts beyond what is currently achievable with other radio telescopes. At  $z \sim 1$ , Chowdhury et al. (2020) have provided the first  $\Omega_{\text{HI}}$  measurement based on a stacked HI emission signal by stacking the signals of 7,653 star-forming galaxies between  $0.74 < z < 1.45$ . This study was supported by a similar study using 400h of the pre-upgraded GMRT, within the redshift range  $1.18 < z < 1.39$  (Chowdhury et al. 2021).

Looking toward the future, one of the major science drivers of the upcoming Square Kilometre Array (SKA) is understanding the formation and evolution of galaxies by

exploring the evolution of their gas content, in particular, the neutral Hydrogen content. Two blind SKA precursor surveys, namely the Deep Investigation of Neutral Gas Origins (DINGO, Meyer 2009) with the Australian SKA Pathfinder (ASKAP) and the Looking At the Distant Universe with the MeerKAT Array (LADUMA, Holwerda, Blyth & Baker 2012; Blyth et al. 2016; Baker, Blyth & Holwerda 2019) will both probe redshifts beyond those currently achievable. These future surveys will be able to overcome the limitations faced with BUDHiES through larger sample sizes and volumes, higher sensitivity and better resolution of direct HI detections. DINGO is a two-tier survey consisting of DINGO-Deep ( $0 < z < 0.26$ ) and DINGO-Ultra Deep ( $0.1 < z < 0.43$ ), over multiple pointings and a total integration time of 2500h. LADUMA is the deepest SKA pathfinder survey defined, covering redshift ranges  $0 < z < 0.42$  with the L-band receivers,  $0.42 < z < 0.58$  where L-band and UHF band receivers overlap, and  $0.58 < z < 1.45$  with the UHF band receivers. Despite the severity of RFI at lower frequencies, they will still be able to detect more galaxies than previously possible.

With these powerful facilities, it will finally be possible to detect fainter galaxies in HI at higher redshifts, allowing the constraint of the low-mass slope of the HiMF, which was not achievable with BUDHiES due to the higher detection limit of the survey along with a large degree of incompleteness at the low-mass end. In addition, they will be able to detect  $M_{\text{HI}}^*$  galaxies throughout most of the surveyed redshift range. In conjunction with the availability of multi-wavelength data, we will not only obtain clearer insights into the redshift evolution of the HiMF but also in its dependence on environment and cosmic variance.

In addition to the HiMF it will also be possible to measure  $\Omega_{\text{HI}}$  through direct detections and stacking. DINGO predicts HIPASS-like errors on the measurement of  $\Omega_{\text{HI}}$  out to  $z \sim 0.43$ , while LADUMA will be able to shed further light on the evolution of the  $\Omega_{\text{HI}}$  out to  $z \sim 1.4$  through direct emission studies and stacking of thousands of optically selected galaxies. It will also provide much needed insight into absorber incidence statistics by probing the connection between CaII and MgII absorption and gas content, which is needed for constraining  $\Omega_{\text{HI}}$  beyond  $z \sim 0.5$ .

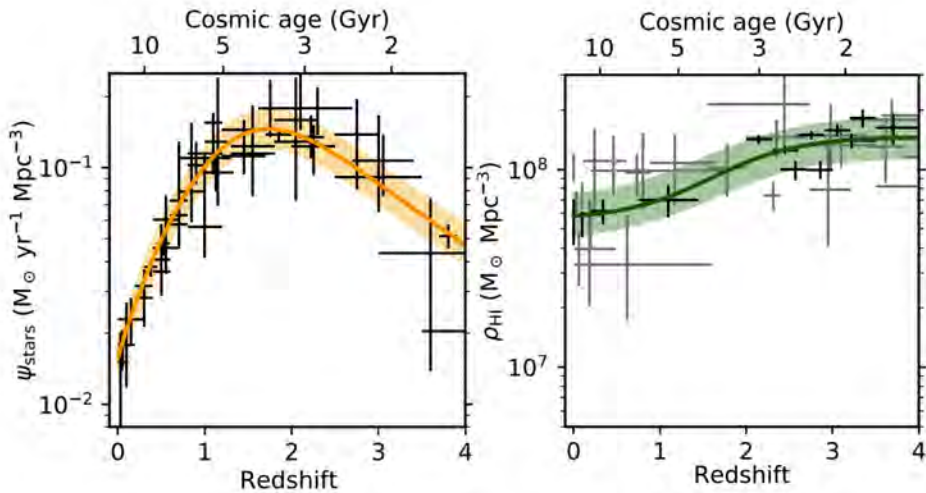
One of the limitations faced in our work on the HI-based TFr and BTFR was that the mass and magnitude range of the BUDHiES TFr sample was not large enough to accurately constrain the slope of the TFr. These upcoming pathfinder surveys will be able to overcome these limitations, through a combination of statistically significant samples over varied mass ranges and available high resolution ancillary optical imaging. Moreover, spatially resolved HI will provide more accurate inclination measurements as well as rotational velocities of galaxies, thus providing more robust TFrs and BTFRs at higher redshifts.

Until the launch of SKA-1, these ongoing and future precursor HI surveys will help bridge the gap between direct HI measurements at  $z \sim 0$  and indirect measurements beyond  $z \sim 1$ . Finally, SKA-1 will deliver unprecedented insights into the distant universe and the role of gas in galaxy evolution.

## Nederlandse Samenvatting

### Motivatie

Dankzij verscheidene methoden die zijn ontwikkeld door astronomen om de veranderende eigenschappen van sterrenstelsels over het verloop van kosmische tijd in kaart te brengen, is inzicht verkregen in de wijze waarop sterrenstelsels zijn ontstaan en welke fysische processen hebben geleid tot de huidige eigenschappen. Met name in de afgelopen decennia heeft het beschikbaar komen van nieuwe gegevens, afkomstig van waarnemingen op verschillende golflengtes, tot nieuwe inzichten geleid. In het kosmologisch  $\Lambda$ CDM model wordt uitgegaan van het idee van de aanwezigheid van donkere materie, waarvan wordt aangenomen dat deze het merendeel van de materie in het heelal uitmaakt. Het model beschrijft een hiërarchisch scenario voor structuurvorming waarin wordt beschreven hoe sterrenstelsels zijn gevormd en geëvolueerd binnen concentraties van donkere materie (zogenoemde potentiaalputten of halo's van donkere materie) door het smelten van kleinere, minder complexe systemen. De eigenschappen van sterrenstelsels worden conform dit model bepaald door hun intrinsieke kenmerken (nature) enerzijds en de invloed van de omgeving waarin ze zich bevinden (nurture) anderzijds. Eén van de belangrijkste factoren in de evolutie van sterrenstelsels is de kosmische stervormingssnelheid (Star Formation Rate - SFR). Studies tonen aan dat de mate waarin sterren worden gevormd, exponentieel met een factor  $\sim 10$ , (is afgenomen sinds  $z \sim 1.9$ , hetgeen overeenkomt met  $\sim 3.4$  miljard jaar sinds de oerknal). Verschillende andere eigenschappen van sterrenstelsels blijken op een vergelijkbare manier te zijn geëvolueerd als de SFR. Over de evolutie van het gehalte aan koud gas, met name het gehalte aan atomaire waterstof (HI), dat van essentieel belang is voor de stervorming, is evenwel weinig bekend als gevolg van de beperkingen van waarnemingen van neutraal waterstof wanneer er verder wordt teruggekeken in de tijd. Te verwachten zou zijn dat het atomaire waterstofgehalte op dezelfde wijze zou evolueren als de SFR, maar het blijkt dat het atomaire waterstofgehalte veel geleidelijker afneemt. Dit blijkt uit figuur 5.1, die de evolutie toont van de kosmische SFR (links) en atomaire waterstof dichtheid (rechts). Teneinde het verband tussen de SFR en het koude atomaire gas beter te kunnen verklaren, is het noodzakelijk om de evolutie van HI buiten het lokale heelal beter in kaart te brengen. Een andere belangrijke factor in de evolutie van sterrenstelsels is de evolutie

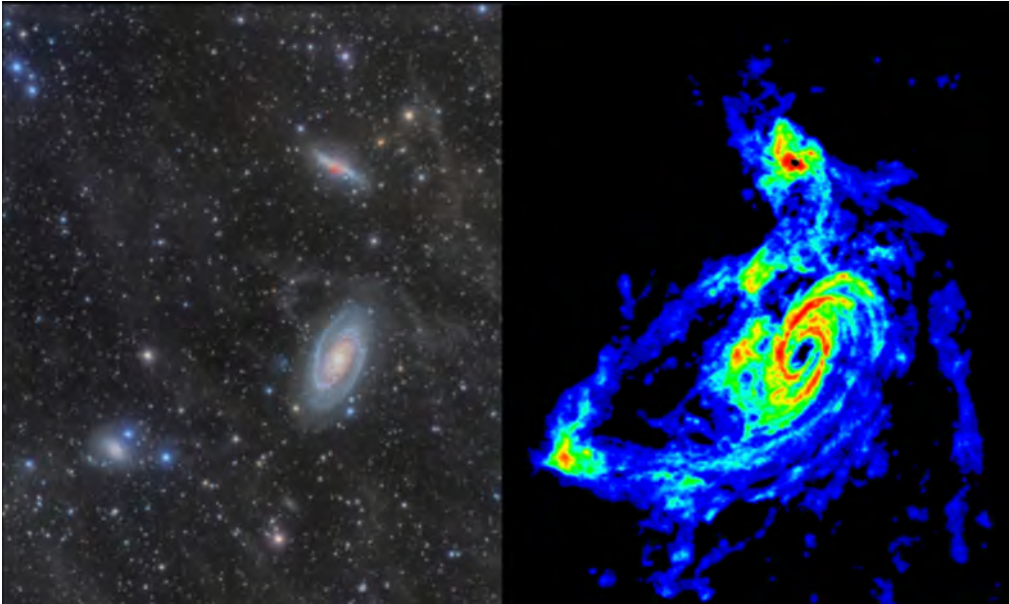


**Figuur 5.1** – Links: De evolutie van de kosmische stervormingssnelheid met een piek bij roodverschuiving 2. Rechts: De evolutie van de atomaire waterstof: Evolutie van atomaire waterstof, die niet dezelfde trend volgt als de SFR. De figuren zijn ontleend aan Walter et al. (2020) en beschreven in Fig. 1.1 van hoofdstuk 1.

van zogenaamde schalingsrelaties. Dit zijn empirisch waargenomen verbanden tussen de eigenschappen van sterrenstelsels, op grond waarvan hun natuurlijke eigenschappen kunnen worden omschreven. Vooral op hogere roodverschuivingen (wanneer er verder wordt teruggekeken in de tijd) is het meten van deze schalingsrelaties tussen de algemene eigenschappen van sterrenstelsels een van de hoofddoelen van grote waarneemprojecten geweest. Of en in hoeverre deze schalingsrelaties over het verloop van de kosmische tijd evolueren, is nog steeds de vraag. Het begrijpen van de spreiding en andere statistische eigenschappen van deze schalingsrelaties is van essentieel belang voor het ijken van theoretische modellen die de vorming en evolutie van sterrenstelsels beschrijven.

## Een HI perspectief op de evolutie van sterrenstelsels

De studie van atomaire waterstof (HI) heeft een revolutie teweeggebracht in het begrip van de vorming en evolutie van sterrenstelsels door ook de omgevingsfactoren in acht te nemen. Een bekend voorbeeld waarin de inzichten uit waarnemingen van het HI gas worden geïllustreerd, is de studie van de M81-groep, te zien in fig 5.2. Links is een optisch beeld te zien van een schijnbaar geïsoleerde groep van sterrenstelsels, met M81 in het midden. Rechts is het HI beeld van hetzelfde veld te zien, waaruit blijkt dat deze groep in feite zeer interactief is. HI schijven van sterrenstelsels reiken over het algemeen veel verder dan optische, stellaire schijven, zelfs tot ver in de halo van



**Figuur 5.2** – De M81 groep van sterrenstelsels: links, het optische beeld (foto credit: Jordi Gallego, APOD) en rechts, het beeld van de HI (de Blok et al. 2018). Met dank aan Thijs van der Hulst.

donkere materie, en blijken zodoende uiterst gevoelige tracers van omgevingseffecten te zijn. Daarnaast geeft HI ook de meest robuuste indicatie van de rotatiesnelheid van de halo van donkere materie waarin sterrenstelsels zijn ingebed, en waardoor op HI gebaseerde schalingsrelaties de meest accurate weergave van de onderliggende natuurkunde zijn. Het enige nadeel van HI is de intrinsieke zwakte van haar signaal, waardoor het aantal studies waarin ook gebieden buiten het lokale heelal worden meegenomen, beperkt is. Dit vanwege de lange integratietijden die radio telescopen nodig hebben en de aanzienlijke toename van radiofrequentie-interferentie (RFI) bij lagere frequenties. Om deze reden zijn er tot op heden maar weinig blinde studies uitgevoerd.

## Dit proefschrift

De gegevens die in dit proefschrift worden gebruikt zijn afkomstig van de Blind Ultra-Deep HI Environmental Survey (BUDHIES), uitgevoerd met de Westerbork Synthese Radio Telescoop (WSRT) tussen 2005 en 2008. De twee waarneembieden aan de hemel zijn elk gecentreerd op een cluster van sterrenstelsels, samen met hun grootschalige structuren op de voor- en achtergrond.

Het onderzoek bestrijkt een roodverschuivingsgebied van  $0,164 < z < 0,224$ , hetgeen overeenkomt met een terugbliktijd van  $2,04 < t_{\text{lookback}} [\text{Gyr}] < 2,68$ . Op zulke afstanden zijn blinde waarnemingen door de intrinsieke zwakte van het signaal tijds-

arbeidsintensief. Met een totale integratietijd van 2000 uur is dit een van de weinige HI studies op een dergelijke roodverschuiving en met een blik op sterrenstelsels die zich in verschillende kosmische omgevingen bevinden. In de toekomst zullen gegevens van lopende onderzoeken zoals CHILES en LADUMA beschikbaar komen. Naast de HI gegevens zijn er ook optische beelden verkregen in de B- en R-band met de Isaac Newton Telescope (INT) op La Palma. Bovendien zijn met de GALaxy Evolution eXplorer (GALEX) satelliet ook nabij- en ver-UltraViolet waarnemingen van de twee velden verricht. Deze ondersteunende data van de INT en GALEX zijn gebruikt bij de identificatie van de stellaire tegenhangers van de HI detecties. Gedetailleerde informatie over de gegevensverwerking en bronopsporing van de HI waarnemingen wordt uiteengezet in hoofdstuk 2.

In hoofdstuk 3 wordt een populaire schalingsrelatie, de zogeheten Tully-Fisher relatie (TFR), in beschouwing genomen. De TFR correleert de rotatiesnelheden van sterrenstelsels met hun lichtkracht. Er wordt gesproken van de Baryonische TFR (BTFR) als de lichtkracht en de hoeveelheid gas vertaald worden naar de massa van de totale hoeveelheid direct waarneembare materie in sterrenstelsels. Rotatiesnelheden die zijn afgeleid van HI-waarnemingen van sterrenstelsels bieden de beste benadering van de rotatiesnelheden van de halo's van donkere materie van deze sterrenstelsels. Omdat er evenwel bij hogere roodverschuivingen geen HI-waarnemingen beschikbaar zijn, wordt doorgaans gebruik gemaakt van andere, vaak minder robuuste tracers van de rotatiesnelheid, hetgeen in de literatuur heeft geleid tot omstreden resultaten betreffende de evolutie in de (B)TFR. Hoofdstuk 3 omvat de eerste HI studie die uitsluitend is gewijd aan de TFR buiten het lokale heelal ( $z \sim 0,2$ ). Met behulp van een zorgvuldig samengestelde collectie van sterrenstelsels die in aanmerking komen voor een robuuste TFR-analyse, werd een geringe evolutie in de TFR aangetroffen maar geen enkele evolutie in de BTFR in vergelijking met een overeenkomstige verzameling sterrenstelsels in het lokale heelal.

Hoofdstuk 4 betreft de meting van de HI-massafunctie (HiMF) en de kosmische dichtheid van HI ( $\Omega_{\text{HI}}$ ) op  $z \sim 0,2$ . Kort gezegd geeft de HiMF de verdelingsfunctie weer van de HI-massa's van sterrenstelsels op een bepaalde kosmische tijd. Hoewel de HiMF in het lokale heelal goed is te bepalen, is er weinig bekend over de evolutie ervan bij hogere roodverschuivingen. Door alle massa's in de HiMF bij elkaar op te tellen, kan de kosmische HI dichtheid ( $\Omega_{\text{HI}}$ ) worden afgeleid. Buiten het lokale heelal wordt de dichtheid doorgaans op andere, indirecte manieren afgeleid. In dit proefschrift wordt voor het eerst een poging gedaan om de HiMF te construeren en de  $\Omega_{\text{HI}}$  te meten door middel van directe HI detecties bij  $z \sim 0,2$  ( $t_{\text{lookback}} \sim 2,5$  Gyrs). Uit de verkregen resultaten blijkt dat de onzekerheden in de HiMF parameters groot zijn en dat daarom geen directe vergelijking met de lokale HiMF kan worden gemaakt. De reden hiervoor is dat bij  $z \sim 0,2$  de gevoeligheid van de waarnemingen aanzienlijk afneemt voor sterrenstelsels met een lagere massa. Desondanks blijkt dat van de drie HiMF parameters de gemeten afwijking het grootst is voor de karakteristieke HI massa,  $M_{\text{HI}}^*$  in vergelijking met andere, overeenkomende studies in het lokale heelal. De verkregen resultaten uit de meting van  $\Omega_{\text{HI}}$  tonen geen noemenswaardige evolutie tot  $z \sim 0,2$ , hetgeen in overeenstemming is met andere indirecte  $\Omega_{\text{HI}}$  metingen en theoretische voorspellingen op vergelijkbare roodverschuivingen.

## Toekomstige onderzoeken

Verdere waarneemprojecten met vergelijkbare wetenschappelijke doelstellingen worden thans uitgevoerd of staan gepland voor de nabije toekomst. Een hiervan is de COSMOS HI Large Extragalactic Survey (CHILES) welke onlangs is voltooid met de Very Large Array (VLA), en  $0 < z < 0.45$  omvat. Op dezelfde wijze zijn er met de upgraded Giant Metrewave Radio Telescope (uGMRT) al waarnemingen gedaan op roodverschuivingen die verder reiken dan wat momenteel mogelijk is met andere radiotelescopen. Met het oog op de verdere toekomst dient de Square Kilometre Array (SKA) te worden genoemd. Eén van de belangrijkste wetenschappelijke drijfveren van dit instrument is het begrijpen van de vorming en de evolutie van sterrenstelsels door de evolutie van hun gasgehalte te onderzoeken, in het bijzonder de hoeveelheid atomair waterstofgas. Twee blind opgezette, voorbereidende onderzoeken, namelijk de Deep Investigation of Neutral Gas Origins (DINGO) met de Australische SKA Pathfinder (ASKAP) en Looking At the Distant Universe with the MeerKAT Array (LADUMA), beogen onderzoek te doen op roodverschuivingen die verder reiken dan momenteel haalbaar is. Naar verwachting zullen deze toekomstige onderzoeken de huidige onzekerheden in de BUDHIES kunnen verkleinen met behulp van grotere verzamelingen sterrenstelsels uit grotere volumes, met een grotere gevoeligheid en een betere resolutie van de directe HI detecties. Op deze wijze zal er, in samenhang met het beschikbaar komen van gegevens op verschillende golflengtes, niet alleen een duidelijker inzicht worden verkregen in de ontwikkeling van de HiMF op hoge roodverschuiving, maar ook in de relatie hiervan met de omgeving van sterrenstelsels en de kosmische variatie in hun verdeling in het heelal.

In dit proefschrift zijn enkele belangrijke aspecten van de evolutie van sterrenstelsels onderzocht, met behulp van unieke, diepe waarnemingen van de 21 cm spectraallijn van atomair waterstofgas, 2,5 miljard jaar in het verleden. Doel was om een referentiekader te bieden voor toekomstige, blind opgezette waarneemprojecten van HI gas in sterrenstelsels die vergelijkbare wetenschappelijke doelstellingen hebben.



## Bibliography

- Abazajian K. N. et al., 2009, ApJS, 182, 543  
Abell G. O., 1958, ApJS, 3, 211  
Allen S. W., Schmidt R. W., Fabian A. C., Ebeling H., 2003, MNRAS, 342, 287  
Allison J. R. et al., 2020, MNRAS, 494, 3627  
Andreon S., Lobo C., Iovino A., 2004, MNRAS, 349, 889  
Andreon S., Quintana H., Tajer M., Galaz G., Surdej J., 2006, Monthly Notices of the Royal Astronomical Society, 365, 915  
Aragón-Salamanca A., Bedregal A. G., Merrifield M. R., 2006, A&A, 458, 101  
Bahé Y. M., McCarthy I. G., Balogh M. L., Font A. S., 2013, MNRAS, 430, 3017  
Baker A. J., Blyth S., Holwerda B., 2019, in American Astronomical Society Meeting Abstracts, Vol. 233, American Astronomical Society Meeting Abstracts #233, p. 333.01  
Baldry I. K. et al., 2002, ApJ, 569, 582  
Balogh M. L., Morris S. L., Yee H. K. C., Carlberg R. G., Ellingson E., 1999, ApJ, 527, 54  
Balogh M. L., Navarro J. F., Morris S. L., 2000, ApJ, 540, 113  
Bamford S. P., Aragón-Salamanca A., Milvang-Jensen B., 2006, MNRAS, 366, 308  
Bamford S. P., Milvang-Jensen B., Aragón-Salamanca A., Simard L., 2005, MNRAS, 361, 109  
Becker R. H., White R. L., Helfand D. J., 1995, ApJ, 450, 559  
Bedregal A. G., Aragón-Salamanca A., Merrifield M. R., 2006, MNRAS, 373, 1125  
Bekki K., Couch W. J., Shioya Y., 2002, ApJ, 577, 651  
Bell E. F., Zheng X. Z., Papovich C., Borch A., Wolf C., Meisenheimer K., 2007, ApJ, 663, 834  
Bera A., Kanekar N., Chengalur J. N., Bagla J. S., 2019, ApJ, 882, L7  
Bera A., Kanekar N., Weiner B. J., Sethi S., Dwarakanath K. S., 2018, ApJ, 865, 39  
Berrier J. C., Stewart K. R., Bullock J. S., Purcell C. W., Barton E. J., Wechsler R. H., 2009, ApJ, 690, 1292  
Bianconi M., Smith G. P., Haines C. P., McGee S. L., Finoguenov A., Egami E., 2018, MNRAS, 473, L79

- 
- Bigiel F., Leroy A., Walter F., Brinks E., de Blok W. J. G., Madore B., Thornley M. D., 2008, *AJ*, 136, 2846
- Bird S., Garnett R., Ho S., 2017, *MNRAS*, 466, 2111
- Blue Bird J. et al., 2020, *MNRAS*, 492, 153
- Blyth S. et al., 2016, in *MeerKAT Science: On the Pathway to the SKA*, p. 4
- Böhm A., Ziegler B. L., 2016, *A&A*, 592, A64
- Böhm A. et al., 2004, *A&A*, 420, 97
- Böhringer H., Briel U. G., Schwarz R. A., Voges W., Hartner G., Trümper J., 1994, *Nature*, 368, 828
- Bond J. R., Kofman L., Pogosyan D., 1996, *Nature*, 380, 603
- Boruah S. S., Hudson M. J., Lavaux G., 2020, *MNRAS*, 498, 2703
- Bottinelli L., Gouguenheim L., Fouque P., Paturel G., 1990, *A&AS*, 82, 391
- Bouwens R. J. et al., 2014, *ApJ*, 795, 126
- , 2015, *ApJ*, 803, 34
- Briggs F. H., 1990, *AJ*, 100, 999
- Broeils A. H., 1992, PhD thesis, -
- Broeils A. H., Rhee M. H., 1997, *A&A*, 324, 877
- Busekool E., Verheijen M. A. W., van der Hulst J. M., Tully R. B., Trentham N., Zwaan M. A., 2021, *MNRAS*, 501, 2608
- Butcher H., Oemler, Jr. A., 1984, *ApJ*, 285, 426
- Cappellari M. et al., 2011a, *MNRAS*, 413, 813
- , 2011b, *MNRAS*, 416, 1680
- Carilli C. L., Walter F., 2013, *ARA&A*, 51, 105
- Casertano S., van Gorkom J. H., 1991, *AJ*, 101, 1231
- Catinella B., Cortese L., 2015, *MNRAS*, 446, 3526
- Catinella B., Haynes M. P., Giovanelli R., Gardner J. P., Connolly A. J., 2008, *ApJ*, 685, L13
- Catinella B. et al., 2012, *MNRAS*, 420, 1959
- Cautun M., van de Weygaert R., Jones B. J. T., Frenk C. S., 2014, *MNRAS*, 441, 2923
- Chen Q., Meyer M., Popping A., Staveley-Smith L., 2021, *MNRAS*, 502, 2308
- Chilingarian I. V., Melchior A.-L., Zolotukhin I. Y., 2010, *MNRAS*, 405, 1409
- Chowdhury A., Kanekar N., Chengalur J. N., Sethi S., Dwarakanath K. S., 2020, *Nature*, 586, 369
- Chowdhury A., Kanekar N., Das B., Dwarakanath K. S., Sethi S., 2021, *ApJ*, 913, L24
- Chung A., van Gorkom J. H., Kenney J. D. P., Crowl H., Vollmer B., 2009, *AJ*, 138, 1741
- Coia D. et al., 2005, *A&A*, 431, 433
- Cole S., Lacey C. G., Baugh C. M., Frenk C. S., 2000, *MNRAS*, 319, 168
- Colless M. et al., 2001, *MNRAS*, 328, 1039
- Condon J. J., 1992, *ARA&A*, 30, 575
- Conselice C. J., Bundy K., Ellis R. S., Brichmann J., Vogt N. P., Phillips A. C., 2005, *ApJ*, 628, 160
- Cook D. O. et al., 2014, *MNRAS*, 445, 890
- Cortese L. et al., 2014, *ApJ*, 795, L37
- Couch W. J., Barger A. J., Smail I., Ellis R. S., Sharples R. M., 1998, *ApJ*, 497, 188
- Couch W. J., Ellis R. S., Sharples R. M., Smail I., 1994, *ApJ*, 430, 121
- Couch W. J., Sharples R. M., 1987, *MNRAS*, 229, 423
- Covington M. D. et al., 2010, *ApJ*, 710, 279
- Crain R. A. et al., 2017, *MNRAS*, 464, 4204

- , 2015, *MNRAS*, 450, 1937
- Crighton N. H. M. et al., 2015, *MNRAS*, 452, 217
- Cybulski R. et al., 2016, *MNRAS*, 459, 3287
- Davé R., Crain R. A., Stevens A. R. H., Narayanan D., Saintonge A., Catinella B., Cortese L., 2020, *MNRAS*, 497, 146
- Davé R., Rafieerantsoa M. H., Thompson R. J., Hopkins P. F., 2017, *MNRAS*, 467, 115
- Davis T. A. et al., 2011, *MNRAS*, 414, 968
- de Blok W. J. G., Walter F., 2014, *AJ*, 147, 96
- de Blok W. J. G. et al., 2018, *ApJ*, 865, 26
- , 2016, *AJ*, 152, 51
- De Lucia G., Blaizot J., 2007, *MNRAS*, 375, 2
- De Lucia G., Weinmann S., Poggianti B. M., Aragón-Salamanca A., Zaritsky D., 2012, *MNRAS*, 423, 1277
- De Propris R. et al., 2014, *Monthly Notices of the Royal Astronomical Society*, 444, 2200
- De Propris R. et al., 2004, *MNRAS*, 351, 125
- Decarli R. et al., 2020, *ApJ*, 902, 110
- , 2019, *ApJ*, 882, 138
- Dekel A. et al., 2009, *Nature*, 457, 451
- Delhaize J., Meyer M. J., Staveley-Smith L., Boyle B. J., 2013, *MNRAS*, 433, 1398
- den Heijer M. et al., 2015, *A&A*, 581, A98
- Dénes H., Kilborn V. A., Koribalski B. S., 2014, *MNRAS*, 444, 667
- Di Teodoro E. M., Fraternali F., Miller S. H., 2016, *A&A*, 594, A77
- Dickey J. M., Kazes I., 1992, *ApJ*, 393, 530
- Djorgovski S., Davis M., 1987, *ApJ*, 313, 59
- Dressler A., 1980, *ApJ*, 236, 351
- Dressler A., Lynden-Bell D., Burstein D., Davies R. L., Faber S. M., Terlevich R., Wegner G., 1987, *ApJ*, 313, 42
- Dressler A. et al., 1997, *ApJ*, 490, 577
- Driver S. P. et al., 2011, *MNRAS*, 413, 971
- Driver S. P., Robotham A. S. G., 2010, *MNRAS*, 407, 2131
- Duc P. A. et al., 2002, *A&A*, 382, 60
- Dutton A. A., van den Bosch F. C., Dekel A., Courteau S., 2007, *ApJ*, 654, 27
- Dutton A. A. et al., 2011, *MNRAS*, 410, 1660
- Efstathiou G., Sutherland W. J., Maddox S. J., 1990, *Nature*, 348, 705
- El-Badry K. et al., 2018, *MNRAS*, 477, 1536
- Ellingson E., Lin H., Yee H. K. C., Carlberg R. G., 2001, *ApJ*, 547, 609
- Ellison S. L., Yan L., Hook I. M., Pettini M., Wall J. V., Shaver P., 2001, *A&A*, 379, 393
- Elson E. C., Blyth S. L., Baker A. J., 2016, *MNRAS*, 460, 4366
- Faber S. M., Jackson R. E., 1976, *ApJ*, 204, 668
- Farouki R., Shapiro S. L., 1980, *ApJ*, 241, 928
- Fasano G., Poggianti B. M., Couch W. J., Bettoni D., Kjærgaard P., Moles M., 2000, *ApJ*, 542, 673
- Fernández X. et al., 2013, *ApJ*, 770, L29
- Fernandez X., van Gorkom J. H., Momjian E., Chiles Team, 2015, in *American Astronomical Society Meeting Abstracts*, Vol. 225, American Astronomical Society Meeting Abstracts #225, p. 427.03

- 
- Ferreras I., Silk J., 2001, *ApJ*, 557, 165  
Ferreras I., Silk J., Böhm A., Ziegler B., 2004, *MNRAS*, 355, 64  
Finkelstein S. L. et al., 2015, *ApJ*, 810, 71  
Fisher J. R., Tully R. B., 1981, *ApJS*, 47, 139  
Flores H., Hammer F., Puech M., Amram P., Balkowski C., 2006, *A&A*, 455, 107  
Förster Schreiber N. M., Wuyts S., 2020, *ARA&A*, 58, 661  
Franx M., de Zeeuw T., 1992, *ApJ*, 392, L47  
Fujita Y., 2004, *PASJ*, 56, 29  
Giovannelli R. et al., 2005, *AJ*, 130, 2598  
Glowacki M., Elson E., Davé R., 2020, arXiv e-prints, arXiv:2011.08866  
—, 2021, *MNRAS*, 507, 3267  
Gnedin N. Y., 1996, *ApJ*, 456, 1  
Gogate A. R., Verheijen M. A. W., Deshev B. Z., van Gorkom J. H., Montero-Castaño M., van der Hulst J. M., Jaffé Y. L., Poggianti B. M., 2020, *MNRAS*, 496, 3531  
Gómez P. L. et al., 2003, *ApJ*, 584, 210  
Greisen E. W., 1990, in *Acquisition, Processing and Archiving of Astronomical Images*, Longo G., Sedmak G., eds., pp. 125–142  
Grogin N. A., Geller M. J., 1999, *AJ*, 118, 2561  
—, 2000, *AJ*, 119, 32  
Gruppioni C. et al., 2015, *MNRAS*, 451, 3419  
—, 2013, *MNRAS*, 432, 23  
Gunn J. E., Gott, III J. R., 1972, *ApJ*, 176, 1  
Gupta N. et al., 2021, *ApJ*, 907, 11  
Haines C. P. et al., 2018, *MNRAS*, 477, 4931  
—, 2015, *ApJ*, 806, 101  
—, 2009, *ApJ*, 704, 126  
Han S., Smith R., Choi H., Cortese L., Catinella B., Contini E., Yi S. K., 2018, *ApJ*, 866, 78  
Haynes M. P. et al., 2011, *AJ*, 142, 170  
Henry J. P., Lavery R. J., 1984, *ApJ*, 280, 1  
Hess K. M. et al., 2019, *MNRAS*, 484, 2234  
Ho L. C., 2007, *ApJ*, 669, 821  
Holmberg E., 1941, *ApJ*, 94, 385  
Holwerda B. W., Blyth S. L., Baker A. J., 2012, in *The Spectral Energy Distribution of Galaxies - SED 2011*, Tuffs R. J., Popescu C. C., eds., Vol. 284, pp. 496–499  
Hopkins A. M., 2004, *ApJ*, 615, 209  
Hopkins A. M., Beacom J. F., 2006, *ApJ*, 651, 142  
Hoppmann L., Staveley-Smith L., Freudling W., Zwaan M. A., Minchin R. F., Calabretta M. R., 2015, *MNRAS*, 452, 3726  
Hu W. et al., 2019, *MNRAS*, 489, 1619  
Huang S., Haynes M. P., Giovannelli R., Brinchmann J., 2012, *ApJ*, 756, 113  
Huchra J. P. et al., 2012, *ApJS*, 199, 26  
Hwang H. S., Geller M. J., Diaferio A., Rines K. J., Zahid H. J., 2014, *ApJ*, 797, 106  
Jaffé Y. L., Aragón-Salamanca A., De Lucia G., Jablonka P., Rudnick G., Saglia R., Zaritsky D., 2011a, *MNRAS*, 410, 280  
Jaffé Y. L. et al., 2011b, *MNRAS*, 417, 1996  
—, 2014, *MNRAS*, 440, 3491  
—, 2018, *MNRAS*, 476, 4753  
Jaffé Y. L., Poggianti B. M., Verheijen M. A. W., Deshev B. Z., van Gorkom J. H.,

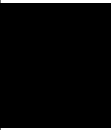
- 2012, *ApJ*, 756, L28
- Jaffé Y. L., Poggianti B. M., Verheijen M. A. W., Deshev B. Z., van Gorkom J. H., 2013, *MNRAS*, 431, 2111
- Jaffé Y. L., Smith R., Candlish G. N., Poggianti B. M., Sheen Y.-K., Verheijen M. A. W., 2015, *MNRAS*, 448, 1715
- Jaffé Y. L. et al., 2016, *MNRAS*, 461, 1202
- Jones M. G., Haynes M. P., Giovanelli R., Moorman C., 2018, *MNRAS*, 477, 2
- Jones M. G., Papastergis E., Haynes M. P., Giovanelli R., 2016, *Monthly Notices of the Royal Astronomical Society*, 457, 4393
- Jorgenson R. A., Wolfe A. M., Prochaska J. X., Lu L., Howk J. C., Cooke J., Gawiser E., Gelino D. M., 2006, *ApJ*, 646, 730
- Kanekar N., Sethi S., Dwarakanath K. S., 2016, *ApJ*, 818, L28
- Kannappan S. J., Fabricant D. G., Franx M., 2002, *AJ*, 123, 2358
- Kapferer W., Sluka C., Schindler S., Ferrari C., Ziegler B., 2009, *A&A*, 499, 87
- Kashibadze O. G., 2008, *Astrophysics*, 51, 336
- Kassin S. A. et al., 2007, *ApJ*, 660, L35
- Kauffmann G. et al., 2003, *MNRAS*, 341, 54
- Kawata D., Mulchaey J. S., 2008, *ApJ*, 672, L103
- Kennicutt, Robert C. J., 1998, *ARA&A*, 36, 189
- Kennicutt R. C., Evans N. J., 2012, *ARA&A*, 50, 531
- Kim H.-S., Wyithe J. S. B., Power C., Park J., Lagos C. d. P., Baugh C. M., 2015, *MNRAS*, 453, 2315
- Kourkchi E. et al., 2020, *ApJ*, 902, 145
- Kreckel K., Platen E., Aragón-Calvo M. A., van Gorkom J. H., van de Weygaert R., van der Hulst J. M., Beygu B., 2012, *AJ*, 144, 16
- Kreckel K. et al., 2011, *AJ*, 141, 4
- Kroupa P., 2001, *MNRAS*, 322, 231
- Lagos C. D. P., Baugh C. M., Zwaan M. A., Lacey C. G., Gonzalez-Perez V., Power C., Swinbank A. M., van Kampen E., 2014, *MNRAS*, 440, 920
- Lah P. et al., 2007, *MNRAS*, 376, 1357
- Lapi A. et al., 2011, *ApJ*, 742, 24
- Larson R. B., Tinsley B. M., Caldwell C. N., 1980, *ApJ*, 237, 692
- Lavery R. J., Henry J. P., 1986, *ApJ*, 304, L5
- Lavezzi T. E., Dickey J. M., 1998, *AJ*, 116, 2672
- Lelli F., McGaugh S. S., Schombert J. M., 2016, *ApJ*, 816, L14
- Lelli F., McGaugh S. S., Schombert J. M., Desmond H., Katz H., 2019, *MNRAS*, 484, 3267
- Lequeux J., Peimbert M., Rayo J. F., Serrano A., Torres-Peimbert S., 1979, *A&A*, 500, 145
- Lerchster M. et al., 2011, *MNRAS*, 411, 2667
- Lewis I. et al., 2002, *MNRAS*, 334, 673
- Lilly S. J., Le Fevre O., Hammer F., Crampton D., 1996, *ApJ*, 460, L1
- Lubin L. M., 1996, *AJ*, 112, 23
- Lupton R., 2005
- Macciò A. V., Udrescu S. M., Dutton A. A., Obreja A., Wang L., Stinson G. R., Kang X., 2016, *MNRAS*, 463, L69
- Madau P., Dickinson M., 2014, *ARA&A*, 52, 415
- Madau P., Ferguson H. C., Dickinson M. E., Giavalisco M., Steidel C. C., Fruchter A., 1996, *MNRAS*, 283, 1388

- 
- Magnelli B. et al., 2015, *A&A*, 573, A45  
Mahajan S., Raychaudhury S., Pimblet K. A., 2012, *MNRAS*, 427, 1252  
Maier C. et al., 2016, *A&A*, 590, A108  
Margoniner V. E., de Carvalho R. R., 2000, *AJ*, 119, 1562  
Martin A. M., Papastergis E., Giovanelli R., Haynes M. P., Springob C. M., Stierwalt S., 2010, *ApJ*, 723, 1359  
Martin D. C. et al., 2005, *ApJ*, 619, L1  
Martinsson T. P. K., Verheijen M. A. W., Bershadsky M. A., Westfall K. B., Andersen D. R., Swaters R. A., 2016, *A&A*, 585, A99  
McGaugh S. S., Schombert J. M., Bothun G. D., de Blok W. J. G., 2000, *ApJ*, 533, L99  
McGee S. L., Balogh M. L., Bower R. G., Font A. S., McCarthy I. G., 2009, *MNRAS*, 400, 937  
Meyer M., 2009, in *Panoramic Radio Astronomy: Wide-field 1-2 GHz Research on Galaxy Evolution*, p. 15  
Meyer M., Robotham A., Obreschkow D., Westmeier T., Duffy A. R., Staveley-Smith L., 2017, *PASA*, 34, 52  
Milvang-Jensen B., Aragón-Salamanca A., Hau G. K. T., Jørgensen I., Hjorth J., 2003, *MNRAS*, 339, L1  
Mocz P., Green A., Malacari M., Glazebrook K., 2012, *MNRAS*, 425, 296  
Moore B., Katz N., Lake G., Dressler A., Oemler A., 1996, *Nature*, 379, 613  
Moorman C. M., Vogeley M. S., Hoyle F., Pan D. C., Haynes M. P., Giovanelli R., 2014, *MNRAS*, 444, 3559  
Morrissey P. et al., 2007, arXiv e-prints, arXiv:0706.0755  
Moster B. P., Somerville R. S., Newman J. A., Rix H.-W., 2011, *ApJ*, 731, 113  
Nakamura O., Aragón-Salamanca A., Milvang-Jensen B., Arimoto N., Ikuta C., Bamford S. P., 2006, *MNRAS*, 366, 144  
Navarro J. F., Steinmetz M., 2000, *ApJ*, 538, 477  
Neeleman M., Prochaska J. X., Ribaudo J., Lehner N., Howk J. C., Rafelski M., Kanekar N., 2016, *ApJ*, 818, 113  
Noeske K. G. et al., 2007, *ApJ*, 660, L43  
Noordermeer E., van der Hulst J. M., Sancisi R., Swaters R. A., van Albada T. S., 2005, *A&A*, 442, 137  
Noordermeer E., Verheijen M. A. W., 2007, *MNRAS*, 381, 1463  
Noterdaeme P. et al., 2012, *A&A*, 547, L1  
Noterdaeme P., Petitjean P., Ledoux C., Srianand R., 2009, *A&A*, 505, 1087  
Obreschkow D., Croton D., De Lucia G., Khochfar S., Rawlings S., 2009, *ApJ*, 698, 1467  
Obreschkow D., Meyer M., 2014, arXiv e-prints, arXiv:1406.0966  
Oman K. A., Hudson M. J., Behroozi P. S., 2013, *MNRAS*, 431, 2307  
Oosterloo T., van Gorkom J., 2005, *A&A*, 437, L19  
Owers M. S. et al., 2019, *ApJ*, 873, 52  
Pavesi R. et al., 2018, *ApJ*, 864, 49  
Pearson W. J. et al., 2019, *A&A*, 631, A51  
Peng C. Y., Ho L. C., Impey C. D., Rix H.-W., 2002, *AJ*, 124, 266  
—, 2010a, *AJ*, 139, 2097  
Peng Y.-j. et al., 2010b, *ApJ*, 721, 193  
Percival W. J. et al., 2001, *MNRAS*, 327, 1297  
Pérez-Martínez J. M., Ziegler B., Dannerbauer H., Böhm A., Verdugo M., Díaz A. I., Hoyos C., 2021, *A&A*, 646, A53

- Perlmutter S., Turner M. S., White M., 1999, *Phys. Rev. Lett.*, 83, 670
- Péroux C., McMahon R. G., Storré-Lombardi L. J., Irwin M. J., 2003, *MNRAS*, 346, 1103
- Persic M., Salucci P., Stel F., 1996, *MNRAS*, 281, 27
- Pisano D. J., Barnes D. G., Staveley-Smith L., Gibson B. K., Kilborn V. A., Freeman K. C., 2011, *ApJS*, 197, 28
- Poggianti B. M. et al., 2017, *ApJ*, 844, 48
- Poggianti B. M., Smail I., Dressler A., Couch W. J., Barger A. J., Butcher H., Ellis R. S., Oemler, Jr. A., 1999, *ApJ*, 518, 576
- Poggianti B. M., van Gorkom J. H., 2001, in *Astronomical Society of the Pacific Conference Series*, Vol. 240, *Gas and Galaxy Evolution*, Hibbard J. E., Rupen M., van Gorkom J. H., eds., p. 599
- Poggianti B. M. et al., 2006, *ApJ*, 642, 188
- Ponomareva A. A. et al., 2021, *MNRAS*, 508, 1195
- Ponomareva A. A., Verheijen M. A. W., Bosma A., 2016, *MNRAS*, 463, 4052
- Ponomareva A. A., Verheijen M. A. W., Papastergis E., Bosma A., Peletier R. F., 2018, *MNRAS*, 474, 4366
- Ponomareva A. A., Verheijen M. A. W., Peletier R. F., Bosma A., 2017, *MNRAS*, 469, 2387
- Popping G., Somerville R. S., Trager S. C., 2014, *MNRAS*, 442, 2398
- Power C., Baugh C. M., Lacey C. G., 2010, *MNRAS*, 406, 43
- Press W. H., Schechter P., 1974, *ApJ*, 193, 437
- Prochaska J. X., Herbert-Fort S., Wolfe A. M., 2005, *ApJ*, 635, 123
- Puech M. et al., 2008, *A&A*, 484, 173
- Ramatsoku M. et al., 2016, *MNRAS*, 460, 923
- Rao S. M., Turnshek D. A., Sardane G. M., Monier E. M., 2017, *MNRAS*, 471, 3428
- Rengelink R. B., Tang Y., de Bruyn A. G., Miley G. K., Bremer M. N., Roettgering H. J. A., Bremer M. A. R., 1997, *A&AS*, 124, 259
- Rhee J., Lah P., Briggs F. H., Chengalur J. N., Colless M., Willner S. P., Ashby M. L. N., Le Fèvre O., 2018, *MNRAS*, 473, 1879
- Rhee J., Lah P., Chengalur J. N., Briggs F. H., Colless M., 2016, *MNRAS*, 460, 2675
- Rhee J., Zwaan M. A., Briggs F. H., Chengalur J. N., Lah P., Oosterloo T., van der Hulst T., 2013, *MNRAS*, 435, 2693
- Rhee M. H., 1996, PhD thesis, -
- Riess A. G. et al., 1998, *AJ*, 116, 1009
- Rix H.-W., Guhathakurta P., Colless M., Ing K., 1997, *MNRAS*, 285, 779
- Rojas R. R., Vogeley M. S., Hoyle F., Brinkmann J., 2004, *ApJ*, 617, 50
- , 2005, *ApJ*, 624, 571
- Rosenberg J. L., Schneider S. E., 2002, *ApJ*, 567, 247
- Rubin V. C., Burstein D., Thonnard N., 1980, *ApJ*, 242, L149
- Sadler E. M. et al., 2020, *MNRAS*, 499, 4293
- Saintonge A. et al., 2011, *MNRAS*, 415, 61
- Saintonge A., Tran K.-V. H., Holden B. P., 2008, *ApJ*, 685, L113
- Sancisi R., Fraternali F., Oosterloo T., van der Hulst T., 2008, *A&A Rev.*, 15, 189
- Schaye J. et al., 2015, *MNRAS*, 446, 521
- Schechter P., 1976, *ApJ*, 203, 297
- Schlegel D. J., Finkbeiner D. P., Davis M., 1998, *ApJ*, 500, 525
- Schmidt M., 1959, *ApJ*, 129, 243
- Schombert J., McGaugh S., Lelli F., 2020, *AJ*, 160, 71

- 
- Schoniger F., Sofue Y., 1994, *A&A*, 283, 21
- Serra P. et al., 2015, *MNRAS*, 448, 1922
- Simard L., Pritchett C. J., 1998, *ApJ*, 505, 96
- Smette A., Claeskens J.-F., Surdej J., 1997, *New Astronomy*, 2, 53
- Smith G. P., Kneib J.-P., Smail I., Mazzotta P., Ebeling H., Czoske O., 2005, *MNRAS*, 359, 417
- Smith R., Davies J. I., Nelson A. H., 2010, *MNRAS*, 405, 1723
- Solanes J. M., Manrique A., García-Gómez C., González-Casado G., Giovanelli R., Haynes M. P., 2001, *ApJ*, 548, 97
- Somerville R. S., Davé R., 2015, *ARA&A*, 53, 51
- Spekkens K., Giovanelli R., 2006, *AJ*, 132, 1426
- Spergel D. N. et al., 2003, *ApJS*, 148, 175
- Springel V., Frenk C. S., White S. D. M., 2006, *Nature*, 440, 1137
- Springob C. M., Haynes M. P., Giovanelli R., 2005, *ApJ*, 621, 215
- Suginohara T., Suto Y., 1991, *PASJ*, 43, L17
- Swaters R. A., van Albada T. S., van der Hulst J. M., Sancisi R., 2002, *A&A*, 390, 829
- Tacconi L. J. et al., 2018, *ApJ*, 853, 179
- Terlouw J. P., Vogelaar M. G. R., 2016, *Kapteyn Package: Tools for developing astronomical applications*
- Tiley A. L. et al., 2016, *MNRAS*, 460, 103
- Tody D., 1986, in *Society of Photo-Optical Instrumentation Engineers (SPIE) Conference Series*, Vol. 627, *Instrumentation in astronomy VI*, Crawford D. L., ed., p. 733
- Tonnesen S., Bryan G. L., 2009, *ApJ*, 694, 789
- Tonnesen S., Bryan G. L., van Gorkom J. H., 2007, *ApJ*, 671, 1434
- Toomre A., Toomre J., 1972, *ApJ*, 178, 623
- Topal S., Bureau M., Tiley A. L., Davis T. A., Torii K., 2018, *MNRAS*, 479, 3319
- Tran K.-V. H., Simard L., Illingworth G., Franx M., 2003, *ApJ*, 590, 238
- Tran K.-V. H., van Dokkum P., Illingworth G. D., Kelson D., Gonzalez A., Franx M., 2005, *ApJ*, 619, 134
- Trenti M., Stiavelli M., 2008, *ApJ*, 676, 767
- Trujillo-Gomez S., Klypin A., Primack J., Romanowsky A. J., 2011, *ApJ*, 742, 16
- Tully R. B. et al., 2013, *AJ*, 146, 86
- Tully R. B., Courtois H. M., Sorce J. G., 2016, *AJ*, 152, 50
- Tully R. B., Fisher J. R., 1977, *A&A*, 54, 661
- Tully R. B., Fouque P., 1985, *ApJS*, 58, 67
- Tully R. B., Pierce M. J., 2000, *ApJ*, 533, 744
- Tully R. B., Pierce M. J., Huang J.-S., Saunders W., Verheijen M. A. W., Witchalls P. L., 1998, *AJ*, 115, 2264
- Tully R. B., Rizzi L., Shaya E. J., Courtois H. M., Makarov D. I., Jacobs B. A., 2009, *AJ*, 138, 323
- Tully R. B., Verheijen M. A. W., Pierce M. J., Huang J.-S., Wainscoat R. J., 1996, *AJ*, 112, 2471
- Tutui Y., Sofue Y., 1997, *A&A*, 326, 915
- Tutui Y., Sofue Y., Honma M., Ichikawa T., Wakamatsu K.-i., 2001, *PASJ*, 53, 701
- Urquhart S. A., Willis J. P., Hoekstra H., Pierre M., 2010, *MNRAS*, 406, 368
- van der Hulst J. M., Terlouw J. P., Begeman K. G., Zwitser W., Roelofsema P. R., 1992, in *Astronomical Society of the Pacific Conference Series*, Vol. 25, *Astronomical Data Analysis Software and Systems I*, Worrall D. M., Biemesderfer C., Barnes J.,

- eds., p. 131
- van Dokkum P. G., Franx M., Fabricant D., Illingworth G. D., Kelson D. D., 2000, *ApJ*, 541, 95
- van Eymeren J., Jütte E., Jog C. J., Stein Y., Dettmar R. J., 2011, *A&A*, 530, A29
- Verheijen M., van Gorkom J. H., Szomoru A., Dwarakanath K. S., Poggianti B. M., Schiminovich D., 2007, *ApJ*, 668, L9
- Verheijen M. A. W., 1997, PhD thesis, -
- Verheijen M. A. W., 2001, *ApJ*, 563, 694
- Verheijen M. A. W., Sancisi R., 2001, *A&A*, 370, 765
- Vogelsberger M. et al., 2014, *MNRAS*, 444, 1518
- Voges W. et al., 1999, *A&A*, 349, 389
- Vogt N. P., Haynes M. P., Giovanelli R., Herter T., 2004, *AJ*, 127, 3325
- Vogt N. P. et al., 1997, *ApJ*, 479, L121
- Vollmer B., 2003, *A&A*, 398, 525
- Vulcani B. et al., 2018, *MNRAS*, 480, 3152
- Walter F. et al., 2020, *ApJ*, 902, 111
- Wang J., Koribalski B. S., Serra P., van der Hulst T., Roychowdhury S., Kamphuis P., Chengalur J. N., 2016, *MNRAS*, 460, 2143
- Weiner B. J. et al., 2006, *ApJ*, 653, 1049
- Westmeier T. et al., 2017, *MNRAS*, 472, 4832
- Wetzel A. R., Tinker J. L., Conroy C., van den Bosch F. C., 2013, *MNRAS*, 432, 336
- White S. D. M., 1978, *MNRAS*, 184, 185
- Williams B. A., 1981, PhD thesis, UNIVERSITY OF MARYLAND COLLEGE PARK.
- Williams M. J., Bureau M., Cappellari M., 2010, *MNRAS*, 409, 1330
- Xi H., Staveley-Smith L., For B.-Q., Freudling W., Zwaan M., Hoppmann L., Liang F.-H., Peng B., 2021, *MNRAS*, 501, 4550
- Yoon H., Chung A., Sengupta C., Wong O. I., Bureau M., Rey S.-C., van Gorkom J. H., 2015, *Publication of Korean Astronomical Society*, 30, 495
- Yoon H., Chung A., Smith R., Jaffé Y. L., 2017, *ApJ*, 838, 81
- York D. G. et al., 2000, *AJ*, 120, 1579
- Zabludoff A. I., Zaritsky D., Lin H., Tucker D., Hashimoto Y., Shectman S. A., Oemler A., Kirshner R. P., 1996, *ApJ*, 466, 104
- Zafar T., Péroux C., Popping A., Milliard B., Deharveng J. M., Frank S., 2013, *A&A*, 556, A141
- Zibetti S., Charlot S., Rix H.-W., 2009, *MNRAS*, 400, 1181
- Ziegler B. L. et al., 2002, *ApJ*, 564, L69
- Ziegler B. L., Böhm A., Jäger K., Heidt J., Möllenhoff C., 2003, *ApJ*, 598, L87
- Zwaan M. A., Briggs F. H., Sprayberry D., Sorar E., 1997, *ApJ*, 490, 173
- Zwaan M. A., Meyer M. J., Staveley-Smith L., Webster R. L., 2005, *MNRAS*, 359, L30
- Zwaan M. A. et al., 2003, *AJ*, 125, 2842
- Zwart J. et al., 2015, in *Advancing Astrophysics with the Square Kilometre Array (AASKA14)*, p. 172



## Acknowledgments

Finally, the most important chapter is here at last. Because this journey means little without the involvement of all of you, dear colleagues, friends and family. Many years from now, looking back, I will recall fondly how a beautiful little country called the Netherlands became my second home, where I lived amongst wonderful people and experienced the greatest emotions. I write this section amidst a whirlwind of memories, and it has all begun to feel almost surreal.

**Marc**, I don't know where to begin. I still remember how keen I was to join your group after my interview at Kapteyn. The moment I received your offer letter, I didn't think twice before accepting, packed my bags and came to the Netherlands. Despite all the eventual roadblocks that became a part of my journey, I am extremely grateful for this opportunity. You opened up the wonders of the HI universe to me, and taught me all I needed to come this far. Your keen attention to detail never fails to amaze me. **Marti**, thank you for all the warmth and affection, the lovely dinners, numerous plants and cheerful conversations. You both helped me feel at home, so far away from home. My deep gratitude to you both also for helping me with the Dutch translation of my summary.

**Thijs**, when I first arrived, everyone said you are the nicest astronomer in the world. Over the course of my PhD, I had the pleasure of experiencing this for myself, and I agree wholeheartedly! As my co-promoter, you provided me with several insights and encouragement when I was lost. I was greatly benefited by your promptness at answering my questions and giving me feedback. You were a source of great support for me when times were difficult. Thank you for everything.

To my reading committee members: **Tom, Andrew** and **DJ** - thank you for being a part of this thesis and for providing your time and valuable inputs to help improve this thesis.

To **Lucia** and our dear secretaries - **Christa, Martine, Ramona, Maria**: I have thoroughly enjoyed our little chats in the coffee corner and the corridors over the years. Thank you all for being so awesome and affectionate, and for making the institute a comfortable second home for all of us.

**Inga, Eline, Scott, Leon, Lucia, Dr Flach**, the secretaries and **Marco** from the ISD: my

sincere gratitude to you all for helping me tide through difficult times during the second half of my PhD. A special thanks to **Dr Flach**, because I genuinely believe I wouldn't be where I am today without your timely intervention and huge support.

I'd also like to thank the computer group (**Martin**, **Leon** (Doddema) and **Eite**), who were always available and prompt in any help or action required on technical matters. A special thanks to **Martin** for all the help when I (often) struggled with GIPSY and related python wrappers. To all the staff members (including those mentioned earlier): **Amina**, **Andrey**, **Bob**, **Edwin**, **Else**, **Filippo**, **Floris**, **Harish**, **Karina**, **Lingyu**, **Manuela**, **Mariano**, **Peter**, **Pratika**, **Raffaella**, **Renzo**, **Reynier**, **Rien** and all the rest, thank you all for making the institute a place to be proud of. A special mention goes to our dear **Huug**; the institute is not the same without you. All those interactions with you will forever be cherished by me.

To my officemates from Room 258: **Dorota**, **Bharat** and **Jaco** - in those early days at the institute when everything was new, I felt totally at ease because of your warmth and willingness to help. I am truly grateful. You guys were done with your PhDs long before me and I hope you are doing well wherever you are now.

And my officemates from Room 185: **Olmo**, **Sara**, **Cristiana**, **Niels**: guys, it's been such an amazing ride with you! I'm so happy to have been a part of this office. Niels, I wish I saw you more often. I hope you are doing well. Cristiana - your discipline and your way of working was always very inspirational. You also managed to magically bring order to our otherwise chaotic office. I miss all those fun chats with you and **Davide**. Olmo and Sara: my friends, it has been an absolute pleasure working alongside you guys. Thank you for lending your ears when I needed to rant sometimes. Thanks also for putting up with my many plants in the office and keeping them alive when I was not around. To the new members of the office, **Bram**, **Areli** and **Christopher**: enjoy the wonderful office and good luck with your theses!

Thanks to all the Hi group members: **Anastasia**, **Anqi**, **Danielle**, **Davide** (Punzo), **Filippo** (Maccagni), **Julia**, **Jordan**, **Kelley**, **Kyle**, **Marc**, **Manolis**, **Mpati**, **Nadine** (Guise, Henk), **Nikki**, **Peter**, **Pooja**, **Sarrvesh**, **Suma**, **Thijs**, **Tirna**, **Toli** as well as my collaborators: **Yara**, **Bianca** and **Jacqueline**. It has been fantastic to be a part of this group and have all of you share your knowledge and expertise with me. **Kyle** and **Danielle**: you were just such awesome support systems for me and the others in the group. I really missed having you around towards the end. **Kelley** and **Manolis** - it is a pity that we did not work more closely together, but it has been a pleasure to know you both. **Anastasia** - I am grateful for all your help, especially in the first year of my PhD. **Julia**, it's been a pleasure to know you and work with you. My visit to Cape Town was one of my most memorable trips, all thanks to you!

**Pooja**, my fellow Mumbaikar. How awesome is it that we've been together since our masters, and that we get to remain colleagues at Rabobank! Your composed and calming presence throughout my PhD was really helpful. Our conversations in Marathi made me feel a little closer to home. **Tirna**, we've had great times together, though we could have done so much more if not for my long absences. It was wonderful knowing you and I wish you the best. Thank **you both** for your love and optimism. It felt as though I had two scientific siblings who knew and understood me and my PhD odyssey.

**Punya**, you were my first friend in Groningen. You made those initial cold, wintry days warmer and brighter, and I have thoroughly enjoyed all the time I spent with you and **Suraj** over the years. Every time you resurface after your regular disappearances, I find myself more and more captivated by your new experiences and stories! You are truly an inspiration. I feel

your constant love and encouragement, no matter where you are or how long it has been since we last met.

**Elaheh**, you continue to be a big part of my life and such a great support system at Rabo. I am so lucky! In you, I have a steadfast friend and mentor, especially during the last several extremely challenging months when I was living two lives: that of a PhD student and a model validator. Thank you for all the warmth!

**Katya**, thanks for all the warm hugs and the lovely company! **Pranav** - those initial months after your arrival here were so much fun! Though I missed out on a lot thereafter, *picture abhi baki hai mere dost*. **Pavel**, though we didn't meet often enough, seeing you always brightened my day! **Umit, Seyda and Samira**, thanks for the heavenly teas and the warm chats! To all the other Kapteyners: **Alessandro, Andrea, Andrés, Anne, Antonino, Crecenzo, Daniel** (Montofré), **Enrico, Florent, Francesco, Georg, Giulio, Hannah, Helmer, Hyoyin, Jack, Jonas, Jorrit, Kevin, Kostas, Kirill, Kristiina, Laura, Laurent, Lorenzo, Marisa, Nelvy, Nika, Pandeyji (and family), Robin, Ruslan, Simon, Smaran, Tadeja, Teymoor, Valentina, Yanan, Yuner, Zheng** (and anyone else I may have missed): you made my time here so much fun, thank you! Each and every one of you was a significant part of my journey and I have really enjoyed our interactions.

To all my new friends and colleagues at Rabobank, especially **Pieter, Christian, Maurits** and **Elisa**: despite hardly ever meeting in person due to the pandemic, I was able to discover another world filled with great people like you, and it has made my transition outside academia so much more pleasant. Thanks for all your support in the last several months.

**Lucie** (and **Thomas**), **Jelle** (and **Aziza**), **Dhanya** (and **Dnyaneshwar**): I loved connecting with you all and I look forward to making more fond memories and reliving the fun times we have had. **Manu**, we've been through it all, haven't we? Thanks for being there for me during those early times. My journey here would be incomplete without you. **Nikki**, my half-Indian friend, I feel so lucky to know you and **Musty!** Thank you for the shower of love and encouragement over the years.

**Suma**, I never imagined I'd be lucky enough to find a rock-solid friendship such as yours at the institute. I won't embarrass you with a huge list of things that I admire about you. I'll never forget those late nights and weekends (often with Apu) at the institute when we were (not) working, all the laughter, the endless chit-chats, all the food we cooked/shared and all the songs we sang together. Even when we didn't meet much towards the end of our PhDs, I still felt your constant presence. You've been there for me no matter what, and I can't imagine having made this journey without you.

**Apu**, Apu, Apu. What can I say? While I'm sorry that you had that terrible bike accident, I'm not at all sorry for whatever followed. I'm glad I was the person on your speed dial. After that, you became such a BIG part of my life, it is absolutely insane. Your fake tooth, the penguin mode, the karaokes, the long walks and Thai dinners stand out in the sea of other events we've seen together. How you magically were a part of every special moment in the last four years baffles me. While remembering all these beautiful times, my only hope is that this amazingly crazy roller coaster ride with you never ends.

And to both of you (**Suma and Apu**) together - our sisterhood means the world to me. Thank you for the colossal love and care over all these years. I also forgive you for destroying 'Tyachi dhuna' and changing it perhaps forever.

**Diego**, thanks for all the tips you gave me before I started my PhD. It was really nice to catch

up with you those few times you visited in Groningen.

**Prof. Boksenberg**, I met you in the unlikeliest of circumstances, and you have been my biggest inspiration. You always encouraged me to dream big, and it was only through you that I actually began realising that dreams don't have to stay dreams. I eagerly await another opportunity to meet you again and relive one of the most memorable days of my life, visiting you at the Royal Astronomical Society and talking about your experiences and adventures.

My friends from back home: **Jay, Harshal, Narendra, Karishma, Debayan, Chaitanya, Prachi, Bhakti, Vijay, Yogesh, Markar**: we seldom met since I moved to the Netherlands, but you still managed to be such significant parts of my life nonetheless! I hope we can make up for lost time soon. **Shri**, my partner-in-crime, I have missed you terribly, and yet I have always felt your presence. It has been painfully long since we met, and that just won't do! I can't wait to make new memories with you again, hopefully more often from now on. **Akhila**, so much has changed since we last met 6 years ago, but you continue to remain one of my most favourite people. I miss you and hope we meet again soon.

To my teachers from school, professors from Bhavans and UDP (Kalina) and my project supervisors at CBS and TIFR: I wasn't always the easiest student to deal with, and you all have played a big part in helping me come this far. Thank you for everything. **Gandhi ma'am**, a special thanks to you for backing me during my PhD applications.

My sincere gratitude to my extended family and family friends, for your constant thoughts and good wishes. To my **future in-laws**: I am lucky to have found a second family that has been nothing but affectionate and encouraging of my endeavours. I am deeply grateful. **PK uncle**, I wish so much that you were around to see this day but I will always carry your blessings and wishes with me.

To my **mom, dad**, my brother **Aditya** and my **grandparents**: There are no words to express how great your support has been. You have been my biggest cheerleaders and pillars of strength, giving me all the love and backing I needed to see this PhD through. Thank you. My love for you all is infinite.

Finally, none of this would have even been possible without the unwavering love and support of my fiancé and best friend, **Harsh**. Despite being thousands of miles apart for what felt like an eternity, your presence has been the strongest. You walked with me every step of the way, gently helping me find my bearings when I felt lost. With the end of this chapter, I look forward to the beginning of a new one, with you. Thank you for everything with all my heart.

To my spiritual masters, my deepest gratitude for all your wisdom and teachings.